Transactions of the ASME®

Technical Editor, **T. H. OKIISHI (2003)**
Associate Technical Editors
Aeromechanical Interaction
R. E. KIELB (1999)
Gas Turbine (Review Chair)
D. C. WISLER (1999)
Heat Transfer
M. G. DUNN (1999)
N. NIRMALEN (2000)
Turbomachinery
A. STRAZISAR (2000)

BOARD ON COMMUNICATIONS
Chairman and Vice-President
R. K. SHAH

OFFICERS OF THE ASME
President, **W. M. PHILLIPS**
Executive Director, **D. L. BELDEN**
Treasurer, **J. A. MASON**

PUBLISHING STAFF
Managing Director, Engineering
CHARLES W. BEARDSLEY
Director, Technical Publishing
PHILIP DI VIETRO
Managing Editor, Technical Publishing
CYNTHIA B. CLARK
Managing Editor, Transactions
CORNELIA MONAHAN
Production Coordinator
VALERIE WINTERS
Production Assistant
MARISOL ANDINO

Transactions of the ASME, Journal of Turbomachinery (ISSN 0889-504X) is published quarterly (Jan., Apr., July, Oct.) for $205.00 per year by The American Society of Mechanical Engineers, Three Park Avenue, New York, NY 10016. Periodicals postage paid at New York, NY and additional mailing offices. POSTMASTER: Send address changes to Transactions of the ASME, Journal of Turbomachinery, c/o THE AMERICAN SOCIETY OF MECHANICAL ENGINEERS, 22 Law Drive, Box 2300. Fairfield, NJ 07007-2300.
CHANGES OF ADDRESS must be received at Society headquarters seven weeks before they are to be effective. Please send old label and new address.
PRICES: To members, $40.00, annually; to nonmembers, $205.00.
To countries outside the United States and Canada, add $40.00 for surface postage and $60.00 for airmail postage.
STATEMENT from By-Laws. The Society shall not be responsible for statements or opinions advanced in papers or . . . printed in its publications (B7.1, Par. 3).

INDEXED by Applied Mechanics Reviews and Engineering Information, Inc.
Canadian Goods & Services Tax Registration #126148048

Journal of Turbomachinery

Published Quarterly by The American Society of Mechanical Engineers

VOLUME 121 • NUMBER 1 • JANUARY 1999

TECHNICAL PAPERS

(Contents continued on p. 10)

This journal is printed on acid-free paper, which exceeds the ANSI Z39.48-1992 specification for permanence of paper and library materials.♾™

♻ 85% recycled content, including 10% post-consumer fibers.

(Contents continued)

ANNOUNCEMENTS

R. Emunds
ABB Corporate Research Ltd.,
Baden, Switzerland

I. K. Jennions
ABB Power Generation Ltd.,
Baden, Switzerland

D. Bohn

J. Gier

Institute of Steam- and Gasturbines,
RWTH Aachen,
Aachen, Federal Republic of Germany

The Computation of Adjacent Blade-Row Effects in a 1.5-Stage Axial Flow Turbine

This paper deals with the numerical simulation of flow through a 1.5-stage axial flow turbine. The three-row configuration has been experimentally investigated at the University of Aachen where measurements behind the first vane, the first stage, and the full configuration were taken. These measurements allow single blade row computations, to the measured boundary conditions taken from complete engine experiments, or full multistage simulations. The results are openly available inside the framework of ERCOFTAC 1996. There are two separate but interrelated parts to the paper. First, two significantly different Navier–Stokes codes are used to predict the flow around the first vane and the first rotor, both running in isolation. This is used to engender confidence in the code that is subsequently used to model the multiple blade-row tests; the other code is currently only suitable for a single blade row. Second, the 1.5-stage results are compared to the experimental data and promote discussion of surrounding blade row effects on multistage solutions.

Introduction

Three-dimensional steady-state flow solvers are becoming more and more used inside the industrial design process for turbines as well as for compressors. This is because during the last decade an enormous effort has been invested in the development of stable and fast-running algorithms for solving the governing equations for compressible fluid flow problems. Additional to this development, the power of computers has also increased tremendously. Therefore, turbomachinery designers are now able to calculate complex geometries with reasonable resolution of the flow domain and physically difficult and interesting flow phenomena can be studied by using numerical simulations, e.g., the influence of the tip leakage flow on the flow through a transonic compressor rotor (Chima, 1996). Moreover, a designer is no longer restricted to an isolated blade row analysis when using three-dimensional algorithms. Instead it is possible to consider multiple-blade row configurations to take into account the influence of adjacent blade rows due to wake, shock, and potential interactions (Jennions and Adamczyk, 1995).

The present paper considers results from computation of the flow through a 1.5-stage axial flow turbine. The computations are carried out for isolated blade rows, for a single-stage configuration as well as for the complete 1.5-stage build. All results obtained from the simulations are compared to experimental data (gained from the 1.5-stage build), being provided within the framework of ERCOFTAC 1996, which is becoming a standard test case for computational methods. Additional experimental results, like secondary flow structures, are given in Gallus et al. (1994). Unfortunately within all these experimental studies no surface profile pressure distributions were taken. Experimental results are only available in a crossflow plane located downstream of the trailing edge of each blade row.

To gain confidence in the numerical code used for the multiple-blade row computations, the results obtained for the isolated first vane and the isolated first rotor calculation were compared to those obtained from another, numerically significantly different scheme. Both numerical algorithms have been applied successfully to various turbomachinery applications in the past (Bohn and Emunds, 1995; Dawes, 1992).

Experimental Setup

The experiment was carried out in the 1.5-stage axial turbine shown in Fig. 1. For both stators a Traupel profile and for the rotor a modified VKI-profile is used. All blades are untwisted.

A cross section of the 1.5-stage turbine with midspan velocity triangles is shown in Fig. 2. The basic parameters of the turbine are given in Table 1. In the open literature the cross section of the turbine is always given according to Fig. 2 but the profile geometry data provided from the ERCOFTAC framework are mirrored with respect to the circumferential direction, i.e., the first vane turns the flow from the axial direction towards the top of the page. It is this mirrored geometry that has been computed and discussed in this paper.

The experimental results were gathered 8.8 mm downstream of the trailing edge of each blade row using three-hole and five-hole pressure probes and thermocouples. The five-hole probes were installed between 10 and 90 percent span, which leads to a gap at hub and casing of 5 mm that cannot be resolved due to the probe's thickness of 0.9 mm. In the hub and casing region, i.e., below 10 percent span and above 90 percent span respectively, three-hole probes were used. These three-hole probes might still have some impact on the measured flow values in these regions due to blockage effects.

In the test rig the probes were traversed radially and circumferentially within what is known as a transfer unit. This is an independent unit that contains the traversing gear and guarantees very precise positioning. For each set of flow measurements, the transfer unit was installed in one axial location and measurements taken. The test rig was then shut down and the transfer unit moved to the next axial location (see Fig. 3).

Due to the different ambient conditions on different measuring days, the measurements contain a variation in the reference total pressure and total temperature. Unfortunately, the given experimental data were not corrected to standard conditions. For the computations this problem was solved by taking the dimensionless values for total pressure and total temperature at the inlet boundary of the computational domain and the dimensionless static pressure at the domain exit. Dimensional values for the inlet and exit boundary conditions are then achieved by

Contributed by the International Gas Turbine Institute and presented at the 42nd International Gas Turbine and Aeroengine Congress and Exhibition, Orlando, Florida, June 2–5, 1997. Manuscript received International Gas Turbine Institute February 1997. Paper No. 97-GT-81. Associate Technical Editor: H. A. Kidd.

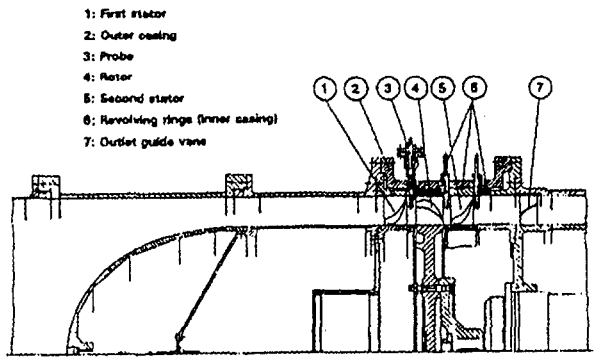

Fig. 1 Turbine test facility

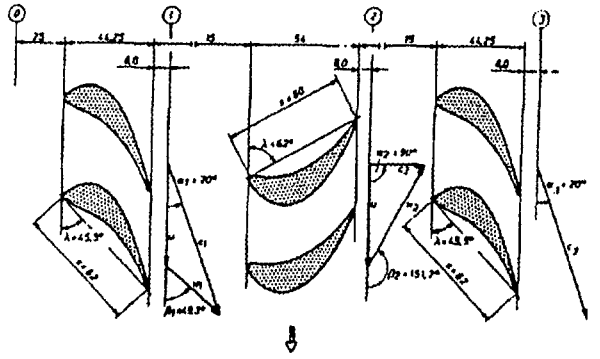

Fig. 2 Turbine geometry and midspan velocity triangles

multiplying the dimensionless values by the reference values given from the experiment in the appropriate inlet cross-flow plane. To be able to compare the multiple-blade row computations with the experimental data, the measured distribution of pressures and temperatures downstream of the rotor and the second vane are corrected to the respective total inlet conditions. For the single rotor and the isolated second vane computation, the nondimensional experimental data were corrected with the total inlet conditions of the considered blade row.

Due to the large number of different circumferentially mass-averaged quantities given from the ERCOFTAC framework downstream of each blade row, only some representative distributions according to the frame of reference for each blade will be shown within this paper. The positions where the solutions will be compared are given in Fig. 3.

Numerical Algorithms

Industrial Numerical Algorithm (Stage 3D). The industrial code was developed from Dawes' structured multiple-blade row Navier–Stokes solver (Dawes, 1992). In the current version of the code, the Reynolds-averaged thin-layer Navier–Stokes equations are solved within a cylindrical coordinate system and relative cylindrical velocity components. To close the system of equations, the ideal gas equation is used for perfect

Table 1 Basic turbine parameters

	Vane 1	Rotor	Vane 2
aspect ratio	0.887	0.917	0.887
pitch (midspan)	47.6 mm	41.8 mm	47.6 mm
rotational speed	-	3500 rpm	-
hub diameter	490 mm	490 mm	490 mm
tip diameter	600 mm	600 mm	600 mm
blade number	36	41	36

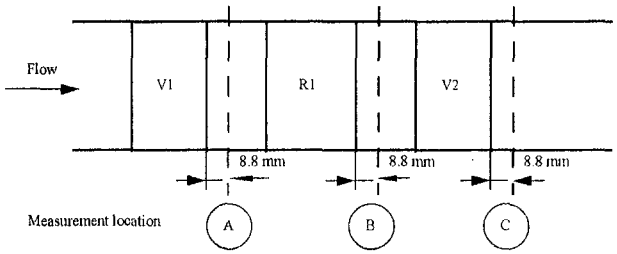

Fig. 3 Position of measurement locations in rig

gas calculations. Turbulence is accounted for by using the algebraic turbulence model of Baldwin and Lomax (1978).

A finite volume scheme is used for spatial discretization. The discretized equations are marched forward in time to a steady state using an explicit, multistep Runge–Kutta scheme. The inviscid fluxes as well as the diffusive fluxes are approximated by central differences. Thus some numerical smoothing is needed to avoid odd–even decoupling. Smoothing is also needed in flow regions containing strong gradients in pressure. Both smoothing tasks are fulfilled by a blend of second and fourth-order smoothing. Different artificial smoothing schemes are available in the code, all being derived from Jameson et al. (1981) and Alonso et al. (1995). Convergence is accelerated by the use of local time-stepping and residual averaging. Furthermore, the wall clock time required for multiple-blade row computations is reduced by the capability to run the code in parallel by using pvm on a blade row by blade row basis. Boundary conditions are specified inside dummy cells upstream and downstream of the numerical domain. The accuracy of Stage3D is similar to the accuracy of Dawes' original BTOB3D for single blade row considerations.

Multiple-blade row computations are carried out by using an interface plane approach to transfer the flow information between adjacent blade rows. For multiple-blade row computations many different interface plane treatments are available in the code but only one is used for the current computations.

One of the main problems in using an interface plane approach to connect the flow state within different blade rows is to find suitable averaged values for the governing flow quantities at the interface plane cell faces, which represent the new circumferentially homogeneous inlet or outlet conditions at the upstream or downstream side of the interface plane for the next time step. According to Dzung (1970) it is useful for an inhomogeneous flow to use throughflow quantities, which can be

Nomenclature

A = area, m^2
p = static pressure, N/m^2
ρ = density, kg/m^3
c_p = specific heat at constant pressure, kJ/kg K
I = momentum, kgm/s^2

Subscripts

x, r, θ = derivative in spatial direction

calculated from the following equations for mass, momentum, and energy:

Massflow:

$$\dot{m} = \int_A \rho c_x dA$$

Momentum

$$\dot{I}_n = \int_A \rho c_x^2 dA + \int_A p dA$$

$$\dot{I}_r = \int_A \rho c_x c_r dA$$

$$\dot{I}_\theta = \int_A \rho c_x c_\theta dA$$

Total enthalpy

$$\dot{H} = \int_A \rho c_x \left(c_p T + \frac{c_x^2}{2} + \frac{c_r^2}{2} + \frac{c_\theta^2}{2} \right) dA$$

With these equations and the state equation for perfect gas, the unknown homogenous quantities $\overline{p}$, $\overline{\rho}$, $\overline{c_x}$, $\overline{c_r}$, $\overline{c_\theta}$ can be calculated.

The physical interpretation of this procedure is that an inhomogeneous flow, which is not influenced by any force from outside, will turn into a homogenous flow with a balanced state due to viscous influences. At the same time, that "mixing out of the flow" results in a growth of dissipation and thus in a higher entropy production. This interface plane treatment is used for all multirow solutions shown here.

University Numerical Algorithm (CHTFlow). The university code solves the full Reynolds-averaged compressible Navier–Stokes equations in conservation form for stationary and rotating coordinates employing a structured finite volume approach. In order to handle complex geometries, the code is formulated in curvelinear coordinates and uses a multiblock technique for geometric flexibility, applying two dummy cells at all domain boundaries.

The inviscid fluxes are calculated using a hybrid Godunov-type/Steger–Warming scheme. The Godunov flux difference splitting scheme, coupled with a van Albada switch, computes the fluxes up to third-order accurate with a characteristic approach. This scheme introduces almost no numerical diffusion in the calculation. A strongly diffusive Steger–Warming flux vector splitting scheme is used additionally to avoid oscillations, especially in regions being dominated by inviscid flow phenomena. The influence of this scheme on the solution can be fine-tuned locally inside the computational domain depending on the local flow solution to increase stability in regions of sharp gradients like shocks. Thus it allows for calculations with as small as possible numerical diffusion. Central differencing is employed for the viscous fluxes.

The time-dependent equations are implicitly discretized by a Newton linearization method to allow large CFL numbers (up to 200) in connection with local time stepping. The resulting system of equations is relaxed using a red-black point Gauss–Seidel algorithm, which can be efficiently used on a vector computer. Preconditioning of the flux Jacobians is done to strengthen diagonal dominance of the system.

Different turbulence models are available for turbulence closure. For the predictions shown in this paper the algebraic Baldwin–Lomax model is employed to simplify comparisons with the industrial numerical procedure. A more detailed description of the basic numerical procedure is given by Schmatz (1989).

Results and Discussion

Isolated Vane Analysis. The isolated vane analysis is done by using the two numerical algorithms described above. To avoid the influence of different meshes for the direct comparison of the two codes a straight H-mesh containing (125, 35, 47) grid points in axial, circumferential, and radial direction is used. Both codes account for turbulence effects by the use of the algebraic Baldwin–Lomax model with transition specified at 60 percent axial chord length.

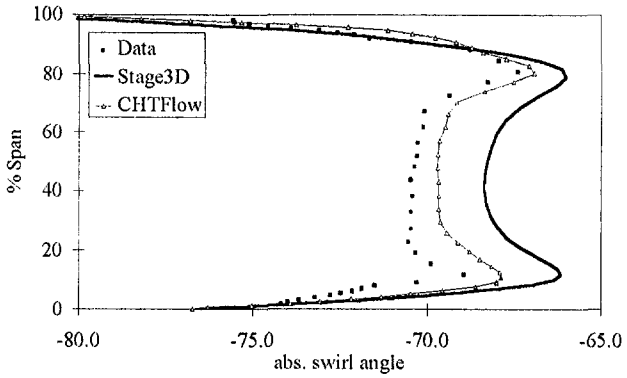

Fig. 4 Absolute swirl angle in plane A

The computations were initially run to the exact inlet boundary conditions given from the ERCOFTAC data with the wall total pressure being reduced to its static value. With this incoming boundary layer profile, no total pressure loss core at plane A downstream of the vane trailing edge was seen, although the overturning due to the two passage vortices was clearly visible within the absolute flow angle distribution.

The reason for this is that the experimentally given distribution of total pressure especially in the near hub region upstream of the vane does not show a boundary layer type profile like the one previously measured (Zeschky, 1991). As this has a major effect on the exit total pressure loss core and as it was thought that the previously measured (Zeschky, 1991) incoming boundary layer was more typical of conditions in the test rig the incoming profile was changed. It was generated from a power law based on the hub static pressure and the free-stream total pressure. The same power law was also applied for the casing boundary layer. The thickness of the inlet hub and casing boundary layer was not changed during this process.

In Fig. 4 the predicted distributions of the mass-averaged swirl angle in plane A are plotted against the experimental data. All positive absolute swirl angles are measured with respect to the axial direction in clockwise direction. Both codes predict the shape of the swirl angle that comes from the two passage vortices. The predicted levels between the two codes are different and both predictions are also different in level to the experimental data with Stage3D giving less turning of the flow than CHTFlow.

Looking at the vane's profile it can be found that the geometric profile metal angle is −70 deg. The experimental distribution indicates that the flow is turned by more than these −70 deg in the bulk region. The reason for this might be a nonsteady separation bubble in the bulk region of the rear suction side ending very close to the vane trailing edge detected in earlier experimental investigations (Zeschky, 1991). This is not detected by either code, both of which exhibit a more standard deviation from the metal angle.

Differences between the two codes are also visible for the spanwise distribution of the circumferentially averaged total pressure distribution in plane A (Fig. 5). For completeness the modified radial inlet profile used for the computations is also shown in this figure.

CHTFlow predicts the total pressure profile across the entire span quite well except inside the region where the casing passage vortex exist (85 percent span). The center of this vortex is predicted too far radially inward. Stage3D underpredicts the

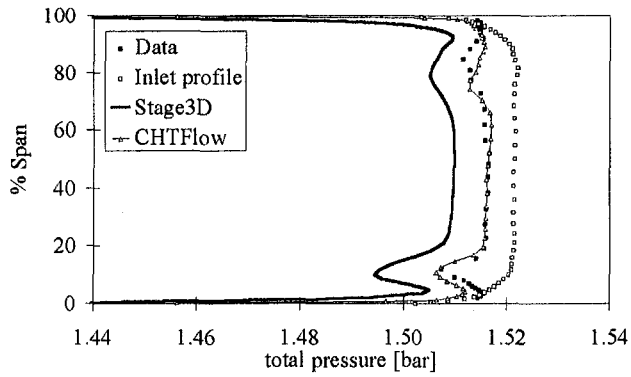

Fig. 5 Total pressure distribution in plane A

total pressure across the entire span due to a small total pressure loss at the leading edge and a larger loss along the vane suction surface. This excess loss is quite uniform across the entire span. Nevertheless Stage3D does predict the overall shape of the total pressure profile quite well including the strong decrease in total pressure when approaching the hub at 10 percent span caused by the presence of the hub passage vortex, which is generated inside the blade channel. This vortex has collected most of the incoming (low total pressure) boundary layer fluid in its core and it leaves behind it good fluid near the hub, hence the peak at 5 percent span, which is well captured by both codes. This collection process has happened before any significant growth of the suction surface boundary layer and hence the suction surface boundary layer loss is added cumulatively to the low total pressure of the vortex. Note that for design purposes it is more important to predict the shape and hence the physics in the total pressure profile than the absolute level. Comparing the predicted circumferentially averaged total temperature profile downstream of the vane, good agreement between the computations and the experimental data was found (not shown).

In Fig. 6, the predicted distribution of total pressure in crossflow plane A from Stage3D is shown. The orientation of Fig. 6 as well as the orientation of all following cross-stream planes is according to the given geometrical orientation of the blade rows, i.e., forward looking aft.

The region of low total pressure fluid near the hub caused by the passage vortex inside the blade channel is clearly visible. Also the wake and the accumulation of low total pressure fluid near the casing region can be seen. The wake is very thick due to the overprediction of the suction surface boundary layer, as already mentioned. Outside of the wake region no change in total pressure is visible in accordance with the data from Zeschky (1991). At the hub and casing thin, low total pressure regions exist. These represent the new endwall boundary layers that build up behind the ones removed by the passage vortex.

The comparison of the two different mass-averaged flow quantities in plane A downstream of the vane trailing edge has shown that CHTFlow does a better job in terms of predicting the level of swirl angle and total pressure than Stage3D, which captures the right shape but not the level of these profiles. The reason for this is thought to be due to the different numerical procedures being used in the two codes. First, the assumption of using the thin-layer approximation inside Stage3D to determine the second-order derivatives is believed to have a significant impact on the underprediction of total pressure. Second, the use of a locally varying sensor to control the amount of artificial diffusion due to the use of a high diffusive Steger–Warming flux vector splitting scheme within CHTFlow seems to be well suited to provide a simulation with as small as possible numerical diffusion. Calculations with very small amount of smoothing have been made with Stage3D but the results seem to be relatively insensitive. Therefore the thin layer approximations are suspected.

Comparing the required CPU time needed to obtain a converged solution, CHTFlow (which was run on a Siemens Fujitsu vector computer VPP 300 to shorten the computational time) takes roughly a factor of 60 times longer than Stage3D when scaling the required CPU time to account for different hardware. The vane calculation with Stage3D took some 13 CPU hours on an IBM workstation. With this, for industrial needs, Stage3D (running on a SP2) becomes an attractive alternative as the major physical features are captured.

Isolated Rotor Analysis. The isolated rotor computations were again carried out using the two numerical algorithms. As for the simulation of the isolated first vane, a straight H-mesh containing (125, 35, 47) gridpoints in axial, circumferential, and radial direction was used for the computations. The tip clearance, which is 0.73 percent of the rotor's blade height, is resolved with three equally spaced grid nodes. To be able to compare the results obtained from the computations, it has to be pointed out that CHTFlow runs only to relative total inlet conditions for rotors while STAGE3D normally runs to absolute inlet conditions. Initially this was not taken into account but the solutions obtained in terms of the predicted level of total pressure downstream of the rotor trailing edge were very different. Further investigation showed that the two simulations were, in fact, run to physically different inlet conditions as can be seen by considering the relationship between the relative total pressure and the absolute total pressure:

$$p_{t,\mathrm{abs}} = p_{t,\mathrm{rel}} \cdot \left(1 + \frac{\gamma - 1}{2} \frac{\Omega^2 r^2 - 2\Omega r v_{\theta,\mathrm{abs}}}{a^2 + \frac{\gamma - 1}{2} v_{\mathrm{abs}}^2} \right)^{-\gamma/(\gamma-1)}$$

It can be seen that for a given relative total pressure the corresponding absolute total pressure depends on the flow solution within the blade passage due to the appearance of the absolute velocity and its circumferential component. Thus, the boundary condition treatment inside STAGE3D was changed for the isolated rotor calculation in order to be able to specify relative total inlet conditions. It should also be noted here that the experimental data were taken in the absolute frame and then, for the rotor, relative conditions were deduced. This leads to a slight uncertainty in the experimental data as comparison to processed rather than fundamental data is being made.

In Fig. 7 the predicted circumferentially averaged relative total pressure distribution at plane B is plotted versus span in comparison to the experimental data.

At first glance the predicted results do not seem to bear much resemblance to the experimental exit data. However, it is first necessary to understand the experimental data before a meaningful comparison can be made. Moving from hub to casing, the experimental data show a number of interesting features. From 8 percent span to 22 percent span the dip in relative total pressure is due to the rotor hub passage vortex. In a similar

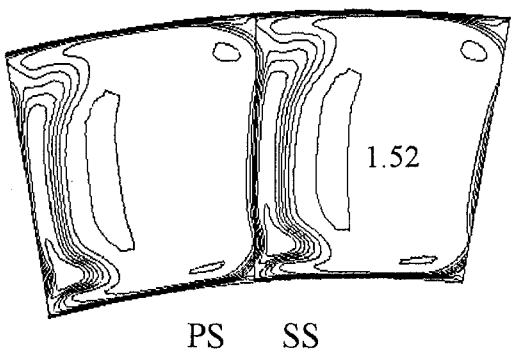

Fig. 6 Total pressure distribution in crossflow plane A (Δ = 0.01 bar, max 1.52 bar)

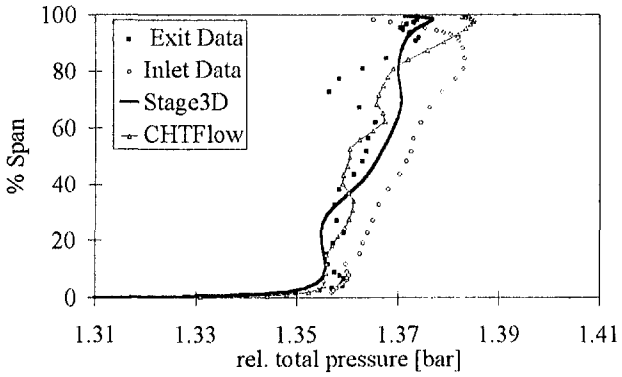

Fig. 7 Relative total pressure in plane B

way to that observed in the vane, the rotor hub passage vortex has taken the incoming endwall flow up the suction surface of the rotor, entraining behind it higher relative total pressure fluid toward the hub. Outboard of this, from 22 to 45 percent span, is the remnants of the vane hub passage vortex. This has moved from a 10 percent span location to a 35 percent span location as it moved through the rotor and has been forced outward by the rotor hub passage vortex. Between 60 and 80 percent span the signature of the vane casing passage vortex that has coalesced with the rotor tip clearance vortex can be clearly seen. Finally, at 95 percent span the rotor casing passage vortex produces a small drop in relative total pressure.

CHTFlow seems to capture the two vortices at the hub. The rotor hub passage vortex, however, does not lead to a very distinct relative total pressure minimum and the vane hub passage vortex seems to have moved too far radially outwards, its center appearing around 45 percent span. Stage3D, on the other hand, has predicted a large and smooth relative total pressure minimum at 30 percent span, which could be interpreted as the loss core of the vane hub passage and the rotor hub passage vortices merging together. The experimental dip in relative total pressure centered at 70 percent span is much more pronounced than either code predicts. CHTFlow shows a trace of the vane casing passage vortex at the same location but the strength is underpredicted. The reduction in relative total pressure between 70 and 95 percent span by Stage3D is a combination of this passage vortex with the tip vortex but again is underpredicted. Neither code appears to have caught the signature of the rotor casing passage vortex.

The distribution of the circumferentially averaged relative swirl angle in plane B (Fig. 8) given from the experiments shows the appearance of the different secondary flow structures downstream of the rotor trailing edge more clearly. This angle is measured clockwise from the axial direction. The rotor hub and casing passage vortices can be clearly identified very close

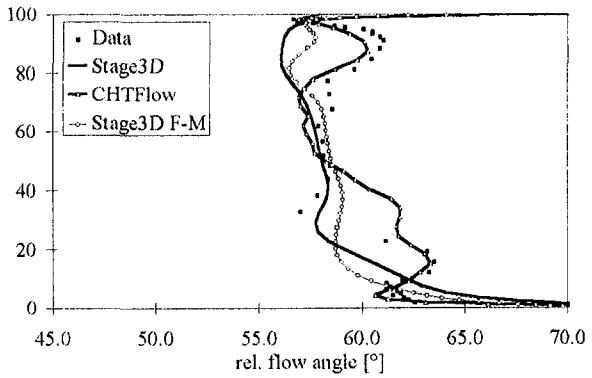

Fig. 8 Relative swirl angle in plane B

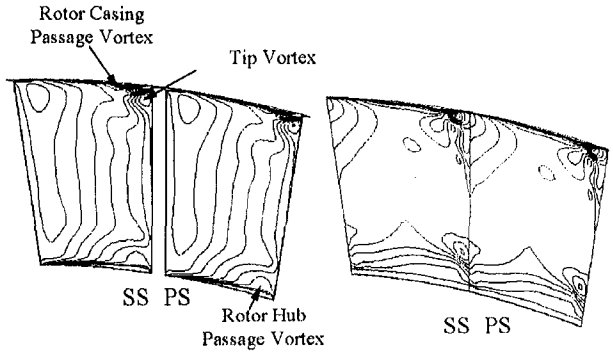

a) cross flow distribution at 90% chord and plane B (maximum 70°, D = 1.8°)

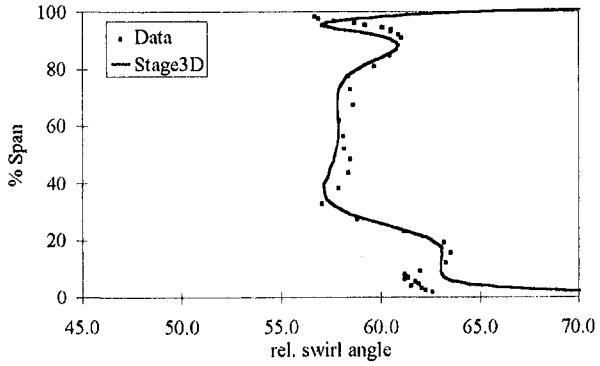

b) spanwise distribution near suction side

Fig. 9(*a*) Crossflow distribution at 90 percent chord and plane B (maximum 70 deg, *D* = 1.8 deg). Fig. 9(*b*) Spanwise distribution near suction side. Fig. 9 Relative flow angle in plane B

to the endwalls. Also the overturning due to the vane hub passage vortex at about 20 percent span is visible. The overturning at about 90 percent span is the signature due to the blade tip vortex and the downstream convected vane casing passage vortex. At about 63 percent span an additional vortex can just be discerned. This vortex was identified by Walraevens and Gallus (1995) as the rotor trailing edge vortex.

CHTFlow shows good agreement across the entire span, except for the vane hub passage vortex region. No explanation is currently known why CHTFlow is able to predicted the relative swirl angle so well compared to the prediction of relative total pressure as shown above. Also no information is currently available regarding the accuracy of the experimental data. With this it would be possible to analyze the sensitivity of the relative total pressure and the relative flow angle to slightly changing flow conditions inside the blade passage. Stage3D misses out most of the secondary flow features, especially the signature from the tip vortex at about 90 percent span. Due to this disagreement between the two codes, Stage3D was rerun on a finer grid containing 47 nodes in circumferential direction and 65 nodes in spanwise direction. The result from that computation is also plotted in Fig. 8. With this mesh, Stage3D starts picking up the shape of the relative flow angle in the near casing region, i.e., the tip vortex and the casing passage vortex. Still, remarkable differences between the results obtained from Stage3D and the experimental data are clearly visible.

The cross-stream swirl angle from Stage3D is shown in Fig. 9(*a*) at two different axial locations. The left picture shows the flow angle distribution at 90 percent axial chord while the right one shows the flow angle distribution at plane B.

From the vortical motion just discussed, we can identify very close to the casing wall the overturning/underturning of the flow due to the casing passage vortex extending from midpitch toward the area influenced by the blade tip vortex and the vane's

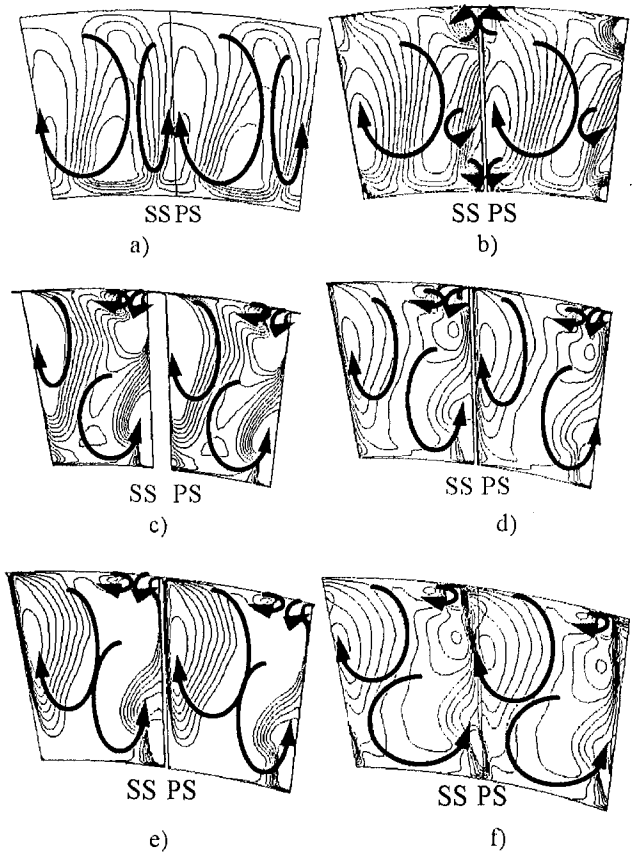

Fig. 10 Spanwise velocity at different locations inside the rotor passage (Stage 3D result)

casing passage vortex joined together. The latter is located very close to the suction surface and inside the computation it is fed with energy from the rotor hub passage vortex, as will be shown later. At the hub the predicted passage vortex can be seen to be stronger than the casing passage vortex. Downstream of the blade trailing edge the breakup of the hub passage vortex can be seen (right picture in Fig. 9(a)) forming a clockwise circulating flow close to the hub. The signature of the combined rotor tip vortex and vane casing passage vortex is also visible but it has become very weak. Thus, this vortex is not spread deep enough inside the blade channel so that its influence gets lost when averaging across the circumference.

Additionally in Fig. 9(b) the radial distribution of the relative total swirl angle at a circumferential location close to the suction surface in plane B is shown. It can be seen from the figure that Stage3D has captured most the flow physics being generated inside the rotor passage and that they are distinguishable. Nevertheless, except for the blade hub passage vortex, the different vortices are underpredicted in strength.

With this in mind it is worthwhile to look at different cross-stream planes showing the distribution of spanwise velocity from Stage3D at different axial locations to obtain a better understanding of the predicted flow features occurring inside the blade passage (Fig. 10). In Fig. 10(a) the distribution of the spanwise velocity is shown in the inlet plane of the computational domain. The distribution represents a combination of the inlet boundary condition and the influence of the blade itself on the inlet plane located 14 percent of axial chord upstream of the leading edge, coinciding with plane A. Two vortical motions of different size within each blade passage are visible. Approaching the blade leading edge (Fig. 10(b)), in the corner of the blade profile and the endwall, horseshoe vortices appear due to the incoming boundary layer profile in total pressure. The clockwise vortical motion observes in the inlet plane is still visible and has extended in the circumferential direction. The smaller counterclockwise rotating vortex is now located close to the blade suction surface radially inward of midspan.

At 90 percent axial chord length (Fig. 10(c)) on the pressure surface outboard of midspan a radially outward directed fluid motion towards the tip exist. Fluid being transported by this motion is partly crossing the blade tip due to the static pressure difference between pressure and suction surfaces. The resulting tip vortex (rotating counterclockwise) close to the blade suction surface can also be seen. At the casing the passage vortex (rotating clockwise) is also captured being closer to the suction side than to the pressure side. At the hub the flow structure due to the hub passage vortex (turning counterclockwise) can be found showing a fluid motion from the pressure side toward the suction side near the endwall. At the suction surface this vortical motion extends to nearly midspan. The vortex is closed by a fluid motion from the suction surface towards the pressure surface radially inward. Figure 10(d) shows the spanwise velocity distribution immediately upstream of the blade trailing edge. At the casing the tip vortex has slightly extended in the circumferential direction, while the casing passage vortex has not changed significantly. At the hub the passage vortex has grown up further. Looking at the predicted fluid motion near the suction side due to the hub passage vortex, it can be found that it is connected with the vortical motion due to the tip vortex, i.e., the computation shows a radially outward directed fluid motion all along the suction surface. This effect is also shown in Fig. 10(e) where only those isolines of spanwise velocity are plotted corresponding to a radially *outward* fluid motion. It can be clearly seen that along the suction surface the fluid is moving toward the casing. Additionally the radial and circumferential extension of the hub passage vortex becomes obvious. This vortex is influencing most of the flow domain in the cross-stream plane located close to the blade trailing edge. This is not in agreement with the secondary flow pattern given by Walraevens and Gallus (1995) showing a much smaller blade hub passage vortex staying near the hub. Finally Fig. 10(f) shows the spanwise velocity distribution in a cross-stream plane located at position B. A significant decrease of the tip vortex is predicted so that this vortex is not really visible anymore. The radially outward direct fluid motion due to the hub passage vortex is still clearly visible. Thus the radial extension of the blade hub passage vortex, especially near the suction surface, is overpredicted yielding, if averaged across the circumference, a large underturning of the flow as shown in Fig. 8. Due to this nonphysical interaction of the hub passage vortex and the combined tip vortex/vane passage vortex, the latter becomes too weak and therefore does not extend deep enough inside the blade passage. Thus the overturning at about 80 percent span due to the tip vortex/vane passage vortex gets underpredicted. Taking this into account, the circumferentially averaged relative flow angle distribution as shown in Fig. 8 from Stage3D can be explained.

Good agreement exists between the calculated and measured distribution of the circumferentially averaged relative total temperature in plane B as shown in Fig. 11. Once again CHTFlow shows more "shape" than Stage3D.

1.5-Stage Analysis

The computation of the complete build of the test turbine was carried out using a mesh containing 35 grid nodes in the circumferential direction, 47 nodes in the radial direction, and 333 nodes in the axial direction. Each of the three profiles is described by 76 points. The interface plane treatment is done with the reversible averaging procedure described above. A computation of the first stage of this rig has also been made for comparison purposes and is referred to when it aids to the overall discussion. It should again be noted that all measured distributions shown in this paper were taken from the complete 1.5-stage build of the turbine.

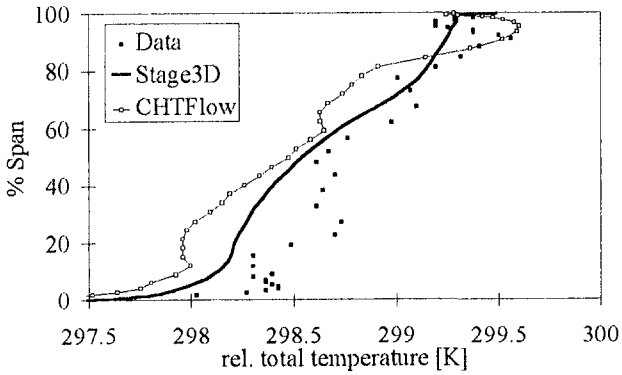

Fig. 11 Relative total temperature in plane B

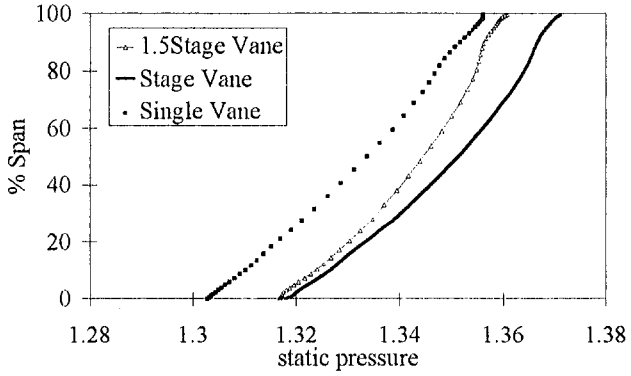

Fig. 13 Static pressure in plane A

First-Vane Flow. In Fig. 12 the computed circumferentially averaged total pressure distribution in plane A is plotted against the experimental data. Additionally the inlet boundary condition as well as the solution obtained from the isolated vane computation is shown.

The absolute total pressure distribution obtained from the 1.5-stage computation is similar in shape to the one taken from the isolated vane computation. Radially outward of 10 percent span, the 1.5-stage computation shows a somewhat higher total pressure level than the isolated vane computation. Near the casing the 1.5-stage calculation also shows better agreement with the experimental data in terms of the position and extent of the casing passage vortex.

The difference in the predicted total pressure level is related to the different static pressure splits between the first vane and the rotor for the two computations. The predicted static pressure distribution in plane A obtained from the 1.5-stage computation is plotted in Fig. 13 along with the static pressure distribution computed by considering only the first stage.

In the near-hub region no significant difference between the single stage computation and the 1.5-stage computation is visible, both predicting a static pressure level higher than the one given from the isolated vane computation. Further radially outward the slope of the static pressure profile becomes less for the 1.5-stage computation than for the single vane computation as well as for the single-stage computation. Approaching the casing this effect gets smaller and the predicted distribution for the 1.5-stage computation approaches the experimental one (being represented by the isolated vane distribution). In contrast the single-stage computation shows a static pressure distribution which, in shape, is very similar to the one obtained for the isolated blade row computation, but the level is shifted to a higher value across the entire span. Thus, the reason for this effect is the existence of the second vane inside the 1.5-stage computation influencing the pressure splits between the different blade rows of the entire machine.

Figure 14 shows the distribution of the circumferentially averaged swirl angle in plane A. Compared to the isolated vane computation, the predicted swirl angle level is lower across the entire span but the shape is very similar. The major difference between the two results is found near the casing.

Considering the distribution given from the experiments, it becomes obvious that the casing passage vortex induces a stronger underturning of the flow than the hub passage vortex. This effect is captured within the 1.5-stage computation. Using the result obtained from the stage computation, which does not show the stronger underturning at the casing, it is concluded that this effect is only introduced by including the second vane in the computation. The physical mechanism operating here is that due to the change in the static pressure splits, a mass flow shift toward the casing occurs, resulting in a change in the flow angle.

Rotor Flow. The results obtained from the 1.5-stage computation for the rotor are again different than those from the isolated rotor calculation and those from the single-stage computation as shown in Fig. 15. The presence of the second vane inside the 1.5-stage computation causes the relative total pressure level to drop closer to the experimental data when compared to the result obtained from the stage computation. Additionally, it shows much more "shape" in the near casing region compared to the isolated row computation. The latter is also valid for the stage computation. At the hub the 1.5-stage calculation still does not predict the blade passage vortex and the vane passage vortex as two separate features. Further radially outward the tip vortex and the vane casing passage vortex seem to be again joined together. No decrease in total pressure due to these vortices can be detected. In the near-casing region (90 percent span) the predicted shape of the relative total pressure

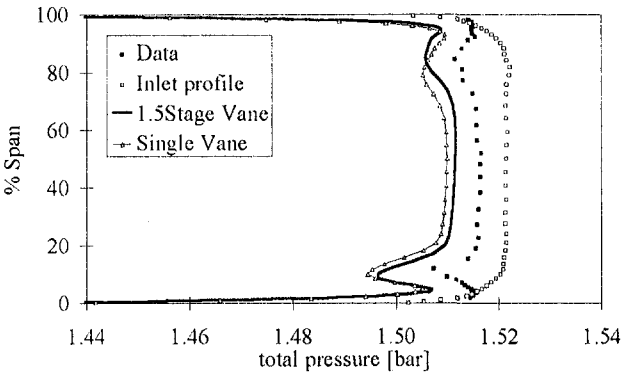

Fig. 12 Total pressure distribution in plane A

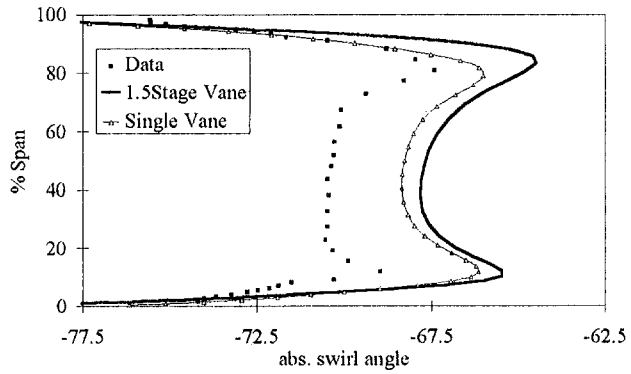

Fig. 14 Swirl angle distribution in plane A

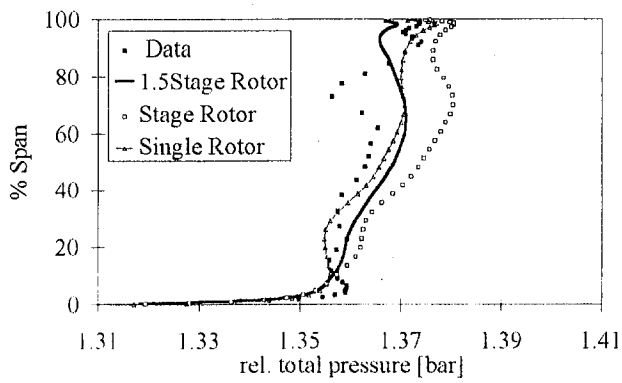

Fig. 15 Relative total pressure distribution in plane B

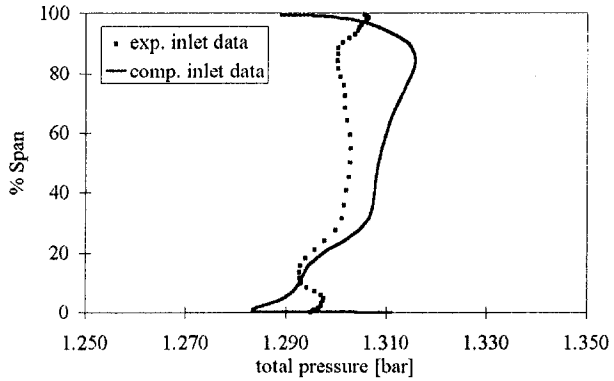

Fig. 18 Absolute total pressure in plane B

is quite similar to the one given from the experimental data, indicating that the influence of the blade casing passage vortex inside the rotor blade is captured. The same features can also be seen in the predicted relative total temperature distribution in plane B (Fig. 16).

Examining the flow from the 1.5-stage computation within different cross-stream planes inside the rotor passage leads to a similar conclusion as for the isolated rotor calculation discussed above. Thus, no significant differences were expected in the radial distribution of the relative flow angle in plane B shown in Fig. 17.

Close to the hub, Fig. 17 shows that the extent of the blade hub passage vortex is again overpredicted. Nevertheless, the signature of the vane's hub passage vortex seems to be present at 17 percent span. In the bulk region of the profile the swirl angle is underpredicted by roughly two degrees in agreement with the underprediction of the swirl angle inside the vane passage (see Fig. 14).

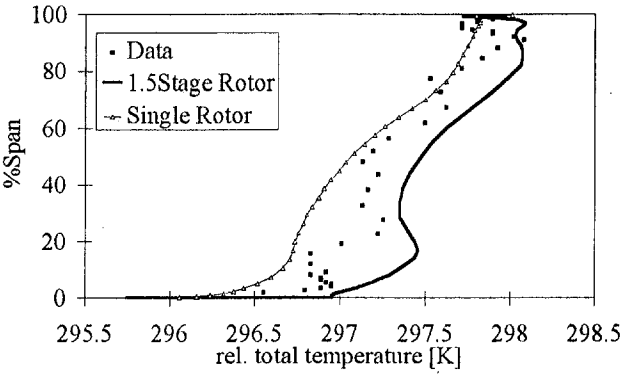

Fig. 16 Relative total temperature distribution in plane B

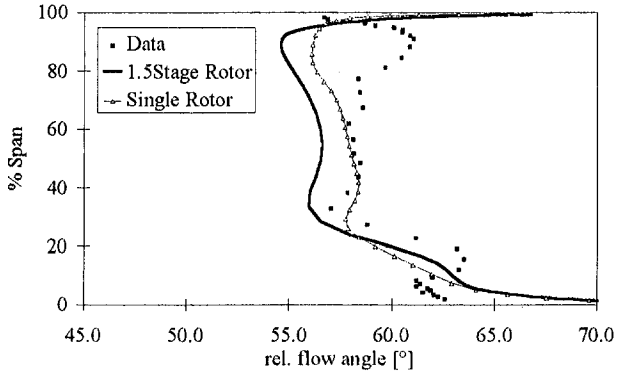

Fig. 17 Relative swirl angle distribution in plane B

Second-Vane Flow. Due to the differences in the relative total pressure distribution downstream of the rotor trailing edge in plane B between the experimental data and the 1.5-stage computation, Fig. 18 shows the resulting differences in the absolute total pressure distribution representing the inlet condition for the second vane computation. Of most importance is the difference in shape of the profiles. As is known from the first vane analysis (having the same geometric profile as the second vane) the total pressure profile is only changed within the endwall regions when convected through the vane passage. Thus, downstream of the second vane's trailing edge in plane C, a comparable difference in total pressure as given in Fig. 18 between the experimental data and the computational result is to be expected.

In Fig. 19 the predicted total pressure distribution in plane C downstream of the second vane's trailing edge is shown in comparison to the experimental data. For further comparison the solution obtained from the computation for the isolated second vane as well as the given inlet conditions from the experiments are also plotted.

Before starting the discussion of the computational results, it is worth noting the experimentally given distribution of total pressure. From Fig. 19 it is obvious that the total pressure distributions upstream and downstream of the second vane are significantly different in shape compared to the ones for the first vane (see Fig. 12), which are very flat in the bulk region of the profile. We return to this point in the discussion of Fig. 20.

The vane hub passage vortex has moved the incoming low total pressure fluid away from the endwall toward the suction surface. The dip in total pressure downstream of the vane trailing edge appears closer to the hub than the corresponding one

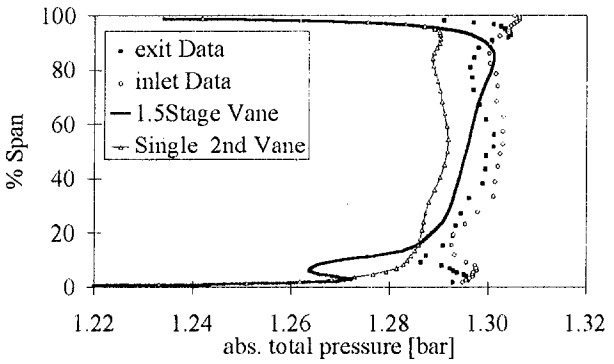

Fig. 19 Total pressure in plane C

given in the inlet profile, indicating that the incoming loss core, due to the rotor hub passage vortex, has been moved closer to the hub by the vane hub passage vortex. Opposite to this, at the casing the low total pressure fluid from the incoming boundary layer has moved from 90 percent span radially inward to 80 percent span. Interestingly, no significant difference in shape between the incoming low total pressure region and the outgoing one, as it occurs at the hub, is visible. In between 15 percent span and 80 percent span the total pressure profile is mainly influenced by the still existing blade passage vortices and the casing trailing edge vortex generated at the rotor trailing edge as discussed by Walraevens and Gallus (1995).

It can be seen from the isolated vane computation that Stage3D predicts the overall shape of the total pressure distribution quite well. Only at the hub due to the thin incoming boundary layer is the low total pressure region due to the passage vortex not predicted. According to the discussion of the isolated first vane computation the level of total pressure is again predicted too low.

As mentioned above also for the 1.5-stage computation, the shape of the total pressure profile downstream of the vane trailing edge in plane C is very similar to the one in plane B except the near-endwall region. Due to the thick incoming hub boundary layer (Fig. 18), the hub passage vortex inside the vane gets very strong. Further radially outward the influences of the upstream rotor's secondary flow structures are not visible according to the uncertainties within the rotor flow prediction. At first glance the 1.5-stage computation does not show the signature of the casing passage vortex in terms of a low total pressure region, although the incoming casing boundary layer is very thick.

Therefore, Fig. 20 shows the computed total pressure distributions in plane B and plane C. According to the discussion above, the computation shows the slight change of the total pressure in the near-casing region between inlet and exit. Because of the total pressure overshoot in the inlet profile, no distinct low total pressure region can be found in plane C.

As the profiles of the first and second vane are identical, it is surprising that the drop in total pressure inside the second vane is smaller than the total pressure drop inside the first vane (Figs. 12 and 19), although the second vane operates on the base of a highly nonuniform inlet flow field. Looking at the given experimental data in detail, it can be found that the total pressure loss in the second vane is on the average roughly a factor 2 lower than inside the first vane. From this the authors conclude that the experimentally given level of total pressure is at least for the second vane somewhat questionable.

Finally, in Fig. 21, the computed distribution of spanwise velocity inside a crossflow plane immediately upstream of the vane trailing edge from the 1.5-stage computation is shown.

Four different vortex motions are visible, two within each near-endwall region. At the hub two vortices of nearly the same

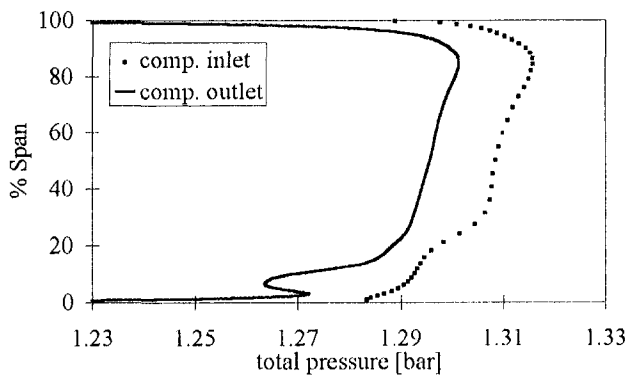

Fig. 20 Computed total pressure in planes B and C

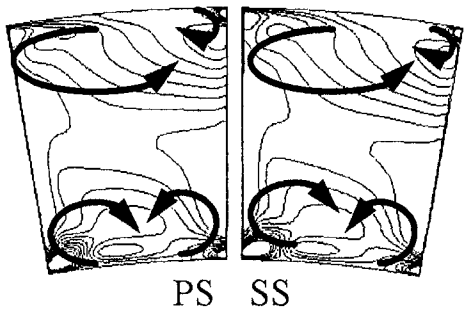

Fig. 21 Spanwise velocity close to the second vane's trailing edge

size are present, representing the hub passage vortex of the second vane rotating clockwise and the blade hub passage vortex rotating counterclockwise. At the casing the vane passage vortex is very strong, while the clockwise rotating blade passage vortex appears small and close toward the vane pressure side. Comparing this result to the given secondary flow analysis of Walraevens and Gallus (1995), it appears that the major (dominating) effects are captured within the computation but the strength of those effects is not predicted correctly. Additionally, the weaker effects like the rotor blade trailing edge vortex and what is called in Walraevens and Gallus (1995) the "combi vortex" in the bulk region of the vane passage are not accounted for at all.

Conclusions

Two significantly different numerical codes have been run against experimental data being provided within the ERCOFTAC framework 1996 for a 1.5-stage axial flow turbine. For code comparison, the first vane and the rotor were considered as running in isolation before the multistage code was run on the combined geometries. All comparisons are made to experimental data obtained from the 1.5-stage configuration. The investigation led to the following conclusions:

- The given inlet total pressure profile ahead of the first vane needs to be modified for both numerical algorithms to be able to predict the total pressure loss cores downstream of the vane trailing edge. This is in accordance with previous experimental data (Zeschky, 1991).
- CHTFlow predicts the flow distribution downstream of the vane trailing edge quite well in terms of level and shape. For the rotor, the predicted relative flow angle downstream of the rotor trailing edge is also predicted reasonably except in the region where the vane casing passage vortex occurs.
- Stage3D predicts the shape of the profiles downstream of the vane trailing edge but the level, especially in total pressure is underpredicted. Downstream of the rotor, all significant secondary flow features are predicted but their strength is inaccurately calculated. Both of these are thought to be related to the thin layer approximation used in determining the viscous stresses. This assumption is currently being removed from the code.
- The presence of the second vane downstream of the rotor in the 1.5-stage computation results in a significant change in static pressure splits across the first vane and the rotor.
- Results obtained from the isolated rotor calculation, the stage calculation, and the 1.5-stage computations shown that the rotor is very sensitive to slight changes in boundary conditions.
- The flow downstream of the second vane is strongly influenced by the secondary flow motions being generated within the upstream rotor. The main secondary flow features were captured from the 1.5-stage computation, i.e., the vane passage vortices and the blade passage vortices could be clearly identified in the exit plane of the second vane.

Acknowledgments

The current work was mostly supported by ABB Power Generation Ltd., and the first two authors wish to thank them for permission to publish this paper.

References

Alonso, J. J., Martinelli, L., and Jameson, A., 1995, "Multigrid Unsteady Navier–Stokes Calculations With Aeroelastic Applications," AIAA Paper 95-0048.

Baldwin, B., and Lomax, H., 1978, "Thin Layer Approximation and Algebraic Model for Separated Turbulent Flows," AIAA Paper No. 78-257.

Bohn, D., and Emunds, R., 1995, "A Navier–Stokes Computer Code for Theoretical Investigations on the Applicability of Various Turbulence Models for Flow Prediction Along Turbine Blades," ASME Paper No. 95-GT-90.

Chima, R., 1998, "Calculation of Tip Clearance Effects in a Transonic Compressor Rotor," ASME JOURNAL OF TURBOMACHINERY, Vol. 120, pp. 131–140.

Dawes, W. N., 1993, "A Comparison of the Measured and Predicted Flow-Field in a Modern Fan-Bypass Configuration," ASME JOURNAL OF TURBOMACHINERY, Vol. 115, pp. 273–282.

Dawes, W. N., 1992, "Toward Improved Throughflow Capability: The Use of Three-Dimensional Viscous Flow Solvers in a Multistage Environment," ASME JOURNAL OF TURBOMACHINERY, Vol. 114, pp. 8–18.

Dzung, L. S., 1970, "Konsitente Mittelwerte in der Theorie der Turbomaschinen für kompressible Medien," Brown Boveri Mitteilung 10-71.

ERCOFTAC Test Case 6, 1.5 Stage Axial Flow Turbine, ERCOFTAC 1995.

Gallus, H. E., Zeschky, J., and Hah, C., 1994, "Endwall and Unsteady Flow Phenomena in an Axial Turbine Stage," ASME Paper No. 94-GT-143.

Jameson, A., Schmidt, W., and Turkel, E., 1981, "Numerical Solution of the Euler Equation by Finite Volume Methods Using Runge–Kutta Time Stepping Scheemes," AIAA Paper No. 81-1259.

Jennions, I. K., and Adamczyk, J. J., 1997, "Evaluation of the Interaction Losses in a Transonic Turbine HP Rotor/LP Vane Configuration," ASME JOURNAL OF TURBOMACHINERY, Vol. 119, pp. 68–76.

Schmatz, M. A., 1989, "Three-Dimensional Navier–Stokes Calculations for Equilibrium Gas," AIAA Paper No. 89-2183.

Walraevens, R. E., and Gallus, H. E., 1995, "Stator-Rotor-Stator Interaction in an Axial Flow Turbine and Its Influence on Loss Mechanisms," AIAA Paper No. 95-000.

Zeschky, J., 1991, "Experimentelle Untersuchung der dreidimensionalen instationären Rotorströmung einer axialen Kaltluftturbine," Dissertation, RWTH Aachen.

Automatic Genetic Optimization Approach to Two-Dimensional Blade Profile Design for Steam Turbines

M. A. Trigg

G. R. Tubby

A. G. Sheard

Allen Steam Turbines,
Bedford, United Kingdom

In this paper a systematic approach to the optimization of two-dimensional blade profiles is presented. A genetic optimizer has been developed that modifies the blade profile and calculates its profile loss. This process is automatic, producing profile designs significantly faster and with significantly lower loss than has previously been possible. The optimizer developed uses a genetic algorithm to optimize a two-dimensional profile, defined using 17 parameters, for minimum loss with a given flow condition. The optimizer works with a "population" of two-dimensional profiles with varied parameters. A CFD mesh is generated for each profile, and the result is analyzed using a two-dimensional blade-to-blade solver, written for steady viscous compressible flow, to determine profile loss. The loss is used as the measure of a profile's "fitness." The optimizer uses this information to select the members of the next population, applying crossovers, mutations, and elitism in the process. Using this method, the optimizer tends toward the best values for the parameters defining the profile with minimum loss.

1.0 Introduction

The design of high-efficiency turbomachinery blading is a complex task, and the introduction of Computational Fluid Dynamics (CFD) has revolutionized the tools available to the designer. This paper describes the method by which CFD tools have been applied to the blade design process.

Allen Steam Turbines produce geared industrial steam turbines in the range 1.0 to 50 MW. The markets served require a great diversity of steam path designs. The throughflow design of a turbine is typically produced using standardized stationary and moving blade profiles, and where possible standard blades. Most market segments are demanding improvements in turbine efficiencies. This has resulted in a quest for improved profile performance to augment the gains in machine efficiency that have been wrought by other means.

Design optimization techniques have been developed and applied to turbine through flow design by Cravero and Dawes (1997). A reduction in rotor underturning and secondary flows was reported, which resulted in an improved overall machine efficiency.

The application of optimization techniques to steam turbine blade design was reported by Cofer (1996). The technique adopted was to define a two-dimensional aerofoil as a set of Bezier curves, then establish the sensitivity of its profile loss to small perturbations of the curves. A manual optimization of the profile for minimum profile loss was then performed by the designer.

The automatic optimization of blade profiles was addressed by Goel et al. (1996). A general purpose engineering design and optimization tool was employed, which could call upon three different optimization techniques. Genetic optimization was not favored, due to the large computational requirement.

The optimization of transonic turbine blade profiles was studied by Shelton et al. (1993). A hill-climbing optimization technique was used in conjunction with an invisid two-dimensional CFD solver. Genetic algorithms were considered, but rejected as too computationally expensive to be applied to CFD analysis in the foreseeable future.

In this paper the first use is reported of an automated two-dimensional steam turbine blade profile design method, incorporating a genetic optimizer and viscous two-dimensional CFD solver to minimize profile loss. This technique has been developed to maximize the production rate of low loss two-dimensional blade profiles.

The overall blade design process is described in Section 2. The method by which blade profile geometry is defined, and profile loss calculated is described in Section 3. The genetic optimizer is described in Section 4, and the improvements in profile performance considered in Section 5.

2.0 Blade Design Process

Some of the most significant advances in blade path design have resulted from the introduction of "throughflow" calculation procedures such as that developed by Denton (1978). Since then further development has involved the two-dimensional and three-dimensional viscous blade-to-blade analysis codes by Dawes (1983, 1992). These calculation methods are essentially analyses from which the designer has to make judgments as to what may or may not effect some improvement in the performance of his design.

Full three-dimensional stage or blade row viscous calculations, although well within the capability of modern high-speed desk-top computers, are computationally intensive, and even with data preparation largely automated, require an engineering effort that is quite significant for a small company. It is therefore useful to develop profiles in a two-dimensional cascade simulation before embarking on a full three-dimensional analysis.

One technique used for two-dimensional profile generation and optimization is that of "Prescribed Velocity Distribution" based on assumption of inviscid flow. Obvious problems with this method are that the postulated ideal velocity distribution involves assumptions, and it may result in a profile mechanically

Contributed by the International Gas Turbine Institute and presented at the 42nd International Gas Turbine and Aeroengine Congress and Exhibition, Orlando, Florida, June 2–5, 1997. Manuscript received International Gas Turbine Institute February 1997. Paper No. 97-GT-392. Associate Technical Editor: H. A. Kidd.

unsuitable for use, or not fitting into a smooth tapered and twisted three-dimensional blade.

The automatic optimization technique described here avoids these problems by using the viscous calculated profile loss as the arbiter of aerodynamic excellence while allowing mechanically necessary features to be incorporated by limiting the range of the relevant parameters controlling the profile geometry.

The use of an automatic two-dimensional profile generation technique does not change the blade design methodology in any way. The throughflow code of Denton (1978) is used to produce an annulus design, plus inlet and exit conditions from each blade row. The two-dimensional CFD solver of Dawes (1983) is used to produce two-dimensional profiles, which are then stacked and analyzed with the three-dimensional solver of Dawes (1992). The use of an optimizer simply takes advantage of the power of modern desk top computers to analyze many more two-dimensional profiles than would be attempted manually.

3.0 Aerofoil Geometry Creation

The method used to generate a two-dimensional aerofoil shape is based on that published by Pritchard (1985), which used 11 basic parameters to fix five points on the aerofoil surface with known gradient at each point. The three curves that formed the aerofoil surface in Pritchard's method were two third-order polynomials and a circle. These gave the designer no control over the shape produced beyond the choice of the original 11 parameters, and the polynomial curves had no means of avoiding inflections.

This scheme has been improved by substituting cubic Bezier curves for the original polynomials, providing two additional control parameters for each curve, Fig. 1. In total 17 parameters are now used to define the aerofoil, with the 6 Bezier control parameters being used to influence the "fullness" of the curves and enable inflections to be avoided. Profiles generated in this way generally have a curvature discontinuity on the suction surface, but this feature has not been identified as a significant source of loss. The parametric equations defining Bezier curves are described by Faux and Pratt (1979).

3.1 Blade-to-Blade Calculations. The blade-to-blade flow is calculated using the two-dimensional code of Dawes (1983) referred to as BTOB. The **H**-type mesh required is simply produced from the analytical curves described above. All mesh size and spacing parameters are kept constant during the optimization process. A mesh size of 82 × 33 was found to be a good compromise between mesh independence, profile geometry independence, and machine run time.

The study undertaken and reported in this paper was purely two dimensional with no stream tube divergence or any other three-dimensional effects being considered. The flow parameters for which an aerofoil is to be designed are derived from the throughflow calculation of Denton (1978).

Comparison of measured and calculated cascade flows has been published by the author of the code (Dawes, 1986), showing good agreement. This has provided confidence in the ability of the code to calculate profile loss on a comparative basis, which is what is required for profile optimisation. The calculation of absolute loss for use in turbine performance prediction is regarded as a separate problem.

High-pressure steam turbine blading runs at relatively high Reynolds numbers, therefore it is reasonable to assume that boundary layers are always fully turbulent. This assumption would not be valid for gas turbine blading where boundary layer transition is a key aspect of blade design.

The only significant modification to BTOB necessary to enable its use as part of an automatic optimizer was the addition of a convergence monitor, which examines the full convergence history of the profile loss (the last parameter to converge) rather as a designer would assess convergence from a plot.

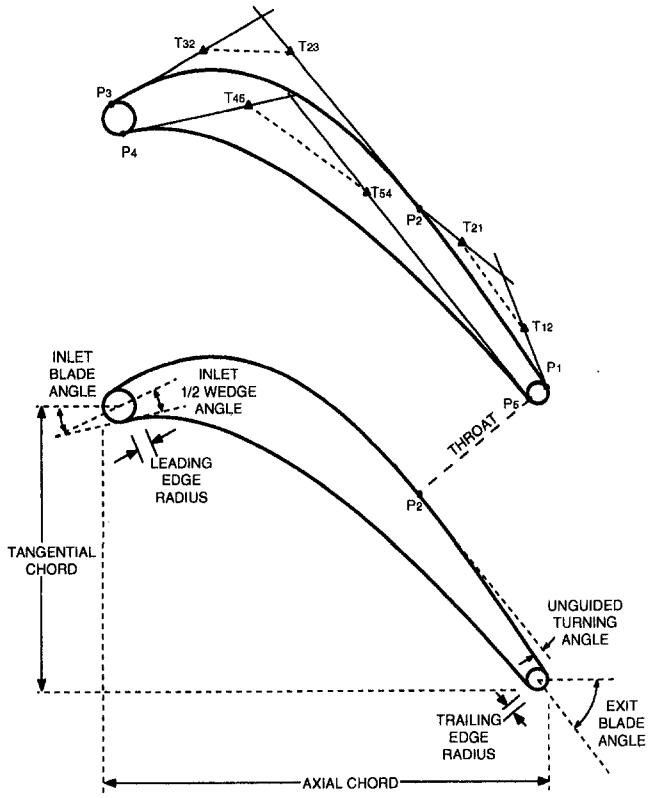

No.	Parameter
1.	Number of blades
2.	Aerofoil radius
3.	Axial chord
4.	Tangential chord
5.	Unguided turning angle
6.	Blade inlet angle
7.	Blade inlet wedge angle
8.	Leading edge circle radius
9.	Blade exit angle
10.	Trailing edge circle radius
11.	Throat/pitch
12.	Tangent proportion (Pt 3–2)
13.	Tangent proportion (Pt 2–3)
14.	Tangent proportion (Pt 2–1)
15.	Tangent proportion (Pt 1–2)
16.	Tangent proportion (Pt 4–5)
17.	Tangent proportion (Pt 5–4)

Fig. 1 Aerofoil parameter list

It is quite normal for the optimizer program to experiment with parameter combinations that do not produce sensible aerofoil shapes and hence cause problems for BTOB. Cases that fail, or that do not produce a converged solution in a reasonable number of iterations, return a large default value of loss to the optimizer program.

The use of a viscous BTOB solver in an automatic optimizer has only become possible because of the recent advances in computer technology. A typical run on a high-speed UNIX work station now takes two minutes; eight hours was a normal overnight run on a mainframe computer in the 1980's. It is therefore now practical to consider performing 1000 BTOB runs on different profiles in the quest for a profile of lowest loss.

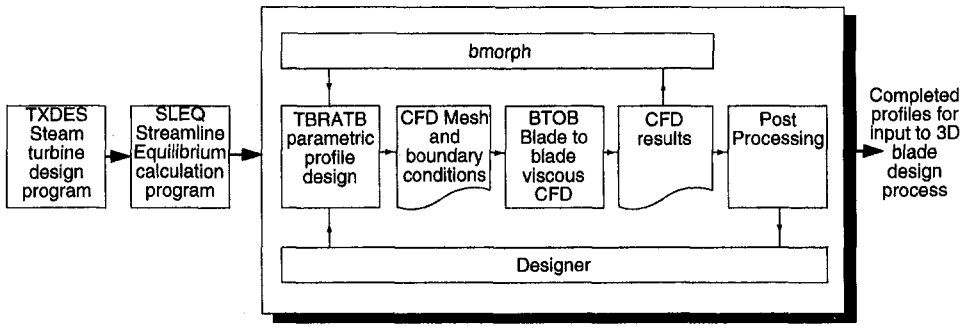

Fig. 2 Two-dimensional blade profile design process

4.0 Genetic Optimizer

Genetic Algorithms (GA's) were originally developed to model computationally the theory of evolution, but have found wider application in totally unrelated fields, described by, among others, Goldberg (1989). The reason for the popularity of GA's is that they are powerful global optimizers that can negotiate complex nonlinear search domains to provide optimal design solutions.

Unlike conventional methods, which usually require the function of interest to be well behaved, GA's are able to tolerate noisy and discontinuous function evaluations. Due to their stochastic nature, they are able to search the entire solution space with more chance of finding the global optimum than conventional methods. They also do not suffer by getting stuck on a relative optimum and so failing to find an absolute optimum.

4.1 Genetic Algorithm. The GA works with a population of individuals, in this case two-dimensional blade profiles. Profiles are defined by the set of 17 parameters, described in Section 3.0. These parameters are the defining features or characteristics of the individual. They are coded into a binary string, which is the "genetic code" of the profile.

The GA is linked into a profile design process loop, Fig. 2. This loop converts the genetic code into an aerofoil definition, produces a CFD mesh with aerodynamic boundary conditions for that aerofoil, and then calculates profile loss.

The GA can begin with a completely random set of parameters for the entire first population. Each profile is analyzed to ascertain its loss, which is used as a measure of the profile's fitness in its environment: the specified flow conditions. The algorithm selects the individuals for the next population from the current population based on their fitness. For this selection, a "roulette wheel" model is used where the profiles with lower loss have a higher likelihood of being selected.

The newly selected individuals are arranged in pairs and a crossover site is selected at a random position along each string. The segment of the string that lies after the crossover site is exchanged with that of the other individual in the pair.

The resulting binary strings are then randomly mutated at a given mutation rate. This rate is several orders of magnitude higher than that observed in living organisms. Increased mutation rate was found to increase convergence rate; however, above a critical mutation rate the optimization process broke down, and became essentially random.

After all the manipulations have been carried out to create the new population, each binary string is converted back into a set of 17 parameters. These parameters are used to define the new aerofoil geometry for each individual in the population. For each individual, a CFD mesh is generated and profile losses calculated. The process is then ready to be repeated. This basic loop continues with a general trend toward lower loss profiles.

The tools used by both designer and GA to produce a two-dimensional profile are identical, Fig. 2. The only difference is that a designer would view the CFD results and make intelligent changes to the profile. The GA simply takes profile loss as a single figure assessment of a profile's worth.

The genetic optimizer process loop has no prescribed end point, Fig. 3. The user must decide if the best profile so far is good enough for the purpose or whether to let the GA continue.

4.2 Optimizer Implementation. GA's are generally robust and relatively easy to apply once the requirements and the objectives have been identified clearly. They are ideal in a case such as this where the GA requires no real understanding of the complex flow analysis carried out by the viscous code, but receives just a single number for each result.

The practical implementation of a GA is often more complex than it first appears. This is due to the effects of collecting together separate manual input programs to form an unsupervised design/analysis program. The application of the GA to two-dimensional profile design proved to be a logical progression to the design process as all the core tools had already been developed for the blade designer, described in Section 2.0.

The GA implementation reported was named "BMORPH." The inputs to BMORPH consist of a range and number of discrete levels for each of 17 parameters that define the profile. Table 1 shows a typical example. This provides the means of constraining parameters to the desired range of values, or of fixing parameters that are not required to vary during a particular study. Additional input parameters were a mutation rate, population size, and flow parameters acting as boundary conditions for the BTOB analysis.

The value of the parameter is stored in the program as a binary string, the number of bits depending on the number of discrete levels required by the user. All these binary strings are put together to form one long binary string for the individual profile, Fig. 4.

The optimization algorithm itself has a number of variables and flags that allow control over its various functions. Once the initial implementation of the GA had been proven to work, a great deal of work was carried out to optimize these variables to provide a tool that was both consistent and easy to use.

The user is allowed a great degree of control over the starting point for an optimization run, enabling a start from a completely random point using a random number seed or beginning with a population of given profiles. A completely random starting value for each parameter for each profile in the first population avoids any preconceived notions of what constitutes a good profile, but necessitates a high degree of robustness from the program. Using a given start with specified values for any or all parameters has not proved to be an important feature as initial convergence is rapid.

Although some work was carried out on parallelism, a much more effective method in terms of execution time on a single machine and complexity for this implementation was found. The method uses a variable population size for dealing with the problem convergence rate of the GA, depending on the random start point. The initial population size is set at a value that is a

factor higher than the normal population size, typically 5 to 10 times the size. This allows the GA to sample a large area of the search space initially before carrying on for subsequent populations with a smaller population size. This allows a dependable convergence of the GA within reasonable time scales. A typical run would use a starting population of 100 to 200 with the following populations of around 20 to 40 individuals.

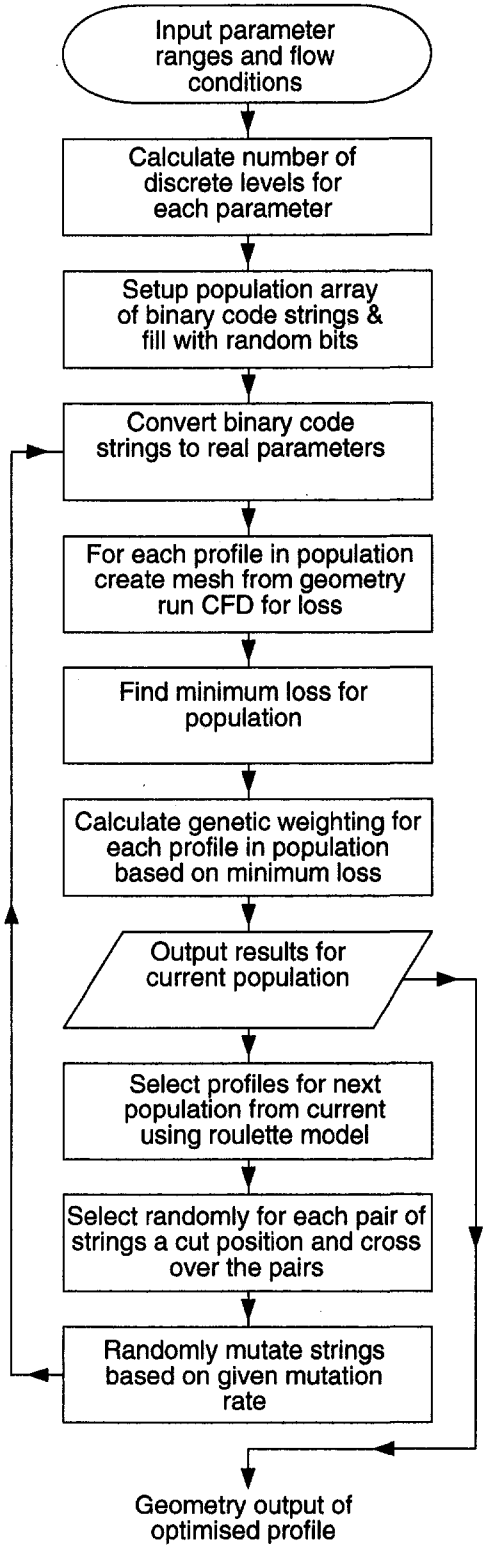

Fig. 3 The genetic optimizer BMORPH process loop

Table 1 BMORPH input parameters

Parameter Title	Min	Max	Levels
Number of Blades	57	57	0
Aerofoil Radius	280	280	0
Axial Chord	15	100	512
Tangential Chord	3	25	512
Unguided Turning Angle	0.5	30	512
Blade Inlet Angle	5	80	1024
Blade Inlet Wedge Angle	5	80	256
LE Circle Radius	0.1	3	32
Blade Exit Angle	-40	-80	256
TE Circle Radius	0.9	0.9	0
Throat To Pitch Ratio	0.32	0.32	0
Tangent Prop. 32	0.1	0.95	512
Tangent Prop. 23	0.1	0.95	512
Tangent Prop. 21	0.0005	0.95	512
Tangent Prop. 12	0.17	1.2	512
Tangent Prop. 45	0.1	0.95	512
Tangent Prop. 54	0.1	0.95	512

Another method used to reduce the overall run time is to record all the individuals encountered, together with their respective loss as the program proceeds. This enables the program to check whether a profile has already been analyzed, avoiding the need to carry out a time-consuming viscous calculation again. This allows the concept to be introduced of "number of unique BTOB runs" as a measure of the computational effort used in a particular run of the optimizer.

Elitism was implemented as an option in this GA, but not found to be of significant benefit. A study of the effect of elitism did not show it to produce an improvement in convergence rate. Both absolute fitness with scaling based on the inverse of the fractional loss and relative fitness based on differences between the losses have been coded as options in the program, with the latter being most commonly used. Future work may involve multi-objective optimization using the mechanical properties of the profile as an added fitness factor for the profile.

4.3 Optimizer Results. In application, BMORPH has been found to reach a practical optimum within 1000 unique BTOB runs, with only very small reductions in loss after this point. Figure 5 shows a typical run of BMORPH, with the lowest loss profile from key populations illustrating the progression of the optimizer. Initially the profiles are clearly absurd; however, after no more than 250 unique runs, the loss is roughly comparable to that typically accepted as satisfactory by a designer producing the profile without the aid of an optimizer.

Once BMORPH has produced a profile that contains no major flaws, reductions of profile loss become less frequent as the profile is "fine tuned."

When the minimum loss for each population analyzed is viewed in conjunction with the minimum overall loss, Fig. 6, the advantage of the genetic algorithm within BMORPH is apparent. Having essentially converged on a local optimum after 500 unique runs other profiles are evaluated, with considerably inferior performance, for about 250 unique runs, before an improvement in profile loss is produced. A further 1000 unique runs are required before the next reduction in profile loss, during which time the lowest loss profile for each population evaluated often has a profile loss no lower than that achieved after the first 250 unique runs.

An extensive study with different starting points did not significantly reduce or increase the time taken to reach an effective optimum. Allowing BMORPH to run significantly longer than 1000 unique runs did produce reductions in loss; however, they were so small as to be of little significance. Theoretically further populations may generate an improved profile no matter how many have gone before. In practice 1000 unique runs was picked as a practical end point.

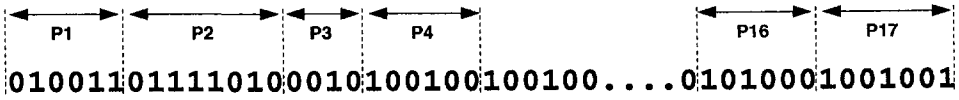

Fig. 4 Binary code parameter string

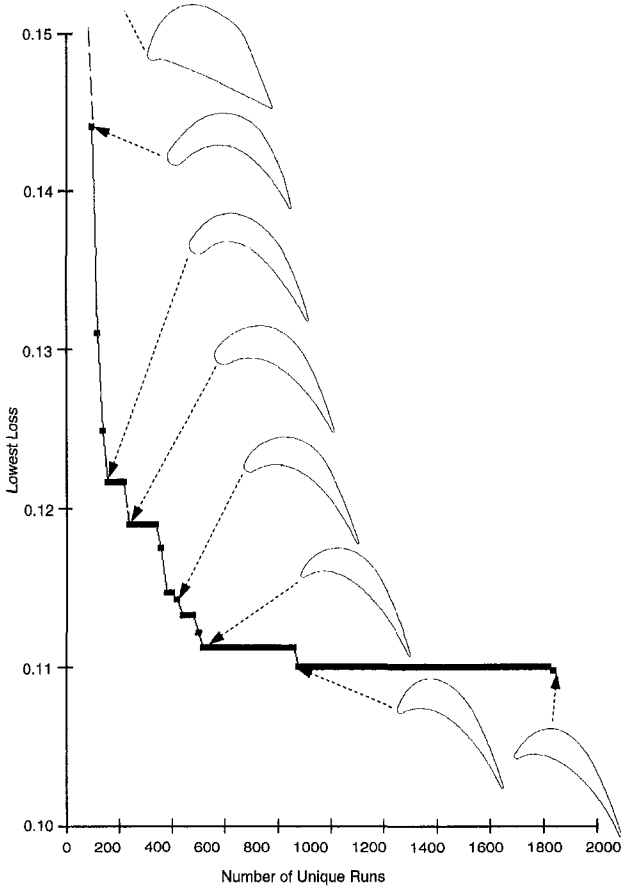

Fig. 5 Lowest loss and key profiles during a BMORPH run

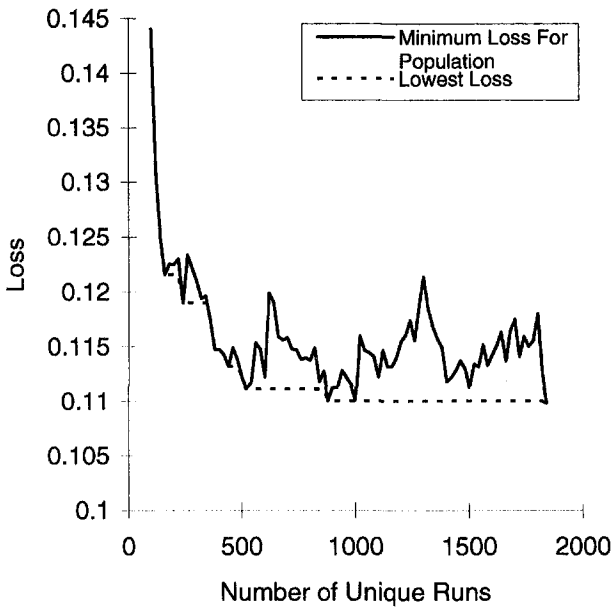

Fig. 6 History for a BMORPH run

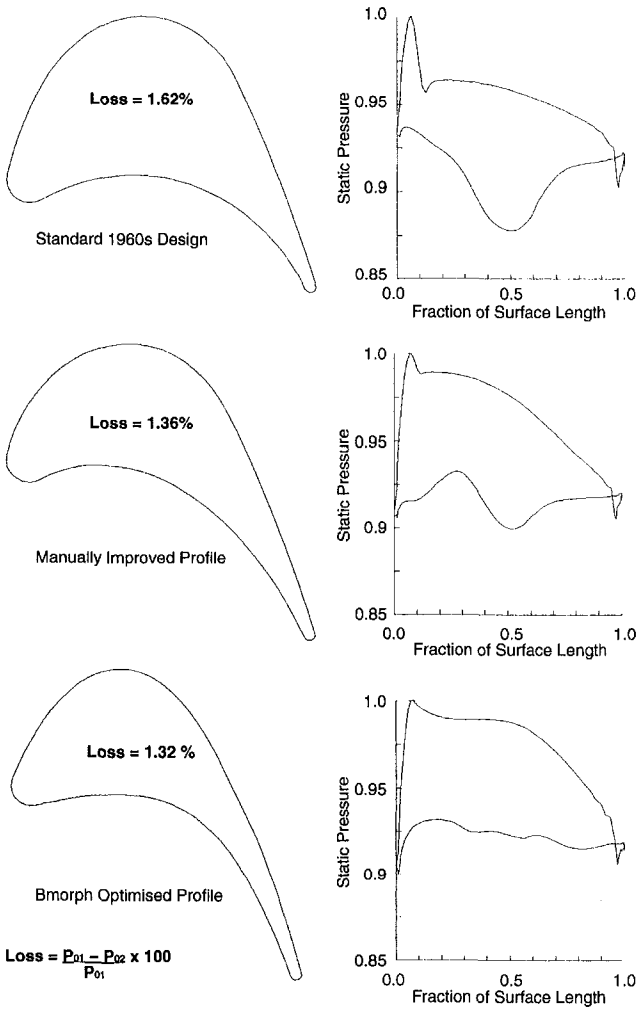

Fig. 7 Blade profiles and static pressure distributions used in the BMORPH evaluation

5.0 Design Evaluation

The application of BMORPH to the blade design process was assessed. The aim of the assessment was to benchmark the profiles produced by BMORPH against those produced before the advent of CFD tools, and those typical of current manual blade design practice.

The profile chosen for optimization runs with a Reynolds number of 400,000 and an isentropic exit Mach number of 0.35. The chosen profile was produced during the 1960s prior to the advent of CFD tools. The profile is from an impulse blade designed with surfaces composed of circular arcs, Fig. 7.

The profile reported was chosen as it had been identified as having a significant shortcoming, and had previously been the subject of improvement undertaken manually using the CFD solver of Dawes (1983) but without the aid of any optimizing tools. The original design exhibited an unfavorable pressure distribution on the suction surface, resulting in pronounced diffusion and local boundary layer separation. The separation may be seen as a negative value for skin friction coefficient between 60 and 80 percent of suction surface length, Fig. 8.

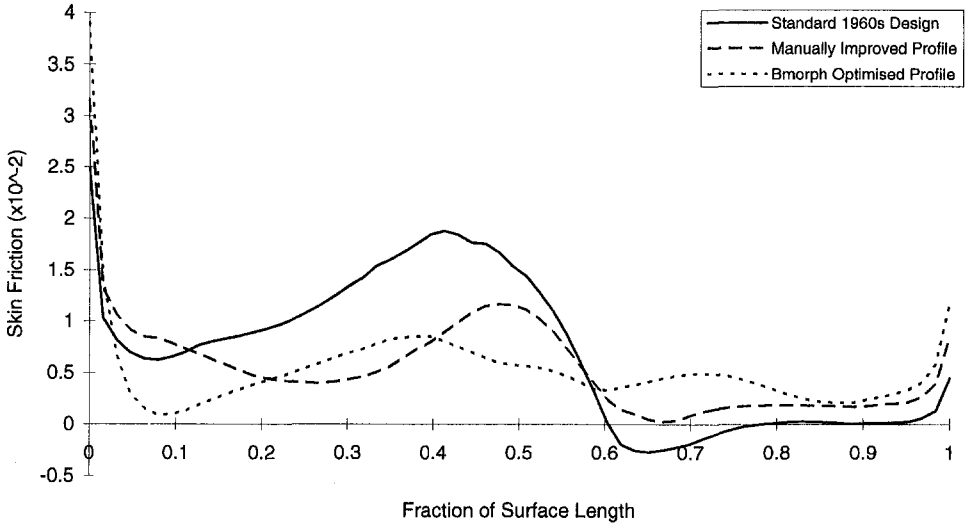

Fig. 8 Comparison of suction surface skin friction

The manually improved profile comes to the point of separation, Fig. 8, but just does not separate. In this respect the manual improvement has been successful, as the gross loss-producing flow feature has been eliminated. A study of the static pressure distribution about the 1960s profile and manually improved profile, Fig. 7, reveals that the manually improved profile still retains an undesirable area of diffusion on the suction surface. The manual improvements to the profile, therefore, constitute a minimization of the bad features of the 1960s profile.

The profile produced by BMORPH is fundamentally different from both the original and manually improved profile, Fig. 7. The undesirable diffusion on the suction surface is totally eliminated, and the pressure is maintained on the pressure surface for a significantly greater fraction of surface length. The skin friction, Fig. 8, does not exhibit the peaks and troughs of the previous profiles.

The BMORPH profile is more than an incremental improvement over its predecessors, it is a completely new profile design without the undesirable flow features of the original. The elimination of these features has effected a 19 percent reduction in profile loss over the 1960s profile and a 5 percent reduction over the manually improved profile. An optimum profile might be judged mechanically unsuitable, but the performance sacrificed in using a modified or constrained profile can be determined.

The manual improvement to the original profile was undertaken by an experienced turbine designer, Fig. 2. Over one week, a systematic study was conducted with the aim of identifying which features affected profile loss. The resulting improved profile was not manually optimized; however, it is considered typical of what would be produced without an optimizer.

The BMORPH optimized profile was set up in an hour, and ran unsupervised overnight. While it is not typical to devote an entire week to improve one two-dimensional blade profile, it is illustrative of the effort that can be spent minimizing profiles loss without the aid of an optimizer. Within this context, the 19 percent reduction in profile loss produced by BMORPH overnight was considered extraordinarily good.

The genetic optimizer has been compared with pre-CFD blade technology and that typically achieved by an experienced turbine designer working without optimization tools. The optimizer produced a profile with 19 percent lower profile loss than the 1960s design in approximately 10 percent of the time that would typically be spent on a profile design without the aid of an optimizer.

It must be remembered that optimization is only a form of design exploration and so is a tool for the designer and not a replacement for the designer.

6.0 Conclusions

1 A genetic optimizer has been developed for minimizing two-dimensional blade profile loss.
2 The genetic optimizer is unsupervised, only requiring setup and occasional monitoring. The time required for an experienced designer to produce a profile is correspondingly reduced by approximately an order of magnitude compared to that taken previously.
3 The genetic optimizer has been shown to reduce two-dimensional blade profile loss by typically 10–20 percent compared to unoptimized blade designs.
4 The genetic optimizer has proven to be a useful development tool for design exploration, showing trends and general behavior. This has facilitated a better understanding by the designer of the effect on profile performance associated with a change in blade profile geometric parameters.
5 The genetic optimizer has been implemented without changing blade design methodology. The laborious task of producing two-dimensional profiles has been automated, which has resulted in the designer focusing on other aspects of blade design.

Acknowledgments

The work reported in this paper was undertaken within the Product Technology department of Allen Steam Turbines; the authors offer thanks to other members of the department and company whose contribution is acknowledged.

The CFD flow solver used by the genetic optimizer was written by Professor W. N. Dawes, Whittle Laboratory, Cambridge University, England. The assistance of Professor Dawes with the CFD solver, and during the production of this paper is acknowledged.

The work reported was funded by Allen Steam Turbines, a Rolls-Royce Industrial Power Group company. The authors offer thanks to David Beighton, General Manager—Allen Steam Turbines, for permission to publish the work reported in this paper.

References

Cravero, C., and Dawes, W. N., 1997, "Through Flow Design Using an Automatic Optimization Strategy," ASME Paper No. 97-GT-294.

Cofer, J. I., 1996, "Advances in Steam Path Technology," ASME *Journal of Engineering for Gas Turbines and Power,* Vol. 118, pp. 337–352.

Dawes, W. N., 1983, "Computation of viscous compressible flow in blade cascades using an implicit iterative replacement algorithm," TPRD/M/1377/N83.

Dawes, W. N., 1986, "Application of Full Navier–Stokes Solvers to Turbomachinery Flow Problems," VKI Lecture Series 2: Numerical Techniques for Viscous Flow Calculations in Turbomachinery Blading, Jan. 20–24.

Dawes, W. N., 1992, "Toward improved through flow capability: the use of three dimensional viscous flow solvers in a multistage environment," ASME JOURNAL OF TURBOMACHINERY, Vol. 114, pp. 8–17.

Denton, J. D., 1978, "Throughflow calculations for transonic axial flow turbines," ASME *Journal of Engineering for Power,* Vol. 100, No. 2, pp. 212–218.

Faux, I. D., and Pratt, M. J., 1979, *Computational Geometry for Design & Manufacture,* Ellis Horwood Ltd.

Goel, S., Cofer, J. I., and Singh, H., 1996, "Turbine Aerofoil Design Optimization," ASME Paper No. 96-GT-158.

Goldberg, D. E., 1989, *Genetic Algorithms in Search, Optimization, and Machine Learning,* Addison-Wesley Publishing Company Inc.

Pritchard, L. J., 1985, "An Eleven Parameter Axial Turbine Aerofoil Geometry Model," ASME Paper No. 85-GT-219.

Shelton, M. L., Gregory, B. A., Lamson, S. H., Moses, H. L., Doughty, R. L., and Kiss, T., 1993, "Optimization of a Transonic Turbine Airfoil Using Artificial Intelligence, CFD and Cascade Testing," ASME Paper No. 93-GT-161.

I. J. Day
Whittle Lab,
Cambridge, United Kingdom

T. Breuer
MTU,
Munich, Germany

J. Escuret
SNECMA,
Paris, France

M. Cherrett
DRA,
Farnborough, United Kingdom

A. Wilson
Rolls-Royce,
Derby, United Kingdom

Stall Inception and the Prospects for Active Control in Four High-Speed Compressors

As part of a European collaborative project, four high-speed compressors were tested to investigate the generic features of stall inception in aero-engine type compressors. Tests were run over the full speed range to identify the design and operating parameters that influence the stalling process. A study of data analysis techniques was also conducted in the hope of establishing early warning of stall. The work presented here is intended to relate the physical happenings in the compressor to the signals that would be received by an active stall control system. The measurements show a surprising range of stall-related disturbances and suggest that spike-type stall inception is a feature of low-speed operation while modal activity is clearest in the midspeed range. High-frequency disturbances were detected at both ends of the speed range and nonrotating stall, a new phenomenon, was detected in three out of the four compressors. The variety of the stalling patterns, and the ineffectiveness of the stall warning procedures, suggests that the ultimate goal of a flightworthy active control system remains some way off.

Background

This project was started 1993 with the financial backing of the European Community under the auspices of the "Brite Euram" program. The four compressors to be tested were provided by Rolls-Royce, SNECMA (Société Nationale D'Etude et de Construction de Moteurs D'Aviation), MTU (Motoren und Turbinen Union Muenchen), and DRA (Defence Research Agency, UK). Experimental coordination, and theoretical modeling (reported separately), were provided by the Whittle Laboratory, Cambridge. The project had three specific aims: to learn more about stall inception in high-speed compressors; to evaluate various data analysis techniques with a view to obtaining early warning of stall onset; and to assess the range of incoming signals with which an active control system might be expected to cope. The background to each of these objectives is set out below.

Stall Inception Process. Previous work on low-speed compressors has identified two fundamental mechanisms of stall inception: the first associated with modal oscillations of the entire flow field (long length-scale disturbances) and the second, with localized disturbances of blade passage proportions called spikes (short length-scale disturbances). It was initially suggested by Day (1993a, b) that the type of stall inception, either modes or spikes, was determined by the design of the compressor, in particular by the size of the tip clearance gap. According to this thinking, a particular compressor would always stall via the same stall inception process. Recent low-speed work, carried out at the Whittle Laboratory in parallel with the current project (Camp and Day, 1998), has shown, however, that stage matching, and radial flow distribution, are far more important parameters than tip clearance when considering the stall inception process.

In a high-speed compressor, the stage matching not only depends on the design of the blading, but also on the speed of rotation of the machine and on the disposition of any variable stator vanes. Apart from some preliminary work by Wilson and Freeman (1994), and Day and Freeman (1994), no systematic investigation has been carried out on the effects of stage matching on stall inception in high-speed compressors. The current work thus fills a gap by providing stall inception measurements covering the full speed range from idle to overspeed. Two of the compressors were fitted with variable inlet guide vanes and these were also used to influence the stage matching of the compressors.

All four compressors in this program were comprehensively instrumented, both circumferentially and axially, so that the stall inception process, whether beginning at the front or rear of the compressor, could be studied in detail. The work presented here concentrates on those aspects of the stall inception process that are common to all the compressors and highlights those features that are unique to an individual machine.

Data Analysis Studies. Extensive data analysis was carried out during the course of this project with two primary objectives: (1) to assist with the interpretation of the data where important features of the flow are not apparent by eying the raw data and, (2) to investigate the possibilities of using real-time analysis of compressor signals to obtain some form of stall warning indicator. A clearly defined warning signal would make possible the semi-active management of an engine, where fast bleed valves, stator re-scheduling, or fuel dipping could be used to pre-empt stall.

The analysis techniques used during the project are described in Section 4, but an evaluation of their respective merits and demerits is not presented here because this paper is primarily concerned with the physical processes associated with stall inception.

Prospects for Active Control. In 1986 Epstein et al. proposed a method of suppressing the onset of stall and surge by actively controlling the stall inception process. Four years later, when the current project was being put together, low-speed laboratory experiments were just beginning to confirm that active control might provide useful improvements in compressor operating range (Paduano et al., 1993; Day, 1993a, b). A decision had therefore to be made whether or not to include active control in the scope of the current program. Little information was available at that time on stall inception in high-speed com-

Contributed by the International Gas Turbine Institute and presented at the 42nd International Gas Turbine and Aeroengine Congress and Exhibition, Orlando, Florida, June 2–5, 1997. Manuscript received International Gas Turbine Institute February 1997. Paper No. 97-GT-281. Associate Technical Editor: H. A. Kidd.

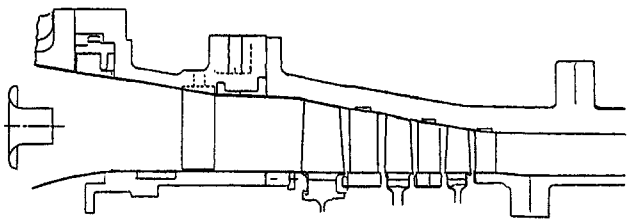

MTU COMPRESSOR

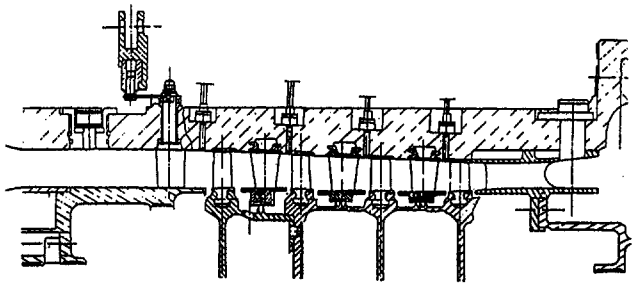

SNECMA COMPRESSOR

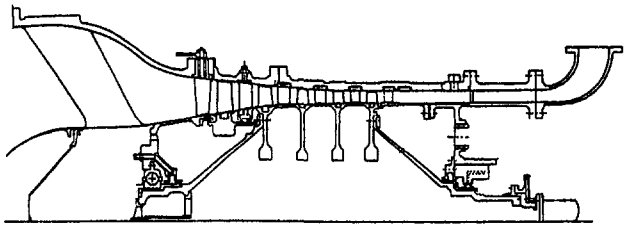

DRA COMPRESSOR

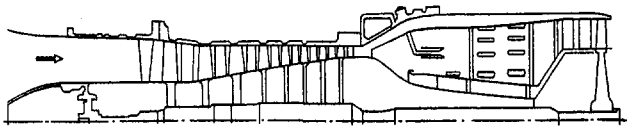

ROLLS-ROYCE VIPER ENGINE

Fig. 1 The four compressors in the Brite Euram civil core compressor program

pressors and it was decided to concentrate on stall inception with the idea that the results would provide a solid basis for any future work on active control. (A follow-on project has not yet been negotiated.)

Four years have passed since the project began. During this time work on active control has continued in other centers throughout the world, some on low-speed machines, (Haynes et al., 1993; Gysling and Greitzer, 1994), and some on a working engine (Freeman et al., 1998). The results so far have been encouraging, but the current work suggests that there is still some way to go before all forms of compressor instability can be controlled.

Equipment

The four compressors used in this study are shown in Fig. 1. They are all of different design but each is representative of aero-engine practice:

1 MTU Compressor: three-stage compressor of Intermediate Pressure design, modern blading, relative tip Mach Number of first rotor 1.080, overall pressure ratio 2.5, 20 percent true chord inter blade row axial spacing, no variables. (Pressure transducer locations: eight probes ahead of each rotor.)

2 DRA Compressor: five-stage compressor of military core design, modern blading, relative tip Mach number of first rotor 1.001, overall pressure ratio 6.0, 60 percent true chord inter blade row axial spacing, variable IGVs. (Pressure transducer positions: four probes between each blade row and a special fifth probe ahead of each of the first four rotors.)

3 SNECMA Compressor: four-stage compressor of High-Pressure design, modern blading, relative tip Mach number of first rotor 0.798, overall pressure ratio 2.0, 50 percent true chord inter blade row axial spacing, variable IGVs. (Pressure transducer positions: eight probes upstream of the IGVs and eight probes ahead of each rotor.)

4 Rolls-Royce Viper Engine: eight-stage single-shaft compressor, traditional blading, relative tip Mach number of first rotor 0.929, overall pressure ratio 5.0, 30 percent true chord interblade row axial spacing, no variables. (Pressure transducer positions: five probes ahead of first rotor, two ahead of second rotor, five ahead of fourth, fifth and sixth rotors, two ahead of seventh rotor, and five ahead of last rotor.)

The high-frequency transducers were arranged in circumferential arrays as equally spaced as mechanical restraints would allow. Higher circumferential densities were possible in the compressors with fewest blade rows. The speed of rotation, mass flow rate, stage-by-stage pressure rise, overall pressure rise, and operating temperatures were all recorded using standard test-bed instrumentation.

The data logging was done according to a prescribed routine with the high-response transducers coupled in both AC and DC modes. Each compressor was tested at speeds between 50 and 105 percent design speed with IGV scheduling, inlet distortion, and reduced Reynolds number tests being undertaken where possible. The data from all the tests has been archived in a standard format database.

Review of Results

In this section the occurrence of modes and spikes in the four compressors will be considered first. Both types of disturbance have previously been observed in high-speed compressors (Tryfonidis et al., 1995; Wilson and Freeman, 1994) and their appearance here is not particularly noteworthy. Of greater interest, however, is the role of stage matching in determining which of these instability patterns will occur in a particular situation. Clear trends were observed and are reported here for the first time. The influence of guide vane setting on stage matching, and hence on the stalling pattern, will also be considered. Following this we look at some of the other stall-related phenomena that occur in these compressors, such as "fixed-location stalling" and the occurrence of high-frequency stall—both new phenomena. The effects of inlet distortion, Reynolds number, and shaft-order perturbations, will also be discussed.

Spikes and Modes. Reference has already been made to the distinction between modal-type stall inception, where the flow becomes unstable due to a large-scale circumferential oscillation, and spike type stalling where flow breakdown originates from a distinctly localized disturbance. In general the physical features of the these processes can be summarized as follows: Modal perturbations revolve comparatively slowly, up to about 50 percent of rotor speed, and appear as gentle waves or undulations in the pressure traces. (Work by Hendricks et al. (1997) suggests, however, that modes of higher frequency can exist in high-speed machines.) Spike-type disturbances, on the other hand, are characterized by sharp peaks or "glitches" in the time traces. As a general rule spikes rotate fairly fast when first detected, 70 to 80 percent of rotor speed, and slow down quite rapidly as they grow in size. Representative exam-

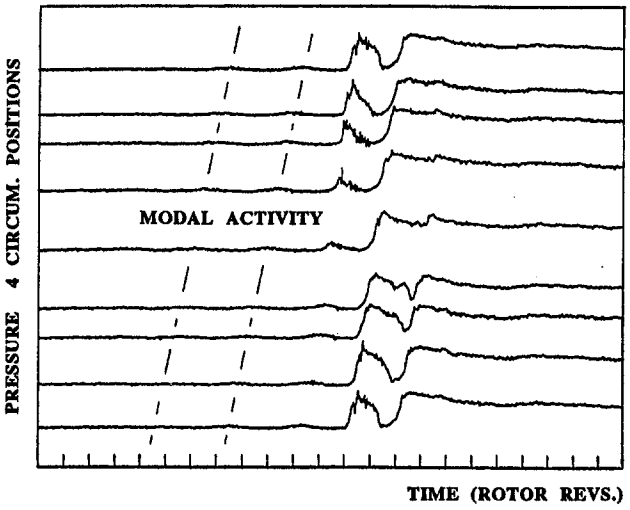

Fig. 2 Example of modes in a high-speed compressor taken from the MTU measurements

ples of modes and spikes from the current project are shown in Figs. 2 and 3. In Fig. 2 the modal perturbations rotates at 33 percent of rotor speed while the spikes in Fig. 3 rotate at 70 percent of rotor speed.

The localized nature of spikes also means that the initial disturbance has a limited detection zone in the axial direction. An example from the SNECMA machine is given in Fig. 4 where a spike is visible on rotor 1 almost a full revolution before it is detected by the probes in the second stage. A similar situation also occurs at low speed in the DRA compressor. The early detection of spikes is thus dependent on the positioning of the measuring probes.

The examples given here suggest that modes and spikes represent two distinctly different stalling mechanisms. This idea is supported by recent low-speed work by Camp and Day (1998). This work also shows that both these disturbances can occur in the same machine and the questions now to be answered are whether or not this is true for high-speed machines, and which compressor operating parameters are responsible for determining the type of stall inception that will occur.

Compressor Matching. The work of Camp and Day (1998) shows that both modes and spikes can occur in the same compressor and that stage matching is one of the parameters that can bring about a change from one stalling pattern to the other. In a high-speed compressor, the stage matching changes automatically as the speed of rotation changes. Compressibility effects mean that the position of highest loading shifts from the front to the rear of the compressor as the speed of rotation

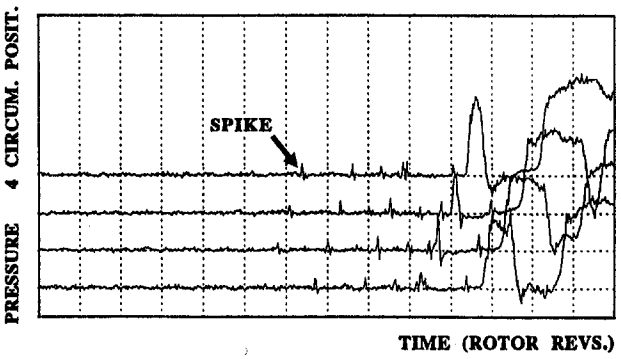

Fig. 3 Example of spikes in a high-speed compressor taken from the DRA measurements

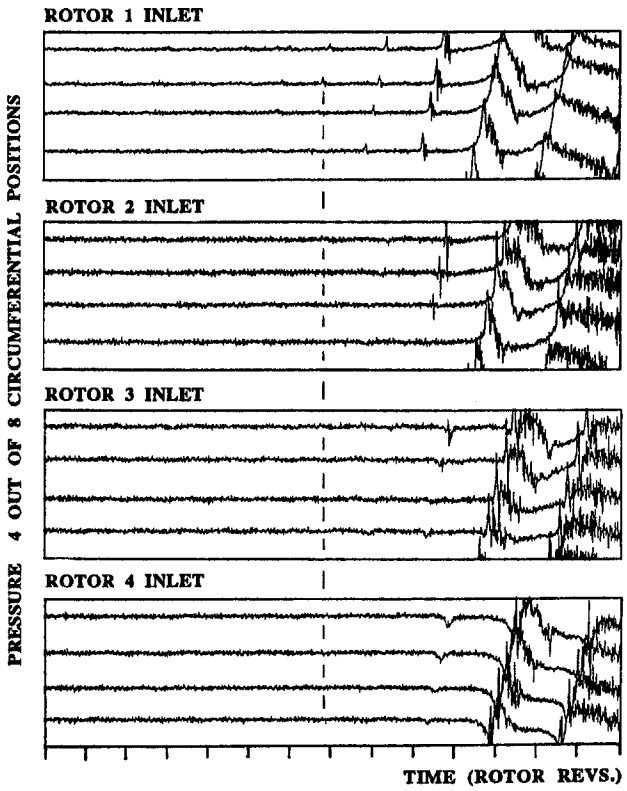

Fig. 4 Example of the localized nature of spike stall inception in the SNECMA compressor

increases. At low speed the front stages are heavily loaded, whereas at high speed the rear stages are the most likely to stall. In the medium-speed range all the stages are evenly matched near the stall point.

As previously mentioned, spike type stalling is a localized phenomenon beginning as a very small disturbance in just one blade row of the compressor. It might therefore be assumed that spike-type stalling will occur at low or high speeds of rotation where individual stages at the front or rear of the compressor are more highly loaded than the rest. At middling speeds of rotation, where all the stages are evenly matched, it might likewise be assumed that modal type stall inception would occur where the perturbations, being of larger proportions, can grow evenly throughout the machine. These ideas about the effect of compressor speed on the stall inception pattern are supported by the current tests.

Three of the four compressors in this study show a systematic change of stalling pattern with change in speed: clear spike-like behavior at low speeds and modal-type behavior in the midspeed range. At high speed, spike-like behavior is sometimes observed, but this is not always the case. In general the stalling process at high speed develops so quickly that it is difficult to classify the initiation mechanism. A clear example of the changing stalling patterns with a change in compressor speed is from the MTU compressor, shown in Fig. 5. Here spike-type stall inception occurs at low speed, and modal type in the midspeed range.

The Rolls-Royce Viper compressor also exhibits a change from spikes to modes as the speed of rotation increases. An example of spike-like behavior is shown in Fig. 6 at 70 percent speed and modal-type activity at 85 percent speed in Fig. 7. In previous work by Wilson and Freeman (1994) and Day and Freeman (1994), the existence of modes in this machine was doubted. It is only with the additional tests carried out in connection with the current project that modal activity has been discovered in a narrow band between 85 and 87 percent speed. Only

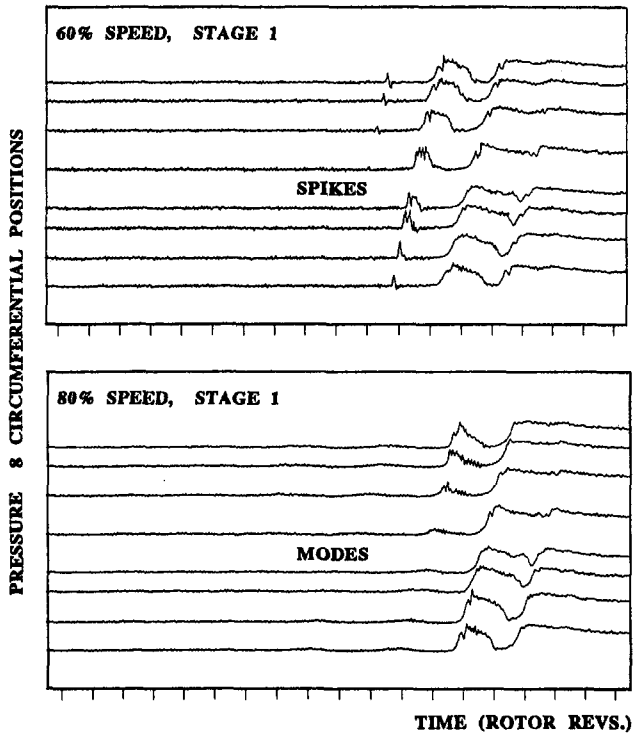

Fig. 5 Measurements from the MTU compressor showing spikes at low speed changing to modes in the midspeed range

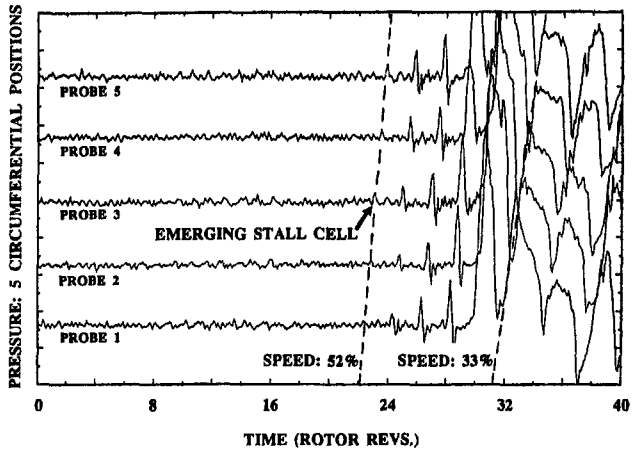

Fig. 6 Spike stall inception in the Viper engine at 70 percent speed

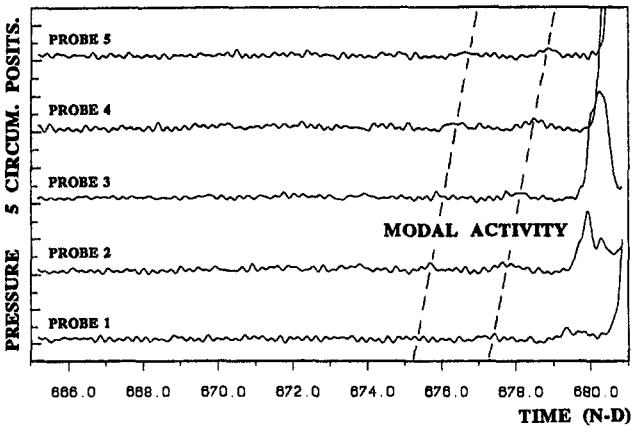

Fig. 7 Modal stall inception in the Viper engine at 85 percent speed

two clear examples were recorded, both showing a modal pattern rotating at 45 percent speed. This compressor has eight stages and the limited range of modal activity is ascribed to the narrowness of the speed range over which all eight stages will be evenly matched. (At 100 percent speed in this compressor where spikes might again be expected, a rotating pattern does precede surge, but the structure of the pattern is ill-defined.)

The DRA compressor also shows a clear change from spikes to modes as the speed of rotation is increased, but again the stalling process at full speed is too complicated to be analyzed in terms of spikes and modes.

The fourth compressor in the series, the SNECMA machine, behaves differently from the others in terms of the change from spikes to modes as the speed increases. In this case stall is initiated by spikes throughout the whole speed range. The reason for this is not clear, except that this compressor has relatively large inter blade row axial gaps and a low overall pressure ratio. Spike type stall is known to be a localized phenomenon originating in a single blade row and therefore it is possible that this machine, with its widely spaced rows, may favor localized disturbances rather than modal activity.

It has thus been shown that both spike-type and modal-type stall inception can occur in the same compressor and that the change from one form to the other is associated with a change in rotational speed, and hence with a change in stage matching. The stage matching of a compressor can, of course, be changed independently of speed through the use of variable stator rows. In the current tests, effective changes in matching were unfortunately not possible because none of the compressors were fitted with a sufficient number of variables. Two of the compressors did have variable IGVs but the effects these produced on the stalling behavior were not straightforward, as is shown below.

Effects of IGV Setting. The DRA and SNECMA compressors were equipped with variable inlet guide vanes and tests at different settings were conducted throughout the speed range. In the case of the DRA machine, the effect on stall inception of changing the IGVs was not significant, despite large (9 deg) changes in both the positive and negative directions. This result is somewhat surprising in view of the low-speed Whittle Laboratory tests where changes in IGV setting produced a dramatic change in stalling behavior (Camp and Day, 1998).

In contrast, the SNECMA machine was very sensitive to changes in IGV setting. This compressor did not exhibit modal activity at any speed and therefore a change from spikes to modes with a change in IGV setting was not expected. However, the IGV setting did have an effect on the axial location of stall inception. At the design setting of the IGV's, spikes appeared at the front of the compressor at low speeds and at the rear at high speeds. A small change in IGV settings was, however, sufficient to reverse this pattern. An example is given in Fig. 8 where, at 92 percent speed, increasing the loading on the first rotor by changing the IGV's by 1 deg was sufficient to switch the point of stall inception from Stage 4 to Stage 1. Changes in stalling pattern were also observed at 87 and 100 percent speed.

Of the two compressors fitted with variable IGVs, one is thus very sensitive to IGV setting and the other not at all. The reason for this difference is not clear and will require further investigation. The anticipated change from modes to spikes, and vice versa, did not occur in either case, but had any of the compressors been fitted with more than one row of variables, the results might have been more revealing.

Stalling Behavior at Low Speeds. At low rotational speeds, around 40 to 60 percent, the DRA, SNECMA, and Rolls-Royce compressors all exhibited so called "front-end" or "start-up" stall. This refers to a stable stall regime, which occurs naturally when the compressor is first started. The stalling comes about because the front stages of a long compressor suffer from low throughflow velocity at low rotational speeds

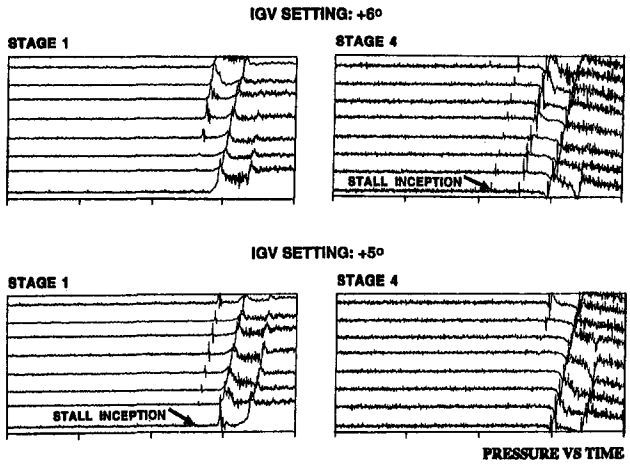

Fig. 8 Example of a small change in guide vane setting affecting the axial location of stall inception

and the blockage created by the stall cells is a self-correcting mechanism for reducing the frontal area of the compressor and thus improving the matching.

Front-end stall is usually confined to the first few rows of a long compressor and the stall cells are nearly always of the part-span type. Multiple cells are a signature of this type of stall and the cells organize themselves in an equally spaced circumferential pattern. If additional throttling occurs while these cells are present, perhaps due to over-fueling in an engine, the cells coalesce through a merging process, giving rise to a single stall cell of larger proportions. Figure 9 from the Viper compressor is a good example of three cells coalescing into one. While the cells remain in their multicell form, they are relatively benign and do little harm to compressor or engine performance. The larger full-span cell, when formed, has a bigger effect on compressor performance because it spreads throughout the length of the compressor and engine shut-down is necessitated. Under normal run-up conditions, where the part-span cells are not forced to coalesce, the cells shrink and disappear as the compressor speed increases and the front-to-back matching improves.

Only the MTU compressor in this series did not exhibit this type of stalling behavior at low speeds. This machine operates without stall at 40 percent speed and when flow throttling is applied, a spike-type pattern is observed prior to single cell rotating stall. Because front-end stall is a consequence of part-speed mismatching, the effect is worst in long compressors.

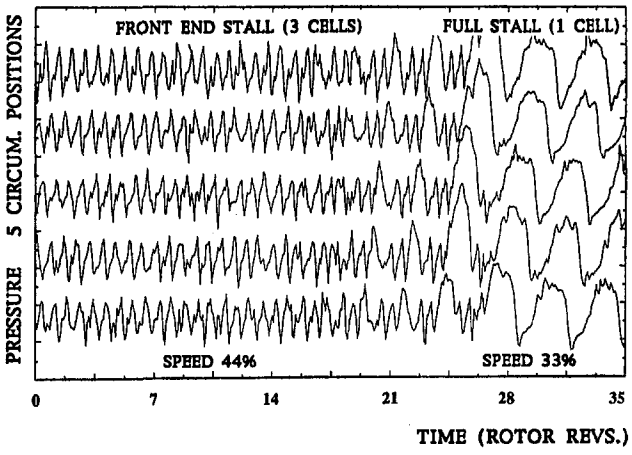

Fig. 9 An example of multicell front end stall changing to single-cell full-span stall in the Viper engine

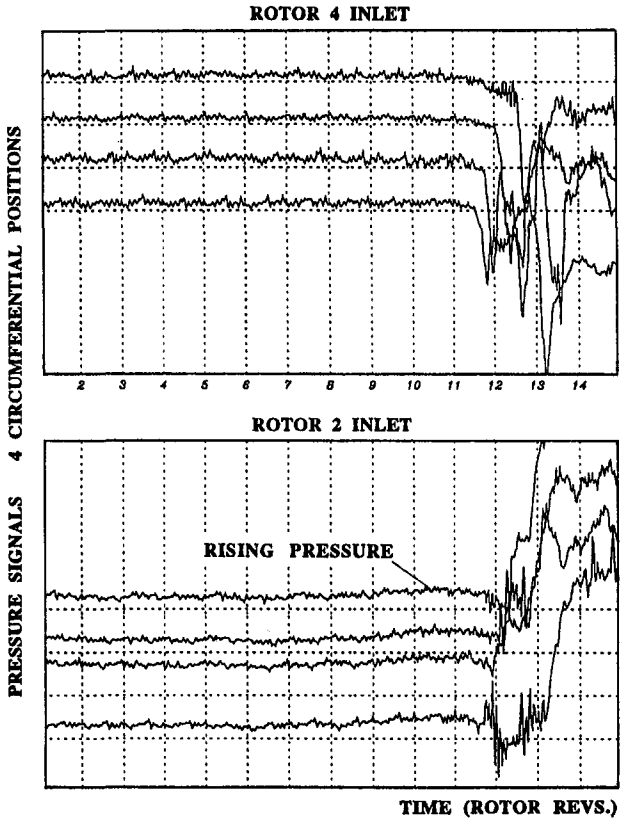

Fig. 10 Nonrotating pressure ramping prior to stall at full speed in the DRA compressor

The MTU compressor has only three stages and therefore the first stage in this machine may not be sufficiently mismatched to sustain front-end stall.

Stall Inception at Full Speed. Each of the four compressors stalls in a different way at high speed and it is difficult to make a clear statement of generic trends. All the compressors surge at this speed and in most cases the surge event is preceded by a brief period of rotating stall. The stalling process occurs very quickly. Less than three rotor revolutions separate the time at which the stall cell first appears and the time when reversed flow is fully established. The three rotor revolutions here should be contrasted with about five at lower speeds where the duration of each revolution is itself longer in time. Surge inception at high speed is thus a very rapid process. This is especially so in the DRA compressor where 10 ms divides axisymmetric forward flow from axisymmetric reversed flow.

In all of the compressors, flow breakdown at high speed seems to begin at a fixed circumferential position in the annulus. This is certainly true for all the SNECMA tests where the spikes preceding stall always appear at the same circumferential position, as confirmed by Escuret and Garnier (1996). In the other compressors, the flow breakdown process is less well defined, but still the impression is that the breakdown process always begins at one particular point on the casing.

Circumferential bias is also a feature of another interesting phenomenon that has been observed for the first time in these tests. In some cases the compressors show signs of protracted, nonrotating prestall flow disruption. In the DRA, Rolls-Royce and MTU compressors, a gentle rise in pressure over a period of three or four rotor revolutions sometimes appears prior to stall. This rise is like a slow ramp and can occur over a wide circumferential area, even axisymmetrically. An example of this type of "fixed-location stall" from the DRA compressor is shown in Fig. 10. Here the rise in pressure appears in the for-

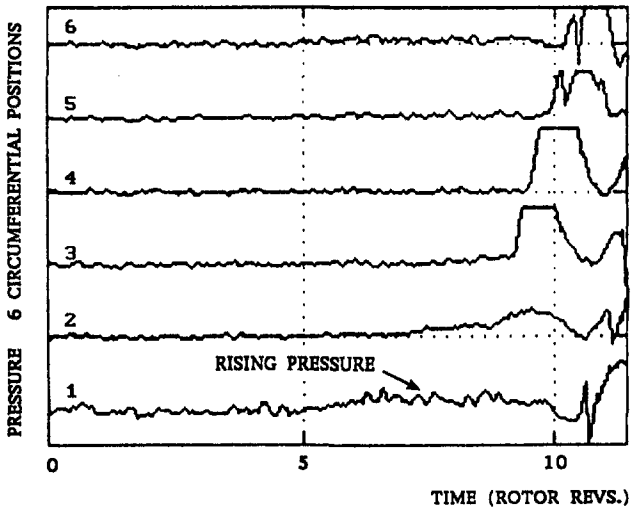

Fig. 11 Fixed location pressure ramping in the fourth stage of the Viper compressor at full speed

ward stages of the compressor all round the circumference. There is nothing to suggest any alteration in flow conditions further back in the compressor, as can be seen from the steadiness of the pressure traces at rotor 4 inlet. In the other compressors the ramping sometimes occurs over a narrower circumferential arc, as in the Viper compressor where only one pressure transducer out of six records the rise, Fig. 11. In this case the ramping occurs in the middle stages of the compressor and has no detectable effect at inlet or exit. (Further work is necessary to establish the physical structure of this type of disturbance.)

Considering all four compressors, the stalling behavior of each machine can be summarized as follows: The MTU machine shows signs of both modes and spikes. When modal activity appears, the speed of rotation of the disturbance is so slow that it could just as well be described as fixed-location pressure ramping. In the DRA compressor, the breakdown process takes place very quickly at the end of a period of fixed-location stall. In Fig. 10, for example, the actual breakdown of axisymmetric flow takes place in just one rotor revolution. Other examples from this compressor show that the breakdown process can occur even quicker than this. The SNECMA compressor exhibits spike-type stall even at high speeds. In the Viper compressor, rotating stall precedes surge, but the actual stalling process is hard to categorize. Fixed-location pressure ramping often occurs before stalling takes place.

Cargill and Freeman (1991) suggested that a blast wave spreading forward through the compressor could occur at high pressure ratios. In the MTU, SNECMA, and Rolls-Royce compressors, there is a clear period of rotating stall prior to flow breakdown and therefore blast wave effects are not expected to be present in these machines. In the DRA compressor, however, the flow break-down process is almost instantaneous and affects the entire circumference of the compressor, from front to rear, so quickly that sonic disturbances are a possibility. In Fig. 10 there is some indication of a sequential flow breakdown process ahead of rotor 4, but this takes place so quickly, in less than one rotor revolution, that an ordinary stall cell could not keep pace. Some of the other stalling events for this compressor are even less structured and occur more abruptly than shown here. While it has been suggested that rotating stall always precedes surge, it is hard to see how this can be true for this compressor, where the disturbance spreads faster than a stall cell can rotate.

The description given above of the peculiarities of each compressor confirms that stalling at high rotational speeds is a very complicated process. Each compressor behaves differently and not always in the same way from test to test.

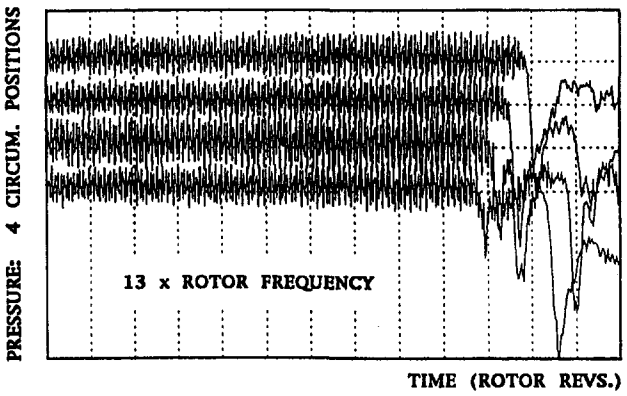

Fig. 12 High-frequency stall in the DRA compressor at full speed

High-Frequency Stall. High-frequency signals, between 10 and 13 times rotor frequency, were observed during testing of the DRA and SNECMA compressors. For both machines, the disturbances were detected at or near full speed and were audible in the test cell. In the case of the DRA compressor, the signal was sensitive to IGV setting. The audibility of the disturbances, and the sensitivity to IGV setting, suggest that data acquisition aliasing is not the origin of the disturbance. An example of the signals from each of the machines is given in Figs. 12 and 13. In both cases the perturbations are strongest at the rear, but detectable throughout the compressor. They appear only at the peak of the characteristic, not at higher flow rates, and can last for hundreds of revolutions before stall.

In a compressor with a large number of blades in each row, it is possible that signals of higher frequency than rotor passing can be generated by an array of very small stall cells. As a general rule, the smaller the stall cell, i.e., the fewer blades it covers, the faster it will rotate, rotor speed being the upper limit. Very small cells, like the spikes seen during stall inception, often rotate at more than 80 percent of rotor speed. An interesting example of a multicell stalling pattern, obtained during low-speed testing at the Whittle Laboratory, is given in Fig. 14. Here 11 part-span cells, affecting one out of every five blade passages and rotating at 82 percent speed, give rise to a passing frequency of 9 times rotor speed. A similar pattern of 10 small stall cells has also been observed in a high-speed industrial compressor (Day, 1993c).

This example of small stall cells creating a high-frequency disturbance seems to fit the SNECMA data very well. To begin

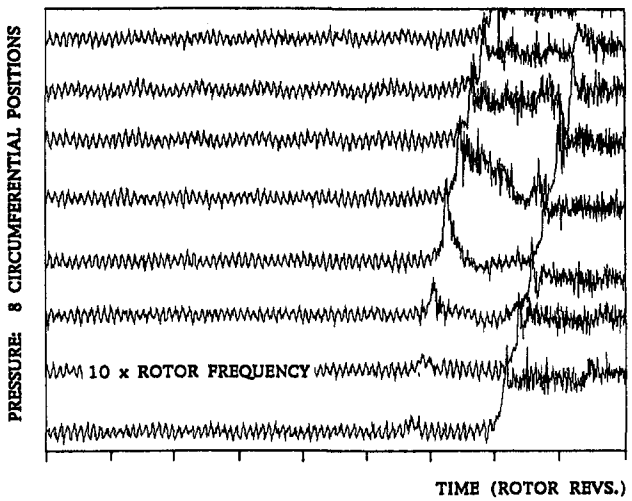

Fig. 13 High-frequency stall in the SNECMA compressor at full speed

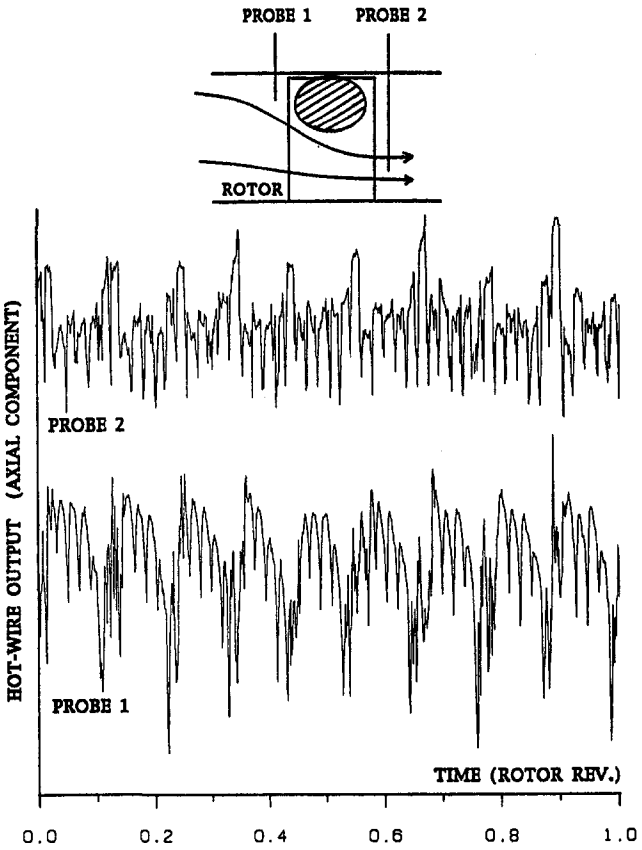

Fig. 14 Low-speed example of a multicell stall pattern in which every fifth blade is affected by a cell one pitch wide

with, the data show that the disturbance is definitely rotating and not axisymmetric. With 70 blades per row and one cell to every five blade passages, as in Fig. 14, we get a total of 14 stall cells. If, for argument's sake, we assume a rotational speed of 82 percent, as in the case above, this would give a passing frequency of 11 times rotor speed, which is fairly close to the measured value of 10 times. For the DRA compressor, a plausible explanation is not so easily found. The disturbance at each point around the circumference appears to be in phase and so the disturbance may be axisymmetric rather than rotating. It is possible of course that the number of stall cells is an exact multiple of the number of measuring probes, only four in this instance, and so the disturbance would have the appearance of being axisymmetric. There are numerous other possible explanations for these disturbances, e.g., acoustic resonance or unsteady shock waves. Further work on this topic is necessary, especially because of the possible excitation of blade vibration.

Shaft Order Perturbations. Shaft order perturbations are present to a greater or lesser extent in all compressors. This is because the concentricity of rotor and casing, the size of the tip clearance gaps, and the uniformity of the blade angles are never absolutely perfect throughout the entire compressor. All four machines in this study show signs of shaft order perturbations. The real point of interest here, however, is not the existence of the perturbations themselves, but whether or not the disturbance actually participates in the stalling process. It has been suggested by Hendricks et al. (1997) that high-speed modal perturbations may lock into shaft order disturbances with the combined effect of triggering stall. The results obtained from the current tests do not openly support this idea, but an in-depth study is in progress.

For the MTU compressor, shaft order disturbances are almost nonexistent at the lower compressor speeds but become more prominent toward the top end of the speed range. At low speeds, the traveling wave energy analysis of Tryfonidis et al. (1995) picks out a small once-per-revolution signal at the front of the compressor. At speeds closer to the maximum, the disturbance increases in intensity and becomes more pronounced at the rear. At full speed, the signal is clear enough to be visible by eye in the data traces. In terms of the growth of the perturbation as stall is approached, the traveling wave energy analysis suggests that the amplitude remains constant for hundred of revolutions before stall, the last twenty of which, at full speed, are shown in Fig. 15.

Analysis of the SNECMA and Rolls-Royce data suggests a similar trend with the shaft order signal becoming more pronounced at higher rotational speeds. The DRA machine exhibits slightly different behavior. In this case the shaft order perturbations are present at all speeds with a slight increase in amplitude at maximum speed. Little or no increase in the strength of the once-per-revolution signal could be detected during the approach to stall, except at 70 percent speed where a notable ramping of the signal occurred over the last 30 revolutions before stall.

Effects of Reynolds Number. Tests were conducted at MTU with the Reynolds number reduced to about half the normal value by throttling the incoming flow. A comparison of the stalling traces for normal and reduced inlet pressures shows no detectable differences in behavior. The differences between the two sets of results are no more than the usual differences between one test and the next. For these tests the average Reynolds number was reduced from 7×10^5 to 4×10^5. The latter number is unfortunately still above the threshold at which Reynolds Number usually has an effect on blade row performance. [Tests at the Whittle Laboratory have shown that the stall inception process is not affected right down to values of 0.4×10^5 (Day, 1993d).]

Inlet Distortion. Both MTU and Rolls-Royce conducted inlet distortion tests. From the Rolls-Royce data it was hard to identify any specific changes in the stalling behavior, especially at high speed where the stalling process is in any case very difficult to categorize. The MTU tests showed little effect on the stalling pattern at low speed, but at full speed the presence of the distortion screen was noticeable.

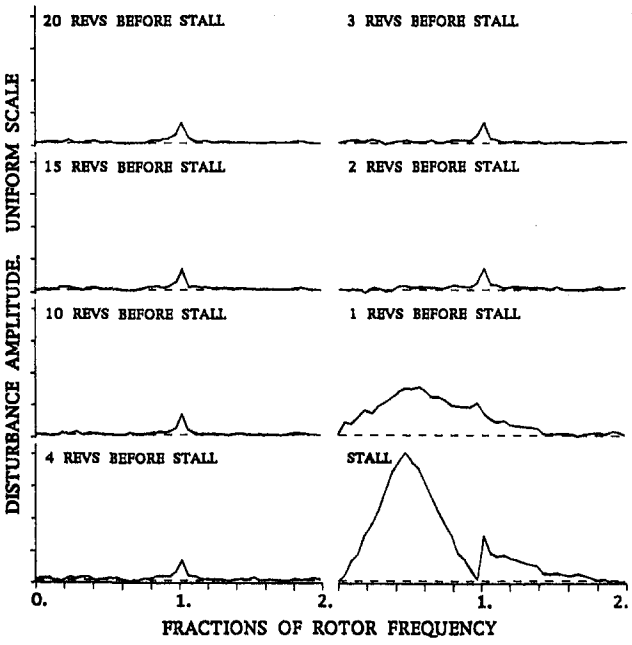

Fig. 15 Traveling wave energy analysis of MTU first-stage signals at full speed

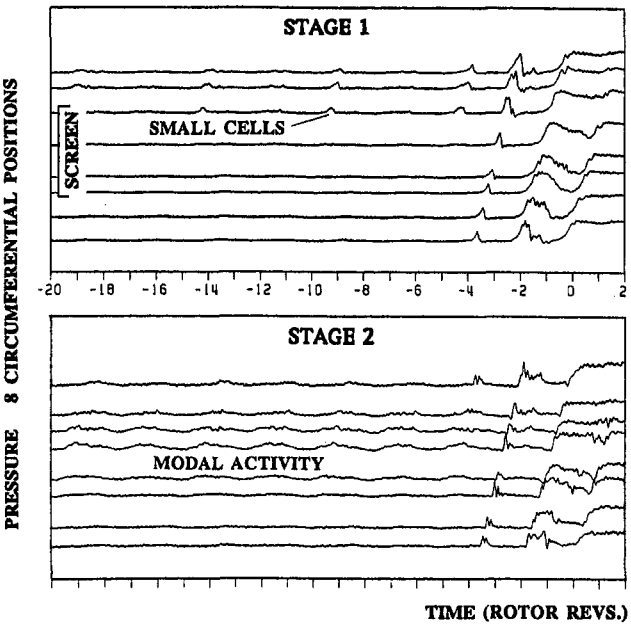

Fig. 16 Inlet distortion experiment in the MTU compressor showing modal activity and localised disturbances

Without the distortion screen at full speed, the MTU time traces show that stall is initiated by a mixture of spikes and modes, the modes sometimes moving so slowly as to be indistinguishable from a fixed-location pressure ramp. When the screen is present, modal activity is greatly increased and the perturbations can be detected many revolutions before stall. The modal oscillations are most pronounced in the middle of the compressor, stage 2, and appear at a frequency of about 42 percent rotor speed. At the front of the compressor, disturbances of shorter length scale, not quite short enough to be described as spikes, appear at regular intervals at the edge of the screen just where the rotor blades leave the distortion; see Fig. 16. These short-length-scale disturbances move at about 65 percent of rotor speed. What appears to happen is that each crest of the modal wave triggers a short-length-scale disturbance, which rotates half way around the annulus and then dies out. The next modal crest then sets off another short-length-scale disturbance and so on. In the end, stalling occurs when one of these disturbances becomes big enough to survive a complete revolution around the annulus and then grows to become a fully developed stall cell. This pattern is similar to that described in the work of Longley (1990). The interesting thing in this case is the noticeable increase in modal activity brought about by the distortion screen.

Data Analysis Studies

The data analysis carried out during this project had two distinct objectives: the first to pick out features of the stall inception process that could not be identified by eye and, the second, to examine the possibility of obtaining early warning of the approach of stall. The latter objective, if it could be achieved reliably, would provide a means of initiating corrective action, e.g., opening bleed valves, before stall actually occurs. This would provide an alternative to active control and would reduce the need for super fast actuators.

In the main, two analysis techniques were used:

1 Spatial Fourier decomposition of modes. This technique was proposed by Longley and used by McDougall et al. (1990). The signals from a circumferential ring of transducers are spatially decomposed at each instant of time to yield information on phase angle and amplitude of any circumferential disturbances.

2 Traveling wave energy analysis. This process was first implemented in a stall precursor context by Tryfonidis et al. (1995). It uses a windowing technique to monitor the build-up of the forward propagating wave energy of spatial modes. The objective here is to detect an increase in wave energy, of all forms, as far ahead of stall as possible.

The spatial Fourier technique proved very useful in identifying the physical details of modal activity prior to stall and provided a quantitative means of comparing the data from the respective compressors. The technique is, however, not well suited to the detection of short-length-scale disturbances and is therefore only useful over a limited range of compressor speeds. The traveling wave energy analysis worked very well, and, in the case of the DRA data, was able to point to the approach of stall some 50 to 100 revolutions before the actual event. For this machine, at compressor speeds where spike-type stall inception was present, the analysis was still effective but the warning period was reduced. For the other three compressors, the traveling wave energy analysis proved less effective as a stall warning technique and in some cases gave no warning at all, as for example in Fig. 15.

Some alternative methods of data analysis were also tried. SNECMA devised a scheme to deal with short-length-scale disturbances using a breadth-and-height filter (Escuret and Garnier, 1996). The results are good and particularly useful for their compressor where spike-type stall inception is predominant. MTU have developed a parameter identification technique aimed at picking out circumferential harmonics. The results are good, with first-order modal perturbations being correctly identified well before stall. Also tried was a noise signal analysis suggested by Rolls-Royce. The technique concentrates on frequencies in the stall propagation range and is often, but not always, able to detect a rise in power level as stall is approached.

Discussion: The Implications for Active Control

Active control, in the classical sense of the word, makes use of real time measurements from within the compressor to detect stalling disturbances and to take action to suppress them. The response of the system is thus tailored to the particular disturbance in the compressor at the time. A control system of this type must be capable of identifying and responding to all forms of stall inception. Any misinterpretation of the incoming signal will result in inappropriate instructions, which could cause the compressor to stall prematurely. The purpose of the current work is to relate the physical disturbances in the compressor to the signals received by the control system, the idea being that improved understanding of what happens in the compressor will lead to improved control systems.

It has been shown that both modal and spike-type stall inception occur in high-speed compressors. The structures of these disturbances are fairly well understood and algorithms are available to detect their presence. Of the two types, modal perturbations are the easiest to detect because they affect the whole compressor at once and therefore all the measuring probes around the compressor contribute toward identifying the disturbance. The more probes there are, the more reliable the detection process will be. The work on the four compressors tested here shows that modal activity is most likely to occur in the midspeed range.

By contrast, spike-type disturbances are most often present at low rotational speeds. In principal these disturbances are more difficult to track than modes because of the localized nature of the disturbance. The disturbance appears to originate from flow breakdown in a particular blade passage, and while the disturbance is small it has no measurable effect anywhere else around the circumference. Out of a circumferential array of probes, only one probe at a time will be affected by the disturbance, making early detection above the background noise

very difficult. In cases where a limited number of probes is deployed, it is even possible for a small disturbance to remain undetected while it travels from one measuring position to the next. As above, this problem can be reduced by using more sensing probes.

Apart from the modes and spikes above, there are other forms of instability in high-speed compressors that could have an influence on the reliable application of active control:

1 Front-end start-up stall: This usually consists of multiple stall cells, which give rise to a high passing frequency: perhaps 1.5 times rotor frequency. The disturbance itself is benign and over a short period of time does not harm the compressor and does not hinder acceleration to higher speeds. From an active control point of view, no corrective action is required in this case, but the control system must remain active to prevent these small cells from merging into a single cell, which could stall the compressor.

2 High-frequency stall: This type of disturbance was detected in the DRA and SNECMA compressors, Figs. 12 and 13. Here the high-frequency signals appear just before stall at full speed and actually mask the start of the surge event. The disturbance produces frequencies well above shaft speed and these can be of sizable amplitude. A successful control system will be expected to ignore these signals but will have to remain tuned to the underlying development of any surge event.

3 Abrupt stalling at full speed: In most of the tests reported here, some form of rotating stall is detected prior to surge. Active response to this type of disturbance is possible with modern actuators (Freeman et al., 1998). In the case of the DRA compressor, however, the flow becomes unstable so quickly, in less than one rotor revolution, that there appears little hope of suppressing the event.

4 Fixed-location stall: When a localized pressure ramp precedes a surge event, as shown in Figs. 10 and 11, the increased warning time may make it easier to sense the onset of instability, but whether or not this type of nonrotating pressure rise will respond to actuation is not known. Further work is necessary for a better understanding of this newly observed phenomenon.

5 Shaft order disturbances: This type of disturbance is present to a greater or lesser extent in all compressors and may or may not play a part in the stalling process. Because the frequency of the disturbance is precisely defined, it can, if necessary, be ignored by the control system.

6 Distorted inlet flow: Where inlet distortion is present, due either to nacelle separation, or to hot gas ingestion, the control system may receive signals of mixed type, i.e., spikes from one side of the compressor and modes from the other. To cope with this situation, the control system may require additional information from sensors external to the compressor to help identify the problem.

The list given above gives some idea of the variety of signals that may be observed during the operation of high-speed compressors. An individual compressor may not, of course, be susceptible to all of these problems, but it is useful to have foreknowledge of the possible range of signal that might be encountered; after all, changes in compressor behavior do occur during the lifetime of an engine and therefore all contingencies should be covered.

An alternative approach to the active control of stall is to disregard the physical details of the flow generating the incoming signals and to simply concentrate on deriving a stall risk index from the sum of all the inputs. The reliability of the index would be essential for a scheme like this, but as yet no system has been found that can provide a suitable signal under all operating conditions; the best scheme so far is the technique suggested by Tryfonidis et al., but this did not work well in all instances. Either way, active control or corrective control, the goal of building a flightworthy control system still seems to be some way off.

Summary and Conclusions

At the start of this project some stall inception information from high-speed machines was available in the literature, but gaps in the test ranges and the inadequacy of the instrumentation used means that very little could be gained from studying these data. A test program covering a range of compressor designs, and using dedicated instrumentation, was therefore set up to obtain the type of detailed information required.

- Both short-length-scale (spikes) and long-length-scale (modes) disturbances were detected in three out of the four compressors. A clear trend was observed with spikes appearing at low rotational speeds changing to modes in the midspeed range. [This trend is in line with the ideas of Camp and Day (1998) in terms of the influence of rotational speed on changes in stage matching.]
- A change of inlet guide vane setting will also change the stage matching in a compressor. The changes possible in the current series of experiments were not sufficient to cause a switch from short to long-length-scale disturbances, but in one compressor changes in the IGV setting certainly did affect the axial position at which short-length-scale disturbances first appeared.
- A new type of high-frequency disturbance was observed for the first time in two of the compressors when operating at full speed. This disturbance is thought to be the result of multiple part-span stall cells. (The findings are supported by similar observations in a low-speed compressor.)
- At full speed in three of the compressors, a nonrotating, fixed-location disturbance was detected just prior to stall. The disturbance extends over three or four rotor revolutions and takes the form of a gradual upward ramping of the pressure signals over part or all of the compressor annulus. The disturbance is usually limited to a particular axial location. There are no known prior references to this type of stalling behavior.
- In most cases rotating stall preceded surge at full speed, but the origins of the stall cell were not clearly identifiable in terms of modes and spikes. The growth of the stall cells also took place over fewer rotor revolutions than at lower operating speeds.
- In one of the compressors, flow breakdown at full speed occurred so quickly that rotating stall could not be detected before the event. The symmetry of the flow throughout the compressor was disrupted in the space of one rotor revolution. Fixed-location pressure ramping usually preceded the event.
- In line with previous low-speed experiments, tests on the effect of Reynolds number on stall inception showed no noticeable effect.
- Shaft order perturbations were detected in all the compressors and the intensity usually increased with the speed of rotation. At any particular speed, no consistent increase in the intensity of the disturbance could be detected as stall is approached.
- The imposition of inlet distortion was found to have little effect on stall inception patterns at low and intermediate speeds. It did, however, amplify the presence of modal perturbations at full speed in one of the compressors. The modes themselves triggered short-lived spikes, which meant that short-length-scale disturbances were detected on one side of the compressor and long-length-scale disturbances on the other.
- Various data analysis procedures were tried during the course of the project. Most were helpful in interpreting the data, but all failed in the search for a reliable stall warning signal.
- From an active control point of view, the results show that just being able to detect modes and spikes will not be sufficient in a high-speed compressor. A whole range of other low and high-frequency disturbances need to be taken into consideration.

Acknowledgments

Grateful acknowledgment is made of the funding for this work from the European Community's Brite Euram Civil Core

Compressor Program. The financial participation of MTU, SNECMA, the Defence Research Agency and Roll-Royce is also gratefully acknowledged. Not to be forgotten are the efforts of the support groups in each of the above organizations.

References

Camp, T. R., and Day, I. J., 1998, "A Study of Spike and Modal Stall Phenomena in a Low-Speed Axial Compressor," ASME JOURNAL OF TURBOMACHINERY, Vol. 120, pp. 393–401.

Cargill, A. M., and Freeman, C., 1991, "High-Speed Compressor Surge With Application to Active Control," ASME JOURNAL OF TURBOMACHINERY, Vol. 113, pp. 303–311.

Day, I. J., 1993a, "Stall Inception in Axial Flow Compressors," ASME JOURNAL OF TURBOMACHINERY, Vol. 115, pp. 1–9.

Day, I. J., 1993b, "Active Suppression of Rotating Stall and Surge in Axial Compressors," ASME JOURNAL OF TURBOMACHINERY, Vol. 115, pp. 40–47.

Day, I. J., 1993c, Letter to Mr. Borthwick, Brite Euram Co-ordinator, 10 May 1993.

Day, I. J., 1993d, Proprietary study for TEXACO OIL after repeated blade failure.

Day, I. J., and Freeman, C., 1994, "The Unstable Behavior of Low and High Speed Compressors," ASME JOURNAL OF TURBOMACHINERY, Vol. 116, pp. 194–201.

Epstein, A. H., Ffowcs Williams, J. E., and Greitzer, E. M., 1986, "Active Suppression of Aerodynamic Instabilities in Turbomachines," AIAA Paper No. 86-1994; also *Journal of Propulsion and Power,* Vol. 5, No. 2, pp. 204–211.

Escuret, J. F., and Garnier, V., 1996, ASME JOURNAL OF TURBOMACHINERY, Vol. 118, No. 4, pp. 690–696.

Freeman, C., Wilson, A., Day, I. J., and Swinbanks, M. A., 1998, "Experiments in Active Control of Stall on an Aeroengine Gas Turbine," ASME JOURNAL OF TURBOMACHINERY, Vol. 120, No. 4.

Gysling, D. L., and Greitzer, E. M., 1994, "Dynamic Control of Rotating Stall in Axial Flow Compressor Using Aeromechanical Feedback," ASME Paper No. 94-GT-292.

Haynes, J. M., Hendricks, G., and Epstein, A. H., 1993, "Active Stabilisation of Rotating Stall in a Three-Stage Axial Compressor," ASME Paper No. 93-GT-346.

Hendricks, G. J., Dabinis, J. S., and Feulner, M. R., 1997, "Analysis of Instability Inception in High-Speed Multi-Stage Axial-Flow Compressors," ASME JOURNAL OF TURBOMACHINERY, Vol. 119, pp. 714–722.

Longley, J. P., 1990, "Measured and Predicted Effects of Inlet Distortion on Axial Compressors," ASME Paper No. 90-GT-214.

McDougall, N. M., Cumpsty, N. A., and Hynes, T. P., 1990, "Stall Inception in Axial Compressors," ASME JOURNAL OF TURBOMACHINERY, Vol. 112, pp. 116–125.

Paduano, J., Epstein, A. H., Valavani, L., Longley, J. P., Greitzer, E. M., and Guenette, G. R., 1993, "Active Control of Rotating Stall in a Low Speed Axial Compressor," ASME JOURNAL OF TURBOMACHINERY, Vol. 155, pp. 48–56.

Tryfonidis, M., Etchevers, J. D., Paduano, J. D., and Epstein, A. H., 1995, "Prestall Behavior of Several High-Speed Compressors," ASME JOURNAL OF TURBOMACHINERY, Vol. 117, pp. 62–80.

Wilson, A. G., and Freeman, C., 1994, "Stall Inception and Development in an Axial Flow Aero-Engine," ASME JOURNAL OF TURBOMACHINERY, Vol. 116, No. 2.

A Shock Loss Model for Supersonic Compressor Cascades

G. S. Bloch

W. W. Copenhaver

Aero Propulsion and Power Directorate,
Wright Laboratory,
Wright-Patterson AFB, OH 45433

W. F. O'Brien

Mechanical Engineering Department,
Virginia Polytechnic Institute and
State University,
Blacksburg, VA 24061

Loss models used in compression system performance prediction codes are often developed from the study of two-dimensional cascades. In this paper, compressible fluid mechanics has been applied to the changes in shock geometry that are known to occur with back pressure for unstarted operation of supersonic compressor cascades. This physics-based engineering shock loss model is applicable to cascades with arbitrary airfoil shapes. Predictions from the present method have been compared to measurements and Navier–Stokes analyses of the L030-4 and L030-6 cascades, and very good agreement was demonstrated for unstarted operation. A clear improvement has been demonstrated over previously published shock loss models for unstarted operation, both in the accuracy of the predictions and in the range of applicability. The dramatic increase in overall loss with increasing inlet flow angle is shown to be primarily the result of increased shock loss, and much of this increase is caused by the detached bow shock. For a given Mach number, the viscous profile loss is nearly constant over the entire unstarted operating range of the cascade, unless a shock-induced boundary layer separation occurs near stall. Shock loss is much more sensitive to inlet Mach number than is viscous profile loss.

Introduction

The detailed design of transonic compressors is typically performed using a streamline curvature method of solution of the equations of fluid motion. The flow is assumed to be axisymmetric, and the effects of entropy generation are included as total pressure losses determined from loss models (e.g., Lieblein, 1954; Novak, 1967). These methods can be used either as analytical tools to predict the flow field from a known geometry, or in an inverse mode to predict the blade shape needed to generate a desired flow.

It has been suggested that the use of streamline curvature methods should be abandoned in favor of Navier–Stokes codes (e.g., Denton, 1994). While a direct numerical solution of the Navier–Stokes equations can yield a very detailed qualitative description of the flow field for a known geometry, there are still several limitations to the use of CFD in the design process. Navier–Stokes methods are quite expensive in terms of computer resources and time required for solution, and are currently unable to predict losses accurately. The inability to quantify loss accurately is a direct result of a poor fundamental understanding of turbulence and boundary layer transition, and this situation is not expected to improve in the near future (Casey, 1994b; Denton, 1993; Vuillez and Petot, 1994; Jennions, 1994). Also, such methods are not presently used in an inverse mode to provide the blade shape required to generate a desired flow field. In spite of these disadvantages, CFD is used extensively to obtain designs that operate closer to the physical separation and choking limits of the machine, and to reduce development time, expense, and risk. However, these CFD optimizations are performed on preliminary designs that are obtained by streamline curvature methods.

It is generally accepted that streamline curvature methods will provide a satisfactory prediction of compressor performance as long as the losses, blockage, and deviation are predicted accurately. As a result, it is expected that the use of these tools in the design process will continue for many years. It follows that there is wide agreement on the need for improvements in loss modeling to support the streamline curvature tools (Koch, 1995; Dunham, 1995; Casey, 1994a).

Miller et al. (1961) assumed that a normal shock extended from the blade leading edge to the suction surface, normal to the mean passage camber line, and calculated the loss from a single shock with a representative upstream Mach number. Wennerstrom and Puterbaugh (1984) also assumed a normal passage shock in the cascade plane, but included the spanwise sweep of the shock that results from the increase in stagger angle from hub to tip, and performed a three-point integration of the shock loss. Koch and Smith (1976) assumed that the passage shock generates the entropy rise equivalent to one oblique shock that reduces a representative passage inlet Mach number to unity, and included an empirical correlation to account for the leading edge bluntness.

The application of these models is restricted to design-point operation because they do not address the changes in shock geometry that occur with changes in back pressure. Calculation of off-design shock losses requires an accurate a priori knowledge of the shock geometry and Mach number (Balzer, 1971) or of flow angle significantly downstream of the shock (Freeman and Cumpsty, 1992), which limits the usefulness of these methods as predictive tools.

It would be desirable to have the ability to generate the entire compressor map from first principles so that a design could be optimized for maximum part-speed efficiency. This is where most man-rated engines spend the majority of their operating lives and this is where the largest benefit to the customer will be obtained. To realize this objective, the compressor designer must have the capability to perform accurate performance calculations over a range of back pressures and rotor speeds, and these calculations must be faster and cheaper than is currently possible with CFD codes.

This paper presents the application of compressible fluid mechanics to the changes in shock geometry that are known to occur with back pressure for unstarted operation of supersonic compressor cascades. This physics-based engineering shock loss model is applicable to cascades with arbitrary airfoil shapes.

Contributed by the International Gas Turbine Institute and presented at the 42nd International Gas Turbine and Aeroengine Congress and Exhibition, Orlando, Florida, June 2–5, 1997. Manuscript received International Gas Turbine Institute February 1997. Paper No. 97-GT-405. Associate Technical Editor: H. A. Kidd.

Table 1 Geometric and design-point aerodynamic parameters for L030 rotor and cascades

	L030-4 45% span	L030-6 68% span
stagger	48.51°	55.71°
s/c	0.621	0.678
t/c	0.05	0.04
LER/s	0.004035	0.003168
M_1	1.0913	1.2237
M_2	0.7167	0.8110
β_1	58.66°	61.95°
β_2	46.17°	54.03°
P_2/P_1	1.464	1.517

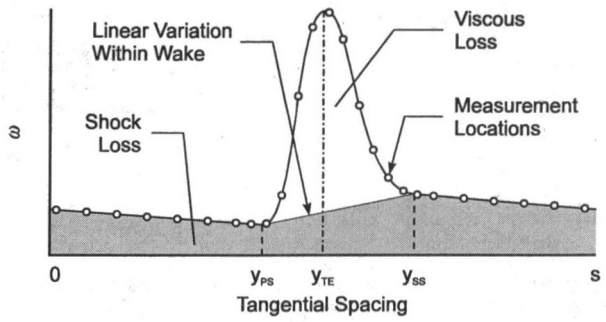

Fig. 1 Shock and viscous losses in the measuring plane downstream of supersonic cascade

Background

To assess the accuracy of the proposed shock loss model, the aero performance data from the L030-4 and L030-6 cascades are considered. These blade sections, which were tested at the DFVLR (now DLR), are the 45 percent span and 68 percent span of the L030 transonic research compressor rotor reported by Dunker et al. (1978) and Dunker and Hungenberg (1980). The major blade geometric parameters and design-point aerodynamic parameters for these cascades are listed in Table 1, and details of the cascade experiment are given by Schreiber (1980, 1981) and by Schreiber and Starken (1981).

The overall total pressure loss coefficients presented for this experiment were obtained by momentum-averaging the exit-plane measurements. The fractions of the overall loss that are the result of the viscous blade boundary layer and the passage shock system were approximated by area-averaging the local total pressure loss coefficient (Schreiber, 1987; Schreiber and Tweedt, 1987). The edges of the viscous wake region were determined from traverse measurements, as shown in Fig. 1, and the profile loss is given by

$$\omega_{\text{profile}} = \frac{1}{s}\int_{y_{ps}}^{y_{ss}} \omega dy - \frac{1}{s}\left(\frac{\omega_{y_{ps}} + \omega_{y_{ss}}}{2}\right)(y_{ss} - y_{ps}) \quad (1)$$

The shock loss was then calculated as the difference between the "mixed-out" overall loss and the approximated value of profile loss.

$$\omega_{\text{shock}} = \bar{\omega} - \omega_{\text{profile}} \quad (2)$$

Shock loss measurements from the aforementioned experiment were presented at discrete inlet flow angles by Schreiber (1987). Two flow angles were presented for the L030-6 cascade, and three flow angles for the L030-4 cascade. A typical curve is shown in Fig. 2.

In an effort to improve the understanding of the qualitative variation of shock loss between the known measurements, Navier–Stokes analyses of the L030-4 and L030-6 cascades have been conducted. These analyses used the RVCQ3D (Rotor Viscous Code Quasi-3-D) solver developed for the analysis of blade-to-blade flows in turbomachinery (Chima, 1987; Chima et al., 1987). Because viscous grids are typically much finer normal to the blade than in the streamwise direction, all viscous derivatives in the streamwise direction are dropped for lack of resolution (the "thin shear layer" approximation).

The RVCQ3D code uses a body-fitted C-type grid, which is typically generated using a version of the GRAPE code developed by Sorenson (1981). An explicit four-stage Runge–Kutta integration scheme was used to march forward in time from an initial guess to a steady-state solution (the number of integration stages is user-specified). A spatially varying time step and implicit residual smoothing were used to accelerate convergence, and the Baldwin–Lomax turbulence model was used. The code uses a fourth difference artificial dissipation term to prevent odd–even decoupling and a second difference artificial dissipation term for shock capturing. The method is generally second-order accurate, although it reduces to first-order near shocks.

For the present investigation, a 321 × 70 grid was used to obtain solutions for both the L030-4 and the L030-6 cascades. Although streamtube contraction is known to have a significant impact on cascade performance, the exit static pressure and the AVDR are strongly coupled and only limited independent variations are possible in the cascade tests. The typical experimental procedure is to set the inlet Mach number and exit static pressure as close as possible to the desired values, and then measure the AVDR obtained from these settings (Schreiber and Tweedt, 1987). Because the streamtube contraction is not measured within the blade passage, and because AVDR information was not published by Schreiber (1987), the CFD solutions were obtained with no streamtube contraction (AVDR = 1.0).

An Engineering Shock Loss Model

The scope of the present model is restricted to the total pressure loss produced by the passage shock system that exists during unstarted operation of a two-dimensional supersonic

Nomenclature

A = relative flow area
AVDR = axial velocity density ratio
c = blade chord
c_p = specific heat at constant pressure
F = compressible mass flow function
h = blade or streamtube height
LER = leading edge radius
$\dot{m}$ = mass flow rate
M = Mach number
P = pressure
s = tangential blade spacing
t = blade thickness
T = temperature
β = relative flow angle
γ = ratio of specific heats
υ = Prandtl–Meyer function
μ = Mach angle = $\sin^{-1}(1/M)$
ω = total pressure loss coefficient $= (P_{01} - P_0)/(P_{01} - P_1)$
$\bar{}$ = averaged property

Subscripts

A = conditions along first captured Mach wave
x = axial component
0 = total property
1 = conditions at upstream location
2 = conditions at downstream location

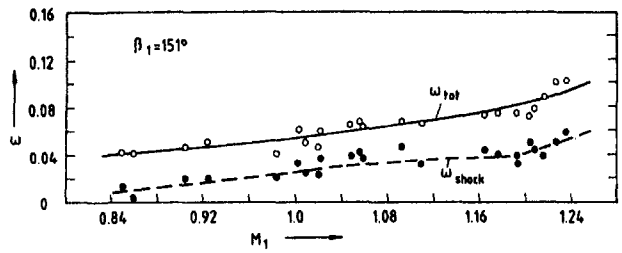

Fig. 2 Influence of inlet Mach number on measured total pressure losses and corresponding shock losses of the L030-6 cascade (Schreiber, 1987)

compressor cascade with arbitrary airfoil shapes. It is recognized that viscous effects related to the blade boundary layer and any shock–boundary layer interactions can have a significant impact on performance, but these effects must be addressed separately. Many treatises on the calculation of the minimum-incidence operating condition exist in the literature (e.g., Kantrowitz, 1950; Levine, 1956; Starken, 1971; Lichtfuss and Starken, 1974) so it will be treated briefly here. This is commonly referred to as the "unique incidence" condition, and these are the inlet conditions that exist at the cascade start/unstart point.

Consider an infinite cascade operating with an inlet flow that is supersonic relative to the blade but has an axial component that is subsonic, as shown in Fig. 3. The flow upstream of the passage shock is assumed to be steady and inviscid. The present investigation is restricted to stationary cascades, so the total temperature is constant everywhere. Because the axial component of the flow is subsonic, the Mach waves emanating from the suction surface move upstream of the blade, allowing the cascade to influence the upstream flow. The curvature of the left-running characteristics caused by the detached bow shock is neglected in the present analysis, although the total pressure loss from the bow shock is included in the continuity equation in an approximate way, as suggested by Starken et al. (1984).

As the flow passes around the leading edge, it will undergo a Prandtl–Meyer expansion from the upstream flow angle to be aligned with the blade suction surface. The first captured Mach wave extends from point A to the point where the stagnation streamline intersects the bow shock at point B. The flow region extending upstream from the first captured Mach wave is generally referred to as the "inlet region" or the "entrance region" of the cascade. The location of point A depends on suction surface curvature and upstream Mach number, and is determined by iteratively solving the Prandtl–Meyer and continuity relations. The Prandtl–Meyer relation is given by

$$\beta_1 + \nu(\mathrm{M}_1) = \beta_A + \nu(\mathrm{M}_A) \tag{3}$$

where ν is the well-known Prandtl–Meyer function:

$$\nu(\mathrm{M}) = \sqrt{\left(\frac{\gamma+1}{\gamma-1}\right)}\tan^{-1}\sqrt{\left(\frac{\gamma-1}{\gamma+1}\right)(\mathrm{M}^2-1)} - \tan^{-1}\sqrt{\mathrm{M}^2-1} \tag{4}$$

The continuity relation is given by

$$\dot{m} = \frac{F(\mathrm{M}_1)P_{01}s\cos\beta_1}{\sqrt{c_pT_{01}}} = \frac{F(\mathrm{M}_A)P_{0A}|\overline{AB}|\sin\mu_A}{\sqrt{c_pT_{0A}}} \tag{5}$$

where F is the following compressible mass flow function:

$$F(\mathrm{M}) = \frac{\dot{m}\sqrt{c_pT_0}}{P_0A} = \frac{\gamma}{\sqrt{\gamma-1}}\mathrm{M}\left\{1+\frac{\gamma-1}{2}\mathrm{M}^2\right\}^{-(\gamma+1)/2(\gamma-1)} \tag{6}$$

In general, supersonic compressor blading has some finite leading edge radius for damage tolerance and this causes the bow shock to be slightly detached from the leading edge. The shape of this detached bow shock is approximated as a hyperbola that is normal to the flow directly ahead of the blade and asymptotically approaches the freestream Mach lines, as suggested by Moeckel (1949). The vertex of this hyperbola is located at the vertex of a wedge, with half-angle 1 deg larger than the half-angle corresponding to shock detachment, placed tangent to the blunt leading edge, as shown in Fig. 4. The shape of the bow shock defined in this manner is uniquely determined by the upstream Mach number and the blade leading edge radius.

The Mach number immediately upstream of the bow shock will not be completely uniform because of the (generally) nonzero suction surface curvature and the deceleration produced by the infinite number of upstream bow waves. These variations are expected to be small, however, and the bow shock is treated as though it were in a uniform stream. The total pressure loss from the bow shock is then estimated by numerically integrating the loss from a single wave between the stagnation streamline, point B, and infinity (Klapproth, 1950):

$$\frac{P_{0A}}{P_{01}} = 1 - \frac{\int_0^\infty (1 - P_{02}/P_{01})dy}{\int_0^s dy} \tag{7}$$

where P_{02}/P_{01} is obtained from oblique shock theory.

If the back pressure is increased enough to unchoke the cascade, the passage shock will detach and move upstream of the blade leading edge by an amount Δx, as shown by the solid lines in Fig. 3. As the passage shock moves upstream, the stagnation streamline will shift toward the suction surface of

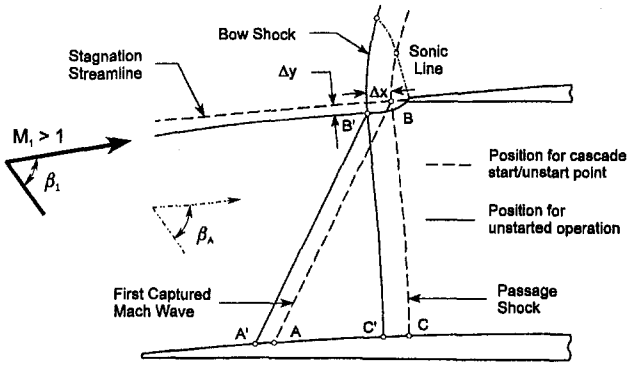

Fig. 3 Idealized wave structure in the entrance region of a supersonic compressor cascade

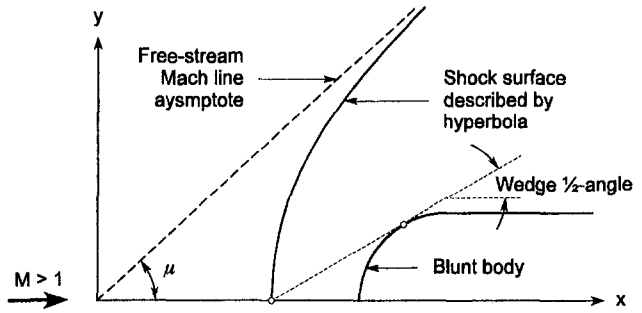

Fig. 4 Detached shock waves approximated by the Moeckel (1949) method

the lower adjacent blade by an amount Δy to provide the typical path for subsonic flow approaching an airfoil. (Point B' is located by extending a line upstream from point B by an amount Δx at an angle β_A relative to the axial direction and translating normal to this line, toward the suction surface, by an amount Δy.) These two effects cause the first captured Mach wave to move upstream and to become shorter. Because Eqs. (3) and (5) must always be satisfied, Δx and Δy are the primary mechanisms that allow the upstream flow angle to increase above the minimum value. Operation with a detached passage shock is commonly referred to as an "unstarted" cascade.

The relation between Δx and Δy for unstarted operation is not currently described by theory. To gain some understanding of this variation, the stagnation streamline was plotted from the unstarted CFD solutions generated for the L030-6 cascade with inlet Mach numbers of 1.100 and 1.200. The variation of Δx and Δy between choking and stall was then scaled from these stagnation streamlines for each Mach number, and was adequately described by the following relation:

$$\Delta x = 6\Delta y \tag{8}$$

To be clear, it is not suggested that this relation will be exactly correct for all blade profiles. Although the relation between Δx and Δy was similar for both of the cases described above it is anticipated that this relation will be slightly different for every blade shape and Mach number combination considered. It is suggested, however, that the shock detachment distance has a much smaller effect on the incidence calculation than does the stagnation streamline shift and that any reasonable variation will likely be within the accuracy of the method. While other investigators have neglected the detachment distance entirely (e.g., Starken, 1971), the present method uses the relation as an approximate means to include more fully the effects of suction surface curvature on the length and position of the first captured Mach wave.

As the operating point moves from choke toward stall, the bow shock moves upstream from the blade leading edge and the strong shock region increases, as was shown in Fig. 3. The bow shock is pushed forward because there is subsonic flow everywhere behind the passage shock and the downstream pressure information can move upstream around the blade leading edge. Although this mechanism is understood in a broad sense, its effects are difficult to quantify and the shape of the unstarted bow shock can only be predicted with difficulty, even if a Navier–Stokes solver is employed.

Because more of the total flow passes through the strong portion of the bow wave during unstarted operation, it is reasonable to anticipate that the loss produced by the bow shock will increase with incidence angle. An approximation of this increased loss has been included in the present model by using an increased "effective leading edge radius" to calculate the bow shock loss for unstarted operation. (The physical coordinates of the blade clearly remain the same, and this increased "effective" leading edge radius is used only in the bow wave loss calculation.)

In the Moeckel (1949) method, the blade leading edge radius is used to calculate the distance between the stagnation streamline and the smooth portion of the blade surface (i.e., the thickness of the forward-most portion of the blade). Because this distance increases by the amount of the stagnation streamline shift during unstarted operation, it is the present authors' opinion that the effective leading edge radius used in the bow shock calculation should be proportional to Δy. Examination of the CFD solutions indicated that the curvature of the sonic line becomes more pronounced after the shock detaches, as represented in Fig. 3, suggesting that the effective leading edge radius should increase by somewhat less than Δy.

Recognizing this as an empirical input, the effective leading edge radius used in the bow shock calculation was adjusted to provide satisfactory agreement with the shock loss extracted from CFD for a *single* operating point. The comparison was made for the L030-6 cascade with $M_1 = 1.200$ and $\beta_1 = 64.83$ deg (near stall), and resulted in the following approximation:

$$\text{LER}_{\text{bow shock loss}} = \text{LER}_{\text{blade}} + \Delta y/2 \tag{9}$$

This relation provided the "effective leading edge radius" used to calculate the bow shock loss for all operating conditions. Clearly, this reduces to the actual blade leading edge radius for the cascade start/unstart point, where $\Delta y = 0$. The Moeckel (1949) method is used to approximate the shape of the detached bow shock using the Mach number along the first captured Mach wave, M_A, and this "effective leading edge radius." The total pressure loss caused by this wave is then calculated from Eq. (7).

Before leaving this subject, an important point must be made. While a number of simplifying assumptions have been introduced in the present analysis, Eq. (9) represents the only strictly empirical input. The remainder of the present method is obtained by using fundamental fluid mechanics, with certain simplifications and approximations, to analyze the known flow physics.

Passage Shock Position. The passage shock for the cascade start/unstart point is slightly curved and has no supersonic flow downstream. A hyperbola, as described by Moeckel (1949), is used to represent the curved portion of the passage shock between the vertex, B, and the point where the downstream flow is exactly sonic, s, as shown in Fig. 5. From the sonic point to the blade suction surface, the passage shock is approximated by a straight line normal to the stagnation streamline at point B. The decrease in total pressure caused by this shock is obtained by numerical integration using 200 points across the passage. The number of points used in this integration was chosen to allow accurate physical-space location of the shock transition point, s.

The integration steps are determined by equally dividing the axial distance between the blade suction surface coordinate at the first captured Mach wave and at the passage shock intersection point (points A and C in Fig. 3). At each point along the blade surface, the Mach number is calculated as a Prandtl–Meyer expansion (or compression) from the upstream condition and a Mach line is extended to the passage shock. For precompression blades, the deceleration produced by the suction surface is assumed to occur isentropically, as a Prandtl–Meyer expansion of opposite sign. As such, this method is applicable to arbitrary airfoil shapes. The variations of upstream Mach number and shock angle are included in the passage shock integration, and the mass-averaged total pressure downstream of the passage shock is given by

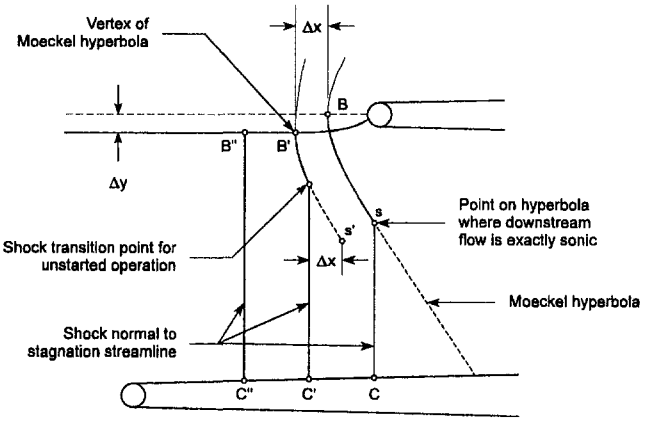

Fig. 5 Assumed shape of passage shock for unstarted operation

$$\frac{\bar{P}_{02}}{P_{0A}} = \frac{\int_B^C \rho V_x \, (P_{02}/P_{0A}) dy}{\int_B^C \rho V_x dy} \tag{10}$$

As the incidence angle increases, the shock detachment distance increases by an amount Δx and the stagnation streamline shifts by an amount Δy. The vertex of the hyperbola is assumed to follow these translations from point B to point B' so that it is always located where the stagnation streamline intersects the bow/passage shock. The curved portion of the shock is reduced by moving the shock transition point forward of the new sonic point, s', by an amount Δx. When the shock transition point reaches the vertex of the hyperbola, the entire shock is approximated as a straight line normal to the stagnation streamline at point B'. As the shock detachment distance continues to increase, the passage shock is approximated as a straight line, normal to the stagnation streamline, from point B'' to point C''. The total pressure ratio across the passage shock is given by Eq. (10).

Model Predictions

The total pressure loss coefficients for unstarted operation of the L030-6 cascade with an inlet Mach number of 1.20 are shown in Fig. 6. As stated previously, the CFD solutions were obtained with no sidewall variation (AVDR $\equiv$ 1). The points labeled "Experiment" were obtained from Schreiber (1980), while the points labeled "Fit to Data" were obtained from the shock loss curves fit by Schreiber (1987) to his measurements (i.e., by evaluating the dashed curve labeled ω_{shock} in Fig. 2). The CFD solutions are shown to provide fairly accurate prediction of the overall loss for the entire operating range of this cascade. This suggests that the RVCQ3D Navier–Stokes analysis tool can be used to supplement the available measurements and that the differences between these predictions and the measurements are likely to be small.

The most significant point made by this figure is the dramatic increase in shock loss as the inlet flow angle increases. This is shown clearly by the data, by the CFD solutions, and by the model predictions. The viscous profile loss predicted by the CFD is seen to be nearly constant over the entire unstarted operating range, with a variation of less than 0.010 between the minimum and maximum unstarted loss coefficients. The actual viscous loss is likely to be slightly larger near stall than indicated by the CFD solutions, which show a suction surface boundary layer separation downstream of the passage shock. It

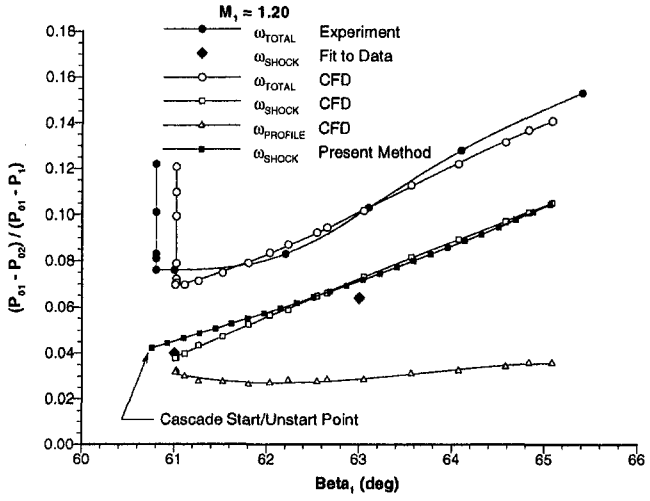

Fig. 6 Loss coefficient comparison for unstarted operation of the L030-6 cascade with M_1 = 1.20

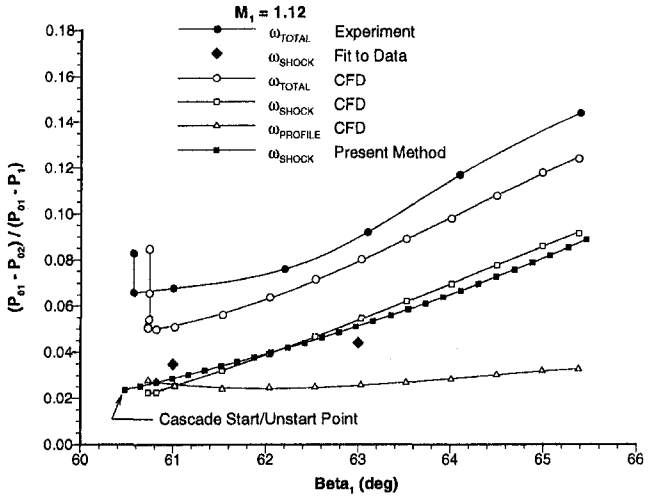

Fig. 7 Loss coefficient comparison for unstarted operation of the L030-6 cascade with M_1 = 1.12

is the authors' opinion, however, that the actual variation of viscous loss between stall and choke will still be significantly smaller than the variation of shock loss over the same operating range.

To understand the significance of the level of accuracy demonstrated in this figure, it is helpful to consider the recent ASME turbomachinery CFD "blind" test case (Strazisar and Denton, 1995). To obtain an accuracy of ± 1–2 percent in pressure rise and of ± 1 percent in efficiency in that test case, the predicted total pressure loss coefficient must be accurate within 0.010 (Dunham, 1995). Although the viscous loss has not been addressed in the present method, the accuracy of the predicted shock loss coefficients in Fig. 6 clearly falls within this range.

Figure 7 shows the total pressure loss coefficients for unstarted operation of the L030-6 cascade with an inlet Mach number of 1.12. As before, there is a significant increase in shock loss with incidence, the viscous profile loss is nearly constant (0.009 difference between maximum and minimum), and the present shock loss model predictions are within the desired 0.010 accuracy.

To illustrate another trend shown in the two previous figures, the shock loss and viscous profile loss coefficients obtained from the CFD solutions for the L030-6 cascade are plotted in Fig. 8. The shock loss is clearly much more sensitive to Mach number than is the profile loss. For the Mach number range considered, the increase in shock loss with Mach number is 3 to 18 times as large as the increase in profile loss (assuming β_1 is held fixed). This observation supports Schreiber's (1987) conclusion that the increase in total pressure loss that occurs with increasing Mach number is predominantly caused by an increase in shock loss.

The present shock loss predictions have shown good agreement with both the experimental measurements and the CFD results for unstarted operation of the L030-6 cascade over the range of inlet Mach numbers considered. Agreement with this data set alone, however, cannot be considered as proof of the general applicability of the method because the empirical constant in the bow shock model was adjusted to match the performance of this cascade (although at a single near-stall condition). To further establish the validity of the present shock loss model, the performance of the L030-4 cascade was predicted. Because there are significant differences in profile shape and blade angles between these two configurations, and because empirical information from the L030-4 cascade test was not used to develop the model, this is a true prediction that can be used to evaluate the accuracy of the present method.

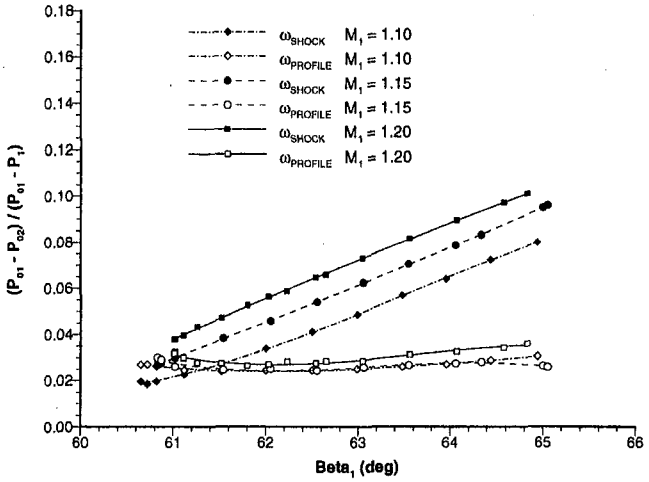

Fig. 8 Comparison of the shock loss and viscous profile loss coefficients obtained from the CFD solutions for unstarted operation of the L030-6 cascade

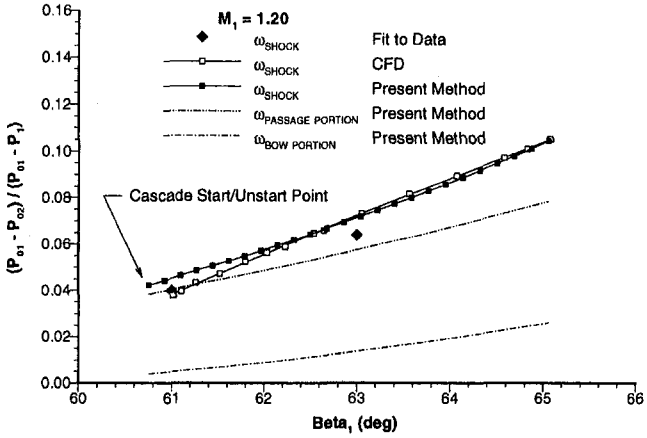

Fig. 10 Identification of loss attributed to passage shock and to bow wave for unstarted operation of the L030-6 cascade with $M_1 = 1.20$

The total pressure loss coefficients for unstarted operation of the L030-4 cascade with an inlet Mach number of 1.10 are shown in Fig. 9. The CFD solutions show a strong increase in shock loss with increasing inlet flow angle, as was shown for the L030-6 solutions, while the viscous profile loss is nearly constant (0.007 difference between maximum and minimum). As in the previous figures, the desired accuracy of 0.010 between the present shock loss model predictions and the available validation tools has been demonstrated for the L030-4 cascade.

Discussion. The present prediction method considers the total pressure deficit that is produced by the detached bow waves that stand ahead of the cascade. While Starken et al. (1984) suggested this effect be included in the continuity equation for the minimum-incidence calculation, it has not been included in previously published shock loss models. To demonstrate the significance of the bow shock loss as a fraction of the present shock loss prediction, the following bow shock loss coefficient is defined:

$$\omega_{\text{bow}} = \frac{P_{01} - P_{0A}}{P_{01} - P_1} \tag{11}$$

where P_{0A}/P_{01} is the total pressure reduction caused by the detached bow shock (obtained from Eq. (7)). A passage shock loss coefficient is then defined as the difference between the predicted shock loss coefficient and the bow shock loss coefficient:

$$\omega_{\text{passage}} = \omega_{\text{shock}} - \omega_{\text{bow}} \tag{12}$$

Figure 10 identifies the bow-shock and passage-shock loss components of the present prediction method for unstarted operation of the L030-6 cascade with inlet Mach number of 1.20.[1] The trends shown in this figure are representative of the other operating points considered for both the L030-6 and L030-4 cascades. The measured shock loss coefficients and the values obtained from CFD are included for comparison, but the overall loss and the viscous loss obtained from CFD are omitted from this figure for clarity.

The bow shock loss is shown to be small at the cascade start/unstart point, with a value of 0.004. This is consistent with observations of the CFD solutions, which indicate that the rotational effects of the bow shock are small during started operation and, except for a small region near the blade surface, that the entrance-region characteristics are nearly straight. The bow shock loss increases significantly with incidence, and is about 0.025 near stall. This is again consistent with the CFD solutions, which indicate that the strong portion of the bow wave extends farther from the blade as incidence increases.

The present bow wave calculation has significant effects on the predicted shock loss coefficients. While the effect of this bow shock is small at the start/unstart point, it is clearly important as incidence increases. This suggests that the bow shock produces a significant fraction of the shock loss during unstarted operation, and that this mechanism must be included in an off-design performance model. Another effect is that inclusion of the bow shock loss in the continuity equation results in a slightly higher Mach number along the first captured Mach wave. This higher Mach number then produces passage shock loss coefficient that is between 0.002 and 0.010 larger than if the bow wave loss were neglected.

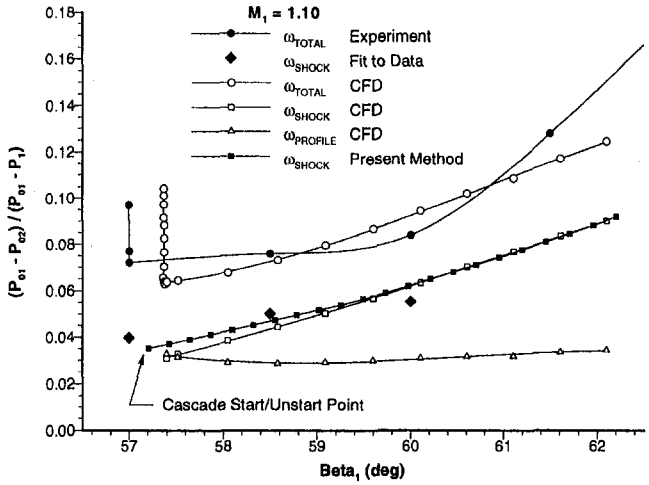

Fig. 9 Loss coefficient comparison for unstarted operation of the L030-4 cascade with $M_1 = 1.10$

Comparison With Previously Published Models. The curved portion of the unstarted passage shock is small and the entire passage shock can be reasonably approximated as a normal shock, as suggested by Miller et al. (1961) and by Wennerstrom and Puterbaugh (1984). Both of these models calculated the Mach number at the suction surface shock impingement point as a Prandtl–Meyer expansion from the upstream condition, as has been done in the present method. In the previous

[1] Symbols are omitted from the bow shock and passage shock loss curves in Fig. 10 to indicate that these are only a *portion* of the present shock loss prediction method and should not be considered separately.

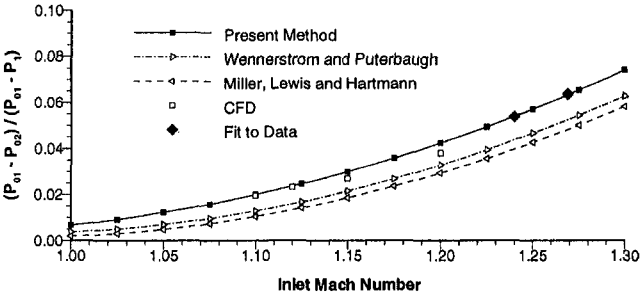

Fig. 11 Comparison of shock loss prediction methods for the L030-6 cascade start/unstart point as a function of inlet Mach number

models, however, the Mach number on the pressure side of the passage (the blade leading edge) was assumed to be the upstream value rather than the value along the first captured Mach wave. Because the flow undergoes a Prandtl–Meyer expansion around the blade leading edge, the Mach number along the first captured Mach wave is generally higher than the upstream value and these methods will slightly underpredict the loss.

In the present investigation, both the upstream Mach number and the shock obliqueness angle are determined by extending a Mach line from the suction surface to the passage shock at 200 locations. This approach allows a more accurate inclusion of the nonlinear effects of Mach number and shock angle on total pressure loss than do the previously published methods. The improved agreement obtained from the present method is shown in Fig. 11 for the start/unstart point of the L030-6 cascade operated over a range of inlet Mach numbers. Comparison with the Miller et al. (1961) and the Wennerstrom and Puterbaugh (1984) shock loss models over a range of inlet flow angles is not possible because the previously published methods are applicable only at the minimum overall loss point (i.e., the cascade start/unstart point).

Conclusions

A physics-based model has been presented for the prediction of shock losses over the entire supersonic operating range of compressor cascades with arbitrary airfoils. This model has been shown to capture the shock loss trends and magnitudes accurately for unstarted operation of both the L030-4 and L030-6 cascades for the range of inlet Mach numbers considered, and the following conclusions can be drawn from this investigation:

- The dramatic increase in overall loss with increasing inlet flow angle is primarily the result of increased shock loss. For a given Mach number, the viscous profile loss is nearly constant over the entire unstarted operating range of the cascade, unless a shock-induced boundary layer separation occurs near stall.
- Much of the increased total pressure loss that occurs with increasing incidence is caused by the detached bow shock.
- Shock loss is much more sensitive to inlet Mach number than is viscous profile loss.

Acknowledgments

The authors wish to thank Rod Chima of the NASA Lewis Research Center for providing the quasi-three-dimensional Navier–Stokes solver used in the present investigation, for explanation of the appropriate boundary conditions, and for general advice on interpretation of the solutions. Gratitude is also expressed to Dan Tweedt of NASA Lewis for some fairly lengthy discussions on the difficult nature of supersonic compressor cascade testing and the limitations of these test results. Heinz-Adolf Schreiber of the DLR has provided the measured blade coordinates from the L030 cascade tests. While these are available in the published literature, the electronic transfer of these coordinates avoided the tedious and error-prone process of typing them in by hand.

In addition, the authors would like to thank the members of the Compressor Aero Research Lab team who have contributed to the present effort. Finally the authors thank the management at Wright Laboratory and Air Force Office of Scientific Research for their continued support of our research efforts.

References

Balzer, R. L., 1971, "A Method of Predicting Compressor Cascade Total Pressure Losses When the Inlet Relative Mach Number Is Greater Than Unity," ASME *Journal of Engineering for Power,* Vol. 93, pp. 119–125.

Casey, M. V., 1994a, "Computational Methods for Preliminary Design and Geometry Definition in Turbomachinery," AGARD LS-195, Paper No. 1.

Casey, M. V., 1994b, "Industrial Use of CFD in the Design of Turbomachinery," AGARD LS-195, Paper No. 6.

Chima, R. V., 1987, "Explicit Multigrid Algorithm for Quasi-Three-Dimensional Viscous Flows in Turbomachinery," AIAA *Journal of Propulsion and Power,* Vol. 3, No. 5, pp. 397–405.

Chima, R. V., Turkel, E., and Schaffer, S., 1987, "Comparison of Three Explicit Multigrid Methods for the Euler and Navier–Stokes Equations," NASA TM-88878.

Denton, J. D., 1993, "Loss Mechanisms in Turbomachines," ASME JOURNAL OF TURBOMACHINERY, Vol. 115, pp. 621–656.

Denton, J. D., 1994, "Designing in Three Dimensions," AGARD LS-195, Paper 3.

Dunham, J., 1995, "Aerodynamic Losses in Turbomachines," AGARD CP-571, Keynote Address.

Dunker, R. J., Strinning, P. E., and Weyer, H. B., 1978, "Experimental Study of the Flow Field Within a Transonic Axial Compressor Rotor by Laser Velocimetry and Comparison With Through-Flow Calculations," *Transactions of the ASME,* Series A, Vol. 100, p. 279.

Dunker, R. J., and Hungenberg, H. G., 1980, "Transonic Axial Compressor Using Laser Anemometry and Unsteady Pressure Measurements," *AIAA Journal,* Vol. 18, pp. 973–979.

Freeman, C., and Cumpsty, N. A., 1992, "A Method for the Prediction of Supersonic Compressor Blade Performance," AIAA *Journal of Propulsion and Power,* Vol. 8, No. 1, pp. 199–208.

Jenions, I. K., 1994, "The Role of CFD in the Design Process," AGARD LS-195, Paper No. 8.

Kantrowitz, A., 1950, "The Supersonic Axial-Flow Compressor," NACA Report 974.

Klapproth, J. F., 1950, "Approximate Relative-Total-Pressure Losses of an Infinite Cascade of Supersonic Blades With Finite Leading-Edge Thickness," NACA RM E9L21.

Koch, C. C., 1995, "Loss Mechanisms and Unsteady Flows in Turbomachines," AGARD CP-571, Technical Evaluation Report.

Koch, C. C., and Smith, L. H., 1976, "Loss Sources and Magnitudes in Axial-Flow Compressors," ASME *Journal of Engineering for Power,* Vol. 98, pp. 411–424.

Levine, P., 1956, "The Two Dimensional Inflow Conditions for a Supersonic Compressor With Curved Blades," Wright Air Development Center TR 55-387.

Lichtfuss, H.-J., and Starken, H., 1974, "Supersonic Cascade Flow," DFVLR Sonderdruck Nummer 376, reprinted in *Progress in Aerospace Science,* Pergamon Press Ltd., Vol. 15.

Lieblein, S., 1954, "Review of High-Performance Axial-Flow Compressor Blade Element Theory," NACA RM E53L22.

Miller, G. R., Lewis, G. W., and Hartmann, M. J., 1961, "Shock Losses in Transonic Compressor Blade Rows," ASME *Journal of Engineering for Power,* Vol. 83, pp. 235–242.

Moeckel, W. E., 1949, "Approximate Method for Predicting Form and Location of Detached Shock Waves Ahead of Plane or Axially Symmetric Bodies," NACA TN 1921.

Novak, R. A., 1967, "Streamline Curvature Computing Procedures for Fluid-Flow Problems," ASME *Journal of Engineering for Power,* Vol. 93, pp. 478–490.

Schreiber, H.-A., 1980, "Untersuchungen am Verdichtergitter L030-6 im transsonischen Machzahlbereich von $M_1 = 0,8$ bis 1,24-Schaufelschnitt des Transsonikverdichter-Laufrades 030 bei 68 percent Schaufelhöhe," DFVLR IB 352-80/2.

Schreiber, H.-A., 1981, "Experimentelle Untersuchung des Verdichtergitters L030-4 mit Variation des axialen Massenstromdichteverhältnisses im transsonischen Machzahlbereich," DFVLR IB 325|4|1981.

Schreiber, H.-A., 1987, "Experimental Investigations on Shock Losses of Transonic and Supersonic Compressor Cascades," AGARD CP-401, Paper 11.

Schreiber, H.-A., and Starken, H., 1981, "Evaluation of Blade Element Performance of Compressor Rotor Blade Cascades in Transonic & Low Supersonic Flow Range," presented at the Fifth International Symposium on Airbreathing Engines, Paper No. 67, Bangalore, India.

Schreiber, H.-A., and Tweedt, D. L., 1987, "Experimental Investigation and Analysis of the Supersonic Compressor Cascade ARL-2DPC," DFVLR IB-325-02-87.

Sorenson, R. L., 1981, "A Computer Program to Generate Two-Dimensional Grids About Airfoils and Other Shapes by the Use of Poisson's Equation," NASA TM-81198.

Starken, H., 1971, "Untersuchung der Strömung in ebenen Überschallverzögerungsgittern (Investigation of the Flow in Planar Supersonic Compressor Cascades)," DFVLR FB 71-99.

Starken, H., Zhong, Y., and Schreiber, H.-A., 1984, "Mass Flow Limitation of Supersonic Blade Rows Due to Leading Edge Blockage," ASME Paper No. 84-GT-233.

Strazisar, A. J., and Denton, J. D., 1995, "CFD Code Assessment in Turbomachinery—A Progress Report," IGTI *Global Gas Turbine News.*

Vuillez, C., and Petot, B., 1994, "New Methods, New Methodology: Advanced CFD in the SNECMA Turbomachinery Design Process," AGARD LS-195, Paper No. 7.

Wennerstrom, A. J., and Puterbaugh, S. L., 1984, "A Three-Dimensional Model for the Prediction of Shock Losses in Compressor Blade Rows," ASME *Journal of Engineering for Gas Turbines and Power,* Vol. 106, pp. 295–299.

A Study of Acoustic Resonance in a Low-Speed Multistage Compressor

T. R. Camp
Rolls-Royce plc,
Derby, United Kingdom

Measurements are presented of a resonant acoustic phenomenon occurring in a low-speed multistage compressor. The results show that this phenomenon shares many characteristics with acoustic resonance as measured in high-speed compressors. These similarities include a rotating pressure field, several acoustic frequencies corresponding to different circumferential modes, step changes in frequency as the flow rate is increased, and acoustic frequencies that are independent of flow coefficient, shaft speed, and the axial length of the compression system. The paper includes measurements of the helical structure of the rotating pressure field and of the variation in amplitude of the acoustic signal over a stator exit plane.

Introduction

An important consideration during the design and development of axial flow compressors is that the amplitudes of blade stresses must remain below critical values at all operating points to ensure adequate fatigue life. Blade vibrations can be excited by a number of mechanisms, of which the most documented phenomena include blade row interaction effects (resulting from the wakes and potential fields of adjacent blade rows), flutter, rotating stall and surge. In recent years another source of blade excitation has been observed, characterized by:

- frequencies of excitation that are not necessarily integral multiples of the shaft frequency,
- frequencies that change in a way not closely related to blade stiffness,
- step changes in the excitation frequency as the compressor shaft speed is changed,
- large-amplitude pressure fluctuations, which lead to high blade stresses when the pressure fluctuation frequency is coincident with a natural frequency of blade vibration,
- high amplitudes of fluctuating pressure and blade stresses occurring in regions of irregularities in the flow-field such as bleed slots or blade rows operating at extreme incidence.

Although at present the phenomenon is poorly understood, the limited amount of experimental data available suggests that this excitation is associated with a resonant acoustic condition of the compressor annulus and/or bleed cavities. The link with the acoustics of the system has been revealed by measurements of a fluctuating pressure field, which rotates about the compressor axis at a speed near the local speed of sound. Results also show that the phenomenon is sensitive to the annulus geometry and to the compressor inlet conditions in a manner consistent with an acoustic signal. Although in the past this phenomenon has been confused with other failure mechanisms such as flutter, sufficient evidence now exists to regard this as a distinct source of blade vibration, which has been termed "acoustic resonance."

The details of this phenomenon are not well understood, partly because there exists only a very limited amount of test data. Measurements of acoustic resonance in high-speed machines have been difficult to obtain for three reasons. First, experimental studies of acoustic resonance on high-speed compressors are difficult to perform because the high blade stresses normally lead rapidly to blade failure. Second, when the phenomenon has been detected in a high-speed compressor, the demands of commercial time scales have meant that once the source of vibration has been removed, by whatever means, compressor development has continued without a thorough investigation of the phenomenon. Third, the financial cost of running a high-speed compressor for sufficient time to complete a full investigation of the phenomenon is very high. In contrast, low-speed compressor rigs offer much lower running costs and are subject to stresses several orders of magnitude below their high-speed equivalents. For these reasons, a study of acoustic resonance on a low-speed multistage compressor is very desirable, provided that it can be shown that the low-speed and high-speed phenomena are similar. In the past, measurements of an acoustic resonance on a low-speed compressor have been limited to a single-stage machine (first reported by Parker, 1967).

The C106 compressor at the Whittle Laboratory, Cambridge University, is a four-stage low-speed compressor, containing blading that is representative of modern high-speed compressors. The compressor includes a variable stator mechanism that allows the inlet guide vanes and stator blade rows to be easily restaggered. The compressor has a constant outer radius of 254 mm and a hub–tip ratio of 0.75. A more detailed description of the compressor is given by Camp (1995). By operating the C106 compressor at high flow coefficients, with the variable stators at certain off-design settings, it was found that the compressor emitted tones at a series of discrete frequencies that could be clearly heard above the blade passing frequency and the background broad-band noise. Because the C106 is a multistage compressor with a flow-field representative of contemporary high-speed compressors, this rig is very suitable for a study of acoustic resonance relevant to high-speed machines.

Review of Previous Work

Acoustic resonance has been detected in the past in high-speed and low-speed, single-stage and multistage machines, but there is little consistency in the understanding of the phenomenon between different classes of machine. This is particularly true of the distinction between low-speed compressors, on which most previous research work has concentrated, and high-speed machines, for which very few detailed measurements of acoustic resonance exist. In this section a brief introduction is given to the structure of acoustic waves in annular ducts. Following this, we consider vortex shedding from struts or blade

Contributed by the International Gas Turbine Institute and presented at the 42nd International Gas Turbine and Aeroengine Congress and Exhibition, Orlando, Florida, June 2–5, 1997. Manuscript received International Gas Turbine Institute February 1997. Paper No. 97-GT-259. Associate Technical Editor: H. A. Kidd.

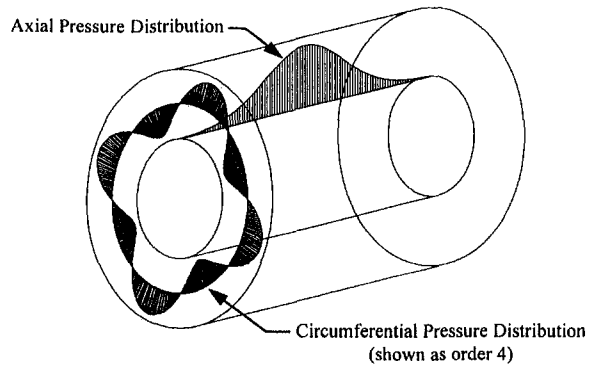

Fig. 1 Illustration of circumferential and axial pressure distributions

rows in the compressor as a possible mechanism for exciting a resonant condition.

Structure of Acoustic Waves in Annular Ducts. The structure of acoustic signals in annular ducts can be calculated by solving the homogeneous wave equation in cylindrical coordinates, as outlined in a pioneering paper by Tyler and Sofrin (1962). In a stationary fluid the three-dimensional wave equation simplifies to

$$\frac{\partial^2 p}{\partial t^2} - c^2 \nabla^2 p = 0 \tag{1}$$

If we assume a narrow duct and therefore neglect variations in the radial direction, we can assume a solution of the form $p(\theta, t, x) = \Theta(\theta)T(t)X(x)$. If we consider one component of the time-dependent function T at frequency ω and one component of the circumferentially varying function Θ with order m, amplitude a_m, and phase ϕ_m, then the functions Θ and T can be combined and, for $x = 0$, the solution written as,

$$p(\theta, t, 0) = a_m \exp i(m\theta - \omega t + \phi_m)$$

where the real part is implied. Note that it is necessary for m to be an integer so that the variation of pressure in the θ direction is continuous and repeats every 2π rad, as required by the cylindrical geometry. In this form the pressure distribution at any axial plane can be interpreted as an m-lobed pattern, as illustrated in Fig. 1. This pressure distribution rotates at ω/m rad/s and generates at every point a fluctuating pressure at frequency ω. The pattern sweeps the annulus walls at a velocity $r_o\omega/m$ where r_o is the radius of the duct. This velocity can be expressed as a Mach number by dividing by the velocity of sound in free space c,

$$\mathrm{M}_\theta = \frac{r_o \omega}{mc} \tag{2}$$

By substituting the expression

$$p(\theta, t, x) = a_m \exp i(m\theta - \omega t + \phi_m) \times X \tag{3}$$

into Eq. (1), an ordinary differential equation is obtained for the function X. This can be solved to find

$$X = b_m \exp(\pm i k_x x) \tag{4}$$

where b_m is a constant and k_x is the axial wavenumber defined by

$$k_x = \frac{m}{r_o}\sqrt{M_\theta^2 - 1} \tag{5}$$

The axial variation in the pressure distribution takes one of two very different forms, depending on the magnitude of the circumferential Mach number M_θ. If M_θ is less than unity, k_x is imaginary and the function X is real. In this case the pressure field decays exponentially in the axial direction with no change of phase. There is no energy transfer in the axial direction and the acoustic wave is described as "cut-off." Because energy cannot propagate through cut-off regions, energy that is input to the system by any source of excitation accumulates, and is manifested by high amplitudes of the fluctuating pressure field. If M_θ is greater than unity, k_x is real and the function X is complex. This case corresponds to a pressure wave, which propagates in the axial direction with changing phase and no reduction in amplitude. The structure of this wave, which allows energy to propagate in the axial direction, is described as "cut-on." The wavefronts of this wave trace out m helices, which rotate about the axis of the duct at ω/m rad/s.

The solution method outlined above assumes a narrow, empty duct at constant radius with no flow. In a real compressor, however, the annulus has a finite span and encloses rotating and stationary blade rows, while the mean flow velocity is normally a significant proportion of the local speed of sound. The annulus areas of real compressors vary in the axial direction, and the temperature of the fluid (and therefore the speed of sound) increases with axial distance. Each of these factors adds considerable complication to the solution of the wave equation, which, as a result, cannot generally be solved without approximation. Despite these effects, the structure of the wave in the circumferential and axial directions, whether cut-on or cut-off, remains similar to the expressions given above.

Vortex Shedding as an Excitation Mechanism. Having described the structures with which acoustic waves may resonate and propagate in annular ducts, we note that significant amplitudes will only result when there is a source of excitation that provides an energy input to the disturbance. Extensive work by Parker and his colleagues at the University College of Swansea has shown that a possible source of excitation is the mechanism of vortex shedding from struts or blade rows at high incidence (Parker and Stoneman, 1989). The phenomenon of wake excitation of resonances is well known in other areas of engineering; bridges and chimneys, for example, can be forced to resonate by the shedding of vortices. In a similar way, bluff bodies in ducts can shed vortices in their wakes, which interact with the flow-field. In the cases of external structures, the surrounding fluid is effectively infinite in extent and resonance occurs when the frequency of vortex shedding is equal to, or close to, the natural frequency of mechanical vibration of the structure. In a duct the condition for resonance is subtly different: In this case, acoustic resonance occurs when the natural frequency of vortex shedding is approximately equal to the

Nomenclature

a, b = signal amplitude
c = speed of sound in free space
Ch = blade chord
D = characteristic dimension
f = frequency, Hz
k = wavenumber
m = circumferential order
M = Mach number
p = static pressure
r = radius
St = Strouhal number
t = time
T = function of time
U = blade velocity
v = flow velocity
v_a = axial flow velocity
x = axial distance
X = function of axial distance
θ = circumferential angle
λ = wavelength
ϕ = phase angle
Θ = function of θ
ω = frequency, rad/s

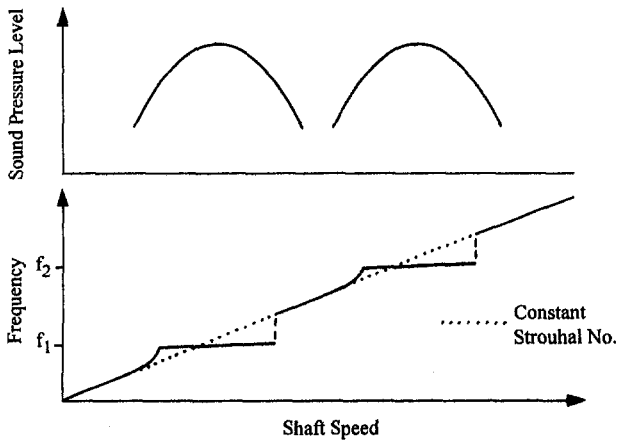

Fig. 2 Two "locked-on" resonant frequencies (after Parker and Stoneman, 1989)

acoustic resonant frequency of the duct. It has been found that when the natural frequency of vortex shedding is close to the resonant frequency of the duct, the frequency of vortex shedding will "lock on" to the acoustic frequency (Cumpsty and Whitehead, 1971). If this frequency is also equal to one of the natural frequencies of blade vibration, then the amplitude of the acoustic signal is reinforced and the vibration of the blade can lead to very high mechanical stresses. Blade stresses are found to be particulary large if the vibrating blade is also the source of the shed vortices because the correlation between the vortex shedding and the mechanical vibration is then very high.

For significant blade vibration to occur as a result of a vortex-driven acoustic resonance, there are therefore three frequencies that must approximately coincide: a natural frequency of vortex shedding, an acoustic resonant frequency of the duct (including blades), and a natural frequency of blade vibration. The occurrence of such an event is not as rare as it might first appear when one considers the number of blade rows in a typical compressor, each of which can shed vortices at a number of frequencies (Welsh and Gibson, 1979) and vibrate in several flexural and torsional modes. Acoustic resonance of the duct may also occur at several frequencies corresponding to different circumferential and radial orders.

The frequency at which vortices are shed by a body can be related to its dimensions and the velocity of the fluid by an approximately constant value of the Strouhal number, defined by

$$\text{Strouhal number St} = \frac{fD}{v} \tag{6}$$

Previous measurements have shown that the natural frequency of vortex shedding for an isolated flat plate or strut is given by a Strouhal number of approximately 0.20, based on trailing edge thickness. At a resonant condition, however, this value of Strouhal number may change significantly, as shown by Koch (1985). If the boundary layer thickness at the trailing edge of the body is significant, or if the plate or aerofoil is stalled, the distance between the shear layers on either side of the wake is a more appropriate dimension for the Strouhal number calculation.

For vortex shedding at a constant Strouhal number, the frequency of vortex shedding f is proportional to the velocity v. For a compressor blade row operating at a constant value of flow coefficient, v_a/U, the frequency of vortex shedding is proportional to U and therefore to the shaft speed. As the shaft speed of the compressor increases or decreases, the frequency of vortex shedding will sweep a range of frequencies and will tend to excite the acoustic modes in that range. As the frequency of vortex shedding "locks on" to different acoustic modes, step changes occur in the frequency of the acoustic signal as illustrated in Fig. 2. This stepping in mode or wavenumber is observed in high-speed compressors as one of the distinctive characteristics of acoustic resonance. This observation therefore supports the hypothesis that vortex shedding is the mechanism by which the resonance is excited. However, at the present time this has only been confirmed experimentally at low Mach numbers in cascades and in a single-stage low-speed compressor.

Experimental Results From a Low-Speed Compressor

Rig Geometry and Instrumentation. An acoustic phenomenon was first detected on the C106 compressor at a high flow operating point when the stagger angles of the IGV and stator blade rows were reduced by 10 deg from their design settings. Because the main purpose of these experiments was to assess the similarity of the phenomenon to acoustic resonance as found in high-speed machines, no attempt was made to map the phenomenon over a range of stagger angles or flow coefficient. Instead, a geometry and flow coefficient were chosen at which the amplitude of one of the acoustic signals (at 1420 Hz) was significantly larger than signals at surrounding frequencies, thereby making this signal easier to measure. Accordingly, all experiments were performed with the stagger of the IGV and all stator rows reduced by 10 deg from their design values and, unless otherwise stated, at a flow coefficient of 0.85.

At this operating point the rotor incidence angle was −9.6 deg at midspan while the stator incidence was approximately −25 deg. Previous experience from high-speed compressors suggests that when acoustic resonance is associated with a mismatched blade row, it is normally associated with high positive incidence. However, negative incidence angles can cause similarly wide wakes and could therefore cause vortices to be shed at similar frequencies. The axial velocity field was measured downstream of the stator 3 exit plane at the test operating point. In Fig. 3 the measured flowfield is compared with the flowfield at the design operating condition, showing the increased width of the stator wake on the pressure side of the blade at the acoustic resonance condition.

For most of the experiments described in this paper, the acoustic signal was measured using arrays of Kulite transducers. These transducers were mounted flush with the outer annulus wall of the compressor, a position that gave two advantages: First, the annulus walls are always pressure antinodes regardless of the radial order of the signal (the radial pressure gradient must be zero at a hard wall) and so the pressure signal was

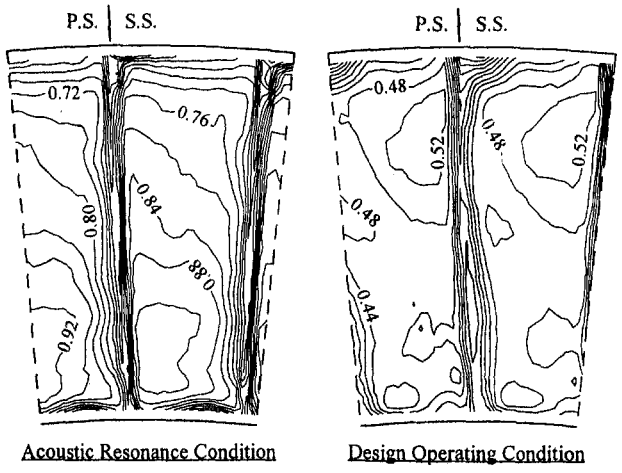

Fig. 3 Contours of axial velocity at the stator 3 exit plane (nondimensionalized by midheight rotor speed)

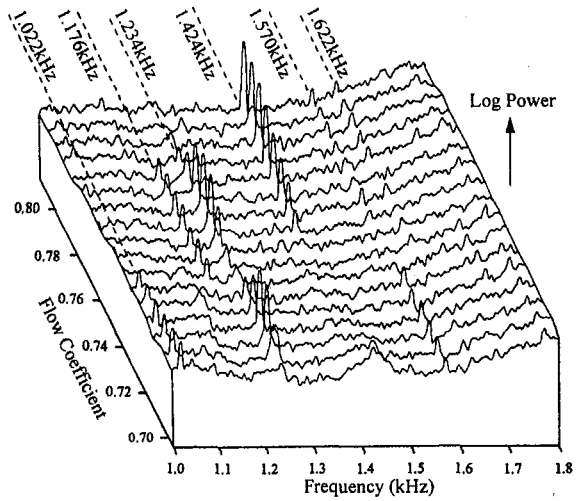

Fig. 4 Pressure amplitude spectra as a function of flow coefficient

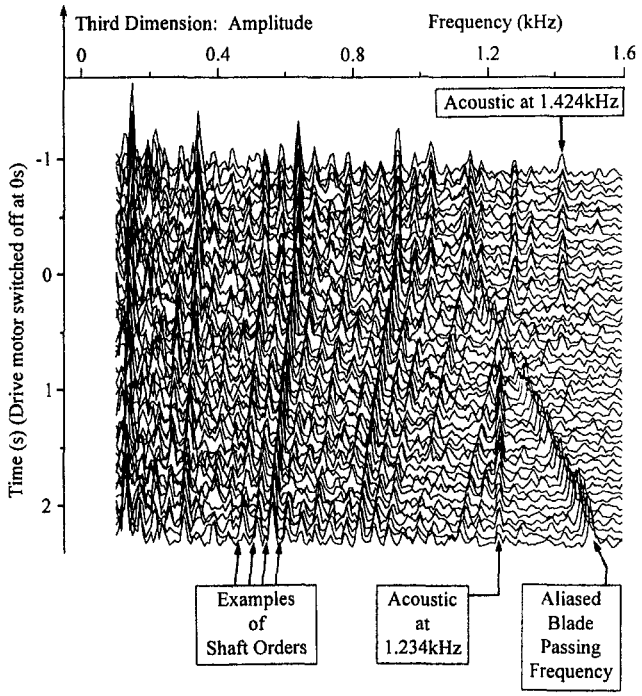

Fig. 5 Pressure amplitude spectra as a function of deceleration time

always clear, and second, in this position the transducers offered no obstruction to the flow. It was found that high frequency-response pressure transducers were more sensitive to the acoustic signal than hot-wire probes.

Preliminary Spectral Analysis. After first detecting the acoustic signals as audible tones above the background noise of the compressor, a preliminary investigation was made using a pressure transducer and a spectrum analyzer. The transducer was used to measure static pressure perturbations at the compressor inlet plane over a range of flow coefficient between 0.70 and 0.81. Figure 4 shows the measured spectra for frequency components between 1.0 and 1.8 kHz. The spectra in Fig. 4 show clear peaks at six frequencies, of which the most prominent and most audible signal was at 1.424 kHz. Although this figure suggests that each peak covers a considerable range of frequencies, this is a consequence of the short sampling period used by the spectrum analyzer. Measurements made using a longer sampling period showed that each acoustic signal occupied a very narrow bandwidth. Of the six peaks identified in Fig. 4, four of these occur at frequencies close to integral multiples of 204 Hz, as shown in Table 1. This relationship was first identified by Cargill (1993).

Table 1 suggests that the four signals are consistent with rotating pressure patterns of orders 5, 6, 7, and 8. (The observation that the relationship between frequency and mode number is not *exactly* linear is consistent with previous measurements, such as those reported by Parker, 1968.) Assuming that this is the case, a Mach number based on the circumferential phase velocity at the tip radius and the speed of sound in free space can be calculated approximately using Eq. (2) as follows:

$$M_\theta = \frac{2\pi r_{tip} f}{mc}$$

Taking $m = 1$, $f = 204$ Hz, $r_{tip} = 254$ mm, $c = 344$ m/s (speed of sound at 295 K), gives $M_\theta = 0.95$. We see that these modes

Table 1 Measured acoustic frequencies expressed as factors of 204 Hz

Frequency (Hz)	Multiple of 204Hz
1022	5.01
1234	6.05
1424	6.98
1622	7.95

are cut-off because the value of M_θ is less than unity at the tip radius (and therefore lower still at other radii). A more rigorous calculation of this Mach number (or "cut-off ratio") can be performed for a particular mode at the respective propagation radius (at which a plane uniform wave appears to propagate at the velocity of sound). For a mode 7 pattern the propagation radius is 223.9 mm and M_θ equals 0.83. This value is consistent with values that have been measured on high-speed compressors, which have been found to lie between 0.8 and 0.9.

It is likely that the two remaining signals shown in Fig. 4 at 1176 Hz and 1570 Hz are the 23rd and 31st harmonics of the shaft frequency (49.1 Hz). Close examination of Fig. 4 reveals that as the flow coefficient through the compressor was increased, the amplitudes of the acoustic signals varied such that the largest amplitudes moved to higher frequency components. At a flow coefficient of 0.70 the largest amplitude of the acoustic signals occurs at 1022 Hz. At a higher flow coefficient of 0.76 the largest amplitude acoustic signal occurs at 1234 Hz, while at a still higher flow coefficient of 0.81 the largest amplitude acoustic signal occurs at 1424 Hz. This stepping in frequency of the signal is a characteristic of acoustic resonance and is consistent with the hypothesis that vortex shedding is the excitation mechanism.

Changes in Spectrum With Shaft Speed. A characteristic of acoustic resonance as observed in high-speed compressors is that the frequency associated with any particular wave structure is approximately independent of shaft speed. (The degree to which the frequency is exactly constant is a function of the damping of the acoustic signal, as found by Smith, 1991.) Although the C106 compressor does not have variable speed control, a series of spectra was measured using a Kulite transducer mounted at the IGV inlet plane while the power to the drive motor was switched off and the shaft allowed to decelerate. The results of these measurements are shown in Fig. 5 as a carpet plot of pressure spectra. During the first two seconds of deceleration, the most prominent acoustic signal is the component at 1234 Hz, which remains at a constant frequency while the frequencies of the surrounding shaft orders fall. This characteristic of the C106 acoustic phenomenon is therefore consistent with experience of acoustic resonance in high-speed compres-

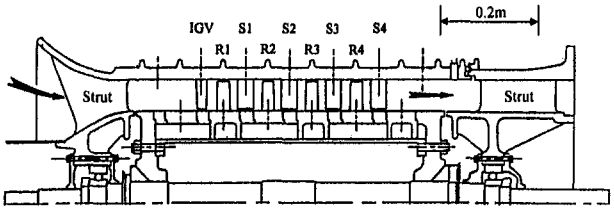

Fig. 6 Cross-sectional view of the C106 compressor

sors. (The aliased component at blade passing frequency shown in this figure was present despite low-pass filtering the signal at 2 kHz owing to the very large amplitude of this signal.)

Changes in the Spectrum With Duct Length. When studying an acoustic phenomenon, it is necessary to consider all volumes of the compression system. Figure 6 shows details of the compressor and the positions of six struts in the bearing housings at compressor inlet and exit, while Fig. 7 shows the associated ducting upstream and downstream of the compressor. The frequency of an acoustic resonance signal, as described above, depends on the circumferential order of the wave, m, and on the effective speed of sound in the circumferential direction, $M_\theta c$. From Eq. (2),

$$\omega = \frac{m M_\theta c}{r_o} \tag{7}$$

where M_θ depends principally on the solidity of the blading, as shown by Meyer and Neumann (1972). The frequencies of acoustic resonance signals are therefore not predicted to depend on the axial length of the compression system. To test the C106 acoustic phenomenon against this criterion, tests were performed using three different lengths of ducting between the compressor and the downstream throttle. The short, datum, and long ducts produced distances of 1070 mm, 1270 mm, and 1770 mm between the stator 4 exit plane and the throttle valve, respectively. In each case the exit ducting was annular with the same inner and outer radii as the compressor section. For each length of duct, the compressor geometry and flow coefficient were set to give the same operating point (as previously described) and pressure spectra were measured using a Kulite transducer mounted at the stator 4 exit plane.

The results of these measurements are summarized in Table 2, which shows the frequencies corresponding to the peak amplitude of the acoustic signal and the ambient temperatures at which the spectra were measured. After normalizing these frequencies to account for variations in the speed of sound with temperature, it was found that the acoustic frequency was exactly constant at 1402.1 Hz for each of the three duct lengths. These results show that the frequency of the acoustic signal was independent of changes in the axial length of the compression system and that, in this respect, the structure of the wave is consistent with the theoretical description given earlier.

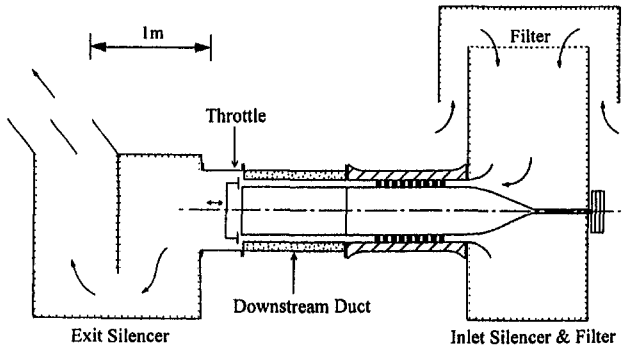

Fig. 7 Schematic layout of the C106 facility

Table 2 Comparison of acoustic frequencies measured at 3 duct lengths

Duct Length: S4 t.e.→throttle (mm)	Frequency at Peak Amplitude f_{pk} (Hz)	Ambient Temperature T_{amb} (K)	$f_{pk} \times \sqrt{\frac{288}{T_{amb}}}$
1067	1417.5	294.4	1402.1
1274	1418.9	295.0	1402.1
1771	1422.5	296.5	1402.1

Phase Variation. The structure of the acoustic signal in the C106 was investigated using arrays of 8 Kulite transducers to measure changes in the phase and amplitude of the signal in the axial and circumferential directions in the compressor and downstream duct. The distributions of amplitude and phase were measured by calculating the cross spectra of the signals from transducers 2–8 using transducer 1 to provide a datum signal. To calculate the spectra from each channel, 4096 samples were measured from each transducer with a sampling period of 170 μs, thereby giving a resolution in the frequency domain of 0.7 Hz. To improve the consistency of the results, 50 cross spectra were calculated for each of transducers 2–8 during each sampling event. These were ensemble-averaged to give 7 cross spectra (one for each of transducers 2–8), which were subsequently used to compare phase and amplitude. Prior to these measurements the gains and phase shifts introduced by the different transducers were measured and these were accounted for during the data processing to ensure valid comparisons of signal amplitude and phase.

Measurements were made for a large number of distributions of the 8 transducers in both the compressor and the downstream duct. The transducers were mainly distributed either axially or circumferentially, although a number of rectangular arrays were also used. Spectra were measured for each of the three lengths of downstream ducting, although only the results for the datum duct are presented here as the results for the longer and shorter ducts were found to be similar. The measurements were performed at the same compressor geometry and flow coefficient as previously described and the acoustic signal at approximately 1420 Hz was therefore the main subject of the investigation. Small changes in this frequency were observed during the course of the experiments but these changes were found to be consistent with changes in the ambient temperature.

Phase Variation in the Compressor. Figure 8 shows the results of a circumferential measurement of phase in the compressor section at the stator 4 exit plane. These results are significant because they confirm that the structure of the 1420 Hz signal has order 7 in the circumferential direction, as suggested by the preliminary results given in Table 1. The sign of the gradient of the phase distribution in Fig. 8 indicates that the pressure field rotates in the opposite direction to rotor rotation (a "backward" traveling wave). Both forward and backward traveling waves have been observed in high-speed compressors. The distribution of phase shown in Fig. 8 is not an exactly straight line; however, when the measurements were repeated, an almost identical phase distribution was found, suggesting that the departure of the points from the straight line shown in the figure is not due to inadequate averaging. Instead, it indicates that there may be more than one acoustic mode present at this frequency, although the mode with circumferential order 7 is the most prominent. The confirmation of a mode of circumferential order 7 in the compressor also confirms the value of M_θ as 0.83 and that the structure of the wave in the compressor is cut-off.

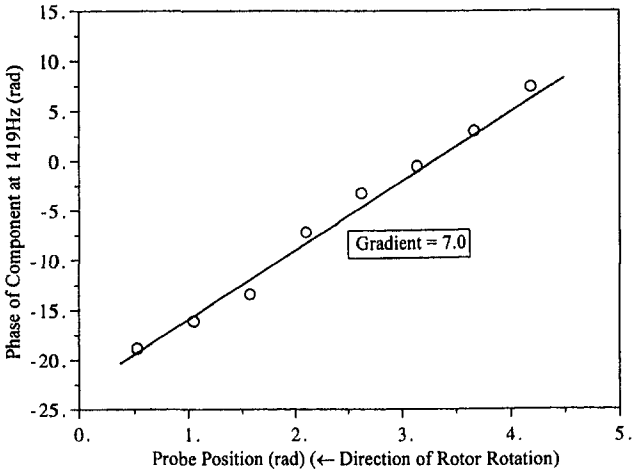

Fig. 8 Circumferential phase distribution in the compressor

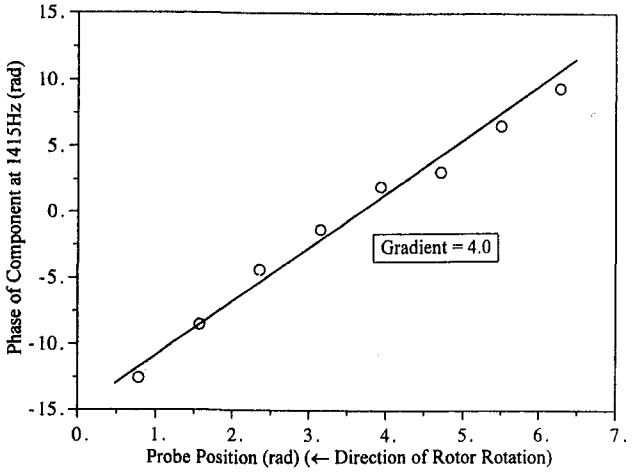

Fig. 10 Circumferential phase distribution in the downstream duct

Measurements of phase change with axial distance in the compressor section were found to be more difficult to interpret than the circumferential measurements, owing to the regular, wide spacing of the measurement planes in the compressor and the unknown effects of spatial aliasing. Figure 9 shows the results that were obtained when the 8 transducers were aligned axially, from the IGV exit plane (0 mm), through the stator exit planes (91.5 mm to 366 mm) and continuing into the downstream bearing housing (457.5 mm to 652.5 mm). To identify trends in the data, it was found helpful to plot the measured phase values and points at $\pm 2\pi$ rad, as shown in the figure. Because of the possibility of spatial aliasing, lines A, B, and C in Fig. 9 (and lines of progressively more positive and more negative gradient) are equally valid interpolations between the measured data points. To increase confidence in one of these possible solutions, it would be necessary to repeat these measurements with a narrower or alternatively less regular spacing of the transducers. At the time of performing these experiments, transducer access was limited to regularly spaced instrumentation planes between the blade rows and so it was not possible to increase the spatial definition beyond that observed in Fig. 9. The issue of spatial aliasing did not confuse the interpretation of circumferential phase measurements, however, first because the circumferential order is constrained to be an integer value and second because the frequency measurements in Table 1 suggest that an order 7 mode existed, and therefore that the phase results did not describe a structure with a fundamental order of 14, 21, 28, etc.

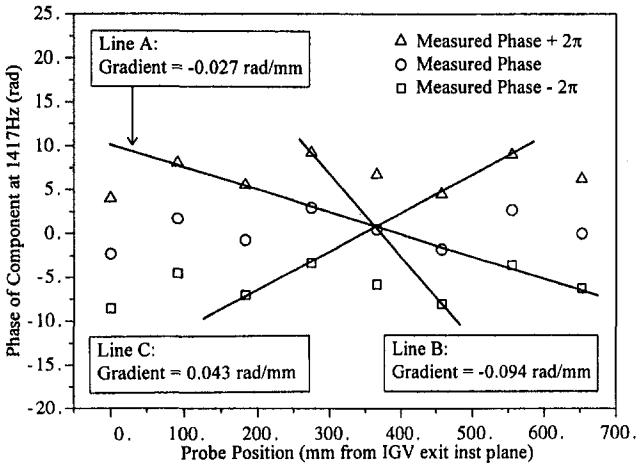

Fig. 9 Axial phase distribution in the compressor

Phase Variation in the Duct. Circumferential and axial distributions of phase were measured in the downstream ducting in a similar manner to the phase measurements in the compressor. Measurements in the duct benefited from arrays of instrumentation holes that were more closely spaced than in the compressor section. In the case of axial measurements of phase, this reduced the uncertainty in the interpretation of the data introduced by the possibility of spatial aliasing. Despite the frequency of the acoustic signal being the same in the bladed region and downstream ducting, the structure of the acoustic wave was found to be very different in the two sections. In particular, the results of phase measurements in a circumferential direction, summarised in Fig. 10, suggest that the wave has a circumferential order of 4 in the duct, as opposed to order 7 in the compressor. This difference in structure between the waves in the compressor and duct sections is somewhat surprising, but is supported by the results of a number of separate circumferential phase measurements in both sections. Once again, the small deviations of the data points from the straight line in Fig. 10 were found to be repeatable, suggesting the presence of more than one mode at this frequency. The circumferential Mach number of this mode, calculated using Eq. (2), was found to be 1.45, showing that this wave is cut-on. At present it is not understood how these two modal structures interface at the boundary between the compressor and the duct. It may be that modes of order 4 and 7 are both generated by the acoustic phenomenon; the order 7 mode dominates in the compressor but, being cut-off, decays rapidly with axial distance in the duct, where the order 4 mode is dominant.

The measurements of phase in an axial direction in the duct are plotted in Fig. 11, which shows that the phase of the signal changes at a rate of 0.018 rad per mm of duct length. The slopes of the lines shown in Figs. 10 and 11 suggest that the wave in the duct has a helical structure and that it propagates downstream, rotating in a direction against rotor rotation. The direction of rotation is thus the same as the mode 7 wave detected in the bladed section.

Amplitude Variation. The axial variation of the acoustic amplitude was measured using 8 Kulite transducers positioned in various axial arrays through the compressor and downstream duct. The cross-spectrum method was used to measure the ensemble-averaged distribution of amplitude, relative to the amplitude measured by the first transducer.

The results of these amplitude measurements are summarized in Fig. 12, which shows the measured amplitudes from a widely spaced array of transducers positioned over the blading, the rear struts, and the downstream duct. This figure shows that the amplitude of the acoustic signal increases rapidly with axial

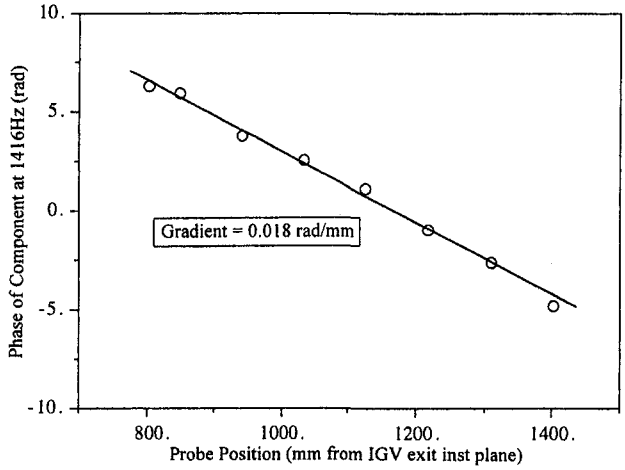

Fig. 11 Axial phase distribution in the downstream duct

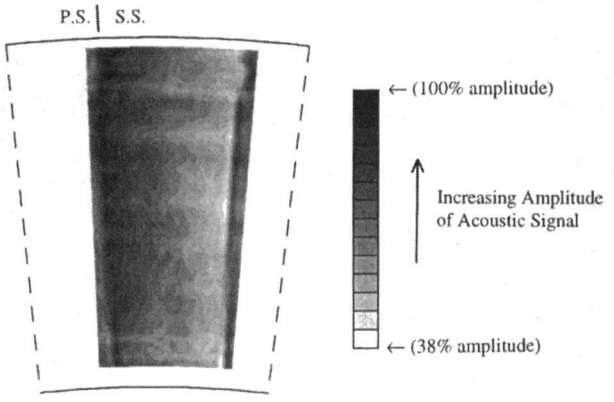

Fig. 13 Amplitude distribution of the acoustic signal over the stator 4 exit plane

distance through the compressor and reaches a maximum close to the stator 4 exit plane, as confirmed by more detailed measurements in this region. The amplitude reduces with distance through the rear bearing housing and strut and shows varying levels in the downstream duct. We might speculate that energy does not propagate beyond the throttle (and therefore that energy is trapped within the system) if the acoustic wave is reflected by the flat surface of the throttle plate, which is perpendicular to the compressor axis as shown in Fig. 7.

To measure the amplitude of the acoustic signal over the stator exit flow-field, a total pressure probe containing a Kulite transducer was traversed in the stator 3 and stator 4 exit planes at the acoustic resonance condition. The probe used for these traverses was specially designed to have a high frequency response. The probe was traversed over a grid of 37 radial by 25 circumferential points, which covered one stator passage. At each point, the probe was rotated to face the direction of the time-averaged flow (previously measured by traversing a hot-wire probe) and the pressure signal was sampled. Twenty spectra were calculated at each point from measurements of the pressure signal, and these were ensemble averaged to give a representative spectrum at each point. Although it is not clear that perturbations in total pressure can be classified as an *acoustic* signal, the spectra that were measured using the total pressure probe contained clear peaks at the previously determined acoustic frequencies. In Fig. 13 the amplitudes of these components are shown contour plotted, using results of the traverse at the stator 4 exit plane. These results suggest that the amplitude of the acoustic signal is greatest on the suction side of the stator wake and that it gradually decreases toward the pressure side of the adjacent blade. The amplitude of the signal changes rapidly over the stator wake but varies very little in the spanwise direction. A similar result was found at the stator 3 exit plane. These results are the first measurements of the amplitude of an acoustic resonance signal to be made inside a compressor flow-field. They confirm recent theoretical work by Parker (1995), which suggests that the amplitude of an acoustic signal varies in the pitchwise direction.

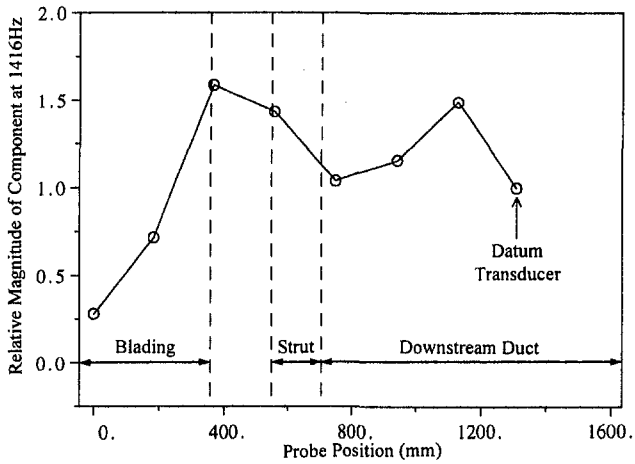

Fig. 12 Axial distribution of the amplitude of acoustic signal at 1416 Hz

Strouhal Numbers. Finally, we consider the Strouhal numbers of the support struts and the rotor and stator blades at the experimental operating point to find possible sources of vortex shedding in the compressor. As noted earlier it cannot be assumed that Strouhal numbers are exactly equal to 0.2 at a resonant condition; however, this value provides a useful guide in the absence of detailed measurements of the flow-field in the blade trailing edge regions.

The six struts in each of the upstream and downstream bearing housings are aligned axially and have a trailing edge thickness of 8 mm. For a vortex shedding frequency of 1420 Hz at a flow coefficient of 0.85, these struts have a Strouhal number based on trailing edge thickness of 0.195. This value is clearly very close to the value of 0.20 at which isolated flat plates are observed to shed vortices, suggesting that the struts are possible sources of vortex shedding. Conflicting evidence is given, however, by the axial distribution of amplitude (Fig. 12), which shows that the acoustic signal is weak in the region of the upstream struts and that the amplitude is decaying in the region of the downstream struts.

Because the rotor and stator blades are subject to large values of incidence, the calculation of the Strouhal numbers of these blades is complicated by the requirement that the length scale used to define the Strouhal number should represent the width of the wake and not simply the trailing edge thickness. As Fig. 3 shows, the width of the stator 3 wake at the experimental operating point is considerably wider than the thickness of the trailing edge. If D represents the trailing edge dimension, which gives a Strouhal number, based on this dimension, of 0.2, then D/Ch can be calculated as the ratio of the Strouhal number based on D, to the Strouhal number based on chord,

$$\frac{D}{Ch} = \frac{fD/v}{fCh/v} = \frac{0.2}{\mathrm{St}_{\mathrm{chord}}} \tag{8}$$

The dimension D can also be expressed as a proportion of the blade spacing s by dividing D/Ch by the space-chord ratio. In Table 3 below, the values of $\mathrm{St}_{\mathrm{chord}}$, D/Ch, and D/s are tabulated for the inlet guide vane, rotor and stator rows, assuming that each sheds vortices corresponding to the measured signal at

Table 3 Strouhal number results

Blade Row	St_{chord}	D/Ch	D/s
IGV	0.86	0.23	0.36
Rotor	0.79	0.25	0.37
Stator	0.86	0.23	0.36

1420 Hz at a flow coefficient of 0.85. The Doppler shift in frequency experienced by the rotor was accounted for in these calculations.

Although it has not been proved that vortex shedding is the excitation mechanism that drives acoustic resonance in high-speed compressors, general experience of gas turbine manufacturers suggests that Strouhal numbers based on chord for blade rows that are exciting acoustic resonance are approximately 0.6 if vortex shedding is present. Table 3 shows that the Strouhal numbers of all blade rows in the C106 exceed this value although the values of D/s (the wake dimension as a proportion of blade spacing) look plausible for each row. In particular, the value of D/s for the stator is close to a value that one might estimate from Fig. 3. From this study of Strouhal numbers we conclude that the struts and blade rows in the compressor are all possible sources of vortex shedding. More detailed measurements of the flow in the vicinity of the trailing edges would be necessary to determine with certainty which blade rows, if any, are exciting acoustic resonance by a vortex shedding mechanism.

Conclusions

The results of the experiments on the C106 compressor presented in this paper comprise the first systematic measurements of a resonant acoustic phenomenon in a low-speed multistage compressor. The experiments revealed that the C106 phenomenon shares many characteristics with acoustic resonances measured in high-speed compressors. These include:

1 A lobed pressure pattern that rotates around the annulus with a circumferential Mach number of 0.83 (values measured on high-speed compressors have been found to lie between 0.8 and 0.9).

2 Several acoustic frequencies at equal intervals, corresponding to different circumferential orders of the rotating pressure field.

3 Step changes in frequency as modes change to higher circumferential order as the flow coefficient through the compressor is increased.

4 An acoustic frequency (of the most studied mode) that is approximately independent of flow coefficient, shaft speed and axial length of the downstream duct.

5 Additionally, the first measurements of an acoustic signal within the blade-to-blade flow-field showed that at the stator exit planes the amplitude of the signal varies considerably in the pitchwise direction but that it changes very little across the span.

Acknowledgments

The author would like to thank Rolls-Royce plc for supporting the research described in this paper and for allowing publication of the results.

References

Camp, T. R., 1995, "Aspects of the Off-Design Performance of Axial Flow Compressors," Ph.D. Dissertation, Cambridge University Engineering Department, United Kingdom.

Cargill, A. M., 1993, private communication, Mar. 31.

Cumpsty, N. A., and Whitehead, D. S., 1971, "The Excitation of Acoustic Resonance by Wake Shedding," *Journal of Sound and Vibration,* Vol. 18, No. 3, pp. 353–369.

Koch, W., 1985, "Local Instability Characteristics and Frequency Determination of Self-Excited Wake Flows," *Journal of Sound and Vibration,* Vol. 99, No. 1, pp. 53–83.

Meyer, E., and Neumann, E. G., 1972, *Physical and Applied Acoustics,* New York Academic Press, pp. 191–192.

Parker, R., 1967, "Resonance Effects in Wake Shedding From Compressor Blading," *Journal of Sound and Vibration,* Vol. 6, No. 3, pp. 302–309.

Parker, R., 1968, "An Investigation of Acoustic Resonance Effects in an Axial Flow Compressor Stage," *Journal of Sound and Vibration,* Vol. 8, No. 2, pp. 281–297.

Parker, R., and Stoneman, S. A. T., 1985, "An Experimental Investigation of the Generation and Consequences of Acoustic Waves in an Axial Flow Compressor: Large Axial Spacings Between Blade Rows," *Journal of Sound and Vibration,* Vol. 99, No. 2, pp. 169–182.

Parker, R., and Stoneman, S. A. T., 1989, "The Excitation and Consequences of Acoustic Resonances in Enclosed Fluid Flow Around Solid Bodies," *Proc. IMechE,* Vol. 203, pp. 9–19.

Parker, R., 1995, private communication, Jan. 22.

Smith, N. H. S., 1991, "Investigation into the Supression of Acoustic Resonances," Ph.D. Dissertation, University College of Swansea.

Tyler, J. M., and Sofrin, T. G., 1962, "Axial Flow Compressor Noise Studies," *Trans. Society of Automotive Engineers,* Vol. 70, pp. 309–332.

Welsh, M. C., and Gibson, D. C., 1979, "Interaction of Induced Sound With Flow Past a Square Leading Edged Plate in a Duct," *Journal of Sound and Vibration,* Vol. 67, No. 4, pp. 501–511.

A Numerical Investigation of Transonic Axial Compressor Rotor Flow Using a Low-Reynolds-Number $k-\epsilon$ Turbulence Model

T. Arima

T. Sonoda

M. Shirotori

HONDA R&D Co., Ltd.,
Wako Research Center,
Saitama, Japan

A. Tamura

K. Kikuchi

National Aerospace Laboratory,
Tokyo, Japan

We have developed a computer simulation code for three-dimensional viscous flow in turbomachinery based on the time-averaged compressible Navier–Stokes equations and a low-Reynolds-number $k-\epsilon$ turbulence model. It is described in detail in this paper. The code is used to compute the flow fields for two types of rotor (a transonic fan NASA Rotor 67 and a transonic axial compressor NASA rotor 37), and numerical results are compared to experimental data based on aerodynamic probe and laser anemometer measurements. In the case of Rotor 67, calculated and experimental results are compared under the design speed to validate the code. The calculated results show good agreement with the experimental data, such as the rotor performance map and the spanwise distribution of total pressure, total temperature, and flow angle downstream of the rotor. In the case of Rotor 37, detailed comparisons between the numerical results and the experimental data are made under the design speed condition to assess the overall quality of the numerical solution. Furthermore, comparisons under the part-speed condition are used to investigate a flow field without passage shock. The results are well predicted qualitatively. However, considerable quantitative discrepancies remain in predicting the flow near the tip. In order to assess the predictive capabilities of the developed code, computed flow structures are presented with the experimental data for each rotor and the cause of the discrepancies is discussed.

Introduction

With the rapid progress of technology for computers and numerical schemes for computational fluid dynamics (CFD), it has become possible to apply the Navier–Stokes equations to the three-dimensional viscous flow phenomena in turbomachinery as an industrial design tool. Due to the requirements of small size and light weight, high efficiency and high loading, which are opposing technical goals, the blade row geometry of modern gas turbine engines has become three dimensional in order to reduce the losses due to secondary flow. We therefore need to understand the complex flow field in such blade rows in detail.

Three-dimensional viscous flow codes have also been developed, validated, and used by many researchers (Hah, 1987; Dawes, 1985; Nakahashi et al., 1989; Kunz and Lakshminarayana, 1992; Arnone, 1994, for example) to compute the flow through blade rows. However, it has been reported that the results computed using CFD show a wide scatter depending on who performed the calculation and the method employed. For example, Shabbir et al. (1996) reported that, in a blind test case for a rotor compressor (Rotor 37) organized by the 1994 ASME/IGTI (Wisler and Denton, 1994) to assess the predictive capabilities of turbomachinery CFD tools, the results computed by participants varied widely when compared with experimental data. They pointed out that the discrepancies could be partly attributed to deficiencies in the turbulence models. They assessed different turbulence models from the same numerical platform in order to evaluate the turbulence model performance. Denton (1996) reviewed the flow in the test case and the comparisons of CFD solutions with the test data and reported several comparisons of computed results for all participants. From these studies, it was found that the results computed using CFD were widely scattered due to factors such as the numerical scheme, the turbulence model, the method of implementing the model in the CFD code, the computational grid and the operator. It is important to investigate the effect of these factors on numerical solutions in order to make good use of CFD as an industrial design tool.

Therefore, we have developed a computer simulation code for three-dimensional viscous flow in turbomachinery based on the time-averaged compressible Navier–Stokes equations and have investigated the numerical characteristics of this code. In this study, flow fields for two rotors are calculated and compared with experimental data. One is the NASA Rotor 67, and the other is the NASA Rotor 37.

In the following sections, we first outline the basic equations and the numerical method, which includes a method of implementing the low-Reynolds-number $k-\epsilon$ turbulence model. Comparisons of computed results with the experimental data for both rotors are then presented and discussed.

Rotors 67 and 37. The geometry of Rotor 67 and the experimental data obtained using both aerodynamic probes and laser anemometer measurements were reported by Strazisar et al. (1989). The locations measured are shown in Figure 1 and the basic design specifications are shown in Table 1.

The details for Rotor 37 were reported by Reid and Moore (1978). Rotor 37 is a NASA Stage 37 rotor designed at the

Contributed by the International Gas Turbine Institute and presented at the 42nd International Gas Turbine and Aeroengine Congress and Exhibition, Orlando, Florida, June 2–5, 1997. Manuscript received International Gas Turbine Institute February 1997. Paper No. 97-GT-82. Associate Technical Editor: H. A. Kidd.

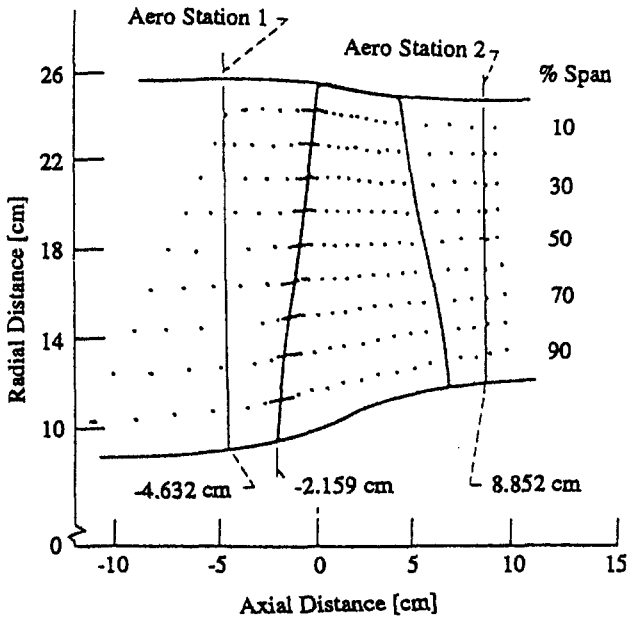

Fig. 1 Meridional view of Rotor 67 showing laser anemometer and aerodynamic survey locations (Strazisar et al., 1989)

NASA Lewis Research Center as a test compressor for a core compressor of an aircraft engine. In the CFD assessment, the rotor was tested in isolation (Suder, 1996). The locations measured using aerodynamic probes and laser anemometer measurements are shown in Fig. 2 and the basic design specifications are shown in Table 2.

For these rotors, not only are experimental data available for assessing the predictive capabilities of the CFD code, but the flow fields have also been investigated by several authors (Chima, 1991; Hah and Reid, 1992; Jennions and Turner, 1993; Arnone, 1994, for Rotor 67; Suder et al., 1994; Dalbert and Wiss, 1995; Chima, 1998; Shabbir et al., 1996, for Rotor 37, for example). We use the same expression for locations as used by these previous authors. The difference in the definition of percent span for Rotors 67 and 37 (see Figs. 1 and 2) should be noted.

Governing Equations

The basic equations governing the viscous flow through blade rows are the time-averaged Navier–Stokes equations, which

Table 1 Basic specifications of NASA Rotor 67

NASA Rotor 67			
Number of Rotor Blades			22
Rotational Speed	[rpm]		16043
Mass Flow	[kg/s]		33.25
Pressure Ratio	[—]		1.63
Rotor Tip Speed	[m/s]		429
Tip Clearance at Design Speed	[cm]		0.061
Inlet Tip Relative Mach Number	[—]		1.38
Rotor Aspect Ratio (based on average span/root axial chord)	[—]		1.56
Rotor Solidity	[—]	Hub	3.11
		Tip	1.29
Tip Diameter	[cm]	Inlet	51.4
		Exit	48.5
Hub/Tip Radius Ratio	[—]	Inlet	0.375
		Exit	0.478

can be written in a normalized form in a generalized curvilinear coordinate system fixed to a rotating blade, as

$$\frac{\partial Q}{\partial t} + \frac{\partial F_{\xi_i}}{\partial \xi_i} = \frac{1}{\mathrm{Re}} \frac{\partial S_{\xi_i}}{\partial \xi_i} + H, \tag{1}$$

where

$$Q = \frac{1}{J}\begin{pmatrix} \rho \\ \rho u_1 \\ \rho u_2 \\ \rho u_3 \\ e \end{pmatrix}, \quad F_{\xi_i} = \frac{1}{J}\begin{pmatrix} \rho U_{\xi_i} \\ \rho u_1 U_{\xi_i} + \xi_{i,1} p \\ \rho u_2 U_{\xi_i} + \xi_{i,2} p \\ \rho u_3 U_{\xi_i} + \xi_{i,3} p \\ (e + p) U_{\xi_i} \end{pmatrix}, \tag{2a}$$

Nomenclature

a = speed of sound
e = total energy per unit volume
$g_{ij} = \xi_{i,k}\xi_{j,k}$
I = identity matrix
J = Jacobian of transformation $= \partial(\xi_1, \xi_2, \xi_3)/\partial(x_1, x_2, x_3)$
k = turbulent energy
M = scaling matrix used to avoid the stiffness problem
p = static pressure
Pr = laminar Prandtl number
Pr_T = turbulent Prandtl number
q_i = heat flux vector
r = radius
Re = Reynolds number
R_T = turbulent Reynolds number
T_u = free-stream turbulence intensity
u_i = x_i component of relative velocity
U_{ξ_i} = ξ_i component of contravariant velocity $= \xi_{i,j} u_j$
U_τ = friction velocity
v_θ = absolute tangential velocity
x_i = Cartesian coordinate
y = normal distance from wall
γ = specific heat ratio
Δ = forward difference operator
δ_{ij} = Krönecker delta
ϵ = isotropic turbulent kinetic energy dissipation rate
μ = molecular viscosity
μ_T = turbulent viscosity
ν = kinematic viscosity $= \mu/\rho$
ν_T = turbulent kinematic viscosity $= \mu_T/\rho$
ξ_i = curvilinear coordinate
ρ = density
$-\overline{\rho u_i' u_j'}$ = Reynolds stress tensor
τ_{ij} = viscous stress tensor
τ_w = wall shear stress
Ω = angular velocity of rotation around the x_1 axis
∇ = backward difference operator

Superscripts and Subscripts

in = inflow boundary
n = time step
r = radial direction
std = standard day
tip = value at blade tip
T = turbulent
w = wall
x = axial direction
θ = circumferential direction
$'$ = fluctuating quantity
$\bar{}$ = time-averaged quantity

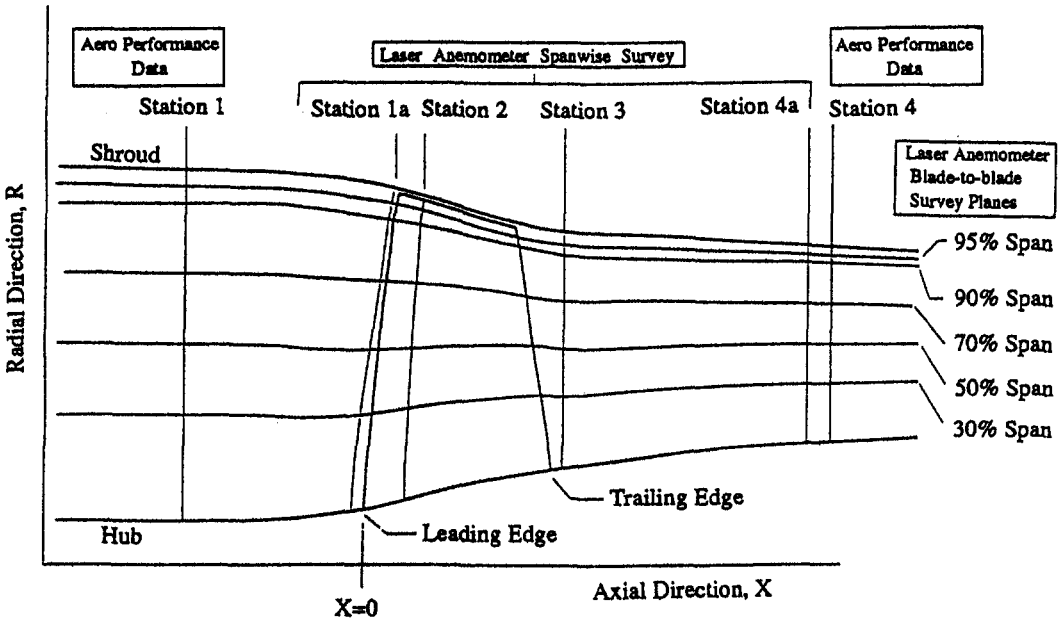

Station	1	1a	2	3	4a	4
X[cm]*	-4.19	-5% chord	20% chord	4.57	10.16	10.67
*X=0 at Intersection of hub and leading edge						

Fig. 2 Meridional view of NASA Rotor 37 showing locations at which experimental data were acquired (Strazisar, 1996)

$$S_{\xi_i} = \frac{1}{J}\begin{pmatrix} 0 \\ \xi_{i,j}\tau_{1j} \\ \xi_{i,j}\tau_{2j} \\ \xi_{i,j}\tau_{3j} \\ \xi_{i,j}(\tau_{jk}u_k + q_j) \end{pmatrix},$$

$$H = \frac{\rho}{J}\begin{pmatrix} 0 \\ 0 \\ \omega^2 x_2 + 2\Omega u_3 \\ \omega^2 x_3 - 2\Omega u_2 \\ 0 \end{pmatrix}. \tag{2b}$$

e is the total energy, which is represented as

$$e = \frac{p}{\gamma - 1} + \frac{1}{2}\rho(u_i u_i - (r\Omega)^2). \tag{3}$$

The viscous stress tensor, τ_{ij}, and the heat flux vector, q_i, can be evaluated as

Table 2 Basic specifications of NASA Rotor 37

NASA Rotor 37		
Number of Rotor Blades		36
Rotational Speed	[rpm]	17188.7
Pressure Ratio	[—]	2.106
Rotor Tip Speed	[m/s]	454.14
Tip Clearance at Design Speed	[cm]	0.0356
Inlet Tip Relative Mach Number	[—]	1.48
Rotor Aspect Ratio	[—]	1.19
Hub/Tip Radius Ratio	[—]	0.7

$$\tau_{ij} = \mu(u_{i,j} + u_{j,i} - \tfrac{2}{3}\delta_{ij}u_{l,l}) - \rho\overline{u_i' u_j'}, \tag{4}$$

$$q_i = \left(\frac{\mu}{\mathrm{Pr}} + \frac{\mu_T}{\mathrm{Pr_T}}\right)\frac{a_i^2}{\gamma - 1}, \tag{5}$$

where the Reynolds stress tensor $-\rho\overline{u_i' u_j'}$ is defined as

$$-\rho\overline{u_i' u_j'} = \mu_T(u_{i,j} + u_{j,i} - \tfrac{2}{3}\delta_{ij}u_{l,l}) - \tfrac{2}{3}\delta_{ij}\rho k \,\mathrm{Re}, \tag{6}$$

and μ_T is evaluated as

$$\mu_T = C_\mu f_\mu \rho \frac{k^2}{\epsilon}\cdot \mathrm{Re}, \tag{7}$$

where k and ϵ are obtained by solving the following transport equations:

$$\frac{\partial Q_T}{\partial t} + \frac{\partial F_{T\xi_i}}{\partial \xi_i} = \frac{1}{\mathrm{Re}}\frac{\partial S_{T\xi_i}}{\partial \xi_i} + H_T \tag{8}$$

$$Q_T = \frac{1}{J}\begin{pmatrix}\rho k \\ \rho\epsilon\end{pmatrix} F_{T\xi_i} = \frac{1}{J}\begin{pmatrix}\rho k U_{\xi_i} \\ \rho\epsilon U_{\xi_i}\end{pmatrix} \tag{9a}$$

$$S_{T\xi_i} = \frac{1}{J}\begin{pmatrix}\left(\mu + \frac{\mu_T}{\sigma_k}\right) g_{ij}\frac{\partial k}{\partial \xi_j} \\ \left(\mu + \frac{\mu_T}{\sigma_\epsilon}\right) g_{ij}\frac{\partial \epsilon}{\partial \xi_j}\end{pmatrix} \tag{9b}$$

$$H_T = \frac{1}{J}\begin{pmatrix} G - \rho\epsilon - \dfrac{2\mu k}{y^2\,\mathrm{Re}} \\ (C_1 G - C_2 f_2 \rho\epsilon)\dfrac{\epsilon}{k} - \dfrac{2 f_3 \mu\epsilon}{y^2\,\mathrm{Re}}\end{pmatrix} \tag{9c}$$

The rate of production of turbulent energy, G, is given by

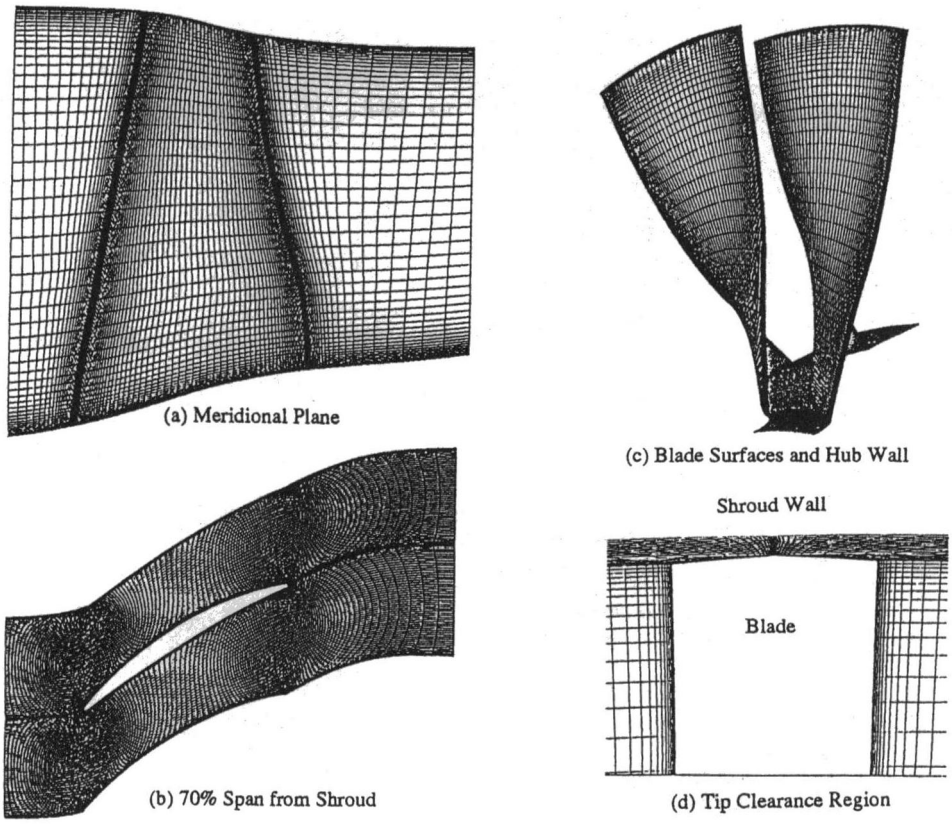

Fig. 3 Computational grid for NASA Rotor 67

$$G = -\frac{1}{\mathrm{Re}}\rho\overline{u_i' u_j'}u_{i,j} = \frac{\mu_T}{\mathrm{Re}}\left(u_{i,j} + u_{j,i} - \frac{2}{3}\delta_{ij}u_{l,l}\right)u_{i,j} - \frac{2}{3}\delta_{ij}\rho k u_{i,j}. \quad (10)$$

The following constants and damping functions proposed by Chien (1982) are used:

$$\sigma_k = 1.0,\ \sigma_\epsilon = 1.3,\ C_1 = 1.35,\ C_2 = 1.8,\ C_\mu = 0.09,$$

$$f_\mu = 1 - \exp(-0.0115y^+),\ f_2 = 1 - \frac{2}{9}\exp\left(-\frac{R_T^2}{36}\right),$$

$$f_3 = \exp(-0.5y^+), \quad (11)$$

where

$$y^+ = \frac{\rho_w U_r y}{\mu_w}\cdot\mathrm{Re},\quad U_r = \sqrt{\frac{\tau_w}{\rho_w}},\quad R_T = \frac{\rho k^2}{\mu\epsilon}\cdot\mathrm{Re}. \quad (12)$$

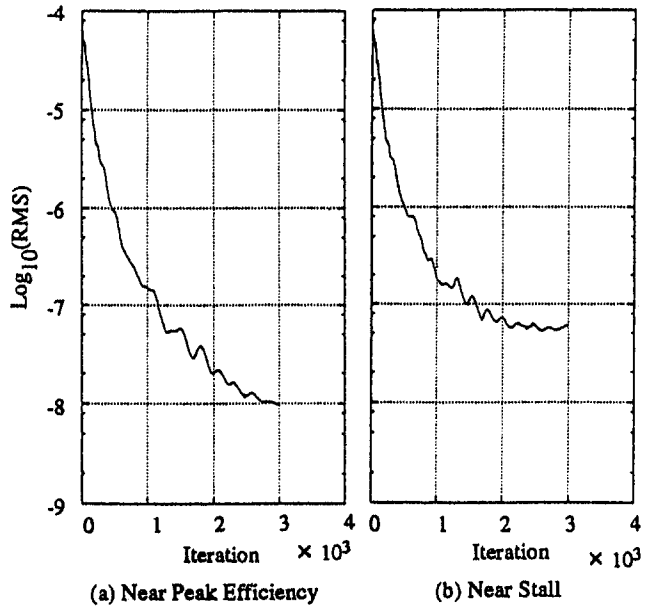

Fig. 4 Convergence history (NASA Rotor 67)

Numerical Method

Navier–Stokes Equations. The governing equations are solved using an implicit time-marching finite difference scheme to obtain a steady-state solution. To discretize the equations, Euler backward time differencing is used:

$$\frac{Q^{n+1} - Q^n}{\Delta t} = -\left\{\left(\frac{\partial F_i}{\partial \xi_i}\right)^{n+1} - \frac{1}{\mathrm{Re}}\left(\frac{\partial S_i}{\partial \xi_i}\right)^{n+1}\right\} + H^{n+1} \quad (13)$$

Then, the discretized equations are written in the conventional delta form as

$$\left[I + \Delta t\frac{\partial}{\partial \xi_i}\left\{\left(\frac{\partial F_i}{\partial Q}\right)^n - \frac{1}{\mathrm{Re}}\left(\frac{\partial S_i}{\partial Q}\right)^n\right\} - \left(\frac{\partial H_i}{\partial Q}\right)^n\right] \times (Q^{n+1} - Q^n) = \mathrm{RHS}, \quad (14)$$

where

$$\mathrm{RHS} = -\Delta t\left\{\left(\frac{\partial F_i}{\partial \xi_i}\right)^n - \frac{1}{\mathrm{Re}}\left(\frac{\partial S_i}{\partial \xi_i}\right)^n - H^n\right\}. \quad (15)$$

The implicit approximate factored (IAF) scheme proposed by Beam and Warming (1976) is applied:

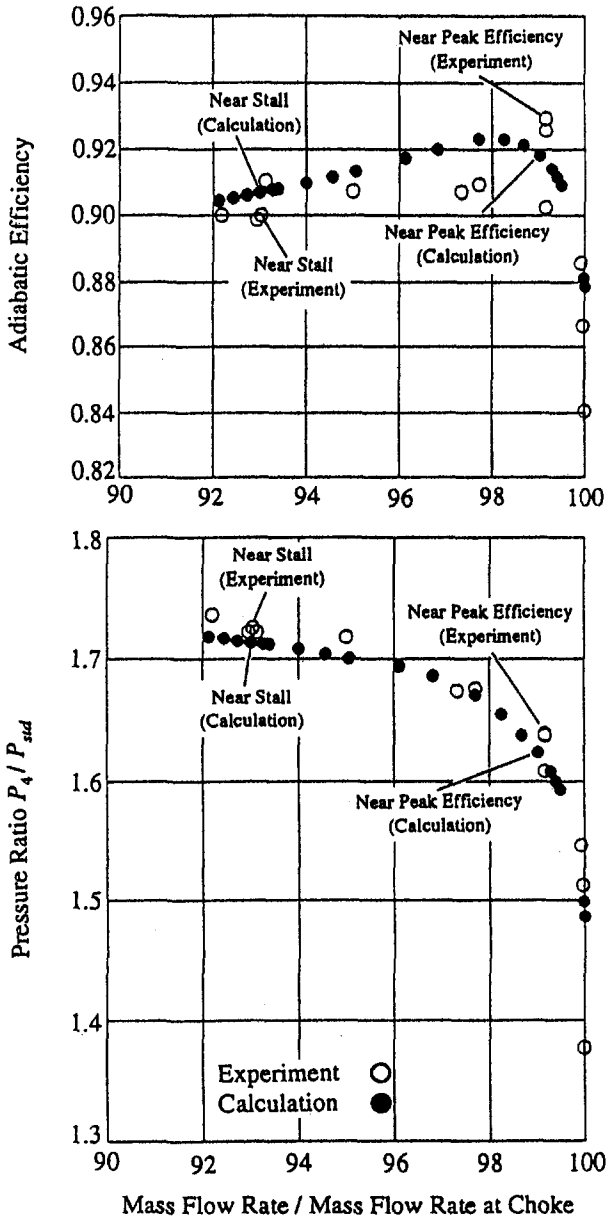

Fig. 5 Comparison of rotor performance at design speed (NASA Rotor 67)

$$\left[I + \Delta t \frac{\partial}{\partial \xi_1}\left\{\left(\frac{\partial F_1}{\partial Q}\right)^n - \frac{1}{\mathrm{Re}}\left(\frac{\partial S_1}{\partial Q}\right)^n\right\}\right] \times \left[I + \Delta t \frac{\partial}{\partial \xi_2}\left\{\left(\frac{\partial F_2}{\partial Q}\right)^n - \frac{1}{\mathrm{Re}}\left(\frac{\partial S_2}{\partial Q}\right)^n\right\}\right] \times \left[I + \Delta t \frac{\partial}{\partial \xi_3}\left\{\left(\frac{\partial F_3}{\partial Q}\right)^n - \frac{1}{\mathrm{Re}}\left(\frac{\partial S_3}{\partial Q}\right)^n\right\}\right] \times \left[I - \Delta t\left(\frac{\partial H}{\partial Q}\right)^n\right](Q^{n+1} - Q^n) = \mathrm{RHS}. \quad (16)$$

In order to reduce the amount of computer memory required and the high operating count for block inversions, the diagonal form of the IAF scheme developed by Pulliam and Chaussee (1977) is applied. The Jacobian matrix for the inviscid flux can be decomposed using the theory of characteristics, as

$$\left(\frac{\partial F_i}{\partial Q}\right) = R_i \Lambda_i L_i. \quad (17)$$

The matrices Λ_i are split into the matrices Λ_i^+, which include only positive eigenvalues, and Λ_i^-, which include only negative eigenvalues:

$$R_i \Lambda_i L_i = R_i(\Lambda_i^+ + \Lambda_i^-)L_i = R_i \Lambda_i^+ L_i + R_i \Lambda_i^- L_i, \quad (18)$$

where R_i, L_i, and Λ_i are the right eigenvector matrices, the left eigenvector matrices, and the diagonalized matrices with the eigenvalues of the Jacobian matrix, respectively. In order to maintain stability, the Jacobian matrix for viscous flux is not omitted but is simplified as

$$\left(\frac{\partial S_i}{\partial Q}\right) = R_i P_i L_i \approx R_i \{2(\nu + \nu_T) g_{ii} I\} L_i. \quad (19)$$

Using the these relationships, the fundamental equations can be rewritten as

$$R_1[I + \Delta t(\nabla_1 \Lambda_1^+ + \Delta_1 \Lambda_1^- - \mathrm{Re}^{-1} \nabla_1 \Delta_1 (\nu + \nu_T) g_{11} I)] L_1 \times R_2[I + \Delta t(\nabla_2 \Lambda_2^+ + \Delta_2 \Lambda_2^- - \mathrm{Re}^{-1} \nabla_2 \Delta_2 (\nu + \nu_T) g_{22} I)] L_2 \times R_3[I + \Delta t(\nabla_3 \Lambda_3^+ + \Delta_3 \Lambda_3^- - \mathrm{Re}^{-1} \nabla_3 \Delta_3 (\nu + \nu_T) g_{33} I)] L_3 \times \left[I - \Delta t\left(\frac{\partial H^n}{\partial Q^n}\right)\right](Q^{n+1} - Q^n) = \mathrm{RHS}. \quad (20)$$

In order to maintain numerical stability, the first-order upwind difference is utilized for the inviscid terms on the left-hand side.

Finally, Q^{n+1} can be determined by solving these linear equations using a tridiagonal matrix, which can be easily solved using the tridiagonal matrix algorithm (TDMA).

On the other hand, the high-accuracy total variation diminishing (TVD) formulation is used for the inviscid terms on the right-hand side of Eq. (20). The present approach is based on the method proposed by Chakravarthy and Osher (1985). If the flux difference is represented as

$$\frac{\partial F}{\partial \xi} = \frac{1}{\Delta \xi}(F_{j+1/2} - F_{j-1/2}), \quad (21)$$

then the numerical flux is evaluated as

$$F_{j+1/2} = \frac{1}{2}(F_{j+1} + F_j) + R_{j+1/2}\left[-\frac{1}{2}(\sigma^+_{j+1/2} - \sigma^-_{j+1/2}) - \frac{1-\phi}{4}\,\mathrm{minmod}\,(\sigma^-_{j+3/2}, \beta\sigma^-_{j+1/2}) - \frac{1+\phi}{4}\,\mathrm{minmod}\,(\sigma^-_{j+1/2}, \beta\sigma^-_{j+3/2}) + \frac{1+\phi}{4}\,\mathrm{minmod}\,(\sigma^+_{j+1/2}, \beta\sigma^+_{j-1/2}) + \frac{1-\phi}{4}\,\mathrm{minmod}\,(\sigma^+_{j-1/2}, \beta\sigma^+_{j+1/2})\right], \quad (22)$$

where

$$\sigma^{\pm}_{j+1/2} = \Lambda^{\pm}_{j+1/2} L_{j+1/2}(Q_{j+1} - Q_j). \quad (23)$$

The minmod limiter function is defined as

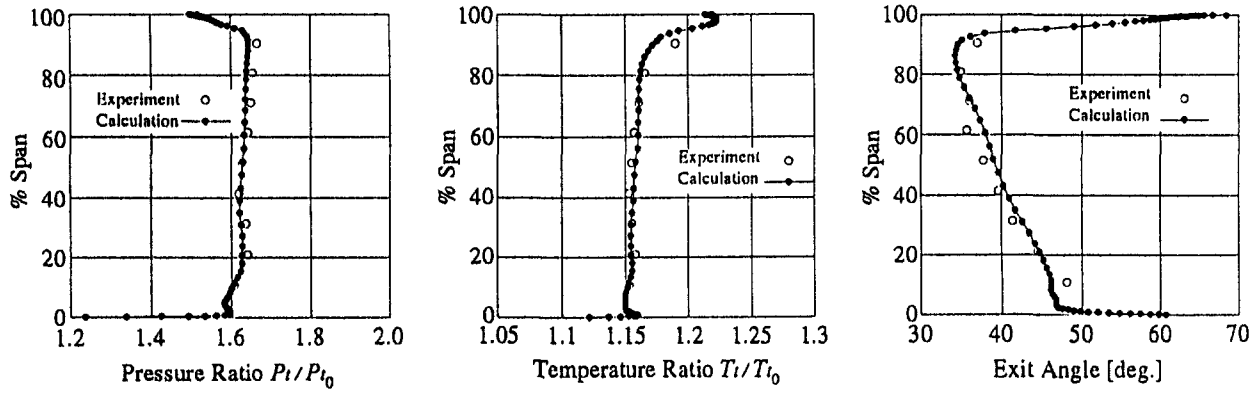

(a) Comparisons for condition near peak efficiency

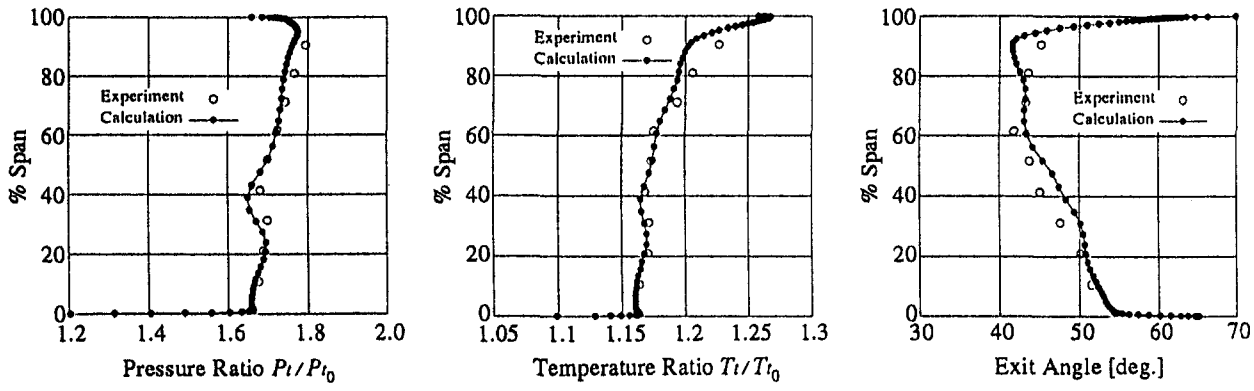

(b) Comparisons for condition near stall

Fig. 6 Spanwise distributions of pressure ratio, temperature ratio, and flow angle (NASA Rotor 67)

minmod $[x, y]$

$$= \text{sign}\,(x) \times \max\,[0, \min\,\{|x|, y \times \text{sign}\,(x)\}]. \quad (24)$$

The cell interface values for the state variables are calculated using Roe's averaging method. For the TVD condition to be satisfied, the values of ϕ and β must be such that

$$1 \le \beta \le \frac{3-\phi}{1-\phi}. \quad (25)$$

The viscous terms are evaluated using standard second-order central difference formulae. In order to speed up convergence to a steady-state solution, the spatially varying time-stepping technique is employed.

$k-\epsilon$ Equations. The turbulence quantities are obtained by lagging when the mean flow equations have been updated. Typical difficulties that occur in the calculation of the low-Reynolds-number $k-\epsilon$ turbulence model are the occurrence of instabilities in the start-up phase, regardless of the size of the time step, and the well-known stiffness problem, which is due to the rapid change in the source term of the turbulence transport equations near the wall with variations in the turbulence quantities. In order to avoid the stiffness problem, the IAF scheme used for mean flow was extended to the turbulence equations by Matsuo and Chyu (1993) to give

$$\left[M + \Delta t\left(\frac{\partial A_{\xi_1}}{\partial \xi_1} - \text{Re}^{-1}\frac{\partial^2}{\partial \xi_1^2}A^{\nu}_{\xi_1}\right)\right]\Delta Q_T^{**} = \text{RHS}_{k-\epsilon}$$

$$\left[M + \Delta t\left(\frac{\partial A_{\xi_2}}{\partial \xi_2} - \text{Re}^{-1}\frac{\partial^2}{\partial \xi_2^2}A^{\nu}_{\xi_2}\right)\right]\Delta Q_T^{*} = M\Delta Q_T^{**}$$

$$\left[M + \Delta t\left(\frac{\partial A_{\xi_3}}{\partial \xi_3} - \text{Re}^{-1}\frac{\partial^2}{\partial \xi_3^2}A^{\nu}_{\xi_3}\right)\right]\Delta Q_T = M\Delta Q_T^{*}$$

$$\Delta Q_T^{n+1} = Q_T^n - \Delta Q_T, \quad (26)$$

where

$$\text{RHS}_{k-\epsilon} = -\Delta t\left(\frac{\partial F_{T\xi_i}}{\partial \xi_i} - \frac{1}{\text{Re}}\frac{\partial S_{T\xi_i}}{\partial \xi_i} - H_T\right). \quad (27)$$

The Jacobian matrices for the inviscid and viscous flux are inherently diagonal, as follows:

$$A_{\xi_i} = U_{\xi_i}\begin{pmatrix}1 & 0\\ 0 & 1\end{pmatrix} \quad (28)$$

$$A^{\nu}_{\xi_i} = \begin{pmatrix}\left(\mu + \frac{\mu_T}{\sigma_k}\right)g_{ii}/\rho & 0\\ 0 & \left(\mu + \frac{\mu_T}{\sigma_\epsilon}\right)g_{ii}/\rho\end{pmatrix} \quad (29)$$

M is the scaling matrix used to avoid the stiffness problem. In keeping with the spirit of the diagonal algorithm, and to simplify the implicit treatment of the source function, the matrix M is replaced by the diagonal approximation, which is

$$M = I - \Delta t\left(\frac{\partial H_T}{\partial Q_T}\right) \approx I - \Delta t\begin{pmatrix}d_{11} & 0\\ 0 & d_{22}\end{pmatrix}. \quad (30)$$

The diagonal elements of the Jacobian matrix M should always

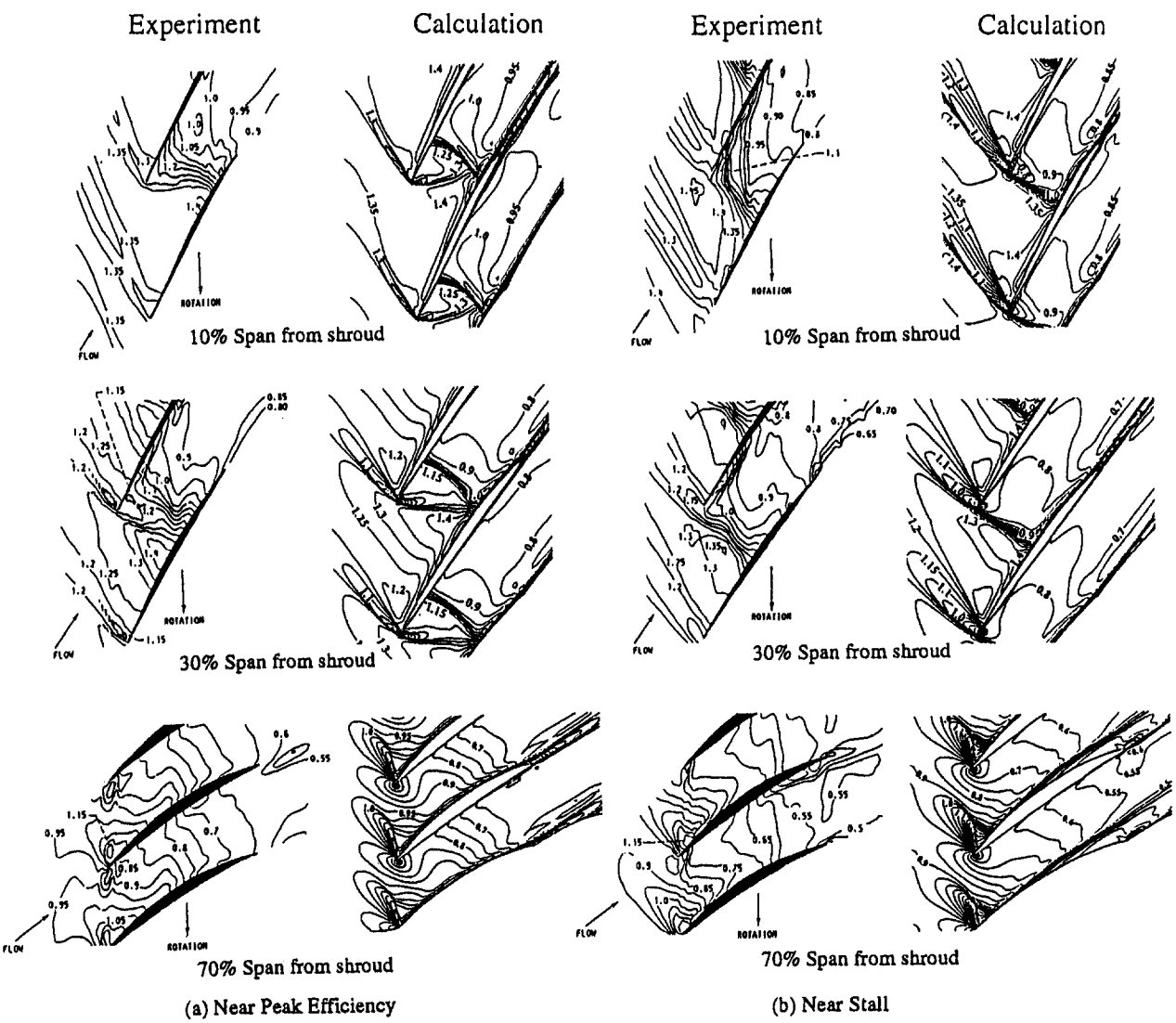

Fig. 7 Relative Mach number contours at intervals of 0.05 (NASA Rotor 67)

be negative for the scheme to be stable. For Chien's model, the diagonal elements are defined as

$$d_{11} = -\left\{\frac{2}{3}C_\mu\frac{\theta^2}{\omega} + \frac{2}{3}\max(\theta, 0) + \omega + \chi\right\},$$

$$d_{22} = -\left\{\frac{2}{3}C_1C_\mu\frac{\theta^2}{\omega} + C_1\frac{2}{3}\max(\theta, 0) + C_2f_2\omega + f_3\chi\right\}, \tag{31}$$

where

$$\theta = u_{i,i}, \quad \omega = \epsilon/k, \quad \chi = \frac{2\nu}{y^2\,\mathrm{Re}}. \tag{32}$$

The instabilities that occurred in the start-up phase may be removed by choosing physically realistic initial values for the turbulence variables. In this study, the initial values are determined so that they satisfy the local equilibrium relations.

Boundary Conditions

Along the blade surfaces, the nonslip condition is imposed on the velocities, the pressure is extrapolated from the adjacent grid points, and the density is computed using the adiabatic wall condition. The turbulent kinetic energy and isotropic dissipation rate are set to zero along the solid boundaries. At the inflow boundaries, the total pressure and temperature profiles and two inlet flow angles are specified, and the static pressure is extrapolated from the interior flow field domain. The turbulent kinetic energy and dissipation rate imposed at the inflow boundary are

$$k_{in} = \tfrac{3}{2}(T_uV_{in})^2, \quad \epsilon_{in} = C_\mu k_{in}^2\,\mathrm{Re}, \tag{33}$$

which are derived from the specified free-stream turbulence intensity and the unit eddy viscosity at the inflow boundary. At the outflow boundaries, the static pressure is specified at the hub wall. A simplified radial equilibrium momentum equation,

$$\frac{\partial p}{\partial r} = \rho\frac{v_\theta^2}{r} \tag{34}$$

is used to integrate a specified hub exit static pressure in the radial direction in order to determine the exit static pressure distribution. The density and velocity components, k and ϵ, are extrapolated from those at interior points. At the periodic boundaries upstream of the leading edge and downstream of the trailing edge, the values at two corresponding points should be equal. The tip clearance region is also handled by imposing

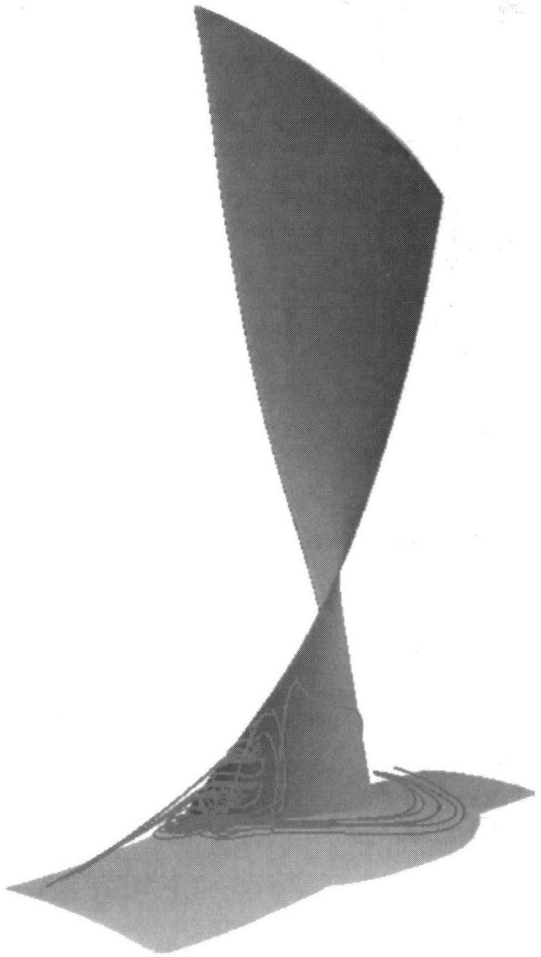

Fig. 8 Separation region observed at the hub/suction surface trailing edge corner (Rotor 67 for near peak efficiency condition)

periodic conditions across the blade and collapsing the blade thickness to zero at the tip.

Results and Discussion

Rotor 67. To validate the code, the NASA Rotor 67 transonic fan flow was studied. The basic specifications of the NASA Rotor 67 transonic fan rotor are shown in Table 1. For this rotor, detailed experimental data obtained near the peak efficiency and stall conditions, and the rotor geometry were reported by Strazisar et al. (1989). Several authors (Chima, 1991; Hah and Reid, 1992; Jennions and Turner, 1993; Arnone, 1994) have investigated this rotor in order to determine its complex flows.

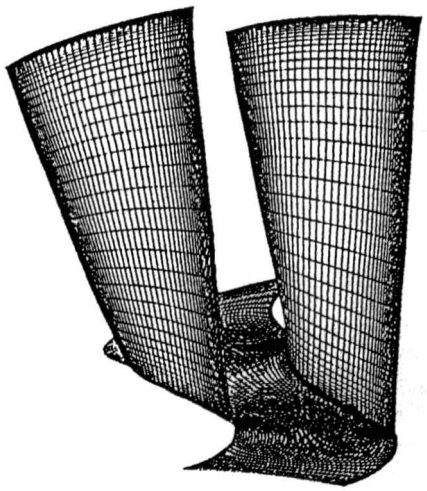

Fig. 9 Computational grid for NASA Rotor 37

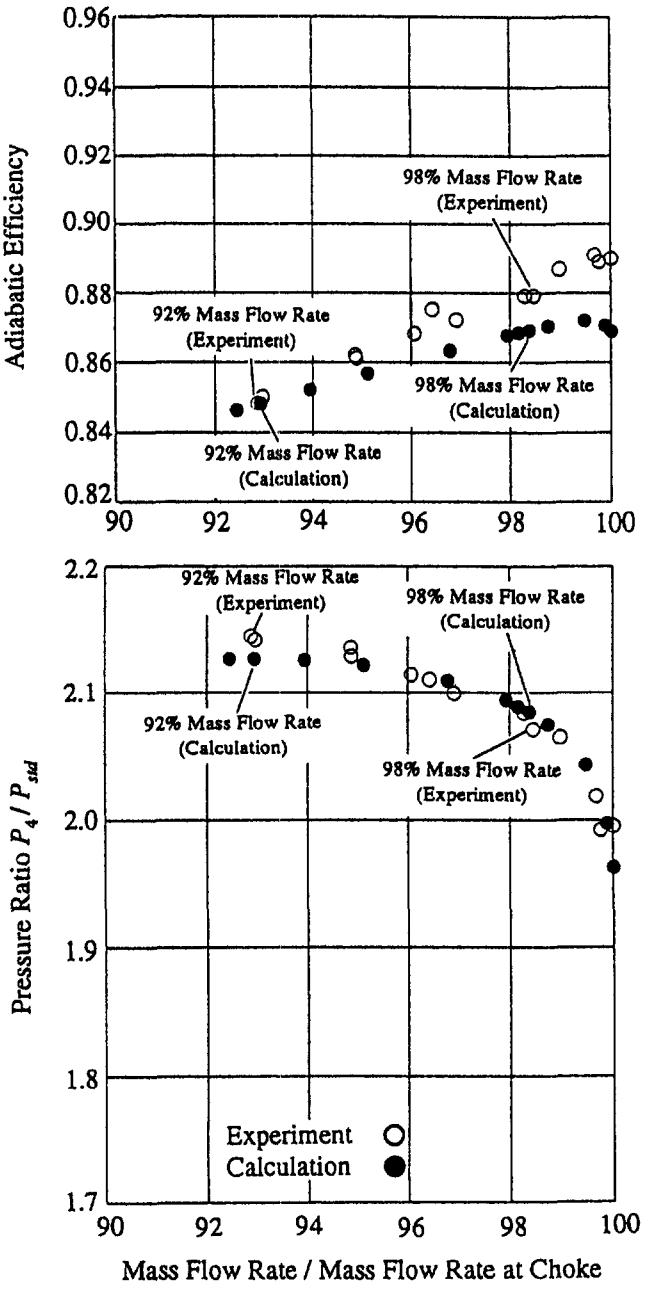

Fig. 10 Comparison of rotor performance at design speed (NASA Rotor 37)

The computational grid is shown in Fig. 3. This is produced by stacking the two-dimensional grids generated by solving the elliptical equations proposed by Sorenson (1980) on the stream surfaces. Figures 3(*a*) to 3(*c*) show a meridional view of the grid, a grid section at a distance of 70 percent of the span from the shroud, and a three-dimensional view of the grids on the blade surface and hub endwall, respectively. The grid consists of 156 nodes in the streamwise direction, 81 nodes in the spanwise direction, and 61 nodes in the blade-to-blade direction. Eleven nodes in the spanwise direction are used to describe the tip clearance, which is 0.024 in. The grid in the tip clearance region

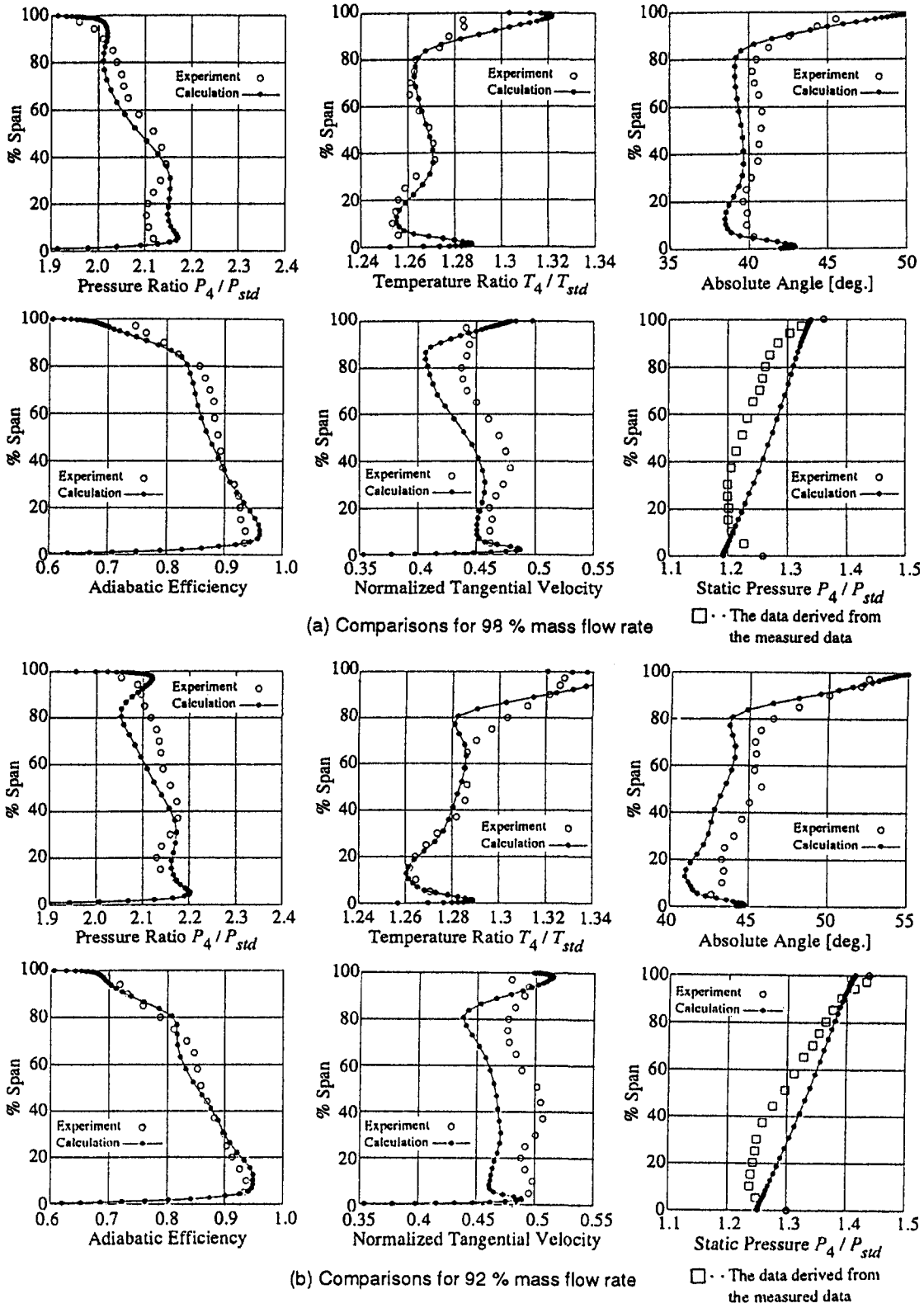

Fig. 11 Spanwise distributions of pressure ratio, temperature ratio, flow angle, adiabatic efficiency, normalized tangential velocity, and static pressure at Station 4 (NASA Rotor 37)

is shown in Fig. 3(*d*). This is believed to be fine enough to resolve the wall boundary layers, the leakage flow from the tip gap, and the shock system. Using the low-Reynolds-number k–ϵ turbulence model (Chien, 1982), the nearest grid point to the solid wall should satisfy $y^+ < 1$. Since this criterion is satisfied, the grid spacing at the blade is set to 1×10^{-5} times the blade span height. The grid spacing at the hub and the shroud is set to 1×10^{-4} times the blade span height due to the relatively thick inlet boundary layer. The calculation takes about 4 hours using a HONDA Fujitsu VX2 to produce results for one operating point on the rotor performance map. The convergence history of the root mean square of the norm of the residuals

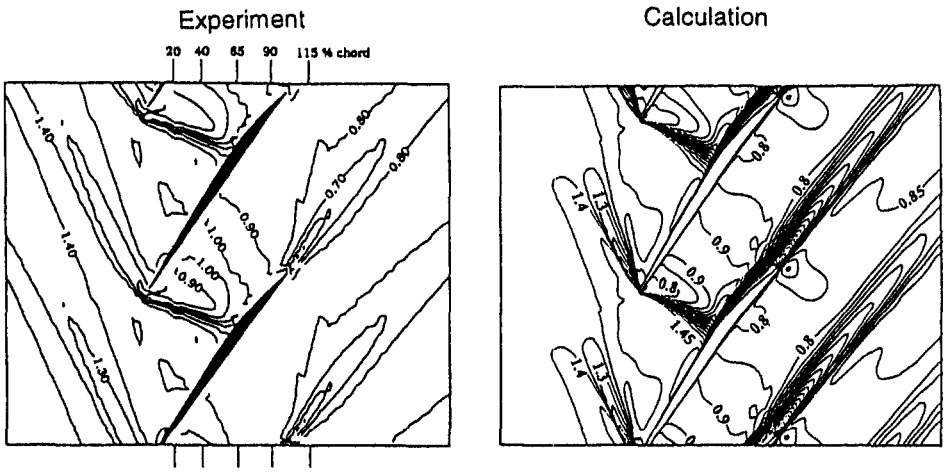

Fig. 12 Relative Mach number contours at 70 percent span for 98 percent mass flow rate (NASA Rotor 37); experimental data taken from Suder et al. (1994)

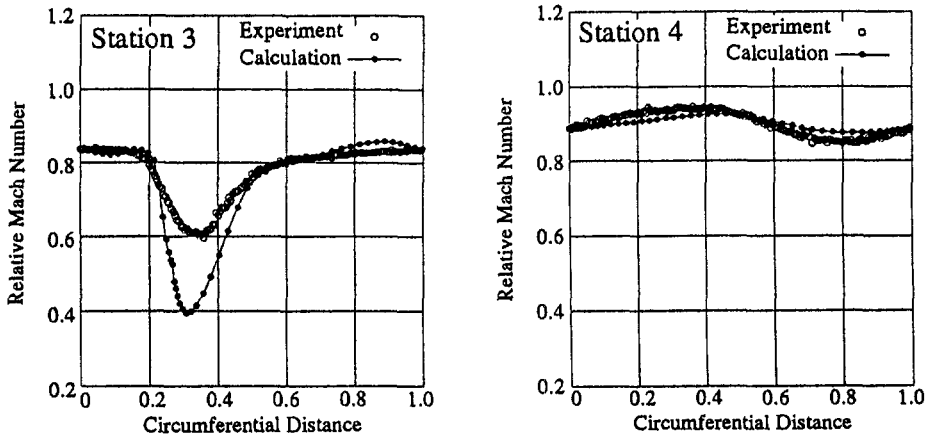

Fig. 13 Relative Mach number wake profile at 70 percent span for 98 percent mass flow rate (NASA Rotor 37)

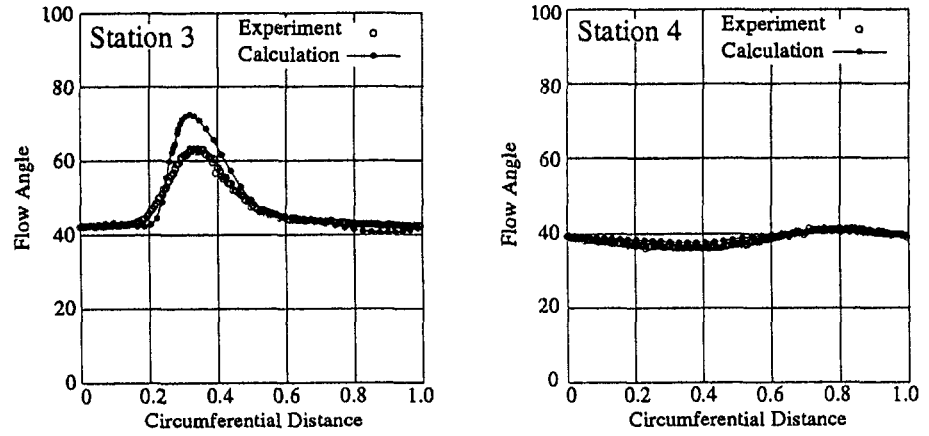

Fig. 14 Flow angle wake profile at 70 percent span for 98 percent mass flow rate (NASA Rotor 37)

obtained in calculations under conditions of near-peak efficiency and near-stall is shown in Fig. 4.

Figure 5 shows a comparison of the computed overall rotor performance with the experimental data. Twenty different operating conditions were considered to produce the overall rotor performance map at the design speed. Both calculated and experimental data are nondimensionalized using the corresponding choked mass flow rate as the equivalence criterion as in previous studies (Chima, 1991; Hah and Reid, 1992; Jennions and Turner, 1993; Arnone, 1994). The calculated mass flow rate was 34.79 kg/s, while that measured was 34.96 kg/s. The discrepancy between these values is only 0.5 percent. In this case, the inlet total pressure profile is determined using the boundary layer thickness, which is derived from experimental

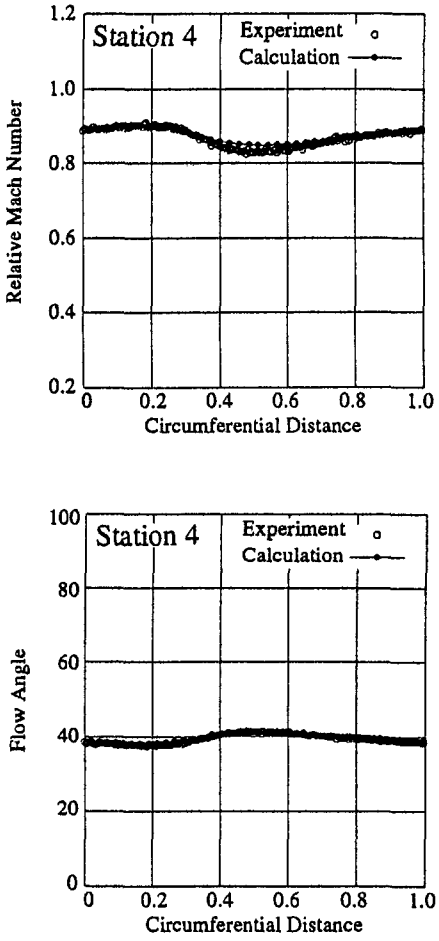

Fig. 15 Relative Mach number and flow angle wake profiles at 50 percent span for 98 percent mass flow rate (NASA Rotor 37)

data for the peak efficiency, and the velocity profile, which is obtained using the power law. The total temperature profile is assumed to be uniform at a constant value of 288.17 K. Identical inflow boundary conditions are used for calculating all of the operating points. Although the peak efficiency is predicted at a slight lower mass flow rate, the calculated efficiencies are quite good.

The computed spanwise variations of the energy-averaged total pressure, and the mass-averaged total temperature and flow angle at Aero Station 2, are shown in Fig. 6 with experimental data for conditions near peak efficiency and near stall (labeled "Near Peak Efficiency" and "Near stall" in Fig. 5). The comparisons agree reasonably well. However, the flow angle is overestimated, as in the calculations of Jennions and Turner (1993) and Arnone (1994). One reason for this discrepancy is that although the calculated total pressure ratio and total temperature ratio are almost the same as the experimental values; the calculated mass flow rate is lower than the experimental mass flow rate. At near-stall point, the calculations predicted the low total pressure ratio at 40 percent span. This feature can be seen in the experimental data, but it is interesting to note that previous authors do not seem to have caught this feature in their calculations. Although a similar feature exists in the experimental data at near-peak efficiency, it cannot be found in the calculation. We have tried to deduce the mechanism from the calculation at near-stall point. A the reason for this feature could not be identified. However, a more radial migration of the endwall flow and a larger separation at the hub/trailing edge corner at the near stall point than at the near-peak efficiency point may be related to this feature.

Figure 7 shows comparisons of the computed and experimental relative Mach number contours at 10, 30, and 70 percent of the span from the shroud for conditions near peak efficiency and stall. The comparisons generally agree well and a shock structure is clearly observed. At near-peak efficiency, bow shock and passage shock appear in the form of a lambda structure at distances of 10 and 30 percent of the span from the shroud. Bow shock is attached to the leading edge of the blade. Near stall, passage shock is not observed. Bow shock impinges on the location of about 50 percent of the chord of the suction surface of the adjacent blade. A skewed contour line is observed over the suction surface of the blade. This is due to grid skewing in this region caused by the large blade stagger angle. It may

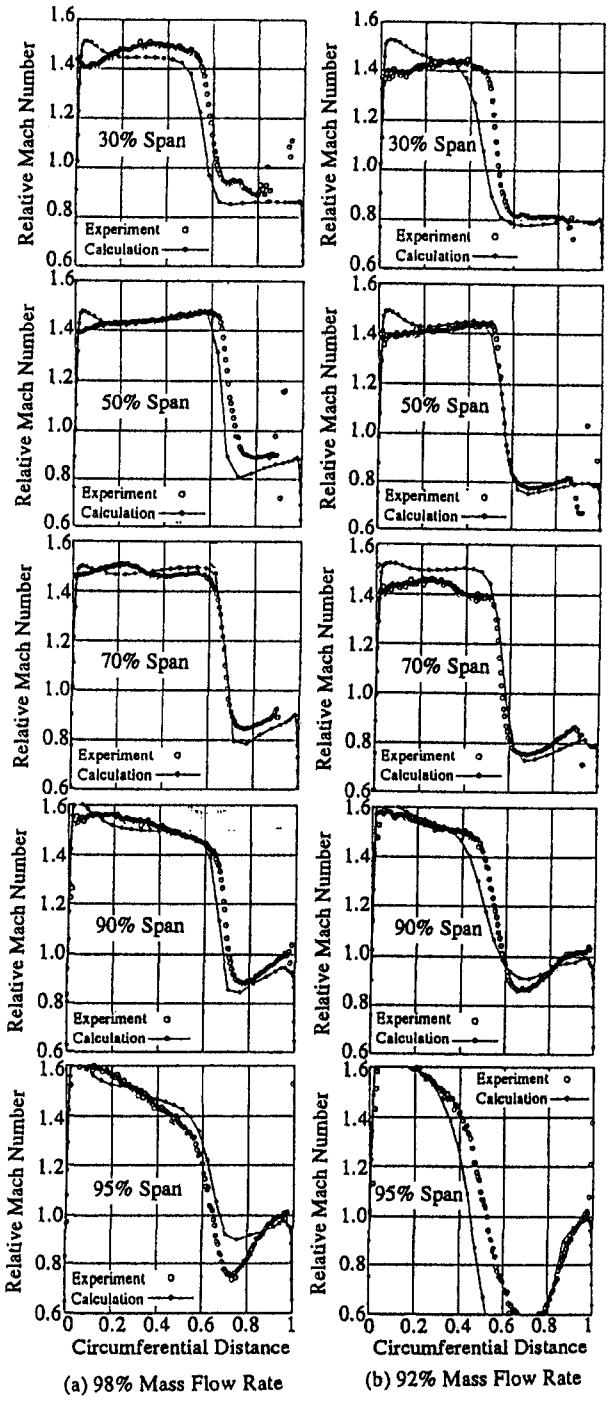

Fig. 16 Pitchwise relative Mach number distributions at 30, 50, 70, 90, and 95 percent span at Station 2 (NASA Rotor 37)

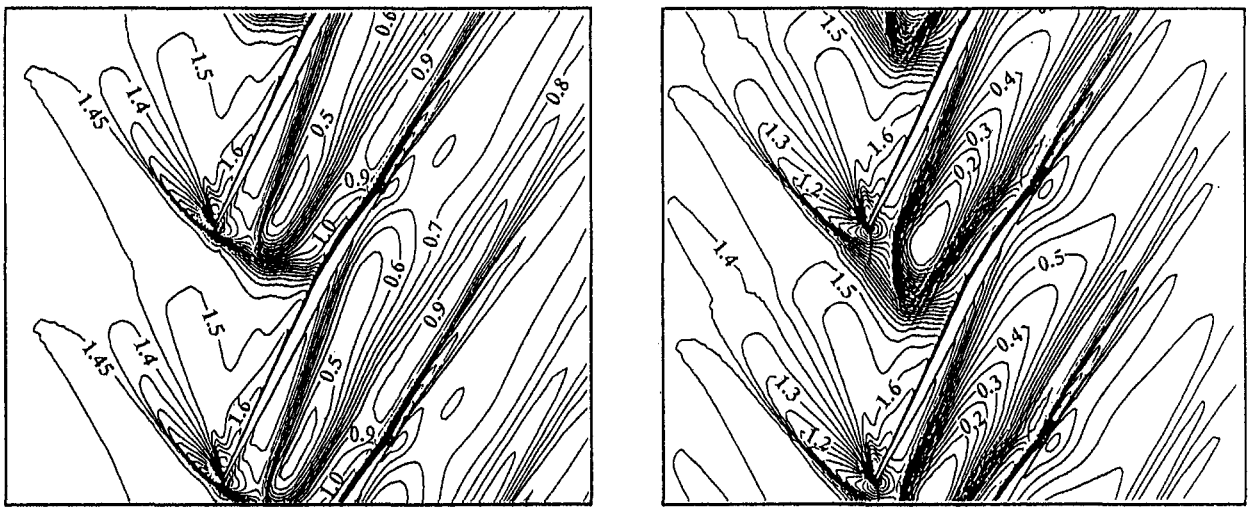

(a) 98% Mass Flow Rate

(b) 92% Mass Flow Rate

Fig. 17 Relative Mach number contours computed at intervals of 0.05 at 95 percent span (NASA Rotor 37)

need to be improved hereafter by revising the method of grid generation.

Finally, we observed a separation region near the hub/suction surface trailing edge, which is shown in Fig. 8.

The occurrence of separation was observed by Chima (1991). Jennions and Turner (1993) also discussed a similar feature observed in their calculations. As Chima (1991) pointed out, this separation bubble, fed by fluid from the endwall, migrates radially outward and ends up in the wake. In our understanding, a high blade incidence at the leading edge of the blade near the hub allows the blade to be high loading, and thus a hub/corner stall seems to occur in this region.

Rotor 37. Rotor 37 is designed so that the outflow angle is constant from hub to shroud at the design operating point. The basic specifications of the NASA Rotor 37 compressor rotor are shown in Table 2. Rotor 37 was used to assess the predictive capabilities of turbomachinery CFD tools in a blind test organized by the 1994 ASME/IGTI. Several participants computed the complex flow field of this rotor (Denton, 1996). The computed results were reported by several authors (Suder et al., 1994; Dalbert and Wiss, 1995; Shabbir et al., 1996; Chima, 1996). Therefore, theoretical predictions from different codes are available in the literature for comparison and discussion.

Figure 9 shows a three-dimensional view of the grids on the blade surface and hub endwall. The grid consists of 141 nodes in the streamwise direction, 81 nodes in the spanwise direction, and 51 nodes in the blade-to-blade direction. Eleven nodes in the spanwise direction are used to describe the tip clearance, which is 0.014 in. The inflow boundary was positioned at Station 1 and the outflow boundary was positioned at Station 4 (see Fig. 2). A stationary wall boundary condition was applied in the region of $x < -0.264$ cm, $x > 4.521$ cm, and a rotational wall condition was applied in the region of $-0.264 \leq x \leq 4.521$ cm for the hub endwall.

The calculations were carried out for twelve different operating conditions to produce the overall rotor performance map at the design speed. The results are shown in Fig. 10. The computed and experimental mass flow rates were nondimensionalized using the corresponding choked mass flow. The computed mass flow was 20.77 kg/s, while that measured was 20.93 $\pm$ 0.14 kg/s. The total pressure ratio is in good agreement with the experimental data. The computed rotor adiabatic efficiency is about 2 percent lower than that observed in the experiments on the higher mass flow side and is close to that observed in the experiments on the lower mass flow side. This tendency may result from the inlet boundary conditions. Given an identical total pressure profile as the inflow boundary condition for different operating points, the predicted adiabatic efficiency for the low mass flow condition tends to be comparatively high. It seems that the boundary layer profile corresponding to the mass flow rate should be used. As Denton (1996) pointed out, the difference of a process in averaging data between calculations and experiments may result in the underestimation of value.

Figure 11 shows the computed spanwise variations of the energy-averaged total pressure, the mass-averaged total temperature, the flow angle, the adiabatic efficiency, the tangential velocity normalized using a tip speed of 454.14 m/s, and the static pressure at Station 4 with experimental data for conditions of 98 and 92 percent mass flow rate. The square symbols in the static pressure distribution in Fig. 11 represent data derived from the experimental data, i.e., total pressure, total temperature, absolute flow angle, and tangential velocity. The calculated and experimental data are in qualitative agreement except near the tip. However, the total pressure distribution is overestimated from the hub up to about 40 percent of the span, and underestimated from 40 to 90 percent of the span for both mass flow rates. Upon averaging the total pressure distribution from hub to shroud, the overall total pressure agrees with the measured data shown in the rotor performance map (Fig. 10). It is interesting to note that the computations predicted, to some extent, the low-pressure region near the hub up to about 30 percent of the span, as is seen in the BTOB3D calculation by Dalbert and Wiss (1995). Although we investigated the origin of this low-pressure region, we could not identify any cause, such as flow separation. Meanwhile, considering the static pressure distributions (which are shown by square symbols in Fig. 11), the gradient of the static pressure is negative from the hub up to 20 percent of the span. This negative gradient seems to induce a flow separation from the hub wall. In our calculation, however, since the static pressure at the outflow boundary was calculated using the simple radial equilibrium equation, the gradient was always positive. The static pressure profile at the outflow boundary needs to be determined using a more realistic method in order to simulate the negative gradient. The computed total temperature is in good agreement with the experimental data from the hub up to about 90 percent of the span for 98 percent mass flow rate. For 92 percent mass flow rate, although the agreement is good from the hub up to about 70 percent span, the discrepancy is significant in the region from about 70 percent of the span to the tip. The computed flow angle is in good

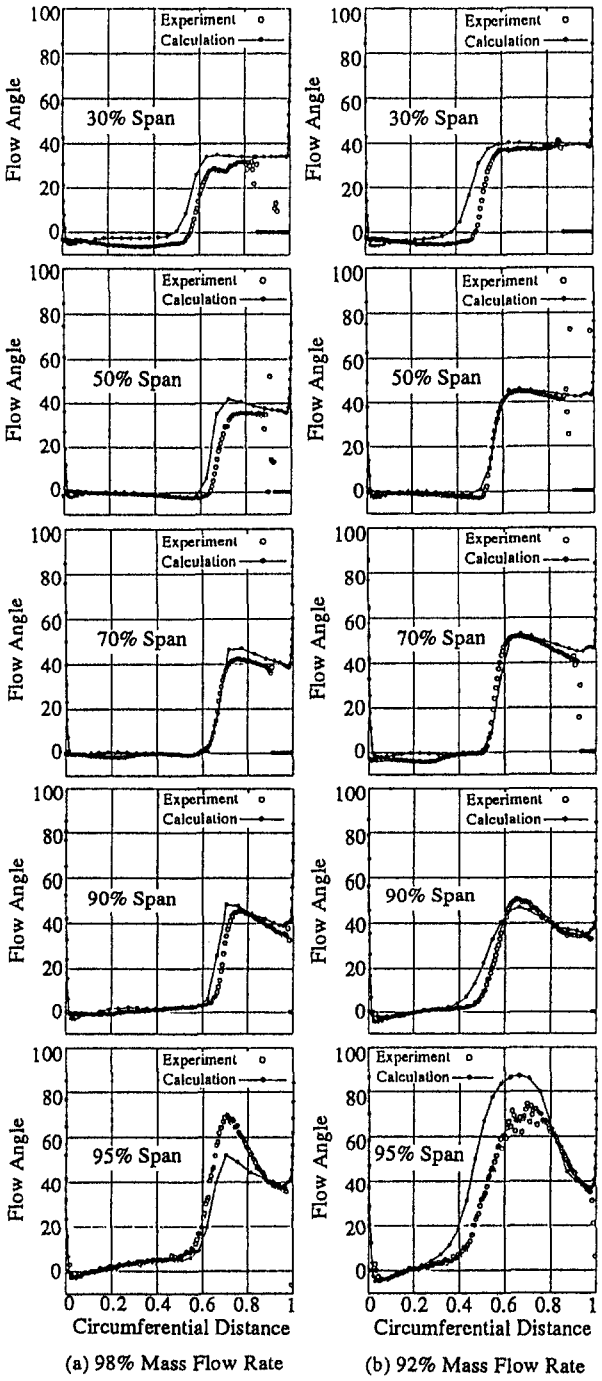

Fig. 18 Pitchwise flow angle distributions at 30, 50, 70, 90, and 95 percent span at Station 2 (NASA Rotor 37)

qualitative agreement. It is constant at about 40 deg from 10 to 90 percent of the span for 98 percent mass flow rate, as designed. Quantitatively, it is underestimated by about 1 to 2 deg for 98 percent mass flow rate and about 2 to 3 deg for 92 percent mass flow rate. For 92 percent mass flow rate, the computed adiabatic efficiency is lower than that measured from 40 to 80 percent of the span for both mass flow rates, which corresponds to the underestimation of the total pressure in this region.

In order to investigate the underestimation of the total pressure and the adiabatic efficiency from 40 to 80 percent of the span, the computed results obtained at 70 percent of the span are compared with the experimental data in detail. The relative Mach number contours are compared in Fig. 12. The relative Mach number wake profiles and the flow angle wake profiles at 70 percent of the span are compared with experimental data obtained at both Station 3 and Station 4 in Figs. 13 and 14, respectively. The relative Mach number contours are in good agreement with the experimental data. Although the computed wake profiles are sharper than the experimental profiles close to the trailing edge of the blade, they are similar to the experimental data at Station 4. In addition, the relative Mach number wake profile and flow angle wake profile at 50 percent of the span are shown in Fig. 15 with experimental data obtained at Station 4, and the agreement with the experimental data is good. These good agreements for the wake profile of the relative Mach number and the absolute flow angle mean that the underestimation of the total pressure at Station 4 may be caused by reduced axial velocity, because the static pressure obtained by solving the simple radial equilibrium equation, which is used as the outflow boundary condition at Station 4, is higher than that measured.

The relative Mach number distributions across the blade pitch on the 30, 50, 70, 90, and 95 percent span stream surfaces at Station 2 are shown in Fig. 16 with experimental data. The computed results for shock locations and values are in good agreement with the data. However, at 95 percent of the span, the values downstream of the shock are higher than that measured for 98 percent mass flow rate and much lower than that measured for 92 percent mass flow rate.

In order to gain a better understanding of the flow mechanism at 95 percent span, the Mach number contours on the 95 percent span stream surface are shown in Fig. 17. For 98 percent mass flow rate, bow shock is attached to the leading edged, while for

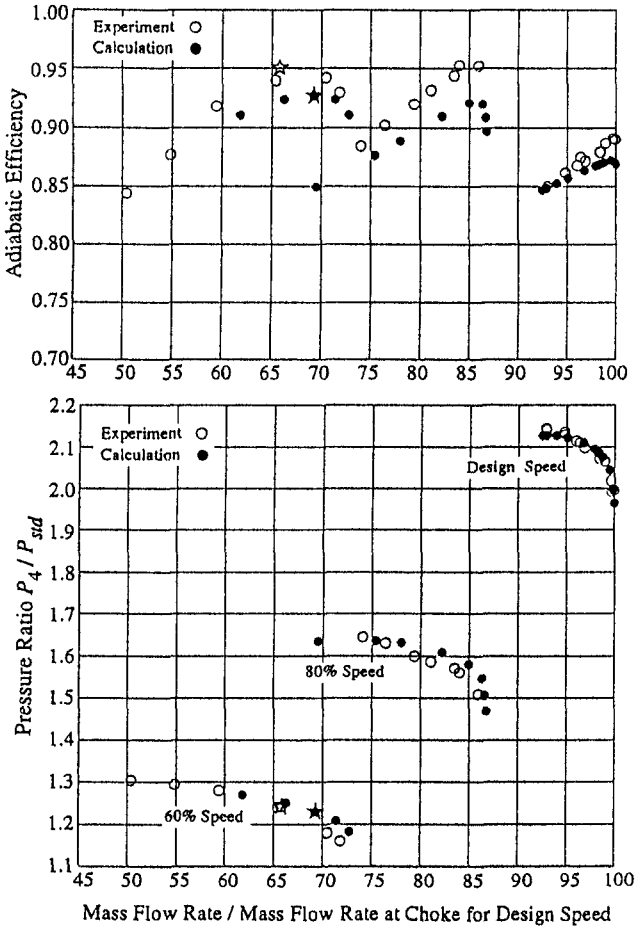

Fig. 19 Computed rotor performance for NASA Rotor 37 at 60, 80, and 100 percent design speed. Stars indicate operating conditions for which spanwise distributions of flow properties are presented. Experimental data are taken from Suder et al. (1994).

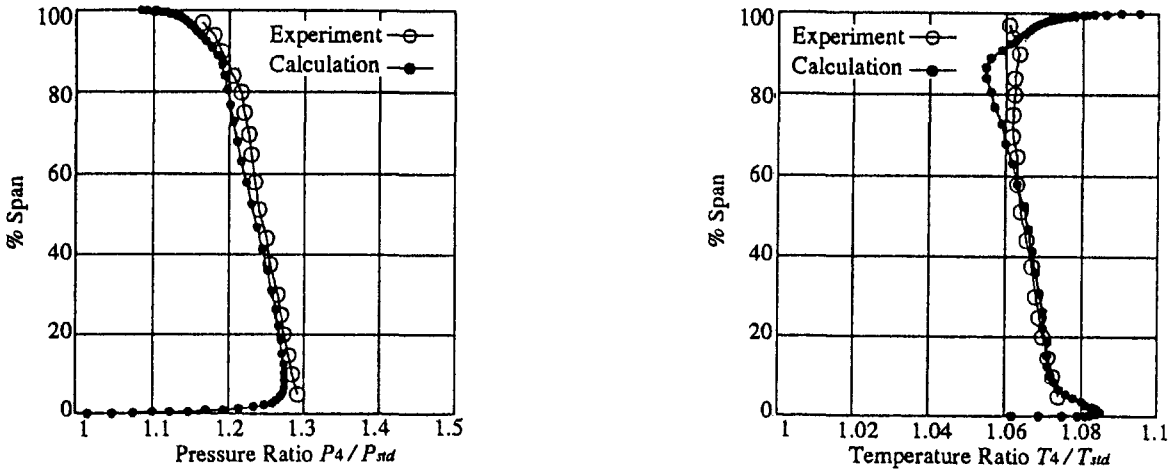

Fig. 20 Spanwise distributions of pressure ratio and temperature ratio at 60 percent of design speed (NASA Rotor 37). Experimental data are taken from Suder et al. (1994).

92 percent mass flow rate, the shock is detached from the leading edge. Under both operating conditions, a low-Mach-number region related to tip clearance flow can be observed near midpitch just downstream of the shock. As shown in Fig. 16, the predicted low Mach number region for 92 percent mass flow rate is too large.

The flow angle distributions across the blade pitch on the 30, 50, 70, 90, and 95 percent span stream surfaces at Station 2 are shown in Fig. 18. The computed results agree well with the experimental data, except at 95 percent of the span. The flow angles at 95 percent of the span are lower for the 98 percent mass flow rate and higher for the 92 percent mass flow rate than the measurements, which correspond to the discrepancies in the relative Mach numbers in the low Mach number region. There are probably several reasons for these discrepancies. They may indicate limitations of numerical models, such as the turbulence model and the simple tip clearance model, which results in the extremely shared grid in the tip clearance region (see Fig. 3(*d*)).

In summary, the predicted flow fields are qualitatively good, but quantitative discrepancies remain in predicting the overall performance, such as the rotor performance map and the spanwise distributions of the aerodynamic parameters. The probable reason for these discrepancies is the boundary condition. For example, the static pressure profile, which includes a negative gradient in the radial direction, cannot be determined using the simple radial equilibrium equation. There are considerable discrepancies in predicting the flow near the tip.

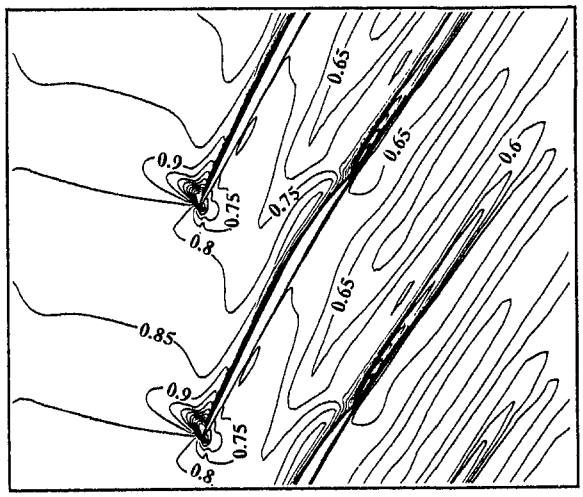

Fig. 21 Relative Mach number contours computed at 95 percent span for 60 percent of design speed (NASA Rotor 37)

Part-Speed Computations for Rotor 37. In order to investigate the numerical characteristics of the developed code for a flow field without passage shock, we have also calculated the flow field of Rotor 37 at 60 percent of the design speed, which was numerically and experimentally investigated by Suder and Celestina (1996) to clarify the tip clearance flow under an off-design condition. The computed results were compared with the results of Suder et al. (1994).

The computations utilized the same blade geometry as that used at the design speed and the change in blade twist, which results from the change in the centrifugal force, was not taken into account, similarly to the calculations of Suder et al. (1994). The same inlet total pressure and total temperature profiles used at the design speed were applied as the inflow boundary conditions.

The overall rotor performance maps computed for 60 percent and 80 percent of the design speed are shown in Fig. 19 with that calculated for the design speed. The pressure rise characteristics are in good agreement with the data obtained by Suder et al. (1994), while discrepancies remain in the mass flow rate. The adiabatic efficiency characteristics are 2 to 3 percent lower than the measured values.

Figure 20 shows the spanwise variations in the total pressure ratio and the total temperature ratio with the experimental data for the operating point marked with a star in Fig. 19. The mass flow rate chosen for comparison at 60 percent speed corresponds to the peak efficiency mass flow rate. The calculation results for 60 percent speed are in good agreement with the experimental data, except the total temperature ratio near the tip. At 60 percent design speed, the low-pressure region, which was observed at design speed, has not yet formed.

Figure 21 shows the relative Mach number contours at a distance of 95 percent of the span from the hub. They agree qualitatively with those measured by Suder et al.

Conclusions

A three-dimensional compressible Navier–Stokes code with a low-Reynolds-number $k-\epsilon$ turbulent model has been developed and used to compute the flow fields for Rotor 67 and Rotor 37. The calculated results were compared with experimental data to validate the code and assess the quality of the numerical solution.

The following conclusions were drawn:

1 For Rotor 67, the overall performance, including the rotor performance map and the spanwise distributions of the averaged

total pressure, total temperature, and flow angle at the rotor exit, is predicted reasonably well. The Mach number contours at each span height are qualitatively well predicted. The shock structure is clearly captured, although slightly skewed contour lines due to skewing of the mesh are observed.

2 For Rotor 37 at the design speed, the predicted flow fields are qualitatively good. However, uncertainties related to the boundary conditions, for example, the boundary layer profile at the inlet boundary and the static pressure profile at the outflow boundary, seem to result in discrepancies in flow prediction. There are considerable discrepancies in predicting the flow near the tip. These may indicate limitations of the numerical models, such as the turbulence model and simple tip clearance model.

3 For Rotor 37 at 60 percent of the design speed, the predictions are in reasonably good agreement with the experimental data.

The computed results provide much useful information for industrial design. In future work, we will calibrate this code using various experimental data and enhance its applicability to various flow fields.

Acknowledgments

The authors are grateful to Dr. Kenneth Suder and Dr. Anthony Strazisar of the NASA Lewis Research Center not only for providing the blade geometry and experimental data, but also for helpful discussion. We would also like to thank Dr. Chunill Hah of NASA Lewis Research Center for his useful comments. Finally, we thank Honda R&D Co., Ltd., for permission to carry out this work.

References

Arnone, A., 1994, "Viscous Analysis of Three Dimensional Rotor Flow Using a Multigrid Method," ASME JOURNAL OF TURBOMACHINERY, Vol. 116, pp. 435–445.

Beam, R. M., and Warming, R. F., 1976, "An Implicit Factored Scheme for the Compressible Navier–Stokes Equations," *AIAA Journal,* Vol. 16, pp. 393–402.

Chakravarthy, S. R., and Osher, S., 1985, "A New Class of High Accuracy TVD Schemes for Hyperbolic Conservation Laws," AIAA Paper No. 85-0363.

Chien, J. Y., 1982, "Predictions of Channel and Boundary Layer Flows With a Low-Reynolds-Number Two Equation Model of Turbulence," *AIAA Journal,* Vol. 20, pp. 33–38.

Chima, R. V., 1991, "Viscous Three-Dimensional Calculations of Transonic Fan Performance," AGARD 77th Symposium on CFD Techniques for Propulsion Applications, Paper No. 21.

Chima, R. V., 1998, "Calculation of Tip Clearance Effects in a Transonic Compressor Rotor," ASME JOURNAL OF TURBOMACHINERY, Vol. 120, pp. 131–140.

Dalbert, P., and Wiss, D. H., 1995, "Numerical Transonic Flow Field Predictions for NASA Compressor Rotor 37," ASME Paper No. 95-GT-326.

Dawes, W. N., 1985, "Computations of Off-Design Flows in a Transonic Compressor Rotor," ASME Paper No. 85-GT-1.

Dawes, W. N., 1986, "Numerical Techniques for Viscous Flow Calculations in Turbomachinery Bladings," von Karman Institute for Fluid Dynamics, Lecture Series 1986-02.

Denton, J. D., 1996, "Lesson From Rotor 37," presented at The 3rd ISAIF, Beijing.

Hah, C., 1987, "Calculation of Three-Dimensional Viscous Flow in Turbomachinery With an Implicit Relaxation Method," *AIAA Journal of Propulsion and Power,* Vol. 3, No. 5, pp. 415–422.

Hah, C., and Reid, L., 1992, "A Viscous Flow Study of Shock-Boundary Layer Interaction, Radial Transport and Wake Development in a Transonic Compressor," ASME JOURNAL OF TURBOMACHINERY, Vol. 114, pp. 538–547.

Jennions, I. K., and Turner, M. G., 1993, "Three-Dimensional Navier–Stokes Computations of Transonic Fan Flow Using an Explicit Flow Solver and an Implicit $k-\epsilon$ Solver," ASME JOURNAL OF TURBOMACHINERY, Vol. 115, pp. 261–272.

Kunz, R., F., and Lakshminarayana, B., 1992, "Three-Dimensional Navier–Stokes Computation of Turbomachinery Flows Using an Explicit Numerical Procedure and a Coupled $k-\epsilon$ Turbulence Model," ASME JOURNAL OF TURBOMACHINERY, Vol. 114, pp. 627–642.

Matsuo, Y., and Chyu, W. J., 1993, "Computations of Separated Aerodynamic Flows Using a Low Reynolds Number $k-\epsilon$ Model," *Proc. The 5th ISCFD,* Sendai, Vol. 2, pp. 355–358.

Nakahashi, K., Nozaki, O., Kikuchi, K., and Tamura, A., 1989, "Navier–Stokes Computations of Two- and Three-Dimensional Cascade Flowfields," *AIAA Journal of Propulsion and Power,* Vol. 5, No. 3, pp. 320–326.

Pulliam, T. H., and Chaussee, D. S., 1977, "A Diagonal Form of an Implicit Approximate Factorization Algorithm," *Journal of Computational Physics,* Vol. 39, pp. 372–397.

Reid, L., and Moore, R. D., 1978, "Design and Overall Performance of Four Highly Loaded, High-Speed Inlet Stages for an Advanced High-Pressure-Ratio Core Compressor," NASA Technical Paper 1337.

Shabbir, A., Zhu, J., and Celestina, M., 1996, "Assessment of Three Turbulence Models in a Compressor Rotor," ASME Paper No. 96-GT-198.

Sorenson, R. L., 1980, "A Computer Program to Generate Two-Dimensional Grids About Airfoils and Other Shapes by the Use of Poisson's Equation," NASA Technical Memorandum 81198.

Strazisar, A. J., Wood, J. R., Hathaway, M. D., and Suder, K. L., 1989, "Laser Anemometer Measurement in a Transonic Axial-Flow Fan Rotor," NASA Technical Paper 2879.

Strazisar, A. J., 1996, Private Communication.

Suder, K. L., Chima, R. V., Strazisar, A. J., and Roberts, W. B., 1994, "The Effect of Adding Roughness and Thickness to a Transonic Axial Compressor Rotor," ASME Paper No. 94-GT-339.

Suder, K. L., and Celestina, M. L., 1996, "Experimental and Computational Investigation of the Tip Clearance Flow in a Transonic Axial Compressor Rotor," ASME JOURNAL OF TURBOMACHINERY, Vol. 118, pp. 218–229.

Wisler, D. C., and Denton, J. D., 1994, "Rotor 37 Blind Test Case," presented at the ASME/IGTI Turbo Expo, The Hague, The Netherlands.

Computation and Measurement of the Flow in Axial Flow Fans With Skewed Blades

M. G. Beiler

T. H. Carolus

University of Siegen, Germany

A numerical analysis of the flow in axial flow fans with skewed blades has been conducted to study the three-dimensional flow phenomena pertaining to this type of blade shape. The particular fans have a low pressure rise and are designed without stator. Initial studies focused on blades skewed in the circumferential direction, followed by investigations of blades swept in the direction of the blade chord. A Navier–Stokes code was used to investigate the flow. The simulation results of several fans were validated experimentally. The three-dimensional velocity field was measured in the fixed frame of reference with a triple sensor hot-film probe. Total pressure distribution measurements were performed with a fast response total pressure probe. The results were analyzed, leading to a design method for fans with swept blades. Forward swept fans designed accordingly exhibited good aerodynamic performance. The sound power level, measured on an acoustic fan test facility, improved.

Introduction

Designing axial flow turbomachinery such as fans, propellers, propfans, and compressors with skewed blades, also known as swept blades, has several advantages. The noise emission is mostly lower and the performance can be improved by skewing the blades. The blade skew has to be accounted for in the design phase. If this is not done properly, the design specifications are not achieved.

The concept of sweep originated in aircraft design where it has been successfully applied to reduce flow losses and drag at transonic speed. The airfoil is said to have sweep when it is tilted within the flow direction. The airfoil has dihedral when it is tilted in the direction perpendicular to the flow direction. In this study, the term sweep refers only to curved blades without dihedral. For all other cases, the more general term skew, incorporating both sweep and dihedral, is used.

Küchemann (1952) studied swept airfoils and derived a method to calculate the spanwise and chordwise loading for swept aircraft wings. He addressed the interaction of the wing with a bounding wall, in particular the nacelle. Godwin (1957) investigated the aerodynamics of an axial flow compressor with 30 deg swept-back blades. The experiments revealed that stall does not occur abruptly, which he could explain by qualitative reasoning. Smith and Yeh (1963) analyzed sweep and dihedral in axial flow turbomachinery in a detailed and generalized approach. Cordes (1963) provided a simplified method to treat tilted blades, considering the radial equilibrium of the flow. According to Dejc and Trojanovskij (1973), the flow distribution and losses can be adjusted by sweeping the blades of axial flow turbines. Presently, the effort to design and optimize the flow by skillfully skewing the blades continues (Smith, 1987). Even for modern gas turbines, it is possible to improve the efficiency (Dejc et al., 1990).

The objective of this work is to study the flow phenomena within axial flow rotors with skewed blades. Computational Fluid Dynamics (CFD) provides a useful tool to conduct a systematic study, identifying the effects of various geometric parameters. This study focuses on the case of axial flow fans for which, to the best of our knowledge, no experience and validation of CFD application is available. The calculated flow field of several rotors was checked by measurements. Based on theoretical reasoning as well as on the numerical results, a design method, which accounts for blade skew, was developed. Several fans were designed accordingly and their performances were investigated.

Skewed Airfoils

In general the flow through a rotor is three dimensional. To simplify the flow analysis, it is assumed that the flow can be considered on two separate, two-dimensional surfaces. For axial flow machines, the throughflow and the blade-to-blade surfaces are such surfaces. In the simple case, the throughflow surface is the meridional plane and the blade-to-blade surface is an axisymmetric surface. Airfoil theory or experimental cascade data are frequently used to determine the appropriate blade section on the blade-to-blade surface. The flow distribution on throughflow surfaces can be treated with the simple radial equilibrium equation.

For the analysis of the fan stage, the blade-to-blade flow is assumed to be aligned on axisymmetric surfaces. Although the flow on such surfaces deviates from the flow through a cascade of parallel airfoils, the difference is assumed to be negligible.

Fan blades are frequently skewed in the circumferential direction θ (Fig. 1(a)). For blade angles between 0 and 90 deg, this results in a combination of sweep λ and dihedral ν (Fig. 1(b)). It has been suggested to include the effect of skew by replacing the blade action with a force acting in the direction normal to the blade surface (Vavra, 1960; Cordes, 1963; Dejc and Trojanovskij, 1973). The force is divided into its radial, tangential, and axial components. The radial component is assumed to act similarly to a distributed body force, which in turn can be included in the radial equilibrium equation. The radial force can be expressed in terms of the swirl velocity distribution V_θ, using Euler's turbine equation (Cordes, 1963). However, with a high space-chord ratio (Dixon, 1978), as is the case with axial flow fans, the representation of the blade using a distributed body force is no longer suitable.

Another approach is to shape the blade in such a way that it has sweep but no dihedral. This corresponds to the case where the angle $\nu = 0$ deg in Fig. 1(b) and eliminates the radial component of the force representing the blade action. The body force can thus be eliminated in the radial equilibrium equation, which simplifies matters.

Contributed by the Turbomachinery Committee for publication in the JOURNAL OF TURBOMACHINERY. Manuscript received by the Turbomachinery Committee April 1, 1997; revised version received at ASME Headquarters September 5, 1997. Associate Technical Editor: R. A. Delaney.

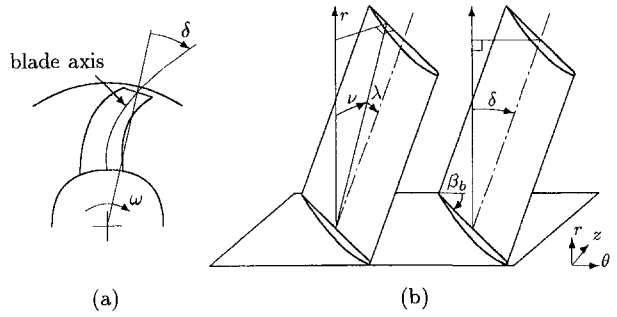

Fig. 1 (*a*) Forward skewed fan blade with variable skew angle $\delta = \delta(r)$ and (*b*) blades tilted in the circumferential direction

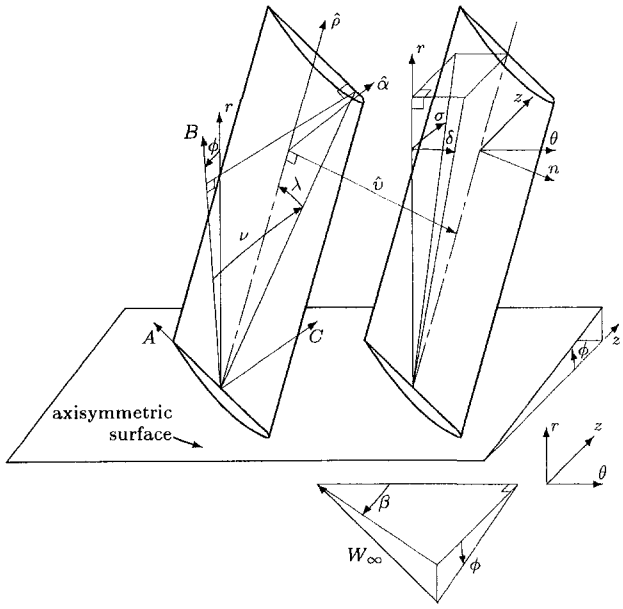

Fig. 2 Axisymmetric flow surface with fan blades

Treating the fan blade similarly to an infinitely long swept airfoil, the reduced pressure rise across the swept stage is

$$\Delta p^* = \Delta p \cos \lambda \tag{1}$$

The effect of a bounding wall, such as hub and shroud, on the pressure rise needs to be incorporated. The spatial blade geometry has to be determined for a given flow angle β, sweep λ, and dihedral ν. In the general case, the axisymmetric surface does not necessarily fall on a cylindrical surface, but is inclined by an angle ϕ. This configuration is shown schematically in Fig. 2 for a blade row of infinitely large rotor radius. It is in analogy to the representation suggested by Smith and Yeh (1963), but the angle β is defined differently.[1] Figure 2 indicates that the sweep angle is positive for the swept-back blade. In the representation of results, λ is specified positive for forward-swept blades to correspond to the positive angle δ for forward-skewed blades. The inclination of the blade in circumferential and axial direction can be calculated from the equations:

$$\sin \sigma = \frac{\theta_3 z_2 \hat{\alpha}_1 + (\theta_1 z_3 - z_1 \theta_3)\hat{\alpha}_2 - \theta_1 z_2 \hat{\alpha}_3}{\sqrt{\hat{\alpha}_1^2 + \hat{\alpha}_2^2 + \hat{\alpha}_3^2}} \tag{2}$$

$$\sin \delta = \frac{\theta_3 z_2 n_1 + (\theta_1 z_3 - z_1 \theta_3) n_2 - \theta_1 z_2 n_3}{\sqrt{n_1^2 + n_2^2 + n_3^2}} \tag{3}$$

The input variables are the angles of sweep and dihedral and the angles β and ϕ. The coefficients θ, z, $\hat{\alpha}$ and n are calculated from the equations provided in the appendix. For axial flow fans, the angle ϕ is set to $\phi = 0$ deg.

Table 1 Design parameters

Fan rotor	A	B
Pressure coefficient ψ_{ts}	0.135	0.152
Flow coefficient φ	0.180	0.153
Swirl distribution V_θ [m/s]	$4 + 0.552/r$	$1 + 0.760/r$
Rotational speed n [min^{-1}]	3000	3000
Total efficiency η_{tt}	0.80	0.90
Hub-to-tip ratio r_i/r_o	0.4	0.4
Outer fan diameter d [m]	0.305	0.305
Tip clearance s/d	0.0015	0.0015
Number of blades z	6	6

Fan Design

The swirl imparted to the flow by axial flow fans of low pressure rise is sufficiently small to omit a stator. Omitting the stator has the benefit that the noise emission, caused by rotor interaction with the stator, is avoided.

Two fans of different flow and pressure coefficients were designed according to elementary airfoil theory (Eck, 1972). The design points were selected to cover the range of designs which have proven successful (Eck, 1972; Carolus, 1988). Different swirl velocity distributions were specified at the rotor outlet, using the relationship suggested by Horlock (1958):

$$V_\theta = ar^n + b/r \tag{4}$$

The values for a, b, and n have to be specified. The corresponding axial flow distribution at the outlet was calculated from the radial equilibrium equation. Table 1 contains salient design parameters.

Both fans were initially equipped with straight (unskewed) blades. NACA airfoil sections were selected from Abbott and

[1] Replacing β by $-\beta$ and $\tan \beta$ by $1/\tan(-\beta)$ yields a form compatible with the form of Smith and Yeh (1963), who defined β positive for a compressor and negative for a turbine.

Nomenclature

C_L = lift coefficient
L_w = sound power level
p = pressure
r = radius
r, θ, z = cylindrical coordinates
u = blade speed
V = absolute velocity
$\dot{V}$ = volume flow rate
W = relative velocity
β = flow angle; $\tan \beta = W_z/W_\theta$
δ = skew angle in plane (r, θ)
σ = skew angle in plane (r, z)
λ = sweep angle
η = efficiency
ν = dihedral angle
ψ = pressure coefficient $= 2\Delta p/(\rho u_o^2)$
ϕ = inclination of stream surface
φ = flow coefficient $= \dot{V}/(u_o \pi r_o^2)$
ρ = density

Subscripts

1, 2 = upstream, downstream
i, o = inner, outer
b = blade
ts = total-to-static
tt = total-to-total

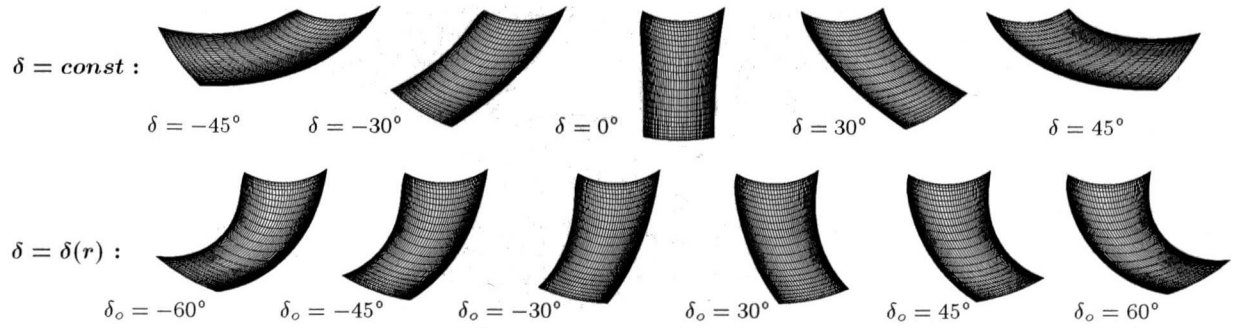

Fig. 3 Blade shapes of different skew (plan view)

Von Doenhoff (1959) (NACA 0010-65). In the second phase, a series of fans with systematically skewed blades in the circumferential direction were developed from each fan. Different skew angles were considered: First, a constant skew angle in circumferential direction δ (positive and negative) was selected from hub to shroud. Second, a variable skew angle $\delta(r)$ was specified, starting with 0 deg at the hub and ending with a maximum of ± 60 deg at the shroud. The skew angle at different radial positions is measured between the blade axis and a radial line (Fig. 1(a)). Typical blade shapes are depicted in Fig. 3. Finally, the blades were systematically skewed in such a way that they exhibit sweep but no dihedral. Starting at the hub and moving incrementally in the radial direction toward the shroud, the blade sections were shifted in the direction of the respective blade chords on coaxial cylindrical planes. This was done in such a way that the blade axis assumes the specified sweep angle at each radial position. The axial and circumferential coordinates of the blade axis were determined using Eqs. (2) and (3).

Numerical Flow Analysis

The flow field as well as the blade surface pressure distribution was studied for the different blade shapes. A fully three-dimensional viscous CFD code, TASCflow, was used for this purpose. The code solves the Reynolds-averaged Navier–Stokes equations in primitive variable form. It employs a finite volume method with Linear Profile Skew upwinding discretization. The two essential components of this discretization scheme are the directionally sensitive upwind discretization and the physically based advection correction term. It is of second-order accuracy. The pressure is linked with the velocity via a fourth-order pressure redistribution, a so-called pressure based code (*TASCflow Documentation,* 1994). The turbulence is modeled by the standard $k-\epsilon$ turbulence model. In the wall regions, the model uses logarithmic wall functions. Despite the fact that eddy viscosity models do not correctly mimic the turbulent stress generation due to Coriolis forces associated with rotating conditions (Launder, 1989), the $k-\epsilon$ model was employed, because, first, the results were validated experimentally and, secondly, the model appears to be sufficiently accurate for this comparative study. The flow is assumed to be incompressible. Convergence was accepted when the maximum of all normalized residues is less than 1×10^{-4}.

Structured grids were used for this application. The C-grid proved to be most successful. Figure 4 presents an example of a grid. The main grid contains 25 nodes in the radial direction, 18 nodes in the direction normal to the blade and 147 nodes wrapping around the blade. The main grid extends in the upstream direction, where a second grid of $25 \times 21 \times 8$ nodes is attached.

The number of grid nodes were not increased, because of limited computing resources. Consequently, the region in the vicinity of the hub and shroud has not been highly resolved. It was found that refining the grid improves the accuracy of the calculated results somewhat. However, the selected grid size provided sufficiently accurate results for the purpose of this investigation.

The tip clearance was omitted from the calculations, because a structured grid could not be applied in the tip region and because the large number of nodes necessary to fully resolve the flow within the tip region overstrained available computing resources. In order to minimize any difference between computation and measurement, the clearance was kept as small as possible on the experimental rotors. It is assumed that neglecting the tip clearance for moderately loaded blades can be accommodated without severely affecting the flow.

The boundary conditions specified at the hub and blade are fixed walls in the rotating frame of reference, whereas the shroud is a counterrotating wall, i.e., a stationary wall in the fixed frame of reference. Inlet and outlet boundaries are indicated in Fig. 4. The plane between adjacent blade segments is expressed as periodic boundary.

The flow field through the rotating flow passage and the fan performance was evaluated by use of the governing equations in integral form. Replacing the integration by a summation over the control volume, data such as momentum across control surfaces and circumferential averages of mass flow and pressure forces can be calculated. Global parameters such as pressure and flow coefficients were determined by using averaged flow parameters across the relevant control surfaces.

Experimental Investigation

The velocity and total pressure distribution were measured in the absolute frame of reference, using fast response probes,

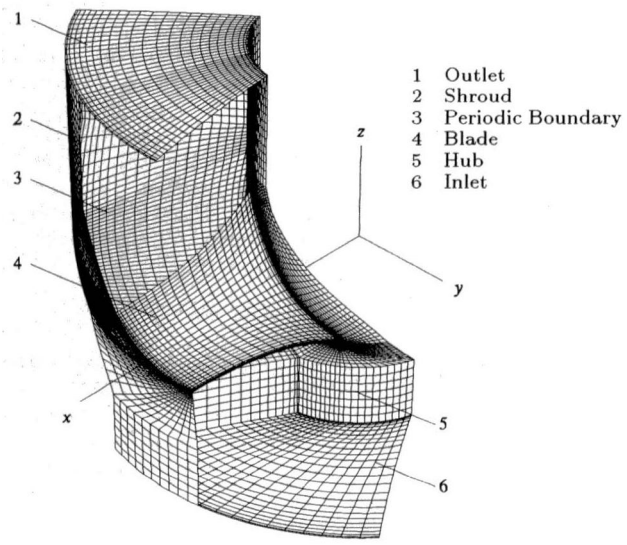

Fig. 4 Computational grid showing mesh boundaries

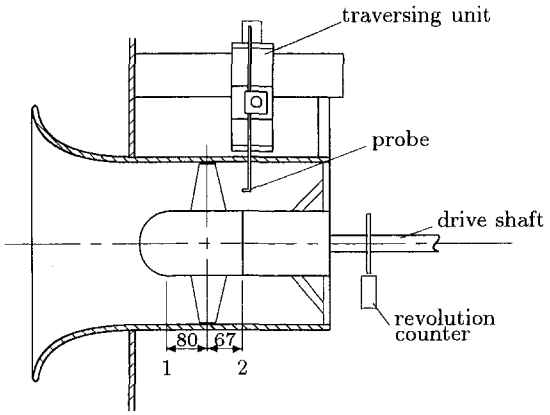

Fig. 5 Fan test unit

to validate the computational results. Further information such as the static pressure and flow losses were determined from the measurements. The fan performance has been evaluated from the fan characteristics, which were measured on an aerodynamic fan test facility.

The test facility has been designed in accordance with the standard DIN 24 163. The fan test unit, depicted in Fig. 5, is attached to the test facility and enables the flow measurements. The probes are mounted onto the traversing unit, which can be moved in the radial direction. The revolution counter also acts as trigger to allocate the measuring signal to the appropriate circumferential position. The drive shaft extends to the driving unit and incorporates a torque meter. The fan rotors, manufactured from aluminum on a CNC milling machine, are mounted within the test unit.

A hot-film probe with three mutually orthogonal sensors (TSI 1299A-20, Fig. 6(a)) was employed to measure the three-dimensional velocity distribution downstream of the rotor at measuring plane 2 in Fig. 5. Probes with an integrated piezoelectric sensor have been built to trace the rapidly fluctuating total pressure distribution. Figure 6(b) depicts the probe, which proved to be suitable to measure the total pressure accurately within a cone of acceptance of -25 to $+25$ deg. This is less than the typically wider range of Kiel probes, but the response characteristic is improved by exposure of the sensor to the fluid.

The data acquisition comprised a fast A/D converter with a maximum sampling frequency of 5 MHz. The analog signal from the pressure probe is pre-amplified by a DC amplifier, while the hot-film signals are amplified by the anemometer before being digitized. The flow field was measured over 120 revolutions with 200 measurements per revolution at 23 radial positions from hub to shroud. The data was reduced by ensemble-averaging.

The sound power level of fans with straight as well as forward-swept blades was measured on a standardized acoustic fan test facility. The facility has been manufactured in accordance with the standard DIN EN 25 136. The volume flow rate was measured with a calibrated flow meter.

Experimental Results

Flow Field. The total pressure and velocity field was measured for three rotors with conventional straight blades, with blades skewed in the circumferential direction ($\delta = +30$ deg), and with blades skewed against the circumferential direction ($\delta = -30$ deg) at design flow rate $\varphi = 0.18$. A set of representative results downstream of the straight bladed fan are provided here.

The calculated flow field, being solved in the rotating frame of reference, was converted to the fixed frame of reference to facilitate comparison with the experimental results. The velocity at the downstream plane 2 is presented by the axial, circumferential, and radial components in Fig. 7.

In the vicinity of the hub, the agreement between calculation and experiment is good. In the shroud region, some discrepancy can be observed. A higher axial velocity is predicted here. The circumferential velocity deviates in magnitude and pattern. This is partly attributed to the tip clearance, which has been excluded from computations. But as the tip clearance prevailing in the experiment was extremely small, the reason for this deviation is expected to be the relatively high relative-to-absolute speed ratio, i.e., a high rotational speed. With the ratio increasing, the accuracy of computational flow results, converted to the fixed frame of reference, deteriorates. The measured total pressure distribution (Fig. 7) matches well with the computation.

In general, the computed and measured flow is in good agreement for all three fans. This holds true for grids with approximately 1×10^5 nodes. Severe discrepancies were observed for grids containing only approximately 1×10^4 nodes.

Design procedures are commonly simplified by using circumferentially averaged flow variables. Figure 8 depicts a comparison of the circumferentially averaged axial velocity downstream of the three rotors mentioned above. The axial velocity distribution, predicted in the design of the straight bladed fan by the simple radial equilibrium, is included. The comparison reveals that the blades skewed in the direction of rotation tend to increase the flow in the hub region as compared to the straight blade. This stabilizes the flow in the hub region, which is usually endangered by flow separation. Mohammad and Raj (1977), who tested an axial flow fan with slightly forward swept blades of 10 deg, observed a similar trend. They reported that the sweep-induced secondary flow is acting inward for the swept blade. Figure 8 shows that the blade skewed against the direction of rotation slightly increases the flow in the shroud region if compared to the straight blade.

Fan Characteristics. The performance of a fan, reflected in the pressure rise and efficiency, changes when its blades are skewed. Figure 9 depicts the measured pressure coefficient and static efficiency for the rotor with straight as well as with skewed blades.

The performance of the fan with blades skewed in the direction of rotation reveals that flow separation tends to occur at a lower flow rate, which is attributed to the flow deflection toward the hub. Hence, these fans can work at a higher pressure rise (i.e., decreased volume flow) without flow separation. However, the flow separation occurs more abruptly and the pressure rise is lower than for the fans with straight blades.

For the blades skewed against the direction of rotation, it can be deduced that flow separation already starts at a higher volume flow rate when the flow is throttled. The region of flow separation extends over a wide range of volume flow. The pressure rise is lower than in the case of straight blades. The fan static efficiency is substantially lower than for the other two fans.

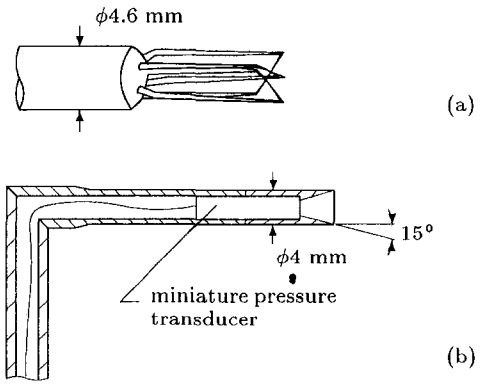

Fig. 6 (a) Triple-sensor and (b) total pressure probe

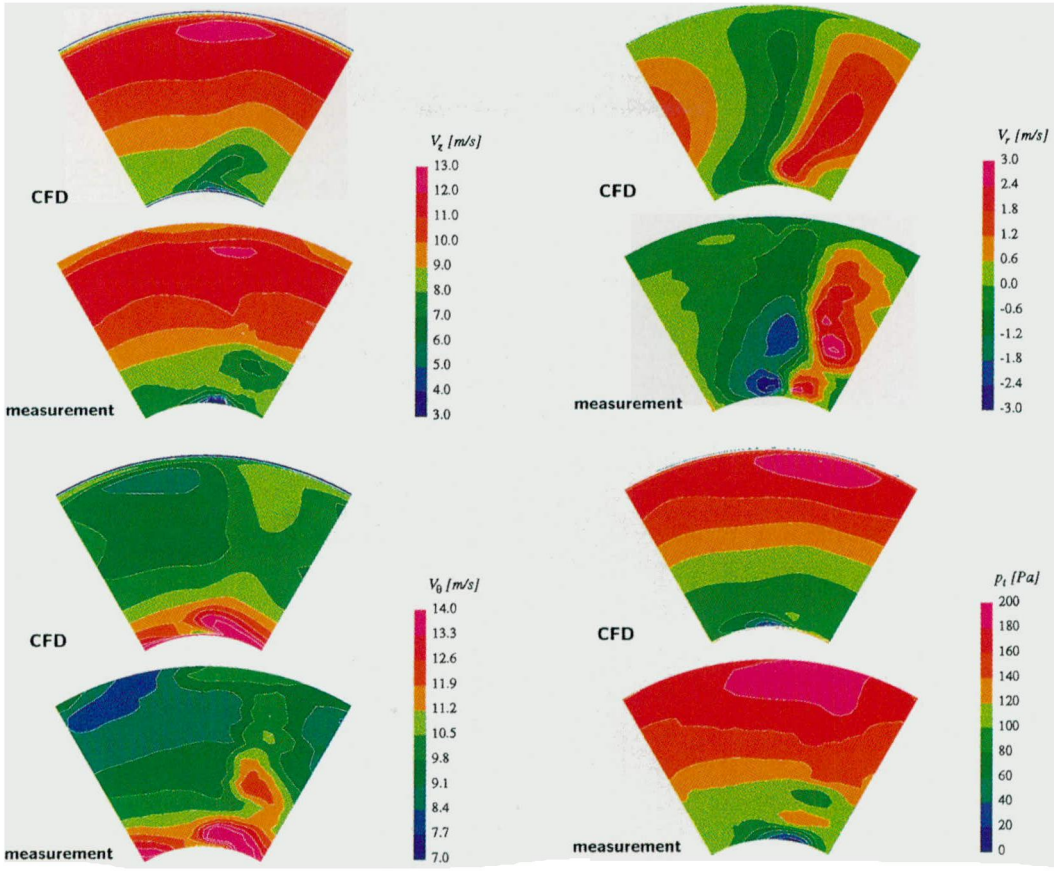

Fig. 7 Flow field downstream of straight bladed rotor (fan A)

The accuracy of the experimental results was checked in a measurement uncertainty analysis. The error in results was estimated not to exceed 2 percent for a 95 percent confidence interval.

Numerical Flow Results

Circumferential Skew. The blades of the two fan rotors A and B are the subject of the parametric study. The blades have skew angles in the circumferential direction with constant values of $\delta = -45, -30, 30$, and 45 deg as well as variable angles starting at $\delta_i = 0$ deg at the hub and increasing linearly to $\delta_o = -60, -45, -30, 30, 45$, and 60 deg at the shroud.

In Fig. 10, the pressure coefficient is compared at different skew angles. The pressure coefficient has a maximum for the straight fan blade. This is also reflected in a reduced blade loading, i.e., the lift coefficient C_L is highest for the straight blade. Positive blade skew increases the axial flow in the vicinity of the hub and vice versa as already indicated by Fig. 7.

Swept Blades. For the blades exhibiting sweep but no dihedral, the sweep angle was varied incrementally in a similar way to the previous variation of the skew angle. Sweep decreases the blade loading and pressure rise across the rotor. The forward-swept blades still increase the flow in the hub region. It would be expected that sweep would not influence the radial flow distribution. However, it can be shown that swept rotor blades affect the radial flow distribution (Beiler, 1996). Sweeping the blade tip in the downstream direction causes the flow to shift toward the casing.

The flow results indicate that the lift distribution does not decrease gradually along the blade span as the theory of infinitely long airfoils would predict (Fig. 11). This is attributed to the interference with the hub and shroud surfaces. The results reveal a pronounced wall effect in the vicinity of the shroud. This interference has been addressed by Küchemann (1952) when he investigated a wing with an adjacent wall (Thwaites, 1960). In the vicinity of a wall, the lift coefficient for a swept-forward airfoil increases. The opposite holds true for a swept-back airfoil. A swept-back fan blade is swept-back with respect to the hub but swept-forward with respect to the shroud.

The blade loading can be estimated. As the loading for a swept airfoil is theoretically reduced according to the cosine of the sweep angle, a correction to compensate for this reduction is applied. Another correction is made to compensate for the wall interference. It is only applied in the vicinity of the shroud as the interference is less pronounced close to the hub and attractive swept fan shapes usually have a low sweep angle at the hub. The predicted loading is derived from the loading of the fan with straight blades.

For example, consider the blade with 30 deg back sweep. The predicted loading in Fig. 11 matches well with the loading derived from the flow simulation. Similar results could be obtained for swept-forward blades.

Extended Design Procedure

The fan design method described in a previous section was extended to cover swept blades as well. This was realized by considering the theory of airfoils and the results of the numerical flow investigations.

The method expands on the elementary airfoil theory as described, for instance, by Eck (1972) in the following way:

1 The design volume flow rate and pressure rise, the swirl velocity distribution, and the total efficiency are specified.
2 The outlet axial flow distribution corresponding to this design point is derived by considering radial equilibrium of the flow at the outlet of the fan stage.

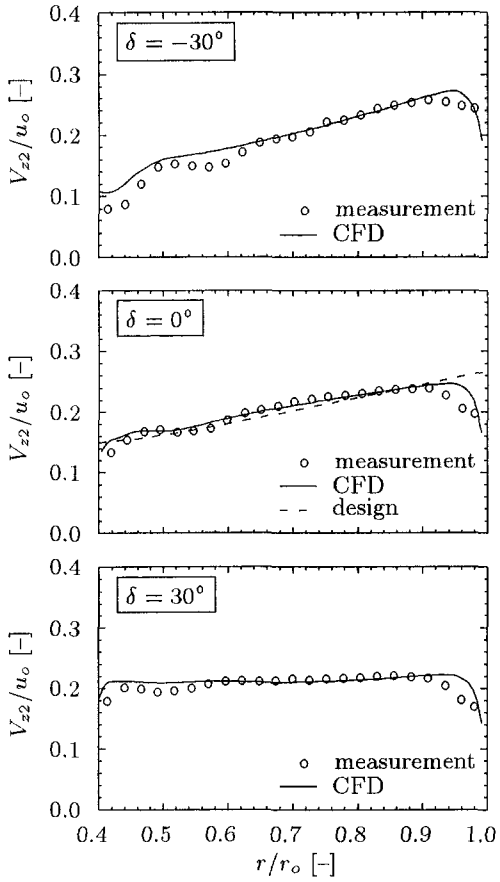

Fig. 8 Comparison of the calculated and measured, circumferentially averaged axial velocity downstream of three rotors (A series) at design flow rate

3 The stage pressure rise is corrected by the total efficiency and for the specified sweep. For varying sweep angles from hub to shroud, the locally corrected pressure rise is integrated along the radius to give the average pressure rise. The pressure rise is corrected for the wall interference in the shroud region.

4 The blade sections at different radial positions are determined according to airfoil theory.

5 The blade geometry is calculated by Eqs. (2) and (3), setting the dihedral angle to zero. The blade sections are stacked on the three-dimensional running blade axis.

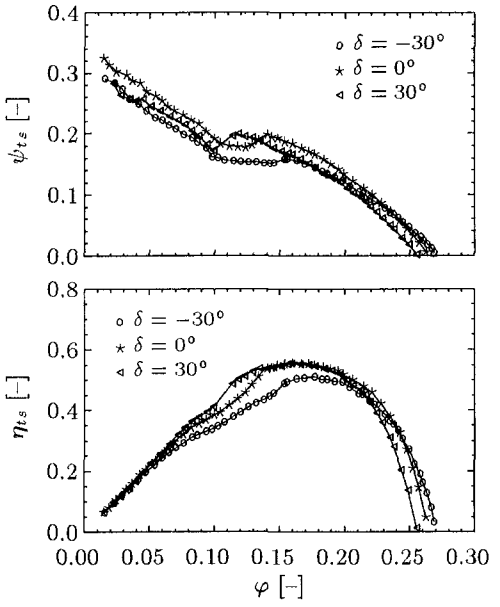

Fig. 9 Measured pressure coefficient and efficiency for fans with straight and circumferentially skewed blades (A series)

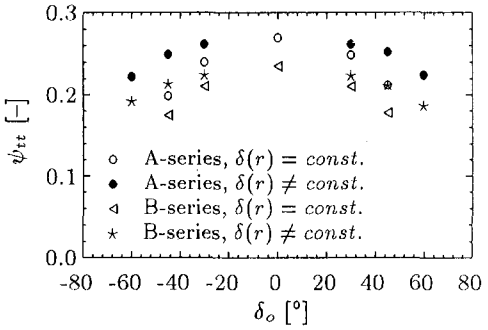

Fig. 10 Calculated pressure coefficient at different blade skew angles at design flow rate

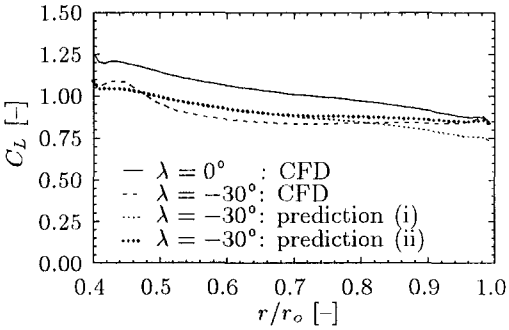

Fig. 11 Calculated and predicted lift distribution along the blade span for straight and swept-back blades, (*i*) excluding and (*ii*) including wall correction

Several fans were designed accordingly and analyzed using CFD. One fan, designated as G-fan, was manufactured and tested. The fan blades are swept in the forward (upstream) direction. The sweep angle increases linearly from hub to shroud, starting with 5 deg back sweep and ending with 55 deg forward sweep to provide a favorable blade shape. A similar pressure and flow rate as for the fan with straight blades (fan A), but a total efficiency of 92 percent, was specified in the design. Figure 12 illustrates the pressure rise at various flow rates. The small deviation in pressure at design point ($\varphi = 0.18$) is attributed to the difference in the specified total efficiency.

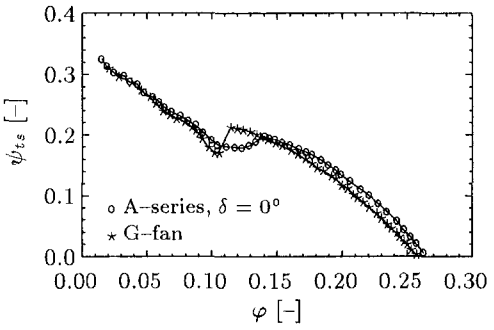

Fig. 12 Comparison of the measured pressure coefficient for a straight bladed fan (fan A) and G-fan

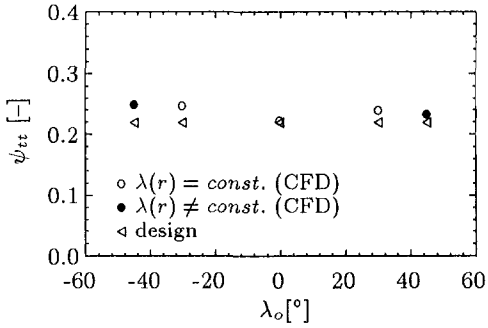

Fig. 13 Calculated and design pressure coefficient at design flow rate for different sweep angles including theoretical corrections

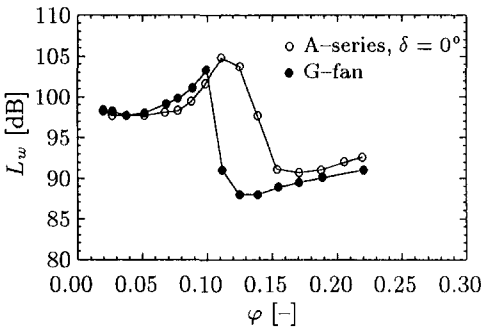

Fig. 15 Measured sound power level of straight and swept-forward fans (n = 3000/min)

Flow simulations were performed for a series of blades with systematically altered sweep angles, including sweep and wall corrections. The swept fans achieve the desired pressure, presented as pressure coefficient in Fig. 13. However, the pressure coefficient is slightly too high. This is attributed to the real flow, which deviates from the theoretical analysis. Contemplating the results of several numerical flow computations, it was found that fans designed with a sweep correction of $(\cos \lambda)^{0.62}$ instead of $\cos \lambda$ achieve the given pressure rise more accurately. Figure 14 shows the calculated pressure coefficients. The pressure coefficients for 30 deg swept-back blades are missing, since the computations did not converge, due to the adverse flow conditions encountered with swept-back blades. The theoretical wall correction was not adjusted.

The measured total efficiency of the fans investigated is approximately 95 percent at design flow rate. The designs based on this value achieved the specified design point.

Sound Power Level

The sound power level of several fans was measured on the acoustic fan test facility. Figure 15 presents the sound power level of the A-series fan with straight blades and the G-fan at various flow rates. Comparing the results to the fan pressure rise in Fig. 12 reveals the negative impact of flow separation on the noise emission. As soon as the flow separates, the noise increases significantly. The swept-forward fan runs more quietly over a wider flow range. There appears to be no advantage at flow rates left to the point where both fans operate in the region of separated flow.

Concluding Remarks

The study shows that the three-dimensional flow in axial flow turbomachinery of high rotational speed and low pressure rise can be simulated well.

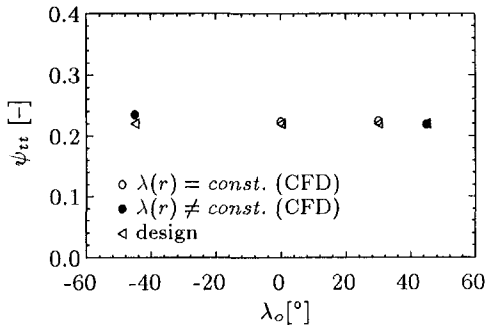

Fig. 14 Calculated and design pressure coefficient at design flow rate for different sweep angles including corrections based on theory and CFD analysis

The blades skewed in the circumferential direction exhibit a combination of sweep and dihedral. Blades with sweep but without dihedral can be treated similarly to swept airfoils. An evaluation of the flow simulation results indicates that theoretical predictions match well with computational results. The predictions, however, rest on several assumptions and the complex flow phenomena cannot be predicted by theory alone.

Fans designed to compensate for sweep as well as for the interference between shroud and blade achieve the specified design point quite accurately. Modifying the corrections by utilizing results from the parametric study further improves the agreement between design and actual operating point.

For this type of fan of specified pressure rise, Mach number and incorporated shroud, swept-back blades exhibit deficiencies. The flow separates at relatively high flow rates. This corresponds to a poor aerodynamic performance and an increased noise emission. Swept-forward blades tend to improve the fan performance. The outlet flow distribution is more uniform, reducing the dynamic discharge losses. The improved acoustic performance is also beneficial. Swept-forward blades appear to have the potential of wide-spread application.

Acknowledgments

The authors would like to acknowledge the Deutsche Forschungsgemeinschaft for the support of this research project. Gratitude is expressed to Mr. M. Stremel who performed the acoustic measurements.

References

Abbott, I. H., and Von Doenhoff, A. E., 1959, *Theory of Wing Sections,* Dover Publications, New York.

Beiler, M. G., 1996, "Untersuchung der dreidimensionalen Strömung durch Axialventilatoren mit gekrümmten Schaufeln," Dissertation Universität Siegen, VDI-Verlag, Reihe 7, No. 298, Düsseldorf.

Brown, N. A., 1977, "The Use of Skewed Blades for Ship Propellers and Truck Fans," *Noise and Fluids Eng.,* ASME, pp. 201–207.

Carolus, T. H., and Scheidel, W., 1988, "Bemerkungen zum Einsatz schnellläufiger Axiallüfter in Motorkühlsystemen von Kraftfahrzeugen," *Mitteilungen Institut für Strömungsmechanik und Strömungsmaschinen,* Universität' Karlsruhe, Heft 39, pp. 19–26.

Cordes, G., 1963, *Strömungstechnik der gasbeaufschlagten Axialturbine,* Springer-Verlag, Dresden.

Dejc, M. E., and Trojanovskij, B. M., 1973, *Untersuchung und Berechnung axialer Turbinenstufen,* VEB Verlag Technik, Berlin.

Dejc, M. E., Trojanovskij, B. M., and Filippov, G. A., 1990, "Effective Way of Improving the Efficiency of Turbine Stages," *Thermal Engineering,* Vol. 37, No. 10, pp. 520–523.

DIN 24163, 1985, "Ventilatoren," Teil 2, Beuth Verlag, Berlin.

DIN EN 25136, 1994, "Bestimmung der von Ventilatoren in Kanälen abgestrahlten Schalleistung," Beuth Verlag, Berlin.

Dixon, S. L., 1978, *Fluid Mechanics, Thermodynamics of Turbomachinery,* 3rd ed., Pergamon Press.

Eck, B., 1972, *Ventilatoren,* 5th ed., Springer-Verlag, Berlin.

Godwin, W. R., 1957, "Effect of Sweep on Performance of Compressor Blade Sections as Indicated by Swept-Blade Rotor, Unswept-Blade Rotor and Cascade Tests," NACA TN 4062.

Horlock, J. H., 1958, *Axial Flow Compressors Fluid Mechanics and Thermodynamics,* Butterworth Publications Limited, London.

Küchemann, D., 1952, "A Simple Method of Calculating the Span and Chordwise Loading on Straight and Swept Wings of Any Given Aspect Ratio at Subsonic Speeds," Aeronautical Research Council, Reports and Memoranda No. 2935.

Launder, B. E., 1989, "Second-Moment Closure and Its Use in Modelling Turbulent Industrial Flows," *International Journal for Numerical Methods in Fluids,* Vol. 9, pp. 963–985.

Mohammad, K. P., and Raj, D. P., 1977, "Investigations on Axial Flow Fan Impellers With Forward Swept Blades," ASME Paper No. 77-FE-1.

Smith, L. H., Jr., and Yeh, H., 1963, "Sweep and Dihedral Effects in Axial-Flow Turbomachinery," ASME *Journal of Basic Engineering,* Vol. 9, pp. 401–416.

Smith, L. H., Jr., 1987, "Unducted Fan Aerodynamic Design," ASME JOURNAL OF TURBOMACHINERY, Vol. 109, pp. 313–324.

TASCflow Theory Documentation, 1994, Version 2.3, Advanced Scientific Computing, Waterloo.

Thwaites, B., 1960, *Incompressible Aerodynamics,* Clarendon Press, Oxford.

Vavra, M. H., 1960, *Aero-Thermodynamics and Flow in Turbomachines,* Wiley, New York.

APPENDIX

The coefficients in Eqs. (2) and (3), as derived by Beiler (1996), are:

$$\hat{\alpha}_1 = \hat{\rho}_2\theta_3 - \theta_2\hat{\rho}_3$$

$$\hat{\alpha}_2 = -\hat{\rho}_1\theta_3 + \theta_1\hat{\rho}_3$$

$$\hat{\alpha}_3 = \hat{\rho}_1\theta_2 - \theta_1\hat{\rho}_2$$

$$n_1 = z_2\hat{\rho}_3 - \hat{\rho}_2 z_3$$

$$n_2 = -z_1\hat{\rho}_3 + \hat{\rho}_1 z_3$$

$$n_3 = z_1\hat{\rho}_2 - \hat{\rho}_1 z_2$$

$$\hat{\rho}_1 = (1 + \tan^2\nu + \tan^2\lambda/\cos^2\nu)^{-1/2}\tan\lambda/\cos\nu$$

$$\hat{\rho}_2 = (1 + \tan^2\nu + \tan^2\lambda/\cos^2\nu)^{-1/2}$$

$$\hat{\rho}_3 = (1 + \tan^2\nu + \tan^2\lambda/\cos^2\nu)^{-1/2}\tan\nu$$

$$\theta_1 = -\cot\beta\cos^2\phi\,\frac{(1 + \tan^2\phi + \cot^2\beta)^{1/2}}{1 + \cot^2\beta\cos^2\phi}$$

$$\theta_2 = 0$$

$$\theta_3 = (1 + \cot^2\beta\cos^2\phi)^{-1/2}$$

$$z_1 = (1 + \tan^2\phi + \cot^2\beta)^{1/2}/(\cot^2\beta + 1/\cos^2\phi)$$

$$z_2 = -\sin\phi$$

$$z_3 = \cos^2\phi\cot\beta(1 + \cot^2\beta\cos^2\phi)^{-1/2}$$

Development of Hub Corner Stall and Its Influence on the Performance of Axial Compressor Blade Rows

C. Hah
NASA Lewis Research Center,
Cleveland, OH 44135

J. Loellbach
ICOMP/NASA Lewis Research Center,
Cleveland, OH 44135

A detailed investigation has been performed to study hub corner stall phenomena in compressor blade rows. Three-dimensional flows in a subsonic annular compressor stator and in a transonic compressor rotor have been analyzed numerically by solving the Reynolds-averaged Navier–Stokes equations. The numerical results and the existing experimental data are interrogated to understand the mechanism of compressor hub corner stall. Both the measurements and the numerical solutions for the stator indicate that a strong twisterlike vortex is formed near the rear part of the blade suction surface. Low-momentum fluid inside the hub boundary layer is transported toward the suction side of the blade by this vortex. On the blade suction surface near the hub, this vortex forces fluid to move against the main flow direction and a limiting stream surface is formed near the hub. The formation of this vortex is the main mechanism of hub corner stall. When the aerodynamic loading is increased, the vortex initiates further upstream, which results in a larger corner stall region. For the transonic compressor rotor studied in this paper, the numerical solution indicates that a mild hub corner stall exists at 100 percent rotor speed. The hub corner stall, however, disappears at the reduced blade loading, which occurs at 60 percent rotor design speed. The present study demonstrates that hub corner stall is caused by a three-dimensional vortex system and that it does not seem to be correlated with a simple diffusion factor for the blade row.

Introduction

Design trends for modern multistage compressors continue to increase blade loadings and decrease aspect ratios. Sophisticated design tools are required to account for the increased complexity of the resulting flow fields. During the last decade, numerical methods based on the Reynolds-averaged Navier–Stokes equations have made remarkable progress in turbomachinery design applications. Currently, steady and unsteady three-dimensional viscous flow calculations are routinely performed during the design cycle.

Although various CFD codes have been successfully applied to turbomachinery component design, further advances in numerics as well as physical modeling should be pursued. During the 1994 ASME/IGTI-sponsored CFD validation exercise (see Strazisar and Denton, 1995), many questions were raised concerning widely scattered blind CFD predictions. One of the issues was whether the current generation of CFD codes can calculate compressor hub corner stall. The importance of accurate calculations of endwall flows for multistage compressor designs has been pointed out by previous studies (Adamczyk et al., 1993; Copenhaver et al., 1993; Smith, 1970; etc.).

Various studies concerning the three-dimensional aspects of endwall flows in axial compressors have been reported. Dring et al. (1982, 1983) investigated the flow in an isolated rotor with high aerodynamic loading and low aspect ratio. The observed regions of high loss were near the end walls. At the hub, the high loss was associated with the flow separation of the blade and endwall surface boundary layers near the trailing edge of the suction surface. At the tip, the high loss region was thought to be due to the rotor tip leakage flow. When the flow coefficient was reduced, the high loss region near the hub extended radially over the entire span. On the rotors of a two-stage machine (Dring et al., 1983), large areas of separated flow on the surfaces near the hub were identified through flow visualization. Joslyn and Dring (1985) performed a similar study of the flow field in a second-stage stator. A stalled region with high aerodynamic loss in the corner of the suction surface and the hub end wall was reported in their study. This corner stall extended up to 75 percent span at a reduced flow rate. They found that the flow incidence angle at the stator hub leading edge was increased due to the rotor hub corner stall, which caused severe flow separation on the stator suction surface near the hub end wall. Dong et al. (1987) investigated flow and loss mechanisms in a single-stage low-speed axial flow compressor. They did not find endwall flow separation in the rotor. However, large separated areas were observed at both endwalls of the stator. Schulz and Gallus (1988) performed detailed flow measurements in an isolated subsonic compressor stator at various blade loadings. Their extensive measurements included blade and endwall flow visualization, steady and unsteady static pressure measurements, blade boundary layer investigations with hot wires and hot films, and five-hole probe measurements at the stator exit. In their study, hub corner stall was observed at all blade loadings. The hub corner stall and the related secondary flows were responsible for the high loss region observed at the stator exit.

Certain high-speed fan/compressor designs use the concept of high-performance hub design to prevent possible hub corner stall and its related performance deterioration. During the 1994 ASME/IGTI CFD code assessment exercise, a large dip in the measured spanwise distribution of total pressure was observed near the hub for the case under study. Because the measurements

Contributed by the International Gas Turbine Institute and presented at the 42nd International Gas Turbine and Aeroengine Congress and Exhibition, Orlando, Florida, June 2–5, 1997. Manuscript received International Gas Turbine Institute February 1997. Paper No. 97-GT-42. Associate Technical Editor: H. A. Kidd.

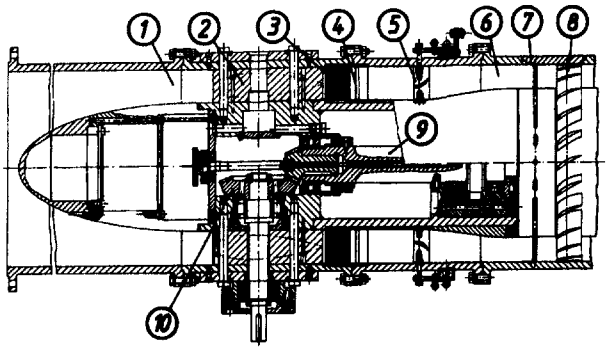

Fig. 1 Annular cascade test facility

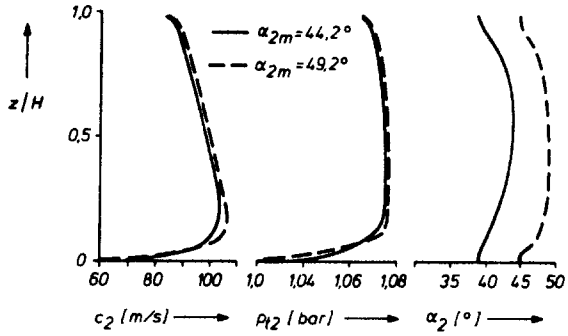

Fig. 3 Flow properties at cascade inlet

did not include flow visualization or LDV data near the hub, no direct explanation could be made. This total pressure deficiency near the hub, however, disappeared at the reduced blade loading, which occurred at 60 percent rotor speed. Hub corner stall was considered to be one of the possible causes of the observed total pressure deficiency near the hub at 100 percent rotor speed at near-peak efficiency.

The primary objective of the current study is to advance our understanding of the basic mechanism of compressor hub corner stall. Both experimental data and numerical results are analyzed in detail for the flows in a subsonic compressor stator and in a transonic compressor rotor.

Hub Corner Stall in a Subsonic Compressor Stator

A detailed experimental study to investigate hub corner stall was conducted by Schulz and Gallus (1988). The test facility is shown in Fig. 1. The extensive and comprehensive data base includes the following measurements:

1 Visualization of the flow on the blades, hub, and casing (dye injection and oil flow technique)
2 Wall static pressure measurements
3 Steady and unsteady blade pressure measurements
4 Blade boundary layer investigations with hot-wire and hot-film probes
5 Five-hole probe measurements at the stator exit

A turbocompressor set provides continuous airflow to the test rig. The swirl angle of the flow can be varied by means of 48 adjustable inlet guide vanes (⑤ in Fig. 1). The test compressor cascade (⑧ in Fig. 1) consists of 24 untwisted blades mounted on the hub, with a hub-to-tip ratio of 0.75 and a tip diameter of 428 mm. The aspect ratio is 0.86 and the solidity at midspan is 0.78. The blade profiles are radially stacked at their center of gravity and the blade metal angles at inlet and exit are 44 and 15 deg respectively. Other geometric parameters are shown in Fig. 2.

For the investigation described in this paper, the experiment was performed with the rotor removed during the test. The properties of the incoming flow were surveyed with pneumatic five-hole and boundary layer probes at 56 percent blade chord upstream of the stator leading edge. Inlet flow conditions were specified at the same location for the calculation as well. The inlet angle to the stator, and therefore the blade loading, were varied, and the measurements were taken at five different points of operation identified by the inlet angles at midspan. The data were taken at inlet angles of 40, 44.2, 49.2, 54.6, and 57.6 deg. These angles are measured from the axial direction, and zero-incidence occurs at an inlet angle of 42 deg. The spanwise distributions of inlet velocity, total pressure, and inlet angle for the midspan inlet angles of 44.2 and 49.2 deg are shown in Fig. 3. The instrumentation and the accuracy of the measurements are described in more detail by Schulz and Gallus (1988) and Gallus et al. (1991).

The steady Reynolds-averaged Navier–Stokes equations are solved for the current problem. For the present numerical study, the entire flow field is assumed to be turbulent and no transition is considered. To close the system of equations, a closure model for turbulence stresses must be applied. Although no existing closure model accurately represents all salient flow features, the main flow phenomena in turbomachinery can be adequately calculated by the current generation of turbulence models. For

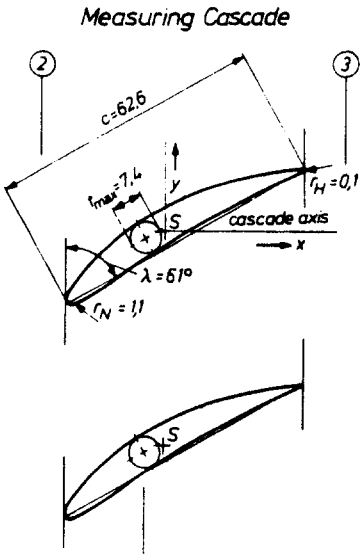

Fig. 2 Midspan cascade geometry

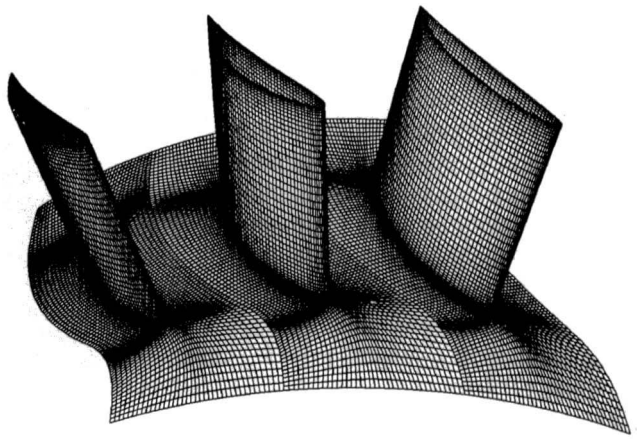

Fig. 4 Computational grid for compressor stator

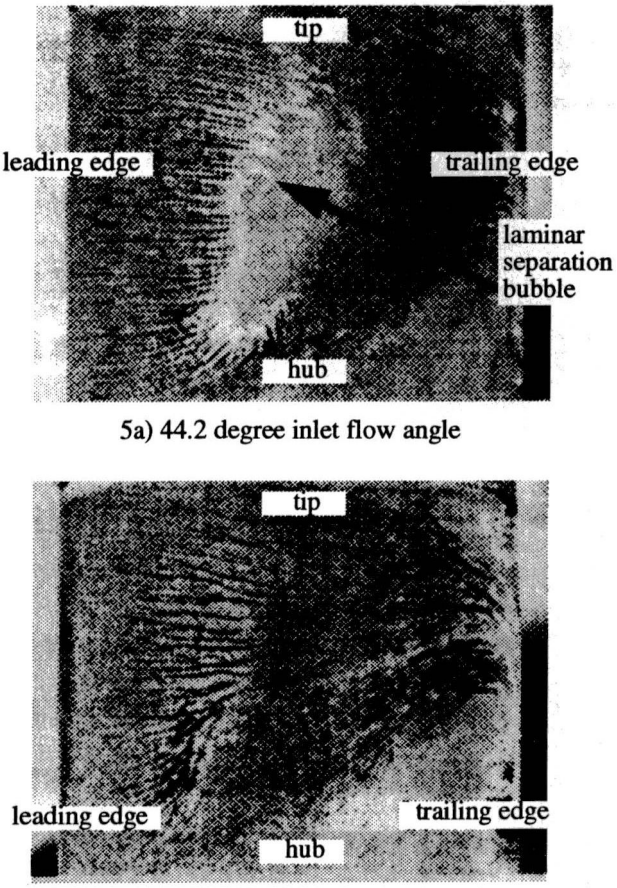

Fig. 5 Oil flow visualization on blade suction surface

the current numerical study, a standard two-equation turbulence model with a low-Reynolds-number modification is applied. Standard values for the various coefficients in the turbulence model are used for the current hub corner stall study. The details of the applied turbulence model are given by Hah and Wennerstrom (1991). The governing steady Reynolds-averaged Navier–Stokes equations are solved with a pressure-based implicit relaxation method using a fully conservative control volume approach described by Hah (1987).

At the inflow boundary, the measured distributions of total pressure, total temperature, and inlet flow angle are fixed. At the outflow boundary, the static pressure is fixed at the shroud and all the other flow variables are extrapolated. The experimental value of the turbulence kinetic energy is prescribed at the inflow boundary and a standard equilibrium condition is used to estimate the length scale for the turbulence dissipation. Periodicity conditions are applied between individual blades. Residuals of each finite difference equation are integrated over the entire domain. When the total integrated residuals of all the equations are reduced by four orders of magnitude from the initial values, the solution is considered to be converged. The computational grid, shown in Fig. 4, has 50 nodes in the blade-to-blade direction, 47 nodes in the spanwise direction, and 102 nodes in the streamwise direction. Typical computing time is about one hour on a Cray-YMP.

Flow Field Near Blade Suction Surface and Hub Wall. Experimental flow visualizations, created by dye injection, on the blade suction surface at inlet flow angles of 44.2 and 49.2 deg are shown in Fig. 5. At both blade loadings, the reversed flow region near the hub is larger than that near the tip. This is because the incoming hub boundary layer is thicker than that at the shroud, as shown in Fig. 3. A hub surface flow visualization at an inlet flow angle of 44.2 deg is shown in Fig. 6. This hub flow visualization indicates that there are two distinct vortices on the hub wall. Calculated flows near the suction surface and on the hub wall are shown in Fig. 7 in the form of surface particle traces and velocity vectors. The numerical solutions also show that the reversed flow region near the hub is larger than that near the shroud. The stalled flow region also increases with higher blade loading. The numerical results agree very well with the measurements.

The flow visualizations and numerical results indicate that two distinct vortices exist near the hub surface. The larger vortex is centered away from the suction surface at approximately 80 percent axial chord downstream from the leading edge. The smaller vortex is located very close to the trailing edge. The two vortices are clearly seen at both blade loadings in the calculated results. The hub surface flow visualization supports the calculated results. The blade suction surface flow visualization shown in Fig. 5 indicates that there exists a laminar flow separation bubble near the middle of the blade span. This laminar separation bubble was also confirmed through hot-film measurements (Schulz and Gallus, 1988). Inside the separation bubble, the flow undergoes transition and reattaches as turbulent flow. In the computations, the flow is assumed to be completely turbulent. This assumption might contribute to the deviation between the measurements and the calculations. However, the measured incoming flow near the hub is turbulent and the flows near the end walls seem to remain turbulent. Therefore, the current fully turbulent flow calculations appear to be adequate for the hub corner stall investigation.

Topological Structure of Hub Corner Stall. Comparisons between the surface flows from the measurements and the calculation indicate that the numerical solution represents the hub corner stall reasonably well. Therefore, an attempt was made to use the numerical solution to shed some new light on the complex structure of the hub corner stall. Although surface flow visualization is very helpful in understanding flow near solid walls, surface flow patterns do not necessarily explain complex flow patterns away from the walls. For the current problem, experimental flow visualization is not possible away from the wall surfaces because of high flow velocity. Probe measurements exhibit large errors and disturb the flow itself beyond tolerable limits, and laser velocimetry for this type of three-dimensional separated flow near the endwall has not been practical due to seeding problems. Numerical solutions, however,

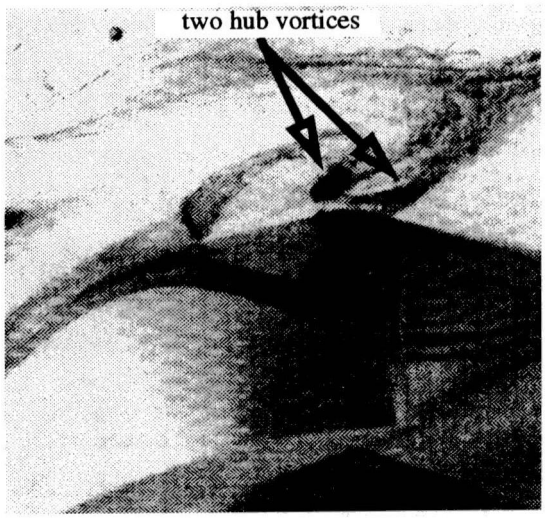

Fig. 6 Oil flow visualization on hub surface

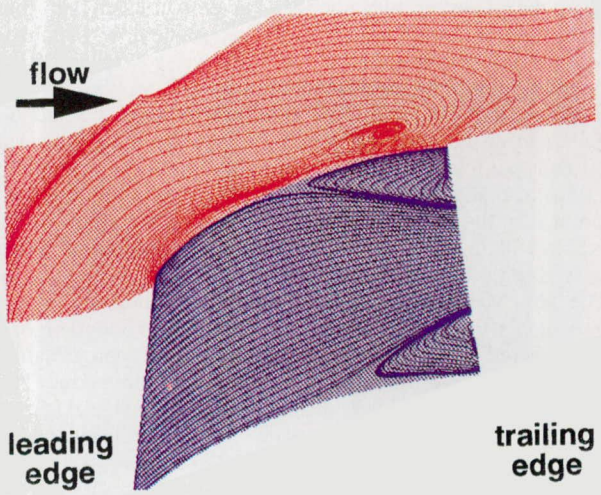

Oil flow visualization

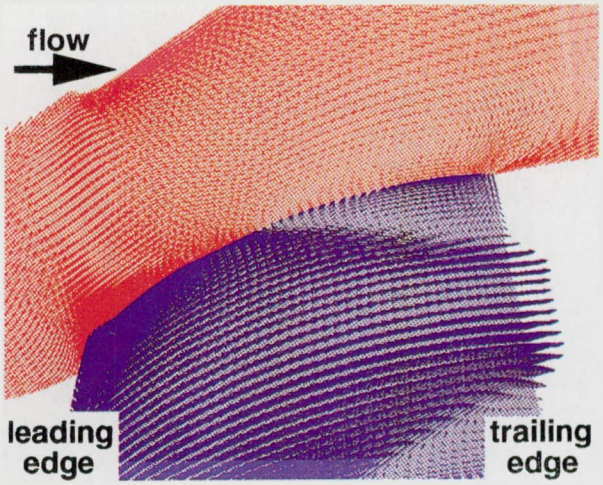

Velocity vectors near surface

Fig. 7(*a*) Calculated flow near hub and suction surface (44.2 deg inlet flow angle)

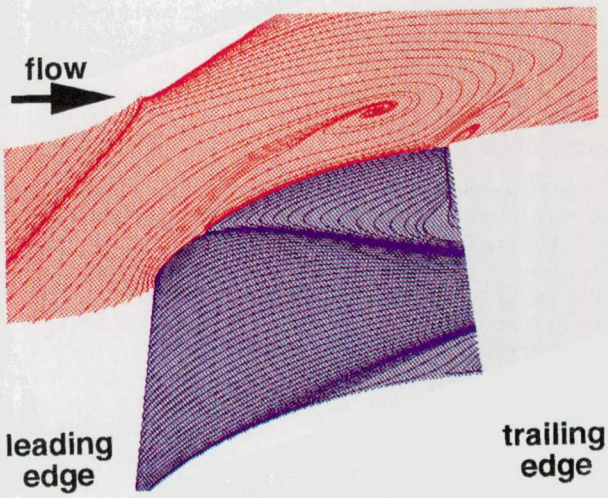

Oil flow visualization

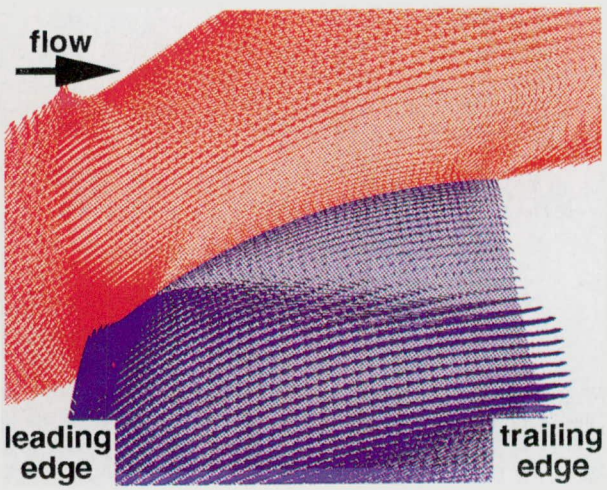

Velocity vectors near surface

Fig. 7(*b*) Calculated flow near hub and suction surface (49.2 deg inlet flow angle)

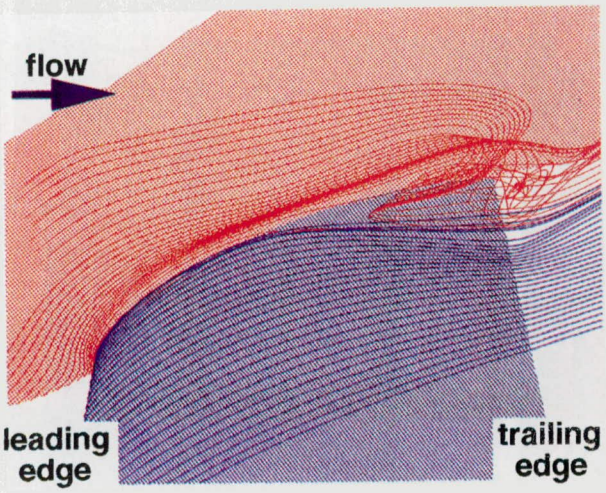

Fig. 8 Particle traces in vortex (44.2 deg inlet flow angle)

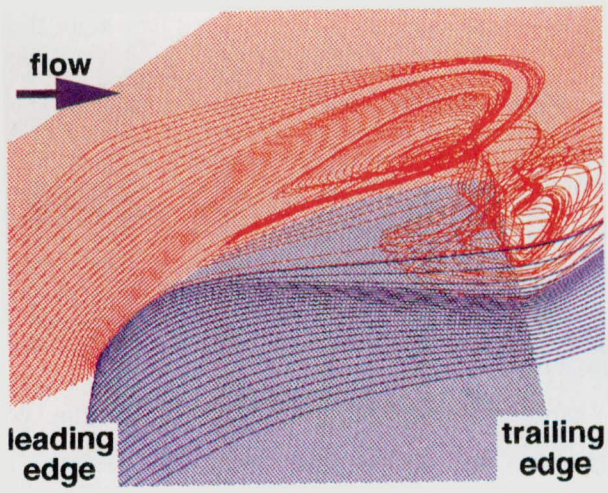

Fig. 9 Particle traces in vortex (49.2 deg inlet flow angle)

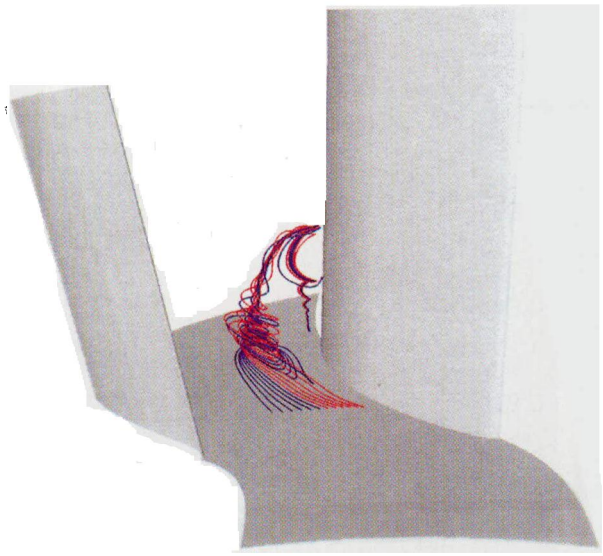

Fig. 10 Structure of hub corner stall vortex

compliment the experimental data by filling in the gaps where measurements cannot be made.

According to Fig. 7, two distinct vortices are clearly shown on the hub wall. On the other hand, no clear vortex structure can be identified on the suction surface, although a reversed flow region is clearly visible near the corner. The flow structures visualized on the hub wall and the suction surface must be part of a three-dimensional structure of hub corner stall. To visualize this three-dimensional structure, particle traces were generated from the numerical solution. Figures 8 and 9 show particle traces inside the hub corner stall at two blade loadings. The structures of the hub corner stall are very similar at the different loadings, but the details of the flow structure are clearer at the higher blade loading. The structure of the vortex itself is shown in Fig. 10. The dominant features of the hub corner stall appear to be two vortices. One is located near the suction surface at approximately 80 percent axial chord, and the other is located close to the trailing edge. These two counterrotating vortices extend radially outward and connect outside the wall boundary layer. Thus, the vortices visualized on the hub wall are actually

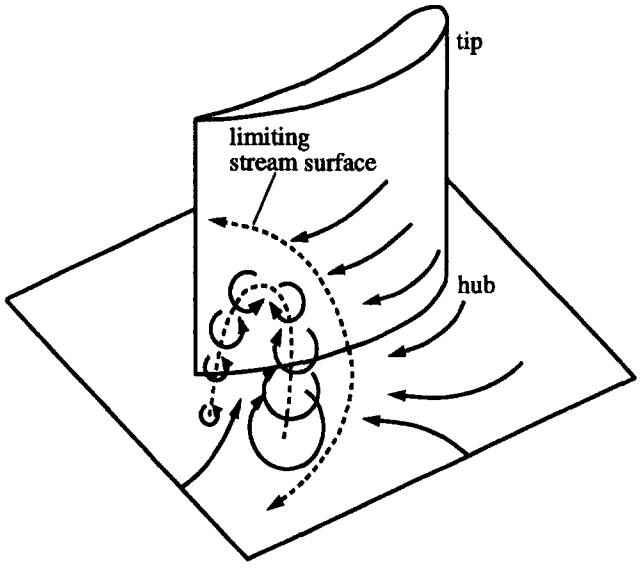

Fig. 11 Topology of hub corner stall

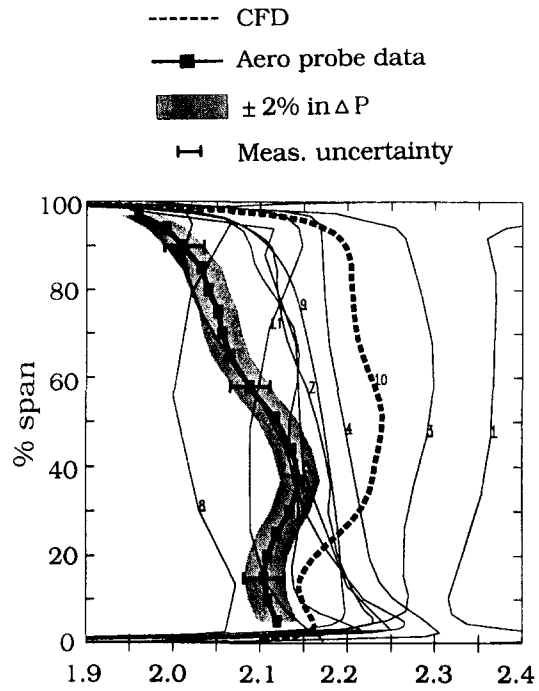

Fig. 12 Radial total pressure distributions for Rotor 37

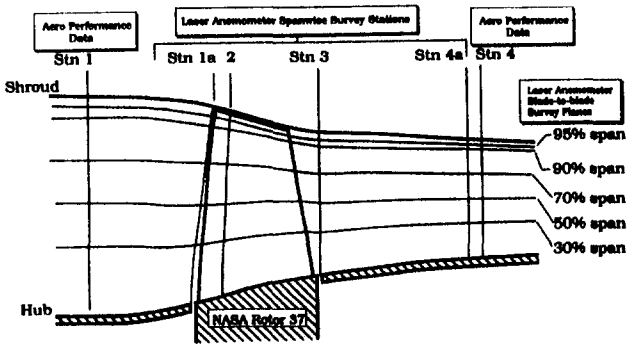

Fig. 13 Experimental measurement stations for Rotor 37

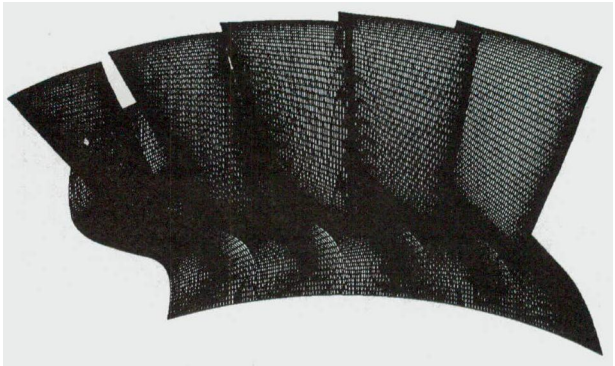

Fig. 14 Computational grid for Rotor 37

two legs of a single vortex. Because of the strong particle motion around this vortex, a reversed flow region and a limiting streamline are created on the suction surface. The structure of the hub corner stall is also illustrated in Fig. 11. The single vortex, whose two legs originate from the hub, clearly explains the measured flow pattern on the hub and the blade suction surface. Again, the dominant feature of the hub corner stall in a compres-

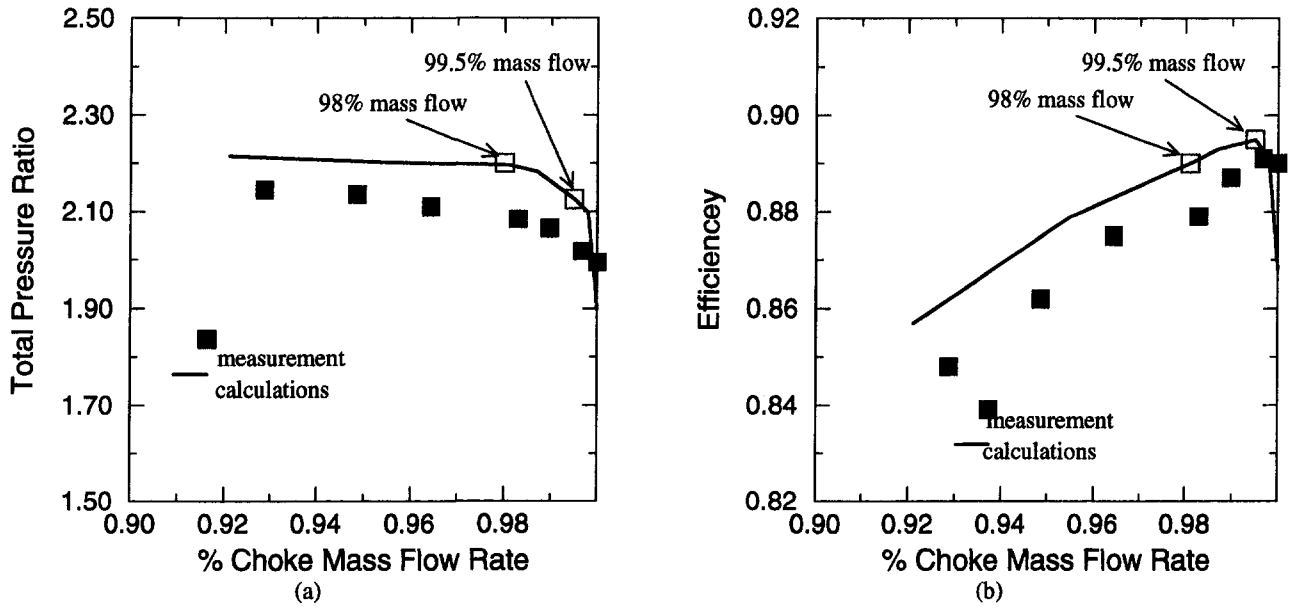

Fig. 15 Comparison of rotor performance for Rotor 37

sor stator is a twisterlike vortex that has two legs attached on the hub wall. The location and the strength of this vortex depend on the blade loading (or diffusion factor) and the incoming flow characteristics, among other factors. The tested airfoils operate below the conventionally accepted limit of the diffusion factor. Therefore, a simple diffusion factor cannot be used as a criterion for the occurrence of compressor hub corner stall. Design optimization to remove or control this hub corner stall vortex with currently available numerical tools might improve the performance of multistage compressors.

Hub Corner Flow in a Transonic Compressor Rotor

During the 1994 ASME/IGTI Turbo Expo, a CFD code assessment exercise was organized by the Turbomachinery technical committee. The objective of this exercise was to provide an objective view of CFD capabilities to the turbomachinery aerodynamics community. Both CFD users and CFD developers were invited to submit solutions for a "blind test case" to the organizers. The flow in a transonic axial compressor, designated as Rotor 37, was used for the test. Eleven blind computations were submitted. Comparisons between the calculations and the measurements were presented during the 1994 IGTI Conference (Strazisar and Denton, 1995). The experimental results were reported by Suder and Celestina (1996) and Suder (1996). The flow field was also used extensively as a test case in CFD validation for propulsion system components (Dunham, 1998).

As is widely recognized in the turbomachinery aerodynamics CFD community, the current generation of CFD codes provides very useful numerical solutions for design purposes. The most useful information from CFD solutions is obtained by calculating variations between different designs. Because current turbulence models do not accurately represent the complexity of real flows, and numerical procedures need further refinements, CFD calculations do not always predict absolute values of aerodynamic properties accurately. However, accurate prediction of changes in aerodynamic parameters due to changes in the design can be more important than the prediction of absolute values.

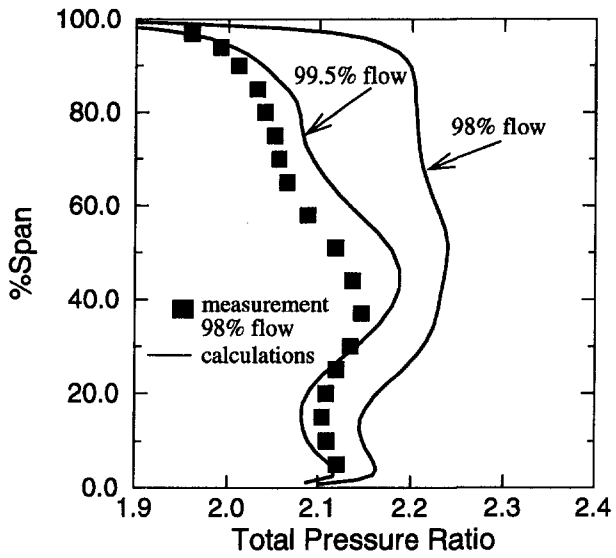

Fig. 16 Comparison of total pressure distribution

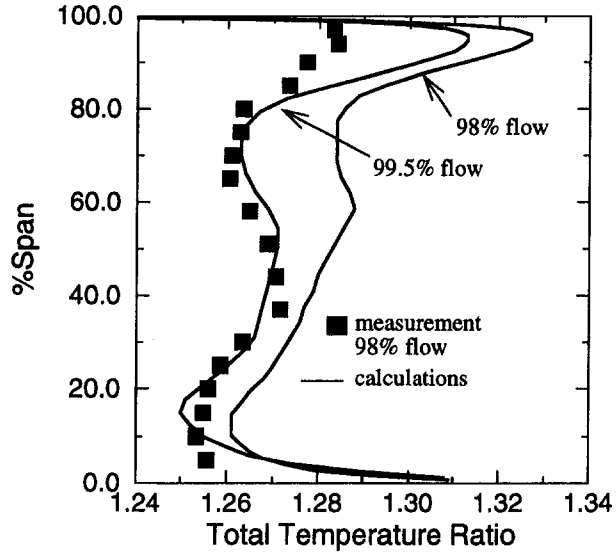

Fig. 17 Comparison of total temperature distribution

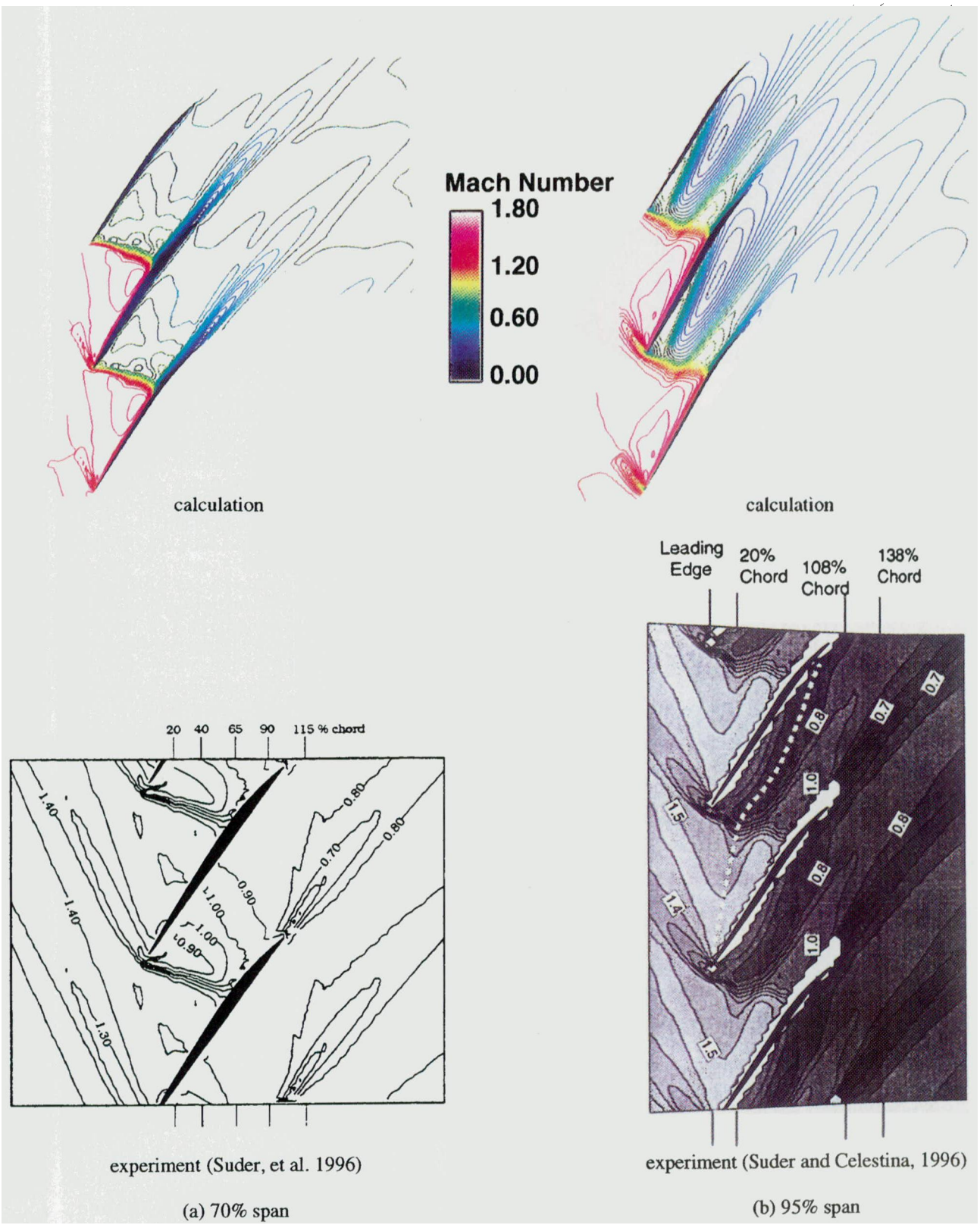

Fig. 18 Calculated and experimental relative Mach number distributions for Rotor 37

Accurate prediction of the shapes of spanwise property distributions can also be more useful than absolute values of integrated properties. Although the numerical results for the blind test case showed wide variations, the various numerical solutions revealed many interesting flow features and the exercise was very helpful in understanding the current level of the technology.

One of the observations during the exercise was that the spanwise shape of the total pressure distribution was not predicted very well, as shown in Fig. 12. Some solutions matched

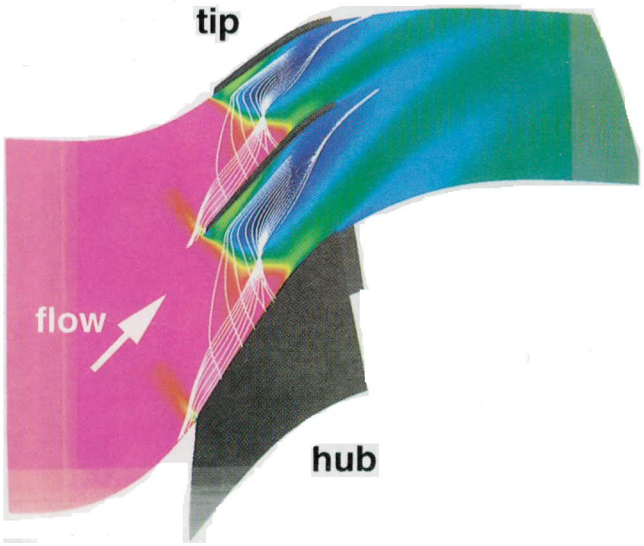

Fig. 19 Tip clearance vortex and passage shock interaction

the overall integrated level well without matching the shape at all. The measurement shows a large dip in the total pressure distribution near the hub. The measured shape of the total pressure distribution near the hub was predicted by solution 10, which was submitted by the authors. However, solution 10 overpredicted the total pressure rise significantly in the outer half-span. During the workshop, it was pointed out that solution 10 shows a mild hub corner stall at the specified operating condition, and this was proposed as the reason for the dip in the spanwise profile of total pressure near the hub.

In this section, the calculated flow fields of Rotor 37 at different flow conditions are further analyzed and compared with the available data. The objective of the analysis is to investigate whether hub corner stall occurs at the given flow conditions and to compare the flow structures with those observed in the subsonic compressor stator. The analysis is based on the numerical solutions submitted during the blind test exercise. No new calculations were performed to better match the measurements in terms of absolute values.

The flow field was calculated with the same CFD code that was used to calculate the flow in the subsonic compressor stator reported in the previous section. The applied turbulence model is also the same. The measurement stations and the computational grid are shown in Figs. 13 and 14. The grid consists of 58 nodes in the blade-to-blade direction, 51 nodes in the spanwise direction, and 151 nodes in the streamwise direction. To describe the blade tip geometry, ten computational nodes are distributed tangentially across the blade tip and 10 nodes are located radially between the blade tip and the shroud. After the blind test exercise, the computational grid was refined to 114 $\times$ 91 $\times$ 181. However, changes in the calculated solutions due to the grid refinement were not significant.

The measured and the calculated rotor speed lines are shown in Fig. 15 in the form of the total pressure ratio and the adiabatic efficiency. Previous code validation experiences have indicated that the code predicts slightly optimistic performance relative to that indicated by measurements. The deviation shown in Fig. 15, especially in terms of the total pressure ratio, is significantly larger than normally observed. Some possible causes of the deviation will be discussed later in this section.

Various aerodynamic measurements were made near the peak efficiency condition. Although the measured peak efficiency occurs very close to the choke condition (between 99 and 99.5 percent of the choke mass flow rate) according to the data shown in Fig. 15, the comparisons were made at 98 percent of the choke mass flow rate. Calculated spanwise distributions of total pressure at measurement station 4 are compared with the measurements in Fig. 16. Calculated values at 99.5 percent of the choke mass flow rate are also presented in Fig. 16. The solution at 98 percent of choke mass flow rate, which was presented during the original exercise, shows a much higher pressure rise near shroud than the measurement. This observation suggests that another comparison at lower back pressure might show better agreement with the measurements. A comparison of total temperature distributions at station 4 is given in Fig. 17. The comparisons in Figs. 16 and 17 indicate that relatively small shifts in the operating condition produce quite different absolute values of total pressure and total temperature. It is very interesting to observe that the numerical results at 99.5 percent of choke mass flow rate agree much better with the measurements than those at 98 percent of the choke mass flow rate. As shown in Fig. 16, the calculated spanwise distributions of total pressure at both flow conditions show a dip near the hub like the experimental data.

Figure 18 compares relative Mach number distributions between the measurements and the calculation at 70 and 95 percent span. The results indicate that the calculated flow field agrees well with the measured flow field in terms of location and strength of the passage shock structure. As shown in Fig. 18, a low Mach number region is formed after the passage shock near the pressure surface at 95 percent span. Figure 19 shows particle traces generated from the numerical solution to identify the origin of this region, which is considered to have a strong link to the onset of compressor stall. According to the particle traces shown in Fig. 19, the tip clearance vortex, which initiates near the leading edge, interacts with the passage shock, and the interaction seems to contribute to the formation of this low momentum area. Because of this interaction, the front of the passage shock moves forward at the interaction location. This forward movement of the passage shock is more clearly seen at 98 percent span, as shown in Fig. 20.

Flow Structure Near Hub and Blade Suction Surface Corner. Velocity vectors and particle traces near the hub and the suction side of the blade are shown in Fig. 21 at 98 percent of the choke flow rate. Figure 22 shows velocity vectors and corresponding particle traces at 99.5 percent of the choke mass flow rate. Very similar structures are observed at the two mass flow rates. A weak hub corner stall is observed in Fig. 22. Three-dimensional particle traces were generated to identify any existing vortex structure and the results are shown in Fig. 23. A weak vortex structure is identified. Compared to the hub corner stall vortex observed in the compressor stator, this vortex has only one leg on the hub wall and the other end of the vortex is diffused in the free stream before touching the hub wall again. Less pronounced hub corner stall in the rotor compared to that

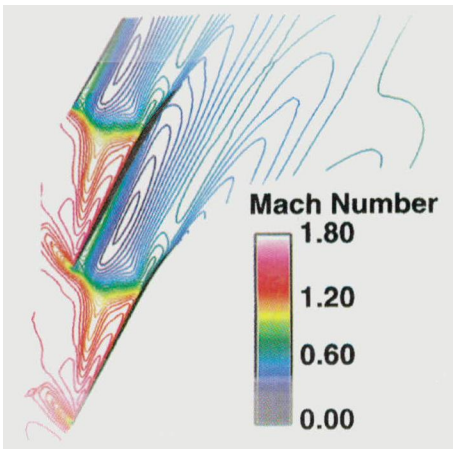

Fig. 20 Relative Mach number distribution at 98 percent span

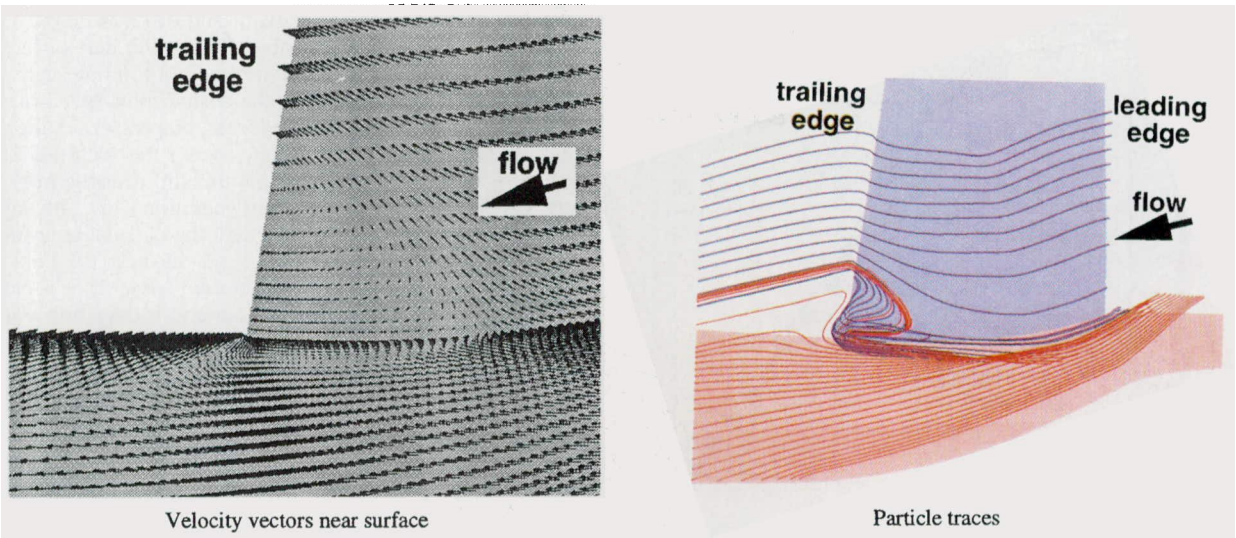

Fig. 21 Calculated flow near hub at 98 percent choke mass flow rate

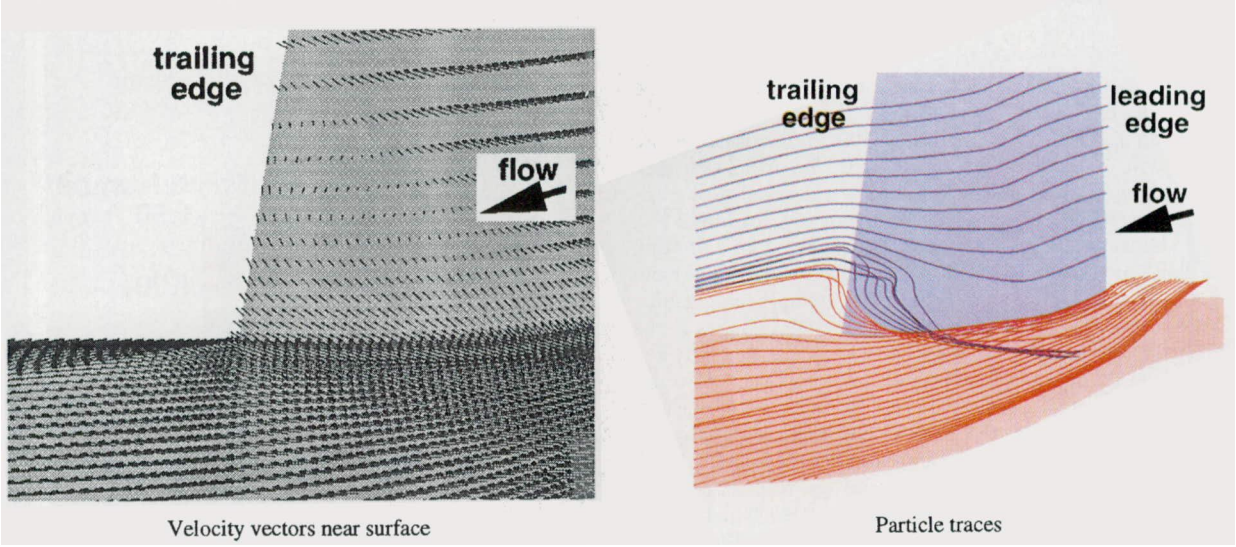

Fig. 22 Calculated flow near hub at 99.5 percent choke mass flow rate

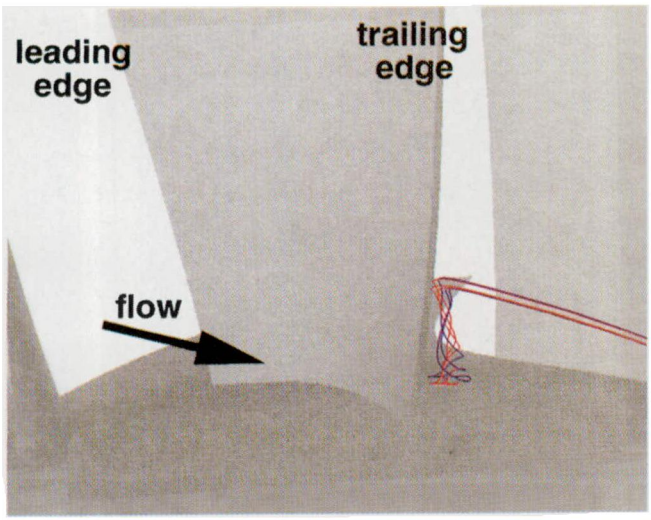

Fig. 23 Particle traces for hub corner flow at 98 percent choke mass flow rate

in the stator has been reported by Dring et al. (1982) and Dong et al. (1987).

Further aerodynamic performance measurements (Suder et al., 1996) show that the dip in the total pressure distribution shown in Fig. 12 disappears at the reduced blade loading that occurs at 60 percent rotor speed. In Fig. 24, the spanwise distribution of total pressure ratio at this operating condition is compared between the measurements and the calculation. Calculated and measured relative Mach number distributions at 95 percent span at this operating condition are compared in Fig. 25. Again the calculated flow field represents the measured flow field very well. Calculated velocity vectors and particle traces at this operating condition are given in Fig. 26. The results in Figs. 24 and 26 indicate that the hub corner stall does not occur at this reduced blade loading. The results shown in Figs. 16–26 suggest that the dip in the radial total pressure distribution near the design rotor speed is due to compressor hub corner stall. The possibility of any direct experimental verification of the existence of hub corner stall in Rotor 37 is very remote at the moment. Because of the twisted blade shape, access of a laser beam to the hub location from an optical window located on the shroud is almost impossible. The rotor speed also prohibits any useful flow visualization near the hub.

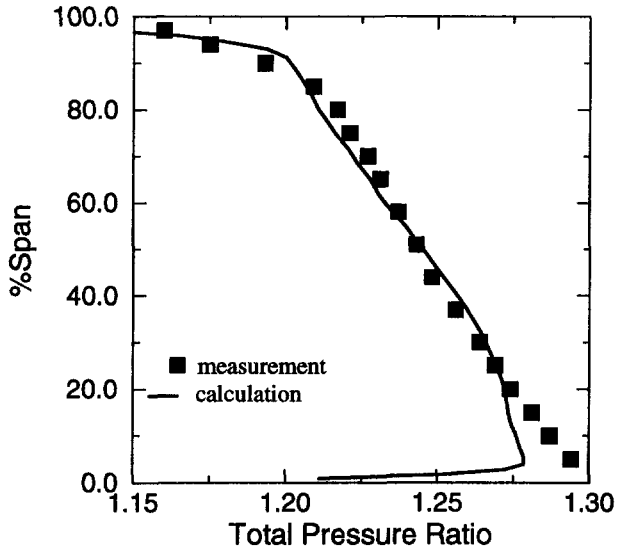

Fig. 24 Comparison of spanwise total pressure distribution near peak efficiency at 60 percent rotor speed

Some of the disagreements between the calculation and the measurements can be attributed to the following facts. For the numerical analysis, it is assumed that all 36 rotor passages are identical, with a uniform clearance gap. The measurements, however, show considerable variations in measured flow variables between blade passages. As shown in Fig. 13, there is a small gap between the stationary part of the hub and the rotating part of the hub, and there might be a small leakage flow from this gap. As is widely known, the flow field in a transonic compressor rotor is extremely sensitive to small changes in the geometry or flow condition. All of these differences between the numerical set up and the experimental conditions may contribute to differences in the effective blockage in the passage, which could explain why the values calculated at the slightly higher mass flow rate match the measured values better.

At both operating conditions at the design rotor speed, the numerical solutions show a mild hub corner stall, which corresponds to the observed dip in the total pressure distribution. At the reduced rotor speed, the measurements do not show this dip in the radial distribution of total pressure. The numerical solution predicts neither hub corner stall nor a dip in the total pressure near the hub, in agreement with the measurements. Therefore, the observed dip in total pressure rise near the hub at the design rotor speed may be caused by hub corner stall. Another possible cause may be leakage into the main stream from the small gap just upstream of the rotor at the hub, as investigated by Shabbir et al. (1997).

Concluding Remarks

This study was performed to advance our understanding of compressor hub corner stall. Three-dimensional flow fields in a subsonic compressor stator and in a transonic compressor rotor were used for the study. Numerical solutions based on the Reynolds-averaged Navier–Stokes equations and available experimental data were analyzed to construct detailed flow structures of compressor hub corner stall. The current study reveals that a vortex is formed at the corner of the hub and the blade suction surface toward the rear of the blade passage. The strong twisterlike vortical motion causes reversed flow regions on the hub surface as well as on the blade suction surface. In the compressor stator, the end of the vortex turns back to the hub surface. According to the numerical results, the two counterrotating vortices that have been identified through oil flow visualization are actually two legs of a single vortex. In the rotor, this vortex bends downstream and diffuses quickly, and only one leg of the vortex is observed on the hub surface. A measured dip in the spanwise distribution of total pressure near the hub of the transonic rotor at the design rotor speed may be due to hub corner stall. At the reduced compressor loading that occurs at 60 percent rotor design speed, the measured total pressure distribution does not show this dip near the hub. The numerical solution at this operating condition shows no sign of hub corner stall in particle traces, and the calculated spanwise distribution of total pressure shows no dip near the hub. The present study reveals that compressor hub corner stall is caused by a three-dimensional vortex system and it does not seem to be correlated with a simple diffusion factor. Design concepts for high-performance stages can possibly be developed to remove or control hub corner stall using currently available nu-

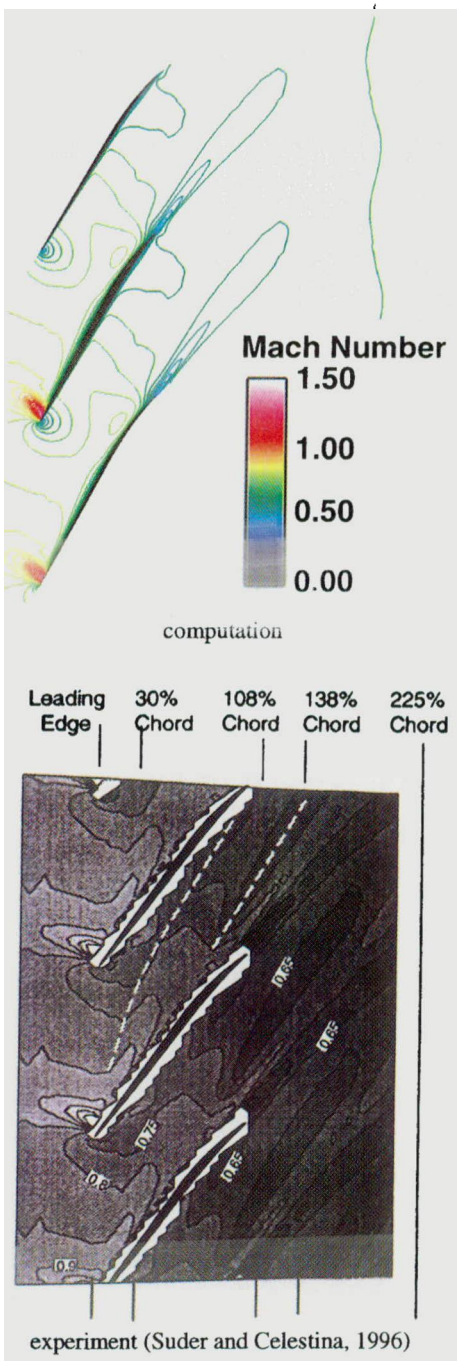

Fig. 25 Comparison of relative Mach number at 95 percent span and 60 percent rotor speed

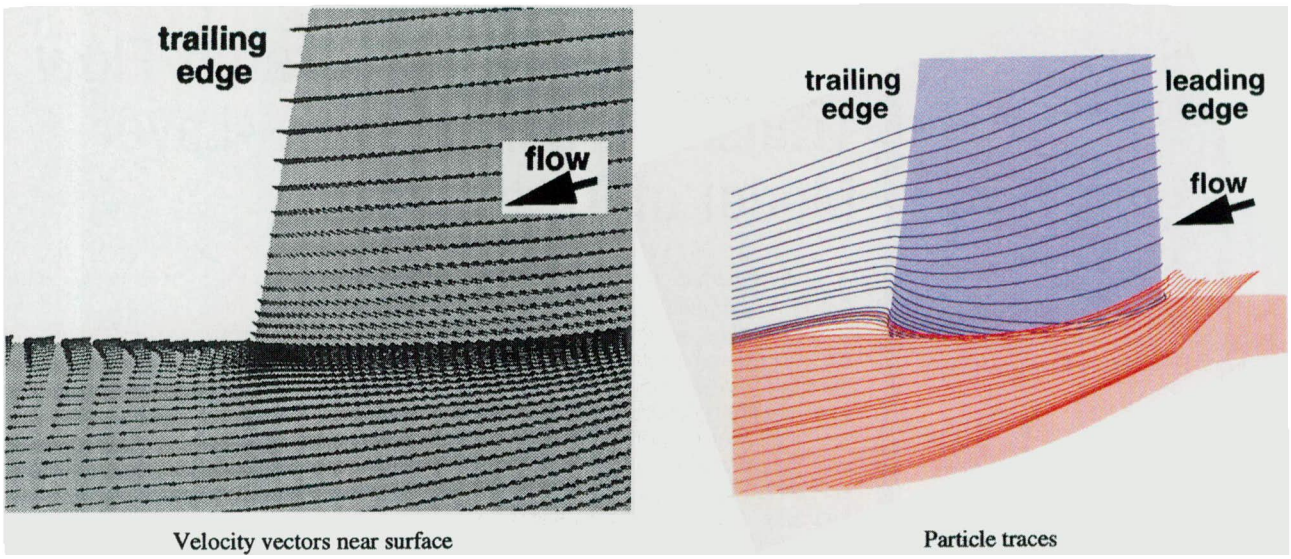

Fig. 26 Calculated flow near hub at 60 percent rotor speed

merical techniques. More detailed experimental data bases for hub corner stall, especially in compressor rotors, will be very useful in calibrating numerical tools as well as in developing such concepts.

Acknowledgments

The authors would like to acknowledge the contribution of F. Tsung of ICOMP at NASA Lewis Research Center in preparing the illustrations. Also, we would like to thank Dr. A. J. Strazisar and Dr. K. L. Suder of NASA Lewis Research Center for many valuable discussions about the experimental data.

References

Adamczyk, J. J., Celestina, M. L., and Greitzer, E. M., 1993, "The Role of Tip Clearance in High-Speed Fan Stall," ASME JOURNAL OF TURBOMACHINERY, Vol. 115, No. 1, pp. 28–39.

Copenhaver, W. W., Hah, C., and Puterbaugh, S. L., 1993, "Three-Dimensional Flow Phenomena in a Transonic, High-Throughflow Compressor Stage," ASME JOURNAL OF TURBOMACHINERY, Vol. 115, pp. 240–248.

Dong, Y., Gallimore, S. J., and Hodson, H. P., 1987, "Three-Dimensional Flows and Loss Reduction in Axial Compressors," ASME JOURNAL OF TURBOMACHINERY, Vol. 109, pp. 354–361.

Dring, R. P., Joslyn, H. D., and Hardin, L. W., 1982, "An Investigation of Compressor Rotor Aerodynamics," ASME *Journal of Engineering for Power,* Vol. 104, pp. 84–96.

Dring, R. P., Joslyn, H. D., and Wagner, J. H., 1983, "Compressor Rotor Aerodynamics," AGARD-CP-351, Copenhagen.

Dunham, J., 1998, "CFD Validation for Propulsion System Components," AGARD Advisory Report 355.

Gallus, H. E., Hah, C., and Schulz, H. D., 1991, "Experimental and Numerical Investigation of Three-Dimensional Viscous Flows and Vortex Motion Inside an Annular Compressor Blade Row," ASME JOURNAL OF TURBOMACHINERY, Vol. 113, No. 1, pp. 198–206.

Hah, C., 1987, "Calculation of Three-Dimensional Viscous Flows in Turbomachinery With an Implicit Relaxation Method," AIAA *Journal of Propulsion and Power,* Vol. 3, No. 5, pp. 415–42.

Hah, C., and Wennerstrom, A. J., 1991, "Three-Dimensional Flowfields Inside a Transonic Compressor With Swept Blades," ASME JOURNAL OF TURBOMACHINERY, Vol. 113, No. 1, pp. 241–251.

Joslyn, H. D., and Dring R. P., 1985, "Axial Compressor Stator Aerodynamics," ASME *Journal of Engineering for Gas Turbines and Power,* Vol. 107, pp. 485–493.

Schulz, H. D., and Gallus, H. D., 1988, "Experimental Investigations of the Three-Dimensional Flows in an Annular Compressor Cascade," ASME JOURNAL OF TURBOMACHINERY, Vol. 110, pp. 467–478.

Shabbir, A., Celestina, M. L., Adamczyk, J. J., and Strazisar, A. J., 1997, "The Effect of Hub Leakage Flow on Two High Speed Axial Flow Compressor Rotors," ASME Paper 97-GT-346, to be published in the ASME JOURNAL OF TURBOMACHINERY.

Smith, L. H., Jr., 1970, "Casing Boundary Layers in Multistage Axial Flow Compressors," in: *Flow Research on Blading,* L. S. Dzung, ed., Elsevier Publishing Company, Amsterdam, No. 3, pp. 688–690.

Strazisar, A. J., and Denton, J. D., 1995, "CFD Code Assessment in Turbomachinery—A Progress Report," *IGTI Global Gas Turbine News,* May/June, pp. 12–14.

Suder, K. L., Chima, R. V., Strazisar, A. J., and Roberts, W. B., 1995, "The Effect of Adding Roughness and Thickness to a Transonic Axial Compressor Rotor," ASME JOURNAL OF TURBOMACHINERY, Vol. 117, No. 4, pp. 491–505.

Suder, K. L., 1996, "Experimental Investigation of the Flow Field in a Transonic, Axial Flow Compressor With Respect to the Development of Blockage and Loss," NASA TM 107310.

Suder, K. L., and Celestina, M. L., 1996, "Experimental and Computational Investigation of the Tip Clearance Flow in a Transonic Axial Flow Compressor Rotor," ASME JOURNAL OF TURBOMACHINERY, Vol. 118, No. 2, pp. 218–229.

Computation of Separated-Flow Transition Using a Two-Layer Model of Turbulence

E. L. Papanicolaou
Institut für Thermische Strömungsmaschinen, Universität Karlsruhe (TH), Karlsruhe, Federal Republic of Germany

W. Rodi
Institut für Hydromechanik, Universität Karlsruhe (TH), Karlsruhe, Federal Republic of Germany

A model for predicting transition in flows with separation is presented in this study. The two-layer model of turbulence is employed, along with a suitably defined intermittency function, which takes appropriate values in the laminar-, transitional- and turbulent-flow regions. Correlations derived from measurements are used for this purpose. Two test cases were selected: the flow over a long horizontal body with semi-circular leading edge and the flow over the backward-facing step of small height (expansion ratio of 1:1.01). In the former, oncoming flows with free-stream *turbulence level encountered in practical applications was considered (0.2–5.6 percent) whereas in the latter the corresponding level was much lower. The Reynolds numbers, based on the diameter in the first case and on the step height in the second, lie in the range of 1600–6600, in which limited numerical investigations were previously available and where bubbles with laminar separation and turbulent reattachment are expected. The predictions were found to compare well with the corresponding measurements, both in terms of the lengths of the separation and the transition regions and of velocity and turbulence intensity profiles at various streamwise locations. The results show that, for the transition criterion chosen, in all cases transition is completed downstream of the reattachment point and that the rate at which it is completed increases with the* free-stream *turbulence level.*

Introduction

The successful numerical prediction of the flow around surfaces or bodies such as airfoils and turbine or compressor blades depends to a great extent on the ability to account for and adequately simulate the transition from laminar to turbulent flow. Although a large number of experimental observations and quantitative data are available to characterize transition in various flows of practical interest, the numerical predictions are still lagging behind and are mostly limited to simple geometries. As far as transition mechanisms are concerned, one can distinguish between *natural transition* and *bypass transition,* while more recently a third type, the *separated-flow transition,* has received increasing attention. The first two apply to boundary layers attached to a surface, while the third one refers to separated shear layer transition.

The different features of each transition type have been described by Mayle (1991). The natural transition is closely related to the development of Tollmien–Schlichting waves in a laminar boundary layer, which is a well-known problem in fluid mechanics and has been treated by linear stability analysis (Schlichting, 1979). It normally occurs in flows with low free-stream turbulence. Bypass transition is due to the entrainment and subsequent growth of turbulent spots in the laminar boundary layer and occurs at high free-stream turbulence levels. Its analytical treatment is based on the turbulent spot theory of Emmons (1951). Separated-flow transition occurs when a laminar boundary layer separates from a surface and a separation bubble is formed. Then a free-shear layer develops, along which the transition takes place. In most cases, the separation bubble is laminar and the flow is turbulent at or soon after the reattachment point, in which case the flow situation can be described as laminar separation–turbulent reattachment.

A large number of computational studies has been presented over the past decades on boundary-layer transition, considering mainly attached flow configurations. Most of them were based on modifications of previously existing turbulence models, and as research in the area of turbulence modeling itself advanced, so did transition modeling. An extensive account of the recent modeling efforts in transition, particularly those made by European researchers, has been presented by Savill (1995). This reflects the activities of the Special Interest Group (SIG) on Transition formed within ERCOFTAC.[1] The most popular approach seems to be the low-Reynolds $k-\epsilon$ model, both in a parabolic and an elliptic form, but also integral methods, nonisotropic $k-\epsilon$ models, Reynolds stress models, models including transport equations for intermittency, and large eddy simulation have been used among others. All these have been used for computations under a variety of external flow conditions, such as level of free-stream turbulence and pressure gradient, the latter of which can have zero or nonzero values and can be of favorable or adverse nature.

In the study of separated-flow transition, the most common configuration has been the leading edge separation bubbles on airfoils. The various methods that have been adopted for this purpose have been classified by Walker et al. (1988) as: (*a*) *Semi-empirical methods,* (*b*) *Viscous–inviscid interaction methods,* and (*c*) *Navier–Stokes solutions,* of which the first two classes are the most widely encountered in the literature. An example of semi-empirical methods and correlations was offered by the work of Roberts (1980), which aimed at analyzing the phenomena associated with leading-edge separation bubbles on airfoils. He discussed in detail the features of the two main types of separation bubbles, namely *short* and *long* bubbles. The short ones have a local effect on the flow and only slightly affect the inviscid flow outside the bubble. Long bubbles, on the other hand, exhibit a significant interaction with the external flow, so that the pressure distribution deviates markedly from the inviscid case. He defined four flow regimes based on

Contributed by the International Gas Turbine Institute and presented at the 42nd International Gas Turbine and Aeroengine Congress and Exhibition, Orlando, Florida, June 2–5, 1997. Manuscript received International Gas Turbine Institute February 1997. Paper No. 97-GT-454. Associate Technical Editor: H. A. Kidd.

[1] European Research Community On Flow Turbulence And Combustion.

very low, low, medium, and high chord Reynolds numbers, which give complete separation, long bubbles, short bubbles, and no separation respectively.

Some of the earliest attempts to investigate transition in separation bubbles were based on analytical methods, which distinguished between an inviscid region outside the bubble, where potential-flow theory could be employed, and a viscous region inside the bubble where boundary-layer analysis could be used. Thus each region was treated independently and an iterative procedure was followed, during which an attempt was made to match the two results at the interface between the two regions. Among the most representative studies in this area are those by Crimi and Reeves (1976) and Kwon and Pletcher (1979). Both were interested in leading-edge separation bubbles on airfoils and the prediction of the phenomenon of "bursting," which could lead to stall at a given angle of attack. A constant-thickness airfoil with a cylindrical nose was the configuration used by Arena and Mueller (1980) for low-speed wind tunnel measurements in an attempt to study leading-edge separation bubbles. Different angles of attack, flap angles, and chord Reynolds numbers in the range 150,000–460,000 were investigated. Bellows and Mayle (1986) performed heat transfer measurements on a similar body, at Reynolds numbers, based on the diameter, Re = 80,000, 100,000 and 120,000 and free-stream turbulence level of 0.4 percent.

In this study, some of the ideas used in previous efforts to model separation bubbles as described above are employed, in conjunction with a full, elliptic simulation of the flow over a body with a semi-circular leading edge and a backward-facing step of small height. The two geometries are shown in Fig. 1. These were proposed in the course of the activities of the ERCOFTAC SIG on Transition mentioned earlier (Savill, 1992). The first flow situation has not been very extensively investigated in the past and only the experimental studies of Arena and Muller (1980), Bellows and Mayle (1986), and Malkiel and Mayle (1996) are on similar flows, but the authors considered higher Reynolds numbers and mostly nonzero angles of attack.

The second test case, the backward-facing step, has been much more frequently investigated. Many test calculations have been carried out for laminar flow (Re $\leq$ 800, based on the step height) and fully turbulent flow (Re $\geq$ 5000), but very few attempts have been made to simulate the flow in the transition

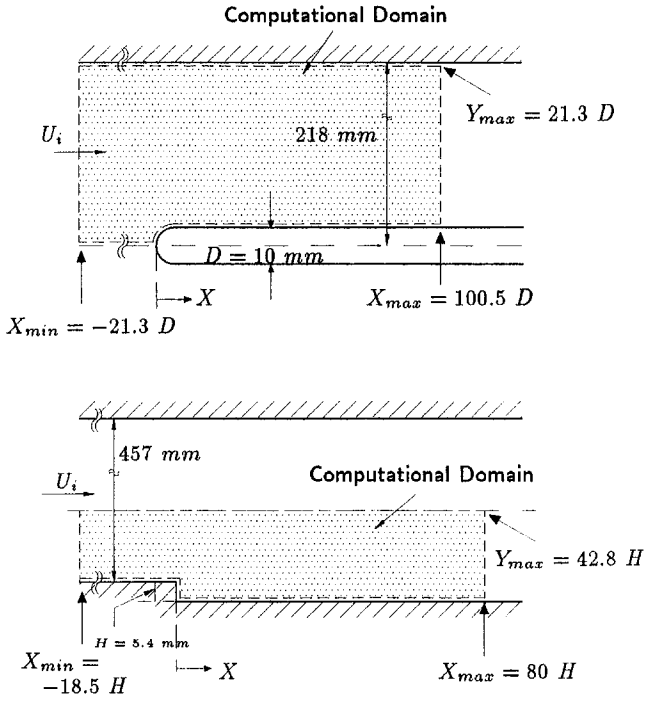

Fig. 1 Schematic of the two test cases with the corresponding significant dimensions. Case 1: Long horizontal body with semi-circular leading edge (top). Case 2: Backward-facing step of small height (bottom).

regime, such as for instance the studies of Karniadakis et al. (1990) and Kaiktsis et al. (1991). The latter has reported bifurcations to three-dimensional and oscillatory flow patterns at the early stages of transition. The expansion ratios (outlet height/inlet height) associated with the step were in most cases 1.5 or larger. On the other hand, the present value is very close to unity, due to the very small step height, namely 1.012. The step-height Reynolds number is equal to 4095.

Here, both test cases described are simulated numerically in the transitional regime. In both of them laminar separation is expected, with a separation point whose location is either not known in advance (case 1) or is fixed (case 2, step corner).

Nomenclature

C_f = skin friction coefficient = $\tau_w/(\rho U_\infty^2)$
C_p = pressure coefficient = $(p - p_i)/(\rho U_\infty^2)$
D = leading-edge diameter of the body in test case 1
H = height of the backward-facing step (test case 2)
H_{12} = shape factor = δ_1/δ_2
$\mathbf{J}$ = Jacobian of the coordinate transformation matrix = $\partial(x, y)/\partial(\xi, \eta)$
k = turbulent kinetic energy, nondimensionalized by U_i^2
L = length scale of turbulence
p = pressure
P = dimensionless pressure = $p/(\rho U_i^2)$
Re = Reynolds number based on a characteristic length for each test case (D or H), e.g., Re = $(U_i D\rho)/\mu$
Re_x = local Reynolds number based on the streamwise coordinate x
Re_2 = local Reynolds number based on momentum thickness δ_2
Tu = free-stream turbulence, percent
u, v = vertical and horizontal Cartesian velocity components, respectively
U, V = dimensionless Cartesian velocity components; $U = u/U_i$, $V = v/U_i$
x, y = vertical and horizontal Cartesian coordinate distance, respectively
X, Y = dimensionless Cartesian coordinate distances, e.g., $X = x/D$, $Y = y/D$ (or $X = x/H$, $Y = y/H$ for case 2)
γ = intermittency function
δ = boundary layer thickness
δ_1 = displacement thickness
δ_2 = momentum thickness
ϵ = rate of dissipation of turbulent kinetic energy, nondimensionalized by U_i^3/D or U_i^3/H
ξ, η = coordinates in the curvilinear (transformed) system
μ = molecular viscosity of air
μ_t = turbulent viscosity
μ_t^* = viscosity ratio = μ_t/μ
ρ = density of the fluid
$\sigma_k, \sigma_\epsilon$ = Prandtl number for the turbulent kinetic energy and its rate of dissipation, respectively
τ_w = wall shear stress

Subscripts

i = inlet
r = reattachment point
s = separation point
t (or tr) = start of transition
T = end of transition
∞ = local free-stream conditions
$\infty, 6$ = free-stream conditions 6 mm from the leading edge (reference point for case 1)

Eventually a fully turbulent reattached flow is expected. The full elliptic, two-dimensional flow equations are solved, along with a two-layer model of turbulence, where the viscosity is adjusted through an intermittency function in the laminar, transitional, and turbulent flow regions. This function is defined in such a manner that previous findings on separated flows can be incorporated into the transition model, thus allowing some elements of the physics of these particular flows to be accounted for. Experimental data for test case 1 were obtained at the Rolls-Royce Applied Science Laboratory (RRASL), Derby, UK (Coupland, 1995) and for test case 2 at the Engineering Department of Cambridge University, Cambridge, UK (Savill, 1992).

Mathematical Model

Model Equations. In a two-dimensional, Cartesian coordinate system, the steady equations governing incompressible flow and using the $k-\epsilon$ turbulence model, can be written in the following dimensionless and compact form:

$$\frac{\partial \mathbf{F}}{\partial X} + \frac{\partial \mathbf{G}}{\partial Y} = \frac{\partial \mathbf{F_d}}{\partial X} + \frac{\partial \mathbf{G_d}}{\partial Y} + \mathbf{S} \tag{1}$$

where $\mathbf{F}$ and $\mathbf{G}$ are the convective flux vectors, defined as:

$$\mathbf{F} = \begin{bmatrix} \bar{U} \\ \bar{U}\bar{U} + P \\ \bar{U}\bar{V} \\ \bar{U}k \\ \bar{U}\epsilon \end{bmatrix}, \quad \mathbf{G} = \begin{bmatrix} \bar{V} \\ \bar{V}\bar{U} \\ P + \bar{V}\bar{V} \\ \bar{V}k \\ \bar{V}\epsilon \end{bmatrix}, \tag{2}$$

$\mathbf{F_d}$, $\mathbf{G_d}$ are the diffusive flux vectors and $\mathbf{S}$ is a source term vector. $\mathbf{F_d}$ and $\mathbf{S}$ are defined as:

$$\mathbf{F_d} = \frac{1}{\mathrm{Re}} \begin{bmatrix} 0 \\ (1 + \gamma\mu_t^*)\left(2\dfrac{\partial \bar{U}}{\partial X}\right) \\ (1 + \gamma\mu_t^*)\left(\dfrac{\partial \bar{U}}{\partial Y} + \dfrac{\partial \bar{V}}{\partial X}\right) \\ \left(1 + \dfrac{\gamma\mu_t^*}{\sigma_k}\right)\left(\dfrac{\partial k}{\partial X}\right) \\ \left(1 + \dfrac{\gamma\mu_t^*}{\sigma_\epsilon}\right)\left(\dfrac{\partial \epsilon}{\partial X}\right) \end{bmatrix}, \quad \mathbf{S} = \begin{bmatrix} 0 \\ 0 \\ 0 \\ S_k \\ S_\epsilon \end{bmatrix} \tag{3}$$

and $\mathbf{G_d}$ is defined accordingly, whereas:

$$S_k = \gamma P_k - \epsilon, \quad S_\epsilon = C_1 \gamma P_k \left(\frac{\epsilon}{k}\right) - C_2\left(\frac{\epsilon^2}{k}\right) \tag{4}$$

$$P_k \equiv \frac{1}{\mathrm{Re}}\,\mu_t^*\left(\frac{\partial \bar{U}_i}{\partial X_j} + \frac{\partial \bar{U}_j}{\partial X_i}\right)\frac{\partial \bar{U}_i}{\partial X_j}, \quad \mu_t^* = C_\mu \frac{k^2}{\epsilon}\,\mathrm{Re} \tag{5}$$

The standard values of the $k-\epsilon$ model constants are used: $\sigma_k = 1$, $\sigma_\epsilon = 1.3$, $C_1 = 1.44$, $C_2 = 1.92$, $C_\mu = 0.09$. γ is the intermittency function used to model transition and will be defined below. Since here a two-layer model is employed, the $k-\epsilon$ model is used only in the outer region. In the near-wall region a one-equation model is used as explained below, whereby the ϵ equation is not solved. For computational domains of nonrectangular shape, such as the one in test case 1, a curvilinear, boundary-fitted coordinate system (ξ, η) is employed. The chain rule is used for the transformation of the derivatives from the Cartesian to the curvilinear system and Eq. (1) can be written as:

$$\frac{\partial \bar{\mathbf{F}}}{\partial \xi} + \frac{\partial \bar{\mathbf{G}}}{\partial \eta} = \frac{\partial \bar{\mathbf{F}}_d}{\partial \xi} + \frac{\partial \bar{\mathbf{G}}_d}{\partial \eta} + \mathbf{J}\bar{\mathbf{S}} \tag{6}$$

Boundary Conditions. In both cases an inlet velocity and an inlet free-stream turbulence level are specified. At the outflow, placed sufficiently far from the separation bubble, all streamwise gradients are taken as zero. On the solid surfaces the no-slip conditions are applied. In test case 1, the computations extend all the way to the opposite wall, where the viscous sublayer is not resolved but wall functions are used. Due to the symmetry of the geometry, only the upper half of the flow is calculated and a symmetry condition is imposed at the symmetry plane upstream of the body. In test case 2, due to the large distance of the opposite wall in the experiments, the upper boundary is taken midway across the channel height, where symmetry conditions are imposed.

Of utmost importance in transition modeling are the inlet conditions for the turbulence quantities. For test case 1, it was specified (Savill, 1992) that the free-stream turbulence Tu, under the prevailing zero-pressure-gradient conditions, decays in a power-law fashion, while the dissipation length scale L_ϵ increases with the square-root of the streamwise distance. Depending on the properties of the turbulence-generating grids used in each subcase, suitable constants of the power-law expression were computed, using measured values of free-stream turbulence above the body surface that were provided. Once the expressions for Tu and L_ϵ are fully determined, their corresponding inlet values can be determined by upstream extrapolation. The value of dissipation rate at the inlet is in turn obtained from the relationship $L_\epsilon = k^{3/2}/\epsilon$ and the turbulent viscosity at inlet from Eq. (5). In test case 2, Blasius conditions at the inlet are proposed, along with a measured, given profile for the turbulence intensity, while for the dissipation length scale a profile obtained from the relationship: $L_\epsilon = \min\,[\kappa y, 0.085\delta]/C_\mu^{3/4}$ was recommended (Savill, 1994), where $\kappa = 0.41$ (von Karman's constant) and y is the distance from the bottom surface of the inlet channel.

Two-Layer Model. The two-layer model as described in the paper by Rodi (1991) is used in the present computations. It is a combination of the standard $k-\epsilon$ model, used in the outer region, and the Norris–Reynolds one-equation model applied in the near-wall region. Since the computations here are carried out in nondimensional variables, the various relationships are presented in a dimensionless form. Therefore, in the Norris–Reynolds approach, the turbulent viscosity is given by the following expression:

$$\mu_t^* = \mathrm{Re}\, f_\mu C'_\mu \sqrt{k} L \tag{7}$$

where:

$$f_\mu = 1 - \exp\left(-\frac{\mathrm{Re_y}}{A_\mu}\frac{25}{A^+}\right)$$

$$\mathrm{Re_y} = \mathrm{Re}\sqrt{k} Y_n, \quad L = C_D \kappa Y_n \tag{8}$$

and: $C'_\mu = 0.084$, $A_\mu = 50.5$, $C_D = 6.41$, $\kappa = 0.41$. Y_n is the dimensionless distance normal to the wall. Only the k equation is solved in the near-wall region, with the source term S_k of Eq. (4) using the following value of ϵ:

$$\epsilon = \frac{k^{3/2}}{L}\left(1 + \frac{1}{\mathrm{Re}}\frac{C_\epsilon}{\sqrt{kL}}\right), \quad C_\epsilon = 13.2 \tag{9}$$

The criterion for switching between inner and outer region modeling is determined by the value $f_\mu \approx 0.95$ (Rodi, 1991) or the boundary layer edge, whichever is attained first as one moves away from the wall. This model has been previously used to compute transitional, attached flows in turbine cascades (Cho

et al., 1993). Transition was effected by an empirical relation for changing A^+ from a large value in the laminar flow to $A^+ = 25$ in fully turbulent flow. The start of transition was determined with the empirical formula of Abu-Ghannam and Shaw (1980). Here, the latter procedure is not used, but A^+ is kept constant at $A^+ = 25$ (turbulent flow) and the transition process is controlled instead through the intermittency function γ, as shown in Eqs. (3) and (4) and as will be described below.

Transition Model Parameters. The intermittency function γ, appearing in Eqs. (3)–(4) as a multiplication factor for the eddy viscosity, represents the fraction of time during which a flow at the given location is turbulent (Mayle, 1991). The values of γ range from 0, corresponding to laminar flow, to 1, which indicates a fully turbulent flow. Values between 0 and 1 represent a state of transition from laminar to turbulent flow at a particular point. The rate at which the values of γ increase from 0 to 1 during transition is determined by the rate of the turbulent spot production (Emmons, 1951) and is generally of exponential nature. Different investigators have proposed different parameters that control this exponential growth and presented γ as a one-dimensional function of the streamwise coordinate, corresponding to values near the wall (near-wall intermittency) (Mayle, 1991). Such expressions, accompanied by correlations for the onset of transition and the extent of the transition region, may then be used for modeling the flow in the transition region.

Here, the following expression is used for intermittency:

$$\gamma(x) = 1 - \exp\left[-G(x - x_{tr}) \int_{x_{tr}}^{x} \frac{dx}{U_\infty}\right] \tag{10}$$

where:

$$G = \frac{\exp(0.99Tu)}{100} \frac{U_\infty^3}{\nu^2} \mathrm{Re}_{2,\mathrm{tr}}^{-8/3} \tag{11}$$

proposed by Rodi and Schönung (1987) as an extended version of the work by Chen and Thyson (1971). This expression involves the value of the Reynolds number $\mathrm{Re}_{2,\mathrm{tr}}$ based on the momentum thickness at the transition point and the coordinate of the transition point x_{tr}. $\mathrm{Re}_{2,\mathrm{tr}}$ is obtained at each streamwise location from the following correlation:

$$\mathrm{Re}_{2,\mathrm{tr}}^2 = \left(1 + \frac{0.05}{\exp(0.365Tu)}\right) \mathrm{Re}_{2,\mathrm{sep}}^2 + \frac{17{,}000}{\exp(0.509Tu)} \tag{12}$$

The coordinate at the start of transition x_{tr} is taken as the location at which the local value of Re_2 exceeds the value of $\mathrm{Re}_{2,\mathrm{tr}}$ computed from Eq. (12). The expression given above has been developed by Rodi and Schönung (1987), by modifying previous published correlations, which incorporated the coordinate of the separation point (see, for instance, Kwon and Pletcher, 1979). These were based on the assumption that transition starts when the maximum displacement thickness due to separation is attained, which coincides with the end of the constant pressure region. Rodi and Schönung (1987) introduced the momentum-thickness Reynolds number instead of the local Re in the correlations, along with the effect of the free stream turbulence. The various coefficients involved were obtained by optimization, based on the experimental data of Gotthardt (1983) and Haas et al. (1987). As can be observed, this correlation involves the Reynolds number at the separation point and therefore it is particularly suited for separated flows. The good prediction of the separation point and the accurate estimation of the various boundary layer thicknesses are essential to the successful use of this model.

Computational Scheme

Main Features. The code FAST-2D[2] (Zhu, 1991a) was used for the present computations. This was developed at the Institute for Hydromechanics, at the University of Karlsruhe, Germany over the past decade by various researchers. A detailed description of it, or more strictly its three-dimensional version, is given in the paper by Majumdar et al. (1992). Its main features consist of a control-volume approach, discretization of Eq. (6) in a generalized, nonorthogonal coordinate system, where the Cartesian velocity components are used to describe the flow field. The code is based on the pressure-correction algorithm SIMPLE (Patankar, 1980) and its variant SIMPLEC (Van Doormal and Raithby, 1984), the latter of which was used in the present computations. A nonstaggered grid arrangement and the momentum interpolation procedure of Rhie and Chow (1983) are used to avoid the checkerboard splitting. The convective terms are discretized using the HLPA scheme (Hybrid Linear/Parabolic Approximation) described by Zhu (1991b). This is a higher-order, bounded scheme, with good stability properties.

Computational Domain and Grid. The extent of the computational domains for both cases is shown in Fig. 1. For the first test case, the horizontal surface of the body is equal to exactly 100 diameters, while vertically the domain is extended up to the wind tunnel wall, as specified by the experimental setup. For the step, the distances chosen (80H downstream of the step, 42.8H vertically) were eventually found to be sufficient to avoid any undesirable boundary influence on the solution, after several possibilities were tested. At the midheight of the test channel, a symmetry condition was employed. The grids used in the computations for the two test cases are shown in Fig. 2. After several attempts, the final grid dimensions, which were considered necessary for a good resolution of the body surface in case 1, were 142 × 102, with 142 points in the streamwise direction. The grid spacings were stretched in the streamwise direction toward the curved surface of the body. In the second test case, the same number of points was used. Here the emphasis in the stretching of the grid was toward the shear layer expected to develop as the flow separates at the corner. Therefore stretching in both the upward and downward direction was used toward the approximate vertical location of the shear layer. In both cases, the grid dimensions and stretching factors used yielded values of Y^+ at the first grid point from the wall of the order of 1 or less, therefore ensuring a fair amount of grid points inside the boundary layers.

Procedure and Stability Considerations. The velocity components and the pressure were initialized with the laminar flow solution obtained on the same configuration for a sufficiently lower Reynolds number. The computations proceeded until the root-mean square residuals of all variables were reduced to the order of 10^{-5} or less. During the early attempts, it became evident that the numerical procedure tended to become unstable, especially in test case 2 where the level of free-stream turbulence is very low, and multiple separation bubbles developed. It was soon realized that this was due to setting $\gamma = 0$ in the laminar-flow regions. It was therefore found necessary to avoid letting the turbulent viscosity go to zero in the diffusion terms of Eq. (3) in these regions. The intermittency was instead set to 1 in the diffusion terms (but not in the production terms) in the laminar region in the free stream. A small amount of diffusion was also allowed in the laminar boundary layer, by setting γ to a small value, in the range 0.1–0.2, again in the diffusion terms only. Such values were found to be adequate for numerical stability without affecting the overall results, after experimentation in several cases with various flow conditions,

[2] F-low A-nalysis S-imulation T-ool of 2-D.

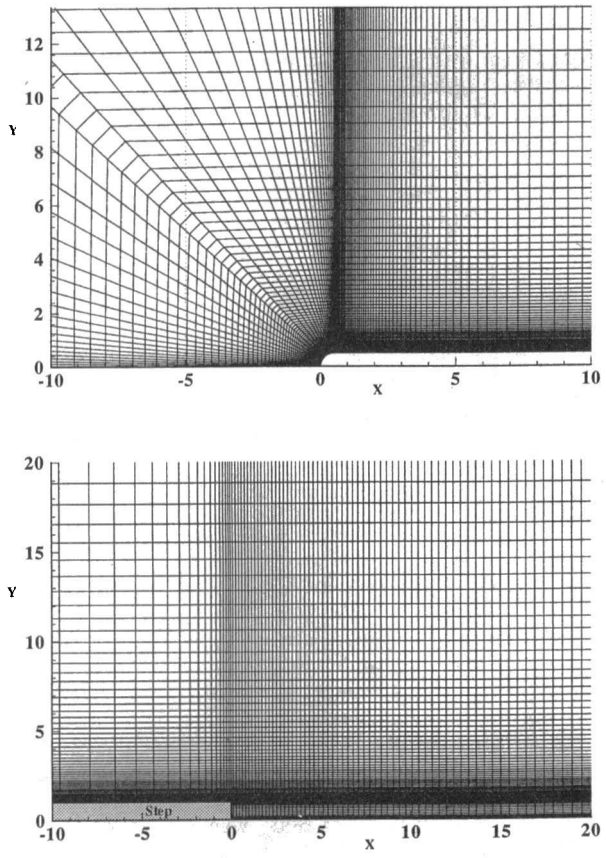

Fig. 2 Section of the computational grid for the two test cases shown in Fig. 1

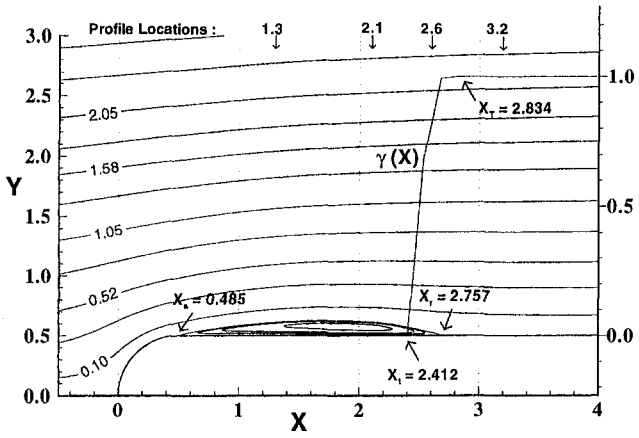

Fig. 3 Streamlines and intermittency distribution $\gamma(X)$ for case 1c (U_i = 5 m/s, $Tu_{\infty,6}$ = 2.31 percent)

and they were maintained in that range in all subsequent calculations. This practice was also directed by physical reasoning, since otherwise the diffusion of free-stream turbulence into the laminar boundary layer would not have been properly accounted for and since it was also known from the measurements that the oncoming flow carried some amount of turbulence with it, both in the free stream and within the laminar boundary layer before transition.

Results and Discussion

Test Case 1. The flow conditions specified for the body with the semi-circular leading edge are listed in Table 1. Each subcase is characterized by a letter "a–f." Results for all these subcases could not be presented here due to limited space, but the reader is referred to the report by Papanicolaou (1996) for additional results. Here only 1c and 1f are presented in detail.

Results for U_i = 5 m/s, Re = *3293.* In Fig. 3 a typical streamline plot is shown. A quite sizable separation bubble is present, whose size varies from case to case, as will be demonstrated below. The bubble in case 1c, for instance, had a length roughly equal to 2.3 diameters. The separation point is located slightly upstream of the beginning of the horizontal surface of the body. On the same figure, the streamwise intermittency distribution $\gamma(X)$ is also shown. The predicted transition point is located at X_t = 2.41 diameters from the leading edge. This corresponds to a distance equal to 85 percent of the bubble length. The transition ends at a streamwise coordinate of X_T = 2.83, yielding a total length of transition equal to 0.42 diameters. The predicted transition behavior appears to be more in accord with the findings of Walker (1993), than those of Mayle (1991), as far as the end-of-transition point is concerned. More specifically, here the transition process seems to be completed downstream of the reattachment point, i.e., the flow is not fully turbulent at reattachment. However, the end-of-transition locations here, obtained for γ = 0.99, were the outcome of a stricter transition criterion, which used the intermittency values computed as a function of the free-stream value of Tu (Eq. (11)). Since assuming a crossflow variation for the intermittency was outside the scope of this work, using the free-stream conditions to represent each streamwise coordinate was the most convenient choice. It is expected that by taking into account a crossflow distribution of intermittency, such as those measured recently by Malkiel and Mayle (1996) or Hazarika and Hirsch (1996), and by using the local peak value of the intermittency to monitor transition instead, an earlier end-of-transition point X_T will be found. Unfortunately, based on the available data, there is no clear experimental evidence regarding the relative position of the end-of-transition and reattachment points.

The various subcases corresponding to an inlet velocity of 5 m/s can be compared in terms of the values shown in Table 1. The separation point varies only slightly with the free-stream turbulence level Tu, while the reattachment point and the start-, end-of-transition points are shifted further upstream with an increase in Tu. In Fig. 4, for case 1c, calculated and measured values of the boundary-layer thickness δ, maximum velocity of the external flow U_{max}, and shape factor are plotted versus the horizontal coordinate X. δ is defined as the wall distance where the velocity is 0.99 of the maximum value. The comparison with the experimental results can be seen to be good, both in terms of δ and maximum velocity. The plot of U_{max} indicates that the effect of the bubble extends down to about five body diameters from the leading edge. The shape factor plot exhibits a sharp peak typical of a separation bubble (somewhat excessive

Table 1 Flow conditions and computed separation-transition data for test case 1

Case	U_i (m/s)	Re	$Tu_{\infty,6}$ (%)	X_s	X_r	X_t	X_T
a	5	3293	0.17	0.448	3.247	3.159	6.695
b	5	3293	0.63	0.466	2.913	2.412	3.336
c	5	3293	2.31	0.485	2.759	2.169	2.834
d	5	3293	5.56	0.466	2.005	1.854	2.058
e	2.5	1646.5	2.30	0.500	3.829	4.158	5.495
f	10	6586	2.50	0.448	1.550	1.181	1.953

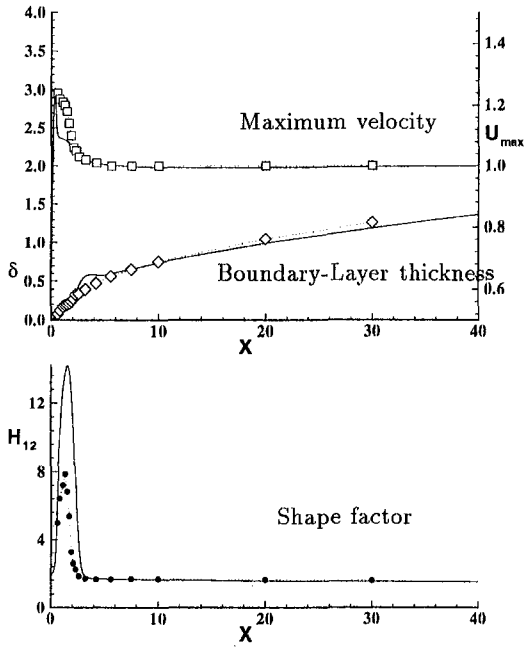

Fig. 4 Numerical (solid lines) against experimental results (points) versus *X* for case 1c

in the calculations) before an asymptotic value of 1.44 is attained. This is very close to the value reported by Schlichting (1979) for turbulent boundary layers on a flat plate. The comparison with the measurements appears fairly good, except for some underprediction of U_{max} in the separation region.

In Fig. 5 additional comparisons with measured data are shown, this time for the skin friction coefficient C_f and the Reynolds number Re_2 based on the momentum thickness, both plotted against the local Reynolds number Re_x. The bubble location in the plot of C_f is indicated by zero values in the measurement data and by negative values in the computations. It can be readily observed that the predicted length and location for the separation bubble agrees quite well with the measurements. The analytical result for the variation of C_f in a turbulent boundary layer over a flat plate, given by a $Re_x^{-0.2}$ relationship (Schlichting, 1979), is also plotted and coincides with the numerical result in the fully turbulent region. The flow behavior in the laminar region is very different from that of a boundary layer over a flat plate, both due to the curvature and the separated region; therefore it would be meaningless to include the analytical result for C_f in the laminar region. Figure 5 includes a graphic representation of the relationship between Re_2 and

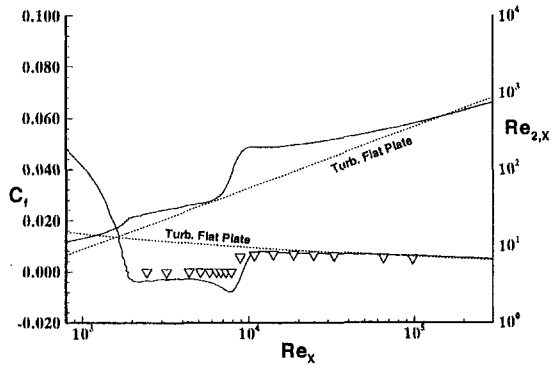

Fig. 5 Numerical (solid lines) versus experimental results (points) and flat-plate correlations (dashed lines) for case 1c. Skin friction coefficient C_f and local Re_2 are both plotted versus Re_x.

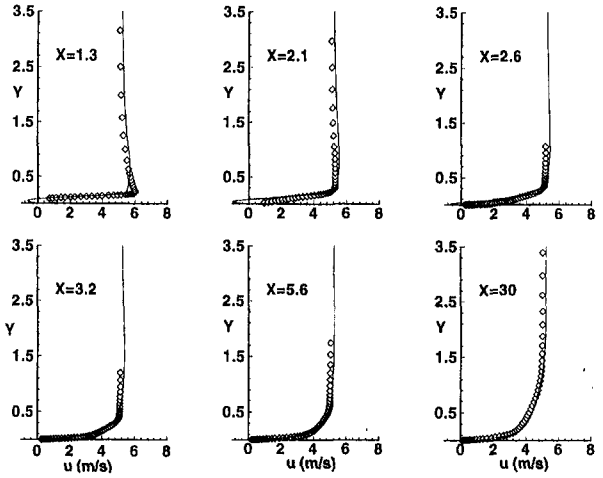

Fig. 6 Numerical (lines) versus experimental (points) velocity profiles for case 1c

Re_x, as predicted numerically, in comparison with the analytical result for a flat plate. This can be obtained using the corresponding expression for δ_2 (Schlichting, 1979) and indicates a $Re_x^{0.8}$ dependence. In the laminar region the corresponding result is $Re_x^{0.5}$ but, for the same reasons as discussed for C_f, the laminar-flow correlation is not shown as not applicable. However, Fig. 5 shows clearly that, as the turbulent regime establishes, the analytical curve is asymptotically approached by the numerical results.

Figure 6 compares predicted velocity profiles for case 1c with the corresponding measured ones, at several streamwise distances from the leading edge. The region of reversed flow can be observed in the first three profiles and the comparison is generally good, except for some indication of delayed reattachment. For the same streamwise locations, Fig. 7 compares predicted turbulence intensity profiles for case 1c with the corresponding measured values. The comparison is reasonably good for most profiles. In the last profile, an underprediction of the maximum value of the intensity is observed, which is a known shortcoming of the Norris–Reynolds model and it is due to an overestimation of ϵ (see Rodi et al., 1993). Equally good results were also obtained for the other three values of free-stream turbulence listed on Table 1 and corresponding to $U_i = 5$ m/s. The transition was found to be very abrupt for the highest value of *Tu* and the length of the bubble the smallest of all cases (roughly 1.5 diameters). For the lowest value of *Tu*, the transition process was slow, but the length of the bubble was not

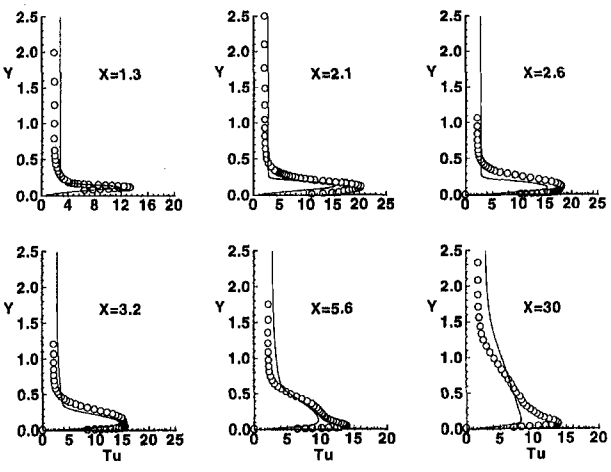

Fig. 7 Turbulence Intensity $\sqrt{u'^2}/U_i$ profiles (percent) for case 1c

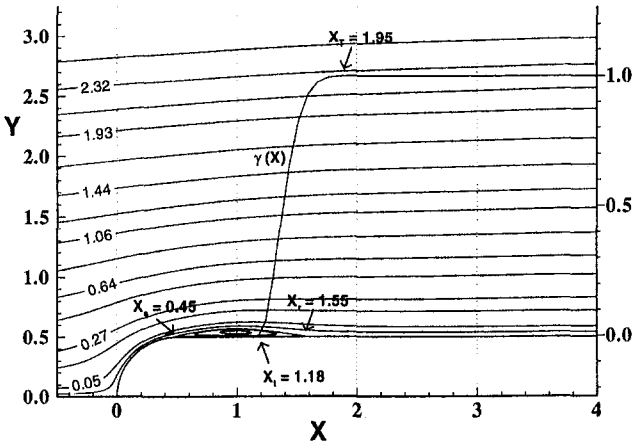

Fig. 8 Streamlines and intermittency distribution $\gamma(X)$ for case 1f (U_i = 10 m/s, $Tu_{\infty,6}$ = 2.5 percent)

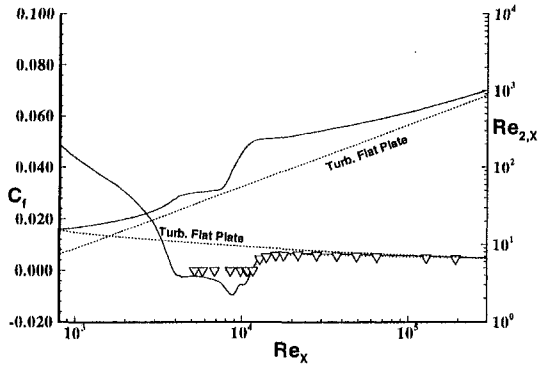

Fig. 10 Numerical (solid lines) versus experimental results (points) and flat-plate correlations (dashed lines) for case 1f. Skin friction coefficient C_f and local Re_2 are both plotted versus Re_x.

significantly affected. By reducing the inlet velocity to 2.5 m/s (case 1e), and at the same value of Tu as for case 1c, a longer bubble was obtained and a significantly delayed start of transition.

Results for U_i = 10 m/s, Re = 6586. The results that follow are for test case 1f, which has a similar value of free-stream turbulence as in case 1c (2.5 percent), but a higher velocity, namely 10 m/s. The corresponding streamline plot for this case is shown in Fig. 8 and shows that the length of the bubble ($1.1D$) is much smaller than for case 1c. Transition starts therefore much earlier, but the total length of the transition region (approximately 0.7 diameters) is not significantly different from case c, indicating that it is mainly dependent on the free-stream turbulence level and not so much on the Reynolds number.

Figures 9 and 10 show the various boundary layer quantities that were previously presented for case 1c. Again, overall good agreement can be observed. In particular the plot of C_f shows a very good prediction of the reattachment point. The Re_2 versus Re_x plot shows again the attainment of turbulent flow conditions at increasing Re_x when compared with the analytical curve. The velocity profiles and turbulent intensities for this case verified once again the good prediction of the reattachment point and exhibited a good overall agreement. In Fig. 11 the pressure coefficients are plotted along the separation and transition regions for cases 1c and 1f. The features typical of a separation bubble, such as a region of constant pressure followed by a downstream region of pressure recovery (Mayle, 1991), can be identified in both cases. The plots further indicate that the start of transition almost coincides with the end of the constant pressure region, as pointed out by Kwon and Pletcher (1979). The pressure recovery is also shown to be complete at the reattachment point.

To summarize, good comparisons with the measured values were obtained for all six cases shown on Table 1. Some discrepancies were observed only in the prediction of turbulence intensities for the smallest value of the free-stream turbulence, Tu_∞ = 0.17 percent (case 1a), and for the smallest value of the inlet velocity, U_i = 2.5 m/s (case 1e). Clearly, some experimentation with alternative values of the parameters involved in Eqs. (11) and (12) would be necessary to produce a more universal model, but this was considered outside the scope of the present work.

Comparisons With Experimental Correlations. The lengths of separation and transition regions for all six computed cases 1a–1f were subsequently compared against each other in a more systematic way. By using the distances X_s, X_t, and X_T listed on Table 1 one can calculate and plot three suitably defined Reynolds numbers Re_{sT}, Re_{st}, and Re_{LT}, often used to characterize transition, versus the momentum-thickness Reynolds number at the separation point $Re_{2,s}$. For instance, Re_{sT} is computed as:

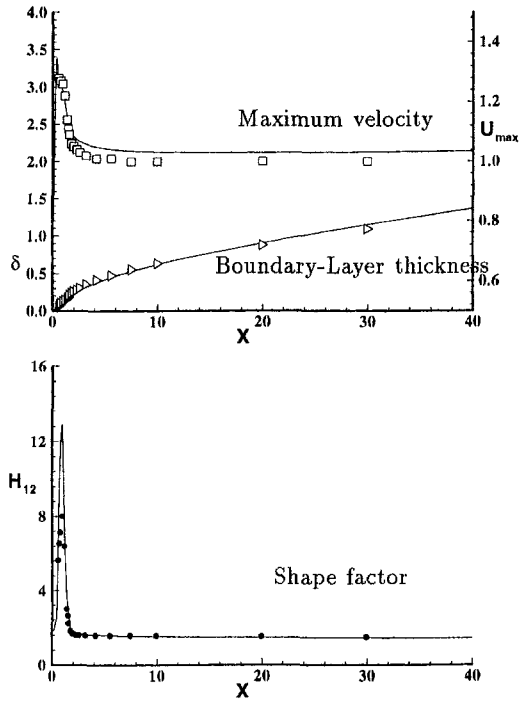

Fig. 9 Numerical (solid lines) against experimental results (points) versus X for case 1f

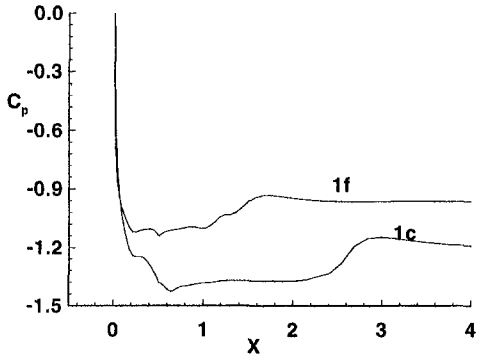

Fig. 11 Pressure coefficient C_p versus X for test cases 1c (X_t = 2.41) and 1f (X_t = 1.18)

$$\mathrm{Re}_{sT} = \frac{u_s(x_T - x_s)\rho}{\mu} = \mathrm{Re}\ U_s(X_T - X_s) \qquad (13)$$

and similarly the other two numbers. In this manner, plots similar to those presented by Mayle (1991) are constructed and shown in Fig. 12. The correlations proposed by Mayle (1991) and Walker (1993) are also included in this figure. The values of $\mathrm{Re}_{2,s}$ appearing here represent a relatively narrow band compared to the results plotted by Mayle (1991) and therefore a new correlation cannot be derived based on the present data. However, one can see that the computed values of Re_{sT} (Fig. 12(a)) are in reasonable agreement with the correlation of Mayle for long bubbles. There is however one data point that falls exactly on the correlating line for short bubbles and this corresponds to the highest value of Tu used (5.56 percent); for this value the transition is completed shortly after reattachment. Figure 12(b) is also showing the data points to be closer to the correlating line of Mayle (1991) for Re_{st} for long bubbles. The short bubble correlation is also plotted and cases (d) and (f), where the bubbles are indeed short, are the closest to it. Both correlations have a $\mathrm{Re}_{2,s}^{0.7}$ dependence, but are multiplied by a different factor. In Fig. 12(c), the values of Re_{LT} are plotted against two different correlations, one proposed by Mayle (1991), valid for both short and long bubbles and suggesting a $\mathrm{Re}_{2,s}^{0.7}$ dependence and another one by Walker (1993) where the dependence is $\mathrm{Re}_{2,s}^{1.5}$. Interestingly enough, although qualitatively this study agrees more with the findings of Walker (1992)

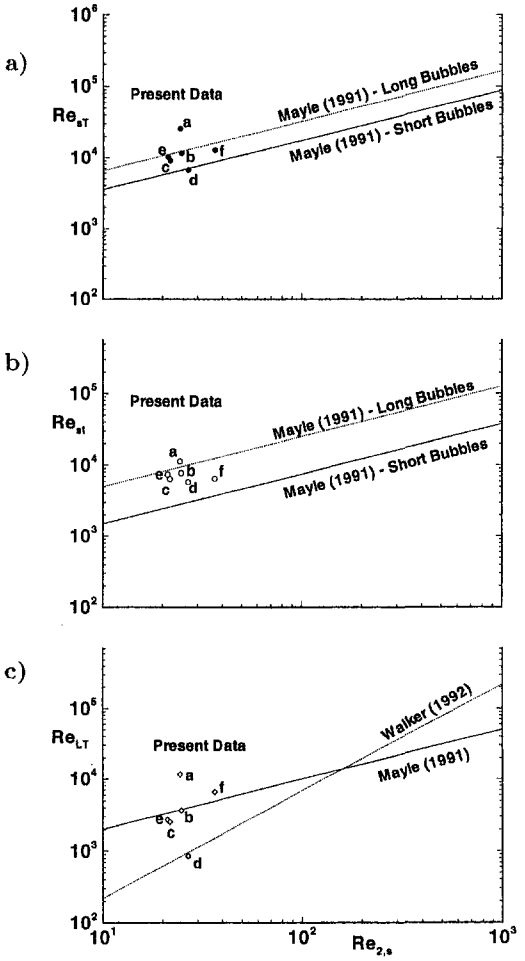

Fig. 12 Separation-bubble data for case 1 versus $\mathrm{Re}_{2,s}$ and against available correlations. The ordinate Re is expressed in terms of: (a) the length of the constant-pressure region (Re_{sT}), (b) the distance between separation and transition points (Re_{st}), (c) the length of the transition region (Re_{LT}).

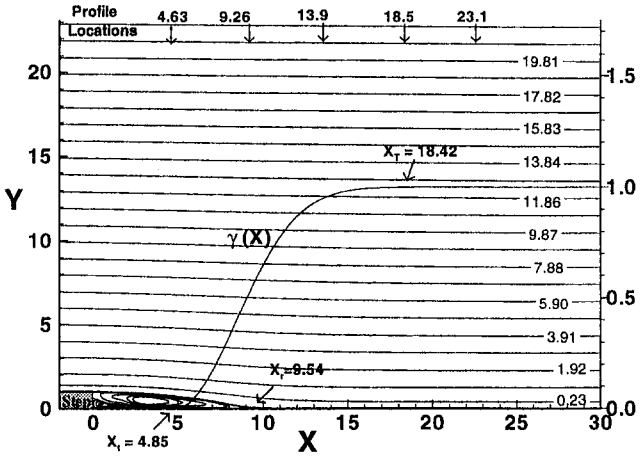

Fig. 13 Streamlines and intermittency distribution for test case 2 (U_i = 11.38 m/s, Tu_∞ = 0.011 percent)

as far as the end-of-transition is concerned, the present results seem to agree quantitatively better with the correlation of Mayle (1991) for Re_{LT}, except for one data point, corresponding to the highest free-stream turbulence level (5.56 percent). Although the correlations of Mayle (1991) where derived from experimental data corresponding to low free-stream turbulence levels (0.2–0.5 percent), here a good agreement is observed in the range 0.63–2.5 percent (cases b, c, e, and f).

Test Case 2. Although experimental data were available in this case for three different Reynolds numbers (based on the inlet velocity), Re = 1830, 2535, and 4095 (Savill, 1994), with essentially the same free-stream turbulence level Tu of the order 10^{-2} percent, only the case with the highest Reynolds number (Re = 4095) could be calculated because of numerical instabilities encountered at this low Tu. In Fig. 13 the streamline plot for this case is shown, along with the corresponding streamwise distribution of the intermittency function. The computed flowfield is characterized by a relatively long separation bubble (9.54 step heights) immediately downstream of the step, with a small secondary eddy at the foot of the step. The transition process appears to be relatively slow, a fact that was to be expected considering the very low free-stream turbulence level of the oncoming flow. Transition starts at about 4.8 step heights downstream of the step and is completed at a distance of about 18.4 step heights.

The experimental data available for this test case were in terms of streamwise varying values of the momentum thickness, the maximum velocity of the external flow, and the shape factor. In Fig. 14 these quantities are compared with the predicted values along the streamwise distance x/H. The agreement is very good for all three quantities and the extent of the separated region is well predicted. Figure 15 shows the variation of the skin friction coefficient and Reynolds number based on the momentum thickness. No experimental data were provided for these two quantities and the results are only compared with the analytical flat-plate boundary layer correlations. What can be observed is that the reattached shear layer in this test case deviates somewhat from the results for turbulent flow over a flat plate.

In Fig. 16 velocity profiles are compared at several streamwise locations downstream of the step with the experimental ones. The experimental data in the first two profiles (separation region) are given as zero or constant, positive values, i.e., no negative velocities were measured. Generally the agreement is good, except for some indication of early reattachment in the numerical results. In Fig. 17 the corresponding turbulence intensities, both numerical and experimental, are shown, at the same streamwise locations as the velocities. It can be observed that

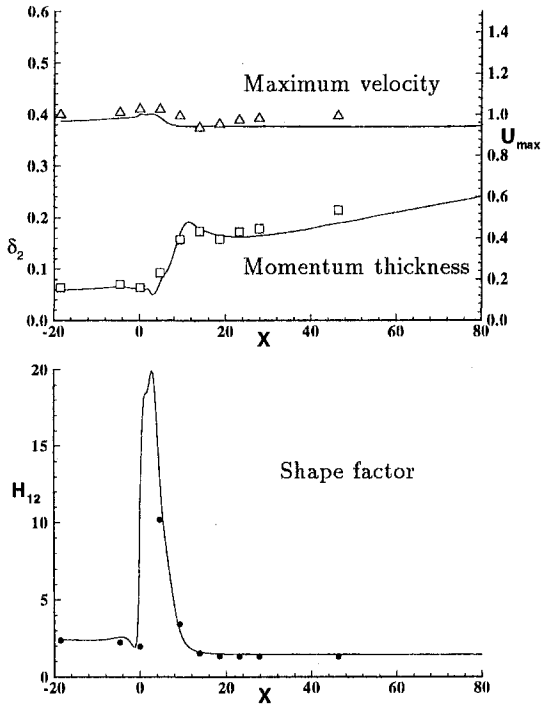

Fig. 14 Numerical (solid lines) against experimental results (points) versus *X* for test case 2

there is some overprediction of the intensity values at the first station, but gradually the numerical values approach the experimental ones. The transition process appears to be very rapid at its early stages in the numerical predictions.

Conclusions

A computational approach based on a two-layer turbulence model and an empirical intermittency function was presented for calculating transition in separated flows. Two test cases were investigated, one involving flow separation due to curvature and the other one due to sudden expansion (step). The transition process was modeled by means of an intermittency function defined through empirical correlations, based on experimental data. These allowed for the effect of separation to be included in the modeling. The results appear promising as for a relatively wide range of external flow conditions (free-stream velocity, level of turbulence) corresponding to values of practical interest in turbomachinery flows, generally good agreement with experimental data was obtained. This can be said both for global

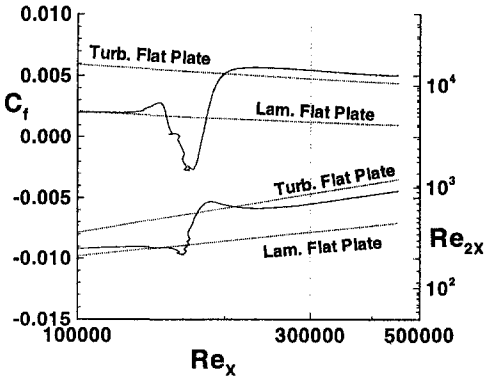

Fig. 15 Numerical results (solid lines) versus Re_X and against flat-plate correlations (dashed lines) for test case 2. Skin friction coefficient and momentum-thickness Reynolds number.

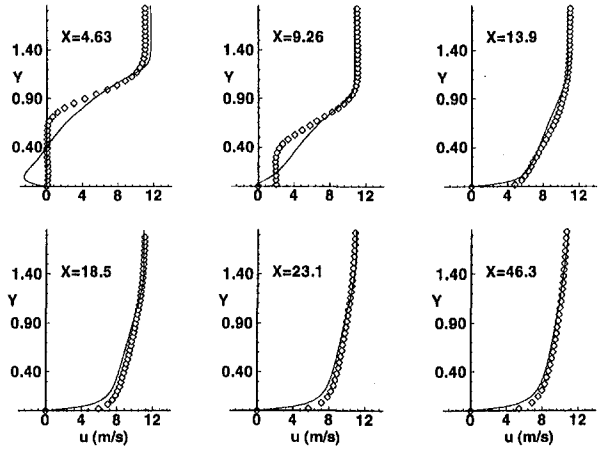

Fig. 16 Numerical (lines) versus experimental (points) velocity profiles downstream of the step for test case 2

quantities such as separation length and location of transition, as well as for local velocity and turbulent intensity profiles.

The model behaved better for free-stream turbulence levels in the range 0.6–5.6 percent, but has been tested also for levels one order of magnitude lower, where it still produced reasonably good results. This study has proven that the intermittency function can be used in several ways in transition modeling, such as for instance in combination with the two-layer model used here, and can lead to successful predictions, but it is necessary to handle with care the laminar-flow regions where this function vanishes, to obtain numerically stable computations.

Available correlations for separated flows based on experimental data such as the ones used here can provide valuable inputs to transitional modeling. However, further experimentation with the various parameters involved in such correlations is needed in order to improve the universality of the models. It is also necessary to investigate additional effects such as rotation or buoyancy and to compute more realistic blade configurations.

Acknowledgments

This work was sponsored by the German Federal Ministry of Research and Technology through program TURBOTECH, under contract No. 0326801G. Many thanks are due to Dr. Mark Savill of Cambridge University, Cambridge, UK, for his valuable work in the ERCOFTAC Transition SIG and for providing the experimental results for test case 2 and to Dr. John

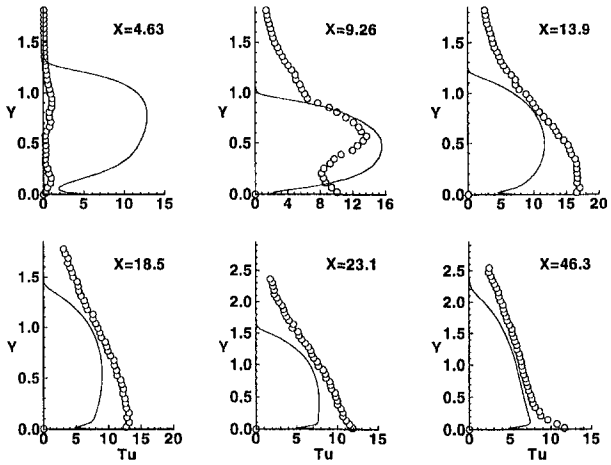

Fig. 17 Turbulence intensity $\sqrt{u'^2}/U_l$ profiles (percent) downstream of the step for test case 2

Coupland from the Rolls-Royce Applied Sciences Laboratory, Derby, UK, for providing us with the experimental data for test case 1.

References

Abu-Ghannam, B. J., and Shaw, R., 1980, "Natural transition of Boundary Layers—The effects of turbulence, pressure gradient, and flow history," *J. of Mech. Engg. Science,* Vol. 22, No. 5, pp. 213–228.

Arena, A. V., and Mueller, T. J., 1980, "Laminar separation, transition and turbulent reattachment near the leading edge of airfoils," *AIAA J.,* Vol. 18, No. 7, pp. 747–753.

Bellows, W. J., and Mayle, R. E., 1986, "Heat Transfer Downstream of a Leading Edge Separation Bubble," ASME JOURNAL OF TURBOMACHINERY, Vol. 108, pp. 131–136.

Chen, K. K., and Thyson, N. A., 1971, "Extension of Emmons' spot theory to flows on blunt bodies," *AIAA J.,* Vol. 9, No. 5, pp. 821–825.

Cho, N.-H., Liu, X., Rodi, W., and Schönung, B., 1993, "Calculation of wake-induced unsteady flow in a turbine cascade," ASME JOURNAL OF TURBOMACHINERY, Vol. 115, pp. 675–686.

Coupland, J., 1995, "Transition modelling for turbomachinery flows," *ERCOFTAC Bulletin,* No. 24, pp. 5–8, 1995.

Crimi, P., and Reeves, B. L., 1976, "Analysis of leading-edge separation bubbles on airfoils," *AIAA J.,* Vol. 14, No. 11, pp. 1548–1555.

Emmons, H. W., 1951, "The laminar–turbulent transition in a boundary layer—Part I," *J. of the Aeronautical Sciences,* Vol. 18, pp. 490–498.

Gotthardt, H., 1983, "Theoretische und experimentelle Untersuchungen an ebenen Turbinengittern mit Pfeilung und V-Stellung," Dissertation, Universität Braunschweig.

Haas, W., Rodi, W., Schönung, B., and Swamy, N. V. C., 1987, "Experimentelle Untersuchung von lokalen Ablöseblasen an Gasturbinenschaufeln," *Z. Flugwiss. Weltraumforschung,* Vol. 11, pp. 261–270.

Hazarika, B. K., and Hirsch, C., 1996, "The effect of Reynolds number on the behaviour of a leading edge separation bubble," ASME Paper No. 96-GT-410.

Karniadakis, G. E., Orszag, S. A., and Yakhot, V., 1990, "Large-eddy/RNG simulation of flow over a backward-facing step," in: *Engineering Turbulence Modelling and Experiments,* W. Rodi and E. N. Ganić, eds., pp. 269–278, Elsevier, New York.

Kaiktsis, L., Karniadakis, E. M., and Orszag, S. A., 1991, "Onset of three-dimensionality, equilibria, and early transition in flow over a backward-facing step," *J. of Fluid Mech.,* Vol. 231, pp. 501–528.

Kwon, O. K., and Pletcher, R. H., 1979, "Prediction of incompressible separated boundary layers including viscous–inviscid interaction," ASME *Journal of Fluids Engineering,* Vol. 101, pp. 466–472.

Majumdar, S., Rodi, W., and Zhu, J., 1992, "Three-dimensional finite-volume methods for incompressible flows with complex boundaries," ASME *Journal of Fluids Engineering,* Vol. 114, pp. 496–503.

Malkiel, E., and Mayle, R. E., 1996, "Transition in a Separation Bubble," ASME JOURNAL OF TURBOMACHINERY, Vol. 118, pp. 752–759.

Mayle, R. E., 1991, "The role of laminar-turbulent transition in gas turbine engines," ASME JOURNAL OF TURBOMACHINERY, Vol. 113, pp. 509–537.

Papanicolaou, E., 1996, "Computation of Separated-Flow Transition Using a Two-Layer Model of Turbulence," Rep. No. 733, Institute for Hydromechanics, University of Karlsruhe, Germany.

Patankar, S. V., 1980, *Numerical Heat Transfer and Fluid Flow,* Hemisphere, Washington, D.C.

Rhie, C. M., and Chow, W. L., 1983, "Numerical study of the turbulent flow past an airfoil trailing edge separation," *AIAA J.,* Vol. 21, No. 11, pp. 1525–1532.

Roberts, W. B., 1980, "Calculation of laminar separation bubbles and their effect on airfoil performance," *AIAA J.,* Vol. 18, No. 1, pp. 25–825.

Rodi, W., and Schönung, B., 1987, "Interaktives-Inverses Grenzschichtverfahren zur Berechnung von lokalen Ablöseblasen an Turbinenschaufeln," *Z. Flugwiss. Weltraumforschung,* Vol. 11, pp. 271–280.

Rodi, W., 1991, "Experience with two-layer models combining the $k-\epsilon$ model with a one-equation model near the wall," AIAA Paper No. 91-0216, presented at the 29th Aerospace Sciences Meeting, Reno, Nevada.

Rodi, W., Mansour, N. N., and Michelassi, V., 1993, "One-Equation Near-Wall Turbulence Modelling With the Aid of Direct Simulation Data," ASME *Journal of Fluids Engineering,* Vol. 115, pp. 196–205.

Savill, A. M., 1992, "A T3 Test Case Project Report—Predicting Transition Induced by Free-Stream Turbulence," presented at the IAHR/ERCOFTAC Turbulence Modelling SIG Seminar, Delft, The Netherlands.

Savill, A. M., 1994, T3D Test Case Problem Specification (private communication).

Savill, A. M., 1995, "A Summary report on the COST ERCOFTAC Transition SIG project evaluating turbulence models for predicting transition," *ERCOFTAC Bulletin,* No. 24, pp. 57–61.

Schlichting, H., 1979, *Boundary Layer Theory,* McGraw-Hill, New York.

Van Doormal, J. P., and Raithby, G. D., 1984, "Enhancements of the SIMPLE Method for Predicting Incompressible Fluid Flows," *Num. Heat Transfer,* Vol. 7, pp. 147–163.

Walker, G. J., Subroto, P. H., and Platzer, M. F., 1988, "Transition modeling effects on viscous/inviscid interaction of low Reynolds number airfoil flows involving laminar separation bubbles," ASME Paper No. 88-GT-32.

Walker, G. J., 1993, "The role of laminar–turbulent transition in gas turbine engines: a discussion," ASME JOURNAL OF TURBOMACHINERY, Vol. 115, pp. 207–217.

Zhu, J., 1991a, "FAST-2D: A computer program for numerical simulation of two-dimensional incompressible flows with complex boundaries," Rep. No. 690, Institute for Hydromechanics, University of Karlsruhe, Germany.

Zhu, J., 1991b, "A low-diffusive and oscillation-free convection scheme," *Comm. in Applied Num. Methods,* Vol. 7, pp. 225–232.

Modeling Unsteady Boundary Layer Transition on a Curved Plate Under Periodic Unsteady Flow Conditions: Aerodynamic and Heat Transfer Investigations

P. Chakka

M. T. Schobeiri

Turbomachinery Performance Laboratory,
Texas A&M University,
College Station, TX 77843

A boundary layer transition model is developed that accounts for the effects of periodic unsteady wake flow on the boundary layer transition. To establish the model, comprehensive unsteady boundary layer and heat transfer experimental investigations are conducted. The experiments are performed on a curved plate at zero-streamwise pressure gradient under periodic unsteady wake flow, where the frequency of the periodic unsteady flow is varied. The analysis of the time-dependent velocities, turbulence intensities, and turbulence intermittencies has identified three distinct quantities as primarily responsible for the transition of an unsteady boundary layer. These quantities, which exhibit the basis of the transition model presented in this paper, are: (1) relative intermittency, (2) maximum intermittency, and (3) minimum intermittency. To validate the developed transition model, it is implemented in an existing boundary layer code, and the resulting velocity profiles and the heat transfer coefficients are compared with the experimental data.

1 Introduction

The flow in a turbomachine stage is highly turbulent and unsteady due to the interactions between the stator and the rotor. The trailing edge thickness, together with the boundary layer thickness, in association with the rotational motion of the rotor, generates unsteady wakes. The unsteady wake exhibits mean velocity defects with a high level of turbulence intensity that passes through the blade rows affecting the natural boundary layer transition. The effect of these wakes on boundary layer transition is important to the design of turbomachinery blades. Successful prediction of transition start and length would help in efficient design of turbine or compressor stages. However, the transition process under the influence of periodic unsteady wakes is not predicted reliably with the existing steady transition models. For this reason, the current investigation focuses on the transition process and its effect on the boundary layer velocity profiles and heat transfer coefficients under unsteady wake flow condition.

The transition process was first explained by Emmons (1950) through the turbulent spot production theory. This theory was later promoted by Dhawan and Narasimha (1958), who proposed a universal profile for intermittency factor for natural transition. Studies by Abu-Ghannam and Shaw (1980), Gostelow and Blunden (1989), Gostelow et al. (1996), and Dullenkopf and Mayle (1994) were conducted to determine the effect of free-stream turbulence and pressure gradient on the spot production rate and the intermittency factor. Experiments for the effect of unsteady wake flow on the boundary layer transition were conducted by Walker (1989), Hodson (1990), Paxson and Mayle (1991), and Orth (1993). Hodson developed a method for calculating boundary layer parameters under unsteady flow conditions using the strip calculation method and the space–time diagrams. He compared the loss coefficient for a turbine blade calculated using the strip calculation method with the time-averaged results. Paxson and Mayle investigated the effect of unsteady passing wakes on the laminar boundary layer near the stagnation region. Dullenkopf and Mayle (1994) proposed a time-averaged transition model. Although this model produces satisfactory results, it is not appropriate for the unsteady flow situation. Few of these researchers have addressed the effect of wake frequency and the structure on boundary layer transition.

The calculation of intermittency factor under the unsteady flow situation is a difficult task because of the free stream, which periodically changes from almost nonturbulent to high turbulent intensity values. The process of turbulent/nonturbulent decisions from the instantaneous signals measured under these unsteady conditions is reviewed by Hedley and Keffer (1974). They proposed derivatives of velocity signals as the detector function to identify the turbulent and nonturbulent parts in the signals. This method was also used by Antonia and Bradshaw (1971), Kovasznay et al. (1970), and Bradshaw and Murlis (1973). Paxson and Mayle (1991) and Mayle (1991) used a similar method for unsteady flows.

Significant contributions to unsteady boundary layer research were made by Pfeil and his co-researchers (Pache, 1976; Eifler, 1975; Schobeiri, 1979; Herbst, 1980; Orth, 1993). Pfeil and Herbst (1979), using the squirrel-cage-type wake generator and a flat plate, developed a wake-induced transition model that is now generally accepted as correct. They also showed that in between the induced transition regions by wakes, the boundary layer grew naturally. Comprehensive investigations on the effect of periodic unsteady flow on a curved plate were performed by Schobeiri and Radke (1993), and Schobeiri et al. (1995a). They showed that an increase in wake passing frequency as a result of reducing the wake spacing results in changing the wake turbulence structure and a shift of transition region toward the leading edge.

Development of an accurate unsteady transition model is essential in predicting the unsteady boundary layer characteristics

Contributed by the International Gas Turbine Institute and presented at the 42nd International Gas Turbine and Aeroengine Congress and Exhibition, Orlando, Florida, June 2–5, 1997. Manuscript received International Gas Turbine Institute February 1997. Paper No. 97-GT-399. Associate Technical Editor: H. A. Kidd.

such as skin friction and heat transfer coefficients. With an appropriate transition model, it is possible to solve the boundary layer equations numerically using the methods proposed by Launder and Spalding (1972), Crawford and Kays (1976), and Schmidt and Patankar (1991). Bearing this in mind, the current investigation focuses on the calculation of the intermittency factor and development of an unsteady model that can be used in Navier–Stokes and boundary layer codes to predict the parameters necessary for the efficient design of turbomachinery stages.

The present investigation includes the aerodynamic and heat transfer experiments detailed in section 2 to provide a comprehensive set of data. Instantaneous velocity signals are used to determine the intermittency throughout the boundary layer. Details on the calculation and analysis of intermittency for unsteady flows is discussed in section 3. The implementation of the model in the boundary layer code is explained in section 4, followed by the results and discussion.

2 Experimental Investigations

To understand the effect of wakes on the aerodynamic and heat transfer characteristics, detailed experiments are performed on the curved plates. The experimental data are collected using a subsonic wind tunnel test facility, which is shown in Fig. 1. Since this facility was already described by Schobeiri and Radke (1994) and Schobeiri et al. (1995a) only a brief description will be given below.

The facility consists of a large centrifugal fan, a settling chamber, a nozzle, a wake generator, and a curved test section. Through the use of a throttle mechanism located at the exit of the fan, the velocity at the inlet of the test section is set at 11 m/s. The rest of the inlet flow conditions can be found in Table 1. The free-stream turbulence intensity of steady flow into the test section is about 1.2 percent. As explained by Schobeiri and Radke (1994), the facility was designed to generate a turbulence intensity about 1 percent without wakes. For unsteady flow cases, however, higher free-stream turbulence intensities are established by secondary wakes.

The *squirrel cage* type wake generator shown in Fig. 2 is used to generate the unsteady flow condition present at the inlet of the test section. The wake generator consists of two parallel rotating, circular disks in which rods can be arranged circumferentially. To determine the effect of wake passing frequency and structure on boundary layer transition, five different rod spacings are used (see Table 1). The unsteady flow produced by the wake generator is characterized by an unsteady parameter Ω. This parameter is similar to the Strouhal number and is defined as $\Omega = \sigma/\phi$, where σ is the ratio of the arc length of the plate s_o and the spacing between the rods s_R, and ϕ is the ratio of the inlet velocity U_{in} and the circumferential velocity of the wake generator U_w. Physically, Ω is the ratio of the transit time of the flow across the test section to the wake passing period. The values of Ω cover a broad range that are typical of a turbomachine and they are specified in Table 1.

Two distinct curved plates, which simulate the pressure surface of a turbine blade, were utilized in this investigation. The first was a curved plate for aerodynamic measurements and the second a heat transfer curved plate with the same concave dimensions as the aerodynamic plate. The test section with the wake generator, curved plate, and the instrumentation is shown in Fig. 2. Boundary layer measurements were taken on the aerodynamic curved plate and heat transfer plate (heater foil not energized) and temperature measurements were taken on the heat transfer plate with liquid crystal instrumentation. All measurements were taken on the concave surface of the curved plate only. For a detailed discussion of boundary layer measurements, we refer to Schobeiri and Radke (1994) and Schobeiri et al. (1995a). The heat transfer measurements are discussed in detail by Wright and Schobeiri (1996). Boundary layer measurements were taken on the concave surface of the aerodynamic plate for $\Omega = 0$, 1.033, 1.725, 3.443, and 5.116 using a TSI single-wire hot-wire probe with a 4 μm tungsten filament. The probe was mounted on a computer-controlled linear traversing system. This system is capable of traversing in increments of 2.5 μm, which is essential in measuring the laminar sublayer. To capture the major portion of the transition onset, the probe was traversed in the longitudinal direction in steps of 2 deg until 50 percent of the plate was reached. The next 25 percent of the plate was traversed in increments of 3 deg, and the last quarter was traversed in increments of 5 deg. For each streamwise position, the boundary layer measurements were started 0.1 mm above the surface of the plate and extended until 10.0 mm above the curved plate. Starting with a high sampling frequency of 10,240 Hz, the preliminary frequency variations showed that the same velocity, turbulence intensity, and intermittency can be reproduced with reduced sampling frequencies. Spectral analysis revealed that the sampling frequency of 2560 Hz is sufficient for boundary layer investigations. Thus, this frequency was chosen for all Ω values. Aerodynamic measure-

Nomenclature

b = intermittency wake width
C = threshold level
h = heat transfer coefficient, W/m^{2}K
$I(t)$ = step function (square wave)
Nu = Nusselt number based on concave arc length = hs_0/k
Pr = Prandtl number = ν/α
Re_x = local Reynolds number based on longitudinal distance = $(\bar{U}s)/\nu$
$\text{Re}_{x,s}$ = Reynolds number at the beginning of transition
$\text{Re}_{x,e}$ = Reynolds number at the end of transition
s = longitudinal distance from plate leading edge, mm
s_0 = arc length of concave surface of curved plate = 690 mm
s_R = rod spacing
$S(t)$ = detector function
St = Stanton number = $h/(\rho C_p \bar{U})$
t = time, s
T = time for one revolution of wake generator
Tu = reference turbulence intensity
$\langle Tu \rangle$ = ensemble-averaged reference turbulence intensity
U = instantaneous velocity, m/s
$\bar{U}$ = time-averaged velocity, m/s
U_{in} = inlet velocity in streamwise direction, m/s
U_w = circumferential velocity of the wake generator, m/s
y = lateral distance from plate surface, mm
α = thermal diffusivity, m^2/s
$\langle \gamma(t) \rangle_{\max}$ = maximum ensemble-averaged intermittency
$\langle \gamma(t) \rangle_{\min}$ = minimum ensemble-averaged intermittency
$\bar{\gamma}$ = time-averaged intermittency
$\langle \gamma(t) \rangle$ = ensemble averaged intermittency
Γ = relative turbulence intermittency
ϵ_H = eddy diffusivity for heat
ζ = nondimensional coordinate = ξ_2/b
ν = kinematic viscosity of air, m^2/s
ξ_2 = transformed co-ordinate = ts_R/τ
ρ = density of air, kg/m^3
σ = length spacing ratio = s_0/S_R
τ = one wake passing period
ϕ = velocity ratio = U_{in}/U_w
Ω = non-dimensionalized unsteady parameter = σ/ϕ

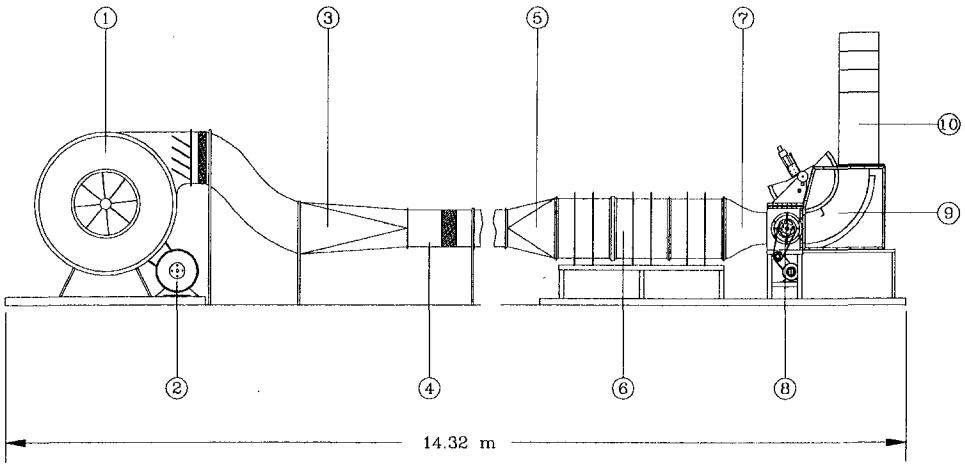

Fig. 1 Overall layout of the test facility: (1) fan, (2) motor, (3) transition duct, (4) straight pipe, (5) diffuser, (6) settling chamber, (7) nozzle, (8) wake generator, (9) test section, (10) exit duct

ments were taken on the heat transfer plate to insure that the new plate provided similar boundary layer results so that a comparison could be made between the boundary layer measurements and the heat transfer measurements.

The power required for heating the heat transfer blade is supplied by a Sorensen DCR40-70B DC power supply. The current passing through the test blade is measured with a multimeter connected across a shunt resistor. A separate multimeter is connected across the output leads of the power supply to measure the voltage. The yellow band of the liquid is used for recording the data. The location of the yellow band is controlled through the power supply to the heater plate and the voltage and the current reading are recorded for different locations of the yellow band on the curved plate. The data are collected for the concave and the convex side of the curved plate. Note that no effect of Görtler vortices in the spanwise direction is observed while taking the liquid crystal measurements. We refer to Schobeiri and Radke (1994) for a discussion of the effect of curvature and Görtler vortices on boundary layer transition.

3 Intermittency Analysis

Intermittency distribution that identifies the flow being laminar or turbulent inside the boundary layer is calculated following the method of Hedley and Keffer (1974). Instantaneous velocities are used to identify this intermittency distribution. Representative plots of ensemble-averaged velocity signal are given in Fig. 3 inside the boundary layer. The instantaneous velocity is sensitized to increase its discriminatory capabilities between turbulent and nonturbulent parts of the signal. For this purpose, the second derivative of the velocity signal is used and squared for further analysis, and is called the detector function, $S(t)$. Several other detector functions were used by Antonia and Bradshaw (1971), Antonia (1972), and Kovasznay et al. (1970). A threshold level C is then applied to this detector function to distinguish between the true turbulence and the signal noise.

$$I(t) = \begin{cases} 1 & \text{when} \quad S(t) \geq C, \\ 0 & \text{when} \quad S(t) < C. \end{cases} \tag{1}$$

After applying the threshold level to the detector function $S(t)$, the result is a random square wave with 0's representing the laminar case and 1's representing the turbulent behavior of the boundary layer. This square wave is ensemble averaged to get the ensemble-averaged intermittency as follows

$$\langle \gamma_i(t_i) \rangle = \frac{1}{n} \sum_{j=1}^{n} I_{ij}(t_i) \tag{2}$$

where n is the number of revolutions of the wake generator for

Table 1 Specifications of inlet flow and wake generator characteristics

Parameters	Values	Parameters	Values
Nozzle exit Reynolds number	$Re_h = 0.43 \times 10^6$	Nozzle exit turbulence intensity	Tu = 1.20%
Nozzle exit height	h = 420.00 mm	Nozzle exit width	w = 593.00mm
Rod diameter	$d_R = 2$ mm	Radius of curvature of curved plate	r = 702.5 mm
Steady reference (no rods)	$s_R = \infty$ mm	Ω - parameter steady case	$\Omega = 0.0$
Set 1 rod spacing	$s_R = 314.0$ mm	Ω - parameter for set 1	$\Omega = 1.033$
Set 2 rod spacing	$s_R = 188.4$ mm	Ω - parameter for set 2	$\Omega = 1.725$
Set 3 rod spacing	$s_R = 94.2$ mm	Ω - parameter for set 3	$\Omega = 3.443$
Set 4 rod spacing	$s_R = 62.8$ mm	Ω - parameter for set 4	$\Omega = 5.166$
No. of rods in set 1	$n_R = 3$	No. of rods in set 2	$n_R = 5$
No. of rods in set 3	$n_R = 10$	No. of rods in set 4	$n_R = 15$

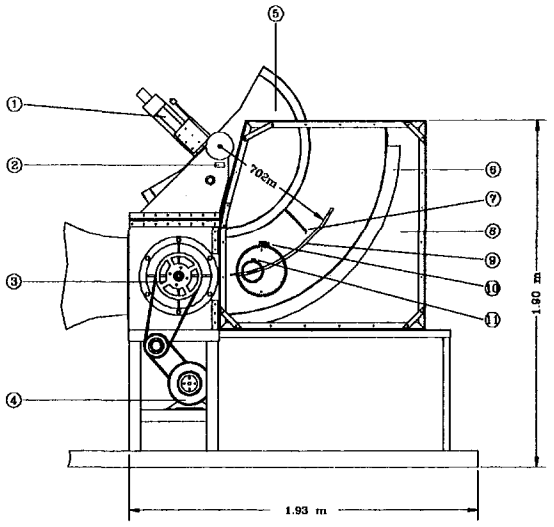

Fig. 2 Test section: (1) traversing system, (2) nozzle, (3) wake generator, (4) electric motor, (5) convex wall, (6) concave wall, (7) hot-wire probe, (8) plexiglass wall, (9) curved plate, (10) small vernier, (11) large vernier

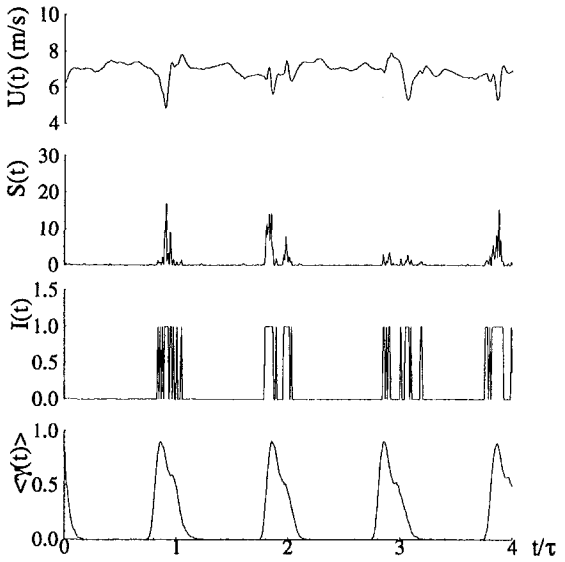

Fig. 4 Calculation of ensemble-averaged intermittency function from instantaneous velocities for $\Omega = 1.725$ (five rods) and $y = 0.1$ mm

which the data are collected. For time-averaged intermittency, $\langle \gamma_i(t_i) \rangle$ is integrated with respect to time to give

$$\bar{\gamma} = \frac{1}{T} \int_{t=0}^{T} \langle \gamma_i(t_i) \rangle dt \tag{3}$$

Figure 4 shows the processing of instantaneous velocities. Ensemble-averaged intermittency distribution as a function of nondimensional time is shown in Figs. 5(*a*, *b*) for three-rod and ten-rod cases. Similar plots are seen for other rod cases. Only the first two wakes are plotted for a better comparison of the effects of impinging wake frequency on the transition process. Intermittency is approximately equal to zero outside the wake region near the leading edge showing the nonturbulent behavior of the flow. The wake is represented by a thin strip with intermittency values near one, typical of a turbulent flow. As these wakes pass through the channel, the boundary layer periodically switches from laminar to turbulent depending on the presence of the wakes. The natural transition of the boundary layer is affected by periodic passing of wakes resulting in wake induced transition. The intermittency distributions in Figs. 5(*a*, *b*) show clearly the unsteady nature of the boundary layer transition.

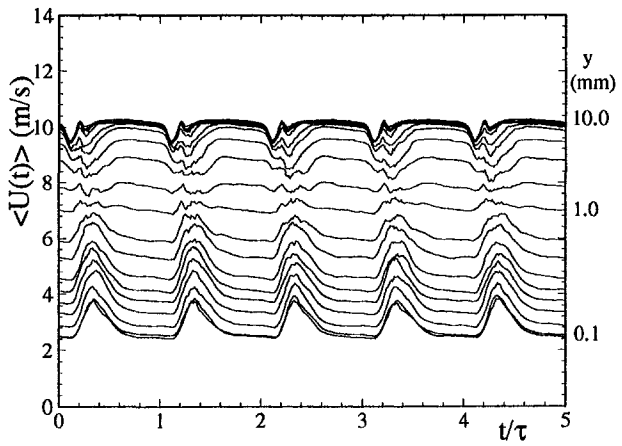

Fig. 3 Ensemble-averaged velocity distribution as a function of nondimensional time at different *y* locations at $s/s_0 = 0.25$ for $\Omega = 1.725$ (five rods)

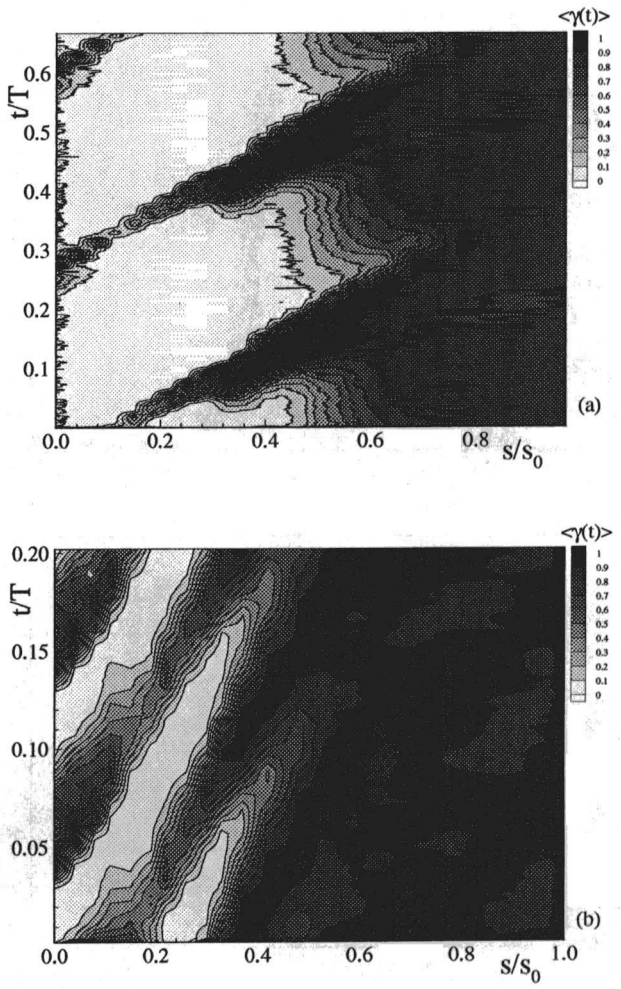

Fig. 5 Contour plots of intermittency factor as a function of normalized axial distance s/s_0 for (*a*) $\Omega = 1.033$ (three rods) and (*b*) $\Omega = 3.443$ (ten rods) at $y = 0.1$ mm.

However, in this form, they cannot be used to describe the complex unsteady transition process quantitatively. To establish the basic relations essential for a quantitative description of the unsteady boundary layer transition, we resort to the fundamental studies by Schobeiri and his co-workers (Schobeiri et al. (1995b), Schobeiri et al. (1996), John and Schobeiri (1996) that deal with the physics of steady and unsteady wake development in a curved environment. These studies clearly show that the turbulence structure of the steady and unsteady wake flow is determined by the wake defect, which is a Gaussian function. Following these studies, we define a dimensionless parameter:

$$\zeta = \frac{tU_w}{b} = \frac{ts_R}{\tau b} = \frac{\xi_2}{b} \quad \text{with} \quad b = \frac{1}{\sqrt{\pi}} \int_{-\infty}^{+\infty} \Gamma d\xi_2 \qquad (4)$$

that relates the passing time t of a wake impinging on the plate surface with the wake passing velocity in the lateral direction U_w and the intermittency width b. The latter is directly related to the wake width introduced by Schobeiri and his co-workers. In an analogous way, to find the defect function, we define the relative intermittency Γ as:

$$\Gamma = \frac{\langle \gamma_i(t_i) \rangle - \langle \gamma_i(t_i) \rangle_{\min}}{\langle \gamma_i(t_i) \rangle_{\max} - \langle \gamma_i(t_i) \rangle_{\min}} \qquad (5)$$

In this equation, $\langle \gamma_i(t_i) \rangle$ is the time-dependent ensemble-averaged intermittency function, which determines the transitional nature of an unsteady boundary layer. The maximum intermittency $\langle \gamma_i(t_i) \rangle_{\max}$ exhibits the time-dependent ensemble-averaged intermittency value inside the wake vortical core. Finally, the minimum intermittency $\langle \gamma_i(t_i) \rangle_{\min}$ represents the ensemble-averaged intermittency values outside the wake vortical core. The relative intermittency function Γ is shown in Figs. 6(a, b), for frequency values of Ω = 1.033 (three rods) and 3.443 (ten rods), respectively, with the dimensionless longitudinal distance s/s_o as a parameter. Again, similar results are observed for other rod frequencies listed in Table 1. The symbols represent the experimental data. For the reduced frequencies and longitudinal positions presented in these plots, the measured relative intermittency functions for wakes impinging on the plate surface follow very closely a Gaussian distribution, given by:

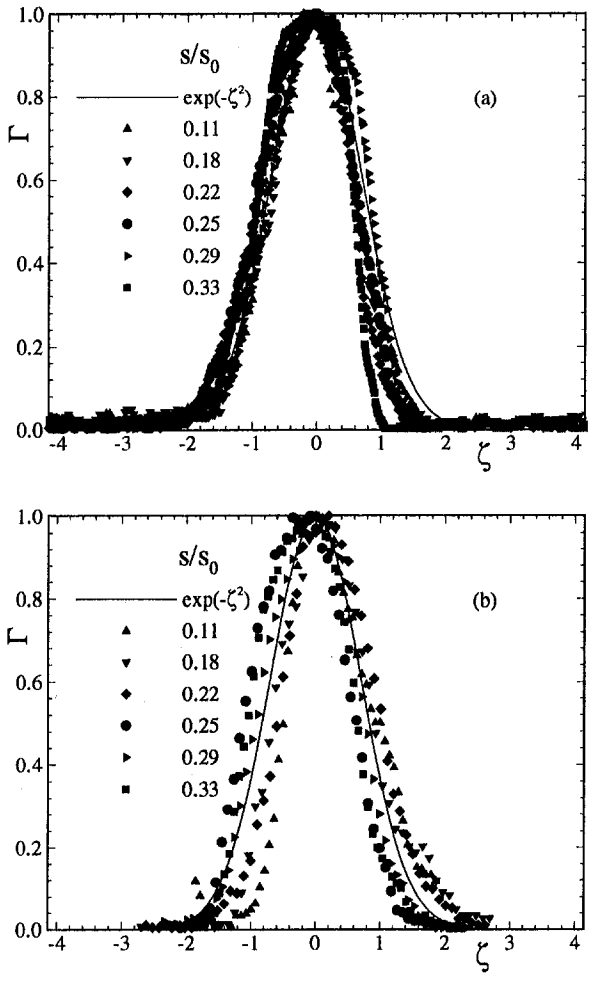

Fig. 6 Relative intermittency as a function of nondimensionalized lateral coordinate for (*a*) Ω = 1.033 (three rods) and (*b*) Ω = 3.443 (ten rods) at y = 0.1 mm

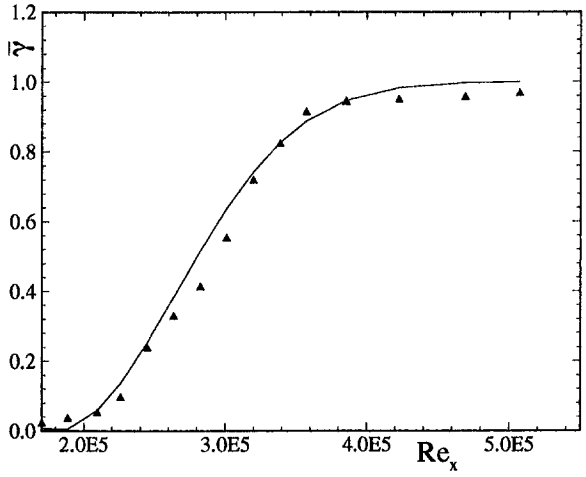

Fig. 7 Intermittency as a function of Re_x for no-rod or steady case on the concave surface of the curved plate at y = 0.1 mm.

$$\Gamma = e^{-\zeta^2} \qquad (6)$$

Here, ζ is the nondimensionalized lateral length scale. Using this function as a generally valid intermittency relationship for zero-pressure gradient cases, the intermittency function $\langle \gamma_i(t_i) \rangle$ is completely determined if additional information about the minimum and the maximum intermittency functions $\langle \gamma_i(t_i) \rangle_{\min}$ and $\langle \gamma_i(t) \rangle_{\max}$ are available. The distribution of $\langle \gamma_i(t_i) \rangle_{\min}$ and $\langle \gamma_i(t_i) \rangle_{\max}$ in streamwise direction are plotted in Fig. 8 for Ω = 1.033 (three rods). The steady case (no-rod case) shown in Fig. 7 serves as the basis of comparison for these maximum and minimum values. In the steady case, the intermittency starts to rise from zero at a streamwise Reynolds number $Re_{x,s} = 2 \times 10^5$ and gradually equals unity corresponding to the fully turbulent state. This is typical of natural transition and follows the intermittency function introduced by Narasimha (1957). The distributions of maximum and minimum turbulence intermittencies $\langle \gamma_i(t_i) \rangle_{\min}$ and $\langle \gamma_i(t_i) \rangle_{\max}$ in the streamwise direction are shown in Fig. 8. For each particular streamwise location on the blade surface with a streamwise Reynolds number, for example $Re_{x,s} = 1 \times 10^5$, two corresponding distinctively different intermittency states are periodically present. At this location, $\langle \gamma_i(t_i) \rangle_{\max}$ corresponds to the condition when the wake with its high turbulence intensity core impinges on the plate surface. Once the wake has passed over the surface, the same streamwise location is exposed to a low turbulence intensity flow regime with an intermittency state of $\langle \gamma_i(t_i) \rangle_{\min}$, where no wake is present. As seen, $\langle \gamma_i(t_i) \rangle_{\min}$ tends to follow the course of steady (no-wake) intermittency distribution exhibited in Fig. 6, with a gradual increase from an initial *nonturbulent* state with a value of zero approaching a final state of 0.8. The final state does not approach to the fully turbulent value of 1.0 due to the *calming* effect of the boundary layer. This tendency is expected as $\langle \gamma_i(t_i) \rangle_{\min}$ is calculated outside the wake region where turbu-

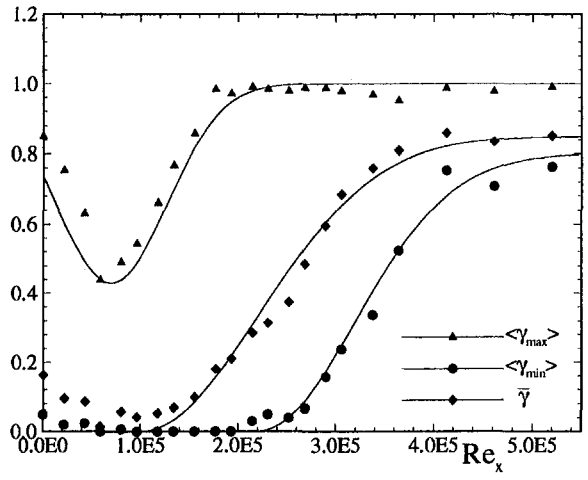

Fig. 8 Maximum, minimum and time-averaged intermittency distributions as a function of axial Reynolds number for Ω = 1.033 (3-rods) at y = 0.1 mm.

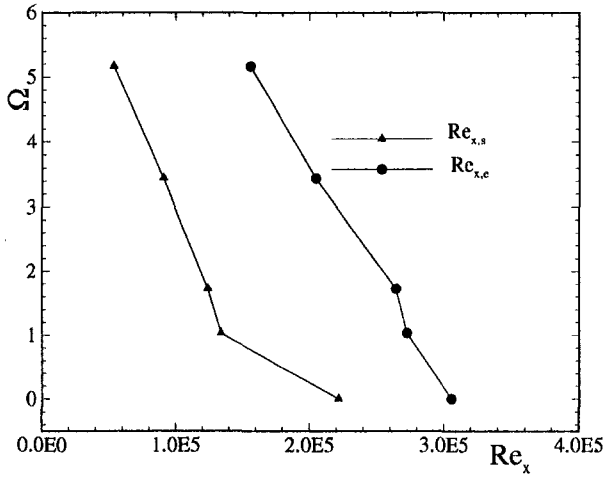

Fig. 9 Effect of wake frequency Ω on start and end Reynolds numbers $Re_{x,s}$ and $Re_{x,e}$

lence intensity is relatively small. On the other hand, $\langle \gamma_i(t_i) \rangle_{max}$ reveals a fundamentally different behavior that needs to be discussed further. As Fig. 8 shows, the wake flow with an intermittency close to 1 impinges on the blade surface. By convecting downstream, its turbulent fluctuations undergo a strong damping by the wall shear stress forces. The process of damping continues until $\langle \gamma_i(t_i) \rangle_{max}$ reaches a minimum. At this point the wall shear forces are not able to further suppress the turbulent fluctuations. As a consequence, the intermittency again increases to approach unity, showing the combined effect of *wake-induced* and *natural transition* due to increased turbulence intensity level. Figure 8 also shows the average intermittency that is a result of the integral effect of periodic wakes with respect to time. The maximum intermittency is described by

$$\langle \gamma(t) \rangle_{max} = 1.0 - c_1 e^{-((Re_x - Re_{x,s})/(Re_{x,s} - Re_{x,e}))^2} \quad (7)$$

where the constant c_1 is dependent on Ω. The minimum intermittency is described by:

$$\langle \gamma(t) \rangle_{min} = c_2(1.0 - e^{-((Re_x - Re_{x,s})/(Re_{x,s} - Re_{x,e}))^2}) \quad (8)$$

where the constant c_2 is again dependent on Ω. The time-averaged intermittency is described by:

$$\bar{\gamma} = c_4(1.0 - c_3 e^{-((Re - Re_{x,s})/(Re_{x,s} - Re_{x,e}))^2}) \quad (9)$$

The four constants for the frequencies under investigation are given in Table 2. Constant c_1 represents the extent of wall damping (the magnitude of trough in $\langle \gamma_i(t_i) \rangle_{max}$), whereas constant c_2 is introduced as the asymptotic value of the minimum intermittency. It can be seen from Table 2 that constant c_2 shows an increase in trend as the wake frequency is increased.

Table 2 Constants in the intermittency correlation

Const	Reduced Frequency, Ω			
	1.033	1.725	3.443	5.166
c_1	0.57	0.22	0.50	0.35
c_2	0.80	0.85	0.86	0.88
c_3	1.00	0.82	0.80	0.80
c_4	0.85	0.92	0.92	0.94

Constants c_3 and c_4 give the combined effect of c_1 and c_2 for $\bar{\gamma}$. It is also possible to derive c_3 and c_4 from Eq. (3) by backworking $\langle \gamma_i(t_i) \rangle$ through Eq. (5). For natural transition, all the constants approach unity. Also, the Reynolds numbers at the start and end of transition, $Re_{x,s}$ and $Re_{x,e}$, differ for different wake frequencies. The values of $Re_{x,s}$ and $Re_{x,e}$, for the Ω values under investigation, are shown in Fig. 9. It will be seen from this figure that the transition starts earlier as the wake frequency Ω is increased. Also, the wake-induced transition length is higher when compared to the steady or no-wake transition length, but shows a decrease in length as the wake frequency is increased.

Free-Stream Turbulence Intensity. One major parameter that affects the boundary layer transition onset is the free-stream turbulence intensity. Also, turbulence scales are important as well. They are currently under investigation and their treatment is beyond the scope of this paper. The presence of wakes, particularly their spacing and interaction, contributes significantly to an increase of the freestream turbulence. Figure 10 shows the free-stream time-averaged turbulence intensity distribution as a function of inlet wake frequency. For the investigated reduced frequency range, it is observed to approach a maximum value of 4.2 percent as the wake frequency is increased.

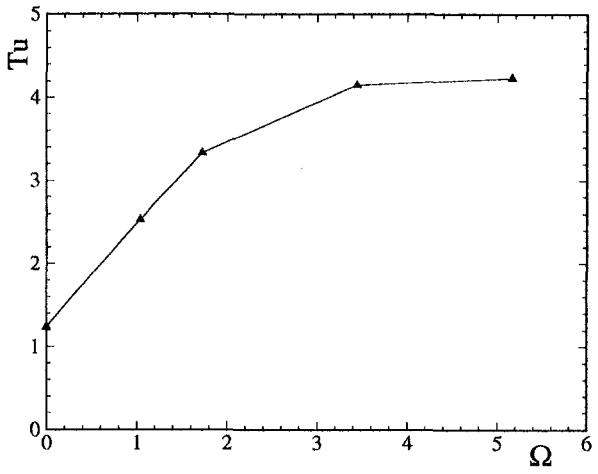

Fig. 10 Time-averaged inlet free-stream turbulence intensity as a function of Ω

4 Implementation of the Transition Model Into Calculation Procedures

The developed transition model can be implemented into any Navier–Stokes or differential boundary layer code. We have chosen TEXSTAN, which simultaneously solves differential equations of continuity, momentum, and energy. All these equations are time averaged and are written to describe the flow over an axisymmetric body. The time averaged momentum equation in the x direction is:

$$\rho U \frac{\partial U}{\partial x} + \rho V \frac{\partial U}{\partial y} = -\frac{dp}{dx} + \frac{1}{r}\frac{\partial}{\partial y}\left[r\left(\mu \frac{\partial U}{\partial y} - \rho\overline{u'v'}\right)\right] \quad (10)$$

In this momentum equation, the turbulent shear stress is modeled by the eddy diffusivity for momentum and is defined as

$$-\overline{u'v'} = \epsilon_M \frac{\partial U}{\partial y} = \frac{\mu_t}{\rho}\frac{\partial U}{\partial y} \quad (11)$$

where μ_t is the turbulent viscosity, which combines with the laminar viscosity to give

$$\mu_{\text{eff}} = (\mu + \mu_t) = \rho(\nu + \epsilon_M) \quad (12)$$

Similarly, after introducing the concept of eddy diffusivity for heat, ϵ_H, the energy equation becomes

$$\rho U \frac{\partial I^*}{\partial x} + \rho V \frac{\partial I^*}{\partial y} = \frac{1}{r}\frac{\partial}{\partial y}\left\{r\left[\frac{\mu_{\text{eff}}}{\text{Pr}_{\text{eff}}}\frac{\partial I^*}{\partial y} + \frac{\mu_{\text{eff}}}{J}\left(1 - \frac{1}{\text{Pr}_{\text{eff}}}\right)\frac{\partial}{\partial y}\left(\frac{U^2}{2}\right)\right]\right\} \quad (13)$$

where I^* is the stagnation enthalpy and Pr_{eff} is the effective Prandtl number, defined as

$$\text{Pr}_{\text{eff}} = \frac{\mu_{\text{eff}}}{(k/c)_{\text{eff}}} = \frac{1 + \frac{\epsilon_M}{\nu}}{\frac{1}{\text{Pr}} + \frac{\epsilon_M}{\nu}\frac{1}{\text{Pr}_t}} \quad (14)$$

and Pr_t is the turbulent Prandtl number. A constant value of 0.85 is used for Pr_t in the solution process.

The eddy viscosity term is modeled through the mixing length theory and the intermittency model developed in the current investigation is implemented through

$$\epsilon_M = \gamma l^2 \left|\frac{\partial U}{\partial y}\right| \quad (15)$$

where l is the mixing length and γ is the intermittency. The expressions developed in Eqs. (7), (8), and (9) are used in the equation in place of γ. The solution process uses Patankar-Spalding's (1970) omega (nondimensional stream function) transformation. In stream function coordinates the momentum equation without the body forces becomes

$$U\frac{\partial U}{\partial x} + U\frac{\partial}{\partial \Psi}\left[U\nu_{\text{eff}}\frac{\partial U}{\partial \Psi}\right] = -\frac{1}{\rho}\frac{dp}{dx} \quad (16)$$

The boundary layer equations are integrated after nondimensionalizing the stream function and solved numerically through the mixing length model. Here, Eq. (12) and Eq. (15) are used for solving momentum equation, Eq. (16). Similarly, Eq. (14) and Eq. (15) are used for solving the energy equation, Eq. (13).

5 Results and Discussions, Aerodynamic Study

5.1 Experimental Results, Intermittency Distribution. The entire set of ensemble-averaged data was utilized to generate the temporal-spatial distribution of the ensemble-averaged turbulence intermittency. Figures 5(a) and 5(b) show a few cases as representative examples at $y = 0.1$ mm. As shown in Fig. 5(a) ($\Omega = 1.033$, three rods), the boundary layer is periodically disturbed by the wakes that cause periodically high turbulence strips and *extended becalmed regions.* These extended becalmed regions were produced by strong damping of turbulence fluctuations in the wall region that leads to an exponential decrease of the maximum intermittency $\langle \gamma_i(t_i)\rangle_{\max}$. These regions are observed between the leading edge and the streamwise position of $s/s_o > 0.4$. As seen, the wake strips are separated from the becalmed regions, indicating the absence of any visible interaction near the leading edge. Increasing the frequency Ω of the wake by reducing the rod spacing (Fig. 5(b) with $\Omega = 3.443$, ten rods) results in an earlier transition start compared to the above three-rod case. Two mechanisms are considered instrumental in effecting the transition start. The first one is an earlier mixing of the wakes due to the reduction of their spacing that leads to higher free-stream turbulence, which inherently affects the onset of the transition. The second mechanism is the increased impinging frequency of the primary wake strips that introduce an excessive turbulent kinetic energy transport to the boundary layer causing a shift of transition start toward the leading edge. It is conceivable that the combination of these two mechanisms would make additional contribution to the shift of the transition start. Further increase of Ω results in a higher free-stream turbulence and increased impinging frequency and thus a significant shift of the transition toward the leading edge as the consequence of the mechanisms discussed above. A similar turbulence intermittency pattern is observed for other y positions.

5.2 Calculation Results, Velocity Distributions. The implementation of the intermittency model into the calculation procedure enables the prediction of time-averaged velocity distribution. As representative examples, the time-averaged velocity profiles for $\Omega = 0$ and 1.725 are plotted in Figs. 11(a, b) for the laminar, transitional, and turbulent flow regions. These are obtained by using the expression for time-averaged intermittency developed in Eq. (9) in the solution process. The solid lines exhibit the calculation results, which are in good agreement with the experimental results represented by symbols. It can be seen from Fig. 11(b) that the transition starts much earlier for $\Omega = 1.725$ (five rods) when compared to $\Omega = 0.0$ (No rods) case shown in Fig. 11(a).

6 Results and Discussions, Heat Transfer Study

6.1 Heat Transfer Coefficient Calculation. The heat transfer coefficient is calculated from the following expression:

$$h = \frac{Q_{\text{foil}} - Q_{\text{rad}}}{(T_{yl} - T_\infty)} \quad (17)$$

where Q_{rad} is the radiation heat loss from the surface of the curved plate, Q_{foil} is the heat flux of the inconel foil, T_{yl} is the yellow line temperature, and T_∞ is the free-stream temperature. Q_{foil} and Q_{rad} are given by:

$$Q_{\text{foil}} = \frac{VI}{A_{\text{foil}}} \quad (18)$$

and

$$Q_{\text{rad}} = \epsilon\sigma(T_{yl}^4 - T_\infty^4) \quad (19)$$

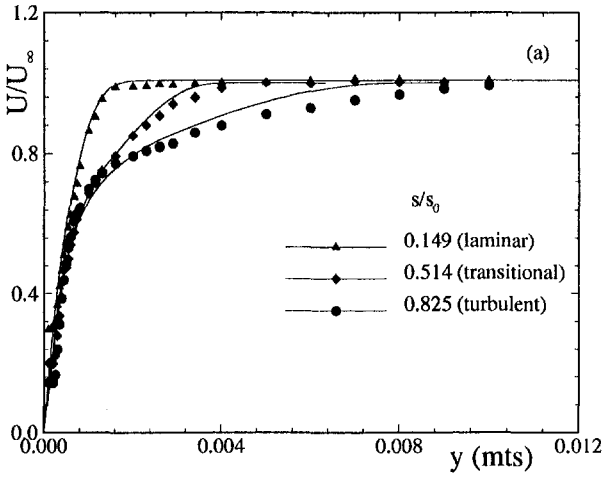

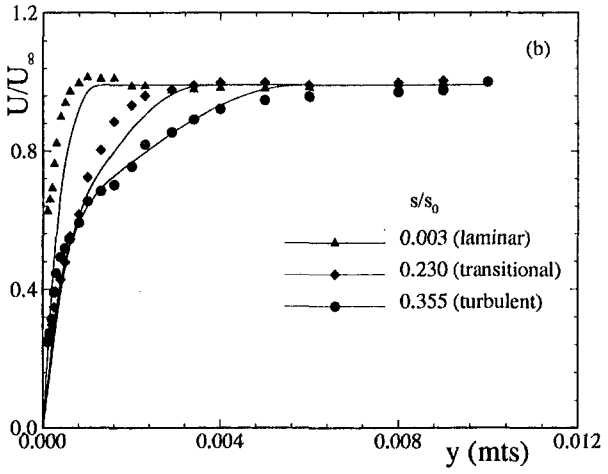

Fig. 11 Velocity profiles as a function of lateral coordinate for three axial locations for (*a*) Ω = 0.0 (No = rods) and (*b*) Ω = 1.725 (five rods)

where V and I are the voltage and current supplied from the power supply respectively, and A_{foil} is equal to the total heat transfer surface area of the Inconel 600 foil. Finally, the Stanton number is defined by:

$$\mathrm{St} = \frac{h}{\rho C_p \bar{U}} \tag{20}$$

6.2 Heat Transfer, Steady Inlet Flow Reference Case. As indicated previously, for heat transfer measurement, we used the liquid crystal technique which was developed by Hippensteele (1981), and is being applied by numerous researchers. It has the advantage of not affecting the turbulence structure at the surface, as thermocouples or surface-mounted hot-wire/film probes do. However, its slow response does not allow extracting valuable unsteady information. As a result, in unsteady cases, only the time-averaged response can be acquired. Using this technique, first for comparison purposes, the steady state case Ω = 0 (no rod) is presented in Fig. 12, where the model is applied. Good agreement between calculation and experiment is shown in Fig. 12 for a wide range of Re_x from leading edge via transition portion to trailing edge. For comparison purposes, Mayle's model (1991) shows some discrepancies between the experiment and theory. However, it should be pointed out that Mayle's correlation gives reasonably good results for time-averaged unsteady cases.

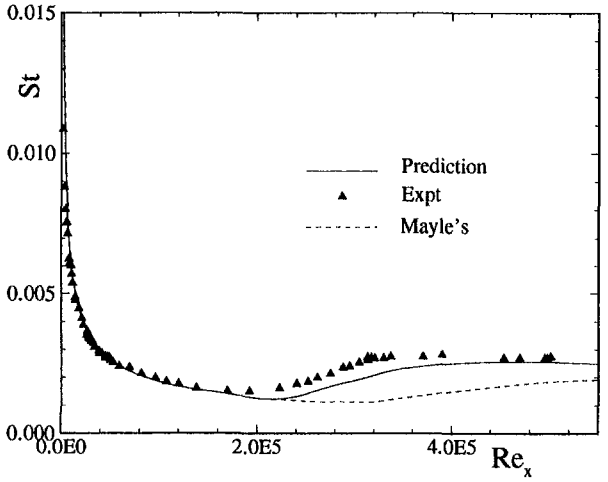

Fig. 12 Heat transfer coefficients as a function of axial Reynolds number for no-rod or steady case

6.3 Heat Transfer, Unsteady Inlet Flow Cases. For unsteady flow cases with a reduced frequency (see Table 1) values of Ω = 1.033 and 5.166, calculated Stanton numbers are compared with the experimental results and shown in Figs. 13(*a*, *b*), where the experimental results are represented by symbols.

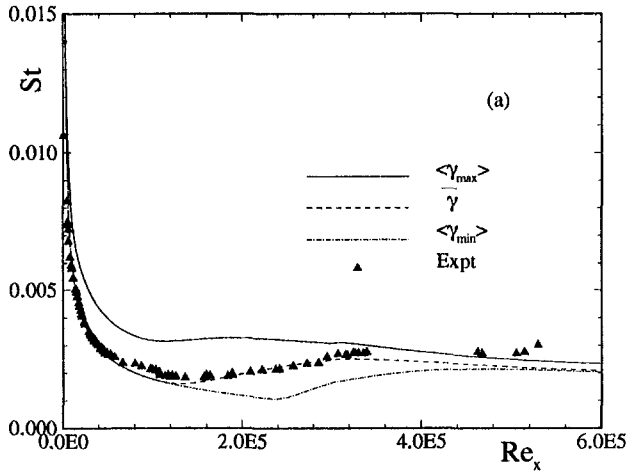

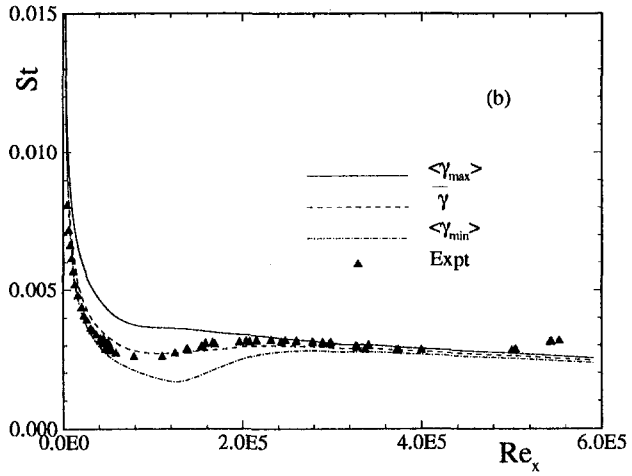

Fig. 13 Heat transfer coefficients as a function of axial Reynolds number for (*a*) Ω = 1.033 (three rods) and (*b*) Ω = 5.166 (15 rods)

Furthermore, three curves are plotted in each diagram representing the calculation results. Starting with a reduced frequency of $\Omega = 1.033$ (three rods), the upper solid curve represents the streamwise Stanton number distribution when the plate is subjected to an inlet flow intermittency state of $\langle\gamma(t)\rangle_{max}$. On the other hand, if the plate is subjected to $\langle\gamma(t)\rangle_{min}$, the lower point-dashed curve depicts its Stanton number distribution. However, because of the periodic character of the inlet flow associated with unsteady wakes, the plate would experience a periodic change of heat transfer represented by upper and lower Stanton number curves (solid line and point-dashed line) as an envelope. The liquid crystal responds to this periodic event with time-averaged signals. This time-averaged result is reflected by the dashed line, which gives a corresponding time-averaged intermittency. As seen, a reasonably good agreement is found for the entire laminar and transitional portions. Close to the plate trailing edge, the theory under predicts slightly. It should be mentioned that in this area, heat transfer measurements were associated with certain difficulty.

As the experimental results (symbols in Fig. 13(*b*)) show, increasing the reduced frequency to $\Omega = 5.166$ (15 rods) causes the transition point to shift toward the leading edge, resulting in a slightly higher Stanton number. This shift of the transition point is in full accord with the aerodynamic findings explained previously. Similar to the case with $\Omega = 1.033$, the upper solid curve represents the streamwise Stanton number distribution if the plate is subjected to an inlet flow intermittency state of $\langle\gamma(t)\rangle_{max}$. The lower point-dashed curve depicts the Stanton number distribution pertaining to the minimum intermittency $\langle\gamma(t)\rangle_{min}$. The time-averaged result is reflected by the dashed curve, which gives a corresponding time averaged intermittency. Figure 13(*b*) exhibits reasonably good agreement between the theory and experiment in the transition and turbulent regions with $Re_x > 1.2 \times 10^5$. In the laminar region, however, the theory slightly overpredicts the heat transfer resulting in marginally higher Stanton numbers. In this region, better agreement can be reached by utilizing the minimum intermittency $\langle\gamma(t)\rangle_{min}$. Similar tendencies are seen for other Ω's of 1.725 (five rods) and 3.443 (ten rods). As discussed previously, a combined effect of wake mixing and the increased impinging frequency of the wake strips that introduce an excessive turbulent kinetic energy transport to the boundary layer cause a shift of transition start toward the leading edge.

7 Conclusions

A transition model that includes the effects of periodic unsteady wakes on the boundary layer and heat transfer of a concave surface of a curved plate is developed for zero pressure gradient. Instantaneous velocities using hot-wire anemometry are measured in the boundary layer for four wake passing frequencies. Steady or no-wake case is also used to determine the intermittency distribution inside the boundary layer. The method of Hedley and Keffer is used to distinguish between turbulent and laminar parts in the instantaneous velocity signals and the result is ensemble averaged to give ensemble-averaged intermittency. Based on the results from these investigations, the following conclusions are drawn:

1 The unsteady wake flow periodically changes the boundary layer transition from natural transition to wake-induced transition depending on the presence of turbulent core inside the wake region.

2 A transition model has been developed that includes the effects of periodic unsteady flow on the boundary layer transition on a curved plate.

3 The relative intermittency factor is seen to follow a gaussian distribution. The minimum intermittency factor, $\langle\gamma_{min}\rangle$, represents the boundary layer behavior in between the turbulent wake strips. It is shown to follow the natural transition process as the free-stream is almost nonturbulent. On the other hand, $\langle\gamma_{max}\rangle$ being the value inside the turbulent core, starts with a value of 1.0 and goes through a minimum. This is due to the viscous damping of the turbulent core by the boundary layer.

4 The transition process starts earlier as the wake frequency is increased. The length of wake-induced transition is higher when compared to the steady case. However, wake-induced transition length decreases as the wake frequency is increased.

5 The heat transfer coefficients and the velocity distribution by the numerical solution using the developed transition model compare well with the experimental data and the maximum and the minimum limits of heat transfer coefficients are predicted.

Acknowledgments

The authors would like to express thanks and appreciation to Mr. Hippensteele of NASA Lewis Research Center for his advice on liquid crystal instrumentation and to Prof. M. Crawford for making TEXSTAN available to them. They also would like to thank DOE for support of this research.

References

Abu-Ghannam, B. J., and Shaw, R., 1980, "Natural Transition of Boundary Layers—The Effects of Turbulence, Pressure Gradient and Flow History," *J. Mech. Eng. Sci.,* Vol. 22, pp. 213–228.

Antonia, R. A., and Bradshaw, P., 1971, Imp. College Aero. Rep., No. 71-04.

Bradshaw, P., and Murlis, J., 1973, Imp. College Aero. Tech. Note, No. 73-108.

Crawford, M. E., and Kays, W. M., 1976, "STAN5 (TEXSTAN Version)—A Program for Numerical Computation of Two Dimensional Internal and External Boundary Layer Flow," NASA CR-2742.

Dhawan, S., and Narasimha, R., 1958, "Some Properties of Boundary Layer Flow During the Transition From Laminar to Turbulent Motion," *Journal of Fluid Mechanics,* Vol. 3, pp. 418–436.

Dullenkopf, K., and Mayle, R. E., 1994, ASME Paper N. 94-GT-174.

Eifler, J., 1975, "Zur Frage der freien turbulenten Strömungen, insbesondere hinter ruhenden und bewegten Zylindern," Dissertation D-17, Technische Hochschule Darmstadt, Germany.

Emmons, H. W., 1951, "The Laminar-Turbulent Transition in Boundary Layer—Part I," *J. Aero. Sci.,* Vol. 18, pp. 490–498.

Gostelow, J. P., and Blunden, A. R., 1989, "Investigations of Boundary Layer Transition in an Adverse Pressure Gradient," ASME JOURNAL OF TURBOMACHINERY, Vol. 111, pp. 366–375.

Gostelow, J. P., Melwani, N., and Walker, G. J., 1996, "Effects of Streamwise Pressure Gradient on Turbulent Spot Development," ASME JOURNAL OF TURBOMACHINERY, Vol. 118, pp. 737–743.

Gostelow, J. P., and Ramachandran, R. M., 1983, "Some Effects of Free Stream Turbulence on Boundary Layer Transition," *Proc. 8th Australasian Fluid Mechanics Conference.*

Halstead, E. D., et al., 1997, "Boundary Layer Development in Axial Compressors and Turbines," ASME JOURNAL OF TURBOMACHINERY, Vol. 119, Part 1: pp. 114–127; Part 2: pp. 426–444; Part 3: pp. 225–237; Part 4: pp. 128–139.

Hedley, B. T., and Keffer, F. J., 1974, "Turbulent/Non-Turbulent Decisions in an Intermittent Flow," *Journal of Fluid Mechanics,* Vol. 64, pp. 625–644.

Herbst, R., 1980, "Entwicklung von Strömunggrenzsschichten bei instationärer Zuströmung in Turbomaschinen," Dissertation D-17, Technische Hochschule Darmstadt, Germany.

Hippensteele, S. A., Russell, L. M., and Stepka, S., 1981, "Evaluation of a Method for Heat Transfer Measurements and Thermal Visualization Using a Composite of a Heater Element and Liquid Crystals," ASME *Journal of Heat Transfer,* Vol. 103, pp. 184–189.

Hodson, H. P., 1990, "Modeling Unsteady Transition and Its Effects on Profile Loss," ASME JOURNAL OF TURBOMACHINERY, Vol. 112, pp. 691–701.

John, J., and Schobeiri, M. T., 1996, "Development of Two-Dimensional Turbulent Wakes in a Curved Channel at Positive Streamwise Pressure Gradient," ASME *Journal of Fluids Engineering,* Vol. 118, pp. 292–299.

Kovasznay, L. S. G., Kibens, V., and Blackwelder, R. F., 1970, *J. Fluid Mech.,* Vol. 41, pp. 283.

Launder, B. E., and Spalding, D. B., 1972, *Mathematical Models of Turbulence,* Academic Press, New York.

Liu, X., and Rodi, W., 1992, "Measurement of Unsteady Flow and Heat Transfer in a Linear Turbine Cascade," ASME Paper No. 92-GT-323.

Mayle, R. E., 1991, "The Role of Laminar–Turbulent Transition in Gas Turbine Engines," ASME JOURNAL OF TURBOMACHINERY, Vol. 113, pp. 509–537.

Narasimha, R., 1957, "On the Distribution of Intermittency in the Transition Region of a Boundary Layer," *J. Aero. Sci.,* Vol. 24, pp. 711–712.

Orth, U., 1993, "Unsteady Boundary-Layer Transition in Flow Periodically Disturbed by Wakes," ASME JOURNAL OF TURBOMACHINERY, Vol. 115, pp. 707–713.

Pache, W., 1976, "Zur Frage der Entwicklung von Strömungsgrenzsschichten bei instationärer Zuströmung in Turbomachinen," Dissertation D-17, Technische Hochschule Darmstadt Germany.

Patankar, S. V., and Spalding, D. B., 1970, *Heat and Mass Transfer in Boundary Layers,* 2nd ed., International Textbook Company Ltd., London.

Paxson, D. E., and Mayle, R. E., 1991, "Laminar Boundary Layer Interaction With an Unsteady Passing Wake," ASME JOURNAL OF TURBOMACHINERY, Vol. 113, pp. 419–427.

Pfeil, H., and Herbst, R., 1979, "Transition Procedure of Instationary Boundary Layers," ASME Paper No. 79-GT-128.

Pfeil, H., Herbst, R., and Schröder, T., 1983, "Investigation of the Laminar–Turbulent Transition of Boundary Layers Disturbed by Wakes," ASME *Journal of Engineering for Power,* Vol. 105, pp. 130–137.

Schmidt, R. C., and Patankar, S. V., 1991, "Simulating Boundary Layer Transition With Low-Reynolds-Number $k-\epsilon$ Turbulence Models: Part I—An Evaluation of Prediction Characteristics; Part II—An Approach to Improving the Predictions," ASME JOURNAL OF TURBOMACHINERY, Vol. 113, pp. 10–26.

Schobeiri, M. T., 1979, "Theoretische und experimentelle Untersuchungen laminarer und turbulenter Strömungen in Diffusoren," Dissertation D-17, Technische Hochschule Darmstadt, Germany.

Schobeiri, M. T., and Radke, R., 1994, "Effects of Periodic Unsteady Wake Flow and Pressure Gradient on Boundary Layer Transition Along the Concave Surface of a Curved Plate," ASME Paper No. 94-GT-327.

Schobeiri, M. T., Read, K., and Lewalle, J., 1995a, "Effect of Unsteady Wake Passing Frequency on Boundary Layer Transition: Experimental Investigation and Wavelet Analysis," ASME Paper No. 95-GT-437.

Schobeiri, M. T., Pappu, K., and John, J., 1995b, "Theoretical and Experimental Study of Development of Two-Dimensional Steady and Unsteady Wakes Within Curved Channels," ASME *Journal of Fluids Engineering,* Vol. 117, pp. 593–598.

Schobeiri, M. T., John, J., and Pappu, K., 1996, "Development of Two Dimensional Wakes Within Curved Channel: Theoretical Framework and Experimental Investigations," ASME JOURNAL OF TURBOMACHINERY, Vol. 118, pp. 506–518.

Walker, G. J., 1989, "Modeling of Transitional Flow in Laminar Separation Bubbles," *Proc. 9th Int. Symp. Air Breathing Engines,* pp. 539–548.

Wright, L., and Schobeiri, M. T., 1996, "Effect of Unsteady Wake Flow on Heat Transfer Along a Concave Surface," to be submitted.

Intermittent Flow and Thermal Structures of Accelerating Transitional Boundary Layers: Part 1—Mean Quantities

T. Wang

F. J. Keller[1]

Department of Mechanical Engineering,
Clemson University,
Clemson, SC 29634

A conditional sampling technique was employed to separate the turbulent and nonturbulent parts of accelerated boundary layers undergoing laminar–turbulent transition on a uniformly heated flat plate. Tests were conducted with zero pressure gradient and two levels of streamwise acceleration parameter: $K = 0.07 \times 10^{-6}$ and 0.16×10^{-6}. The conditionally sampled distribution of the skin friction coefficients revealed that the values for C_f in the nonturbulent and turbulent portions deviated significantly from the respective laminar and turbulent correlations. These deviations increased as acceleration increased. Reconstructing the local average C_f values using the laminar and fully turbulent correlations consistently overestimated the unconditioned C_f values. Using the conditionally sampled data for reconstructing C_f values provided better results, but does not necessarily result in the same unconditioned C_f values. The mean velocity profiles from the turbulent portions had the appearance of a low-Reynolds-number turbulent boundary layer with a large wake region. In the late transition region, as acceleration increased, the wake region in the turbulent portion was suppressed relative to the unconditioned result. The integral parameters, δ^*, θ, and shape factor, H, were conditionally sampled and analyzed.

Introduction

A better understanding of momentum and thermal transport during the laminar–turbulent transition process is one of the key factors toward improving the prediction of the thermal load on gas turbine blades (Graham, 1979, 1984; Mayle, 1991). Transition from laminar to turbulent boundary layer flow significantly increases the local wall shear stresses and the convective heat transfer rates. These increases must be appropriately factored into the design of gas turbine blades, since as much as 50 to 80 percent of the surface of a typical turbine blade is commonly covered by flow undergoing transition (Turner, 1971). A recent four-part paper by Halstead et al. (1997) specifically pointed out, through rotating multistage tests, the importance of laminar–turbulent transition in axial compressors and turbines. In the newest heavy-frame industrial H-type Advanced Gas Turbine Systems (Farmer and Fulton, 1995), adoption of closed-loop steam cooling eliminates the need for conventional air film cooling in the first two stages; therefore, correct prediction of the laminar–turbulent transition becomes more essential. An unsatisfactory prediction of the location and streamwise coverage of transition on gas turbine blades can result in either reduced longevity and reliability of the blade or reduced engine performance below design objectives. For example, Graham (1979) shows that a 56°C error in temperature prediction can result in an order-of-magnitude decrement in vane life.

One of the undeniable features in the laminar–turbulent transition is the intermittent behavior between nonturbulent and turbulent flows. Among many different transitional flow models, the intermittency model (Dhawan and Narasimha, 1958) is always physically more realistic than any other model, since the actual transitional flow is intermittent. For the purpose of engineering practice, statistical measurements of flow and thermal structures in this intermittent heat flow play an important role in improving understanding of fundamental aspects of flow mechanisms, as well as contributing to the database and methodologies of prediction models. In nonaccelerated flows, Kuan and Wang (1990) and Kim et al. (1994) have pointed out that the turbulent part of the transitional flow is different from the fully developed turbulent flow, and the nonturbulent part is not an extension of the upstream laminar flow. Blair (1992) investigated the intermittent flow in accelerating transitional boundary layers. He concluded that the turbulence kinetic energy within the turbulent parts exceeded fully turbulent boundary layer levels. He also conducted spectral analysis for the turbulent parts of flow and observed that the ratio of dissipation to production increased through transition. Sohn et al. (1989) analyzed conditionally sampled transitional flow for various FSTI cases and concluded that the transport processes occurring in the turbulent spots will not be well modeled by standard turbulence models used in equilibrium turbulent boundary layers. Solomon et al. (1995) incorporated the linear-combination method with a calculation method that continuously adjusts the spot growth parameters in response to the changes in the local pressure gradient through transition. The results showed reduced sensitivity to errors in predicting the onset of transition. Therefore, providing the information regarding the individual flow and thermal characteristics of the nonturbulent and turbulent parts, respectively, of the transitional flows is indispensable for the intermittency model, for example, the model proposed by Steelant and Dick (1996), and the linear-combination integral boundary layer method presented by Dey and Narasimha (1988).

In gas turbine throughflows, the accelerated boundary layers typically occur in the transition pieces downstream of the combustor, near the leading edge of the suction side of the blades, and near the aftbody of the pressure side of the blades. The effects of streamwise favorable pressure gradients on the flow

[1]Current address: Accuracy Microsensors, Inc., Pittsford, NY.

Contributed by the International Gas Turbine Institute and presented at the 42nd International Gas Turbine and Aeroengine Congress and Exhibition, Orlando, Florida, June 2–5, 1997. Manuscript received International Gas Turbine Institute February 1997. Paper No. 97-GT-402. Associate Technical Editor: H. A. Kidd.

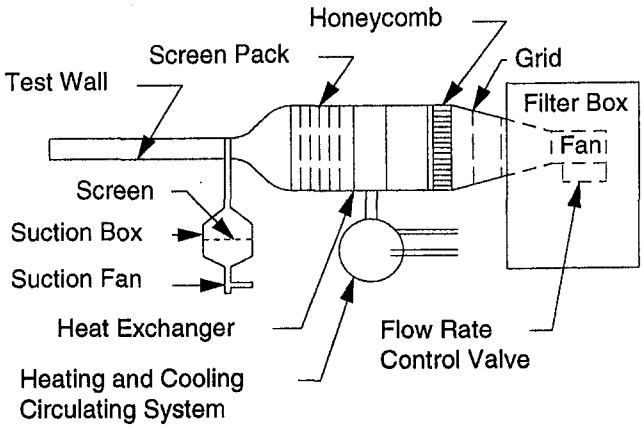

Fig. 1 Wind tunnel test facility

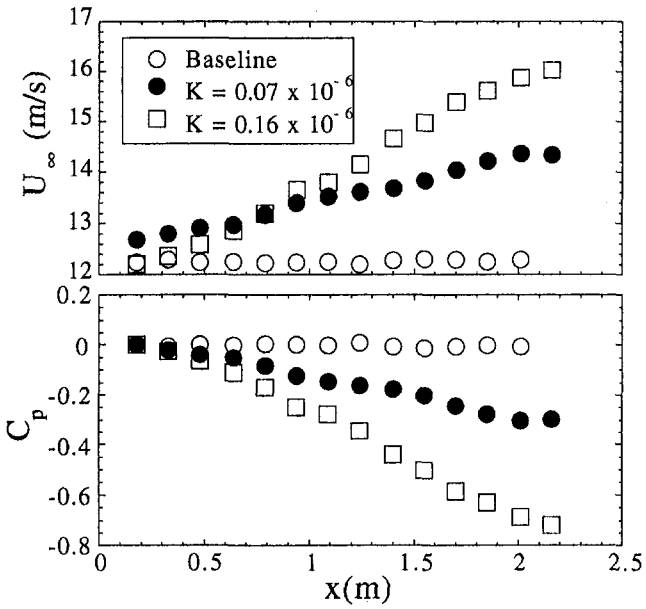

Fig. 2 Free-stream velocity and corresponding Cp values for each case

and thermal structures of unconditionally sampled transitional flow have been reported by Keller and Wang (1996). This paper will present conditionally sampled results of the same flows.

The objectives of this paper are: (*a*) to investigate the intermittent flow and thermal structures of the transitional boundary layers, (*b*) to study the effects of streamwise acceleration on the intermittent behavior of these structures, (*c*) to provide a database for transitional flow modeling, and (*d*) to provide information for studies in elevated free-stream conditions (Wang and Zhou, 1998).

Experimental Program

The detailed experimental facility, instrumentation, data acquisition and experimental procedures have been documented by Wang et al. (1992). Therefore, only a brief description of the experimental program will be provided.

Wind Tunnel. The present study employed a two-dimensional, open circuit, blowing-type wind tunnel, as shown in Fig. 1. The flow rate could be adjusted from 0.5 to 35 m/s. The steadiness of the free-stream velocity and temperature could be maintained, respectively, within 1 percent and 0.5°C for a 24-hour period; the uniformity was within 0.7 percent and 0.1°C.

Test Section. The rectangular test section was 0.15 m wide, 2.4 m long, and 0.92 m high with an aspect ratio of 6. This large aspect ratio reduced edge effects and ensured two dimensionality of the boundary layer flow in the center span of the test section. One of the test section walls served as the test wall. The heat patch inside the test wall was constructed of a serpentine heater foil sandwiched between glass cloth and silicon rubber sheets. The surface temperature was measured by 184 76-mm (3-mil) E-type thermocouples embedded between the heater and the plexiglass surface. Fourteen measuring holes were drilled along the centerline of the outer observation wall. Measurements were obtained by traversing probes through the holes into the test section. The spacing between the centerline thermocouples was 2.54 cm (1 in.), and the spacing between the measuring holes was 15.24 cm (6 in.). Boundary layer suction was applied at the leading edge of the test section.

The outer observation wall was manipulated to achieve constant-K flows. Three different cases were conducted in the present study: baseline ($K = 0$), $K1 = 0.07 \times 10^{-6}$ and $K2 = 0.16 \times 10^{-6}$. The pressure coefficient distributions are shown in Fig. 2. The detailed geometry of the test section was described in Keller and Wang (1996).

Instrumentation and Data Reduction. A single hot wire and a three-wire sensor were used in this study. The single hot wire was used to measure each station before using the three-wire sensor. Since the single wire can measure very close to the wall (approximately $Y^+ = 2$), the results of the single wire were used to guide the three-wire sensor to locate the wall position ($y = 0$) and to determine the skin friction.

The three-wire sensor was specifically designed to measure simultaneously the two velocity components and the temperature. Basically, the three-wire sensor consisted of an X-array of gold-plated tungsten wires for measuring velocities and a 1.2-μm platinum wire for measuring temperature. The two X-wires were operated in constant temperature mode. The 1.2-μm platinum wire was operated at a very low current of 0.1 mA (cold wire) in the constant current mode.

A TSI Model IFA 100 Intelligent Flow Analyzer System was used as a constant temperature anemometer. A DISA M20 temperature bridge was used for operating the cold wire in the constant current mode. A 12-bit A/D data acquisition board

Nomenclature

C_f = skin friction coefficient = $\tau_W/(\rho\bar{U}_\infty^2/2)$
C_p = $(P - P_{\text{ref}})/(1/2)\rho U_\infty^2$
H = shape factor = δ^*/θ
K = pressure gradient parameter = $(\nu/\bar{U}_\infty^2)(d\bar{U}_\infty/dx)$
P_{ref} = reference pressure at Station 1
$\bar{T}$ = mean temperature
u_τ = friction velocity = $\sqrt{\tau_W/\rho}$
$\bar{U}$ = mean velocity
U^+ = $\bar{U}/u_\tau$
x = coordinate in streamwise direction
x_S = at onset of transition
y = coordinate normal to the surface
Y^+ = yu_τ/ν
Γ = intermittency factor
δ = boundary layer thickness at 0.995 U_∞
δ^* = displacement thickness
ϵ_M = turbulent (or eddy) viscosity
ν = kinematic viscosity
θ = momentum boundary layer thickness
ρ = density
τ_W = shear stress on the wall
∞ = free-stream value

and a high-speed data acquisition software, STREAMER, were used to acquire data. The sampling rate was 2 kHz, and the sampling duration was 20 seconds. For more detailed description of the three-wire sensor, see Shome (1991) or Wang et al. (1996).

Determination of Skin Friction Coefficient and Wall Position

The skin friction coefficient, C_f, is an important parameter for characterizing the boundary layers, since it changes significantly from laminar to turbulent flow through the transition region. Direct measurement of C_f is difficult, expensive, and time consuming, not suitable for the heated wall, and may not be fast enough to sense the instantaneous wall shear stress change of the turbulent spots. However, with the information from the mean velocity profiles, the following can be indirectly determined, based on the nature of the boundary layer:

- In the nonturbulent part, the mean velocity varies linearly with distance from the wall in the near-wall region. The values of $\Delta U/\Delta y$ from several mean velocity data points close to the wall were measured by the single wire and used to approximate the velocity gradient at the wall to calculate C_f.
- In the turbulent part, the mean velocity gradient near the wall is so large that the linear approximation of mean velocity gradient near the wall may lead to a large error. The Clauser technique (Clauser, 1956) was used instead to estimate the value of C_f and the wall position by the best fitting of U^+ falling within the log-linear region. Some subjectivity was exercised to determine the "best fit," since the slope of the log-linear region varies as K changes.

Conditional Sampling Technique

Conditional sampling consists of three primary stages: the choice of a criterion function, the determination of a threshold value, and the generation of an intermittency function. In turbulent/nonturbulent discrimination, one commonly used method for identifying a criterion function is to differentiate the velocity signal with respect to time and square it, thus emphasizing the high-frequency components. As pointed out by Keller and Wang (1995), performing the differentiation procedure was actually equivalent to conducting a digital high pass filtering. They also indicated that using the Reynolds shear stress, uv, as the criterion function for turbulent/nonturbulent discrimination in a heated transitional boundary layer is superior to the scheme of using single velocity or temperature as the criterion function. They indicated that using uv signals as the criterion function possesses the following merits: (a) sharpness in demarcation between the turbulent and nonturbulent portions of the flow, (b) small variation of threshold values across the boundary layer and throughout the transition region, (c) low uncertainty in determining the threshold values, and (d) low sensitivity of the resultant intermittency to the uncertainty in choosing the threshold value. Therefore, squares of the first derivatives of the uv signal were used in this study as the criterion function.

From each data reading, the criterion function was compared to the threshold value. If the value was larger than the threshold, the reading was considered turbulent. If the value was less than the threshold and the next three readings (i.e., hold time) were also less than the threshold, the reading was considered nonturbulent. The value of the intermittency function was equal to 1 if the flow was turbulent; the value was 0 if the flow was nonturbulent. The intermittency distributions for each case are shown in Fig. 3. A single intermittency value at about $y/\delta = 0.1$ was selected as the representative for each station. Keller and Wang (1995) have shown that using near-wall intermittency values at about $y/\delta = 0.1$ best matches the universal intermittency distribution (Dhawan and Narasimha, 1958) in

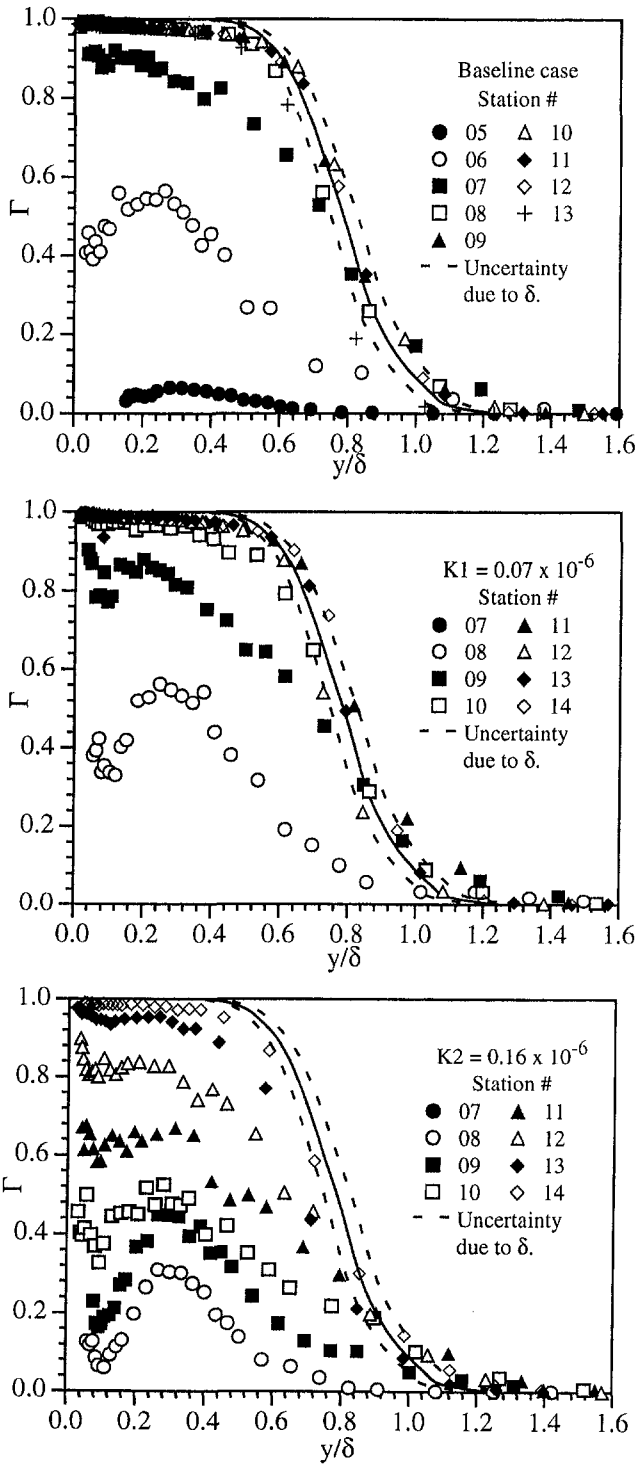

Fig. 3 Intermittency distributions through boundary layers

streamwise direction. Representative velocity signals are presented in the appendix.

The threshold value was determined based on the cumulative intermittency distribution curve originally introduced by Hedley and Keffer (1974). An improved "dual-slope" method based on the cumulative intermittency distribution curve was developed by Kuan and Wang (1990). This curve represents the variation of the integral of the probability density function (PDF) as the threshold value increases from zero. This method uses a graphic approach to find the threshold value at each location. Based on this method, two straight lines of different slopes are apparent most of the time

Table 1 Test conditions for the baseline (K = 0) and two accelerating cases

		Baseline	K1=0.07x10^{-6}	K2=0.16x10^{-6}
FSTI at x_s		0.5	0.4	0.4
U_∞ (m/s) at Sta.1 (x = 18 cm)		12.24	12.68	12.20
Onset of transition	x(cm)	68	107	115
	Re_x	5.50 x 10^5	9.46 x 10^5	10.3 x 10^5
	$Re_{\delta*}$	1294	1322	1233
	Re_θ	492	541	544
End of transition	x(cm)	137	168	213
	Re_x	11.2 x 10^5	15.7 x 10^5	21.7 x 10^5
	$Re_{\delta*}$	1826	1874	1880
	Re_θ	1302	1282	1235
Length of transition	x(cm)	69	61	98
	Re_x	5.70 x 10^5	6.24 x 10^5	11.4 x 10^5
	$Re_{\delta*}$	532	552	647
	Re_θ	810	741	691

when the cumulative intermittency distribution is plotted on a semi-log coordinate with the threshold value. The different slopes are caused by the different characteristics of probability density distributions for the turbulent and nonturbulent part, respectively. A steeper slope represents the nonturbulent part, which indicates smaller standard deviation. The approximate threshold value is then taken to be the value corresponding to the intersection of the straight lines. Fine tuning can be made to make the overall distribution of intermittency factors smooth. The reasoning behind this method and the detailed analysis of using nine different criterion functions for conditionally sampling the heated, accelerating flows, were discussed by Keller and Wang (1995). It should be noted that in the "real" gas turbine environment, the flow is highly disturbed by periodic wakes, a clear discrimination between turbulent patches and nonturbulent parts becomes difficult.

Results and Discussion

The test conditions and the onset and end of transition are shown in Table 1. The unconditionally sampled results were previously analyzed by Keller and Wang (1996). The measurement locations located in the transitional region for each case were conditionally sampled. Flow and thermal structures of four stations for the baseline case, four stations for the K1 case, and seven stations for the K2 case were separated into turbulent and nonturbulent parts.

Skin-Friction Coefficient. The conditionally sampled distributions of the C_f values for the baseline case and the accelerating cases are shown in Fig. 4. The C_f values from the original unconditioned results are included for comparison.

For the baseline case, the nonturbulent C_f values follow the laminar correlation up through station 06 (Γ = 0.50). Beyond this midtransition point, the nonturbulent C_f values show progressive deviation from the laminar correlation. For station 08 (Γ = 0.98), the last transitional station, the nonturbulent C_f value exceeds the laminar correlation by 65 percent. For the turbulent portion, a reverse trend occurs. Significant deviation from the fully turbulent correlation is observed in the early transition regions and the C_f value approaches the fully turbulent correlation as transition ends. A similar observation was made by Kuan and Wang (1990) and Kim et al. (1994) for the zero-pressure gradient flat plate case. Kuan and Wang reported that the C_f values in the nonturbulent portion were significantly greater than the laminar correlation throughout the transition region, and C_f values in the turbulent part were approximately 6 percent higher than the turbulent correlation. For the accelerating cases K1 and K2, a similar trend is observed. The C_f values follow the laminar values obtained from the STAN5 program up through Γ = 0.37 for both cases and then begin to deviate. As the K value increases, the deviation from the laminar values in the late transition stage is not as large as is observed in the baseline case. The C_f values for the turbulent portions deviate significantly from the turbulent correlation in the early transition region and approach the turbulent correlation as the transition process proceeds. Also shown in Fig. 4 are the results for reconstructing the unconditioned C_f values using the local near-wall intermittency with (a) the respective laminar and turbulent correlations and (b) the conditionally sampled experimental data.

Using the laminar and turbulent correlations to obtain a local overall C_f value, as is done in intermittency weighted transitional flow analysis, consistently overestimates the experimentally determined unconditioned C_f values. This result indicates that the skin friction in the nonturbulent and turbulent portions do not behave as a simple extension of laminar and fully turbulent flow, respectively. Reconstructing total C_f using the conditionally sampled experimental data provides better results than using the fully turbulent and laminar correlations but does not necessarily result in the original unconditioned C_f values. This is not surprising since a single representative near-wall intermittency was used in the reconstruction formula for each x-location while the local $\Gamma(y)$ value, which varied with y, was used in separating the velocity data. This result may indicate that a single near-wall intermittency value may not adequately represent the characteristic property for the transition region, and that the $\Gamma(y)$ variation may play an important role. Regarding the issue of $\Gamma(y)$ variation, Dhawan and Narasimha (1958) stated that although the $\Gamma(y)$ variation was probably important to the detailed structure of the turbulent motion associated with the spots, the near-wall value was the characteristic property for the transition region. Nevertheless, with the complexity involved in the transition flow, using a single Γ at each x location to represent the evolution of the transition process is an im-

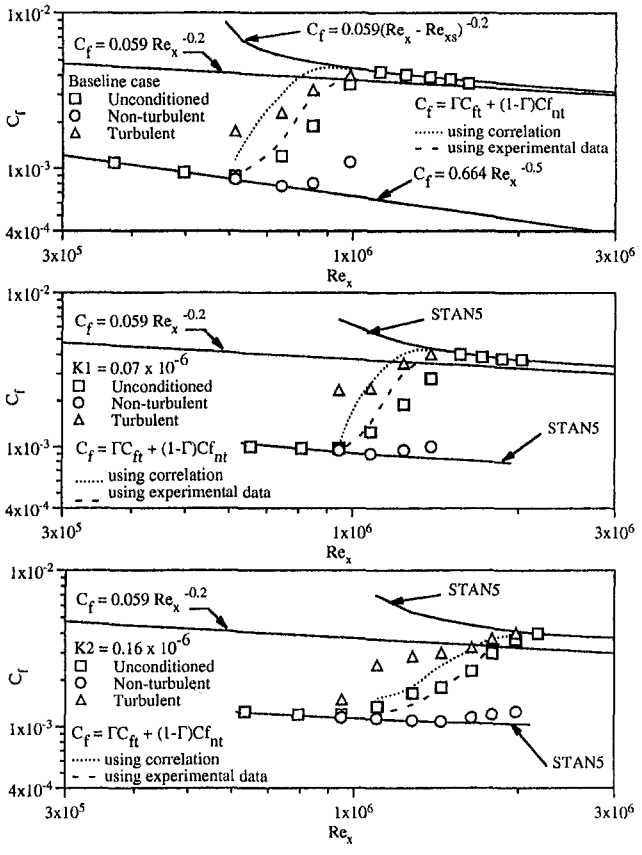

Fig. 4 Comparison of the reconstructed skin-friction coefficient values by using the intermittency model with the conditionally sampled experimental data versus the values from laminar and fully turbulent correlations. Data presentation starts at station 3.

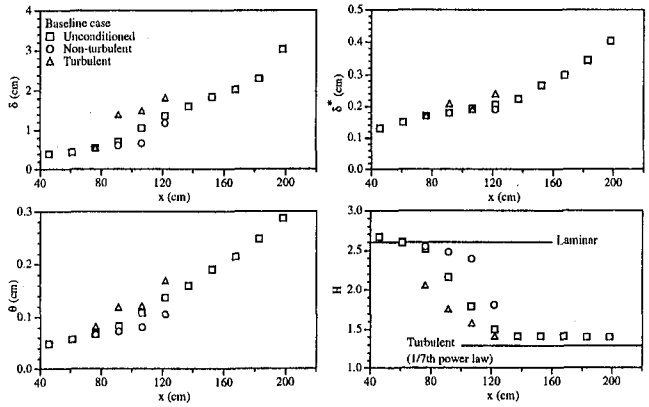

Fig. 5 Conditionally sampled boundary layer integral parameters for the baseline case

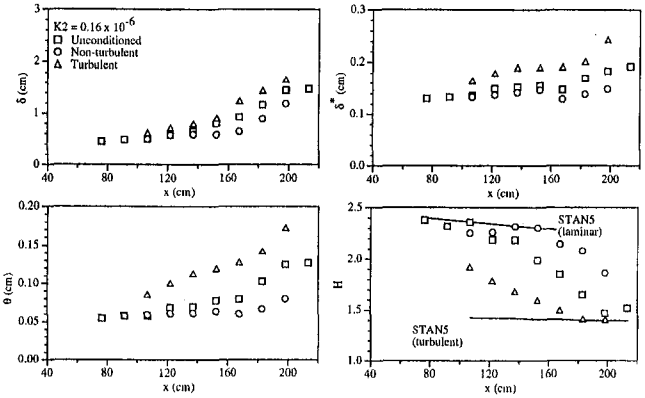

Fig. 7 Conditionally sampled boundary layer integral parameters for the K2 case

portant first step in transition modeling. If a single Γ is to be selected, Keller and Wang (1995) suggested the intermittency value at $y/\delta = 0.1$ would be appropriate. Other opinions about the selection of a single representative intermittency value were discussed by Professor M. W. Johnson in Gostelow and Blunden's paper (1989).

Integral Parameters. A large uncertainty exists in determining boundary layer thickness and integral parameters for the conditionally sampled portions. For the early transition region, low intermittencies provide very few turbulent values for analysis. This results in a large scatter of the data. Similarly, in the late transition region, high intermittencies provide very few nonturbulent values for analysis. The largest uncertainty occurs in the turbulent portions. As the edge of the boundary layer is approached, the intermittency drops off rapidly, resulting in fewer turbulent readings. This results in a larger scatter in the velocity profile in the outer boundary layer at the turbulent portion. Therefore, determination of the boundary layer thickness, displacement thickness, and momentum thickness is more uncertain for the turbulent portion than for the nonturbulent portion. The results for each of the three cases are shown in Figs. 5–7. For each case, the displacement thickness for the nonturbulent portion exhibits little deviation from the unconditioned values. For the turbulent portion, δ^* is consistently greater than the unconditioned values. Evaluation of the momentum thickness confirms that a higher momentum loss is associated with the turbulent portion of the flow. As K increases, significant deviation of these parameters, including the shape factor, from the unconditioned data occurs. This raises further questions about the applicability of treating each portion in the boundary layer as an extension of their respective laminar and fully turbulent counterparts.

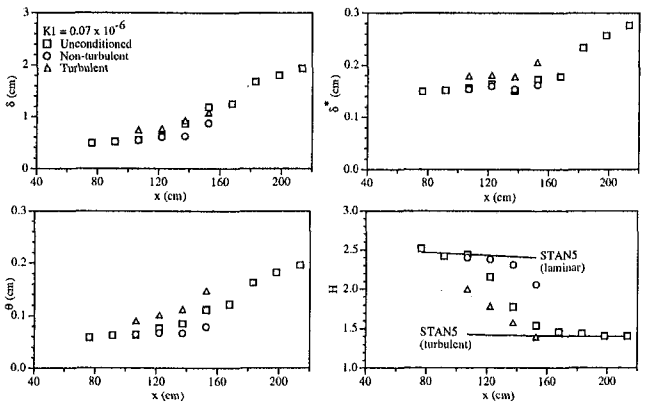

Fig. 6 Conditionally sampled boundary layer integral parameters for the K1 case

Mean Velocity and Temperature Profiles. The conditionally sampled velocity profiles for the baseline case are shown in Fig. 8. The velocity profiles for the nonturbulent part follow the Blasius profile up through station 06. In the late transition region, stations 07–08, the nonturbulent profiles follow the viscous sublayer relation ($U^+ = Y^+$) very well in the inner boundary layer, up to approximately $Y^+ = 30$, but deviate from the Blasius profile in the outer layer. This deviation from the Blasius profile apparently affects the wall shear and explains why the C_f values increasingly deviate from the laminar correlation as transition proceeds. Kim et al. (1994) hypothesized that this higher stress at the wall was due to disturbances in the nonturbulent region as a result of the passage of turbulent spots. Transition at the leading edge of a turbulent spot is abrupt; however, at the trailing edge the flow slowly relaxes back to the nonturbulent value through the calmed region. For a high intermittency, turbulent spots pass frequently and the nonturbulent portion is continually disturbed, which results in higher velocity gradients near the wall, thus increasing the skin friction above the laminar value. Another phenomenon, which is present in the nonturbulent portion and may result in a higher skin friction, is the amplification of sinusoidal oscillations. Both of these behaviors are observed in instantaneous velocity traces, which exhibit the slow relaxation period (calmed region) after the passage of a turbulent spot and the presence of amplified oscillations between spots. The turbulent profiles for stations 06–08 have the appearance of a low-Reynolds-number turbulent boundary layer with a short linear-log region and a large wake region. However, the turbulent profile of station 08 exhibits a depressed wake region. A similar observation for the mean velocity profiles was made by Kuan and Wang (1990), Kim et al. (1994), and Sohn and Reshotko (1991).

The mean velocity profiles for the accelerating case K1 are shown in Figs. 9 and 10. The results are similar to those observed for the baseline case. The nonturbulent velocity profiles follow the profiles obtained from the STAN5 program for the early transition region, up through $\Gamma = 0.37$. In the late transition region, the nonturbulent profiles follow the STAN5 laminar profile very well in the inner boundary layer, but deviate from the laminar profile in the outer layer. A standard $k-\epsilon$ turbulence model with a correction of damping coefficient due to acceleration (Launder and Spalding, 1974) is used in the STAN5 calculation. The turbulent profiles also have the appearance of a low-Reynolds-number turbulent boundary layer with a large wake region. In the late transition region, as K increases, the nonturbulent portion deviates more from the corresponding laminar profile, and the turbulent portion moves more close to the fully turbulent profile, as can be seen by comparing station 9 in Fig.

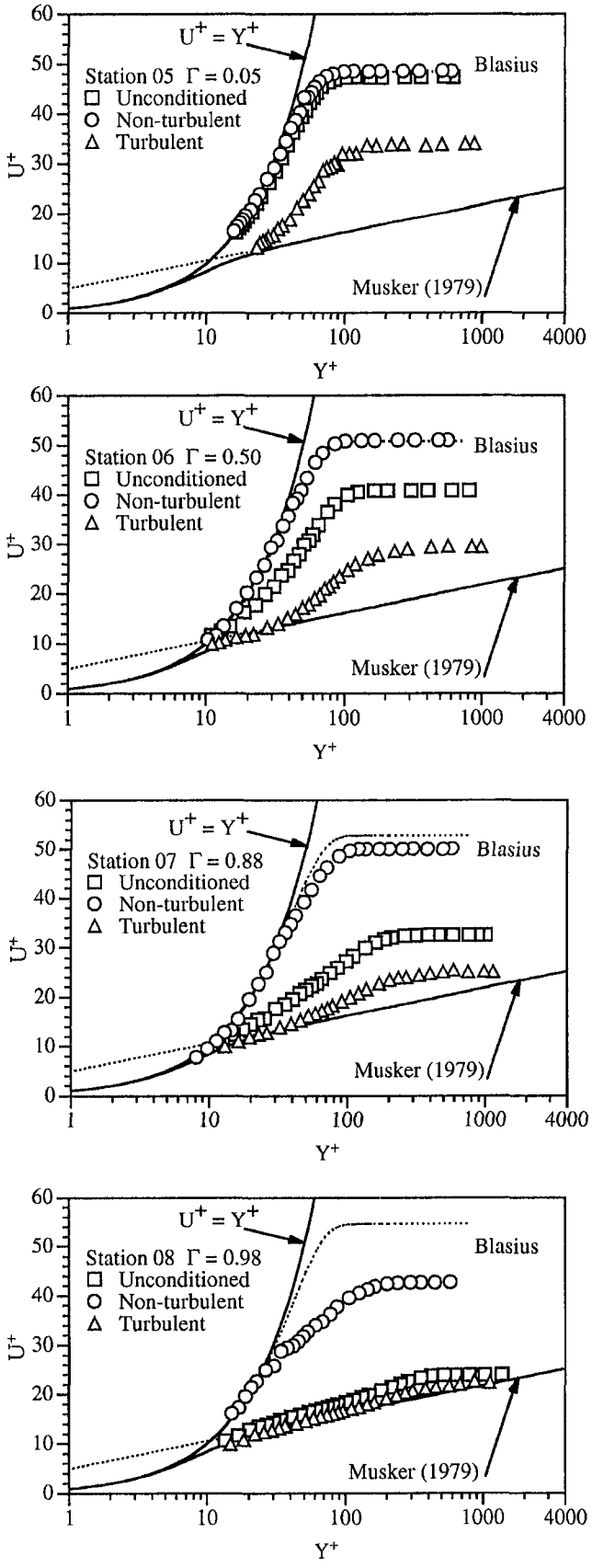

Fig. 8 Conditionally sampled mean velocity profiles for the baseline case (in wall units)

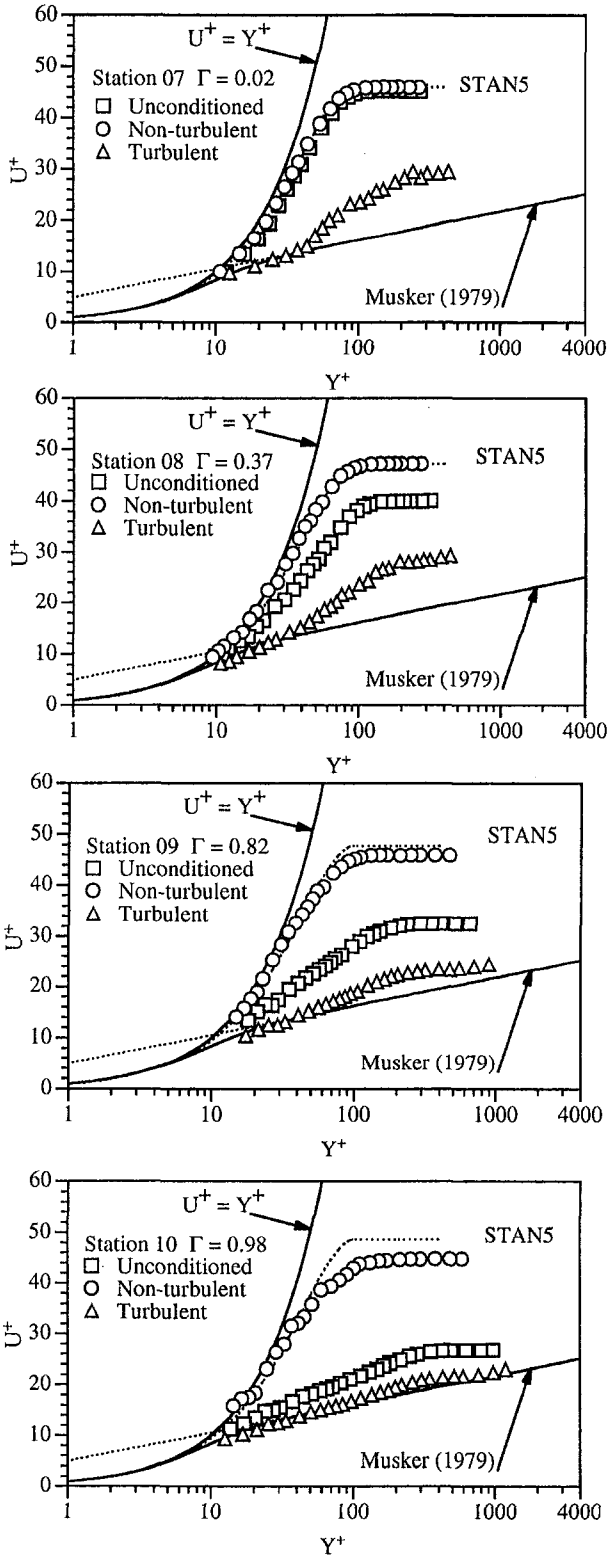

Fig. 9 Conditionally sampled mean velocity profiles for the K1 case (in wall units)

9 and station 12 in Fig. 10. Both have the same intermittency factor, 0.82.

Conditional sampling of the mean temperature profiles was difficult to present in T^+ versus Y^+ coordinates. As a turbulent spot passes over the test surface, the surface temperature begins to change immediately, but the thermocouples, embedded beneath the test surfaces, were not able to respond to the fast passing turbulent spots, which had a duration from 10 ms to 50 ms. Therefore, the conditionally sampled mean temperature profiles are not presented in this paper. However, the thermal

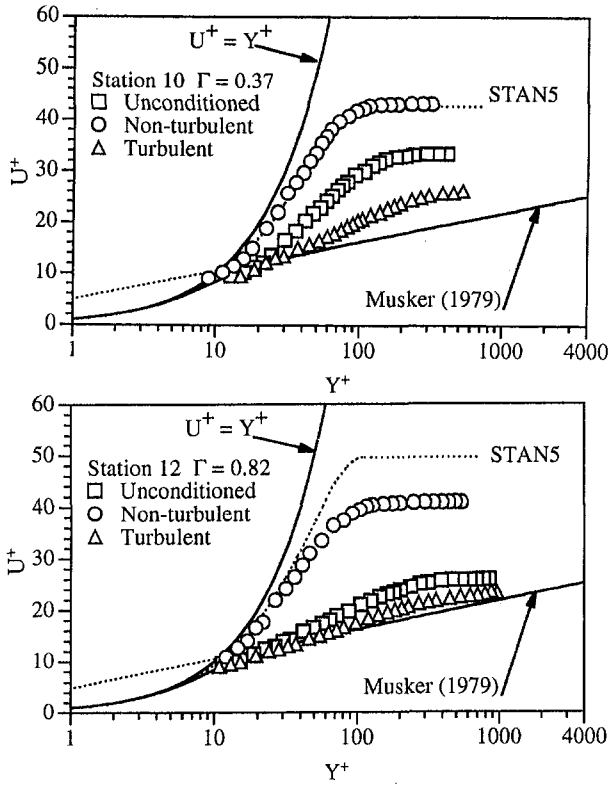

Fig. 10 Conditionally sampled mean velocity profiles for the K2 case

structure in the boundary layer will be presented in Part 2 of this paper.

Conclusion

A conditional sampling technique was employed to separate the turbulent and nonturbulent parts of accelerated boundary layers undergoing laminar–turbulent transition on a uniformly heated flat plate. Tests were conducted with zero pressure gradient and two levels of streamwise acceleration: $K = 0.07 \times 10^{-6}$ and 0.16×10^{-6}. The results are summarized below:

- The values for C_f in the nonturbulent and turbulent portions significantly deviated from the respective laminar and turbulent correlations. These deviations decreased as acceleration increased.
- Reconstructing the local average C_f values using the laminar and fully turbulent correlations consistently overestimated the experimentally determined unconditioned C_f values. Using the conditionally sampled data for reconstructing C_f values provided better results, but does not necessarily result in the same unconditioned C_f values.
- The mean velocity profiles from the turbulent portions had the appearance of a low-Reynolds-number turbulent boundary layer with a large wake region. In the late transition region, as acceleration increased, the wake region in the turbulent portion was suppressed relative to the unconditioned result.
- For each case, the displacement thickness for the nonturbulent portion exhibited little deviation from the unconditioned values. For the turbulent portion, the displacement was consistently greater than the unconditioned values.
- Evaluation of the conditionally sampled momentum thickness confirmed that the higher loss of momentum in the transition region than the corresponding laminar flow was a direct result of the turbulent portion of the boundary layer.

Acknowledgments

This research was sponsored by the Air Force Office of Scientific Research (Grant No. F49620-94-1-0126). The program manager was Dr. James McMichael.

References

Blair, M. F., 1992, "Boundary-Layer Transition in Accelerating Flows With Intense Free-Stream Turbulence: Part 1—Disturbances Upstream of Transition Onset; Part 2—The Zone of Intermittent Turbulence," ASME *Journal of Fluids Engineering,* Vol. 114, pp. 313–332.

Clauser, F. H., 1956, "The Turbulent Boundary Layer," *Advances in Applied Mechanics,* Vol. 4, pp. 1–51.

Dey, J., and Narasimha, R., 1988, "An Integral Method for the Calculation of 2-D Transitional Boundary Layers," Fluid Mechanics Report 88 FM 7, Indian Institute of Science, Bangalore.

Dhawan, S., and Narasimha, R., 1958, "Some Properties of Boundary Layer Flow During the Transition From Laminar to Turbulent Flow," *Journal of Fluid Mechanics,* Vol. 3, pp. 418–436.

Farmer, R., and Fulton, K., 1995, "Design 60% Net Efficiency in Frame 7/9 H Steam-Cooled CCGT," *Gas Turbine World,* May–June, pp. 12–22.

Gostelow, J. P., and Blunden, A. R., 1989, "Investigations of Boundary Layer Transition in an Adverse Pressure Gradient," ASME JOURNAL OF TURBOMACHINERY, Vol. 111, pp. 366–375.

Graham, R. W., 1979, "Fundamental Mechanisms That Influence the Estimate of Heat Transfer to Gas Turbine Blades," ASME Paper No. 79-HT-43; NASA TM-79128.

Graham, R. W., ed., 1984, *Transition in Turbines,* Symposium Proceedings, NASA CP-2386.

Halstead, D. E., Wisler, D. C., Okiishi, T. H., Walker, G. J., Hodson, H. P., and Shin, H., 1997, "Boundary Layer Development in Axial Compressor and Turbines, Part 1: Composite Picture; Part 2: Compressors; Part 3: LP Turbines; Part 4: Computations and Analyses," ASME JOURNAL OF TURBOMACHINERY, Vol. 119, Part 1: pp. 114–127; Part 2: pp. 426–444; Part 3: pp. 225–237; Part 4: pp. 128–139.

Hedley, T. B., and Keffer, J. F., 1974, "Turbulent/Non-turbulent Decisions in an Intermittent Flow," *Journal of Fluid Mechanics,* Vol. 64, pp. 625–644.

Keller, F. J., 1993, "Flow and Thermal Structures in Heated Transitional Boundary Layers With and Without Streamwise Acceleration," Ph.D. Dissertation, Department of Mechanical Engineering, Clemson University, Clemson, SC.

Keller, F. J., and Wang, T., 1995, "Effects of Criterion Functions on Intermittency in Heated Transitional Boundary Layers With and Without Streamwise Acceleration," ASME JOURNAL OF TURBOMACHINERY, Vol. 117, pp. 154–165.

Keller, F. J., and Wang, T., 1996, "Flow and Thermal Behavior in Transitional Boundary Layers With Streamwise Acceleration," ASME JOURNAL OF TURBOMACHINERY, Vol. 118, pp. 314–326.

Kim, J., Simon, T. W., and Kestoras, M. 1994, "Fluid Mechanics and Heat Transfer Measurements in Transitional Boundary Layers Conditionally Sampled on Intermittency," ASME JOURNAL OF TURBOMACHINERY, Vol. 116, pp. 405–416.

Kuan, C. L., and Wang, T., 1990, "Investigation of the Intermittent Behavior of a Transitional Boundary Layer Using a Conditional Averaging Technique," *Experimental Thermal and Fluid Science,* Vol. 3, pp. 157–170.

Launder, B. G., and Spalding, D. B., 1974, "The Numerical Computation of Turbulent Flows," *Computer Methods in Applied Mechanics and Engineering,* Vol. 3, p. 269.

Mayle, R. E., 1991, "The Role of Laminar–Turbulent Transition in Gas Turbine Engines," ASME JOURNAL OF TURBOMACHINERY, Vol. 113, pp. 509–537.

Musker, A. J., 1979, "Explicit Expression for the Smooth Wall Velocity Distribution in Turbulent Boundary Layers," *AIAA Journal,* Vol. 17, No. 6, June, pp. 655–657.

Narasimha, R., 1985, "The Laminar–Turbulent Transition Zone in a Boundary Layer," *Prog. Aero. Sci.,* Vol. 22, pp. 29–80.

Shome, B., 1991, "Development of a Three-Wire Probe for the Measurement of Reynolds Stresses and Heat Fluxes in Transitional Boundary Layers," M.S. Thesis, Department of Mechanical Engineering, Clemson University, Clemson, SC.

Sohn, K. H., O'Brien, J. E., and Reshotko, E., 1989, "Some Characteristics of Bypass Transition in a Heated Boundary Layer," *Proc. 7th Turbulent Shear Flow Symposium,* pp. 61–70.

Sohn, K. H., and Reshotko, E., 1991, "Experimental Study of Boundary Layer Transition With Elevated Free-Stream Turbulence on a Heated Plate," NASA CR-187068.

Solomon, W. J., Walker, G. J., and Gostelow, J.-P., 1995, "Transition Length Prediction for Flows With Rapidly Changing Pressure Gradients," ASME Paper No. 95-GT-241.

Steelant, J., and Dick, E., 1996, "Modelling of Bypass Transition With Conditional Navier–Stokes Equations Coupled to an Intermittency Transport Equation," *International Journal for Numerical Methods in Fluids,* Vol. 23, pp. 193–220.

Turner, A. B., 1971, "Local Heat Transfer Measurements on a Gas Turbine Blade," *Journal of Mechanical Engineering Sciences,* Vol. 13, 1, pp. 1–12.

Wang, T., Keller, F. J., and Zhou, D., 1992, "Experimental Investigation of Reynolds Shear Stresses and Heat Fluxes in a Transitional Boundary Layer," *Fundamental and Applied Heat Transfer Research for Gas Turbine Engines,* ASME HTD-Vol. 226, pp. 61–70.

Wang, T., Keller, F. J., and Zhou, D., 1996, "Flow and Thermal Structures in a Transitional Boundary Layer," *Experimental Thermal and Fluid Science,* Vol. 12, pp. 352–363.

Wang, T., and Zhou, D., 1998, "Conditionally Sampled Flow and Thermal Behavior of a Transitional Boundary Layer at Elevated Free-Stream Turbulence," *International Journal of Heat and Fluid Flow,* Vol. 19, pp. 348–357.

APPENDIX

Representative raw velocity traces at about $y/\delta = 0.1$ in a duration of 0.5 seconds for each transition station are shown in Figs. (A1)–(A3).

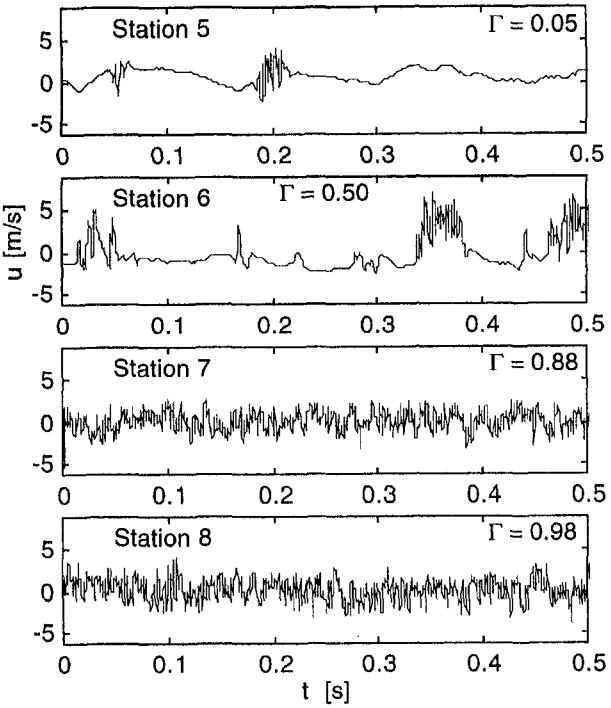

Fig. A1 Instantaneous u signals for the baseline case at $y/\delta \approx 0.1$

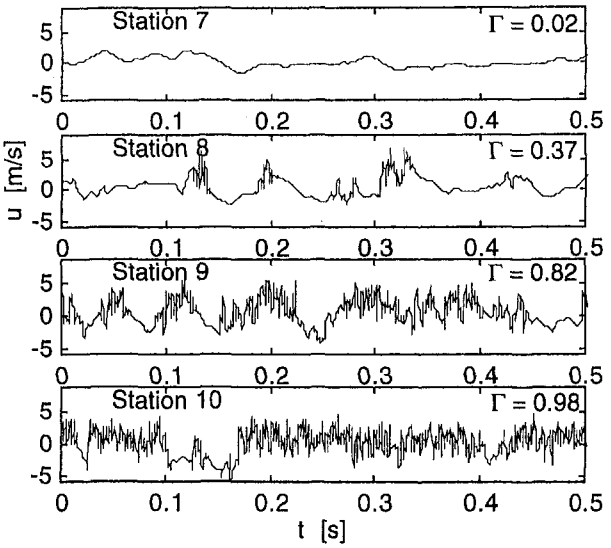

Fig. A2 Instantaneous u signals for the K1 case at $y/\delta \approx 0.1$

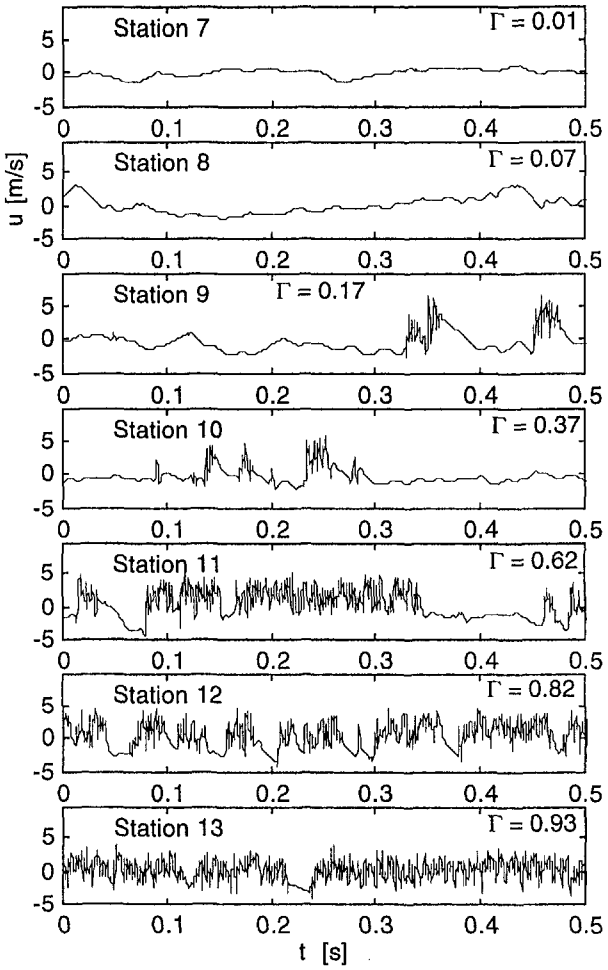

Fig. A3 Instantaneous u signals for the K2 case at $y/\delta \approx 0.1$

Intermittent Flow and Thermal Structures of Accelerating Transitional Boundary Layers: Part 2—Fluctuation Quantities

T. Wang

F. J. Keller[1]

Department of Mechanical Engineering,
Clemson University,
Clemson, SC 29634

The conditionally sampled fluctuation quantities of nonaccelerating and accelerating heated transitional boundary layers were analyzed. The results indicated that the values of u', v', $\overline{uv}$, and $\overline{ut}$ in the turbulent part of the transitional flow were higher than those values in the fully developed turbulent flow. These higher values were believed to be manifestations of the vigorous activities involved in the transition process. The contributions to the unconditioned u' by "mean-step" change due to the alternating behavior between turbulent and nonturbulent flows are about 20 percent in the near-wall region, but are negligible for $Y^+ > 30$. The turbulent part $\overline{uv}$ values are higher than the fully turbulent and unconditioned values in the inner boundary layer but lower in the outer boundary layer. The mean-step change has negligible effect on unconditioned $\overline{uv}$ values. As acceleration increases, both u' and t' in the turbulent part are suppressed; however, turbulent part u' is still higher than the unconditioned u'. Acceleration promotes streamwise Reynolds heat flux ($\overline{ut}$) transport in both turbulent and nonturbulent parts. A second peak of the turbulent part $\overline{ut}$ occurs at around $Y^+ = 120$ as acceleration increases. The turbulent part eddy viscosity values are much lower than those in the fully turbulent flow.

Introduction

The results of Part 1 provided conditionally sampled mean values in the turbulent and nonturbulent parts in the intermittent, transitional boundary layers. Part 2 will focus on the fluctuation quantities. These fluctuation quantities provided information regarding the production of turbulent kinetic energy, turbulent shear stress transports, and turbulent heat flux transport, which are necessary for modeling turbulence and verifying CFD results. The instantaneous traces of velocity or turbulence shear stress can also serve as an important database for verifying the results from direct numerical simulation (DNS).

Blair (1992) employed an ensemble-averaging technique to analyze the turbulent burst profiles of randomly passing turbulent patches in accelerating boundaries with intense free-stream turbulence. He discovered that as much as one-half of the streamwise-component unsteadiness, and much of the apparent anistropy observed near the wall, was not produced by turbulence, but by the steps in velocity between the turbulent and nonturbulent zones of flow. His results regarding the turbulence kinetic energy indicated that the nonturbulent part preserved the characteristics of a highly disturbed laminar boundary layer all the way through transition.

The objectives of this paper are to provide a detailed analysis of the conditionally sampled fluctuation quantities in heated transitional boundary layers and investigate the effects of streamwise acceleration on the development of these fluctuation quantities in the transition process.

Results and Discussion

The effects of acceleration on the unconditioned flow and thermal structures have been discussed by Keller and Wang (1996). This paper will focus on the conditionally sampled results.

Streamwise and Cross-Stream Velocity Fluctuations (u' and v'). For the Reynolds normal stresses, the unconditioned values obtained in the transitional boundary layer are a combination of the nonturbulent and turbulent portions plus the intermittent alternation between the nonturbulent and turbulent mean values, as shown below:

$$u'^2 = \Gamma u_t'^2 + (1 - \Gamma)u_{nt}'^2 + \Gamma(1 - \Gamma)(\bar{U}_t - \bar{U}_{nt})^2. \quad (1)$$

The first and second terms on the right side of Eq. (1) can be directly obtained by conditional sampling and are termed nonturbulent contribution and turbulent contribution, respectively. The last term can be calculated from the conditionally sampled data. It is commonly referred to as the "mean-step contribution" and has been speculated as the cause of the peak values of unconditioned u' found in the transitional boundary layer, which exceed the peak values found in a fully turbulent boundary layer (Schubauer and Klebanoff, 1956). The qualitative value of this "mean-step contribution" may be inferred by comparing the u' values obtained in the nonturbulent and turbulent portions to the unconditioned result. Note, as previously discussed, that the intermittency drops off rapidly at the edge of the boundary layer resulting in fewer turbulent readings. Too few points in this region for the turbulent portion result in a large scatter in the data. Therefore, if the intermittency in the outer boundary layer region of turbulent portion dropped below 0.005, the data were omitted from presentation. The conditionally sampled results of u' for the baseline case are shown in Fig. 1. The nonturbulent portion exhibits a peak intensity of 7.5 percent at $Y^+ \approx 35$ ($y/\delta^* \approx 1.3$) for station 05 ($\Gamma = 0.05$), which is slightly below the 8 percent peak value for the unconditioned result that occurs at the same Y^+ location. The maximum value of u' in the turbulent part is 16 percent and is greater than the 8 percent reached for the unconditioned result, as well as the 10 percent value of the fully turbulent flow at station 13

[1] Current address: Accuracy Microsensors, Inc., Pittsford, NY.

Contributed by the International Gas Turbine Institute and presented at the 42nd International Gas Turbine and Aeroengine Congress and Exhibition, Orlando, Florida, June 2–5, 1997. Manuscript received International Gas Turbine Institute February 1997. Paper No. 97-GT-403. Associate Technical Editor: H. A. Kidd.

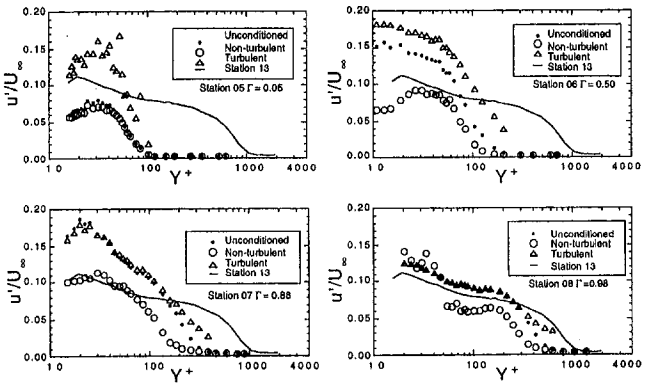

Fig. 1 Conditionally sampled u' for the baseline case

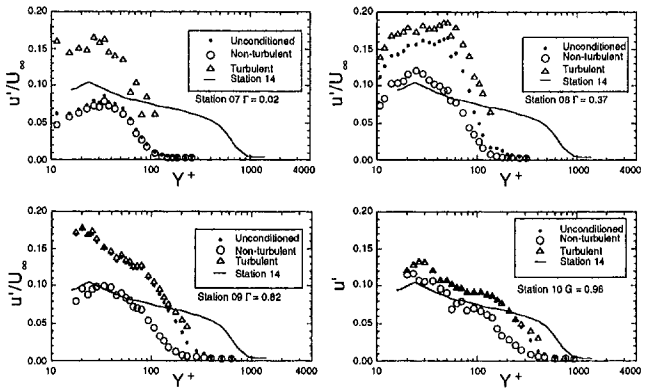

Fig. 2 Conditionally sampled u' for the K1 case

for the same Y^+ location. For station 06 ($\Gamma = 0.50$) the peak intensity for the nonturbulent portion increases to 9.5 percent. The peak magnitude for the unconditioned result is 16 percent at this station and occurs closer to the wall at $Y^+ \approx 15$ ($y/\delta^* \approx 0.3$). The peak magnitude in u' for the turbulent portion for station 06 increases to 18.5 percent and still exceeds the unconditioned value. At station 6 in Fig. 1, the individual contributions from turbulent, nonturbulent, and mean-step change to the unconditioned u' in Eq. (1) are 64, 13, and 23 percent at the third data point ($Y^+ = 14.9$); 73, 23, and 4 percent at the sixth point ($Y^+ = 26.8$); 79, 19, and 2.2 percent at the 14th point ($Y^+ = 58.6$). It is clear that the turbulent part is the major term. The nonturbulent and mean-step change terms are minor terms that actually pull down the turbulent part u' values when the data are not conditionally sampled, i.e., the unconditioned u' values become lower than the conditionally sampled turbulent part values. The contribution from the mean-step change drastically decreases as $Y^+ > 30$.

In the late transition region, stations 07 through 08, the peak intensity in the nonturbulent part continues to increase in magnitude. At station 07 ($\Gamma = 0.88$), u' in the turbulent portion is slightly below the unconditioned result, indicating a contribution from the mean-step alternation. For station 08 ($\Gamma = 0.98$), the peak intensity in u' for the nonturbulent portion exceeds both the turbulent and unconditioned values near the wall. Kuan and Wang (1990) observed a similar occurrence in the late transition region and determined it was a direct result of large-magnitude low-frequency unsteadiness (not turbulence) in the nonturbulent intervals between the turbulent spots. Sohn et al. (1989) had a similar observation. The near-wall peak of turbulent portion decreases in magnitude from station 07 to station 08. This decrease of u' in the late transition region is most probably caused by the effects of viscous dissipation. The conditionally sampled results of u' indicate that large magnitudes observed in the transition region are a direct result of the turbulent fluctuations in the turbulent portion, and the mean-step contribution is not a major factor. Similar observations were made by Kuan et al. (1989), Kim et al. (1989), Sohn and Reshotko (1991), and Blair (1992). These results suggest that the level of turbulent activity indicated by the unconditioned values in the transitional boundary layer is not an accurate measure of the true turbulent activity and that turbulence models using fully turbulent boundary layers to model the transport processes occurring in the turbulent spots require correction.

The conditionally sampled u' profiles for the accelerating cases are shown in Figs. 2 and 3. An interesting difference occurs between the nonturbulent portions of the accelerating cases and the baseline case. For the baseline case, the peak magnitude of u' in the nonturbulent portion increases from

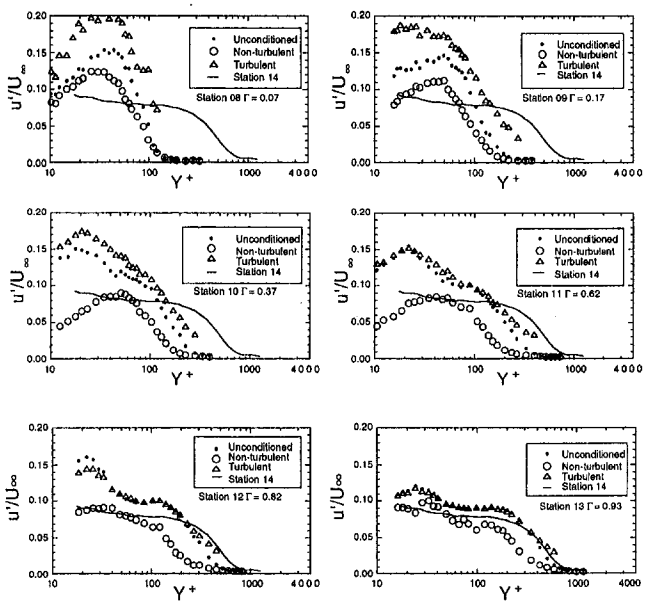

Fig. 3 Conditionally sampled u' for the K2 case

Nomenclature

C_p = specific heat
K = pressure gradient parameter = $(\nu/\bar{U}_\infty^2)(d\bar{U}_\infty/dx)$
q''_w = wall heat flux
Re = Reynolds number
T = instantaneous temperature
t' = rms value of temperature fluctuations
u', v' = rms values of velocity fluctuations
u_τ = friction velocity = $\sqrt{\tau_w/\rho}$
$U^+ = \bar{U}/u_\tau$
$\overline{uv}$ = Reynolds shear stress
$\overline{ut}$ = streamwise Reynolds heat flux
Γ = intermittency factor
$Y^+ = yu_\tau/\nu$
δ = boundary layer thickness at 0.995 U_∞
ϵ_M = turbulent (or eddy) viscosity
ν = kinematic viscosity
ρ = density
τ_w = shear stress on the wall

Subscripts

∞ = free-stream value
t = turbulent
nt = nonturbulent

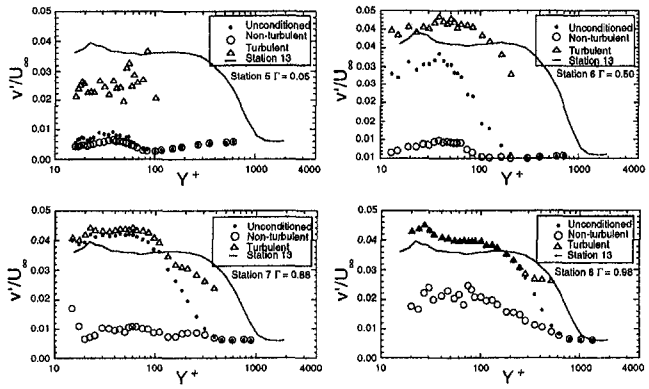

Fig. 4 Conditionally sampled v' for the baseline case

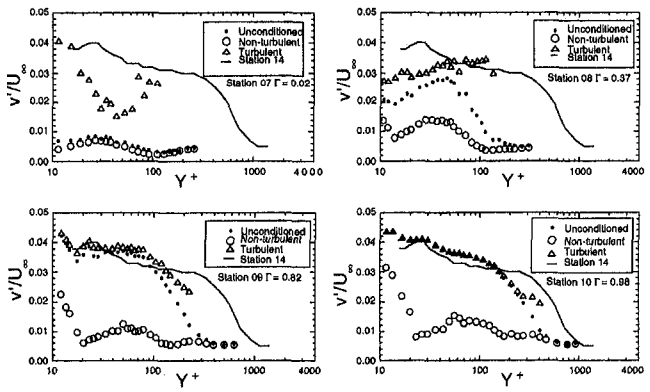

Fig. 5 Conditionally sampled v' for the K1 case

station 05 ($\Gamma = 0.05$) up through station 07 ($\Gamma = 0.88$). For the K1 case, the peak magnitude of u' in the nonturbulent portion increases from 8 percent at station 07 ($\Gamma = 0.02$) to 12.5 percent at station 08 ($\Gamma = 0.37$) and then decreases to 10.5 percent by station 09 ($\Gamma = 0.82$). For the K2 case, the nonturbulent u' peak magnitude increases from 7.5 percent at station 07 ($\Gamma = 0.01$, not shown) to 13 percent at station 08 ($\Gamma = 0.07$). The peak magnitude of nonturbulent u' then decreases to 12 percent at station 09, finally to about 9 percent at station 10 ($\Gamma = 0.37$) and is maintained about 9 to 10 percent through station 13 ($\Gamma = 0.93$). This evolution of the peak value of nonturbulent u' indicates that as K increases, u' of the nonturbulent portion is suppressed at an earlier stage. This can be more clearly observed by comparing the nonturbulent u' values at stations of same intermittency values as shown in Keller's (1993) dissertation, where complete data were presented. This is consistent with the results of Schubauer and Skramstad (1947), which showed a favorable pressure gradient damps boundary layer nonturbulent oscillations in a pretransitional boundary layer and may also suggest that this damping effect continues through the transition process.

The results for u' in the turbulent portions are similar to the baseline case. The u' values are greater than the unconditioned values in the early transition region through $\Gamma = 0.37$ for both K1 and K2 cases. In the late transition region ($\Gamma > 0.6$) the unconditioned values of u' slightly exceed the values in the turbulent portion in the near-wall region indicating a mean-step contribution. This is especially noticed for station 12 of the K2 case shown in Fig. 3. As with the baseline case, the level of turbulent energy indicated by the turbulent portion in the accelerating transitional boundary layer is very different from the turbulence energy in the fully turbulent flow.

The conditionally sampled cross-stream fluctuations, v', for the baseline case is shown in Fig. 4. There are two interesting observations. For the nonturbulent portion, the peak of v' increases from approximately 0.6 percent at station 05 ($\Gamma = 0.05$) to 1 percent at station 06 ($\Gamma = 0.50$) and finally to 2 percent at station 08 ($\Gamma = 0.98$). This increase in v' as the transition process develops is most likely caused by the presence of amplified oscillations still present in the boundary layer and by the relaxation period (calm region) after the passage of a turbulent spot, since part of the low-frequency oscillations in the calm region is grouped into the nonturbulent portions. For the turbulent portion, the v' magnitude reaches the fully turbulent value by station 06 ($\Gamma = 0.50$). As transition proceeds, the location of the peak magnitude migrates closer to the wall but the absolute magnitude of the peak value changes very little.

The conditionally sampled v' profiles for the accelerating cases are shown in Figs. 5 and 6. The effect of increasing K on v' in the nonturbulent portion is similar to the effect on u' (i.e., an applied favorable pressure gradient suppresses the velocity fluctuations in the nonturbulent portion and that this suppression

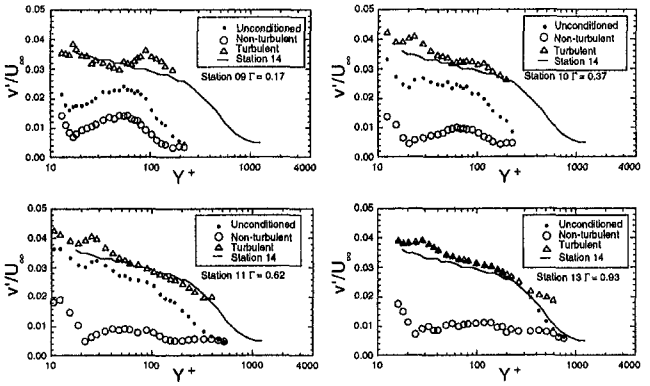

Fig. 6 Conditionally sampled v' for the K2 case

is greater and occurs earlier in the transition process as the pressure gradient increases). The turbulent portion of v' for all three cases is never exceeded by the unconditioned values. This is due to the mean value of the cross-stream velocity, $\bar{V}$, being near zero for both the turbulent and nonturbulent portions. There is no significant mean-step contribution.

Reynolds Shear Stress ($\overline{uv}$). The reconstruction formula for the Reynolds shear stress is given as:

$$\overline{uv} = \Gamma\overline{uv}_t + (1-\Gamma)\overline{uv}_{nt} + \Gamma(1-\Gamma)(\bar{U}_t - \bar{U}_{nt})(\bar{V}_t - \bar{V}_{nt}) \quad (2)$$

Since the results from v' indicate the mean-step between $\bar{V}_t$ and $\bar{V}_{nt}$ is almost null, the last term of Eq. (2) is not expected to have a significant contribution on the overall Reynolds shear stress. The evolution of the conditionally sampled Reynolds shear stress, $\overline{uv}$, for the baseline case is shown in Fig. 7.

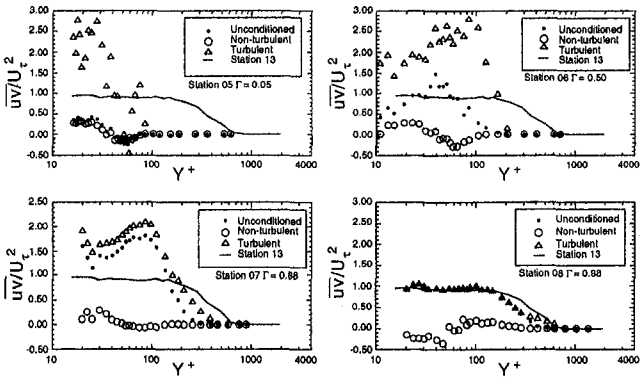

Fig. 7 Conditionally sampled Reynolds shear stress for the baseline case (normalized by unconditioned C_f)

The nonturbulent contribution to the shear stress throughout the transition region is relatively small. This shows the weak correlation between the streamwise and cross-stream velocity fluctuations in the nonturbulent portions. The turbulent portion immediately increases above the wall shear and above the unconditioned result, obtaining a magnitude nearly three times the wall shear at station 05 ($\Gamma = 0.05$). The peak magnitude remains at about three times the wall shear at station 06 ($\Gamma = 0.50$) and then begins to decay, reaching a value of 1 by station 08 ($\Gamma = 0.98$). This evolution of the turbulent shear indicates that the unconditioned values are not representative of the true turbulent shear through the transition process. To provide additional insight into the turbulent shear, the results for the baseline case are replotted in Fig. 8 but are normalized by the individual C_f values obtained for each portion (i.e., the turbulent and nonturbulent values shown in Fig. 4 of Part 1). By presenting the Reynolds shear stress in this manner, the peak magnitudes in the turbulent portion are significantly reduced. The peak magnitude of $\overline{uv}$ in the turbulent portion for stations 05 through 07 still exceed the wall shear but not by the magnitude previously seen in Fig. 7. For station 06 ($\Gamma = 0.50$), $\overline{uv}$ in the turbulent portion reaches a maximum of approximately 1.4 and occurs at $Y^+ \approx 100$, not at $Y^+ \approx 40$ shown by the unconditioned portion. The trend of the Reynolds shear distribution in the turbulent portion for station 07 is similar to that observed in station 06 even though the unconditioned values are not similar. Note that the $\overline{uv}/(U_\tau)^2$ values in the turbulent portion at station 7 in Fig. 8 become lower than the unconditioned values because the C_f values used in the turbulent portion in Fig. 8 are much higher than the unconditioned C_f values used in Fig. 7. For station 07 ($\Gamma = 0.88$) the peak of $\overline{uv}$ in the turbulent portion is 1.3 times greater than the wall shear. This supports the statement that the turbulent shear is generated within the turbulent portion of the flow and away from the wall at approximately $Y^+ = 70 \sim 100$ and that the higher turbulent shear away from the wall is not due to the mean-step contribution.

Figure 7 provides information of the absolute magnitude difference of $\overline{uv}$ between nonturbulent and turbulent parts since a constant value of U_τ is used for all three parts. Figure 8 provides information on normalized $\overline{uv}$ values relative to the wall shear stress of each part respectively. Both presentation methods are informative and provide physical insights to the evolution of turbulence transports in the transition process. However, limited by the paper length, only the second normalization method is used for the accelerating cases in this paper. The complete data presentation can be found in Keller's dissertation (1993).

Selected conditionally sampled results of the Reynolds shear stress for the accelerating cases normalized by the respective C_f values of each portion are shown in Figs. 9 and 10. For the K2 case (Fig. 10), comparison of $\overline{uv}$ between the unconditioned and turbulent portions between station 10 ($\Gamma = 0.37$) and 11

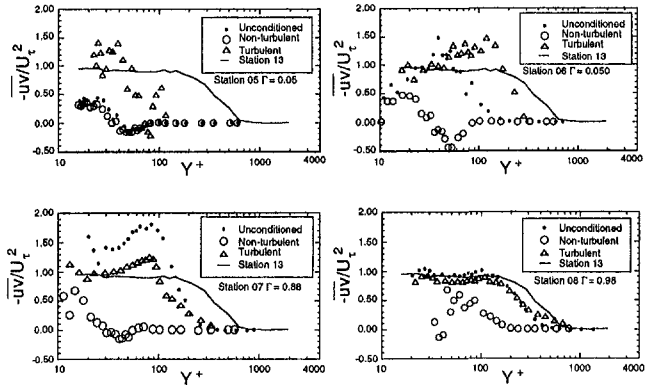

Fig. 8 Conditionally sampled Reynolds shear stress for the baseline case (normalized by individual C_f of each portion)

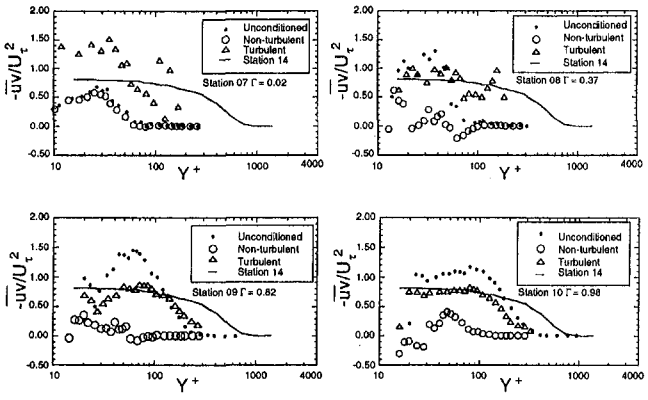

Fig. 9 Conditionally sampled Reynolds shear stress for the K1 case (normalized by individual C_f of each portion)

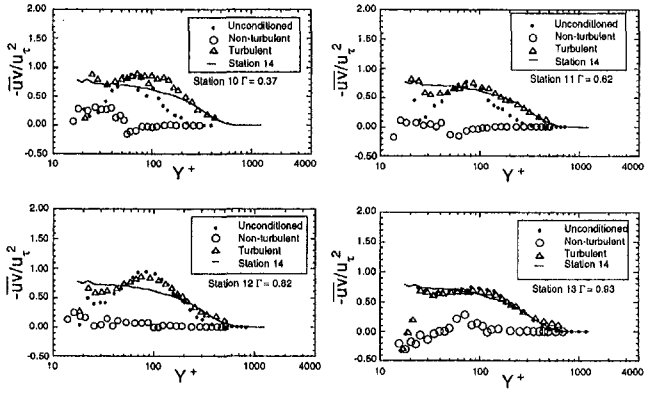

Fig. 10 Conditionally sampled Reynolds shear stress for the K2 case (normalized by individual C_f of each portion)

($\Gamma = 0.62$) reveals that the distribution of turbulent shear is more uniform through the inner boundary layer for the turbulent portion than the unconditioned result. For example, in the inner boundary layer at station 10 ($\Gamma = 0.37$) $\overline{uv}$ for the unconditioned data reaches a maximum value at $Y^+ = 60$ and quickly decreases in magnitude as the wall is approached, while $\overline{uv}$ in the turbulent portion remains at a relatively constant value. In the outer boundary layer, for $Y^+ > 50$, $\overline{uv}$ for the unconditioned data rapidly decreases to a zero magnitude by $Y^+ = 200$, whereas for the turbulent portion, $\overline{uv}$ slowly decays in magnitude in the outer boundary layer. This difference is partly caused by the engulfing of the intermittent irrotational flow from the free stream. As transition progresses, these differences become less pronounced and $\overline{uv}$ for the unconditioned data and the turbulent portion are nearly indistinguishable by station 13.

RMS Temperature Fluctuations (t'). The conditionally sampled rms temperature profiles, normalized by $T_w - T_\infty$ for the baseline case, are shown in Fig. 11. The profiles are similar to those observed in the u' profiles shown in Fig. 1. The nonturbulent portion exhibits a peak intensity of 0.045 at $Y^+ \approx 35$ ($y/\delta^* \approx 1.3$) at station 05 ($\Gamma = 0.05$), which is slightly below the 0.05 peak value for the unconditioned result, which occurs at the same Y^+ location. For station 06 ($\Gamma = 0.50$) the peak intensity for the nonturbulent portion increases to 0.075 and remains at $Y^+ \approx 35$. The peak magnitude for the unconditioned result is 0.12 at this station and occurs closer to the wall $Y^+ \approx 15$ ($y/\delta^* \approx 0.3$). In the late transition region, stations 07–08, the peak intensity in the nonturbulent part continues to increase in magnitude but does not migrate closer to the wall until station 08. For station 08 ($\Gamma = 0.98$), the peak intensity in t', similar to the result of u' for the nonturbulent portion, exceeds both

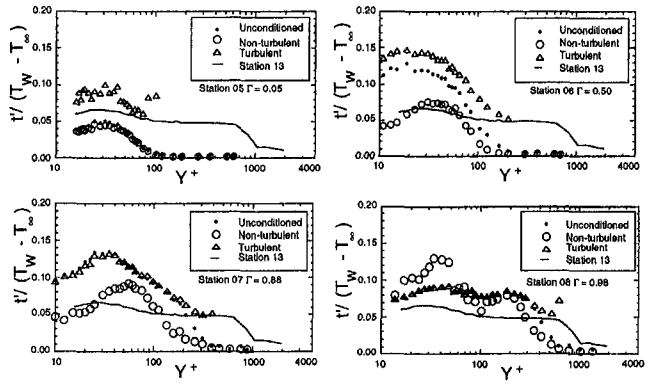

Fig. 11 Conditionally sampled rms temperature for the baseline case

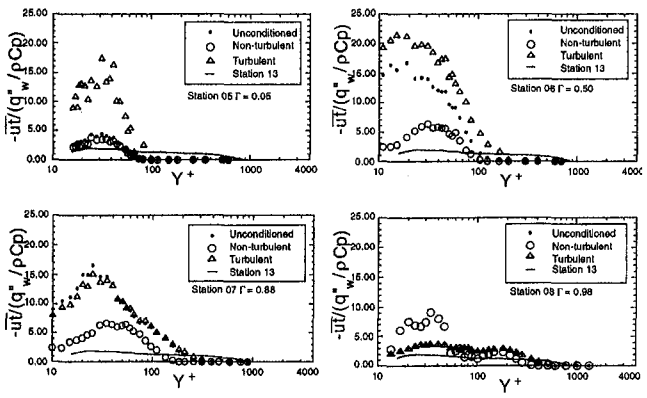

Fig. 14 Conditionally sampled Reynolds streamwise heat flux for the baseline case

the turbulent and unconditioned values near the wall. This can be contributed by the unsteadiness (not turbulence) of the highly disturbed nonturbulent portion. For station 05 (Γ = 0.05), the maximum value of t' in the turbulent part reaches 0.10, which is greater than the 0.05 reached in the unconditioned part for the same Y^+ location. For station 06 (Γ = 0.50), the peak magnitude in t' for the turbulent portion increases to 0.15 at $Y^+ \approx 15$ ($y/\delta^* \approx 0.3$) and still exceeds the unconditioned value. At station 07 ($\Gamma = 0.88$) t' in the turbulent portion for $Y^+ < 40$ is slightly below the unconditioned result; this indicates a contribution from the step alternation in mean temperature. The near-wall peak of turbulent portion decreases in magnitude from station 07 to station 08. The secondary peak that was seen to occur at $Y^+ \approx 200$ for the unconditioned result also occurs in both the nonturbulent and turbulent portions. This indicates that this second peak is not majorly caused by the mean-step contribution but rather is a direct result of the temperature fluctuation.

The conditionally sampled t' profiles for the accelerating cases are shown in Figs. 12 and 13. The effect of a favorable pressure gradient is seen to be most significant in the nonturbulent portion. For the K2 case, the broad peak in the t' profiles for the nonturbulent portion occurring at $Y^+ \approx 40$ for station 09 continually increases in magnitude. At station (Γ = 0.62), the peak intensity in t' occurs at $Y^+ \approx 100$ and is approximately the same magnitude as both the turbulent and the unconditioned value. By station 13 (Γ = 0.93) the peak intensity in t' for this region is greater than both the turbulent part and the unconditioned values. This behavior did not occur in the corresponding u' profiles where the fluctuations in the nonturbulent portion never exceeded the unconditioned or the turbulent part values in the K2 case. The exact reason for this phenomenon is not clear. Probably, this difference is caused by the fact that pressure gradients directly interact with the momentum transport but not with the thermal transport.

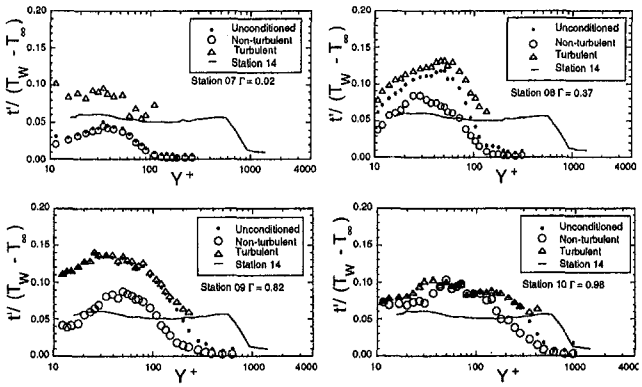

Fig. 12 Conditionally sampled rms temperature for the K1 case

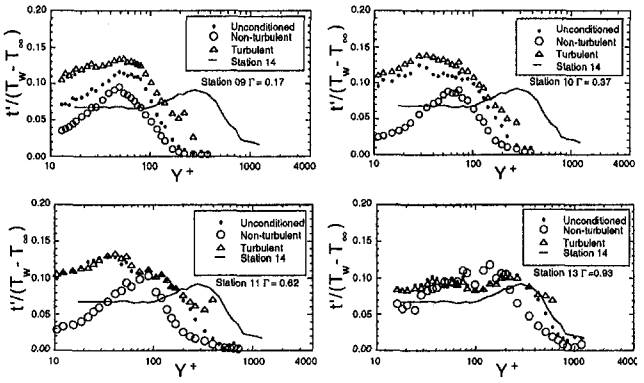

Fig. 13 Conditionally sampled rms temperature for the K2 case

Reynolds Heat Fluxes ($\overline{ut}$). The conditionally sampled streamwise Reynolds heat flux, $\overline{ut}$, for the baseline case is shown in Fig. 14. The peak intensity in the nonturbulent portion occurs at the same cross-stream location as was observed in the t' profiles. At station 05 (Γ = 0.05) the magnitude of the peak intensity is approximately 3.5. By station 06 (Γ = 0.50) this peak intensity in $\overline{uv}$ increases to 7.0 and maintains this level until station 08 (Γ = 0.98). For the turbulent portion, $\overline{ut}$ exceeds the wall heat flux by more than a factor of 15 at station 05. By station 06 (Γ = 0.50) this value has increased to over 20. The large values of convective heat transfer in the streamwise direction, $\overline{ut}$, are a result of the turbulent transport within the turbulent portions.

The conditionally sampled results of $\overline{ut}$ for the accelerating cases are shown in Figs. 15 and 16. The results indicate that the effect of a favorable pressure gradient is to increase the convective heat transfer in the streamwise direction, $\overline{ut}$, in both the turbulent and nonturbulent portions relative to the baseline case. The presence of a relatively large $\overline{ut}$ value in the nonturbulent portion does not necessarily indicate that a significant turbulent transport of heat is occurring but only that u and t are correlated due to the unsteadiness of the flow. A second peak around Y^+ = 12 appears downstream of station 11. The reason for this second peak in accelerating flow is not clear. The results of the cross-stream Reynolds heat flux, $\overline{vt}$, are not presented here due to a large uncertainty in $\overline{vt}$ measurements, as discussed by Wang et al. (1992).

Eddy Viscosity, ϵ_M. The results of the conditionally sampled eddy viscosity, ϵ_M, normalized by the molecular viscosity are shown in Figs. 17 and 18. For the baseline case, the

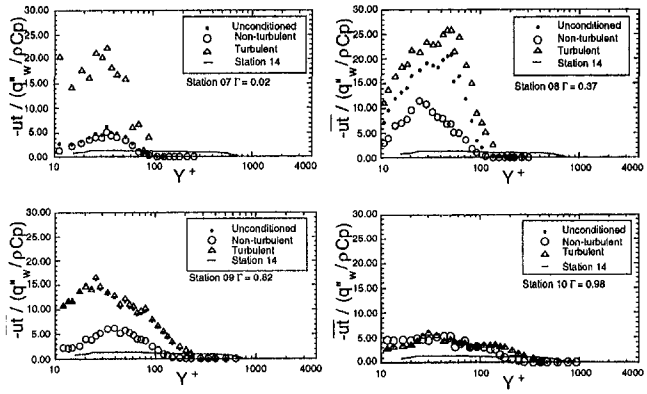

Fig. 15 Conditionally sampled Reynolds streamwise heat flux for the K1 case (in wall units)

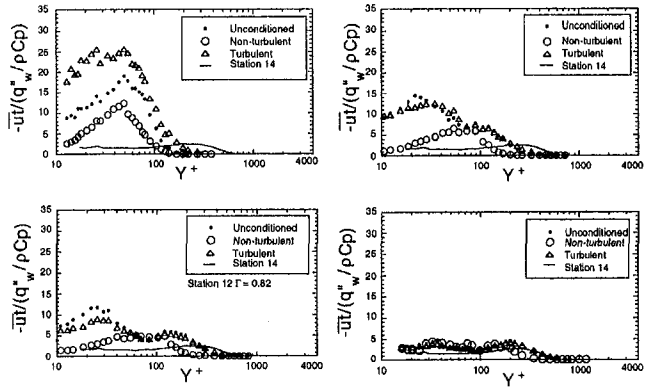

Fig. 16 Conditionally sampled Reynolds streamwise heat flux for the K2 case

values obtained in the turbulent portion are larger than the unconditioned values but are significantly below the fully turbulent values obtained at station 13 (see Fig. 17). As K increases, both the turbulent part and the unconditioned ϵ_M values decrease.

Conclusion

A conditional sampling technique was employed to analyze the fluctuation quantities in the turbulent and nonturbulent parts of accelerated boundary layers undergoing laminar–turbulent transition on a uniformly heated flat plate. The results indicated that the increased magnitudes of the unconditionally sampled u' and t' were discovered to be a direct result of the fluctuations in the turbulent portions. The

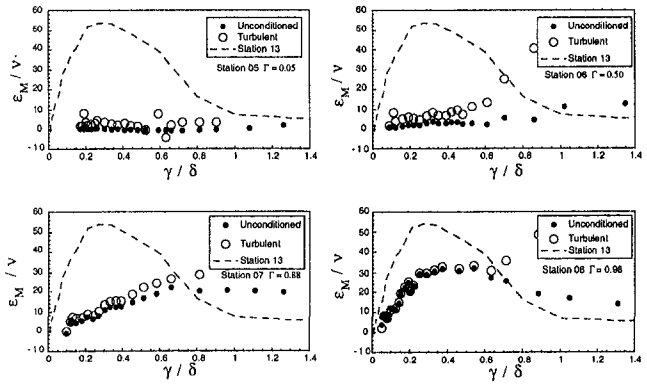

Fig. 17 Conditionally sampled eddy viscosity for the baseline case

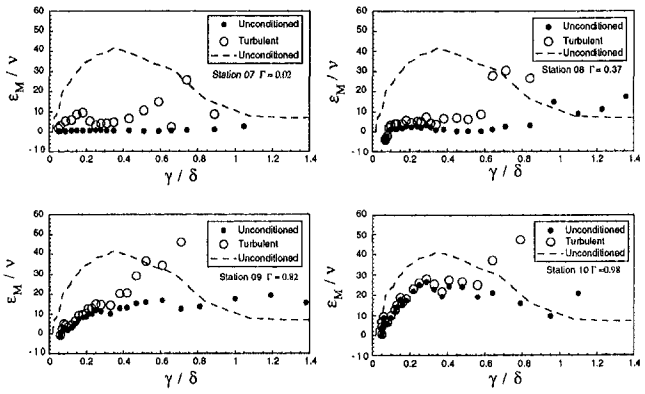

Fig. 18 Conditionally smapled eddy viscosity for the K1 case

"mean-step" contribution to u' due to the alternating behavior between turbulent and nonturbulent flows were about 20 percent in the near-wall region but were negligible for $Y^+ > 30$. The peak intensity of u' and t' in the nonturbulent portion was suppressed at an earlier stage, as acceleration increased. The peak magnitude of $\overline{uv}$ in the turbulent parts of the accelerating cases exceeded the wall shear but not by the magnitude seen in the baseline case. The turbulent part $\overline{uv}$ values were higher than the fully turbulent and unconditioned values in the inner boundary layer but lower in the outer boundary layer. The "mean-step" contribution to unconditioned $\overline{uv}$ values was negligible. As acceleration increased, $\overline{uv}$ in the turbulent portion was more uniformly distributed through the inner boundary layer than the unconditioned results.

In accelerating cases, the peak of v' of the turbulent portion reached the fully turbulent value in the middle of the transition at $\Gamma \approx 0.5$ and changed little downstream. The effect of acceleration on nonturbulent portion v' is similar to nonturbulent portion u'. The unconditionally sampled rms temperature fluctuations, t', exceeded both the turbulent and nonturbulent values throughout most of the boundary layer. This indicated that a mean-step contribution to the large unconditioned t' values was not negligible. The effect of acceleration on t' was seen to be most significant in the nonturbulent portion. The streamwise Reynolds heat flux transport, $\overline{ut}$, increased as acceleration increased in both turbulent and nonturbulent portions of the boundary layers. A second peak of $\overline{ut}$ of the turbulent part at around $y^+ = 120$ appeared as K increased.

For the baseline case, the values of eddy viscosity, obtained in the turbulent portion, were larger than the unconditionally sampled values and were significantly below the fully turbulent values.

Acknowledgments

This research was sponsored by the Air Force Office of Scientific Research (Grant No. F49620-94-1-0126). The program manager was Dr. James McMichael.

References

Blair, M. F., 1992, "Boundary-Layer Transition in Accelerating Flows With Intense Free-Stream Turbulence: Part 1—Disturbances Upstream of Transition Onset; Part 2—The Zone of Intermittent Turbulence," ASME *Journal of Fluids Engineering*, Vol. 114, pp. 313–332.

Keller, F. J., 1993, "Flow and Thermal Structures in Heated Transitional Boundary Layers With and Without Streamwise Acceleration," Ph.D. Dissertation, Department of Mechanical Engineering, Clemson University, Clemson, SC.

Keller, F. J., and Wang, T., 1996, "Flow and Thermal Behavior in Transitional Boundary Layers With Streamwise Acceleration," ASME JOURNAL OF TURBOMACHINERY, Vol. 118, pp. 314–326.

Kim, J., Simon, T. W., and Kestoras, M., 1994, "Fluid Mechanics and Heat Transfer Measurements in Transitional Boundary Layers Conditionally Sampled on Intermittency," ASME JOURNAL OF TURBOMACHINERY, Vol. 116, pp. 405–416.

Kuan, C. L., and Wang, T., 1990, "Investigation of the Intermittent Behavior of a Transitional Boundary Layer Using a Conditional Averaging Technique," *Experimental Thermal and Fluid Science,* Vol. 3, pp. 157–170.

Schubauer, G. B., and Skramstad, H. K., 1947, "Laminar-Boundary Layer Oscillations and Transition on a Flate Plate," NACA Report No. 909.

Schubauer, G. B., and Klebanoff, P. S., 1956, "Contributions on the Mechanics of Boundary-Layer Transition," NACA Technical Note #1289, supercedes NACA TN 3489.

Sohn, K. H., O'Brien, J. E., and Reshotko, E., 1989, "Some Characteristics of Bypass Transition in a Heated Boundary Layer," *Proc. 7th Turbulent Shear Flow Symposium,* pp. 2.4.1–2.4.6.

Sohn, K. H., and Reshotko, E., 1991, "Experimental Study of Boundary Layer Transition With Elevated Free-Stream Turbulence on a Heated Plate," NASA CR-187068.

Wang, T., Keller, F. J., and Zhou, D., 1992, "Experimental Investigation of Reynolds Shear Stresses and Heat Fluxes in a Transitional Boundary Layer," *Fundamental and Applied Heat Transfer Research for Gas Turbine Engines,* ASME HTD Vol. 226, pp. 61–70.

Wang, T., Keller, F. J., and Zhou, D., 1996, "Flow and Thermal Structures in a Transitional Boundary Layer," *Experimental Thermal and Fluid Science,* Vol. 12, pp. 352–363.

The Experimental Study of Matching Between Centrifugal Compressor Impeller and Diffuser

H. Tamaki

H. Nakao

M. Saito

Turbomachinery and Engine Development Department, Ishikawajima-Harima Heavy Industries Co., Ltd., Toyosu Koto-ku, Tokyo, Japan

The centrifugal compressor for a marine use turbocharger with its design pressure ratio of 3.2 was tested with a vaneless diffuser and various vaned diffusers. Vaned diffusers were chosen to cover impeller operating range as broad as possible. The analysis of the static pressure ratio in the impeller and the diffusing system, consisting of the diffuser and scroll, showed that there were four possible combinations of characteristics of impeller pressure ratio and diffusing system pressure ratio. The flow rate, Q_P, where the impeller achieved maximum static pressure ratio, was surge flow rate of the centrifugal compressor determined by the critical flow rate. In order to operate the compressor at a rate lower than Q_P, the diffusing system, whose pressure recovery factor was steep negative slope near Q_P, was needed. When the diffuser throat area was less than a certain value, the compressor efficiency deteriorated; however, the compressor stage pressure ratio was almost constant. In this study, by reducing the diffuser throat area, the compressor could be operated at a flow rate less than 40 percent of its design flow rate. Analysis of the pressure ratio in the impeller and diffusing systems at design and off-design speeds showed that the irregularities in surge line occurred when the component that controlled the negative slope on the compressor stage pressure ratio changed.

Introduction

A centrifugal compressor produces a high pressure ratio with its compactness and toughness. The efficiency of a centrifugal compressor impeller is normally high, sometimes exceeding 90 percent. Absolute impeller discharge Mach number is transonic in case of a high pressure ratio or large volume flow rate. Effective pressure recovery downstream of an impeller is very important to realize a centrifugal compressor with high efficiency and high pressure ratio, and an appropriate selection of a diffuser for a specific impeller is a critical step to develop the compressor accordingly. Klassen and Wood (1977) showed the analysis of the matching characteristics of the impeller and diffuser using mass flow parameters at peak impeller efficiency and peak pressure recovery factor of the diffuser in order to optimize the compressor efficiency. Yoshinaka (1977) related the static pressure recovery at the impeller and diffuser throat to stall of the impeller and diffuser and showed the way of selection of the diffuser throat area using test results. Because of complicated impeller discharge flow, selection of a vaned diffuser for a specific impeller still requires many trial experiments. It is often necessary to change the operating range of the compressor without replacing its impeller. Changing a vaned diffuser throat area seems to be a general method. Hence understanding of the relationship between vaned diffuser throat area and compressor operating range, in particular shift of surge line, is important. The purpose of this study is to investigate the change of surge flow rate with different diffuser throat areas.

Experimental Apparatus

The main dimensions of the impeller for the compressor of a marine use turbocharger with its design pressure ratio of 3.2 used in the present test were:

Impeller outer radius	65.40 mm
Number of blades (full/splitter)	14 (7/7)
Impeller outlet blade angle (from radial direction)	−40 deg
Design peripheral Mach number	1.40

Three kinds of vaned diffusers, shown in Fig. 1, were used in this study. Figure 1-1 is diffuser designed by conformal transformation of NACA-65 series of airfoils. Figure 1-2 is designed based on NACA-65 series of airfoils. Figure 1-3 is a channel diffuser with a log spiral at its leading edge. Dimensions of the tested vaned diffusers are shown in Table 1.

Abdelhamid (1982) and Whitfield et al. (1991) reported the use of vaneless diffusers with throttle rings extended impeller flow range. In order to obtain the impeller characteristics over as broad a range as possible, this study used a vaneless diffuser whose shroud wall was pinched from the position of the impeller radius ratio of 1.0 to 1.7 and a throttle ring was installed at the diffuser exit.

The performance of the compressor was derived with the measurement of static pressure, total pressure, and total temperature in inlet and discharge line. Compressor mass flow rate was measured in the discharge line using an orifice plate flow meter.

Results and Discussion

Analysis of Design Speed

Static Pressure Ratio in Impeller. Measurement of static pressure at impeller exit was done with the vaneless diffuser. Eight static pressure holes were installed at the position of the impeller radius ratio of 1.1. The flow condition at the impeller radius ratio of 1.1 was calculated as follows (Matsutani and Aoki, 1991):

$$Cu_{2m} = R_2/R^*_{2m}\Delta h/U_2 \quad (1)$$

$$A_{2m} = 2*\pi*R^*_{2m}B^*_{2m}(1 - bl) \quad (2)$$

Contributed by the International Gas Turbine Institute and presented at the ASME ASIA '97 Congress & Exhibition, Singapore, September 30–October 2, 1997. Manuscript received by the International Gas Turbine Institute June 19, 1997. Paper No. 97-AA-2. Associate Technical Editor: H. A. Kidd.

Fig. 1-1 NACA-65 (Conformal Transformation)

Fig. 1-2 Airfoil Diffuser

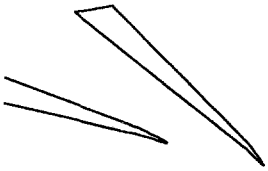

Fig. 1-3 Channel Diffuser

Fig. 1 Tested diffuser shape

$$Cm_{2m} = (W * Rg * t_{2m})/(A^*_{2m} p_{2m}) \quad (3)$$

$$t_{2m} = T_{2m} - 0.5*(Cm^2_{2m} + Cu^2_{2m})/Cp \quad (4)$$

$$\alpha_{2m} = \tan^{-1}(Cu_{2m}/Cm_{2m}) \quad (5)$$

$$M_{2m} = (2*(t_{2m}/T_{2m} - 1)/(\kappa - 1))^{0.5} \quad (6)$$

It was assumed that the total pressure at the impeller exit was the same as the total pressure of the impeller radius ratio of 1.1. The impeller exit condition was calculated by the same manner described above, using R_2 instead of R_{2m}.

Figure 2 shows the total to static pressure ratio of the impeller, π_i, at the design speed. The flow rate in Fig. 2, Q_N, is nondimensionalized by the design volume flow rate. It is well known that surge or flow instability of a compressor occurs, when the slope on the pressure ratio characteristics is positive. The flow rate the impeller achieved at the maximum static pressure ratio, Q_P, was 0.9. The slope of characteristics of π_i started to be positive below the flow rate of 0.9. The impeller could be the main component responsible for surge or flow instability of the compressor, if the impeller is used below the flow rate of 0.9.

Prediction of Vaned Diffuser Operating Range. Figure 3 shows the predicted operating range of tested diffusers with the one-dimensional method. The diffuser's choke flow rate was determined when the Mach number at the throat was 1.0. Throat blockage in the choke calculation was 0.02. Diffuser stall flow rate was determined when the pressure recovery between the diffuser leading edge and throat reached a certain value. The pressure recovery factor of 0.4 and the throat blockage of 0.15 were selected in the stall calculation (Yoshinaka, 1977). The conditions of the impeller discharge flow and diffuser leading edge were calculated with typical one dimensional method. Shift of the diffuser operating range to smaller flow rate as the decreasing diffuser throat area was expected. Figure 3 also includes Q_p and impeller choke flow rate obtained by the experiments.

Table 1 List of tested diffusers

TITLE	R3/R2	R4/R2	α2v	Zv	Ath	AR	Remark
VD-1	1.1	1.5	72	14	1.13	1.40	Fig. 1-1
VD-2	1.2	1.55	66	17	1.07	1.25	Fig. 1-2
VD-3	1.1	1.5	66	17	1.00	1.95	Fig. 1-2
VD-4	1.1	1.7	66	15	0.97	1.94	Fig. 1-3
VD-5	1.1	1.7	66	15	0.94	1.94	Fig. 1-3
VD-6	1.1	1.4	66	15	0.94	1.27	Fig. 1-3
VD-7	1.1	1.7	68	15	0.88	2.12	Fig. 1-3
VD-8	1.1	1.4	66	15	0.87	1.26	Fig. 1-3
VD-9	1.1	1.7	68	15	0.83	2.12	Fig. 1-3
VD-10	1.1	1.5	73	15	0.65	1.91	Fig. 1-3
VD-11	1.1	1.5	80	15	0.38	3.04	Fig. 1-3

Static Pressure Ratio in Diffusing System. The diffusing system of the centrifugal compressor consisted of the diffuser and scroll. The pressure ratio in the diffusing system, π_d, was determined as follows:

$$\pi_d = \pi_t/\pi_i$$

where π_i is total to static pressure ratio between the compressor inlet and the impeller exit calculated from the vaneless diffuser test and π_t is total to static pressure ratio between the compressor

Nomenclature

AR = diffuser area ratio
Ath = diffuser throat area divided by throat area of VD-3
B = diffuser height
bl = blockage factor
Cp = pressure recovery factor or specific heat at constant pressure
Cm = meridional velocity
Cu = tangential velocity
M = Mach number
Mu = peripheral Mach number
P = total pressure
p = static pressure
Q = volume flow rate
Q_P = flow rate where the impeller maximum static pressure ratio is achieved
Q_N = nondimensionalized volume flow rate
R = radius
Rg = gas constant
T = total temperature
t = static temperature
U_2 = impeller tip speed
W = mass flow rate
Z_v = number of diffuser vanes
α = flow angle
α_{2v} = diffuser vane setting angle
Δh = total enthalpy rise in compressor
κ = specific heat ratio
π_i = total to static pressure ratio between compressor inlet and impeller exit (static pressure ratio in impeller)
π_d = static pressure ratio in diffusing system = π_t/π_i
π_t = total to static pressure ratio between compressor inlet and scroll exit (compressor stage pressure ratio)

Subscripts

0 = compressor inlet
2 = impeller exit (diffuser inlet)
$2m$ = position of impeller radius ratio of 1.1
3 = diffuser leading edge
4 = diffuser trailing edge
5 = position of impeller radius ratio of 1.7
6 = scroll exit
th = diffuser throat

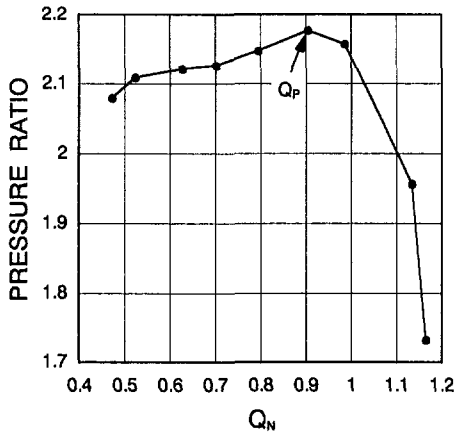

Fig. 2 Impeller static pressure ratio

inlet and scroll exit. Figure 4 shows the characteristics of π_t and π_d. Figure 4 also includes π_i.

According to Fig. 4, there are four possible combinations of the characteristics of the impeller and diffusing system pressure ratio. Figure 5 shows the schematic of these four combinations.

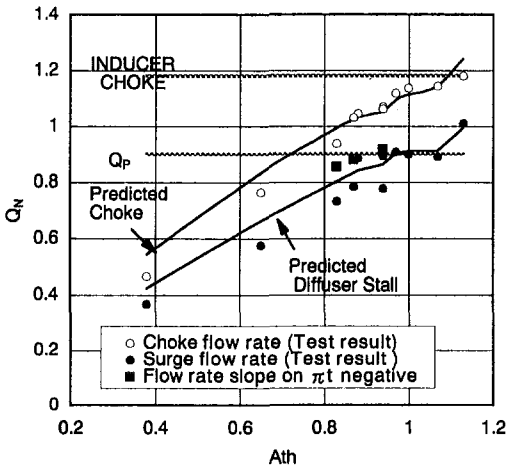

Fig. 3-2 Flow Rate at Surge and Slope on π_t Started to be Negative

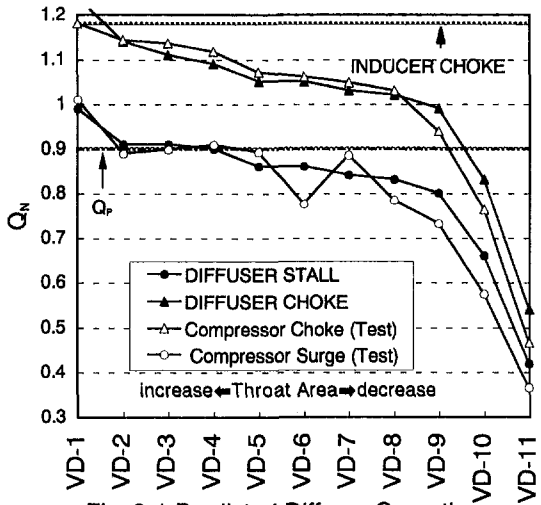

Fig. 3-1 Predicted Diffuser Operating Range

Fig. 3 Diffuser operating range

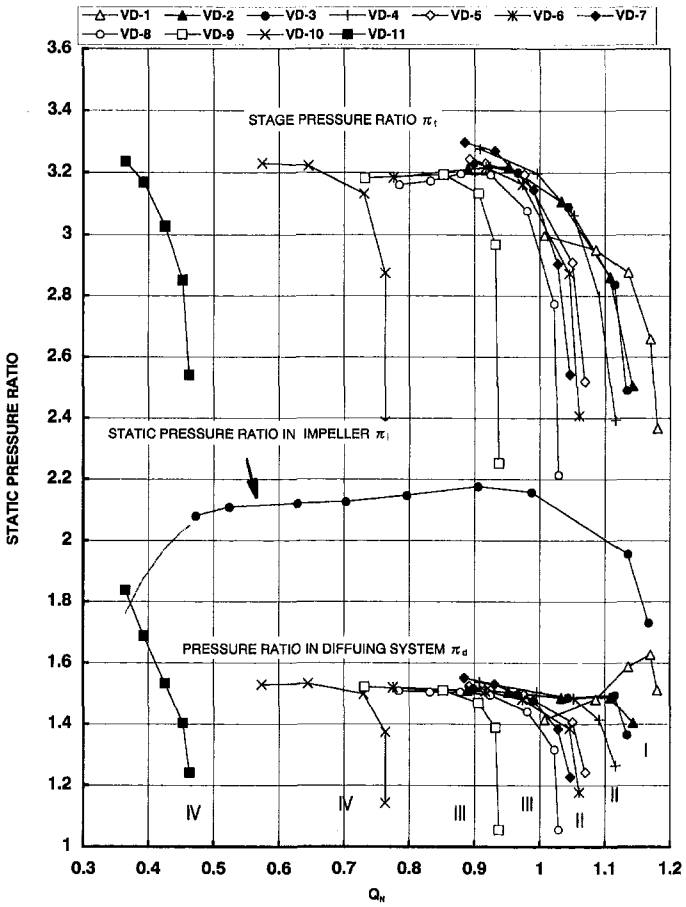

Fig. 4 Pressure ratio in impeller, diffusing system, and compressor stage

Type I: The slope on the impeller pressure ratio, π_i, was negative from surge to choke. The slope on the pressure ratio between the impeller exit and scroll exit, π_d, was positive near surge point. The negative slope of π_i compensated the positive slope on π_d to keep the slope of the compressor stage pressure

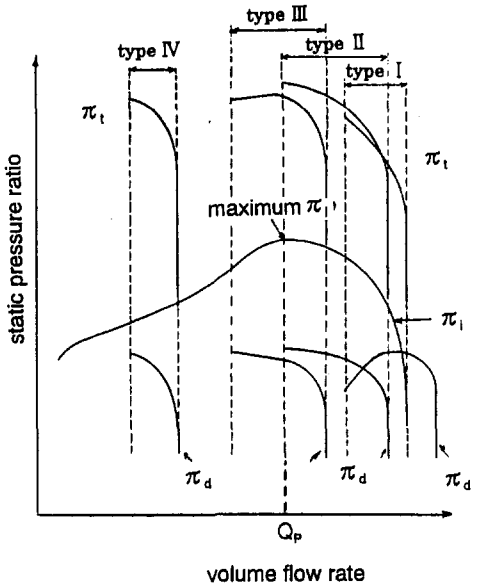

Fig. 5 Schematic of combination of impeller and diffusing system

ratio, π_t, negative. The diffuser characteristic was responsible for surge.

The throat area of VD-1 was too large for the impeller. Pressure recovery between the impeller exit and diffuser throat tended to be high, and hence the diffuser stall occurred at the large flow rate.

In the cases of VD-2 and VD-3 diffuser stall was assumed to be almost correspondent to Q_P and diffuser choke flow rate was near impeller choke flow rate. The impeller used the diffuser operating range as wide as possible.

Type II: In the cases of VD-4, VD-5, and VD-7, it was expected that the flow rate of surge was less than Q_P, but surge occurred at Q_P. The positive slope on impeller pressure ratio, π_i, was steeper than negative slope on the pressure ratio of the diffusing system, π_d. The impeller characteristic was responsible for surge.

Type III: In the cases of VD-6, VD-8, and VD-9, the slope on the impeller pressure ratio, π_i, changed from negative to positive as the flow rate was reduced; on the other hand, the slope on the pressure ratio in the diffusing system, π_d, was negative. Surge occurred at the flow rate below Q_P. These results were correspondent to the one-dimensional prediction.

VD-6 has the same throat area as VD-5. The geometric differences between these diffusers were vaned diffuser trailing edge positions. Figure 6 shows the results of the flow visualization in the vaned diffuser by oil trace at the impeller peripheral Mach number of 0.8. The volume flow rates were the same, near the compressor peak efficiency point. In case of VD-5, separated flow region existed down stream of the throat due to a high area ratio of the diffuser. In case of VD-6, separated flow region did not extend downstream of throat. This example shows the stability of the diffuser is not only determined by the pressure recovery between the diffuser leading edge and throat, but by the flow situation downstream of the throat.

VD-6, VD-8, and VD-9 had the positive slope regions on the compressor stage pressure ratio, π_t. Since the operation of compressor is likely to be unstable in the region of the positive slope on the pressure ratio, the region of the positive slope on the compressor stage pressure ratio is often considered a useless

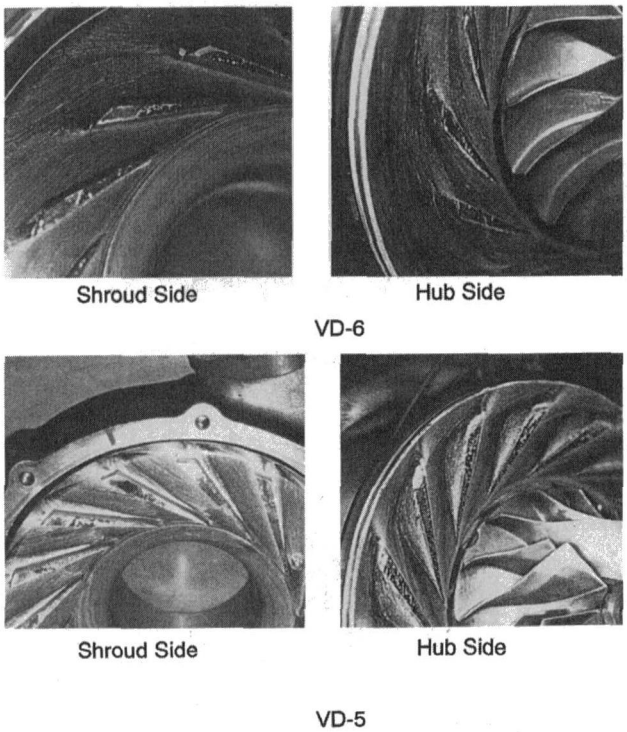

Fig. 6 Results of flow visualization in vaned diffuser

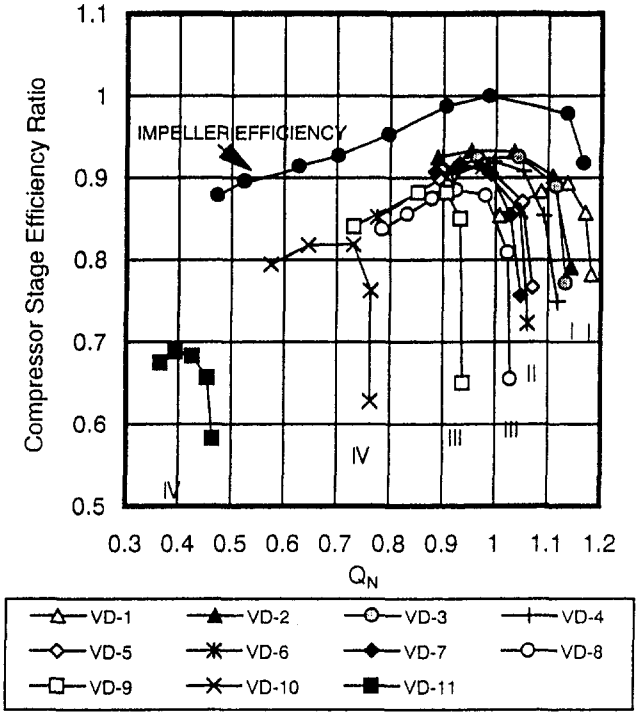

Fig. 7 Impeller and compressor stage efficiency

region for applications to turbochargers or other utilities. These results show the difficulties of keeping the slope on the stage pressure ratio negative below Q_P.

Type IV: In the cases of VD-10 and VD-11, the slope on π_i was positive from surge to choke and that on π_d was negative. In the case of VD-11, the compressor could be operated at the flow rate less than 40 percent of the design flow rate. The steep negative slope by the diffuser near choke kept the characteristic of the compressor stage pressure ratio negative. When volume flow rate was reduced and the negative slope on the pressure ratio of diffusing system became moderate, the compressor tended to go into surge.

The flow rates at surge and at which slope on π_t was negative are plotted on Fig. 3. These figures clearly show Q_P plays a very important role on the compressor operating range.

Compressor Performance. Figure 7 shows the calculated impeller efficiency from the static pressure measurement at the impeller exit and the compressor stage efficiencies. The efficiency in Fig. 7 is nondimensionalized. Impeller efficiency became the maximum value at the volume flow of 0.98. The compressor whose operating range included the flow rate where the impeller efficiency was maximum could achieve high stage efficiency; however, it could not have the negative slope on the stage pressure ratio below Q_P. It was possible to get the negative slope on the stage pressure ratio below Q_P by using the diffuser whose choke flow rate was near or less than Q_P, for example VD-9 or VD-10, at the cost of the compressor efficiency. Using the diffuser throat area less than a certain value, which was VD-4 in this study, the compressor efficiency deteriorated; however, the compressor stage pressure ratio, π_t, was almost constant. The best efficiency was obtained by VD-2. Although the operating range was determined by the diffuser throat area and

Table 2 Pressure recovery factor between diffuser leading edge and throat at surge

Diffuser	VD-3	VD-5	VD-8
$Cp_{3\text{-}th}$	0.342	0.243	0.330

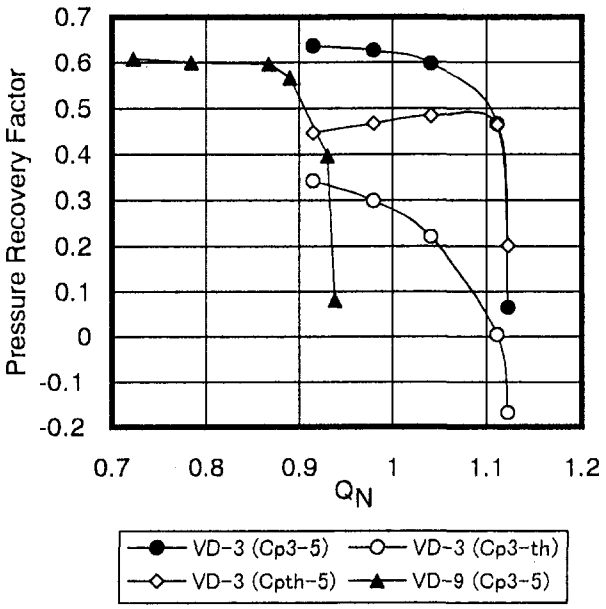

Fig. 8 Pressure recovery factor in diffuser

Q_P, the shape of diffuser plays an important role on the compressor efficiency. In this test, the airfoil diffuser, Figs. 1 and 2, showed good efficiency.

Pressure Recovery Factors in Diffusing System. In the cases of VD-3, VD-5, and VD-8, static pressure was measured at the diffuser throat and trailing edge. Pressure recovery factors between diffuser leading edge and throat at surge conditions were obtained using the impeller total pressure calculated with the static pressure measurement at the impeller exit. Results were shown in Table 2. Pressure recovery factors of VD-3 and VD-8, which surged by the diffusers, were about 0.34. Pressure recovery factor of VD-5, which surged by impeller, was about 0.24, less than 0.34.

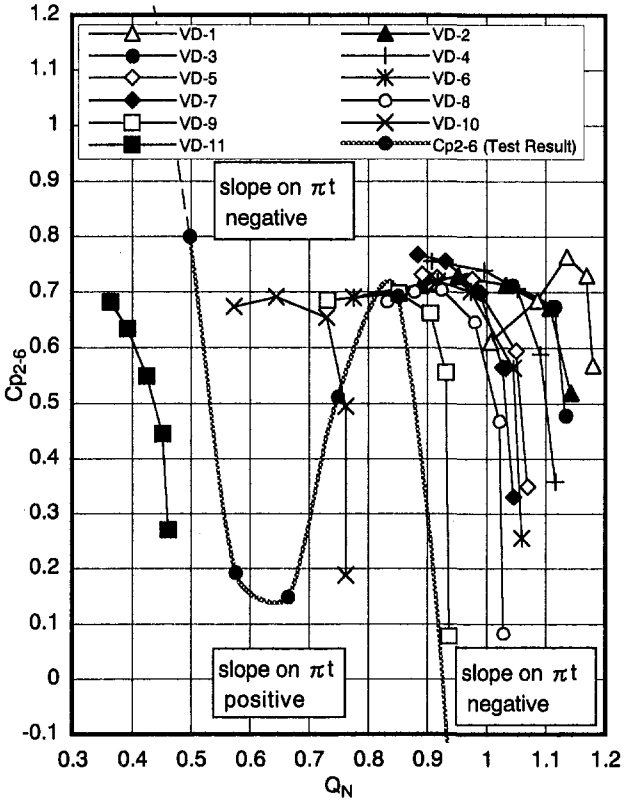

Fig. 9 Pressure recovery factor in diffusion system

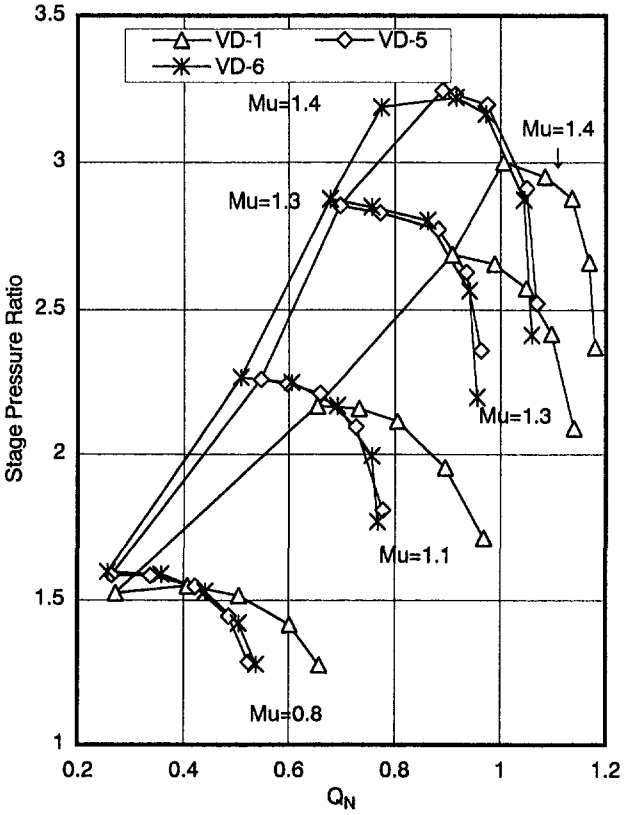

Fig. 10 Compressor stage pressure ratio

Figure 8 shows the pressure recovery factors, Cp_{3-5} of VD-3 and VD-9. In case of VD-3, $Cp_{3\text{-th}}$ and $Cp_{\text{th-5}}$ is also included. It is clear that as the volume flow rate was reduced, the pressure rise at the throat $Cp_{3\text{-th}}$ increased and $Cp_{\text{th-5}}$ decreased. At high flow rate, semi-vaneless space works as nozzle and most of the pressure rise occurred at the channel part. Pressure rise at the throat increased and that at the channel part decreased as the mass flow rate was reduced. Due to the pattern of the pressure recovery of the semi-vaneless space and the channel part as described above, the slope on the static pressure ratio in the diffusing system is likely to be flat except choke.

The negative slope of the compressor pressure ratio π_i is expressed as follows:

$$d\pi_i/dQ = d\pi_i/dQ + d(Cp^*_{2-6}(P_2 - p_2)/P_0)/dQ < 0$$

$$= d\pi_i/dQ + Cp^*_{2-6}d((P_2 - p_2)/P_0)/dQ$$

$$+ (P_2 - p_2)/P^*_0 dCp_{2-6}/dQ < 0 \quad (7)$$

$d((P_2 - p_0)/dQ < 0$ and on the assumption that the change of Cp_{2-6} is very small, Eq. (7) is re-arranged as follows:

$$Cp_{2-6} > -(d\pi_i/dQ)/(d((P_2 - p_2)/P_0)/dQ) \quad (8)$$

Figure 9 shows the calculated Cp_{2-6} from Eq. (8) using the impeller performance derived from the vaneless diffuser test. The upper part of Cp_{2-6} curve is the region where the slope on the compressor pressure ratio is negative without the negative slope on Cp_{2-6}. Figure 9 also includes the pressure recovery factors of diffusion systems. Figure 9 demonstrates that high Cp_{2-6} is required for the tested impeller below Q_P.

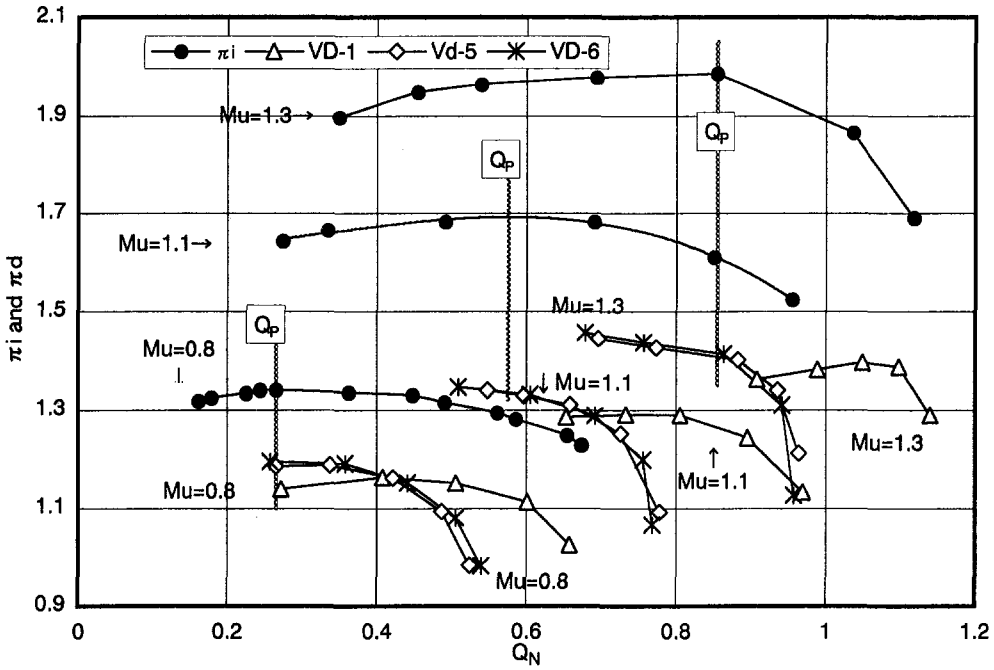

Fig. 11 Pressure ratio in impeller, diffusing system, and compressor stage at off-design speed

In order to keep $d\pi_t/dQ < 0$, $dCp_{2-6}/dQ < 0$ is required according to Eq. (7). Consequently, the diffusing systems whose pressure recovery factor were steep negative slope near Q_P were needed, in order to operate the compressor less than Q_P.

Analysis of Off-Design Speed. Figure 10 shows compressor stage pressure ratios π_t of VD-1, VD-5, and VD-6 at impeller peripheral Mach number, Mu, of 0.8, 1.1, 1.3, and 1.4. It can be seen that surge lines of VD-5 and VD-6 are somewhat irregular.

Analysis of pressure ratio in the impeller and diffusing systems was done with the same way applied to design speed, Mu = 1.4. Figure 11 shows π_i and π_d as function of Q_N.

According to Fig. 11, compressor stage installed VD-1 included the positive slope on π_d for all the rotational speeds, and hence the diffuser controlled surge. Since the slopes on π_d of compressor stages installed at VD-5 and VD-6 were negative below Q_P at Mu = 1.1 and 1.3, diffusers made the compressor stages stable. At Mu = 0.8, both surge flow rates were the same as Q_P, and hence impeller determined surge points.

Combination of π_d and π_i for VD-1, VD-5, and VD-6 were classified in Table 3. Table 3 demonstrates that the irregularities in surge line occurred when the component that controlled the negative slope on the compressor stage pressure ratio changed.

Conclusion

1 Based on the test result with 11 diffuser configurations, the matching between the impeller and diffusing system were categorized into four characteristics.

Table 3 Combination of impeller and diffusing system

	Mu			
	0.8	1.1	1.3	1.4
VD-1	I	I	I	I
VD-5	II	IV	IV	II
VD-6	II	IV	IV	III

2 The pattern of the pressure rise at semi-vaneless space and channel part made the negative slope of the static pressure rise in the diffusing system comparatively flat, so that it is difficult to extend the centrifugal compressor operating range by diffusers below the flow rate, Q_P, where the impeller pressure ratio becomes maximum.

3 The compressor whose operating range included the flow rate where the impeller efficiency was maximum could achieve high stage efficiency; however it could not have the negative slope on the stage pressure ratio below Q_P. It was possible to get the negative slope on the stage pressure ratio below Q_P by use of the diffuser whose choke flow rate was near or less than Q_P at the cost of the compressor efficiency.

4 Using a diffuser throat area less than a certain value, the compressor efficiency deteriorated; however, the compressor stage pressure ratio was almost constant. In this study, the compressor could be operated at a flow rate less than 40 percent of the design flow rate, by reducing the diffuser throat area.

5 Analysis of the pressure ratio in the impeller and diffusing systems at design and off-design speeds showed that the irregularities in surge line occurred when the component that controlled the negative slope on the compressor stage pressure ratio changed.

References

Abdelhamid, A. N., 1982, "Control of Self-Excited Flow Oscillations in Vaneless Diffuser of Centrifugal Compression Systems," ASME Paper No. 82-GT-188.

Klassen, H. A., Wood, J. R., 1977, "Experimental Performance of a 16.10 centimeter Tip Diameter Sweptback Centrifugal Compressor Designed for a 6:1 Pressure Ratio," NASA TM X-3552.

Matsutani, J., and Aoki, S., 1991, "Dawes Code Applied to a High Pressure Ratio Centrifugal Compressor," ASME FED-Vol. 120, *Numerical Simulation in Turbomachinery.*

Whitfield, A., Sutton, A. J., and Leonard, H. J., 1991, "The Development of Turbocharger Compressor With Improved Surge Margin," C433/063 IMechE.

Yoshinaka, T., 1977, "Surge Responsibility and Range Characteristics of Centrifugal Compressors," 1977 Tokyo Joint Gas Turbine Congress.

Numerical Flow Analysis in a Subsonic Vaned Radial Diffuser With Leading Edge Redesign

E. Casartelli

A. P. Saxer

G. Gyarmathy

Turbomachinery Laboratory,
Institute of Energy Technology,
Swiss Federal Institute of Technology,
8092 Zurich, Switzerland

The flow field in a subsonic vaned radial diffuser of a single-stage centrifugal compressor is numerically investigated using a three-dimensional Navier–Stokes solver (TASCflow) and a two-dimensional analysis and inverse-design software package (MISES). The vane geometry is modified in the leading edge area (two-dimensional blade shaping) using MISES, without changing the diffuser throughflow characteristics. An analysis of the two-dimensional and three-dimensional effects of two redesigns on the flow in each of the diffuser subcomponents is performed in terms of static pressure recovery, total pressure loss production, and secondary flow reduction. The computed characteristic lines are compared with measurements, which confirm the improvement obtained by the leading edge redesign in terms of increased pressure rise and operating range.

1 Introduction

It is well known that the stability of a compressor may be limited as the flow rate is reduced from its nominal value by the so-called limit of dynamic stability. This usually coincides with the maximum of the pressure rise characteristic in the stage. Experimental data generally provide global stage and component characteristics such as the pressure rise/volume flow operating lines, thus allowing the definition of the stable operating range. The identification of the different "large-scale" instability phenomena (such as rotating stall and surge) is rendered possible by analyzing the pressure rise and its slope versus mass flow in each of the components or subcomponents of the system. For example, typical subcomponents in a radial compressor are the impeller, the diffuser vaneless and semi-vaneless space, the diffuser channel, and the collecting chamber (Kämmer and Rautenberg, 1986; Hunziker and Gyarmathy, 1993). It has been experimentally shown that the diffuser of a centrifugal compressor is a crucial element for the stability of the stage (Hunziker and Gyarmathy, 1993). The diffuser channel is identified as a typical unstable subcomponent, while the impeller and the diffuser inlet are usually stabilizing elements. Also the experimental studies suggest that up to the stability limit, the flow field in the different components of the centrifugal compressor is mainly steady.

Based on these findings, the analysis of the flow fields of radial diffusers within the stable regime can be supported by steady-state numerical procedures. In particular the major effects of blade redesign should be captured by Navier–Stokes (N–S) programs.

This paper presents numerical investigations of the flow field in a subsonic vaned diffuser based on three-dimensional steady N–S simulations and two-dimensional mixed computations, i.e., viscous analysis and inverse design. The effects on the operating characteristic and the flow structure for three geometric configurations are presented and discussed. The first geometry is a standard (conventional) vane, while the two others were modified in the leading edge area using MISES (Drela and Youngren, 1995).

One objective of the paper is to show that a two-dimensional leading edge redesign of a conventional circular-arc vaned diffuser can lead to an overall improvement of the characteristic line, shown by a higher pressure rise, lower losses, and an increase of the operating range through a flatter, i.e., wider, operating line.

The two-dimensional nose redesign is motivated both by manufacturing and aerodynamic reasons. The two-dimensional blade reshaping avoids additional production costs by keeping the prismatic nature of the original (conventional) blading. Because of the importance of the flow physics occurring in the semi-vaneless space for the stability, it is expected that a selected alteration of this region, though keeping the original throat area, will produce an overall potentially beneficial effect on the operating line (see experimental observations by Hunziker and Gyarmathy (1993), Clements and Arts (1989)). This is in contrast to previous studies, for example Jansen and Rautenberg (1982), where the redesign was three-dimensional even changing the diffuser throat area.

Another objective is to show the mutual complementary use of a state-of-the-art two-dimensional analysis/inverse-design software package, i.e., MISES, and a commercial three-dimensional N–S program such as TASCflow (ASC, 1995). The computationally very fast design predictions of MISES are assessed in two and three dimensions by TASCflow and measurements. The design strategy is based on the following experimental observation. The large axial variation of the inlet flow angle for a given operating point is also observed in a two-dimensional sense, i.e., axially averaged, when varying the mass flow from surge to choke flow conditions. It is therefore expected that a two-dimensional design procedure should potentially improve the overall operating characteristic through reduction of the incidence sensitivity at the leading edge.

The paper is structured as follows: The two software packages are briefly described in Sec. II together with the radial diffuser configuration and the boundary conditions used for the computations. The computed operating lines obtained for two different impeller speeds and diffuser designs are presented in Sec. III and compared to the measurements. This acknowledges the overall consistency and validity of the three-dimensional N–S computations and the improvement in design. A more detailed discussion of the flow behavior in the diffuser for different operating conditions is then presented in Sec. IV. This includes a partitioning between two-dimensional and three-dimensional pressure recovery and loss production and an analysis of

Contributed by the International Gas Turbine Institute and presented at the 42nd International Gas Turbine and Aeroengine Congress and Exhibition, Orlando, Florida, June 2–5, 1997. Manuscript received International Gas Turbine Institute February 1997. Paper No. 97-GT-185. Associate Technical Editor: H. A. Kidd.

the performance of the diffuser subcomponents for different operating points and designs using the three-dimensional N–S program. The design program results and secondary flow structures are presented in Sec. V. Finally, a summary of the major results and the essential conclusions are listed in Sec. VI.

II Numerical Procedures and Geometry

II.1 3D Navier–Stokes Program. The steady three-dimensional flow field computations have been performed with a commercial Navier–Stokes code, TASCflow, V2.4 (ASC Ltd., 1995). Reynolds-stress averaging is applied to the governing equations in strong conservation form for the turbulent flow. A standard $k-\epsilon$ model is used. The discretization procedure is based on a Finite Volume Method. The computational grid is a block structured H-type mesh with 102138 active nodes (see Fig. 1). The periodic boundary condition is surface based, i.e., the number of nodes and their distribution on periodic surfaces can vary. The diffuser blade has been placed in the middle of the computational domain to improve the cell shape at the leading edge. The blade region is a block-off domain in the grid. For all the computed geometries the number of nodes and their distribution are the same.

Also shown in Fig. 1 are several cutting planes along the diffuser, which are used to calculate surface- and mass-averaged values for the pressure rise (Dp), the pressure recovery (Cp) and the total pressure loss (Cp^o) coefficients. For every plane the middle point (bisection of the line in the two-dimensional plane) is located; its radial position is then used to plot the different coefficients along the diffuser from inlet to outlet (abscissa in Figs. 5 and 6).

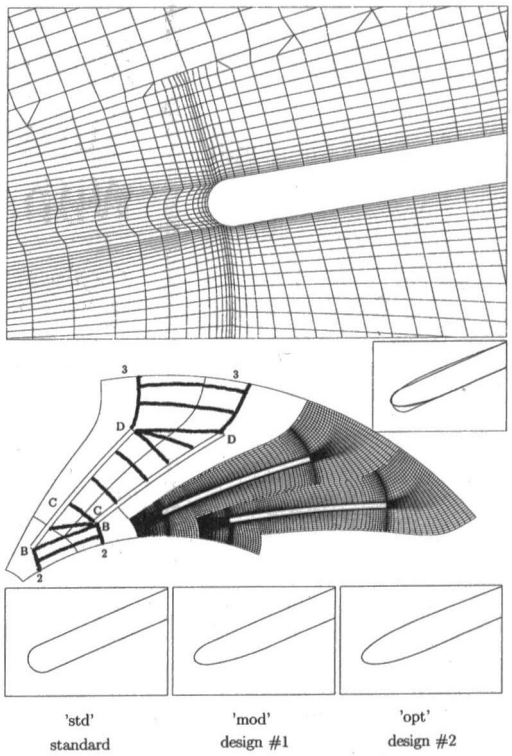

Fig. 1 Mesh (two-dimensional: 3522 nodes, 29 planes) with LE-detail and blow-up of the nose region for the three vanes (with comparison). The cutting planes for the mean-value computations and the diffuser subcomponent stations are marked in the left channel.

II.2 Two-Dimensional Analysis and Design Procedure. The design procedure was performed using MISES, V2.3, MIT, a two-dimensional analysis/inverse-design code with quasi-three-dimensional capabilities. This software package is based on a fully coupled viscous/inviscid method. The flow is modeled with steady Euler equations and the integral boundary layer equations. MISES V2.3 incorporates a modified version of the Abu–Ghannam–Shaw (AGS) bypass transition model. Both the e^n and the AGS model are active all the time and either one may be decisive in inducing transition, which is left free. As opposed to the modal (full) inverse-design option, which allows large overall geometric changes, the mixed inverse-design option has been used. This allows local geometric changes through the prescription of a surface pressure on selected target blade segments. The physical space is mapped through an angle preserving transformation into the computational plane.

II.3 Geometry Description. The standard configuration for the radial diffuser of the single-stage centrifugal compressor of the ETH/Turbomachinery Lab consists of 24 vanes with a

Nomenclature

AS = diffuser aspect ratio = (b_2/l) = 0.17
Cp = pressure recovery coefficient = $(\tilde{p} - \tilde{p}_2)/(\bar{p}_2^o - \tilde{p}_2)$
Cp^o = total pressure loss coefficient = $(\bar{p}^o - \bar{p}_2^o)/(\bar{p}_2^o - \tilde{p}_2)$
D = diameter, m
Dp = pressure rise coefficient = $(\tilde{p} - \tilde{p}_2)/(\rho_E u_2^2/2)$
LE = leading edge
Mu = impeller tip speed Mach number = $u_2/\sqrt{\gamma R T_E^o}$
N = nominal operating point
Op1 = maximum pressure rise operating point
Op2 = high mass flow operating point
Op3 = operating point near choke
PS = pressure side
R = gas constant, J/(kg·K)
Re = Reynolds number = $u_2 b_2/\nu_2$
S = surge operating point
SS = suction side
T^o = total temperature, K
TE = trailing edge
b_2 = diffuser width = 0.0168, m
c = absolute velocity, m/s
c_f = skin friction coefficient
c_r = radial velocity, m/s
c_u = tangential velocity, m/s
c_x = axial chord
l = diffuser blade length = 0.1, m
$\dot{m}$ = mass flow rate, kg/s
m' = streamface coordinate in MISES = log (r^*)
mod = diffuser design #1
opt = diffuser design #2
p = static pressure, bar
p^o = total pressure, bar
r = radius, m
r^* = reduced radius = (r/r_2)
s' = surface arc length ($s' = 0$: LE, $s' = 1$: TE)
std = standard diffuser geometry
u_2 = impeller tip speed = $u(r^* = 1)$, m/s
x, y = physical plane coordinates, m
z = axial length, m
α = flow angle (from tangential direction), deg
ρ = density, kg/m^3
φ = flow coefficient = $\dot{m}/(\rho_E D_2^2 u_2)$
γ = ratio of specific heats
ν = kinematic viscosity, m^2/s
θ = streamface coordinate in MISES = arctan (y/x)

Subscripts

E = impeller inlet
2 = diffuser inlet, $r^* = 1.05$
3 = diffuser outlet, $r^* = 1.79$
B = diffuser leading edge, $r^* = 1.16$
C = diffuser throat
D = diffuser trailing edge, $r^* = 1.54$

Superscripts

$\bar{}$ = mass-averaged
$\tilde{}$ = surface-averaged

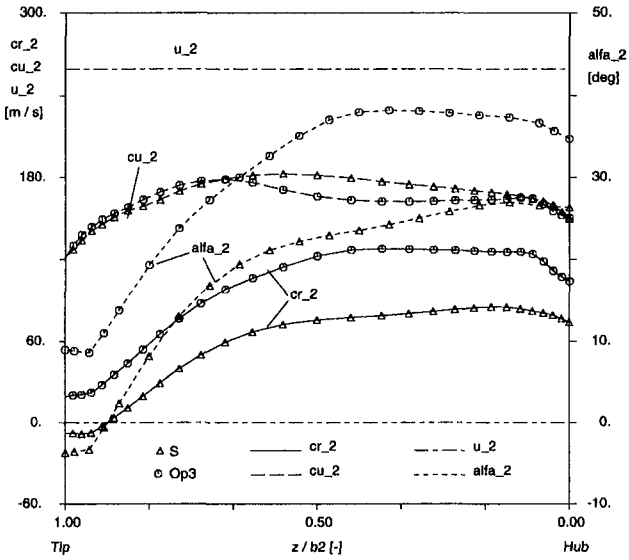

Fig. 2 Velocity and angle profiles for "S" and "Op3" at Mu = 0.75. Note that the velocity and angle distribution of the other operating points ("Op1," "N," and "Op2") lay in between "S" and "Op3."

constant height (i.e., constant diffuser width) mounted at a 25 deg mean line camber angle (see Fig. 1). All vanes of the three investigated variants are prismatic, i.e., the two-dimensional geometry is stacked in the axial direction. A circular-arc mean camber line with constant thickness distribution and a semicircle leading edge defines the standard blading. The "mod" blades are modified only at the suction side, while the "opt" vanes have been redesigned on both the pressure and the suction side leading edge area (see Fig. 1 and Nomenclature). More details on the test rig are given by Hunziker and Gyarmathy (1993).

II.4 Boundary Conditions. The inlet boundary conditions (BC) for the different operating points are gained from time-averaged in-house measurements near the impeller exit ($r^* = 1.05$) of the centrifugal compressor test rig with the standard diffuser.

For the three-dimensional computations, the measured velocity profile and a constant static temperature are imposed at the diffuser inlet. Therefore, the total pressure profile at the inlet is a result of the computation. A uniform exit pressure is applied at the outlet. The measured velocity profiles from hub to tip for the two extreme operating points "S" and "Op3" are shown in Fig. 2. Typical of a radial impeller is the large variation of the radial velocity component from hub to shroud and, since c_u is comparably constant, this leads to an axial variation of the inlet tangential angle of more than 30 deg for all operating points. Note that for the operating points "S" and "Op1" a reverse flow near the shroud is measured and prescribed as inlet BC. As a reference the impeller tip speed is plotted in Fig. 2.

Additionally the $k-\epsilon$ turbulence model in TASCflow requires an inlet value for the turbulence intensity (Tu) and the eddy length scale (L). All TASCflow computations were run in fully turbulent mode with Tu = 5 percent and L = 0.005 m.

For the two-dimensional computations with MISES the inlet Mach number (equivalent to the three-dimensional mass-averaged value) and the inlet mean flow angle in the three-dimensional case, are set, assuming constant stagnation conditions at the inlet. As in the three-dimensional computations, the free-stream turbulence is also set to 5 percent.

For the two-dimensional TASCflow cases, the mean flow angle and the velocity magnitude (mass-average of the three-dimensional case) has been set. The mass flow/diffuser width is matched to the three-dimensional case by adjusting the outlet pressure.

III Computed and Measured Characteristic Line

The three-dimensional computed (CFD) and the measured (Exp) operating lines at the impeller rotational speeds Mu = 0.75 and Mu = 0.6 for the standard and design #1 diffuser profiles are plotted in Fig. 3. The corresponding Reynolds numbers are Re = 300,000 and Re = 230,000 for Mu = 0.75 and Mu = 0.6, respectively. For Mu = 0.75 the selected operating points are tagged with capital letters to aid in the discussion of the results: "S" indicates the onset of mild surge (corresponding to the maximum pressure rise in the stage), "Op1" produces the maximum pressure rise in the diffuser, "N" is a regime with nearly zero incidence for the diffuser, while "Op2" and "Op3" indicate operation at high mass flow rates, i.e., close to choked flow conditions. Measurements have been performed with the standard (std) and the intermediate, design #1 (mod) diffuser. The computed static pressure rise coefficient is calculated from the area-averaged pressure at inlet and outlet, while the measured value is calculated from wall pressures.

The boundary conditions at the diffuser inlet for different blades are identical for equivalent operating points, assuming that the diffuser influence on the impeller discharge velocity profile is negligible within the stable operating regime (Rodgers, 1982; Krain, 1981; Dawes, 1995). However, the inlet velocity profile varies for the different operating points. For the computations, the outlet pressure was adjusted in order to match the measured mass flow.

In general, the computed pressure rise is smaller than the measured one. However, the experimental tendencies are properly captured numerically, except maybe near the stability limit (onset of mild surge). In particular, the slopes in the characteristic as well as the relative gain in static pressure rise between the standard (std) and the design #1 (mod) diffuser are consistent with the measurements for the tendencies as well as for the order of magnitude (for example the computed increase at "Op1" is $\Delta Dp_{CFD}(Op1)$ = 4.2 percent, the measured is $\Delta Dp_{Exp}(Op1)$ = 4.8 percent). Near the stability limit the CFD results present a more pronounced difference from the experiments, which is probably due to the steady nature of the computation not being able to capture unsteady effects that occur at this operating point. The overall comparison between CFD and measurements, i.e., based on the operating line, is completed by the static pressure evolution in the diffuser channel for "Op1," see Fig. 4. While the CFD plot represents a cut at midchannel width, the measured values are based on an arithmetic average between the hub and tip static pressure taps.

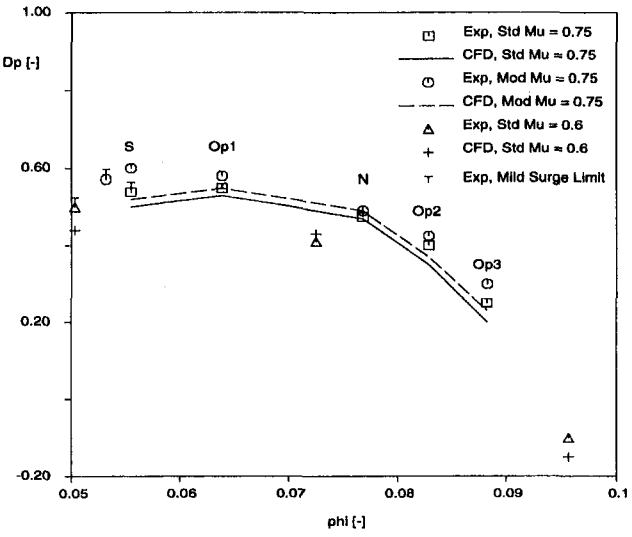

Fig. 3 Measured (Exp) and computed (CFD) characteristic lines at Mu = 0.75 ("std," "mod") and Mu = 0.6 ("std")

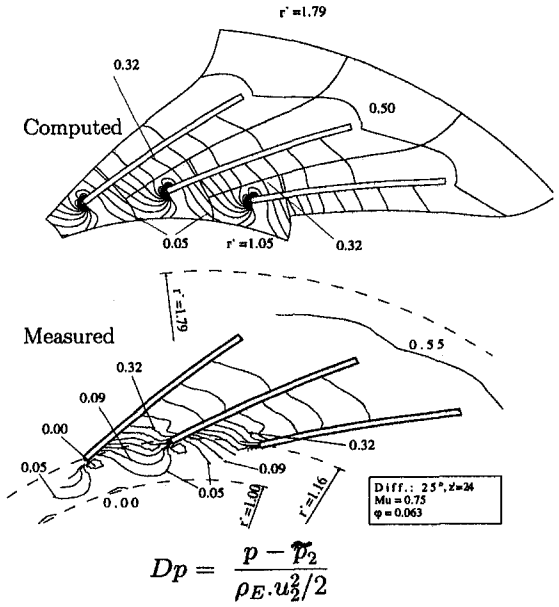

Fig. 4 Measured (mean hub–tip) and computed (midspan) pressure rise (*Dp*) contours for "Op1," *Mu* = 0.75, standard blading ($\Delta Dp = 0.046$)

As already noticed in the characteristic line, the global pressure increase is in the CFD case slightly smaller than for the measured case. Compared to the measurements the computed static pressure rise (especially the gradient) is nearly equal in the diffuser channel and exit region (i.e., from *C* to 3 as marked in Fig. 1). The lack of static pressure rise and the mismatch in contours in the CFD solution occurs essentially within the entry region and the semi-vaneless space, with an overall difference less than 6 percent.

IV Diffuser Behavior at Different Operating Points

IV.1 Comparison Two-Dimensional–Three-Dimensional. Considering the large inlet axial variations ($c_{r2}(z)$, $\alpha_2(z)$) at all flow rates, see Fig. 2, it seemed logical to assess the two-dimensional nature of the diffuser flow field, at least near nominal flow conditions before applying a two-dimensional blade-to-blade design procedure.

The pressure recovery and the total pressure loss coefficient at maximum diffuser pressure rise and nominal flow conditions are shown in Fig. 5 for two-dimensional and three-dimensional diffusers. The *Cp* and ($1 + Cp^o$) are plotted together so that between the *Cp* and Cp^o curves the normalized kinetic energy at every position can be deduced. Comparing the evolution of the two-dimensional with the three-dimensional pressure recovery coefficient a similar behavior is observed. The difference is essentially the higher recovery levels calculated for the two-dimensional diffuser.

In the Renau et al. (1967) two-dimensional diffuser charts, the standard diffuser geometry as defined from the throat to the trailing edge, i.e., station *C* to *D*, is placed in the so-called "no appreciable stall" region. The chart predicts $Cp = 0.5$ to 0.575, assuming a 5 percent blockage at the throat. The two-dimensional simulation at nominal flow conditions, where $\bar{\alpha}_2 = 26.3$ deg is close to the mean line camber angle and where a comparison with the *Cp* of two-dimensional straight diffusers can be made, gives $Cp_{CD} = 0.52$ while the three-dimensional case gives $Cp_{CD} = 0.45$.

It is interesting to note that at near nominal flow rate (case "N") the diffuser entrance area *B* to *C* does not raise the static pressure at all. This suggests that best performance is obtained at a flow rate slightly lower than at "N."

The comparison of the two-dimensional and the three-dimensional loss coefficient reveals the amount of loss produced by the mixing of the inlet shear flow, the diffuser blade itself, and the endwalls. Since the three-dimensional cases take the endwall boundary layers into account, the Cp^o slope along the diffuser is steeper than that for the two-dimensional cases. In this low-aspect-ratio diffuser the endwall losses depend to some extent on the operating point, but typically account for about half of the total losses. "Op1" has also been computed with a constant inlet angle and velocity distribution along the diffuser width, i.e., no inlet shear (see case "Op1_std_3d_co" in Fig. 5), so that this effect can be separated from the endwall effects. Compared to the full three-dimensional case, i.e., "Op1_std_3d," this case exhibits the same *Cp* distribution but a 15 percent reduction in normalized total pressure loss. It is interesting to note that up to the throat area (station *C*) about half of the diffuser losses have already been produced independently of the two-dimensional or three-dimensional nature of the flow. In particular, loss production is increased in the leading edge region (stations *B* and *C*), indicating a need for a blade redesign in this area. For example design #1 was carried out only on the suction side, to reduce the leading edge losses and increase the diffuser pressure recovery, see "Op1_mod_2d" in Fig. 5. The two-dimensional computations with the "mod" diffuser show that the expected performance improvement with lower loss levels, better static pressure recovery, and less exit kinetic energy compared to the standard design is captured.

IV.2 Subcomponents Performance. A comparison between the three-dimensional computations of the standard geometry and the design #2 for *Cp* and Cp^o along the diffuser is presented in Fig. 6 for three operating points, ranging from the stability limit ("S") to near choke conditions ("Op3"). The performance improvement as well as the loss reduction for the new geometry are confirmed over the whole characteristic. Consequently, the residual kinetic energy at the diffuser outlet is always lower for "opt" than for "std" blading.

Vaneless Space (2-B): In this region all the six curves are almost equivalent, i.e., the pressure recovery process in the vaneless space does not depend on the velocity magnitude, on

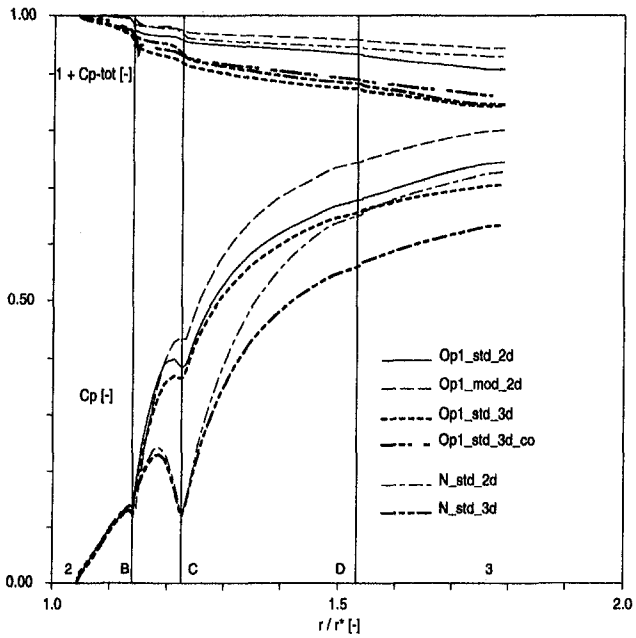

Fig. 5 Pressure recovery and total pressure loss coefficient along the diffuser for two-dimensional and three-dimensional cases at "Op1" and "N" (*Mu* = 0.75). Note that the pressure recovery for "Op1_std_3d" and "Op1_std_3d_co" overlap.

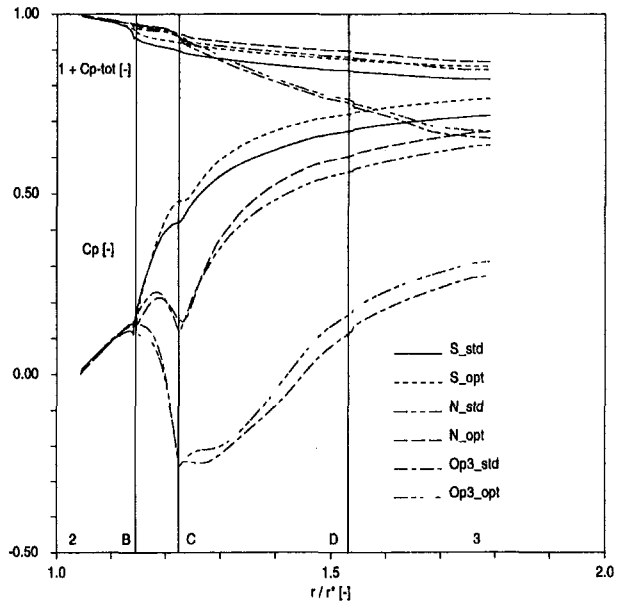

Fig. 6 Three-dimensional computations of the pressure recovery and total pressure loss coefficients along the diffuser for "std" and "opt" at "S," "N" and "Op3" (Mu = 0.75)

the mean flow angle and on the geometry of the following vanes.

Semi-vaneless Space (B-C): In this part of the diffuser the pressure recovery is characterized by the mean flow angle for the global behavior and by the blade shape. In fact, depending on the mean flow angle and on the mass flow, the pressure will monotonously rise (case 'S', $\bar{\alpha}_2$ = 19.0 deg), rise and then decrease toward the throat (case 'N', $\bar{\alpha}_2$ = 26.3 deg) or decrease (case "Op3," $\bar{\alpha}_2$ = 31.2 deg). The state of the flow entering the diffuser channel is influenced by the nose geometry, too. This "preprocessing" of the flow before diffusion in the fully vaned diffuser part seems to be important, considering the difference in the pressure recovery levels reached at the diffuser exit.

At the throat, the pressure recovery coefficient already presents better results for the optimized vane. It is interesting to note that the acceleration in the "Op3" case even hinders the loss production resulting in the lowest total pressure loss until C.

Vaned Diffuser (C–D): For the operating points "S" and "N" the diffuser channel shows a similar behavior. There is a monotonic static pressure increase from the throat to the trailing edge with the initial slope of Cp characterized by the local effects on the flow in the semi-vaneless diffuser. The improvement in static pressure recovery between the "opt" and "std" profiles is $\Delta Cp_{CD} = 0.05$, which represents more than 10 percent of the vaned diffuser pressure rise at "N" and "Op3." As it will be seen later in the next section the better static pressure recovery factor found for design #2 is closely related to the uniformity of the flow conditions found at the throat. For example, the recirculation zones in the diffuser channels are smaller in the "opt" case (Figs. 12 and 13).

At "Op3" the pressure increase begins later, downstream of the throat. The losses present a steep slope, which may indicate that in the first third of the channel there is only dissipation of kinetic energy without pressure gain (the Cp slope in this region is almost zero).

Vaneless Space (D-3): In this region the pressure increase does not present particular phenomena. The larger the available kinetic energy, the better is the recovery in static pressure, as in a usual two-dimensional diffuser for incompressible flow.

The analysis of the relative static pressure rise in the diffuser as seen in Fig. 7 for three operating points shows where, compared to the total rise in static pressure, the diffuser converts the kinetic energy in pressure. This is not exactly the same information as the one deduced from the Cp-Cp^o diagram, since here the rise in static pressure is normalized by a quantity $(\rho_E \cdot u_2^2/2)$, which is constant and does not depend on the operating point. The major difference between the standard geometry and the design #2 lies in the semi-vaneless space $(B–C)$, where the "opt" vanes always produce a larger increase in pressure.

IV.3 Effects of Redesign on the Characteristic Line. In order to avoid instability phenomena during operation, it is customary to define a surge margin. This is usually defined as the mass flow for which a percentage of the maximum pressure rise in the stage is obtained. By applying this idea to the diffuser, the stability behavior of the modified vanes can be compared to the standard ones. Figure 7 shows therefore a blow-up of the computed characteristic line Mu = 0.75 at low flow rates and for the three designs. The surge margin was set for instance to achieve 95 percent of the maximum pressure rise. Thus, the flatter the Cp slope to the right of "Op1" (maximum pressure rise operating point) is, the larger the distance from "S," i.e., from the surge line, obtained and the better the diffuser performs at part load conditions. A flatter slope of the characteristic line to the right of "Op1" also indicates that the difference between the "95 percent $Dp_$max" mass flow ($\varphi_{95\%Dp\_max}$) and the "surge" mass flow (φ_S), as defined in Fig. 7, is increased. In order to keep the same surge margin mass flow rate, i.e., $\Delta\varphi = \varphi_{95\%Dp\_max} - \varphi_S$, the surge margin itself can be shifted to the left, presenting then an overall wider operating range. According to the surge margin criterion, the lowest reachable mass flow rate during save operation is therefore lower than the original one.

Compared to the standard design, the first geometry modification ("mod") produces a pressure increase in the diffuser especially at low flow rates (6.3 percent at "S" and 5.5 percent at "Op1") with a flatter slope to the left of the maximum rise in static pressure. Since only the suction side has been modified, the relative improvement of operating points with $\bar{\alpha}_2$ higher than the mean line camber angle ("N," "Op2," and "Op3")

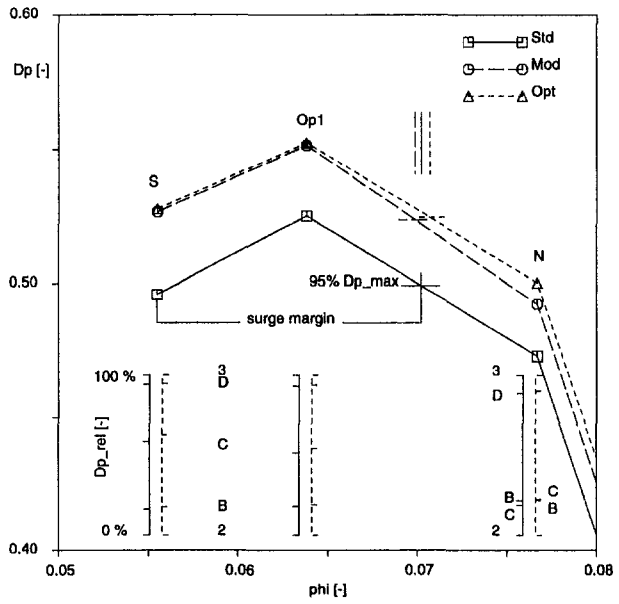

Fig. 7 Computed diffuser characteristic for the three vane profiles (curves) and component breakdown of the pressure rise for the different operating points ("S," "Op1," "N" at Mu = 0.75)

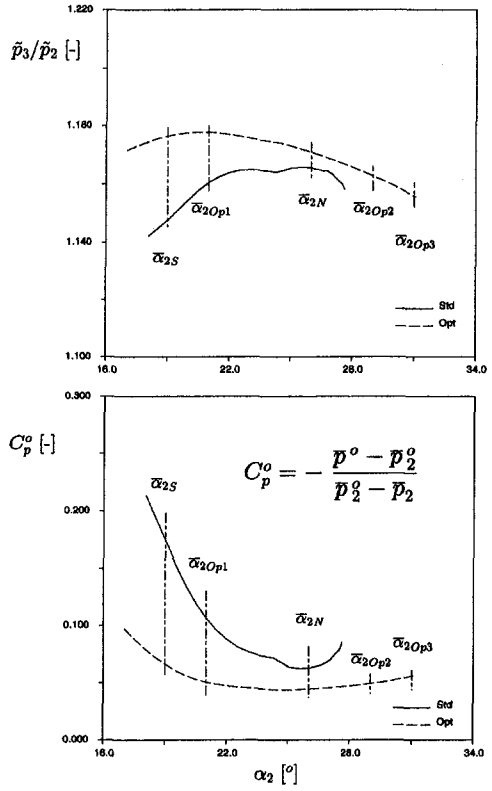

Fig. 8 Two-dimensional comparison of "std" and "opt" profiles: MISES "polars" for pressure ratio and total pressure losses

is not as high as for "Op1"; the "mod" slope to the right of "Op1" even gets steeper. Based on this criterion, this would actually mean a reduction in surge margin. However, the measurements shown in Fig. 3 clearly indicate that for this modified diffuser the instability (mild surge) is reached at a lower mass flow rate than that for the standard geometry. Hence the goals of the design with a larger gain in pressure and a lower instability-onset flow rate (thus increase of surge margin) are reached even if the slope between "Op1" and "N" is steeper.

Through the second design phase ("opt" diffuser), which includes an additional modification of the pressure side, the pressure rise at the nominal flow conditions "N" is increased by 5.5 percent compared to "std." This induces a flatter characteristic line on both sides of the operating point producing the maximum pressure rise, hence a wider operating point producing the maximum pressure rise, hence a wider operating range as discussed in the previous section. Measurements with this geometry have not been done yet, so that a direct comparison can't be made. Anyway, since the computed results at "S" and "Op1" for the design #2 ("opt") are almost equivalent to those for "mod," the stability limit should also be reached at a lower mass flow rate than φ_{S_std}. Combined with the flattening of the slope to the right of "Op1," this diffuser should have a wider operating range than the original one.

V Flow Structure Analysis

V.1 MISES Results. The two-dimensional direct and inverse-design software package MISES has been applied to analyze the effects of modifying the nose region of the standard diffuser blading, which has a semi-circle leading edge. In an effort to improve the diffuser performance at low and high mass flow rates, a "polar" was generated in order to "optimize" the geometry for angles higher and lower than the mean line camber angle (see Fig. 8).

Two approaches can be followed in the "optimization" process, both of them leading to the same optimization criterion. The first approach is based on the mean inlet flow angle (two-dimensional), which essentially controls the operating points, since the mean inlet Mach number variation for the different operating points does not change significantly. This leads to searching for a leading edge geometry, which has low incidence sensitivity for the wider possible angle range.

The second approach is based on the observation that every operating point presents at the inlet a shear flow with a large angle variation from hub to tip (at least 30 deg, three-dimensional effect). Therefore, in reducing the *LE* sensitivity to shear, the same optimization criterion can be applied as previously. These considerations seem to indicate that the improvement that could result from a two-dimensional redesign at one given operating point should actually produce an overall improvement in the characteristic.

Additionally the similarity in the two-dimensional and three-dimensional pressure recovery process, as seen in Fig. 5, seems to justify a two-dimensional redesign.

The total pressure loss coefficients and the ratios of exit to inlet static pressure as predicted by MISES are given in Fig. 8 as a function of the inlet flow angle. Clearly the "opt" design presents a better pressure rise characteristic and lower loss levels at all operating conditions. Also the range for which (almost) smooth flow conditions occur, i.e., no massive separation is present, is extended by 5 deg. Beyond this range the TASCflow and MISES simulations indicate that the two-dimensional flow separates from the leading edge and that the separated region covers almost the whole diffuser channel from blade-to-blade. Contrarily the three-dimensional flow remains attached longer because of the secondary flow effects. For the maximum rise in pressure and the nominal flow conditions, i.e., case "Op1" with $\bar{\alpha}_2 = 21.0$ deg and case "N" with $\bar{\alpha}_2 = 26.3$ deg, the MISES pressure recovery and loss predictions compare very well with the two-dimensional computations of TASCflow, see Figs. 5 and 8. Note that MISES predicts transition from laminar to turbulent flow in the leading edge area, confirming the validity of using a fully turbulent viscous model in the TASCflow computations.

The static pressure coefficients on the blade surface for the "std" and the "opt" design as predicted by MISES are shown in Fig. 9 for the "Op1" operating condition. The major differences are the low-pressure spikes at the leading edge. In the standard case there is a strong acceleration on both sides (even on the PS the pressure is lower than the free-stream value) immediately followed by a strong deceleration. The skin friction coefficient plot shows the high loss production in this region, see Fig. 10. On both sides there is a small separation bubble. This generates a large boundary layer on the suction side, which separates near the trailing edge (about 80 percent chord).

Geometry #2 ("opt") presents a different character. The pressure gradients are smoother and therefore there is no separation at the leading edge. The boundary layer is thinner as in the standard case, even though on the suction side a separation occurs at the same downstream location as for the standard profile. Note that the leading edge redesign reduces the drag over almost the entire blade pressure surface (see Fig. 10).

V.2 Secondary Flow Pattern. The secondary flow in an adiabatic and nonrotating bent duct depends on the presence of stagnation pressure gradients and on the development of the boundary layer as discussed by several authors (see for example Hawthorne, 1974). In the present diffuser case there is a total pressure gradient in the axial direction, which is essentially produced from the axial distribution of the inlet velocity (see Fig. 2) since the static pressure in axial direction at the diffuser inlet is almost constant. Consequently, a secondary flow, which has its origin from the inlet shear, is expected together with the

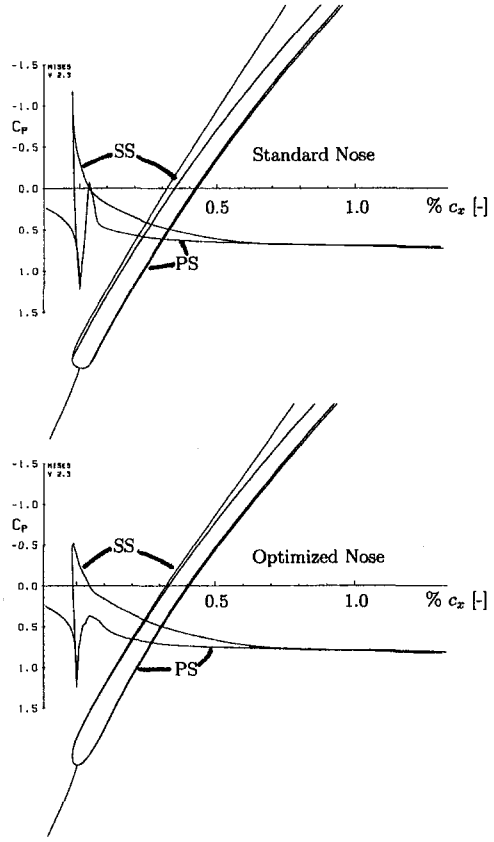

Fig. 9 MISES pressure rise with boundary layer plot for "std" and "opt" designs at $\bar{\alpha}_2$ = 21.0 deg ('Op1' 2D, *Mu* = 0.75). Note that in the (m' – θ) computational plane of MISES pressure and suction side are reversed as compared to the physical plane (x, y).

roll-up of the endwall boundary layers into horseshoe vortices ahead of the cylindrical leading edge.

At the near-surge operating point, the crossflow velocity vectors on a blade-to-blade surface cut behind the diffuser throat are shown in Fig. 11 together with absolute velocity contours. The cutting surface is composed of two grid planes, one perpendicular to the *PS* and the other almost perpendicular to the *SS*. The common line of the two planes is plotted. Note that due to the different orientation of these two surfaces, the projection of the velocity vectors along the intersection line produces two distinguished vectors.

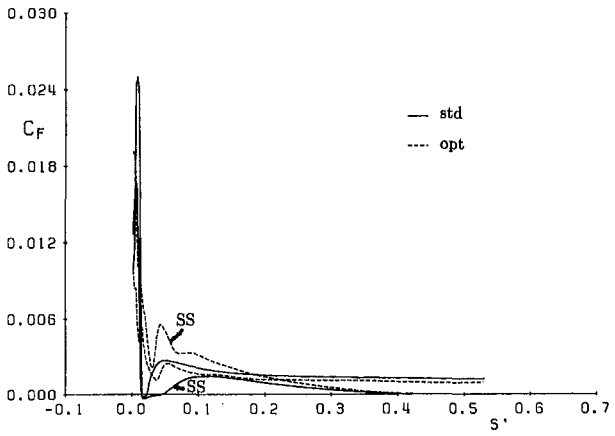

Fig. 10 MISES skin friction coefficient for "std" and "opt" designs at $\bar{\alpha}_2$ = 21.0 deg ("Op1" 2D, *Mu* = 0.75)

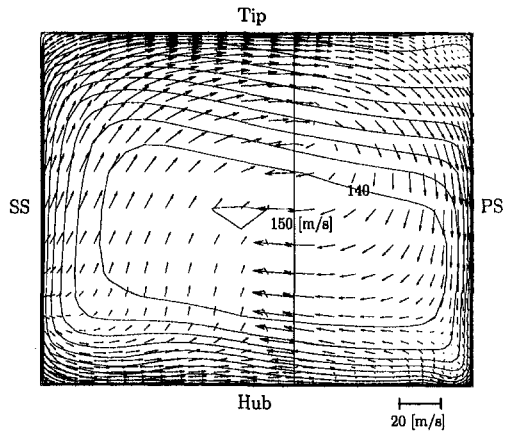

Fig. 11 Velocity vectors projection on a surface behind throat ($\frac{1}{10}$ chord) at operating point "S" (*Mu* = 0.75) with absolute speed contours; standard blading

The hub-to-tip variation of the absolute velocity closely corresponds to the axial variation of the velocity profile at the impeller outlet. A large passage vortex is seen to occupy almost the entire cross section. The flow next to the endwalls migrates toward the pressure side. The vane boundary layers are instead driven by the passage vortex, showing therefore opposite migration, i.e., from hub to tip on the *SS* and from tip to hub on the *PS*.

In the corners on the pressure side there are horseshoe vortices, while on the suction side the horseshoe vortices have already been caught in the passage vortex. The absolute velocity contours mark the core-flow position. The distance between the core-flow center and the suction side remains almost constant along the diffuser channel, while the passage vortex moves towards the pressure side.

Backflow regions have been detected in the diffuser at all mass flow rates. Even though their extent and intensity depends on the operating point and on the vane geometry, some general features can be extracted from the simulations.

From "Op1" to "S" the impeller discharge, hence diffuser inlet, presents regions of inward flow (i.e., $c_r < 0$) near the shroud due to impeller secondary flow (streamline curvature and tip clearance effects), see Figs. 2 and 12. They extend for the standard diffuser over parts of the vaneless and semi-vane-

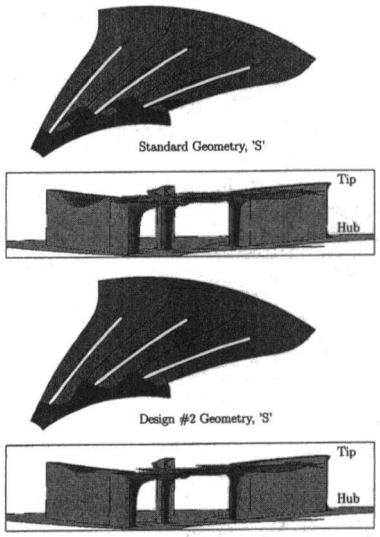

Fig. 12 Inward flow ($c_r < 0$) zones at low flow rate ("S") for "std" and "opt" design

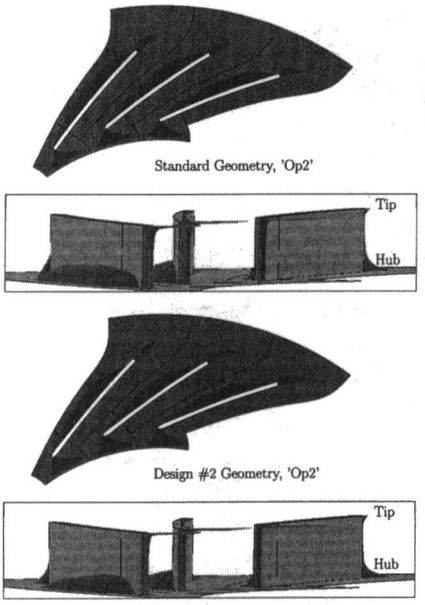

Fig. 13 Inward flow ($c_r < 0$) zones at high flow rate ("Op2") for "std" and "opt" design

less diffuser space. The diffuser design #2 (''opt'') almost eliminates the backflow region in the near-suction-side part of the semi-vaneless space.

The backflow pocket in the channel corner as seen in Fig. 12 near the casing on the pressure side is formed by the inlet layer of low-momentum fluid (c_r is positive but small, see Fig. 2), which is swept into the corner by the passage vortex until it cannot sustain the adverse pressure gradient. By inducing a more uniform flow entering the diffuser channel, design #2 also reduces this backflow pocket.

Contrarily, at the higher mass flow rates (operating points ''N,'' ''Op2,'' Op3''), the backflow region on the pressure side appears near and on the hub, and is generated by another mechanism. The corner recirculation begins near the leading edge and is due to the high incidence, i.e., large flow angle near the hub (see Figs. 2 and 13). It is interesting to note that not only the volume of the pocket of inward flowing fluid, but also the mass flow in these regions, is reduced by the ''opt'' geometry.

VI Summary and Conclusions

The flow field in a subsonic vaned radial diffuser of a single-stage centrifugal compressor has been numerically investigated. Two-dimensional and three-dimensional steady-state Navier–Stokes solutions for three different leading edge vane geometries were presented and discussed. The standard circular-arc vane was modified at the leading edge using the two-dimensional analysis and inverse-design program MISES, by retaining the overall throughflow and prismatic characteristics of the diffuser.

The extension of the stable operating range, the improvement in pressure rise, and the reduced level of total pressure losses predicted by MISES were confirmed by the three-dimensional Navier–Stokes simulations as well as by measurements. Regions of recirculated flow were observed at all flow rates. The near casing backflow is directly produced by the impeller discharge, while for higher mass flow rates the detached flow computed at the hub on the blade pressure side is induced by a high-incidence flow angle.

The flow field performance analysis for the diffuser subcomponents and the observed secondary flow pattern indicate that the two-dimensional leading edge redesign reprocesses the flow in the semi-vaneless space. In particular a more uniform state is reached at the throat when compared to the conventional blading, hence allowing an improved pressure recovery in the vaned diffuser part. Consequently, the improved diffuser and stage stability limits, i.e., the extension of the stable operating range with the locally redesigned blade, and gain in static pressure measured at low flow rates seem to correlate with the magnitude and the extent of the secondary flow.

The analysis of the effects of redesign on the operating line suggests that the suction side leading edge redesign essentially affects the gain in static pressure at low flow rates, while the advantages of a pressure side redesign are more pronounced at higher flow rates.

Acknowledgments

The authors would like to thank Prof. M. Drela, MIT, for providing the design program MISES as well as for the scientific support. The Swiss Kommission für die Förderung der Wissenschaftlichen Forschung (KWF) is acknowledged for its financial support. Sulzer Turbo, ABB Turbo Systems, and Sulzer Innotec are acknowledged as well for their cooperation in the program.

References

ASC, 1995, ''TASCflow Documentation Version 2.4,'' Advanced Scientific Computing, Ltd, Waterloo, Ontario, Canada.

Clements, W. W., and Artt, D. W., 1989, ''The influence of the diffuser vane leading edge geometry on the performance of the centrifugal compressor,'' ASME Paper No. 89-GT-163.

Dawes, W. N., 1995, ''A simulation of the unsteady interaction of a centrifugal impeller with its vaned diffuser: flows analysis,'' ASME JOURNAL OF TURBOMACHINERY, Vol. 117, pp. 213–222.

Drela M., and Youngren H., 1995, ''A User's guide to MISES 2.3,'' MIT Computational Aerospace Science Laboratory.

Hawthorne, W. R., 1974, ''Secondary Vorticity in Stratified Compressible Fluids in Rotating Systems,'' Technical Rpt. CUED/A-Turbo/TR 63, Cambridge University, United Kingdom.

Hunziker, R., and Gyarmathy, G., 1993, ''The operational stability of a centrifugal compressor and its dependence on the characteristic of the subcomponents,'' ASME Paper No. 93-GT-284.

Jansen M., and Rautenberg, M., 1982, ''Design and investigations of a three dimensionally twisted diffuser for centrifugal compressors,'' ASME Paper No. 82-GT-102.

Kämmer, N., and Rautenberger, M., 1986, ''A distinction between different types of stall in a centrifugal compressor stage,'' ASME *Journal of Engineering for Gas Turbines and Power,* Vol. 108, pp. 83–92.

Krain, H., 1981, ''A study on centrifugal impeller and diffuser flow,'' ASME *Journal of Engineering for Power,* Vol. 103, pp. 688–697.

Renau, L. R., Johnston, J. P., and Kline, S. J., 1967, ''Performance and design of straight, two-dimensional diffusers,'' ASME *Journal of Basic Engineering,* Vol. 89, pp. 141–150.

Rodgers, C., 1982, ''The performance of centrifugal compressor channel diffusers,'' ASME Paper No. 82-GT-10.

Swirl Brake Effect on the Rotordynamic Stability of a Shrouded Impeller

E. A. Baskharone
Associate Professor,
Department of Mechanical Engineering,
Texas A&M University,
College Station, TX 77843
Mem. ASME

The swirling motion of the shroud-to-housing leakage flow in pumps is known to have an adverse impact on the impeller rotordynamic stability. Swirl brakes, under such circumstances, would enhance the stability margin by reducing or, ideally, eliminating, the prerotation at the leakage passage inlet station. The numerical analysis outlined in this paper provides a quantitative means of predicting the effectiveness of such devices. The computed results also illustrate the mechanism with which the fluid/rotor interaction, with the aid of a typical brake, is altered towards relative overall rotordynamic stability. This is done through a comparative examination of the pressure perturbation distribution over the shroud surface for a wide range of backward and forward impeller-whirl frequencies. The conclusions in this study are consistent with recent experimental findings and have important design implications.

Introduction

Rotordynamic stability of fluid-encompassed rotors has increasingly become one of the foremost issues, particularly in turbomachinery applications. Of these, the topic of impeller vibration in centrifugal pumps has exclusively gained a special momentum due to its relevance to the Space Shuttle Main Engine turbopumps (Childs, 1989; Childs and Moyer, 1985; Childs et al., 1991). To date, the single most established, yet controversial, parameter affecting the rotordynamic stability of shrouded impellers is the preswirl ratio (tangential velocity/impeller-tip-speed ratio) at the leakage-passage inlet station. According to Childs (1989), values of this ratio in excess of 0.5 would cause abrupt resonance-like fluctuations of the fluid-induced forces within a narrow positive whirl frequency range. This analytical result was later dismissed by Guinzberg et al. (1993) in a comprehensive experimental study where the preswirl velocity was elevated to as much as twice the impeller tip speed.

Total elimination of the secondary flow preswirl in shrouded-impeller turbomachines through a cascade of stationary guide vanes (Fig. 1) is, perhaps, unthinkable. This, in part, is a result of design constraints on such variables as the blades' radial chord, with which a more acceptable solidity ratio would require an unrealistically high blade count. Recalling that any off-design operation mode would more than likely alter the impeller-exit flow angle, it would be unwise to ignore the consequences of what may become excessively large incidence angles, as these deswirl vanes are approached (Fig. 1). Aside from causing its own performance degradation, the premature boundary-layer separation it might cause, coupled with the adverse streamwise pressure gradient, may lead to a cascade-exit flow direction that is virtually unpredictable. The so-called swirl brakes, such as that in Fig. 1, are often designed with the modest intent of reducing the swirl component of the leakage flow stream in the secondary passage. Of these rotordynamic enhancement devices, the two configurations tested by Childs et al. (1991) were reportedly effective. Favoring the vaned-stator swirl brake configuration, it is important to point out that Childs' test results exclusively apply to the design-point flow angle and might have been drastically different had there been any appreciable fluid/vane incidence angle.

The current numerical study aids in understanding the mechanism with which a well-designed swirl brake can alter the rotordynamic behavior of a shrouded pump impeller. Under investigation is a commercial pump stage with a relatively high head capacity resulting in a large swirl velocity component at the impeller discharge radius and, consequently, the leakage-passage inlet station (Fig. 1). Extensively tested and rotor-dynamically analyzed, the force coefficients are computed for a modified stage design, now featuring a swirl brake. The brake is constructed in such a way as to extract the circumferential velocity component slightly upstream from the leakage-flow inlet location. A thorough examination is then made to highlight the manner in which the fluid reaction forces, arising from a cylindrical whirl excitation, are altered in the presence of this added pump component. Reference, in this case, is made to the shroud-surface pressure perturbation redistribution being the origin of the rotordynamic gain.

Computational Development

A finite-element-based perturbation model, initially devised by the author and Hensel for simple annular seals (Baskharone and Hensel, 1991a, b), was upgraded and applied to the existing and modified pump configurations. In both cases, the centered-impeller flow field, throughout the computational domain in Fig. 1, was first obtained. This so-called "zeroth-order" flow solution was then used as input to the perturbation analysis of the pump stage. Of all perturbations in the flow thermophysical properties, the shroud-surface pressure perturbations are then isolated and integrated to find the fluid-exerted forces for each impeller whirl frequency under consideration. These fluid/structure interaction forces are finally processed as stiffness, damping, and added-mass (or inertia) contributors to the impeller eccentric motion.

The flow-governing equations and finite-element formulation of the unperturbed flow field are essentially those of Baskharone and Hensel (1993) for an axisymmetric flow pattern. Obviously, the boundary conditions associated with the original and the swirl-brake-equipped pump configurations (Fig. 2) are different, particularly at the impeller discharge station, as far as the flow component of angular motion is concerned.

The mathematical foundation of the rotordynamic model was fully documented by Baskharone and Hensel (1991a). Referring to Fig. 2, an impeller excitation in the form of a whirling motion around the housing centerline is considered. In this case, the lateral "virtual" eccentricity is perceived to cause infinitesimally small distortions in the twenty-noded isoparametric elements in the shroud-to-housing clearance gap. In a perturbation

Contributed by the Turbomachinery Division for publication in the JOURNAL OF TURBOMACHINERY. Manuscript received by the Turbomachinery Division October 25, 1995. Associate Technical Editor: R. A. Delaney.

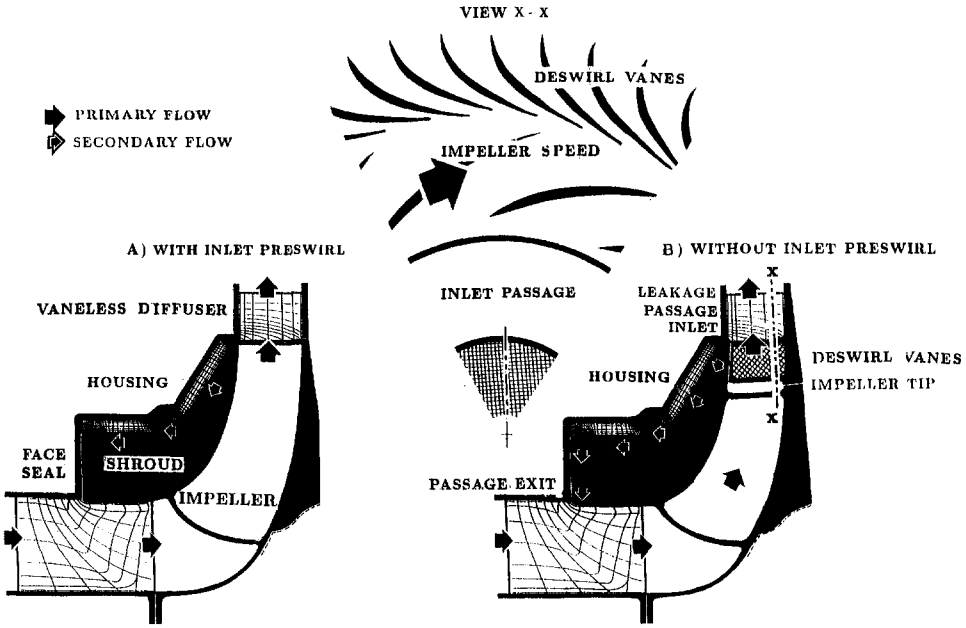

Fig. 1 Finite-element discretization model for the centered-impeller operation mode

approach, the differential changes in the flow thermophysical properties are subsequently computed using the above-referenced perturbation approach. Of these, the perturbations in the shroud-surface pressure magnitudes are properly integrated to find the differential changes in the fluid/shroud interaction forces, which may categorically be restoring or aggravating. In applying this procedure, the centered-impeller flow field is first obtained, then used for each of the existing and modified pump configurations in Fig. 1. Clearly the major difference between these two fields is a direct result of the swirl velocity profile at the secondary-passage inlet station being that of the boundary-layer type with zero core magnitude, on one hand, and a superimposed prerotation value, on the other. It may rightfully seem that such a difference is localized, considering the rather small clearance gap width at this location. However, it is this slight difference in boundary conditions that is a major issue to the impeller rotordynamic characteristics.

Results and Discussion

Figures 3, 4, and 5 illustrate the flow structure in the pump leakage passage with and without the swirl brake. First, the

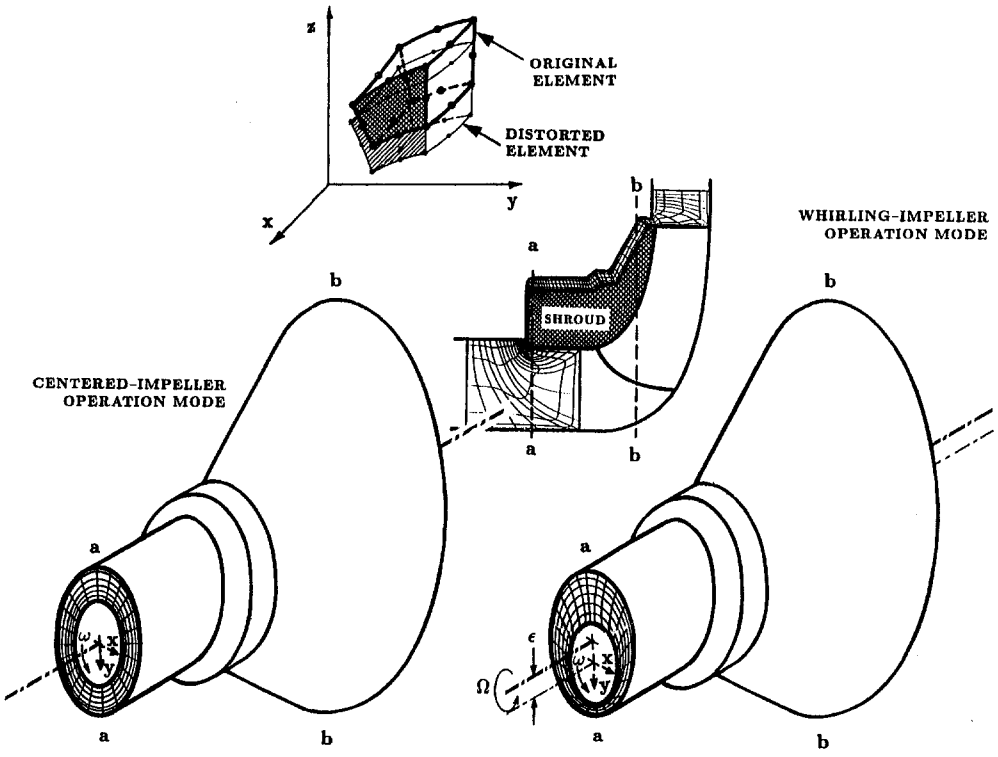

Fig. 2 Distortion of the shroud-to-housing finite element assembly due to the impeller whirl

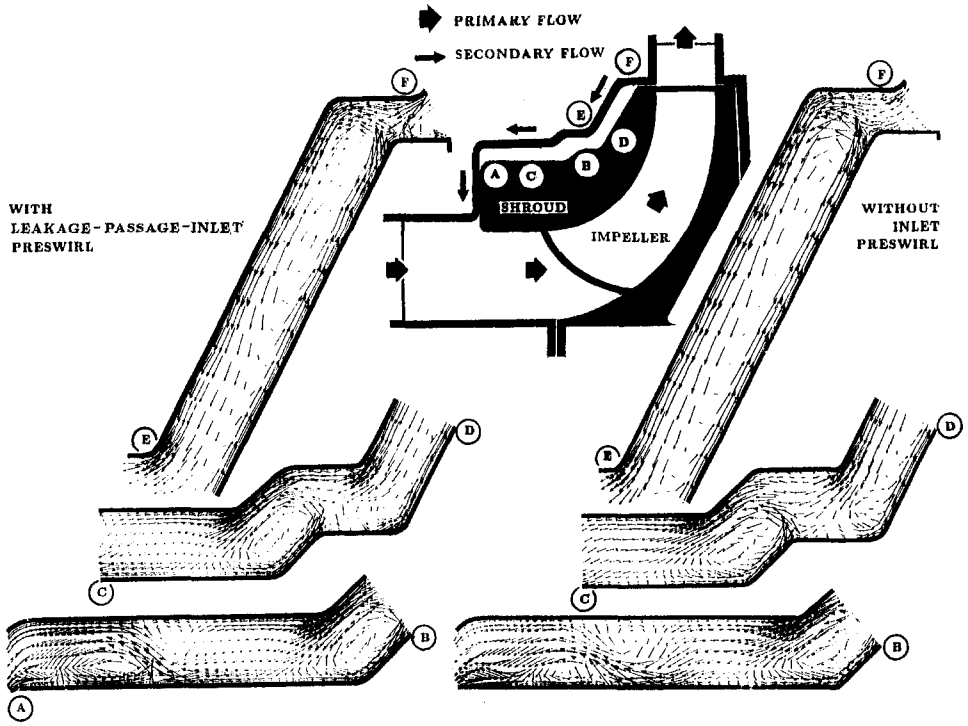

Fig. 3 Vector plot of the meridional velocity component for the centered-impeller operation mode

meridional and tangential velocity components are shown in Figs. 3 and 4, respectively. As was initially expected, distribution of the meridional component of the fluid motion is similar for the two pump configurations, including some isolated, and other massive recirculation zones in the entire secondary passage. These zones are the outcome of two opposing factors: namely, the centrifugal force near the shroud surface and the "unfavorable" streamwise static pressure differential across the entire passage. Also featured in the fluid meridional motion is the vortex breakdown in the axial passage segment leading to the face seal. The tangential velocity component, on the other hand, is markedly dissimilar in the entrance region of the secondary passage for the reasons stated earlier. This is also the impression one gets by examining the static pressure contours in Fig. 5, where the largest pressure decline is notably confined to the face seal itself. Note that the pressure magnitudes in Fig. 5 are nondimensionalized as follows:

$$\bar{p} = \frac{(p - p_i)}{\rho U_t^2}$$

where p and p_i are the local and stage-inlet static pressures, respectively, ρ is the fluid density, and U_t is the impeller tip speed. Further quantification of the difference between the two sets of results is shown in Fig. 6, and is in the form of nondimensional swirl velocity profiles in the shroud-to-housing gap at the secondary-passage inlet station. In interpreting Fig. 6, note that this velocity component is dictated not only by the impeller-

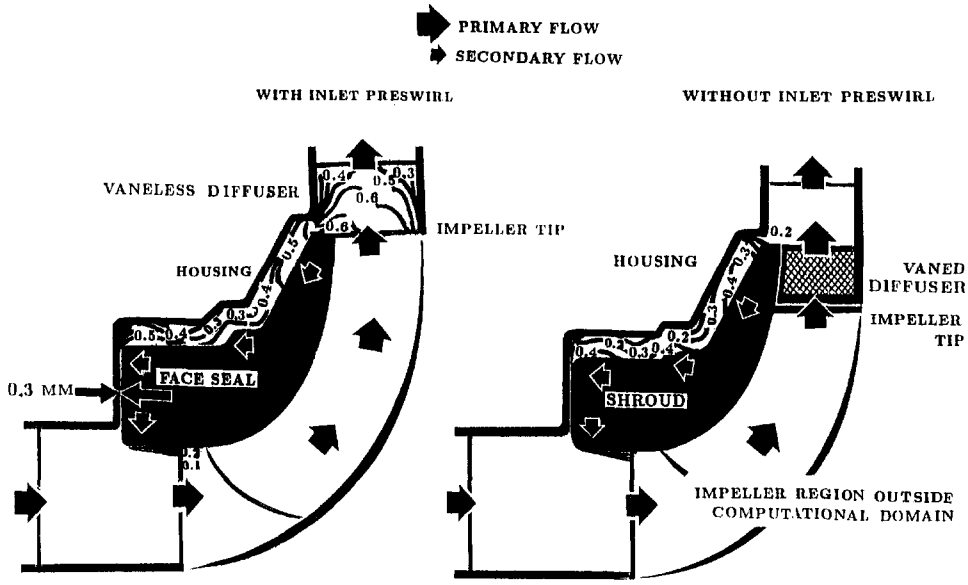

Fig. 4 Contours of the nondimensional swirl velocity

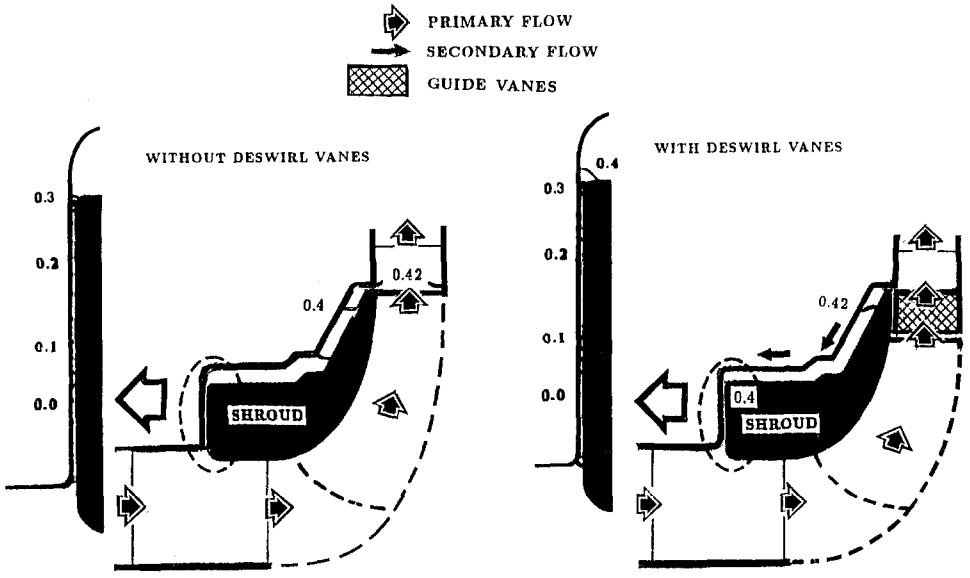

Fig. 5 Comparison of the pressure field

tip velocity triangle in the primary passage, but also by the manner in which the primary and secondary passages are naturally connected. Noteworthy in Fig. 6 is also the boundary layer-like profile near the shroud surface for both pump configurations.

Figure 7 shows the fluid-induced force components for the modified pump configuration over a range of whirl frequencies between −125 and +125 percent of the impeller speed. Reproduced on the same figure are the original-design computed forces and experimental data, both corresponding to the design-point value of the leakage-passage inlet swirl. The first impression one gets by examining the tangential-force curve in this figure is that the no-preswirl pump operation is comparatively more stable (as anticipated), judging by the smaller range of positive whirl frequency within which the tangential force is positive.

The impeller rotordynamic coefficients, corresponding to the zero leakage-passage preswirl, are compared to their numerical and experimental counterparts, *associated with the design-point preswirl, in Table 1.* All three sets of data in this table were obtained through a quadratic least-squares fit of the fluid-exerted forces, as outlined by Baskharone and Hensel (1991). Referring to the angular-motion-contributing coefficients in this table, it is clear that the zero leakage-passage preswirl gives rise to a more stable impeller operation as well. While the direct damping coefficient "C" remains almost unaffected, the cross-cou-

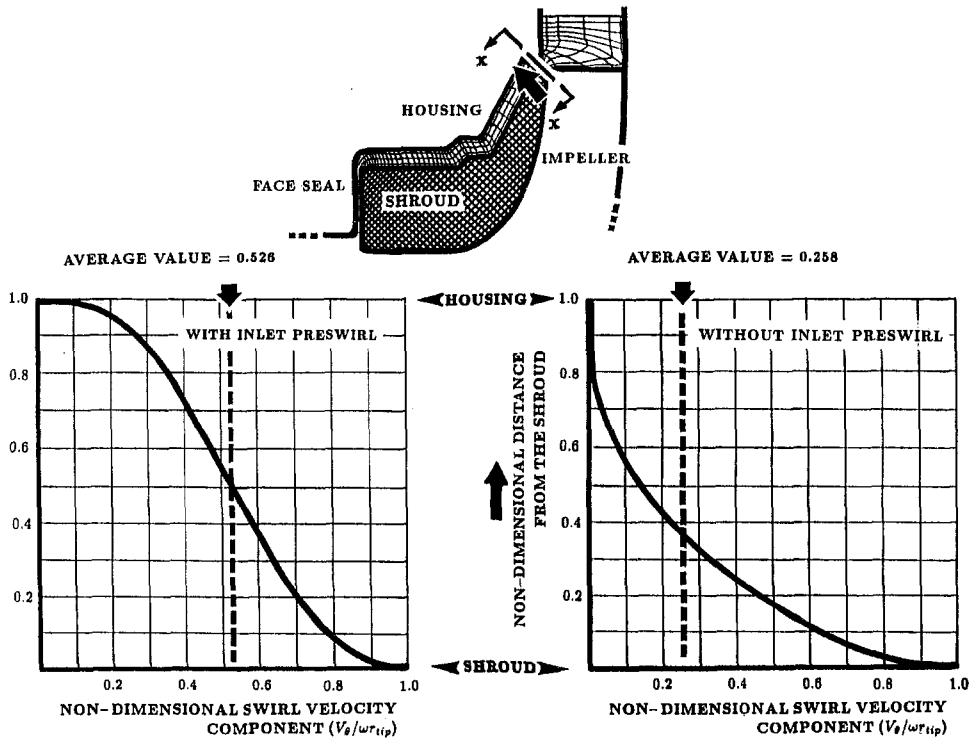

Fig. 6 Profile of the nondimensional swirl velocity near the leakage-passage inlet station

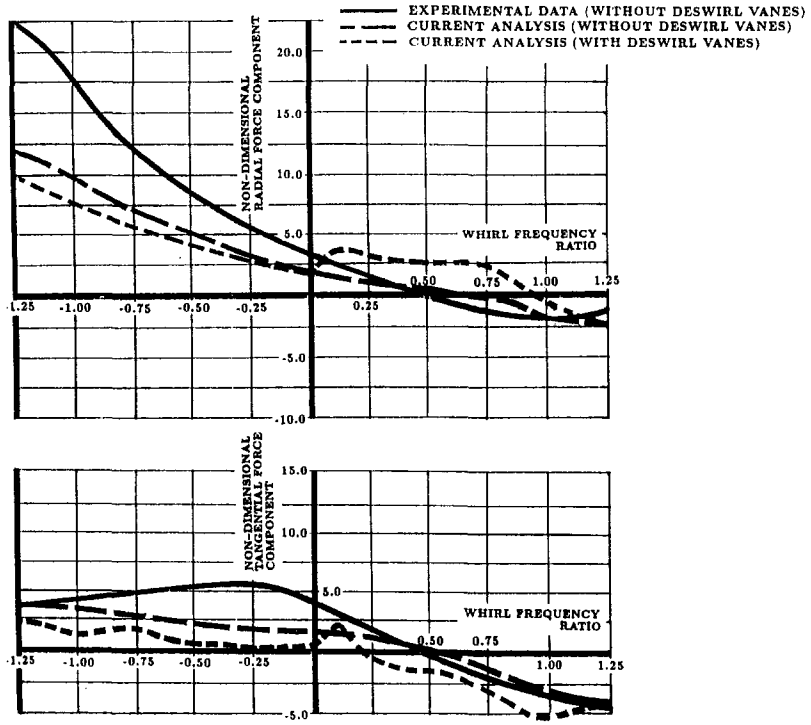

Fig. 7 Comparison of the fluid exerted forces with and without deswirl vanes

Table 1 Comparison of the impeller rotordynamic coefficients with experimental data

	BOLLETER ET AL. (1989)	CURRENT PERTURBATION MODEL	
		WITHOUT DESWIRL VANES	WITH DESWIRL VANES
K (MN/m)	-0.500	-0.268	-0.399
k (MN/m)	0.600	0.165	-0.045
C (Ns/m)	2570	1640.8	1456.8
c (Ns/m)	7610	2916.3	2272.8
M (kg)	29.6	5.034	2.299
m (kg)	10.800	3.035	2.053

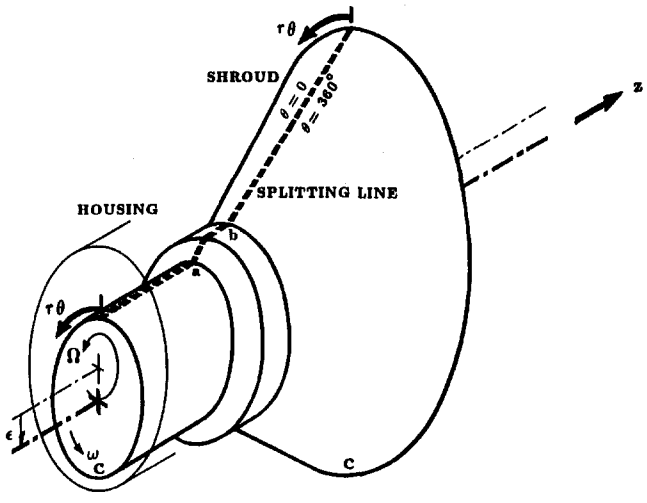

Fig. 8 Splitting and unwrapping the shroud surface

pled stiffness coefficient "k" becomes negative, thus stabilizing, in the zero-preswirl operation mode.

In order to understand the origin of dissimilarities in the rotordynamic forces, a "focused-purpose" post-processor was erected in order to, in effect, "unwrap" the shroud surface in the manner illustrated in Fig. 8. The outcome, in this case, is a display of the distribution of pressure perturbations (i.e., $\partial p/\partial \epsilon$) over the "unwrapped" surface, where "ϵ" is the impeller eccentricity. The main objective here was to see whether there is any substantial redistribution of the pressure perturbation contours as the impeller shifts from slightly negative to slightly positive whirl frequencies.

Figure 9 shows the pressure perturbation contours in the selected whirl-frequency range. For backward whirl (first two whirl frequency ratios), the figure shows that the zero-preswirl pressure perturbations peak is, more or less, at the minimum-clearance position (circumferential position $c-c$ in Fig. 8). The figure also shows that the design-point-preswirl pump operation gives rise to pressure perturbation peaks, which are clearly ahead of the minimum-clearance position in the direction of rotation. The relatively symmetric distribution of the pressure perturbation in the zero-preswirl case is perhaps the reason why the tangential force in Fig. 7 is comparatively small in this negative whirl-frequency range.

Proceeding to the positive whirl-frequency ratios in Fig. 9, it is seen that both pump operation modes give rise to peak pressure perturbations ahead of the minimum-clearance position in the direction of rotation. This occurs in the whirl-frequency-ratio range between 0.0 and +0.2 and, indeed, represents a shift in the zero-preswirl case. This shift causes a notable rise in the tangential force in this frequency range. While the pressure perturbation peak in Fig. 9 continues to exist ahead of the minimum-clearance position ($c-c$) for the pump operation mode, with the original inlet preswirl unaltered, a rather surprising contour redistribution occurs for the zero-preswirl operation. Here, the pressure perturbation peak is at a circumferential location that is lagging the minimum-clearance position (relative to the direction of rotation) for a whirl-frequency ratio of +0.3.

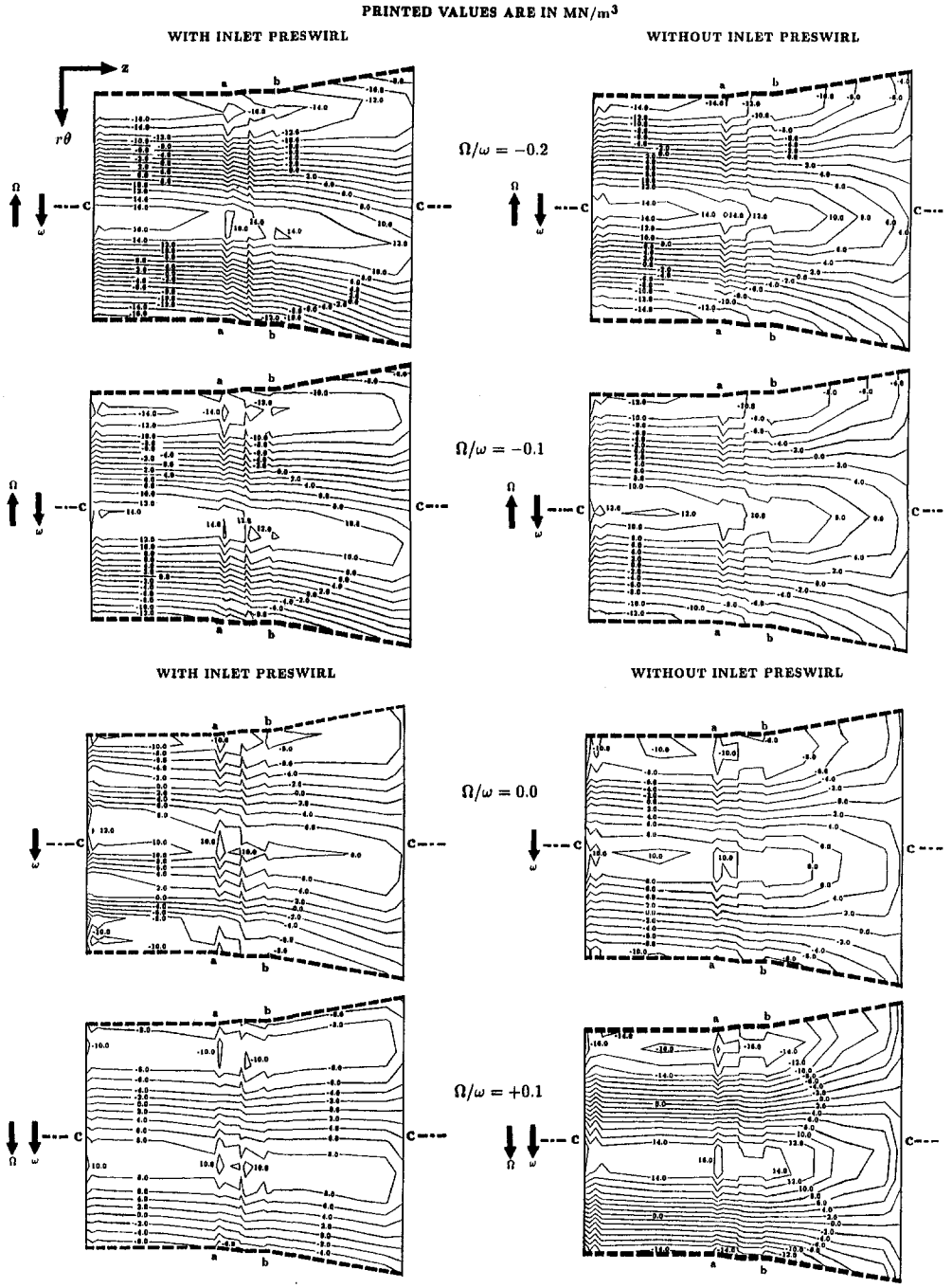

Fig. 9 Shroud pressure perturbation contours with and without inlet preswirl

Referring to Fig. 8, note that this shift causes the tangential force to be negative and, therefore, stabilizing.

Concluding Remarks

In an attempt to comprehend the rotordynamic principle governing the stability role of swirl brakes, an ideally suited category of such devices has been analytically explored. Composed of a simple vaned stator, a so-called "swirl brake" was appropriately constructed and inserted in the primary-flow passage of an existing pump stage, lightly downstream from the exducer. Although a modification such as this would normally be intended to improve the stage static-to-static pressure ratio, only the rotordynamic implications of the design upgrade were investigated. Comparing the resulting secondary flow structure to that of the original pump configuration, a reassuring feature was first detected as the average magnitude of the leakage-passage inlet preswirl was correspondingly reduced by approximately 51 percent. As a result, a drastic shift in the fluid/shroud interaction force was clearly achieved over a relatively wide range of whirl frequencies. For the major part, the tangential component shift of the fluid-induced force appeared to be restoring, as opposed to aggravating under the initial pump design configuration. In terms of rotordynamic performance, the cross-coupled stiffness coefficient was particularly reduced by comparison. With the direct damping coefficient virtually unchanged, the overall relative stability factor was significantly improved as a result. Pursuing the comparison on a rather microscopic basis, the above-referenced stability enhancement appears to have been primarily caused by a characteristically untraditional distribution of the pressure perturbation

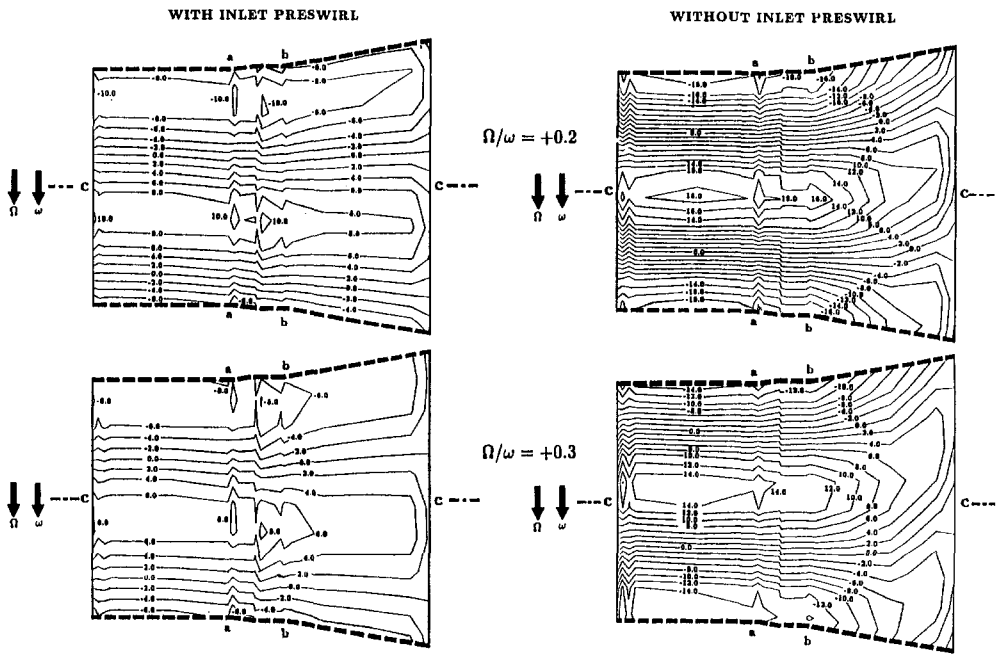

Fig. 9 (continued)

over the shroud surface, including a favorable shift in the tangential location at which the perturbation peak magnitude is attained.

Acknowledgments

This research was funded by NASA Marshall Space Flight Center, Huntsville, Alabama, Contract No. NAS8-37821, Technical Monitor: James Cannon, and the Texas A&M Turbomachinery Research Consortium.

References

Baskharone, E. A., and Hensel, S. J., 1991a, "A Finite-Element Perturbation Approach to Fluid/Rotor Interaction in Turbomachinery Elements. Part 1: Theory," ASME *Journal of Fluids Engineering,* Vol. 113, pp. 353–361.

Baskharone, E. A., and Hensel, S. J., 1991b, "A Finite-Element Perturbation Approach to Fluid/Rotor Interaction in Turbomachinery Elements. Part 2: Application," ASME *Journal of Fluids Engineering,* Vol. 113, pp. 362–367.

Baskharone, E. A., and Hensel, S. J., 1993, "Flow Field in the Secondary, Seal-Containing Passages of Centrifugal Pumps," ASME *Journal of Fluids Engineering,* Vol. 115, pp. 702–709.

Bolleter, U., Leibundgut, E., and Sturchler, R., 1989, "Hydraulic Interaction and Excitation Forces of High Head Pump Impellers," presented at the Third Joint ASCE/ASME Mechanics Conference, University of California, La Jolla, CA.

Childs, D. W., and Moyer, D., 1985, "Vibration Characteristics of the High-Pressure Oxygen Turbopump of the Space Shuttle Main Engine," ASME *Journal of Engineering for Gas Turbines and Power,* Vol. 107, pp. 152–159.

Childs, D. W., 1989, "Fluid-Structure Interaction Forces at Pump-Impeller Shroud Surfaces for Rotordynamic Calculation," ASME *Journal of Vibration, Acoustics, Stress, and Reliability in Design,* Vol. 111, pp. 216–225.

Childs, D. W., Baskharone, E., and Ramsey, C., 1991, "Test Results for Rotordynamic Coefficients of the SSME HPOTP Turbine Interstage Seal With Two Swirl Brakes," ASME *Journal of Tribology,* Vol. 113, No. 3, pp. 577–583.

Guinzberg, A., Brennen, C. E., Acosta, A. J., and Caughey, T. K., 1993, "The Effect of Inlet Swirl on the Rotordynamic Shroud Forces in a Centrifugal Pump," ASME *Journal of Engineering for Gas Turbines and Power,* Vol. 115, pp. 287–293.

Nonlinear Separated Inviscid-Viscous Analysis of Oscillating Cascade Aerodynamics Using an Inverse Integral Method

J. M. Wolff[1]

S. Fleeter
Professor.

Thermal Sciences and Propulsion Center,
School of Mechanical Engineering,
Purdue University,
West Lafayette, IN 47907

A mathematical model is developed to analyze the unsteady flow through an harmonically oscillating cascade of airfoils, including separated flow. The model incorporates an inverse integral boundary layer solution with the time-marching Euler analysis NPHASE. An embedded composite grid formulation is incorporated, specifically a deforming C-grid embedded in a Cartesian H-grid, thereby simplifying grid generation. To reduce computational requirements, Fourier series unsteady periodic boundary conditions are implemented. The integral turbulent boundary layer model is closed with steady correlations adopted in a quasi-steady manner. To couple the inviscid and viscous solutions, the viscous effect is modeled in the unsteady Euler solution in a quasi-steady manner by a transpiration boundary condition. An isolated airfoil is used to compare the steady interaction model with experimental data. Then a flat plate cascade is used to verify the unsteady flow solver with linear theory predictions. An experimental unsteady aerodynamics data set of a loaded cascade with separated meanflow executing torsional oscillations compared favorably with the analysis. The code is then utilized to study the effect of flow separation on the unsteady aerodynamics.

Introduction

Unsteady aerodynamic phenomena continue to produce serious aeroelastic problems in the development of new turbomachinery. To minimize this development problem, accurate fast-running unsteady aerodynamic cascade models are required. Such models are generally inviscid and time linearized, with the validity of these linearized models well established for subsonic flows for low aerodynamic loading (Whitehead, 1987). However, these linearized flow models may not be valid for many situations. In particular, to predict off-design aerodynamic and aeroelastic performance, an unsteady cascade viscous analysis that properly models strong inviscid–viscous interaction effects such as boundary layer separation and shock/boundary layer interaction is needed.

Recently several time-marching solutions for the unsteady Reynolds-averaged Navier–Stokes equations have been developed to analyze blade row interactions (Giles and Haimes, 1993) and oscillating cascades (Huff et al., 1987). These Navier–Stokes solutions have demonstrated the feasibility of analyzing complex two and three-dimensional turbomachinery flows. However, because of the large number of grid points and the requirement that the analysis be both accurate and stable, the maximum allowable time step in the calculations must be small, making these calculations prohibitively expensive for design use.

An alternate approach to using the time-marching Reynolds-averaged Navier–Stokes equations for the computation of unsteady viscous cascade aerodynamics is a zonal solution method, as opposed to the global solution method. Zonal solution methodology involves using different equation sets and possibly different numerical algorithms for various regions of the flow. An advantage of zonal methods is that simpler equations are used in the regions where permissible and, consequently, computational time requirements can be reduced. A disadvantage is that information must be exchanged at zonal boundaries, which can cause convergence and stability problems.

One type of zonal method used for inviscid–viscous interaction is an inviscid flow solution method for the flow away from the body matched to a viscous or boundary layer flow solution method for the flow near the body. For steady airfoil calculations, extensive inviscid–viscous interaction methods have been developed (for example, Whitfield et al., 1982). The boundary layer computational methods are either finite difference or integral methods. As well demonstrated for steady flow calculations, the integral form of the boundary layer equations leads to a more efficient way of including viscous effects in numerical solutions. The integral boundary layer equations can be solved by a direct method. This method has a singularity associated with flow separation. This singularity is removed by formulating the equations in an inverse method, then the calculations can proceed throughout separated regions. Hence, an inviscid–inverse integral viscous coupled approach seems particularly attractive for unsteady flow calculations.

Empirical correlations must be utilized in an integral boundary layer solution. Currently there are no unsteady flow correlations, only experiments on turbulent boundary layers subject to free-stream oscillations, which show that the steady correlations can be applied in a quasi-steady manner (Cousteix et al., 1981; Karlsson, 1959). Very few attempts have been made to apply the viscous–inviscid interaction approach to unsteady turbomachinery flows. One attempt, which shows encouraging results, used a direct unsteady Euler and an entrainment integral boundary layer solution for unsteady flow around oscillating blades with a simultaneous coupling method (He and Denton, 1993).

In this paper, a computationally efficient mathematical model is developed to analyze the unsteady flow through an harmonically oscillating cascade of airfoils, including inviscid–viscous

[1] Current address: Assistant Professor, Department of Mechanical & Materials Engineering, Wright State University, Dayton, OH 45435.

Contributed by the International Gas Turbine Institute and presented at the 42nd International Gas Turbine and Aeroengine Congress and Exhibition, Orlando, Florida, June 2–5, 1997. Manuscript received International Gas Turbine Institute February 1997. Paper No. 97-GT-85. Associate Technical Editor: H. A. Kidd.

interactions. The model incorporates an inverse integral boundary layer solution with the time-marching Euler analysis NPHASE (Huff, 1991). An embedded composite grid formulation is incorporated, specifically a deforming C-grid embedded in a Cartesian H-grid, thereby simplifying grid generation. Fourier series unsteady periodic boundary conditions are implemented in the flow solver to reduce computational requirements. The integral unsteady turbulent boundary layer model is closed with steady correlations adopted in a quasi-steady manner. To couple the inviscid and viscous solutions, the viscous effect is modeled in the unsteady Euler solution in a quasi-steady manner by a transpiration boundary condition. The code is then utilized to predict the unsteady aerodynamics of a cascade executing torsional oscillations.

Inviscid Model

Implicit Finite Volume Scheme. The inviscid flowfield computations are performed using an implicit finite volume Euler solver, NPHASE (Huff, 1991). The discretized integral form of the time-dependent curvilinear Euler equations is obtained by integrating the partial differential equations over a computational volume with the center denoted as (i, j) and changing the resulting volume integral to a surface integral using the divergence theorem

$$\frac{\partial Q}{\partial t} + \frac{\delta_i F}{\Delta \xi} + \frac{\delta_j G}{\Delta \eta} = 0 \tag{1}$$

where the central difference operators $\delta_m(\cdot) = (\cdot)_{m+(1/2)} - (\cdot)_{m-(1/2)}$, $m = i, j$, imply that the flux vectors are evaluated at the surfaces of a cell.

The dissipation aspect of this scheme is improved by a flux-difference split method for the residual based on the solution of approximate Riemann problems, with Roe averaging at the cell faces. With the determination of the eigensystem for the flux vectors using Roe averaging and the knowledge that the interface differential is proportional to the right eigenvectors, a first-order flux is obtained. To obtain higher order spatial accuracy, a corrective flux is then added.

Excellent results have been obtained by evaluating the residual term with the flux-difference split method described above and the left-hand side operator with the flux vector split scheme, which is approximately factored into the product of two operators. This results in a flow solver that is third-order accurate spatially and second-order accurate in time (Huff, 1991).

Embedded Composite Computational Grids. The Euler solution is implemented for an airfoil cascade geometry by a computational **C**-grid embedded in a Cartesian **H**-grid. The

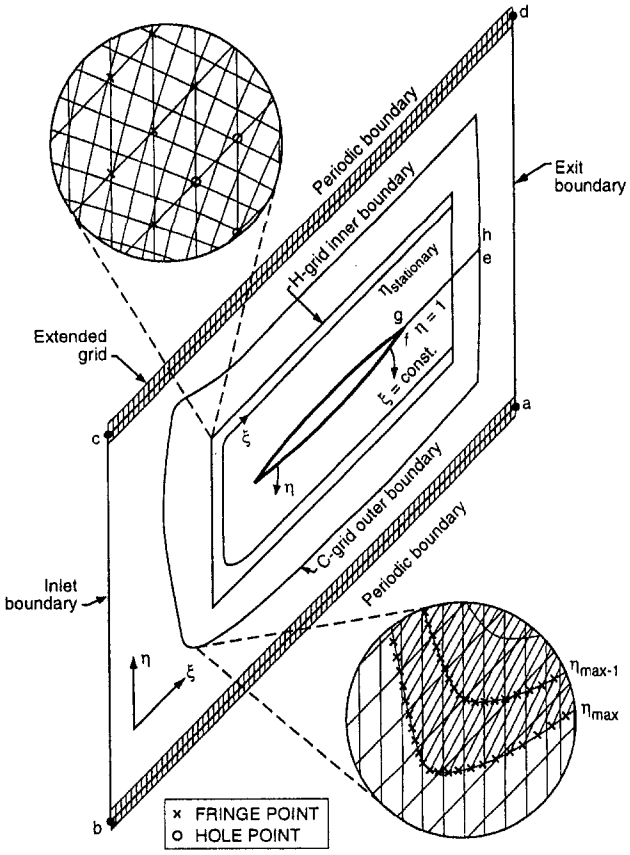

Fig. 1 ***H-C*** **embedded composite grid geometry**

embedded composite grid approach of Wolff and Fleeter (1994b) is utilized to extend the computational grid upstream and downstream of the cascade. The outer boundary condition for the inner **C**-grid is obtained by appropriate interpolation from the Cartesian **H**-grid, Fig. 1, termed fringe points. The inner **H**-grid boundary is defined, thereby indicating the hole grid points that will not be solved by the flow solver, Fig. 1. The grid points adjacent to the hole points are used as fringe points for the Cartesian **H**-grid, Fig. 1.

Bilinear interpolation accounts for the transfer of information from one grid to another at the fringe points. The bilinear interpolation for the conservative variable $f_i(\xi, \eta)(\rho(\xi, \eta), \rho u(\xi, \eta)$, etc.) has the form

Nomenclature

C = airfoil chord
C_p = pressure coefficient = $-(p - p_1)/(\frac{1}{2}\rho_1 V_1^2)$
ΔC_p = pressure difference coefficient = $(p_L - p_U)/(\frac{1}{2}\rho_1 V_1^2 \lvert\alpha_1\rvert)$
c_f = local skin friction coefficient = $2\tau_w/(\rho_e u_e^2)$
$\bar{H}$ = incompressible shape factor = δ^*/θ
k = reduced frequency = $\omega C/2V_1$
M = free-stream Mach number
p = static pressure
P_0 = total pressure
Q = dependent variable vector
R = residual
Re_x = Reynolds number based on x, $(\rho V x)/\mu$
S = cascade spacing
V = velocity
u, v = velocities in the x and y directions
x_{ea} = elastic axis location
x, y = spatial coordinates
α = incidence angle, deg
δ^* = boundary layer displacement thickness
δ^{**} = boundary layer compressibility thickness
θ = boundary layer momentum thickness
θ^* = boundary layer energy thickness
ρ = density
σ = interblade phase angle, deg
τ = time, shear stress
ξ, η = curvilinear coordinate directions
ω = angular frequency, relaxation parameter
ζ = cascade stagger angle, deg

Subscripts

e = boundary layer edge condition
i = inviscid value
v = viscous value
w = wall condition

Superscript

$\bar{}$ = incompressible value

$$f_i = f(i,j) + \Delta f_\xi \bar{\xi} + \Delta f_\eta \bar{\eta} + \Delta f_{\xi\eta} \bar{\xi}\bar{\eta} \quad (2)$$

where $\Delta f_{\xi\eta} = f(i+1, j+1) - f(i+1, j) - f(i, j+1) + f(i, j)$, $\Delta f_\xi = f(i+1, j) - f(i, j)$, $\Delta f_\eta = f(i, j+1) - f(i, j)$, and with $0 < \bar{\xi}, \bar{\eta} > 1$ the interpolation parameters in the ξ and η directions, respectively.

To ensure proper interpolation of information between the **C**-grid and the Cartesian **H**-grid, the outer portion of the **C**-grid remains fixed in space, with a deforming grid technique used to locate the position of the airfoil. Based on the grid point locations in the **C**-grid that are used for interpolating to the **H**-grid inner boundary, the user specifies the portion of the **C**-grid allowed to deform with the airfoil motion. This is accomplished by specifying a η grid line beyond which the **C**-grid will remain stationary, Fig. 1. The grid lines connecting the inner ($\eta = 1$) and outer ($\eta = \eta_s$) boundaries deform with the airfoil motion.

Boundary Conditions. The solid surface boundary conditions, $f-g$ in Fig. 1, implement characteristic variable boundary conditions (CVBC). The CVBC's are consistent with the concept of upwinding in which the signs of the characteristic velocities determine the appropriate propagation directions. The flow variables are averaged across the interface aft of the airfoil solid surface to the exit, $e-f$ and $g-h$.

CVBC are used for proper transmission of information into and out of, $b-c$ and $a-d$, the steady computational domain. The CVBC's are only valid for steady cascade flows because the exit boundary is assumed to have uniform static pressure.

Approximate nonreflecting unsteady inlet and exit boundary conditions are used by assuming that linear theory can be applied. First, the steady flow is solved using the CVBC's. The linearized Euler equations are then solved at the inlet and exit boundary to determine the perturbation flow variables in terms of the characteristic variables. This allows time variations of static pressure at the exit and reduces reflections from the boundaries. For certain unsteady flows, reflections are still a problem. The composite grid method is used to extend the computational domain upstream and downstream to eliminate the reflections.

The flow variables at the unsteady periodic boundaries, $a-b$ and $c-d$, are approximately expressed as a Fourier series for nonzero interblade phase angle (Wolff and Fleeter, 1994a). The Fourier series boundary conditions are applied by expanding the computational grid one node at the upper and lower periodic boundaries. At one node interior of the upper and lower periodic boundaries, the timewise integrations for the Fourier coefficients are performed on the conservative variables. The solutions at the overlapped nodes for the lower and upper periodic boundaries are found by a timewise Fourier series for the conservative variables. The analysis is then run until a periodic solution is achieved.

Integral Boundary Layer Model

Quasi-Steady Assumption. To model the unsteady boundary layer behavior, steady predictions are assumed to apply in a quasi-steady manner. This assumption has been shown to be valid by several researchers. Karlsson (1959) provided pioneering data on unsteady flat plate turbulent boundary layers with no pressure gradient obtained in a wind tunnel with velocity fluctuating sinusoidally in magnitude about a constant mean. The fluctuations varied from 8 to 34 percent of the free-stream mean velocity, with $\mathrm{Re}_x = 1 \times 10^5$ and a reduced frequency range of 0.22 to 27.4. He found that the boundary layer momentum thickness did not vary from the quasi-steady thickness over the entire range of parameters.

Cousteix et al. (1981) obtained experimental data on a similar configuration, but in an adverse pressure gradient. The fluctuations varied from 7 to 15 percent of the free-stream mean velocity, with $\mathrm{Re}_x = 1.5 \times 10^6$ and a reduced frequency range of 0.76 to 5.0. These results support the validity of the quasi-steady boundary layer assumption for reduced frequency values of at least 5.0. Based on the available experimental unsteady turbulent data, a quasi-steady model for unsteady boundary layer calculation is reasonable for unsteady turbomachine flows up to a reduced frequency of at least 5.0.

The two primary methods for modeling the boundary layer equations are (1) finite-difference methods and (2) integral methods. The finite-difference solutions are more complex and require more computational resources, while the integral methods rely on numerical correlations to complete the analysis. Since a goal of this research is to produce an efficient model, an integral method is utilized.

Turbulent Flow. The turbulent integral boundary-layer formulation is based on the mean flow kinetic energy. The formulation was developed originally by Whitfield (1978) and updated to include separated flow. The momentum integral equation can be written as:

$$\frac{1}{\rho_e u_e^2} \frac{\partial}{\partial x} (\rho_e u_e^2 \theta) + \frac{\delta^*}{u_e} \frac{\partial u_e}{\partial x} = \frac{c_f}{2} \quad (3)$$

where the displacement thickness δ^*, momentum thickness θ, and skin friction c_f are

$$\delta^* = \int_0^\infty \left(1 - \frac{\rho u}{\rho_e u_e}\right) dy \quad (4a)$$

$$\theta = \int_0^\infty \frac{\rho u}{\rho_e u_e} \left(1 - \frac{u}{u_e}\right) dy \quad (4b)$$

$$c_f = \frac{2\tau_w}{\rho_e u_e^2} \quad (4c)$$

The mean-flow kinetic energy equation is obtained by multiplying the streamwise momentum equation by the streamwise velocity and integrating normal to the wall:

$$\frac{1}{2\rho_e u_e^3} \frac{\partial}{\partial x} (\rho_e u_e^3 \theta^*) + \frac{\delta^{**}}{u_e} \frac{\partial u_e}{\partial x} = \frac{c_f}{2} D \quad (5)$$

where the compressibility thickness δ^{**}, energy thickness θ^*, and dissipation integral D are

$$\delta^{**} = \int_0^\infty \frac{u}{u_e} \left(1 - \frac{\rho}{\rho_e}\right) dy \quad (6a)$$

$$\theta^* = \int_0^\infty \frac{\rho u}{\rho_e u_e} \left(1 - \frac{u^2}{u_e^2}\right) dy \quad (6b)$$

$$D = \int_0^\infty \frac{\tau}{\tau_w} \frac{\partial}{\partial y} \left(\frac{u}{u_e}\right) dy \quad (6c)$$

The governing equations contain seven unknowns, u_e, δ^*, θ, c_f, δ^{**}, θ^* and D. An analytical expression for attached and separated turbulent boundary-layer velocity profiles permits the evaluation of certain auxiliary correlations necessary for the integral boundary-layer calculation method. A closure procedure is employed that expresses four of the unknowns, θ^*, δ^{**}, c_f, and D, in terms of the remaining three, M_e, $\bar{\Theta}$, and δ^*, by defining the following shape factors, $H_{\delta_*} = \delta^*/\theta$, $H_{\theta_*} = \theta^*/\theta$, $H_{\delta_{**}} = \delta^{**}/\theta$.

The analytical expressions for the shape factors derived by Whitfield (1978) and modified to account for separated flow profiles (Swafford, 1980) are

$$H_{\delta_*} = \bar{H}(1 + 0.113M_e^2) + 0.290M_e^2 \quad (7a)$$

$$(H_{\theta_*})_{M_e=0} = 3.83781e^{-2\bar{H}} + 0.33 - \frac{1}{8.5484}\tan^{-1}\left(\frac{10^{7-\bar{H}} - 1}{1.23}\right) + 1.48061 - \left(0.33 - \frac{\pi}{17.1}\right) \times \tanh^{1/2}[(1.2874 \times 10^{-6})(10^{7-\bar{H}})^{1.45761}] \quad (7b)$$

$$H_{\theta_*} = \frac{(H_{\theta_*})_{M_e=0} + 0.028\mathrm{M}_e^2}{1 + 0.014\mathrm{M}_e^2} \quad (7c)$$

$$H_{\delta^{**}} = \left(\frac{0.064}{\bar{H} - 0.8} + 0.251\right)\mathrm{M}_e^2 \quad (7d)$$

and

$$\frac{\theta}{\bar{\theta}} = 1 - \frac{0.92\mathrm{M}_e^2}{7.09 + \mathrm{M}_e^2}\tanh[1.49(\bar{H} - 0.9)] \quad (7e)$$

The correlation for the skin friction can be written as

$$c_f = \frac{1}{F_c}\frac{0.3e^{-1.33\bar{H}}}{\left[\log_{10}\left(\frac{\mathrm{Re}_\theta}{F_c}\right)\right]^{1.74+0.31\bar{H}}} + 1.1 \times 10^{-4}\left[\tanh\left(4 - \frac{\bar{H}}{0.875}\right) - 1\right] \quad (8)$$

where

$$F_c = \left(1 + \frac{\gamma - 1}{2}\mathrm{M}_e^2\right)^{1/2} \quad \text{and} \quad \mathrm{Re}_\theta = \frac{\rho_e u_e \theta}{\mu_e}.$$

The dissipation integral D is evaluated by using the numerical correlation from Whitfield et al. (1982).

$$\frac{D}{2} = \frac{0.009 - 0.011e^{-0.15\bar{H}^{2.1}} + 3.0 \times 10^{-5}e^{0.117\bar{H}^2} + A(\bar{\mathrm{Re}}_\theta)^{-0.574}}{F_c(1 + 0.05\mathrm{M}_e^{1.4})} \quad (9)$$

with $A = 0.438 - 0.280\bar{H}$ for $\bar{H} \le 3.5$ and $A = 0.160(\bar{H} - 3.5) - 0.550$ for $\bar{H} > 3.5$.

Inverse Solution. The integral boundary layer equations can be formulated to be solved by a direct method, where the pressure distribution is input to the solution. This method has a singularity associated with flow separation. This singularity is removed by specifying the displacement thickness distribution instead of the pressure distribution, i.e., an inverse method, and boundary-layer computations can proceed throughout separated regions, without the separation point being specified prior.

Equations (3) and (5) can be arranged to (Whitfield et al., 1982):

$$(1 + H_{\delta^*})\frac{d}{dx}[\ln(u_e)] - \frac{d}{dx}[\ln(H_{\delta^*})] = \frac{c_f}{2\theta} - \frac{d}{dx}[\ln(\rho_e u_e \delta^*)] \quad (10a)$$

$$\left(1 + 2\frac{H_{\delta^{**}}}{H_{\theta^*}} - H_{\delta^*}\right)\frac{d}{dx}[\ln(u_e)] - \frac{d}{dx}[\ln(H_{\theta^*})] = \frac{c_f D}{\theta H_{\theta^*}} - \frac{c_f}{2\theta} \quad (10b)$$

For a gas with constant specific heat ratio and constant total enthalpy at the boundary-layer edge, these equations can be written with $\bar{H}$ and M_e as dependent variables.

$$\frac{d\mathrm{M}_e}{dx} = \frac{a_{22}b_1 - a_{12}b_2}{\Delta} \quad (11a)$$

$$\frac{d\bar{H}}{dx} = \frac{a_{11}b_2 - a_{21}b_1}{\Delta} \quad (11b)$$

where

$$a_{11} = \frac{1 + H_{\delta^*}}{\mathrm{M}_e F_c^2} - \frac{1}{H_{\delta^*}}\frac{\partial H_{\delta^*}}{\partial \mathrm{M}_e}, \quad b_1 = \frac{c_f}{2\theta} - \frac{d}{dx}[\ln(\rho_e u_e \delta^*)],$$

$$a_{12} = -\frac{1}{H_{\delta^*}}\frac{\partial H_{\delta^*}}{\partial \bar{H}}, \quad a_{21} = \frac{1 + 2\frac{H_{\delta^{**}}}{H_{\theta^*}} - H_{\delta^*}}{\mathrm{M}_e F_c^2} + \frac{1}{H_{\theta^*}}\frac{\partial H_{\theta^*}}{\partial \mathrm{M}_e},$$

$$a_{22} = \frac{1}{H_{\theta^*}}\frac{\partial H_{\theta^*}}{\partial \bar{H}}, \quad b_2 = \frac{c_f D}{\theta H_{\theta^*}} - \frac{c_f}{2\theta}, \quad \text{and}$$

$$\Delta = a_{11}a_{22} - a_{12}a_{21}.$$

The boundary layer calculations are performed separately on the upper and lower airfoil surfaces. The stagnation point is located. The turbulent boundary layer calculations are then started at 0.5 percent chord from the stagnation point on both surfaces. The calculations are continued past the airfoil surface to the computational domain exit using the same numerical scheme except assigning the skin friction, c_f, to 0.00001. For the steady calculations, a flat plate displacement thickness distribution is used to start the inverse boundary layer solution. In addition the starting shape factor, H, is specified as 1.2. For the unsteady calculations, the steady displacement thickness distribution is used along with the same starting shape factor.

Inviscid–Viscous Coupled Solution. A surface source model will be used as a coupling device between the steady viscous and inviscid computational regions. The surface source model imposes a mass flux on the solid wall and numerically simulates the displacement effect caused by the steady boundary layer. The surface model is derived by subtracting the two-dimensional continuity equation from the continuity equation evaluated at the edge of the boundary layer, with the resulting equation then integrated in the y direction, knowing that ρv at the wall is zero. The result is

$$\frac{\partial}{\partial x}(\rho_e u_e \delta^*) = (\rho v)_n \quad (12)$$

The steady surface source model is then applied in a quasi-steady manner.

The term $(\rho v)_n$ is updated as follows. The δ^* distribution at the previous time step is used in the inverse boundary layer code to solve for the distribution of $\rho_e u_e \delta^*$. This quantity is then used in Eq. (12) to calculate $(\rho v)_n$ for the next inviscid calculation. The δ^* distribution for the next viscous calculation is obtained by the expression

$$\delta^*_{\text{new}} = \delta^*_{\text{old}} + \omega\delta^*_{\text{old}}\left[\frac{u_{e,v}}{V_{w,i}} - 1\right] \quad (13)$$

The inviscid solid wall boundary condition is implemented using a characteristic variable formulation. To transpire the

proper amount of artificial mass to account for the viscous effect, Eq. (12) is used in conjunction with the characteristic variables, yielding

$$\left[\eta_x\left(\rho - \frac{P}{c_o^2}\right)\right]_b = \left[\eta_x\left(\rho - \frac{P}{c_o^2}\right)\right]_r \quad (14a)$$

$$\left[\eta_y\left(\rho - \frac{P}{c_o^2}\right)\right]_b = \left[\eta_y\left(\rho - \frac{P}{c_o^2}\right)\right]_r \quad (14b)$$

$$[(\eta_x u + \eta_y v)]_b = [(\eta_x u_n + \eta_y v_n)]_v \quad (14c)$$

$$\left[\frac{P\nabla\eta}{\rho_o c_o} - (\eta_x u + \eta_y v)\right]_b = \left[\frac{P\nabla\eta}{\rho_o c_o} - (\eta_x u + \eta_y v)\right]_r \quad (14d)$$

The subscript r denotes a reference value, selected as the center of the first cell off the boundary inside the computational domain. Equations (14) are solved to obtain the nonconservative flow variables accounting for the proper viscous effect.

$$P_b = P_r \pm \rho_o c_o[(\eta_x u_r + \eta_y v_r) - (\eta_x u_n + \eta_y v_n)] \quad (15a)$$

$$\rho_b = \rho_r + \frac{P_b - P_r}{c_o^2} \quad (15b)$$

$$u_b = u_r - \eta_x[(\eta_x u_r + \eta_y v_r) - (\eta_x u_n + \eta_y v_n)] \quad (15c)$$

$$v_b = v_r - \eta_y[(\eta_x u_r + \eta_y v_r) - (\eta_x u_n + \eta_y v_n)] \quad (15d)$$

For the steady-state analysis, the airfoil is held stationary as the flow solver is marched in time until steady conditions are reached. The viscous and inviscid analyses are calculated at each time step. The relaxation parameter was set to 0.5 for the steady analysis and 1.0 for the unsteady analysis. The inverse integral boundary layer calculations are performed once per time step for the steady analysis, but for the unsteady analysis they are iterated until convergence. Convergence is achieved for each time step when the velocity from the viscous and inviscid solutions agree within 0.1 percent.

Results

In this paper, the two-dimensional unsteady flow through an harmonically oscillating cascade of airfoils is investigated using the time-marching inviscid–viscous interaction code. For comparison, solutions are obtained for an isolated airfoil in a steady flow and for both flat plate and loaded oscillating airfoil cascades.

Isolated Airfoil—RAE 2882. The experimental data of Cook et al. (1979) include surface pressure and boundary-layer information for transonic flow about the isolated RAE 2882 airfoil. In particular, Case 9 will be compared to the inviscid–viscous analysis developed herein. A 223 × 34 C-grid extending 4 chords up and downstream with a spacing of 18 chords was used for the inviscid–viscous analysis. Since a steady isolated airfoil is being analyzed, the composite grid method was not used. The cascade spacing and grid density were increased until solution independence was achieved. The angle of attack correction, $\alpha_c = 2.78$ deg, of Cook et al. (1979) was applied. The momentum thickness and skin friction coefficient results are shown in Fig. 2. Excellent agreement is achieved between the data and the inviscid–viscous solution.

The steady pressure distribution results for the inviscid–viscous and inviscid solutions show the significant effect of viscosity on the upper surface shock location, Fig. 3. The inviscid analysis overshoots the shock location by 8 percent of the airfoil chord. The shock strength is also diminished by the boundary layer effects. These comparisons with the RAE 2822 airfoil experimental data show the accuracy of the inviscid–viscous steady analysis.

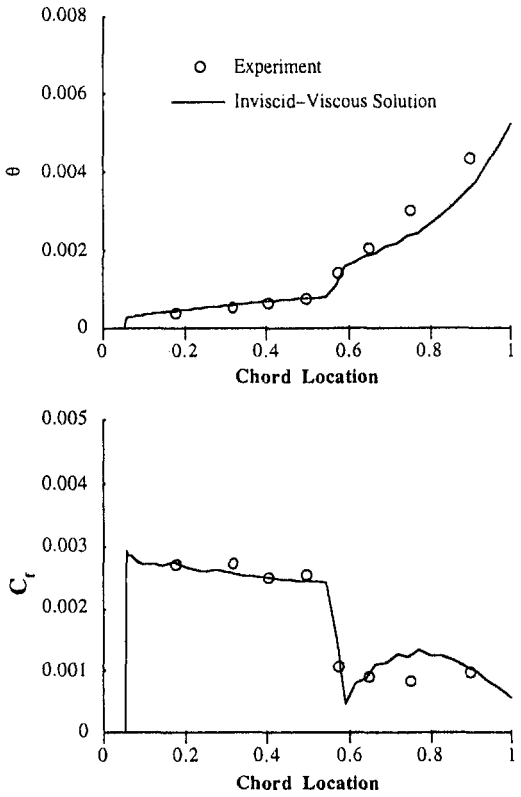

Fig. 2 Inviscid–viscous interaction solution, RAE 2822, Case 9; M = 0.73, α_c = 2.78 deg, Re = 6.5 × 10^6, S/C = 20.0

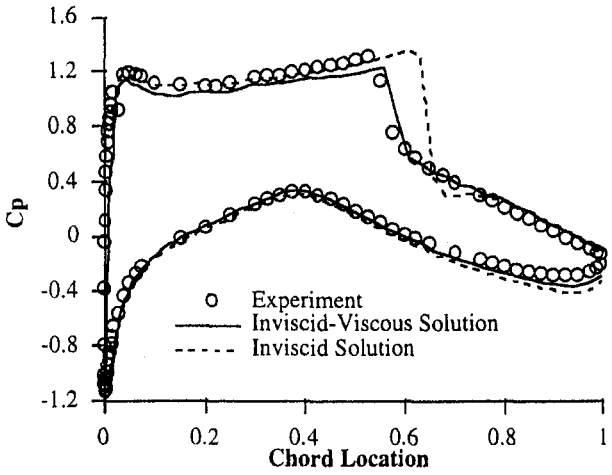

Fig. 3 Steady pressure distribution, RAE 2822, Case 9: M = 0.73, α_c = 2.78 deg, Re = 6.5 × 10^6, S/C = 20.0

Flat Plate Cascade. To validate the unsteady cascade analysis, the flow past an oscillating flat plate cascade is analyzed and compared with linear theory predictions. The cascade consists of flat plates staggered at 45 deg with a solidity of 1.0. The inlet Mach number is 0.7, the mean flow incidence angle is zero, and the reduced frequency k is 0.75. A finite 1 percent thick, rounded nose airfoil is used to approximate the flat plate airfoils. An H-C composite grid, which extended 6.0 chords upstream and downstream of the cascade with 108 × 30 and 145 × 28 grid points, respectively, was used. Initially, the flow variables are set equal to the previously determined steady values. Then the airfoils oscillate for a number of cycles sufficient to achieve a periodic unsteady solution. The airfoil surface unsteady pressures for the last cycle of oscillation are then Fourier

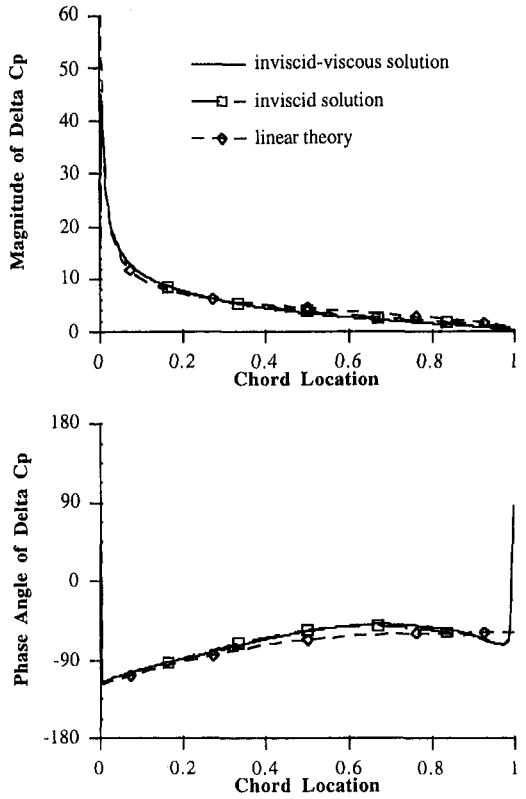

Fig. 4 Flat plate cascade unsteady pressure difference: M = 0.7, k = 0.75, ζ = 45 deg, α = 0 deg, p/P_0 = 0.721, h_1 = 0.01, C/S = 1.0, σ = 90 deg

decomposed to determine the first harmonic unsteady pressure distribution.

Figure 4 shows the magnitude and phase response of the cascade of flat plate airfoils to a 1 percent chord translational amplitude at an interblade phase angle of 90 deg. The predictions of the inviscid–viscous interaction, Re = 5×10^6, and inviscid solvers are shown. The viscous effects are negligible for the flat plate cascade, causing a slight decrease in the magnitude response over the last half of chord and nearly no difference in phase. There is a slight decrease in magnitude over the last half of the chord; otherwise excellent agreement between the current solutions and the linear theory analysis of Whitehead (1987) is evident.

The subiterations required for the inverse boundary layer solution varied between 1 and 2 times. The computational time for the inviscid–viscous analysis was 2.5 CPU hours versus 2 CPU hours on an IBM RS/6000 Model 580 workstation for the inviscid solution. Both solutions required seven cycles of oscillation to converge.

10th Standard Configuration—Subsonic. To demonstrate the inviscid–viscous interaction model, the unsteady aerodynamics of the 10th standard cascade configuration executing torsional oscillations is analyzed. The 10th standard configuration is a cascade of modified cambered NACA 0006 airfoils at 45 deg stagger, 10 deg angle-of-attack, with a solidity of 1.0. A free-stream Mach number of 0.7 and a back pressure of 0.87 are analyzed. These flow conditions result in a flow field that is completely subsonic. An *H-C* composite grid, which extended 6.0 chords upstream and downstream of the cascade with 108 × 30 & 156 × 16 grid points, respectively, was used. Please note: Both a grid and time step convergence study were completed for all the results presented.

The unsteady cascade flow generated by a torsional motion about the midchord with an amplitude of 1.0 deg is analyzed. Figure 5 shows the unsteady magnitude and phase pressure response of the 10th standard configuration cascade oscillating with a 1.5 reduced frequency value, a free-stream Mach number of 0.7, and a 0 deg interblade phase angle for two different Reynolds numbers, together with the inviscid solution. The expected trend with increasing Reynolds number is evident. The magnitude of the unsteady pressure response for Re = 5×10^6 is nearly double the inviscid response at 10 percent chord, with a 50 percent increase for Re = 30×10^6. From the 40 percent chord location to the trailing edge, viscous effects are not as significant, decreasing the magnitude of the unsteady pressure. The phase results show that viscosity causes a phase lead across the airfoil surface. The phase lead is greater in the leading edge region, 40 deg for Re = 5×10^6 and 30 deg for Re = 30×10^6, while near the trailing edge the phase lead is minimal.

The subiterations required for the inverse boundary layer solution varied up to five times, with most time steps requiring just one or two. The computational time for the inviscid–viscous analysis was 2.0 CPU hours versus 1.65 CPU hour for the inviscid solution, with all solutions requiring five cycles of oscillation to converge.

Separated Flow Predictions. Experiments have been performed in the NASA Lewis Transonic Oscillating Cascade facility on an airfoil cascade designed by Pratt & Whitney (Buffum et al., 1998). The test configuration is a cascade of negatively cambered airfoils at 60 deg stagger with a spacing-to-chord ratio of 0.657. A composite grid configuration, 217 × 39 **C**-grid, Fig. 6, embedded in a 108 × 30 *H*-grid, with the inlet and exit plane locations extending six chords upstream and downstream is used for both the inviscid and inviscid–viscous interaction calculations.

Steady pressure distributions are available for a free-stream Mach number of 0.5. Two different incidence angles, 0 and 10, are considered. The corresponding pressure ratios, defined as the ratio of downstream static pressure to the upstream static pressure, are 0.93 and 1.03, respectively. The experimental inci-

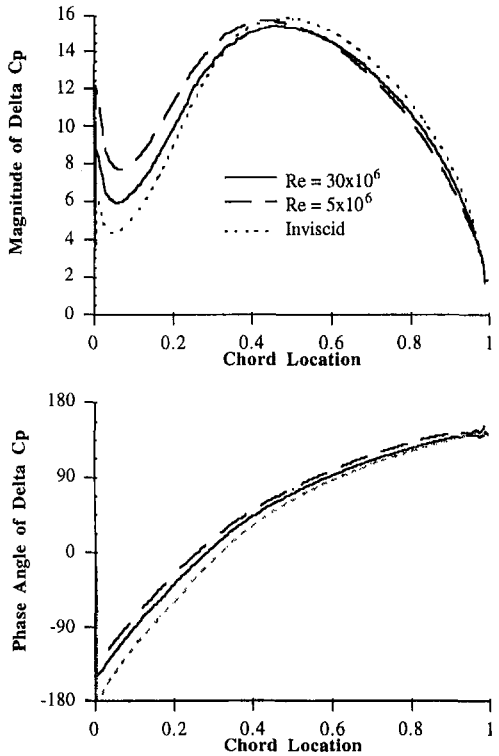

Fig. 5 10th standard configuration unsteady pressure difference: M = 0.7, k = 1.5, ζ = 45 deg, α = 10 deg, C/S = 1.0, p/P_0 = 0.87, α_1 = 1 deg, x_{ea} = 0.5, σ = 0 deg

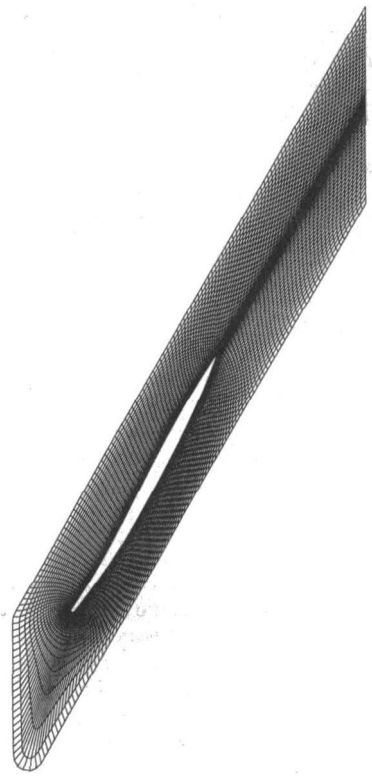

Fig. 6 NASA Pratt & Whitney configuration computational C-grid

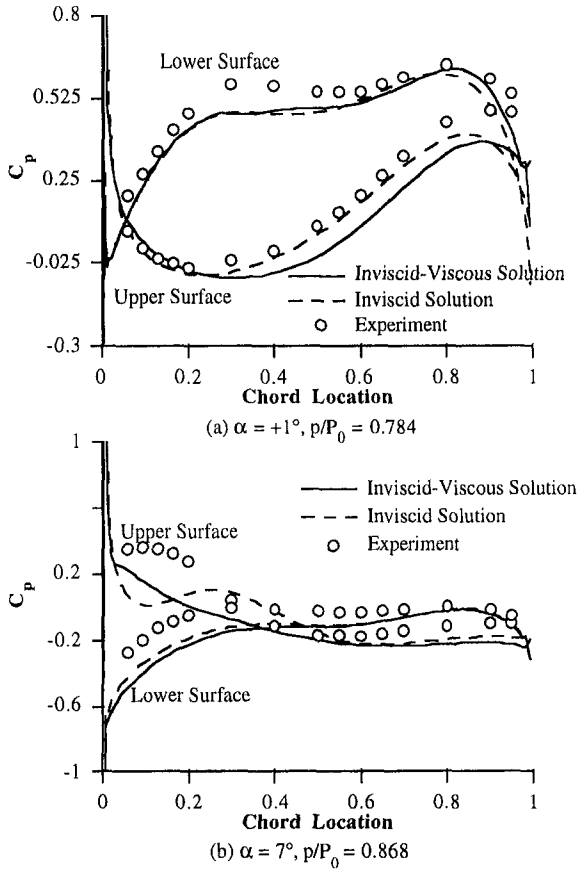

Fig. 7 NASA Pratt & Whitney configuration steady pressure distribution: M = 0.5, ζ = 60 deg, S/C = 0.657, Re = 1 × 10^6

dence angle is set by positioning the upstream walls of the linear cascade to the specified inlet angle, with the actual incidence angle at the cascade inlet plane not measured. Thus, the incidence angle for the computations was determined by analyzing a limited range of incidence angles and selecting the one that best matched the experimental results. These tests were completed using the inviscid analysis.

Figure 7(*a*) shows the experimental steady pressure loading for the 0 deg incidence case together with the computational solutions obtained for a 1 deg incidence angle. The viscous effects are the strongest on the upper airfoil surface. The upper surface viscous effect moves the solution away from the data from 30 percent to 90 percent of the airfoil chord. Except for the upper surface viscous solution, the agreement between the predictions and the experimental data is generally good. Slight modifications to the airfoil shape could explain the differences at the trailing edge. To get a converged steady solution, the trailing edge had to be straighten to provide a better computational grid.

The experimental steady pressure loading for the 10 deg incidence angle case and the computational results obtained with a 7 deg incidence angle are shown in Fig. 7(*b*). The experimental data indicate flow separation on the upper surface from the 5 to 20 percent chord locations. The inviscid analysis on the upper surface underpredicts the pressure through the separation zone and then overpredicts the pressure until midchord. The upper surface viscous effect causes the pressure to flatten out as compared to the inviscid analysis. The pressure is still underpredicted in the separated region, but the viscous solution tends toward the data. The viscous effects on the lower surface are negligible. The lower surface pressure is underpredicted over the first 80 percent of the chord. The agreement with the data shows that the general trendwise behavior of the flow is captured by the analysis. Transition was assumed at 0.5 percent chord, this limitation could be the cause of some of the error.

To understand better the boundary layer effects for the inviscid–viscous, Re = 1 × 10^6, interaction analysis, Fig. 8 shows

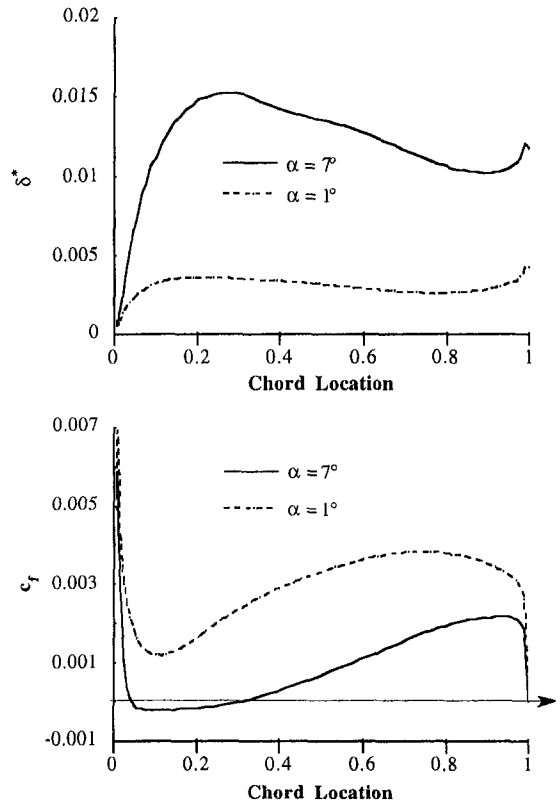

Fig. 8 NASA Pratt & Whitney configuration steady boundary layer parameters: M = 0.5, ζ = 60 deg, S/C = 0.657, Re = 1 × 10^6

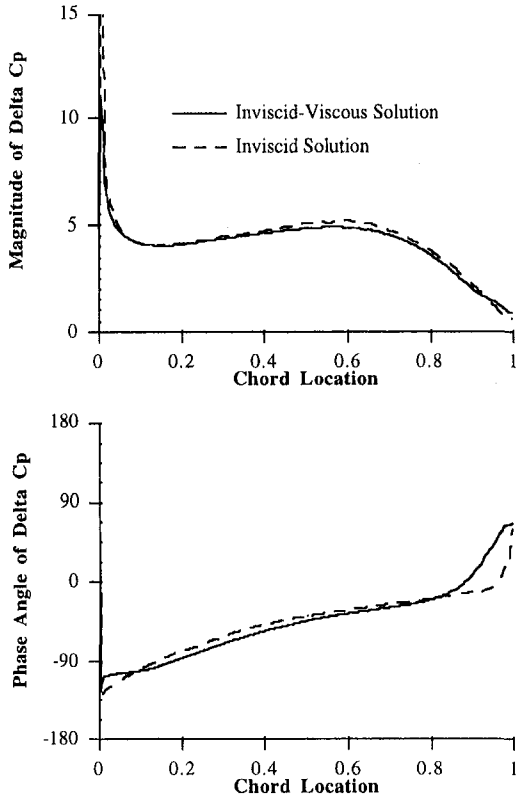

Fig. 9 NASA Pratt & Whitney configuration unsteady pressure difference: M = 0.5, k = 0.4, ζ = 60 deg, S/C = 0.657, α = 1 deg, p/P_0 = 0.784, α_1 = 1.2 deg, x_{ea} = 0.5, σ = 0 deg

the upper surface steady displacement thickness, δ^*, and skin friction, c_f, distributions for both incidence angles. At an incidence angle of 1 deg, the upper surface displacement thickness grows near the leading edge and the skin friction drops to a minimum at 15 percent chord. The flow remains attached to the upper surface. At 7 deg of incidence, the upper surface displacement thickness grows very rapidly at the airfoil leading edge. The skin friction drops below zero from 5 to 30 percent chord, indicating boundary layer separation over this region. The separation zone agrees with the data, which show the separation zone from 5 to 20 percent chord on the upper surface.

Unsteady Torsional Motion. The NASA Lewis Transonic Oscillating Cascade facility is designed to oscillate the cascade in a torsional motion about midchord with an amplitude of ±1.2 deg. The torsional motion analysis at 1 deg of incidence with a reduced frequency of 0.4 and 0 deg interblade phase angle for the inviscid and inviscid–viscous, Re = 1×10^6, interaction methods is shown in Fig. 9. Because of periodicity problems (Buffum, 1996), experimental data are only available for σ = 180 deg. The steady analysis computational grid was used. The unsteady viscous effects on both the magnitude and phase pressure difference distributions are minimal. A small decrease in the unsteady pressure magnitude results from the viscous effects. Also, viscosity results in a slight decrease in the phase response over most of the chord.

Increasing the steady incidence angle to 7 deg, the predicted unsteady inviscid and inviscid–viscous, Re = 1×10^6, interaction magnitude and phase pressure distributions are shown in Fig. 10. Recall that the steady results for this incidence angle showed the boundary layer to be separated from 5 to 30 percent chord location on the airfoil upper surface, Fig. 8. The viscous effects on the unsteady loading, both the magnitude and phase of the unsteady pressure difference, are significant over the first 60 percent of the chord. There are large differences between the viscous and inviscid predictions of the unsteady pressure difference magnitude over the first 60 percent chord, with the viscous solution producing a greatly reduced magnitude that is flattened out through the separation zone. Compared to the inviscid analysis, the inviscid–viscous analysis predicts an increase in the unsteady magnitude from the 30 to 60 percent chord locations. The inviscid and viscous unsteady magnitude predictions agree over the last 40 percent chord. The unsteady phase pressure difference shows a sharp decrease at the beginning of the separated zone. The phase distribution then remains fairly constant until the trailing edge region, where it increases.

Figure 11 shows the variation of the unsteady upper surface boundary layer parameters, δ^* and c_f, as a function of chord location. Surprisingly, the variation in the boundary layer parameters show no significant effects. The time-averaged and steady values are the same. The flow remains separated over the complete oscillation cycle of the airfoil. The area of separation does change as the airfoil oscillates but this movement is not significant. The boundary layer parameters show the greatest unsteady variation near the trailing edge with a maximum unsteady envelope for δ^* of 27 percent and for c_f, 29 percent of their mean values. A negative c_f signifies separated flow, but its numerical size has no physical meaning. Therefore, the maximum, minimum, and time-averaged values of c_f in the separated region have the same negative value. The variation of δ^* shows that the unsteady boundary layer in the separated flow zone is changing as the airfoils oscillate.

The conclusion drawn from these unsteady results is that mean separated flow conditions have significant effects on the unsteady pressure difference across the airfoil chord. The only parameter changed was the cascade incidence angle, but this change caused the flow to separate on the upper surface of the airfoil with significant unsteady viscous effects resulting.

Unsteady Nonlinear Separated Flow. Figure 12 shows the experimental data (Buffum et al., 1998), inviscid, and inviscid–viscous, Re = 1×10^6, interaction analysis prediction for the

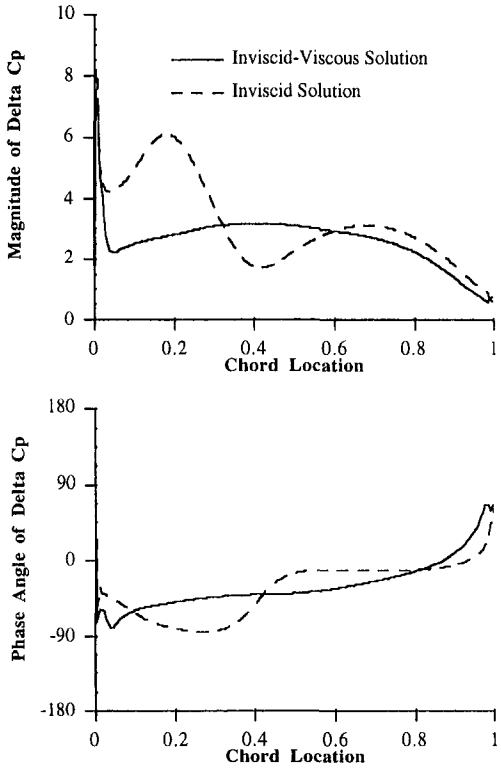

Fig. 10 NASA Pratt & Whitney configuration unsteady pressure difference: M = 0.5, k = 0.4, ζ = 60 deg, S/C = 0.657, α = 7 deg, p/P_0 = 0.868, α_1 = 1.2 deg, x_{ea} = 0.5, σ = 0 deg

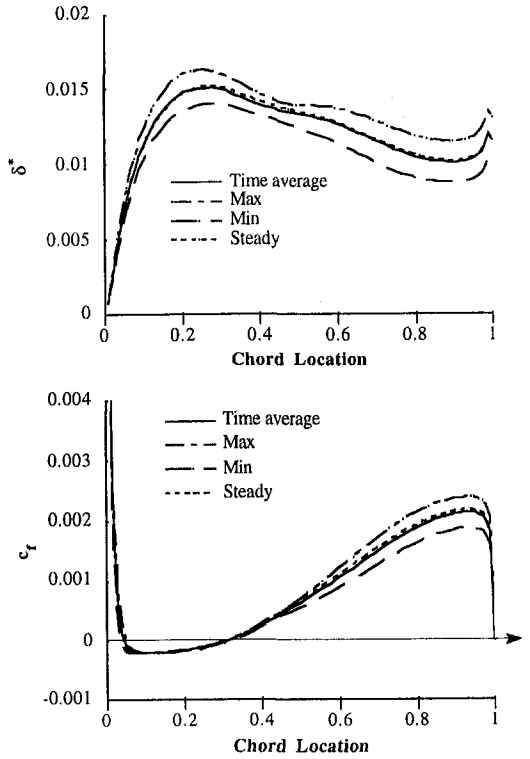

Fig. 11 NASA Pratt & Whitney configuration, unsteady boundary layer parameters: M = 0.5, k = 0.4, ζ = 60 deg, S/C = 0.657, α = 7 deg, p/P_0 = 0.868, α_1 = 1.2 deg, x_{ea} = 0.5, σ = 0 deg

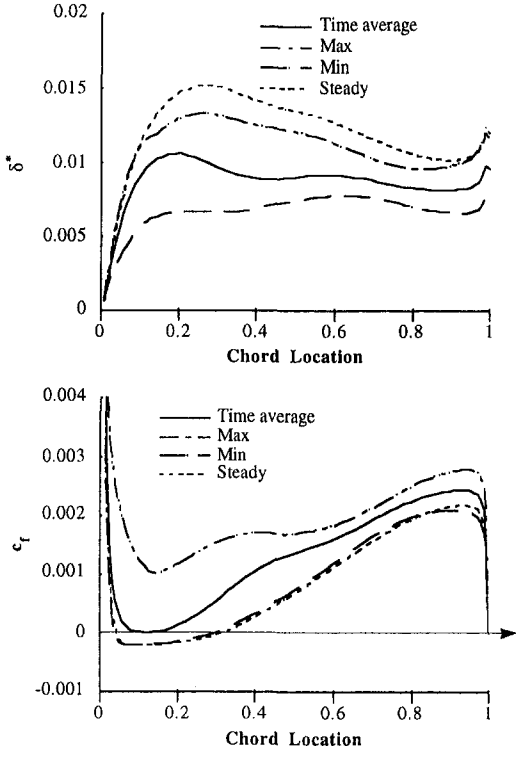

Fig. 13 NASA Pratt & Whitney configuration unsteady boundary layer parameters: M = 0.5, k = 0.4, ζ = 60 deg, S/C = 0.657, α = 7 deg, p/P_0 = 0.868, α_1 = 1.2 deg, x_{ea} = 0.5, σ = 180 deg

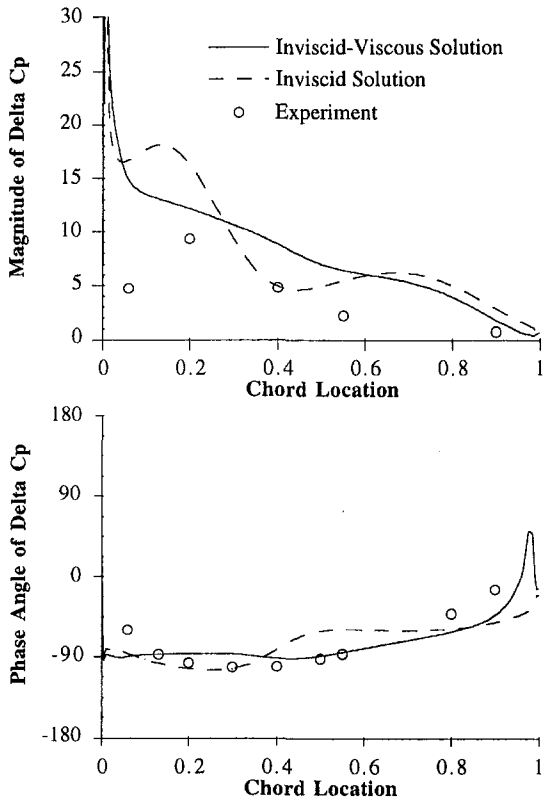

Fig. 12 NASA Pratt & Whitney configuration unsteady pressure difference: M = 0.5, k = 0.4, ζ = 60 deg, S/C = 0.657, α = 7 deg, p/P_0 = 0.868, α_1 = 1.2 deg, x_{ea} = 0.5, σ = 180 deg

7 deg incidence angle case but with a 180 deg interblade phase angle. Analogous to the previous 0 deg interblade phase angle separated unsteady results, there is a large difference between the inviscid and viscous predictions of the unsteady pressure difference magnitude in the region where the steady flow is separated, with the viscous prediction decreased. Both methods overpredict the experimental magnitude, with the viscous solution providing a better trendwise agreement. The unsteady pressure difference magnitude predicted by the viscous analysis is increased as compared to the inviscid analysis from 30 to 60 percent of the airfoil chord, with minimal effect aft of 60 percent chord. The unsteady viscous phase distribution solution shows excellent agreement with the experimental results over the entire chord.

To study the unsteady effects on the boundary layer parameters, Fig. 13 shows the upper surface boundary layer parameters, δ^* and c_f, as a function of chord location. Significant nonlinear effects can be seen in both boundary layer parameters. For the displacement thickness, the entire unsteady envelope is lower than the steady values, while for c_f, the minimum unsteady values are approximately the steady ones. Over part of the airfoil oscillation, the flow is completely attached on the upper airfoil surface, as shown by the c_f distribution. This causes significant differences between the steady and time average values of the skin friction.

At the 15 percent chord location, the time average value of δ^* is closer to the maximum and that of c_f nearer to the minimum. This means that the flow is separated over the majority of the oscillation cycle and is attached for only a short time. At the 30 percent chord location, the opposite is true. Therefore the flow is attached over the majority of the oscillation cycle and separated for a limited time. The unsteady boundary layer solution is significantly affected by the oscillation of the cascade as the steady δ^* values are never reached in the unsteady solution from 10 to 90 percent chord.

An explanation for this phenomenon is obtained by considering the influence of the interblade phase angle on the flow

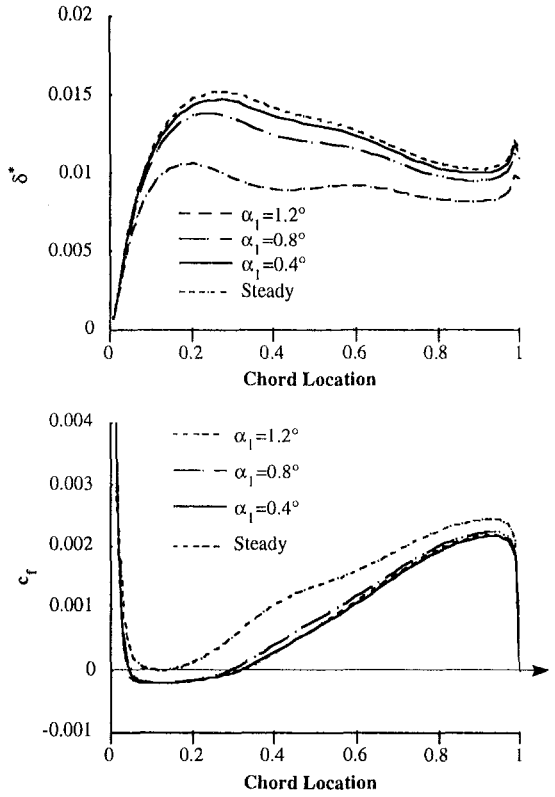

Fig. 14 NASA Pratt & Whitney configuration, time-averaged boundary layer parameters: M = 0.5, k = 0.4, ζ = 60 deg, S/C = 0.657, α = 7 deg, p/P_0 = 0.868, x_{ea} = 0.5, σ = 180 deg

physics. For the 0 deg interblade phase angle analysis, there was no difference between the time average and the steady boundary layer parameters. At 180 deg, the boundary layer is attached over part of the oscillation cycle. The main difference between a 0 and 180 deg interblade phase angle value is that at 180 deg the airfoils are out of phase with one other. When one airfoil is pitched maximum up, the adjacent airfoil is pitched maximum down. This causes a flow restriction between adjacent airfoils, with the adjacent pair of airfoils having an expanded flow area and more favorable flow conditions. Therefore, the flow will be attached on the upper surface of the airfoil that is experiencing the favorable flow conditions.

Assuming the nonlinear effects predicted with the inviscid–viscous interaction analysis at 180 deg interblade phase angle with ±1.2 deg torsional motion are real, then decreasing the amplitude of oscillation should eliminate the nonlinear effects. The time-averaged separated unsteady boundary parameters for three different oscillation amplitudes, ±1.2, ±0.8, and ±0.4 deg, are shown in Fig. 14, along with the steady solution. As the oscillation amplitude is decreased, the time-averaged unsteady results approach the steady ones. The movement of the size of the separation region has significant effects on the downstream boundary layer values. As the separation zone gets smaller, the time-averaged displacement thickness decreases.

Finally, the effect of the nonlinear separated unsteady flow on the first harmonic upper surface pressure distribution is shown, Fig. 15, for the three different oscillation amplitudes. The inviscid solutions show no nonlinear effects as the oscillation amplitude is increased from 0.4 to 1.2 deg. Significant nonlinearities in the inviscid–viscous solutions result from varying the oscillation amplitude. As the oscillation amplitude is increased, the magnitude of the unsteady upper surface pressure difference decreases from 5 to 80 percent of the airfoil surface. A decrease in the phase angle from 30 to 60 percent of the airfoil surface is caused by increasing the oscillation amplitude. This change in phase is caused by the significant movement of the boundary layer reattachment point for the 1.2 deg analysis.

Computational Resources. The computational time penalty required to do the inverse integral boundary layer calculations was approximately 25 percent of the time required for the inviscid analysis. The major computational savings over the Navier–Stokes methods are obtained by being able to use the same grid and time step for the inviscid–viscous interaction analysis as the inviscid analysis. Typically, the difference between inviscid and viscous computational times is 300 percent (Ayer and Verdon, 1995). The computational memory savings are significant for two reasons. First, as the grid density is increased to model the viscous effects properly with the Navier–Stokes methods, the memory requirements go up proportionally. Second, only a few boundary layer parameters need to be stored in one-dimensional arrays compared to including all the viscous flux terms in the whole flow field.

Summary and Conclusions

A computationally efficient mathematical model was developed to analyze the unsteady flow through an harmonically oscillating cascade of airfoils, including inviscid–viscous interactions. The flow solver, which incorporates an inverse integral boundary layer solution with the time-marching Euler analysis NPHASE, was demonstrated for steady flow by analyzing an isolated airfoil and comparing with experimental data. The unsteady flow solver was verified by analyzing a flat plate cascade and comparing the results with linear theory predictions. Also, the unsteady flow solver was compared to an unsteady oscillating cascade data set showing excellent agreement. The analysis method has been compared with high Reynolds number experimental results, but comparison of this method for low-Reynolds-numbers cases is still needed.

The conclusion of this study is that unsteady viscous effects increase the nonlinearity of the oscillating cascade flow. These

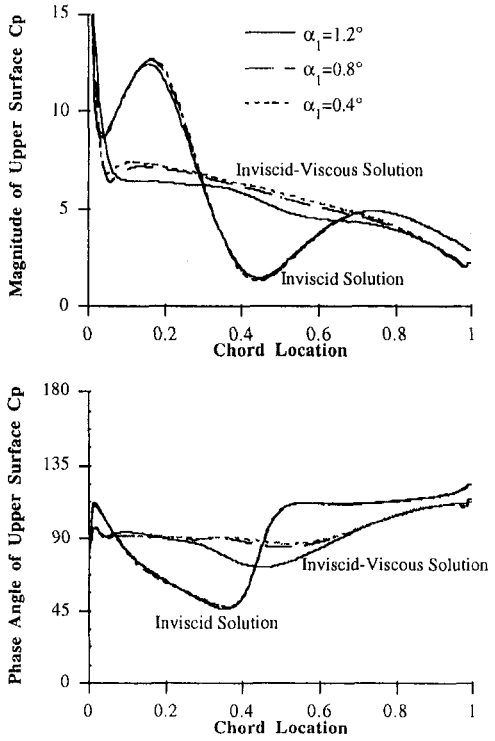

Fig. 15 NASA Pratt & Whitney configuration, unsteady upper surface pressure: M = 0.5, k = 0.4, ζ = 60 deg, S/C = 0.657, α = 7 deg, p/P_0 = 0.868, x_{ea} = 0.5, σ = 180 deg

effects are most significant on the boundary layer parameters, but nonlinear effects are apparent in the unsteady loading. Nonlinear viscous effects were largest for 180 deg interblade phase angle cascade flow conditions, with the viscous effects decreasing as the amplitude of oscillation decreased. In addition, an inverse integral boundary layer viscous/inviscid quasi-steady aerodynamic model has been shown to be a viable unsteady analysis method.

Acknowledgments

This research sponsored in part by the Army Research Office (ARO). This support is most gratefully acknowledged.

References

Ayer, T. C., and Verdon, J. M., 1995, "Numerical Unsteady Aerodynamic Simulator for Blade Forced Response Phenomena," *WL-TR-95-2011*.

Buffum, D. H., 1996, private communication.

Buffum, D. H., Capece, V. R., King, A. J., and EL-Aini, Y. M., 1998, "Oscillating Cascade Aerodynamics at Large Mean Incidence," ASME JOURNAL OF TURBOMACHINERY, Vol. 120, pp. 122–130.

Cook, P. H., McDonald, M. A., and Firmin, M. C. P., 1979, "Airfoil RAE 2822—Pressure Distributions, and Boundary Layer and Wake Measurements," AGARD-AR-138.

Cousteix, J., Houdeville, R., and Javelle, J., 1981, "Response of a Turbulent Boundary Layer to a Pulsation of the External Flow With and Without Adverse Pressure Gradient," in: *Unsteady Turbulent Shear Flows,* R. Michel, J. Cousteix, and R. Houdeville, eds., Springer-Verlag.

Giles, M. B., and Haimes, R., 1993, "Validation of a Numerical Method for Unsteady Flow Calculations," ASME JOURNAL OF TURBOMACHINERY, Vol. 115, pp. 110–117.

He, L., and Denton, J. D., 1993, "Inviscid–Viscous Coupled Solution for Unsteady Flows Through Vibrating Blades," ASME JOURNAL OF TURBOMACHINERY, Vol. 115, pp. 101–109.

Huff, D. L., Wu, J. C., and Sankar, L. N., 1987, "Analysis of Viscous Transonic Flow Over Airfoil Sections," AIAA Paper No. 87-0420.

Huff, D. L., 1991, "Unsteady Flow Field Predictions for Oscillating Cascades," *Sixth International Symposium on Unsteady Aerodynamic, Aeroacoustics and Aeroelasticity of Turbomachines and Propellers,* Springer-Verlag, University of Notre Dame, USA.

Karlsson, S. K. F., 1959, "An Unsteady Turbulent Boundary Layer," *Journal of Fluid Mechanics,* Vol. 5, pp. 622–636.

Swafford, T. W., 1980, "Analytical Approximation of Two-Dimensional Separated Turbulent Boundary-Layer Velocity Profiles," Arnold Engineering Development Center, Report # AEDC-TR-79-99.

Whitehead, D. S., 1987, "Classical Two-Dimensional Methods," AGARD *Manual on Aeroelasticity in Axial-Flow Turbomachines, Vol. 1, Unsteady Turbomachinery Aerodynamics.*

Whitfield, D. L., 1978, "Integral Solution of Compressible Turbulent Boundary Layers using Improved Velocity Profiles," Arnold Engineering Development Center, Report # AEDC-TR-78-42.

Whitfield, D. L., Swafford, T. W., and Donegan, T. L., 1982, "An Inverse Integral Computational Method for Compressible Turbulent Boundary Layers," in: *Recent Contributions to Fluid Mechanics,* W. Haase, ed., Springer-Verlag.

Wolff, J. M., and Fleeter, S., 1994a, "Single Passage Euler Analysis of Oscillating Cascade Aerodynamics for Arbitrary Interblade Phase," *Journal of Propulsion and Power,* Vol. 10, pp. 690–697.

Wolff, J. M., and Fleeter, S., 1994b, "Euler Analysis of Oscillating Cascade Unsteady Aerodynamics Using Embedded Composite Grids," AIAA Paper No. 94-0077.

The Influence of Film Cooling on the Efficiency of an Annular Nozzle Guide Vane Cascade

C. R. B. Day

M. L. G. Oldfield

Department of Engineering Science, Oxford University, United Kingdom

G. D. Lock

Department of Mechanical Engineering, University of Bath, United Kingdom

This paper examines the effect of aerofoil surface film cooling on the aerodynamic efficiency of an annular cascade of transonic nozzle guide vanes. A dense foreign gas (SF_6/Ar mixture) is used to simulate engine representative coolant-to-mainstream density ratios under ambient conditions. The flowfield measurements have been obtained using a four-hole pyramid probe in a short duration blowdown facility that correctly models engine Reynolds and Mach numbers, as well as the inlet turbulence intensity. The use of foreign gas coolant poses specific challenges not present in an air-cooled cascade, and this paper addresses two. First, a novel method for the determination of mass flow from pneumatic probe data in a heterogeneous gas environment is presented that eliminates the need to measure concentration in order to determine loss. Second, the authors argue on the grounds of dimensionless similarity that momentum flux ratio is to be preferred to blowing rate for the correct parameterization of film cooling studies with varying coolant densities. Experimental results are presented as area traverse maps, from which values for loss have been calculated. It is shown that air and foreign gas at the same momentum flux ratio give very similar results, and that the main difference between cooled and uncooled configurations is an increase in wake width. Interestingly, it is shown that an increase in the momentum flux ratio above the design value with foreign gas coolant reduces the overall loss compared with the design value. The data have been obtained both for purposes of design and for CFD code validation.

1 Introduction

The use of discrete-hole film cooling to reduce surface temperatures on nozzle guide vane surfaces has long been recognized as a source of aerodynamic inefficiency, despite its beneficial thermal effects. The loss mechanisms in such an environment can be classified into three areas (King, 1986):

- Uncooled/baseline aerodynamic loss. This encompasses all losses found in an uncooled blade row, including profile loss, secondary loss, and leakage loss.
- Coolant mixing losses.
- Loss of available work due to injection of coolant at a temperature below that of the mainstream.

The loss of available work due to the cold injected coolant is solely a thermodynamic effect, and thus experimental work in this field has concentrated on the first two areas.

The body of literature on uncooled losses is both broad and deep, and Denton (1993) gives a good overview of the state of the field. His emphasis is on the fundamental processes that cause loss, which he analyzes in terms of entropy generation. His convincing argument about the importance of understanding the basic physical mechanisms in loss is echoed in the present study's examination of meaningful methods for the simulation of coolant-to-mainstream density ratio in cooling. Experimentally, Sieverding et al. (1984) studied the evolution of the flow field in a low-speed high-turning annular nozzle guide vane cascade, showing the effect of the radial pressure gradient in the movement of low momentum boundary layer fluid. A later study by Dominy and Harding (1989) showed the importance of the three-dimensional nature of modern blading in the size and distribution of secondary losses. Both these studies emphasize the significance of the highly three-dimensional nature of nozzle flows in modern turbomachines, and indeed the present study has been careful to maintain the full annular geometry typical of a modern aeroengine.

Coolant mixing losses have been investigated in many different configurations. Haller and Camus (1984) studied the effects on loss of coolant ejection from five separate cooling hole locations, finding that ejection downstream of the throat did not generate significantly higher losses than ejection upstream of the throat. Kollen and Koschel (1985) found that loss increased with blowing rate for injection in the leading edge area, while on the suction surface the loss decreased with increasing blowing rate for all but the lowest blowing rates. Both these studies considered film cooling on aerofoil surfaces, and both used carbon dioxide to simulate density ratios. However, Haller and Camus (1984) found that their results were not affected by density ratio, and thus for their later tests used only air as coolant. By contrast Mee (1992), in a study of trailing-edge film cooling, found a definite effect of density ratio, which could nonetheless be correlated by the use of momentum flux ratio as a parameter rather than blowing rate. The present authors believe that the influence of density ratio has not yet been satisfactorily established, and thus careful consideration has been given to this issue in the present study.

Against the background outlined above, the authors believe there is a need for detailed data in fully three-dimensional film cooled cascades, with careful attention given to meaningful coolant simulation. Hence this paper presents experimental data from a large-scale annular cascade under both cooled and uncooled conditions. Experimental issues raised by the use of foreign gas to simulate density ratio are discussed, and the question of defining loss in a cooled annular cascade is addressed. The information is intended to be useful both for design purposes and for the validation of CFD codes.

Contributed by the International Gas Turbine Institute and presented at the 42nd International Gas Turbine and Aeroengine Congress and Exhibition, Orlando, Florida, June 2–5, 1997. Manuscript received International Gas Turbine Institute February 1997. Paper No. 97-GT-521. Associate Technical Editor: H. A. Kidd.

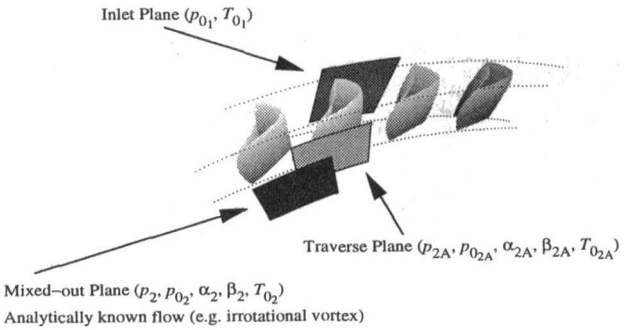

Fig. 1 Schematic of the mixing-out process

2 Loss Calculation in a Cooled Turbine Stator

2.1 Definition of Loss. For any blade row, the process of loss determination typically begins by mixing out the measured exit flowfield (the "traverse" plane) to an analytically known flow (the so-called "mixed-out" plane). The process is illustrated diagrammatically in Fig. 1. The transformation from inlet to exit flow is then compared to an ideal (usually isentropic) reference case, and the losses determined. The mixing-out process is essentially one of averaging. The equations of conservation of mass, momentum, and energy are applied to produce a known flow that is mathematically equivalent to the actual exit flow. For two-dimensional blade rows, this can be uniform flow (Amecke, 1970). For an annular nozzle guide vane row, however, the swirling exit flow must have a radial pressure gradient and hence can be uniform only in the circumferential direction. Main et al. (1997) discuss possible choices for the mixed-out flow, concluding that the free vortex is the most consistent choice.

In the case of an annular stator cascade such as that considered in the present study, the conservation equations are:

Mass:

$$I_{\text{mass}} = \int_{r_i}^{r_o}\int_{0}^{2\pi} \rho_{2A} v_{2A} \cos\beta_{2A} \cos\alpha_{2A} r d\theta dr = 2\pi \int_{r_i}^{r_o} \rho_2 v_2 \cos\beta_2 r dr \quad (1)$$

Axial momentum:

$$I_{\text{axial}} = \int_{r_i}^{r_o}\int_{0}^{2\pi} [\rho_{2A} v_{2A}^2 \cos^2\beta_{2A} \cos^2\alpha_{2A} + p_{2A}] r d\theta dr = 2\pi \int_{r_i}^{r_o} [\rho_2 v_2^2 \cos^2\beta_2 + p_2] r dr \quad (2)$$

Angular momentum:

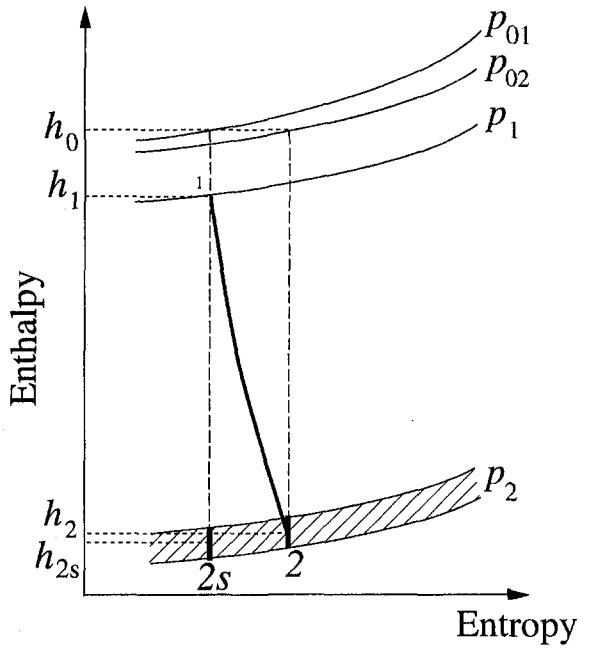

Fig. 2 Expansion through a nozzle as viewed on an enthalpy–entropy chart. Radial pressure gradients in the exit plane may require a range of possible p_2.

$$I_{\text{angular}} = \int_{r_i}^{r_o}\int_{0}^{2\pi} \rho_{2A} v_{2A}^2 \sin\beta_{2A} \cos\beta_{2A} \cos^2\alpha_{2A} r d\theta dr = 2\pi \int_{r_i}^{r_o} \rho_2 v_2^2 \sin\beta_2 \cos\beta_2 r dr \quad (3)$$

Energy:

$$I_{\text{energy}} = \int_{r_i}^{r_o}\int_{0}^{2\pi} c_{p2A} T_{02A} \rho_{2A} v_{2A} \cos\beta_{2A} \cos\alpha_{2A} r d\theta dr = 2\pi \int_{r_i}^{r_o} c_{p2} T_{02} \rho_2 v_2 \cos\beta_2 r dr \quad (4)$$

These are to be solved using experimental measurements of p_0, M, and two flow angles (α and β). A method for using these equations to mix out the flow at exit of an annular non-cooled blade row has been described by Main et al. (1997).

The method of Main et al. (1997) is a fully three-dimensional method, which mixes the outlet flow to a free vortex. For the purpose of loss determination this is then compared to an ideal flow (also a free vortex) having the same static pressure at midspan. This is shown schematically in Fig. 2, where the exit

Nomenclature

a = local speed of sound
A = flow area
B = blowing rate = $\rho_c v_c / \rho_m v_m$
c_{ax} = axial chord
c_p = specific heat capacity at constant pressure
c_v = specific heat capacity at constant volume
h = enthalpy
I = conservation integral
M = Mach number
$\dot{m}$ = mass flow rate
p = pressure
r = radius
R = gas constant
T = temperature
v = flow velocity
x = mass fraction of coolant
α = pitch angle (tip-to-hub angle)
β = swirl angle (blade-to-blade angle)
γ = ratio of specific heat capacities $= c_p/c_v$
θ = circumferential angle
η = efficiency (see Eq. (5))
$\phi = M_{2A}\sqrt{\gamma}(1 + [(\gamma - 1)/2] M_{2A}^2)^{(1+\gamma)/2(1-\gamma)}$
$\psi = p_{02A}/\sqrt{T_{02A}}$
ρ = density
ζ = loss = $1 - \eta$

Subscripts

0 = stagnation value
1 = inlet value
2A = measured value
2 = mixed-out value
c = coolant
i = inner endwall
m = mainstream
o = outer endwall
s = isentropic conditions

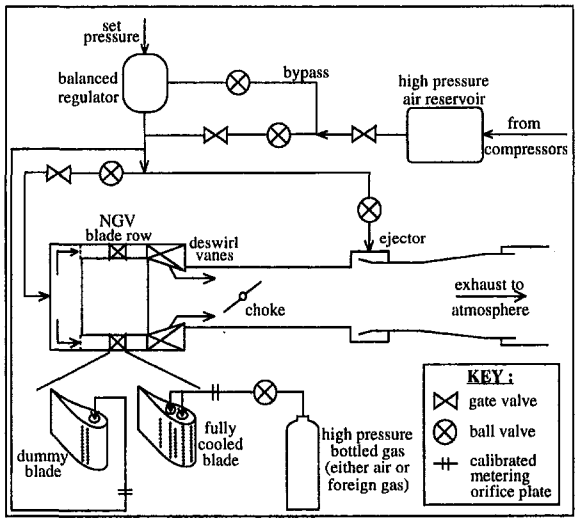

Fig. 3 Schematic diagram of the CHTT

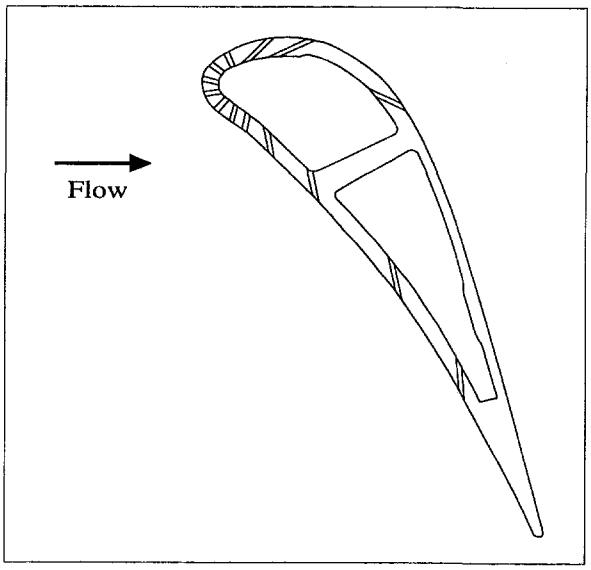

Fig. 4 Cross section through blade showing location of coolant holes

conditions are represented by a range of pressures p_2, because of the radial pressure gradient.

When dealing with a cooled blade row, the definition of ideal flow must be modified because there are now (at least) two separate initial streams. In a two-dimensional analysis it is still possible to expand the two streams separately since the exit condition is defined by a single static pressure. For a three-dimensional analysis, however, there is insufficient information to describe the ideal reference flows adequately for both mainstream and coolant, since they must themselves be mixed somewhere between inlet and outlet. Thus an alternative approach must be adopted as a compromise. The present authors advocate the use of Dzung's (1971) method for this purpose. This uses a swirl-averaging technique to evaluate a set of mean values of the flow at a single radius. Such a method has the advantage that it uses a single point in (enthalpy–entropy)-space to describe the exit flow, in effect removing a dimension from the problem. The ideal flow is then defined as a simple expansion of each stream from inlet to outlet conditions. Although this reduces the physical rigor of the model, the benefit in terms of simplification amply compensates for this. Main et al. (1997) have previously shown that the Dzung method agrees closely with their own for noncooled blade rows. For this reason, this is the method used in the present study. When the Dzung method is used to mix out the flow, the efficiency definition commonly used in two-dimensional flows (Mee, 1992) may be used with $\gamma_c = \gamma_m$, namely:

$$\eta = \frac{\text{Actual Exit Kinetic Energy}}{\text{Isentropic K.E. of mainstream + Isentropic K.E. of coolant}} = \frac{\left(1 + \frac{\dot{m}_c c_{pc} T_{0c}}{\dot{m}_m c_{pm} T_{0m}}\right)\left(1 - \left(\frac{p_2}{p_{0,2}}\right)^{(\gamma-1)/\gamma}\right)}{\left(1 - \left(\frac{p_2}{p_{0,m}}\right)^{(\gamma-1)/\gamma}\right) + \frac{\dot{m}_c c_{pc} T_{0c}}{\dot{m}_m c_{pm} T_{0m}}\left(1 - \left(\frac{p_2}{p_{0,c}}\right)^{(\gamma-1)/\gamma}\right)} \quad (5)$$

2.2 Measurement of Mass Flow. The present study is concerned with loss determination in a *film-cooled* stator blade row. A heavy "foreign gas" (a SF_6/Ar mixture) is used to simulate an engine-representative density ratio of 1.77. The coolant has been carefully chosen to have the same ratio of specific heats ($\gamma = 1.4$) as air. In solving the conservation equations above, the energy balance (Eq. (4)) is redundant as all components are at ambient temperature. Equations (2) and (3) can be solved using the measured variables ($p_{0,2A}$, M_{2A}, α_{2A} and β_{2A}) as they are expressed in terms of the dynamic head ($=(1/2)\rho v^2)_{2A}$. However, Eq. (1) explicitly involves v_{2A}, and this can only be calculated if the spatial variation of R_{2A} (i.e., the concentration of foreign gas) across the annulus is known. In a transient facility the measurement of this is not trivial, and an alternative method for the determination of mass flow must therefore be sought.

For the apparatus described in the present study, independent measurement of mainstream mass flow using, for example, an orifice plate, was not feasible due to the large scale of the apparatus. Hence it was necessary to derive an alternative method for mass flow determination that made use of the downstream measurements. It is shown in the appendix to this paper that an acceptable approximation to the mass flow may be obtained from the formula

$$\dot{m}_{\text{total}} = \dot{m}_{m-\text{air}} + \frac{1}{2}\left(1 - \frac{R_c}{R_m}\right)\dot{m}_c \quad (6)$$

where $\dot{m}_{m-\text{air}}$ is the mass flow calculated from the downstream area traverse assuming that the coolant is air (i.e., ignoring the variation in R_{2A}). The coolant mass flow $\dot{m}_c$ is measured using calibrated orifice plates, and thus all terms in Eq. (6) are known. As is shown in the appendix, this approximation typically introduces an error of <0.1 percent.

3 Using Foreign Gas in Experimental Studies

As indicated above, the current study uses a foreign gas to simulate engine-representative density ratios. The use of a foreign gas to simulate density ratios in film cooling research is a

Table 1 Salient parameters of the CHTT

Mean axial chord (mm)	66.7
Span at exit (mm)	80.8
Mean blade diameter (mm)	1113
Exit Mach number	0.96
Exit Reynolds number	2×10^6
Coolant pressure ratio (p_{0c}/p_{0m}) - standard	1.02
Coolant pressure ratio (p_{0c}/p_{0m}) - strong blowing	1.07
Coolant mass flow as fraction of main flow (foreign gas cooling - standard blowing)	3.6%

widely used technique, and Teekaram et al. (1989) have shown its value in studies of heat transfer. The most common foreign gas used in the literature is CO_2, which produces a density ratio of 1.53 at standard conditions. However, air ($\gamma = 1.4$) and CO_2 ($\gamma = 1.3$) behave differently from a thermodynamic perspective, and thus the present study sought a more compatible gas. A mixture of 30.2 percent w/w SF_6, balance Ar, has density ratio 1.77, and a ratio of specific heats of 1.4, the same as that for air. As will be seen below, the use of a gas with a similar ratio of specific heats gives great benefits in the analysis of results.

Although the present study uses a foreign gas coolant in some experiments, it is also desirable to use air as the coolant in others, and indeed such experiments are reported herein. These experiments aim to demonstrate the influence of density ratio on the aerodynamic phenomena under investigation. However, the design of such experiments must address the question of what constitutes "similarity" in these circumstances. In the literature the most common parameter used to correlate experiments using coolants of difference density ratio is the blowing rate, B, apparently because it is easy to conceptualize and measure. However, as the following analysis shows, it is inappropriate from an aerodynamic perspective.

Aerodynamic equivalence between two cascade cooling experiments using different coolants is achieved if the ratio of the flow area occupied by the coolant and mainstream at any position is the same in both cases. The equation of continuity indicates that the area occupied by a flow is given by

$$A = \left(\frac{\dot{m}}{\rho u}\right) = \left(\frac{\dot{m}\sqrt{RT}}{p\mathrm{M}\sqrt{\gamma}}\right) \tag{7}$$

If the experiments are performed with coolants with the same value of γ, and with the same static pressure at any position, the ratio of coolant to mainstream flow areas is given by:

$$\frac{A_c}{A_f} = \frac{(\dot{m}\sqrt{RT}/\mathrm{M})_c}{(\dot{m}\sqrt{RT}/\mathrm{M})_m} \tag{8}$$

Generally it is required that the mainstream flow be unchanged, and in transonic flows an additional requirement is that the coolant Mach number be the same. Thus the requirement is that the product $\dot{m}\sqrt{RT}$ should be the same for the two coolants for comparable cooling. This requirement is equivalent to matching momentum flux ratio, since $\dot{m}u = \dot{m}\mathrm{M}a = \dot{m}\mathrm{M}\sqrt{\gamma RT}$, which is equal to $\dot{m}\sqrt{RT}$ if the coolant Mach number and ratio of specific heats are the same as before.

Operationally, the flow rate through an orifice is inversely proportional to $\sqrt{RT}$ for a given pressure difference, and thus if the external Mach number distribution is unchanged, then momentum flux ratio will be matched if $p_{0,c}/p_{0,m}$ is constant. The coolant Mach number will then also be the same, as previously assumed. Thus, in summary, the present study simulated the engine coolant by using the correct density ratio and ratio of specific heats, and the momentum flux ratio was set correctly by operating at the engine-design ratio of $p_{0,c}/p_{0,m}$. The blowing rate was not simulated.

It has also been shown experimentally that momentum flux correlates loss better than blowing rate (Mee, 1992), as the analysis above would suggest. It should be noted that the use of a coolant with the same ratio of specific heats as air simplifies the analysis considerably.

4 Description of Experimental Facility

The present study was undertaken in the Cold Heat Transfer Tunnel (CHTT) at Oxford University. The CHTT is an annular cascade of 36 nozzle guide vanes, typical of those found in the high-pressure turbine section of a modern aeroengine. The original configuration has been described in detail elsewhere (Martinez-Botas et al., 1993); however, it has recently been

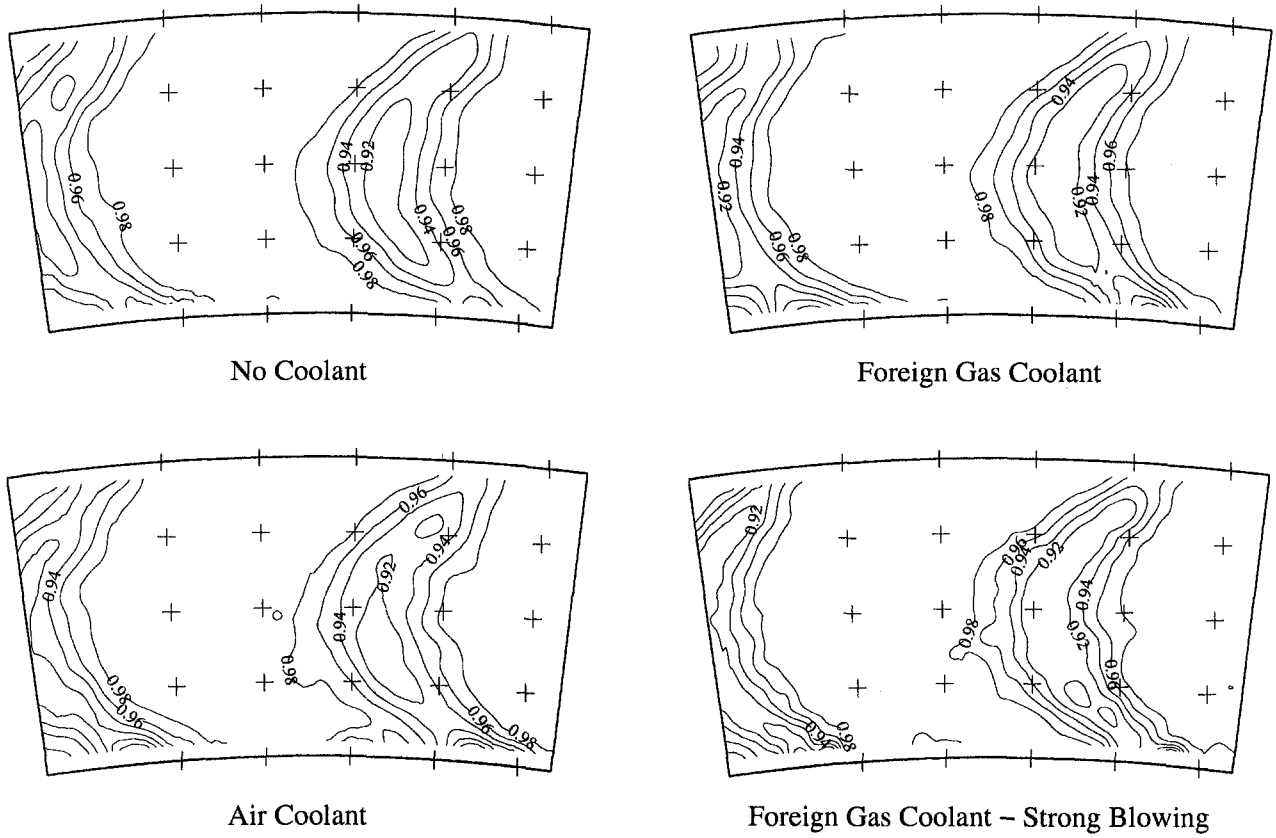

Fig. 5 Traverse plane maps of total pressure, normalized with respect to upstream total pressure

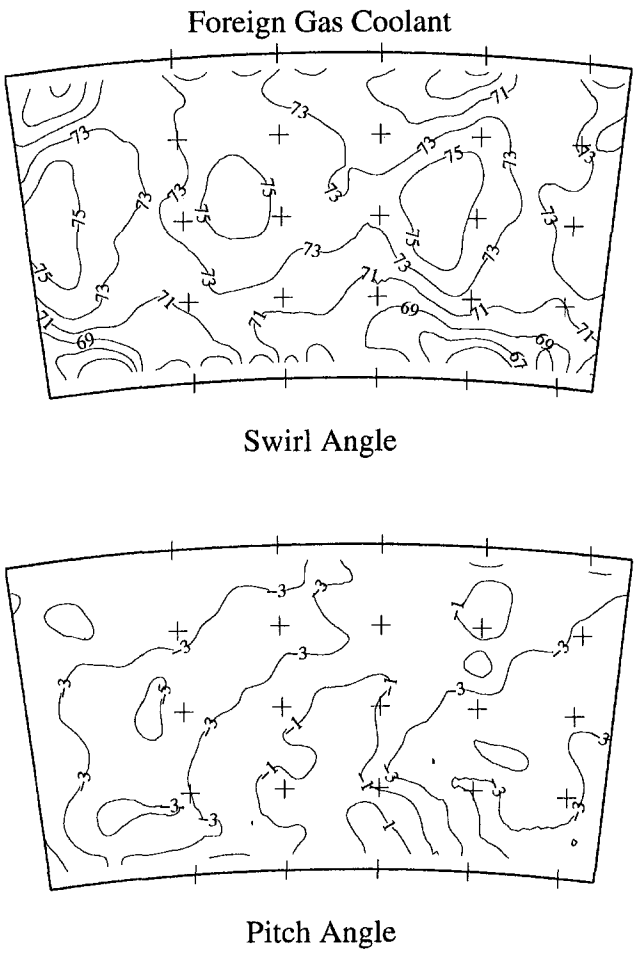

Fig. 6 Traverse plane maps of flow angles; these quantities are not greatly affected by cooling

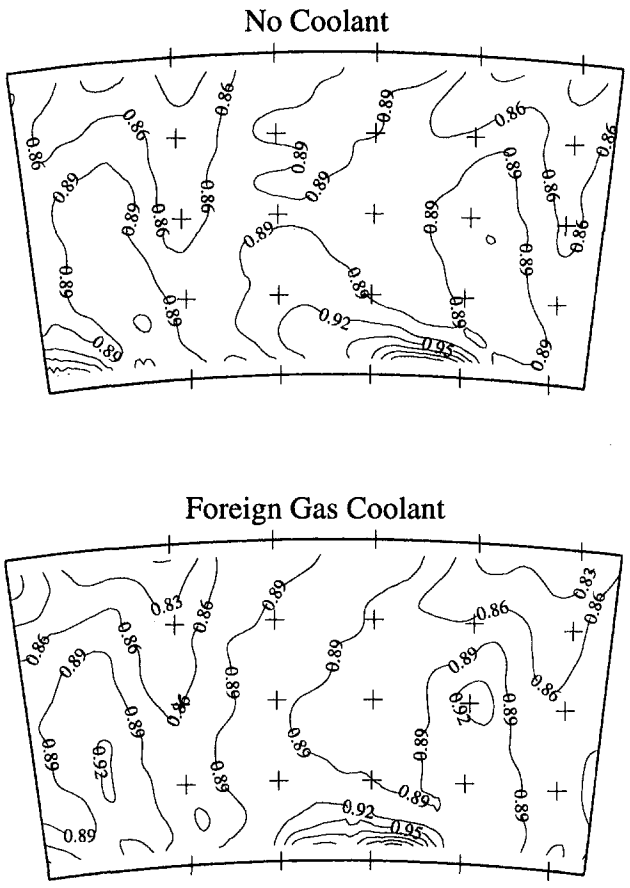

Fig. 7 Traverse plane maps of isentropic Mach number

extended to provide for film cooling of the aerofoil surfaces. The tunnel is a transient facility fed from a large high-pressure reservoir via a balanced regulator (see Fig. 3). At engine design conditions (M_{exit} = 0.96 based on the mean of the endwall Mach numbers, Re = 2×10^6 based on axial chord and exit conditions) a regulated run time of approximately four seconds is attainable. The inlet total pressure is approximately 200 kPa, and the inlet free-stream turbulence intensity of 13 percent reflects the high turbulence level typical of a combustor exit.

The blade coolant system is divided into two subsystems. The first, which accounts for the three vanes under investigation, feeds from three gas bottles (air or SF_6/Ar) through a standard regulation system. The mass flow into each blade is measured using a choked orifice plate. These three blades are configured with an advanced cooling geometry consisting of approximately 300 holes arranged in 14 rows (see Fig. 4). The second coolant subsystem feeds the remaining 33 blades in the annulus, and draws air from the main tunnel regulator. The mass flow rate into each blade is also metered using choked orifice plates, and set to ensure the same momentum flux ratio as in the first coolant subsystem as explained in the previous section. These blades are configured with a simplified cooling geometry consisting of approximately 80 holes arranged in four rows, and maintain periodicity around the annulus while avoiding the cost and complexity of the full coolant geometry. A schematic of the apparatus is shown in Fig. 3, and salient details of the tunnel are given in Table 1.

Traverses downstream of the cascade were conducted using the four-hole pyramid probe described by Main et al. (1996). This was traversed rapidly behind the blade row in both a radial and circumferential direction, and over the course of approximately seven runs of the tunnel, a full area map of the flowfield was produced. Transformation of the raw probe data yielded values of total pressure, Mach number, pitch and yaw angle, which were then interpolated onto a regular grid over the annulus area for the purposes of plotting and loss determination. The calculation of loss was performed using Dzung's (1971) method as outlined above.

5 Experimental Results

Full area traverses of total pressure, Mach number, pitch and yaw angle have been obtained at design conditions for the

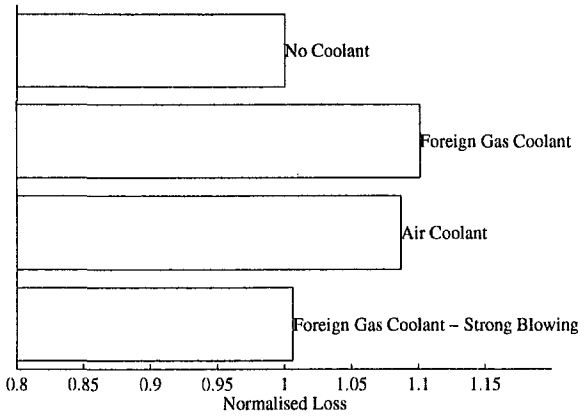

Fig. 8 Comparison of losses for the four cases investigated

situations both with and without foreign gas cooling. In addition, results to investigate the effect of density ratio have been obtained using air as coolant, and the influence of momentum flux ratio has been considered by examining the flowfield with above design $p_{0,c}/p_{0,m}$. In all the area traverses presented here, a gird of crosses is superimposed on the experimental data to indicate the area used in the loss calculation.

Figure 5 shows the total pressure distribution in the measurement plane, normalized relative to the upstream total pressure. Three film-cooled cases are shown, with both air and foreign gas as coolant. It can be seen that the main influence of cooling is to thicken the wake (relative to the uncooled case) for the normal blowing case, while for strong blowing the wake is similarly wider, but to a lesser degree. The depth of the wake is not greatly increased for the normal blowing case, but for the stronger blowing there is a definite increase in average wake depth. In all cases the shape of the wake is remarkably constant. Figure 6 shows the distributions of flow angle, which do not seem to be greatly influenced by cooling.

The results for air and foreign gas cooling at the same momentum flux ratio show considerable similarity, giving confidence in the analysis outlined above, suggesting that this, rather than blowing rate, should be the preferred correlating parameter. One interesting feature that is similarly apparent with both air and foreign gas coolant is the region of low static pressure (high isentropic Mach number, defined using $p_{2A}/p_{0,1}$) on the pressure surface side of the wake near the hub endwall. Figure 7 shows the isentropic Mach numbers for the situation with no coolant and with foreign gas coolant, and it can be seen that the size of this feature is appreciably larger in the presence of cooling.

Using the full area traverse data described above, the aerodynamic loss associated with each configuration may be determined. This has been done as described above, and the results are shown in Fig. 8, which presents loss normalized with respect to the no-coolant configuration, for which the loss $\zeta = 0.0484$. This differs slightly from that reported for the same cascade by Main et al. (1997) due to refinements in the loss calculation algorithm, but (as in that study) it is *relative* loss that is sought, and this is not significantly affected by such refinements. It can be seen that for design-level cooling both foreign gas and air give very similar values for the change in loss. For the strong blowing case, however, the loss is almost identical to that found for the no-coolant case. This trend is similar to that described by Kollen and Koschel (1985), who found that for coolant ejection on the suction surface the loss initially increased and then subsequently decreased as the blowing rate was increased. A detailed explanation of the mechanism for the loss variation is beyond the scope of this paper.

6 Conclusions

This paper has presented the first aerodynamic loss measurements in the presence of film cooling from the Oxford blowdown facility. They are significant because they have been obtained in a large-scale transient environment, which correctly models engine Reynolds and Mach numbers in a full three-dimensional geometry.

The paper addresses two important new issues unique to the film-cooled environment: the definition of an ideal flow to be used in loss calculation, and the measurements that are necessary for such loss calculation. In the latter context a novel method has been developed that uses a series expansion to obtain an accurate approximation of the total mass flow through the cascade. The paper also addresses the question of correct parameterization of coolant density effects, showing that correct correlation requires matching of the momentum flux ratio rather than the blowing rate.

The paper presents results as full area traverses of total pressure, Mach number, pitch and yaw angles. It is shown that the dominant effect of film cooling is a thickening of the main vane wake, and also that the hub flowfield is modified in the presence of cooling. The use of air as coolant rather than foreign gas is shown to produce broadly similar patterns, supporting the use of momentum flux ratio as a correlating parameter. The losses calculated with the two different coolants are similar, and show a small increase of approximately 9 percent over the uncooled losses.

Acknowledgments

The authors would like to thank D. Rowbury for assistance in all phases of the project, and T. V. Jones for advice on coolant issues. This work was funded by Rolls-Royce plc and DRA (MoD and DTI), whose continuing generous support is gratefully appreciated.

References

Amecke, J., 1970, "Anwendung der transsonischen Ahnlichkeitsregel auf die Stromung durch ebene Schaufelgitter," *VDI Forschungsheft,* Vol. 540, pp. 16–28.

Denton, J. D., 1993, "Loss Mechanisms in Turbomachines," ASME JOURNAL OF TURBOMACHINERY, Vol. 115, pp. 621–656.

Dominy, R. G., and Harding, S. C., 1989, "An investigation of secondary flows in nozzle guide vanes," AGARD CP-469.

Dzung, L. S., 1971, "Konsistente Mittelwerte in der Theorie der Turbomaschinen für Kompressible Medien," *BBC-Mitt.,* Vol. 58, pp. 485–492.

Haller, B. R., and Camus, J. J., 1984, "Aerodynamic loss penalty produced by film cooling transonic turbine blades," ASME *Journal of Engineering for Gas Turbines and Power,* Vol. 106, pp. 198–205.

King, P. I., 1986, "Aerodynamics of high performance turbine blading," D. Phil. Thesis, University of Oxford.

Kollen, O., and Koschel, W., 1985, "Effect of film-cooling on the aerodynamic performance of a turbine cascade," AGARD CP-390.

Main, A. J., Day, C. R. B., Lock, G. D., and Oldfield, M. L. G., 1996, "Calibration of a four-hole pyramid probe and area traverse measurements in a short-duration transonic turbine cascade tunnel," *Experiments in Fluids,* Vol. 21, pp. 302–311.

Main, A. J., Oldfield, M. L. G., Lock, G. D., and Jones, T. V., 1997, "Free Vortex Theory for Efficiency Calculations From Annular Cascade Data," ASME JOURNAL OF TURBOMACHINERY, Vol. 119, pp. 247–255.

Martinez-Botas, R. F., Main, A. J., Lock, G. D., and Jones, T. V., 1993, "A cold heat transfer tunnel for gas turbine research on an annular cascade," ASME Paper No. 93-GT-248.

Mee, D. J., 1992, "Techniques for Aerodynamic Loss Measurement of Transonic Turbine Cascades With Trailing-Edge Region Coolant Ejection," ASME Paper No. 92-GT-157.

Sieverding, C. H., Van Hove, W., and Boletis, E., 1984, "Experimental study of the three-dimensional flow field in an annular turbine nozzle guide vane," ASME *Journal of Engineering for Gas Turbines and Power,* Vol. 106, No. 2.

Teekaram, A. J. H., Forth, C. J. P., and Jones, T. V., 1989, "The use of foreign gas to simulate the effects of density ratios in film cooling," ASME JOURNAL OF TURBOMACHINERY, Vol. 111, pp. 57–62.

APPENDIX

Calculation of Mass Flow From Traverse-Plane Data

The isentropic flow equations lead to the following:

$$\rho_{2A}v_{2A} = M_{2A}\sqrt{\gamma}\left(1 + \frac{\gamma - 1}{2}\,\mathrm{M}_{2A}^2\right)^{(1+\gamma)/2(1-\gamma)} \frac{p_{02A}}{\sqrt{R_{2A}T_{02A}}}$$

$$= \varphi\,\frac{p_{02A}}{\sqrt{T_{02A}}}\,\frac{1}{\sqrt{R_{2A}}} \qquad \text{(A1)}$$

where $\varphi = \varphi(\mathrm{M}_{2A}, \gamma)$ is a known function of M_{2A} and γ.

For the situation of coolant and mainstream at the same total temperature, measurements in the traverse plane yield all the quantities in the above equation except for R_{2A}, which depends on the concentration of foreign gas:

$$R_{2A} = (1 - x)R_m + xR_c = R_m - x(R_m - R_c) \qquad \text{(A2)}$$

where the variable x is the mass fraction of coolant at any point in the measured flow. From this equation a series expansion may be used to derive:

$$\frac{1}{\sqrt{R_{2A}}} = \frac{1}{\sqrt{R_m}} + \frac{1}{\sqrt{R_{2A}}}\frac{1}{2}\left(x\left(1 - \frac{R_c}{R_m}\right)\right)$$

$$- \frac{1}{\sqrt{R_{2A}}}\frac{1}{8}\left(x\left(1 - \frac{R_c}{R_m}\right)\right)^2 + \text{higher order terms} \quad \text{(A3)}$$

Substituting Eq. (A3) into Eq. (A1) and thence into Eq. (1), the total mass flow I_{mass} is given by:

$$I_{\text{mass}} = \int_{r_i}^{r_o}\int_0^{2\pi} \rho_{2A}v_{2A}\cos\beta_{2A}\cos\alpha_{2A}rd\theta dr$$

$$= \int_{r_i}^{r_o}\int_0^{2\pi} \varphi\frac{P_{02A}}{\sqrt{T_{02A}}}\frac{1}{\sqrt{R_{2A}}}\cos\beta_{2A}\cos\alpha_{2A}rd\theta dr$$

$$= \int_{r_i}^{r_o}\int_0^{2\pi} \varphi\psi\frac{1}{\sqrt{R_m}}\cos\beta_{2A}\cos\alpha_{2A}rd\theta dr$$

$$+ \frac{1}{2}\left(1 - \frac{R_c}{R_m}\right)\int_{r_i}^{r_o}\int_0^{2\pi} x\varphi\psi\frac{1}{\sqrt{R_{2A}}}\cos\beta_{2A}\cos\alpha_{2A}rd\theta dr$$

$$+ \int_{r_i}^{r_o}\int_0^{2\pi}\frac{1}{8}\left(x\left(1 - \frac{R_c}{R_m}\right)\right)^2\varphi\psi\frac{1}{\sqrt{R_{2A}}}\cos\beta_{2A}\cos\alpha_{2A}$$

$$rd\theta dr + \text{higher order terms.} \quad \text{(A4)}$$

where $\psi = p_{02A}/\sqrt{T_{02A}}$.

The first term on the right hand side of Eq. (A4) is simply the mass flow that would have been calculated if it had been assumed that the coolant and mainstream gases had been the same. Considering the second term, and noting that at the traverse plane the coolant mass flow is x times the total mass flow at any point, it follows that:

$$\dot{m}_c = \int_{r_i}^{r_o}\int_0^{2\pi} x\rho_{2A}v_{2A}\cos\beta_{2A}\cos\alpha_{2A}rd\theta dr$$

$$= \int_{r_i}^{r_o}\int_0^{2\pi} x\varphi\psi\frac{1}{\sqrt{R_{2A}}}\cos\beta_{2A}\cos\alpha_{2A}rd\theta dr \quad \text{(A5)}$$

which is the integral in the second term of Eq. (A4).

The mass flow of the coolant, $\dot{m}_c$, is known from orifice plate data, and thus this term is simply a correction to the first. Thus Eq. (A4) provides a means to calculate the total mass flow through the cascade using only the variables measured in the traverse plane and the coolant mass flow.

In order to estimate the error introduced by this approximation we examine a simplified case. Assume that, at the measurement plane $2A$, the coolant is mixed uniformly in the wake, and zero outside. Thus $x = 0$ outside the wake, and the integrals in the second and third term of Eq. (A4) need only be integrated over the wake. Within the wake x is constant, so the third term is $(x/8)(1 - R_c/R_m)^2\dot{m}_c$. Thus the percentage error is $(x/8)(1 - R_c/R_m)^2(\dot{m}_c/\dot{m}_{\text{total}}) \times 100$. Parameters representative of the current study are $R_c = 162$ kJ/kg K, $R_m = 287$ kJ/kg K, and $(\dot{m}_c/\dot{m}_{\text{total}}) = 0.07$. If the wakes occupy 20 percent of the passage at the measurement plane, the numerical value of this third term is approximately 0.06 percent. This is less than the inherent errors generally encountered in probe measurements in transonic cascade flows.

Mechanisms of Turbulence Transport in a Turbine Blade Coolant Passage With a Rib Turbulator

P. K. Panigrahi

S. Acharya

Department of Mechanical Engineering,
Louisiana State University,
Baton Rouge, LA 70803

This paper provides detailed measurements of the flow in a ribbed coolant passage, and attempts to delineate the important mechanisms that contribute to the production of turbulent shear stress and the normal stresses. It is shown that the separated flow behind the rib is dictated by large-scale structures, and that the dynamics of the large-scale structures, associated with sweep, ejection, and inward and outward interactions, all play an important role in the production of the turbulent shear stress. Unlike the turbulent boundary layer, in a separated shear flow past the rib, the inward and outward interaction terms are both important, accounting for a negative stress production that is nearly half of the positive stress produced by the ejection and sweep mechanisms. It is further shown that the shear layer wake persists well past the re-attachment location of the shear layer, implying that the flow between ribbed passages never recovers to that of a turbulent boundary layer. Therefore, even past re-attachment, the use of statistical turbulence models that ignore coherent structure dynamics is inappropriate.

1 Introduction

The flow in the internal ribbed passages of a gas turbine blade coolant channel is essentially characterized by flow separation about one rib-height upstream of each rib and re-attachment nearly 5 to 6 rib-heights downstream of the rib. The separated shear layer past the rib has been shown (Panigrahi and Acharya [1]; Acharya et al. [2]) to be dominated by coherent structures and it is expected that the flow and heat transport mechanisms would be largely influenced by the dynamics of these structures. Nearly all the reported measurements [3–6], that have presented Reynolds stresses and heat fluxes in ribbed ducts, have done so without carefully identifying the mechanisms associated with the production and transport of these fluxes. Yet this information is critical, not only in understanding the basic flow mechanisms, but also in developing suitable models for turbulent transport.

The quadrant analysis technique of Wallace et al. [7] has been employed to identify the mechanisms associated with the production and transport of the shear stresses in flat plate boundary layer and channel flows. With this analysis, the flow motion is represented by a sequence of events that describe how fluid is swept into or ejected from the shear layer, and allows the partitioning of turbulence production into these events. In flat plate boundary layer and channel flows, it has been shown that the primary production mechanism for shear stresses is due to "ejection" of low-speed fluid from the sublayer followed by an inward "sweep" of high-momentum fluid. The term "bursting" is often used in the literature to describe the ejection process. Such an analysis does not appear to have been performed for a separated and re-attaching shear layer of interest in this study, and is therefore the primary goal of this work.

The flow field of interest here, that of a re-attaching shear layer past the rib, is rather complex, as several studies have shown, and accurate prediction of such flows have been rather difficult (see Acharya et al. [8]). At the re-attachment point, the re-attaching shear layer breaks into two halves: One travels downstream along the wall (forward motion) and the other travels upstream (reversed motion). Hasan [9] observed that the downward motion of the re-attaching shear layer was not continuous, but reversed intermittently. Arnal and Friedrich [10], from their large eddy simulation of backward-facing step flow, observed large departures of the instantaneous flow field from the mean flow field. They therefore concluded that for a complete understanding of the re-attaching shear flow, the instantaneous flow structure is required. Further, for turbulence modeling, the measurements of the time-averaged turbulent shear stresses have been used to guide the development of turbulence models. However, the use of time-averaged measurements alone, without any reference to the flow structures and their motions, may be inadequate in developing universal models. All the previous investigations of re-attaching shear layer have reported only the time-averaged quantities. The objective of this investigation is to use an extension of the quadrant analysis, termed here the octant analysis technique, to characterize the different types of eddy motion taking place in a re-attaching shear layer behind a surface-mounted square rib. The contribution of all important flow motions toward the production of turbulent normal stresses and turbulent shear stresses will be investigated. As noted earlier, the results of this study will serve as a useful guide to the turbulence modeler.

2 Octant Analysis

Corino and Brodkey [11] used high-speed motion-picture photographs of very small particles suspended in the flow of a flat plate turbulent boundary layer, and observed a sequence of motions. These motions were identified as low-speed fluid moving away from the wall called *ejections* ($u' < 0, v' > 0$), high-speed fluid moving toward the wall called *sweep* ($u' > 0, v' < 0$), high-speed fluid from the sweep motion reflected back as *outward interaction* ($u' > 0, v' > 0$), and low-speed fluid being pushed back toward the wall as *wallward interaction* ($u' < 0, v' < 0$). This analysis that partitions the fluid motion into

Contributed by the International Gas Turbine Institute and presented at the 42nd International Gas Turbine and Aeroengine Congress and Exhibition, Orlando, Florida, June 2–5, 1997. Manuscript received International Gas Turbine Institute February 1997. Paper No. 97-GT-119. Associate Technical Editor: H. A. Kidd.

four quadrants is referred to as quadrant analysis. Wallace and Lu [7] and Willmarth et al. [12] used Corino and Brodkey's analysis and observed that the ejection and sweep motions were primarily responsible for the total Reynolds stress production inside the boundary layer. Several other investigators [13–16] have also used the quadrant analysis technique to describe ejections and bursts in turbulent and transitional boundary layer. Volino and Simon [17] used an extended quadrant analysis technique for heated flows known as the octant analysis to study the turbulent and transitional boundary layer on heated flat and curved surfaces.

In a re-attaching shear layer, the flow is intermittent in the flow direction due to the presence of recirculating region behind the rib. In this paper, to partition the motions separately for both instantaneously positive and negative flows, the quadrant analysis technique used in flat plate boundary layer analysis is modified into an octant analysis technique to identify the important physical processes taking place in a re-attaching turbulent shear layer. The fluid motion is classified on the basis of instantaneous flow direction as positive ($u > 0$) or reversed ($u < 0$). For both the positive and reversed flows, the flow motions can be subdivided into four different quadrants depending on the instantaneous signs of the fluctuating velocities u' and v'. This results in a eight-way partitioning, and is termed here as octant analysis. Conceptual drawing of eddies and the notation used in this paper to indicate the different motions in each octant are presented in Fig. 1 (forward motion) and Fig. 2 (reversed motion).

Octants can be further partitioned based on the strengths of the eddies [12]. Eddies of a certain strength characterized by the hole size H_s can be delineated by computing their contribution to $\overline{u'v'}$ only if the signal $|u'v'|$ is greater than the value $H_s|u'v'|$. The central region bounded by eight hyperbole ($|u'v'| < H_s|\overline{u'v'}|$) can be said to be the hole region. When the hole size is large, the Reynolds stress outside the hole region gives the contribution from the strongest eddies.

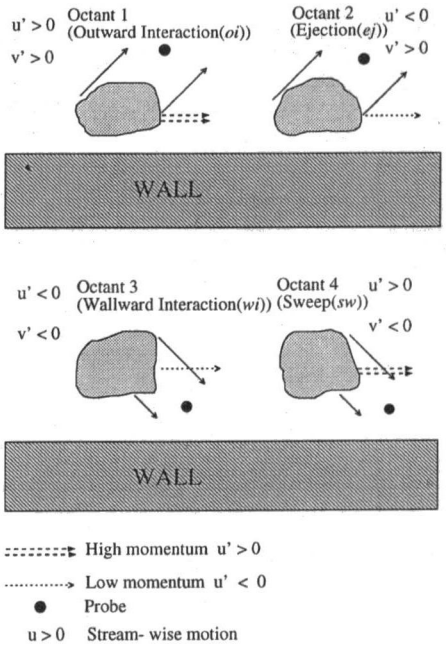

Fig. 1 Conceptual drawing of eddies in different octants for streamwise motions of the re-attaching shear layer

3 Experimental Arrangements and Techniques

The experimental setup for the measurements is shown in Fig. 3. Air is drawn into a 0.3 m by 0.06 m cross-sectional rectangular channel through a 5.25:1 contraction section, honeycomb and turbulence screens, by a blower operating in the suction mode. The rib sizes used here satisfy the two-dimensional flow criterion, i.e., the smallest aspect ratio (ratio of channel width to rib height) is 18.89, which is larger than the aspect ratio 12 required to minimize three-dimensional effects [18–20]. The experiments consisted primarily of velocity measurements using a two-color DANTEC fiber-optic LDV system. The argon-ion laser beam was split into a pair of 488 nm (blue) and 514.5 nm (green) wavelength beams using a color separator and a beam splitter. One beam from each of the two pairs was shifted by 40 MHz using a Bragg cell to eliminate the directional ambiguity in velocity measurements. A 400 mm focal length lens focused the resulting pair of beams to a measurement volume of less than 0.2 mm waist diameter. The flow was seeded with an aerosol mist, obtained by heating a fog fluid supplied by Rosco Inc. Back-scattered light was collected by photomultiplier tubes and processed using the Dantec PDA signal processor and SIZEware software. A program to perform the octant analysis was written, and it used as input the raw data files created by the SIZEware software containing the time stamp and the instantaneous u and v values.

4 Results and Discussions

Results are presented for the flow past a single rib ($h/D_h = 0.0626$) at a Reynolds number of 14,594 and 8260. Measurements will be presented primarily at three streamwise locations: representing an early stage of shear layer separation ($X/h = 3$), representing a near-re-attachment position ($X/h = 6$), and representing a location well past re-attachment ($X/h = 18$).

Velocity profiles at the downstream face of the rib are shown in Fig. 4. Negative velocities close to the rib surface indicate that the shear layer is not re-attached on the top surface of the rib. It is also observed that there is no constant free-stream velocity due to the asymmetry created by the rib located on the bottom surface of the channel. The mean velocity increases to a maximum value and then decreases slowly.

4.1 Octant Analysis. The flow behind a rib can be subdivided into four distinct regions in the cross-stream direction, i.e., the separated flow region, the lower part of shear layer, the

Nomenclature

D_h = hydraulic diameter of the channel $= (2WH/(W + H)) = 0.1013$ m
U_{Av} = average velocity in the wind tunnel $= U(W - 2\delta^*)(H - 2\delta^*)/WH$
W = width of the channel = 0.3 m
H = height of the channel = 0.061 m
h = rib height
U = free-stream velocity in the channel
δ = boundary layer thickness
U_{max} = maximum velocity on the high-speed side of the shear layer
u = instantaneous streamwise velocity
v = instantaneous cross-stream velocity
u' = fluctuating streamwise velocity
v' = fluctuating cross-stream velocity
$u'v'$ = Reynolds shear stress
u'^2 = streamwise normal stress
v'^2 = cross-stream normal stress
μ = dynamic viscosity
X = distance from the downstream edge of the rib in streamwise direction
Y = distance from channel bottom surface in cross-stream direction
H_s = hole size
U_{Mean} = mean streamwise velocity
U_{rms} = rms streamwise velocity
I_r = reversed flow intermittency

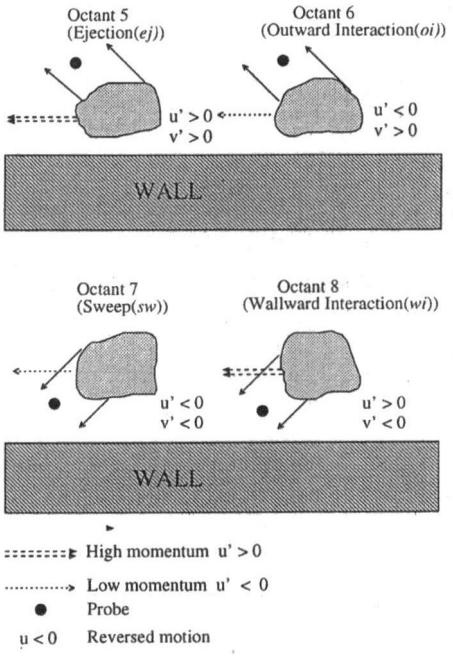

Fig. 2 Conceptual drawing of eddies in different octants for reversed motions of the re-attaching shear layer

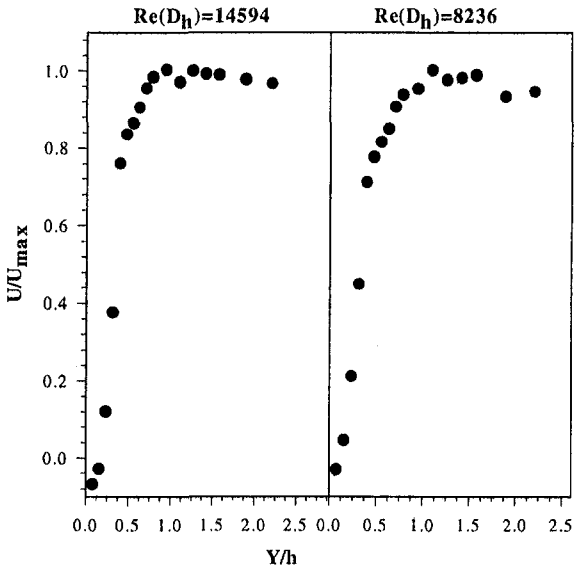

Fig. 4 Velocity profile at downstream rib corner at different Reynolds number

upper part of shear layer, and the region outside the shear layer. To identify these regions, the definition of reversed flow intermittency is used. Reversed flow intermittency (I_r) is the fraction of time during which the flow is in the upstream direction. The separated flow region is characterized by reversed flow intermittencies greater than 0.5. The lower part of the shear layer is the region where the reversed flow intermittency is between 0.0 and 0.5, where upward motions in the shear layer, referred to as shear layer splitting by Hasan [9], may be taking place. This is followed by the upper part of the shear layer, which extends to the Y location where u reaches its maximum value. The locations of the four different flow regions behind the rib are presented in Table 1. In the downstream direction (increasing X/h), the extent of the separated flow region decreases as expected, and the extent of the lower part of the shear layer region increases, attaining its maximum value near the re-attachment point. The importance of different types of fluid motion (ej, sw, oi, wi) in the different regions behind the rib will be examined next.

4.2 Shear Stress. Figures 5, 6, and 7 show the distributions of the normalized shear stresses at X/h = 3, 6, and 18, respectively, apportioned into four distinct events for both instantaneously positive ($u > 0$) flows (octants 1–4) and instantaneously negative ($u < 0$) flows (octants 5–8). Also shown

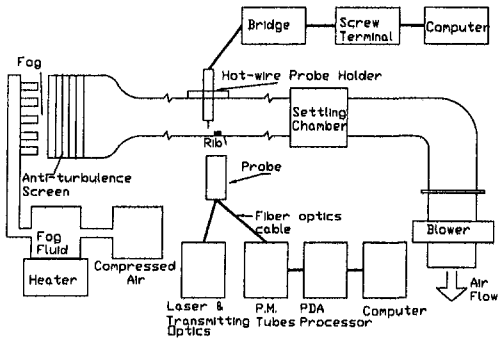

Fig. 3 Schematic of experimental setup

are the mean velocity profile and the reversed flow intermittency.

In the reversed flow region (see Fig. 5), the contributions to the shear stress appear to come primarily from octants 7 and 6 representing sw and oi motions of the instantaneously reversed flows, and from octants 4 and 1 representing sw and oi motions of the instantaneously forward flows. In a typical boundary layer flow, the sweep motion follows an ejected stream that is acted upon and dissipated by small-scale turbulence. This does not appear to be the case in the reversed flow region, where a high-momentum fluid packet swept inward does not lead to any ejections, but is simply reflected outward in an oi motion. This appears to be true for both the instantaneously negative flow from the recirculation region (octants 7 and 6) and the instantaneously positive flow (octants 4 and 1) from the shear layer side. The importance of octants 4 and 1 implies the existence of streaks or bursts of high-speed fluid from the shear layer penetrating into the separated region (down to Y/h values as low as 0.2–0.3). For $Y/h \leq 0.4$, the contributions of the reverse-sw and reverse-oi motions that are of opposite signs are quite significant. The reverse-sw and reverse-oi motions drop off to nearly zero for Y/h = 1.4. This drop-off occurs approximately at the same rate. In the recirculation region, both the reverse and forward motions appear to play important roles, but the reverse-sw and forward-oi counteract the reverse-oi and forward-sw in their contributions to the shear stress. Therefore the peak in $\overline{u'v'}$ occurs not inside the recirculating region, but just outside it in the low-speed side of the shear layer.

The maximum shear stress occurs near a Y/h value of about 1.1 (see Fig. 5) in the lower shear layer region. In this region, the reverse-oi, forward-ej, and forward-sw are the primary Reynolds stress contributing motions. The reverse-oi motion and the forward-sw motion reach their maximum values at a Y/h of 0.944, while the forward-ej motion reaches its maximum value at a Y/h = 1.259; these locations are inside the lower part of the shear layer. The mixing process along the lower edge of the shear layer seems to be characterized by ejection of low-momentum fluid upward (forward-ej) followed by a downward sweep of high-momentum fluid from the shear layer side (forward-sw) and an upward surge of the instantaneously reversed flow from the recirculation region (reverse-oi). The interaction between the forward-sw motion (directed downward) and the reverse-oi motion (directed upward) presumably leads to strong shearing and high values of shear stress. Near

Table 1 Location of different flow regions behind a 6.35 mm rib at different Reynolds numbers

Re(D_h)	X/h	Separated Regn.	Lower Sh. Regn.	Upper Sh. Regn.	Outside Regn.
14594	3	$0 \le Y/h \le 0.708$	$0.708 \le Y/h \le 1.417$	$1.417 \le Y/h \le 2.204$	$Y/h \ge 2.204$
14594	6	– – – – –	$0.0 \le Y/h \le 1.889$	$1.889 \le Y/h \le 2.519$	$Y/h \ge 2.519$
14594	18	– – – – –	– – – – –	$0.0 \le Y/h \le 3.464$	$Y/h \ge 3.464$
8236	3	$0.0 \le Y/h \le 1.023$	$1.023 \le Y/h \le 1.417$	$1.417 \le Y/h \le 2.204$	$Y/h \ge 2.204$
8236	6	$0.0 \le Y/h \le 0.551$	$0.551 \le Y/h \le 1.574$	$1.574 \le Y/h \le 2.204$	$Y/h \ge 2.204$
8236	18	– – – – –	– – – – –	$0.0 \le Y/h \le 3.937$	$Y/h \ge 3.937$

the peak location, the forward-*ej* and forward-*sw* motions each contribute nearly 75 percent to the total stress, while the forward-*oi* and forward-*wi* (octants 1 and 3) motions reduce the shear stress by nearly 30 and 20 percent, respectively. This is qualitatively consistent with the boundary-layer flow observations on a flat plate or a channel where the *ej* and *sw* motions each account for 70 percent of the total shear stress. In the upper part of the shear layer itself, the *ej* and *sw* motions (octants 2 and 4) are the largest contributors to the shear stress, and are of comparable order. Note the development of a local peak in the *sw* and *ej* contributions in the upper part of the shear layer, and this manifests itself as a second local peak in the shear stress profile near $Y/h = 1.6$ at $X/h = 3$.

The location $X/h = 6$ represents the near-reattachment location, and the intermittency is zero everywhere except close to the wall ($Y/h < 0.889$), where flow splitting in both directions maybe occurring (Fig. 6). In this region close to the wall, we note that the largest contributors in order of importance are: reverse-*oi*, forward-*sw*, forward-*oi*, and reverse-*sw*. This indicates that the eddies swept toward the wall (forward-*sw*) are reflected back both in the streamwise (forward-*sw*) and reverse (reverse-*oi*) directions. The larger magnitude of the reverse-*oi* motion indicates the significance of the flow splitting induced by the wall. The peak shear stress occurs close to the wall, and is influenced by this flow splitting, with the forward-*sw* and reverse-*oi* motions providing the largest contributions to the shear stress. For $Y/h \ge 1$, the forward-*sw* and forward-*ej* mechanisms are the most important, but now the peak forward-*wi* and forward-*oi* motions are nearly 40–50 percent of the peak *sw* and *ej* values, and have the opposite sign. Compared to the earlier separated flow regions, the interaction terms have become more important, and represent a departure from traditional boundary layer behavior. The Y/h location of maximum forward-*sw* and reverse-*oi* at $X/h = 6$ is lower than that at $X/h = 3$ due to the downward curvature of the shear layer.

At $X/h = 18$ (Fig. 7), well downstream of reattachment, one would expect recovery to the boundary layer behavior. The reverse-motion contributions have disappeared, as expected, but the forward-*wi* and *oi* motions are significantly greater proportion of the total shear stress than that reported for boundary layer flows. At the peak shear stress location, the *sw*, *ej*, *oi*, and *wi* contributions are roughly in the proportion of 1:1.446:−0.92:−0.99. For the fully developed boundary layer in the channel (measurements made without the rib), the above proportions are 1:1.77:−0.39:−0.39. The larger contributions from the interaction motions (*oi*, *wi*) compared to that in a flat plate boundary layer implies that the wake of the separated shear layer persists well past the reattachment location, and even at a location as far downstream as $X/h = 18$ it is inappropriate to assume that full recovery has taken place.

For Re(D_h) = 8236, the location $X/h = 3$ and $X/h = 6$ (Figs. 8 and 9) represents streamwise locations before reattachment. The general trends are similar to those observed at Re = 14,594 but there are differences in detail. The peak value of reverse-*sw* and reverse-*oi* close to the reattachment point (Fig. 9) are more than five times stronger than that away from the reattachment region (Fig. 8). In reattaching shear layer studies, shear layer splitting has been generally reported to cause the flow to move in both forward and reverse direction from the reattachment point. The peak value of reverse-*oi* is stronger than the peak of the reverse-*sw* motion, as it was at the higher Reynolds number. The maximum reverse-*oi* motion appears to be largest close to the reattachment point where the effect of shear layer splitting or upward motion is most pronounced.

The structure of the flow, as Figs. 5–9 reveal, is as follows. The maximum total shear stress and the peak in the important

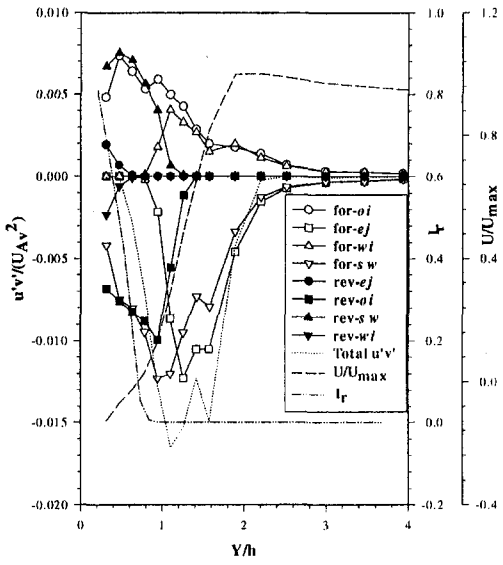

Fig. 5 Normalized Reynolds stress, velocity, and reversed flow intermittency profile behind the rib at $X/h = 3$ and Re(D_h) = 14,594

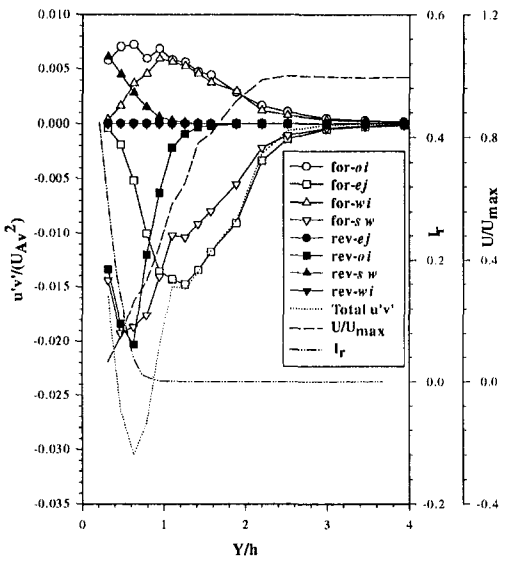

Fig. 6 Normalized Reynolds stress, velocity, and reversed flow intermittency profile behind the rib at $X/h = 6$ and Re(D_h) = 14,594

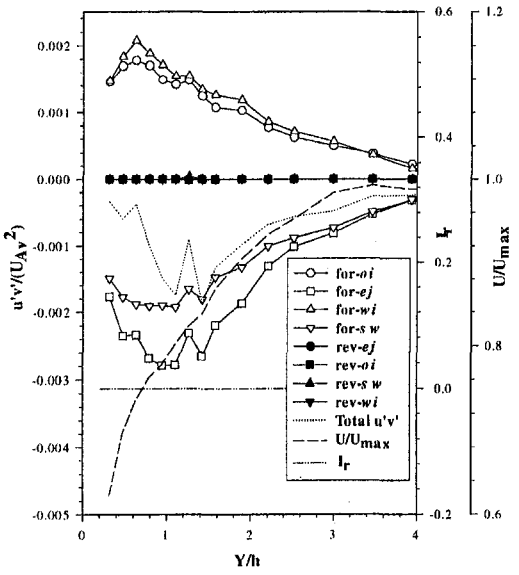

Fig. 7 Normalized Reynolds stress, velocity, and reversed flow intermittency profile behind the rib at X/h = 18 and Re(D_h) = 14,594

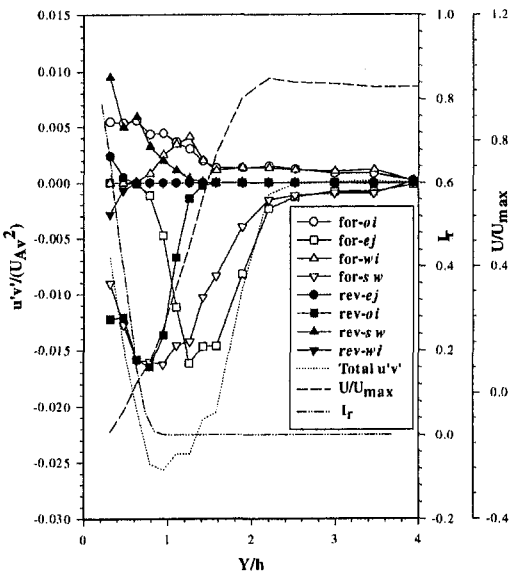

Fig. 9 Normalized Reynolds stress, velocity, and reversed flow intermittency profile behind a 6.35 mm rib at X/h = 6 and Re(D_h) = 8236

shear stress producing motions (i.e., forward-*ej* and *sw* and reverse-*oi*) takes place inside the lower part of the shear layer. Inside the recirculating region, the important motions produce Reynolds stresses of comparable magnitude but opposite sign (reverse-*oi* and forward-*sw* increase the shear stress and reverse-*sw* and forward-*oi* decrease the shear stress) and hence cancel each other, resulting in lower total shear stress. The lower part of the shear layer appears to be the region of intense turbulent mixing supplemented by both streamwise and reversed stress producing motions. Traditionally, most of the re-attaching shear layer studies [9, 21, 22] have focused attention on the upper part of the shear layer in order to study the effect of external excitation on the development of reattaching shear layer. According to this study, the lower part of the shear layer is also an important region, which should be investigated for a complete understanding of the turbulent structure of the reattaching shear layer with or without external excitation.

The total Reynolds stress inside the separated region is less than the contributions from the individual stress producing motion (forward-*sw* and reverse-*oi*) (see Fig. 5). Close to the reattachment point, the total Reynolds stress is more than the individual stress producing motion (see Fig. 6). Past the reattachment point in the streamwise direction, the total Reynolds stress is again less than the individual stress producing motions (see Fig. 7). The reduction in the shear stress after reattachment is due to the importance of interaction motions (octants 1 and 3), which reduces the skin friction. It will be shown later that these interaction motions enhance the turbulent kinetic energy. Thus a flow modulation scheme that enhances the interaction motions is attractive for mixing or turbulence enhancements with comparable reduction in skin friction.

4.3 Eddy Size. For Re(D_h) = 14594, at the reattachment point, Fig. 10 shows the fractional contribution to the shear stress from each octant, and the fraction of points in the octant

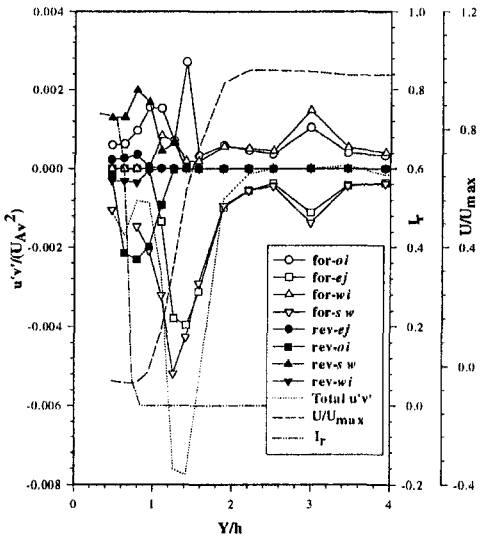

Fig. 8 Normalized Reynolds stress, velocity, and reversed flow intermittency profile behind a 6.35 mm rib at X/h = 3 and Re(D_h) = 8236

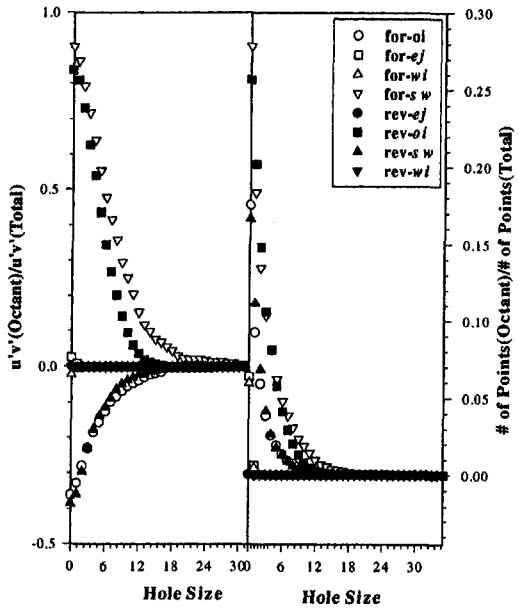

Fig. 10 Variation of fractional contribution from an octant and fraction of points in an octant with respect to hole size behind the rib at X/h = 6, Y/h = 0.3145, and Re(D_h) = 14,594

as a function of the hole size. Close to the wall ($Y/h = 0.3145$), the most energetic eddies appear to be those corresponding to the reverse-*oi* and forward-*sw*. These stress-producing events are about twice as strong as the stress-reducing forward-*oi* and reverse-*sw* motions. These are consistent with the observations in Fig. 6. The forward-*sw* motion is associated with the largest eddy (or hole size). The ejection motions are virtually nonexistent. Thus, at the point of reattachment, the *sw* and the *oi* motions dominate, indicating eddies "sweeping" downward, and reflected "outward" from the surface in either direction. The absence of *ej* motions indicates that close to the wall the "bursting" of eddies (ejection followed by dissipation) does not occur. Farther up from the bottom surface of the channel ($Y/h = 0.63$), the scale and contribution of reversed sweep decrease while the scale and contribution of reverse-*oi* increase (Fig. 11). After $Y/h = 0.63$, the contribution of reversed-*oi* decreases, but the scale is still the largest among all the motions. Hence, the reverse-*oi* motion in the shear layer are due to large scale eddies.

Farther away from the wall (Fig. 12), at $Y/h = 0.944$, the forward-*ej* and the forward-*wi* motions, both associated with low-momentum fluid, become increasingly important. Although the fractional contribution from both ejection and sweep are the same, the ejected eddies are stronger since they are associated with a smaller fraction of points in the octant. The reverse-*oi* motions decrease considerably, but these eddies appear to be relatively strong given the very few points that fall in octant 6, and relatively large in size given that they continue to contribute up to a hole size of 24, while the other motions persist only up to a hole size of about 16. As one moves farther upward ($Y/h = 1.417$) (Fig. 13), the ejected eddies appear to be the strongest and they are also largest in size, implying that the expected process of these eddies breaking up into fine-scale turbulence does not occur fully, and the distinct coherent eddies that are ejected are swept downstream.

From Figs. 14 and 15, at locations well past the reattachment point, the large-scale structures are still observed to contribute significantly to the Reynolds stress production. Contrary to a flat plate boundary layer, both positive and negative Reynolds stress-producing motion have large-scale contributions. Close to the wall, the sweep and wall-ward interactions have the largest scale eddies, while away from the wall, the ejection and wall-ward interaction motions are associated with the largest scale eddies.

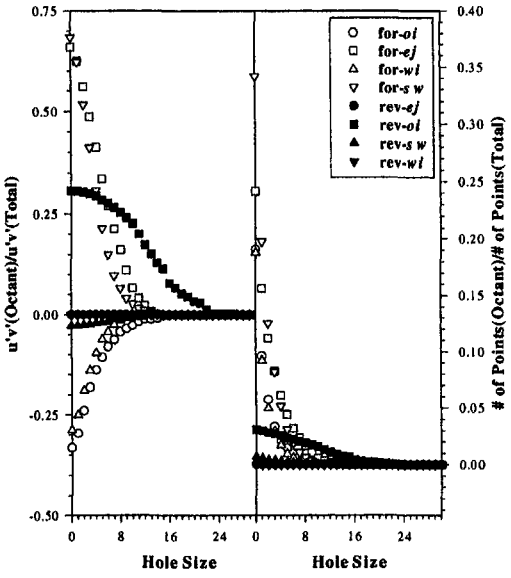

Fig. 12 Variation of fractional contribution from an octant and fraction of points in an octant with respect to hole size behind the rib at $X/h = 6$, $Y/h = 0.944$, and $\mathrm{Re}(D_h) = 14{,}594$

4.4 Normal Stress. Results are also presented of the normal stresses computed from each octant (Figs. 16 and 17). Unlike the shear stresses, the normal stresses are always positive. What is apparent is that the motions that contribute most toward shear stress production also contribute the most for the normal stress production, that is, the forward sweep and the forward ejection motions. The reverse-*sw* and reverse-*oi* motions assume importance in the recirculation region. However, the forward interaction motions that detract from the shear stress production contribute positively to normal stress production. At $X/h = 6$ and $\mathrm{Re}(D_h) = 14{,}594$, it can be observed that $\overline{u'^2}$ and $\overline{v'^2}$ attains high values near the wall while the corresponding $\overline{u'v'}$ are small. This is because close to the wall, the forward-*sw* and reverse-*oi* motions contribute strongly toward the

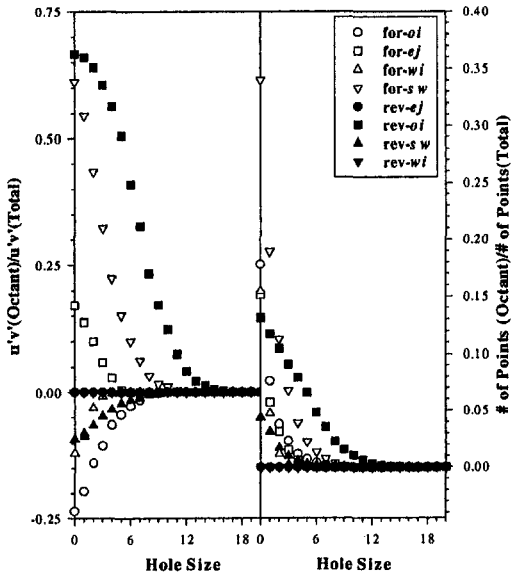

Fig. 11 Variation of fractional contribution from an octant and fraction of points in an octant with respect to hole size behind the rib at $X/h = 6$, $Y/h = 0.63$, and $\mathrm{Re}(D_h) = 14{,}594$

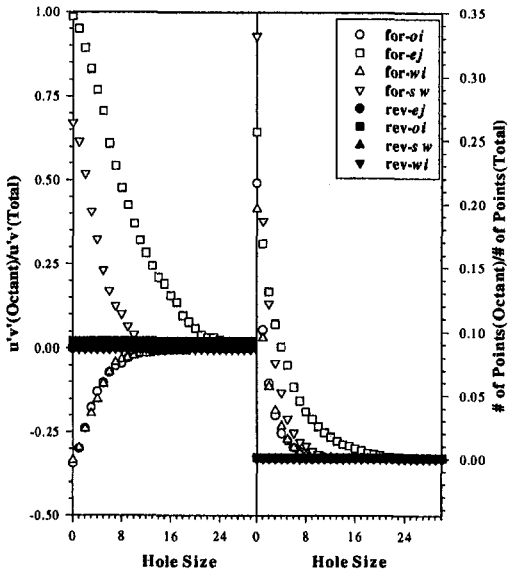

Fig. 13 Variation of fractional contribution from an octant and fraction of points in an octant with respect to hole size behind the rib at $X/h = 6$, $Y/h = 1.417$, and $\mathrm{Re}(D_h) = 14{,}594$

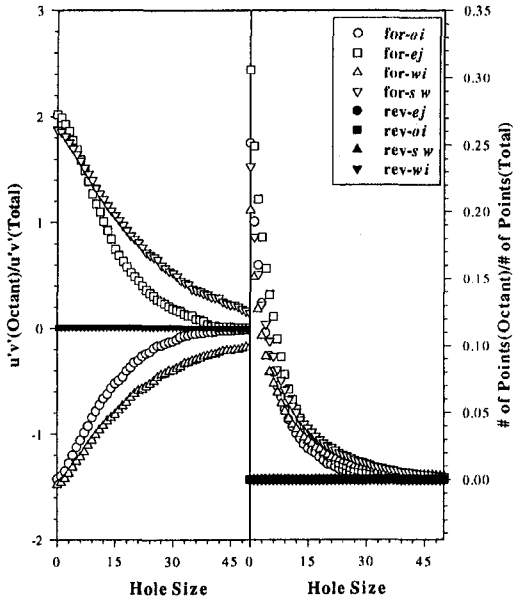

Fig. 14 Variation of fractional contribution from an octant and fraction of points in an octant with respect to hole size behind the rib at X/h = 18, Y/h = 0.3145, and Re(D_h) = 8236

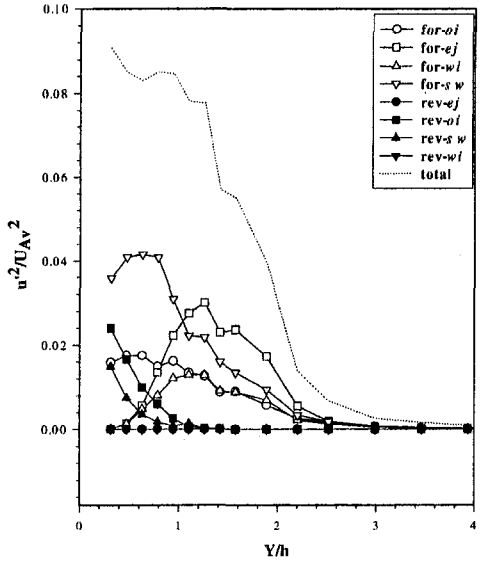

Fig. 16 Streamwise normal stress profile with its contribution from different octants at X/h = 6 and Re(D_h) = 14,594

streamwise and cross-stream normal stress (see Figs. 16 and 17), leading to high values of $\overline{u'^2}$ and $\overline{v'^2}$, while the contributions to $u'v'$ from the forward-*sw*, reverse-*oi* and the forward-*oi*, reverse-*sw* counteract each other and reduce the shear stress near the wall (see Fig. 6). However, away from the wall the u' and v' (and therefore $\overline{u'^2}$, $\overline{v'^2}$, and $\overline{u'v'}$) seem to be well correlated with each other because both the forward-*ej* and the forward-*sw* motions have strong contribution toward the streamwise normal stress, cross-stream normal stress, and shear stress. It should be noted that $\overline{u'^2}$ peaks very close to the wall, yet the traditionally accepted $\overline{u'v'}\dfrac{\delta\overline{u}}{\delta y}$ production term peaks at Y/h = 0.8 and is relatively small at the location corresponding to the $\overline{u'^2}$ peak. Clearly the dynamics of the coherent structures, most notably high-momentum eddies sweeping downwards and reflected outwards in the reverse direction, contribute greatly to the generation of turbulence near the reattachment location.

At X/h = 6, the maximum normal stress in the streamwise direction ($\overline{u'^2}$) takes place inside the recirculating region (see Fig. 16), while the maximum normal stress in the cross-stream direction ($\overline{v'^2}$) takes place inside the lower part of the shear layer (see Fig. 17) at Y/h = 0.8. The maximum shear stress ($\overline{u'v'}$) also occurs near Y/h = 0.8, implying a strong correlation of the shear stress and presumably the heat flux with $\overline{v'^2}$ (rather than with $\overline{u'^2}$).

5 Conclusion

The re-attaching shear layer behind a surface mounted rib is studied using octant analysis. The primary achievement of this study has been to delineate the flow mechanisms that contribute to the production of turbulent stresses.

In the separated region, streaks of high-momentum fluid from the shear layer penetrate into the recirculation region (forward-

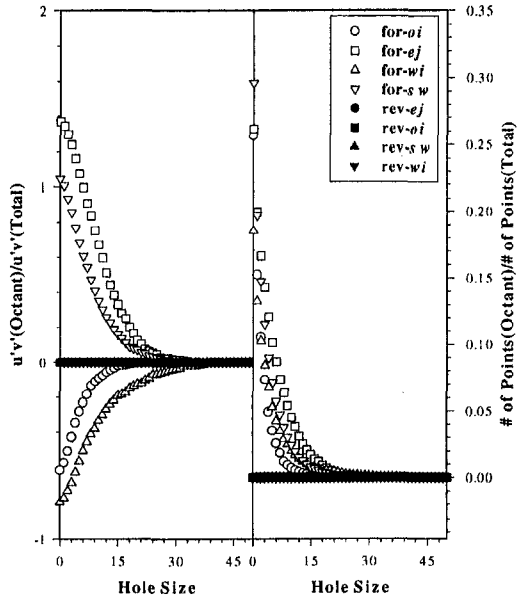

Fig. 15 Variation of fractional contribution from an octant and fraction of points in an octant with respect to hole size behind the rib at X/h = 18, Y/h = 0.787, and Re(D_h) = 8236

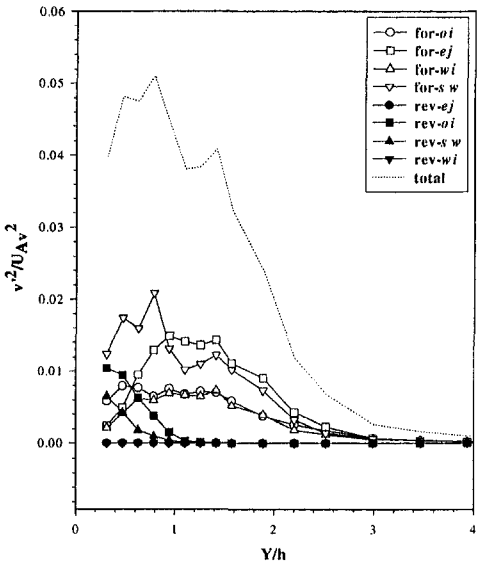

Fig. 17 Cross-stream normal stress profile with its contribution from different octants at X/h = 6 and Re(D_h) = 14,594

sw motion). Accompanying this are bursts of instantaneously reversed flows directed upward from the recirculation into the shear layer (reverse-*oi* motion). These two counterdirected motions provide high shearing rates, which are partially ameliorated by the reverse-*sw* and forward-*oi* motions. The peak shear stress and the peak normal stress occur at the low-speed side of the shear layer, and this region is therefore important from the perspective of turbulent mixing and transport. In the high-speed side of the shear layer, the forward-*sw* and *ej* motions typically associated with the bursting phenomena in wall boundary layer are the most important stress-producing mechanisms. The out-ward and wall-ward interactions ameliorate the magnitude of the shear stresses to a much larger degree (typically 65 percent) than in wall-bounded turbulent boundary layers where the typical reductions associated with each of the interaction motions is around 28 percent.

At the point of reattachment, clear evidence of flow splitting is noted with eddies directed in both the forward and reverse directions. Close to the surface ($Y/h \leq 0.8$) the contributions from the forward-*sw* (high momentum fluid sweeping downwards) and reverse-*oi* (eddies reflected outward in the reverse direction) are the strongest. This is consistent with the observations of intermittent flow reversals by Hasan [9].

Well past reattachment ($X/h = 18$), the interaction motions continue to be very important, unlike that of a typical turbulent boundary layer. This implies that flow recovery does not occur even 18 rib heights past reattachment. The motions continue to be associated with large scales (hole size) implying the dominance of coherent structures well past reattachment, and indicating that use of statistical turbulence models is inappropriate.

In examining the normal stresses, it is noted that all motions contribute positively to the normal stresses, but that the relative importance of the various motions are more or less unchanged from what they were for the shear stresses. The cross-stream turbulence intensity appears to correlate well with the turbulent shear stress.

The overall picture of the separated flow past the ribs appears to be rather complex with large scales persisting well past reattachment, and the absence of flow recovery even as far downstream as $X/h = 18$. Prior to reattachment, the low-speed side of the shear layer is the region associated with the highest shearing rate and turbulent transport.

References

1 P. K. Panigrahi and S. Acharya, "Spectral characteristics of separated flow behind a surface mounted square rib," AIAA Paper No. 96-1931, 1996.

2 S. Acharya, T. A. Myrum, and S. Inamdar, "Subharmonic excitation of the shear layer between two ribs: vortex interaction and pressure field," *AIAA Journal,* Vol. 29, No. 9:1390–1399, 1991.

3 R. A. Antonia and R. E. Luxton, "The response of a turbulent boundary layer to an upstanding step change in surface roughness," ASME *Journal of Fluids Engineering*, pp. 22–34, 1971.

4 C. D. Tropea and R. Gackstatter, "The flow over two-dimensional surface-mounted obstacles at low Reynolds number," ASME *Journal of Fluids Engineering,* 107:489–494, 1985.

5 T. M. Liou and C. F. Kao, "Symmetric and asymmetric turbulent flows in a rectangular duct with a pair of ribs," ASME *Journal of Fluids Engineering,* 110:373–379, 1988.

6 T. A. Myrum, X. Qiu, and S. Acharya, "Heat transfer enhancement in a ribbed duct using vortex generators," *Int. J. Heat Mass Transfer,* 36, No. 14:3497–3508, 1993.

7 J. M. Wallace, H. Eckelmann, and R. S. Brodkey, "The wall region in turbulent shear flow," *J. Fluid Mech.,* 54:39–48, 1972.

8 S. Acharya, S. Dutta, T. A. Myrum, and R. S. Baker, "Turbulent flow past a surface mounted two-dimensional rib," ASME *Journal of Fluids Engineering,* Vol. 116, pp. 238–246, 1994.

9 M. A. Z. Hasan, "The flow over a backward facing step under controlled perturbation: Laminar separation," *J. Fluid Mech.,* 238:73–96, 1992.

10 M. Arnal and R. Friedrich, "The instantaneous structure of a turbulent flow over a back-ward facing step," *Separated Flows and Jets, IUTAM Symposium Novosibirsk/USSR,* pp. 709–717, 1991.

11 E. R. Corino and R. S. Brodkey, "A visual study of turbulent shear flow," *J. Fluid Mech.,* 37, 1, 1969.

12 W. W. Willmarth and S. S. Lu, "Structure of the reynolds stress near the wall," *J. Fluid Mech.,* 55, Part 1:65–92, 1972.

13 D. G. Bogard and W. G. Tiederman, "Burst detection with single-point velocity measurements," *J. Fluid Mech.,* 162:389–413, 1986.

14 D. G. Bogard and W. G. Tiederman, "Characteristics of ejections in turbulent channel flow," *J. Fluid Mech.,* 179:1–19, 1987.

15 T. S. Luchik and W. G. Tiederman, "Timescale and structure of ejections and bursts in turbulent channel flows," *J. Fluid Mech.,* 174:529–552, 1987.

16 L. D. Stetler and D. E. Stock, "On the bursting frequency in wind-generated fully rough turbulent boundary layer flows," *Turbulent Flows,* FED-Vol. 188:25–30, 1994.

17 R. J. Volino and T. W. Simon, "An application of octant analysis to turbulent and transitional flow data," ASME JOURNAL OF TURBOMACHINERY, 116:752–758, 1994.

18 V. De Brederode and P. Bradshaw, "Three dimensional flow in nominally two-dimensional separation bubbles: Flow behind a rearward-facing step," Imperial College of Science and Technology, England, Dept. of Aeronautics. Rept No. 72-19, 1972.

19 F. W. Roos and J. T. Kagelman, "Control of coherent structures in reattaching laminar and turbulent shear layers," *AIAA Journal,* 24, No. 12:1956–1963, 1986.

20 D. M. Driver and H. L. Seegmiller, "Features of a reattaching turbulent shear layer subject to an adverse pressure gradient," Paper No. AIAA-82-1029, 1982.

21 J. K. Eaton and J. P. Johnston, "Low frequency unsteadyness of a reattaching turbulent shear layer," *Proc. Third International Symposium on Turbulent Shear Flows,* Davis, CA, pp. 162–170, 1981.

22 S. Bhattacharjee, B. Scheelke, and T. R. Troutt, "Modification of vortex interactions in a reattaching separated flow," *AIAA Journal*, 24, No. 4:623–629, 1986.

H. Karabay
Department of Mechanical Engineering
Kocaeli Universitesi,
Anitpark Yani,
41100 Izmit, Turkey

J.-X. Chen
Alstom Energy Technology Centre,
Whetstone, Leicester LE8 6LH
United Kingdom

R. Pilbrow
Rolls-Royce plc,
Filton, Bristol, BS12 7QE United Kingdom

M. Wilson

J. M. Owen

Department of Mechanical Engineering,
University of Bath,
Bath BA2 7AY, United Kingdom

Flow in a "Cover-Plate" Preswirl Rotor–Stator System

This paper describes a combined theoretical, computational, and experimental study of the flow in an adiabatic preswirl rotor–stator system. Preswirl cooling air, supplied through nozzles in the stator, flows radially outward, in the rotating cavity between the rotating disk and a cover-plate attached to it, leaving the system through blade-cooling holes in the disk. An axisymmetric elliptic solver, incorporating the Launder–Sharma low-Reynolds-number $k-\epsilon$ turbulence model, is used to compute the flow. An LDA system is used to measure the tangential component of velocity, V_ϕ, in the rotating cavity of a purpose-built rotating-disc rig. For rotational Reynolds numbers up to 1.2×10^6 and preswirl ratios up to 2.5, agreement between the computed and measured values of V_ϕ is mainly very good, and the results confirm that free-vortex flow occurs in most of the rotating cavity. Computed values of the preswirl effectiveness (or the nondimensional temperature difference between the preswirl and blade-cooling air) agree closely with theoretical values obtained from a thermodynamic analysis of an adiabatic system.

1 Introduction

Figure 1 shows a schematic diagram of two preswirl systems that are commonly used to supply cooling air to gas turbine blades. In the so-called direct-transfer (or large-radius) system, the preswirl nozzles are located in a stationary casing, or stator, at a radial position, r_p, approximately equal to the inlet radius of the blade-cooling passages, r_b. In the cover-plate (or small-radius) system, the preswirl nozzles are located in the stator radially inward of the blade-cooling passages, and the air flows outward in the clearance between the turbine disk and a cover-plate attached to it.

By swirling the cooling air in the direction of rotation of the disk, the temperature of the air entering the blade-cooling passages is reduced. In both systems, air is used to remove the windage heating from the turbine disk and to provide a sealing flow to reduce the ingress of hot mainstream gas at the periphery of the system. For the direct-transfer system, most, or all, of the disk-cooling air and some of the ingested mainstream gas ends up in the blade-cooling passages. In the cover-plate system, an inner seal is used to prevent this undesirable contamination of blade-coolant with either disk-cooling air or ingested gas.

In the cover-plate system, a free vortex is created as the air flows radially outward in the rotating cavity between the disk and the cover-plate. For radial outflow in rotating cavities (see Owen and Rogers, 1995), there is usually a source region near the inlet, where inviscid free-vortex flow occurs between two entraining boundary layers; radially outward of the source region, there is a core of inviscid rotating fluid (which is *not* a free vortex) between two nonentraining Ekman-type layers.

The radial extent of the source region depends principally on the preswirl ratio, β_p, of the incoming air and on the turbulent flow parameter, λ_T, where β_p and λ_T are defined in the nomenclature. For sufficiently large values of λ_T, the source region fills the entire cavity; this is usually the case for the preswirl cooling systems considered here. Another feature of rotating cavities is that the flow in the boundary layers is radially outward when the inviscid core rotates more slowly than the disks, and it is radially inward when the core rotates faster. There is, therefore, a stagnation point in the boundary layer at the radial location where $V_\phi = \Omega r$ in the inviscid core.

Computational and experimental studies in preswirl systems, with and without heat transfer, have been conducted by a number of research workers, and the reader is referred to Meierhofer and Franklin (1981), El-Oun and Owen (1989), Chen et al. (1993a, b), Wilson et al. (1997), and Popp et al. (1998). Details of the flow and heat transfer in rotor–stator systems in general, and the subject of ingress in particular, are given by Owen and Rogers (1989).

The work described here is concerned principally with an adiabatic preswirl cover-plate system. In Section 2, the performance of an adiabatic system is analyzed, and expressions are derived for the preswirl effectiveness in both direct-transfer and cover-plate systems. The computational method and the experimental apparatus are described in sections 3 and 4, respectively, and the computational results and the experimental velocity measurements are discussed in Section 5. Conclusions are presented in Section 6.

2 Analysis of an Adiabatic Preswirl System

2.1 Preswirl Effectiveness. Figure 2 shows the control volume used in the analysis. Stations 1 and 1′ are respectively immediately upstream and downstream of the preswirl nozzles, and 2′ and 2 are respectively immediately upstream of and inside the blade-cooling passages; $r_{1'} = r_1$ and $r_{2'} = r_2$. From 1 to 2′ the flow is taken to be isentropic, and from 2′ to 2 work is done to adjust the tangential speed of the air, $V_{\phi 2'}$, to that of the disk, $V_{\phi 2}$.

From the first law of thermodynamics for an adiabatic open system, the rate of work done on the air is equal to the rate of increase of its total enthalpy. Also, as the air moves from stations 1′ to 2, the moment exerted by the rotating surfaces equals the rate of change of angular momentum of the air; the product

Contributed by the International Gas Turbine Institute and presented at the 42nd International Gas Turbine and Aeroengine Congress and Exhibition, Orlando, Florida, June 2–5, 1997. Manuscript received International Gas Turbine Institute February 1997. Paper No. 97-GT-243. Associate Technical Editor: H. A. Kidd.

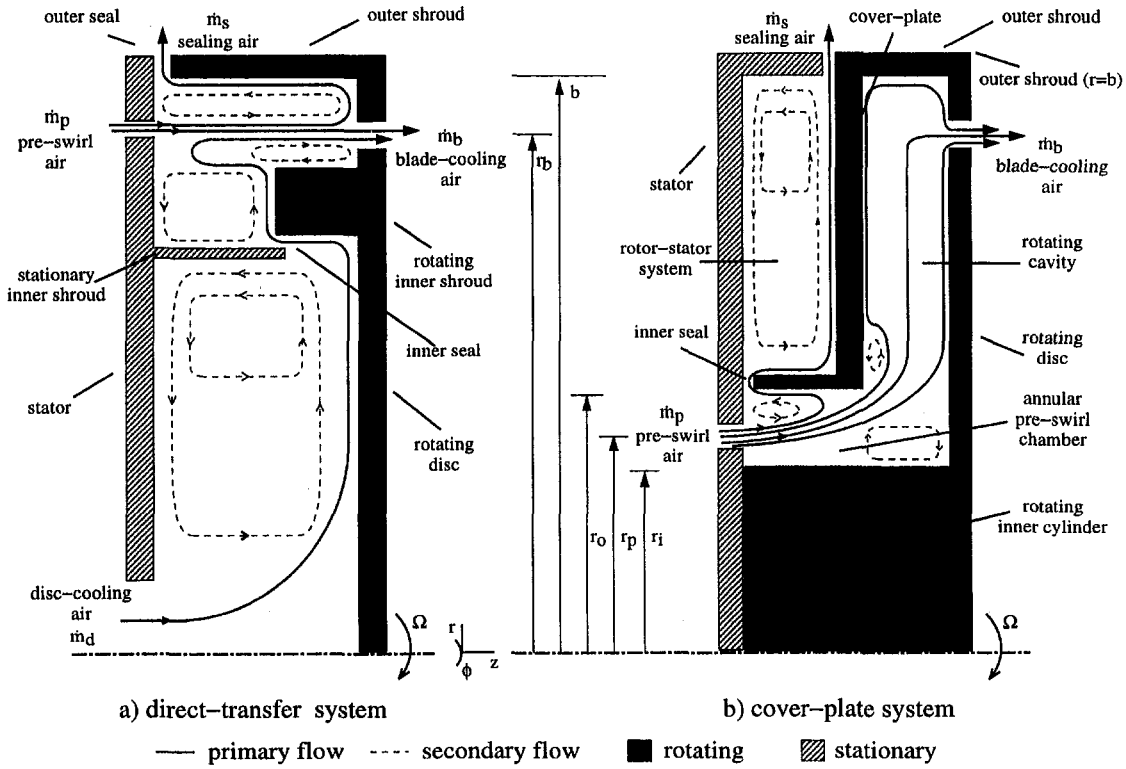

Fig. 1 Schematic diagram of preswirl systems: — primary flow; ---- secondary flow; ■ rotating; ▨ stationary

of this moment and the angular speed of the disc is equal to the rate of work done on the air. Hence,

$$c_p(T_{02} - T_{01'}) = \Omega(r_2 V_{\phi 2} - r_{1'} V_{\phi 1'}) \tag{1}$$

or, as $T_{01'} = T_{01}$ and $V_{\phi 2} = \Omega r_2$,

$$c_p(T_{02} - T_{01}) = \Omega^2 r_2^2 \left[1 - \beta_{p'} \left(\frac{r_1}{r_2} \right)^2 \right] \tag{2}$$

where $\beta_{p'} = V_{\phi 1'}/\Omega r_1$ is the inlet preswirl ratio.

It should be noted that Eq. (2) is valid for viscid and inviscid flow providing all the blade-cooling air originates from the preswirl nozzles. This condition should always be true for the cover-plate system, but it will not be true for a direct-transfer system where the disk-cooling and blade-cooling flows mix, as shown in Fig. 1. In fact, there is computational and experimental evidence (see El-Oun and Owen, 1989, and Chen et al., 1993a, b) that, even when there are discrete blade-cooling holes rather than the annular slot considered here, most or all of the disk-cooling air ends up in the blade-cooling passages, and some of the preswirl air leaves the system through the peripheral seals.

It is convenient to define ϕ as the ratio of the disk-cooling air that enters the blade-cooling passages to the total flow that enters these passages. For the cover-plate system, $\phi = 0$; for the direct-transfer system it is assumed that $\phi = m_d/m_b$. If the disk-cooling air enters the system with zero swirl, Eq. (2) becomes

$$c_p(T_{02} - T_{01}) = \Omega^2 r_2^2 \left[1 - (1 - \phi)\beta_{p'} \left(\frac{r_1}{r_2} \right)^2 \right] \tag{3}$$

Nomenclature

b = outer radius of disk
c_p = specific heat at constant pressure
C_w = nondimensional flow rate, $m/\mu b$
e_Θ = difference between computed and theoretical adiabatic effectiveness
k = turbulent kinetic energy
m = mass flow rate of cooling air
Ma = Mach number
r = radius
r_i, r_o = inner, outer radius of annular preswirl chamber
Re_ϕ = rotational Reynolds number = $\rho\Omega b^2/\mu$
s = axial clearance between rotor and stator
T = static temperature
T_0 = total temperature in stationary frame
T_t = total temperature in rotating frame
V_r, V_ϕ, V_z = radial, tangential, and axial components of velocity in stationary frame
x = nondimensional radius = r/b
z = axial distance from stator
β = swirl ratio = $V_\phi/\Omega r$
γ = ratio of specific heats
ϵ = turbulent energy dissipation rate
Θ = adiabatic effectiveness (Eq. (7))
Θ' = ideal adiabatic effectiveness (Eq. (8))
λ_T = turbulent flow parameter = $C_w\,\mathrm{Re}_\phi^{-0.8}$
μ = dynamic viscosity
ρ = static density
ϕ = fraction of disk-cooling air in blade-cooling passages
Ω = angular speed of rotating disk

Subscripts

b = blade-cooling flow
d = disk-cooling flow
e = edge of source region
eff = effective value
0 = value when $\beta_p = 0$
p, p' = preswirl flow, ideal preswirl flow
s = sealing flow or location of stagnation point
1 = upstream of preswirl nozzles
1′ = downstream of preswirl nozzles
2′ = upstream of blade-cooling passages
2 = inside blade-cooling passages

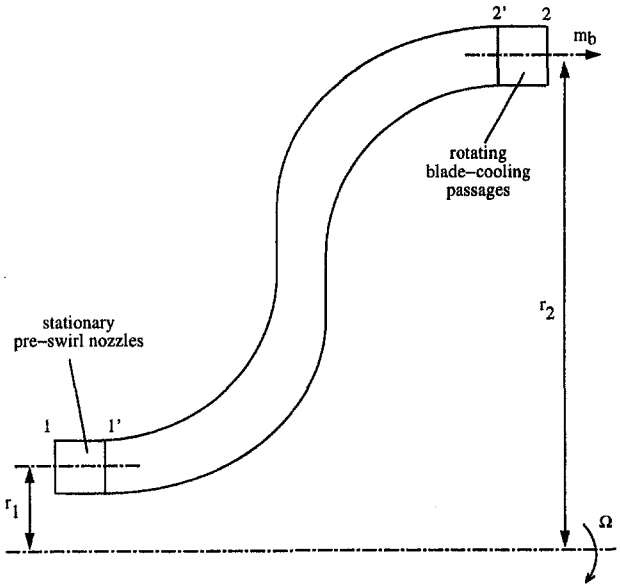

Fig. 2 Axisymmetric control volume for preswirl system

(It should be noted that the adverse effect of the disk-cooling air could be reduced if the air were swirled at inlet to the system.)

Also,

$$c_pT_{02} = c_pT_2\left(1 + \frac{\gamma - 1}{2}\mathrm{Ma}_2^2\right) \tag{4}$$

$$= c_pT_2 + \tfrac{1}{2}(V_r^2 + V_\phi^2 + V_z^2)_2 \tag{5}$$

It is convenient to define T_{t2} as the total temperature in the rotating frame, which is the value that would be measured by a total-temperature probe inside a blade-cooling passage; it is this temperature that controls the heat transfer from the blade to the air. By definition

$$c_pT_{t2} = c_pT_2 + \tfrac{1}{2}V_{r2}^2 + \tfrac{1}{2}V_{z2}^2 \tag{6}$$

where, for axial blade-cooling passages, $V_{r2} = 0$.

It is also convenient to define the nondimensional pre-swirl effectiveness, Θ, as

$$\Theta = \frac{c_p(T_{01} - T_{t2})}{\frac{1}{2}\Omega^2 r_2^2} \tag{7}$$

which is the nondimensional difference in the total temperature between the stationary preswirl nozzles and the rotating blade-cooling passages. A positive value of Θ indicates that the pre-swirl system is effective in reducing the total temperature of the blade-cooling air.

Using Eqs. (3), (5), and (6), it follows that the ideal effectiveness, Θ', is given by

$$\Theta' = 2(1 - \phi)\beta_{p'}\left(\frac{r_1}{r_2}\right)^2 - 1 \tag{8}$$

For the direct-transfer system, where $\phi = m_d/m_b$ and $r_1 = r_2$,

$$\Theta' = 2\left(1 - \frac{m_d}{m_b}\right)\beta_{p'} - 1 \tag{9}$$

For the cover-plate system, where $\phi = 0$,

$$\Theta' = 2\beta_{p'}\left(\frac{r_1}{r_2}\right)^2 - 1 \tag{10}$$

If $\beta_{p'}(r_1/r_2)^2$ is kept the same for both systems (that is, the inlet angular momentum is the same), and if there is no disk-cooling flow, then the effectiveness of both systems will be the same. *Equation (8) holds for all adiabatic systems whether the flow is laminar, turbulent or inviscid and whether the flow is compressible or incompressible.*

El-Oun and Owen (1989) used an "unmixed theory" (where $\phi = 0$) for the adiabatic effectiveness of a direct-transfer pre-swirl system (where $r_1 = r_2$). Their theory was based on the Reynolds analogy in which the work was transferred by shear stresses in the boundary layer on the disk. If a fluid is brought to rest, or to the speed of a moving surface, by viscous shear then the adiabatic surface temperature is related to the total temperature of the fluid by a recovery factor, R, say. For the case where $R = 1$, when viscous recovery and isentropic recovery are identical, Eq. (8) becomes identical to the equation derived by El-Oun and Owen.

Although pressure losses do not affect the preswirl effectiveness directly, in practice they will reduce the amount of swirl that can be imparted to the air when the overall pressure drop in the system is fixed by engine conditions. The pressure loss in the preswirl nozzles is expected to increase with the square of the tangential velocity at inlet, and this loss will therefore be much larger in the cover-plate system, thereby reducing the inlet swirl ratio. However, as shown above, when disk-cooling air is introduced, the effectiveness of the direct-transfer system will be reduced. It is therefore unclear which of these two systems has the better adiabatic performance in practice.

Whatever the relative adiabatic performance, the effects of heat transfer and hot gas ingress are likely to increase significantly the temperature of the blade-cooling air in gas turbines. However, the adiabatic effectiveness provides a datum from which to measure the performance of all practical preswirl systems.

2.2 Source Region in a Rotating Cavity With Radial Outflow. In a rotating cavity with a radial outflow of air, there is a source region where angular momentum is conserved and the incoming fluid is entrained into boundary layers on the two disks. If the incoming flow is rotating faster than the disk ($\beta > 1$) then there will be radial inflow in the boundary layers; radial outflow in the boundary layers will only occur at the larger radii where $\beta < 1$. For free-vortex flow, rV_ϕ is constant, and if

$$\beta_{p'} = \frac{V_{\phi 1'}}{\Omega r_1} \tag{11}$$

it follows that

$$\frac{V_\phi}{\Omega r} = \beta_{p'}\left(\frac{r_1}{r}\right)^2 = \beta_{p'}\left(\frac{x_1}{x}\right)^2 \tag{12}$$

Equation (12) will be referred to as the equation for an "ideal free vortex."

If $\beta_{p'} > 1$, there will be a radius, $r = r_s$, say, where $V_\phi/\Omega r = 1$. It follows from Eq. (12) that

$$r_s = \beta_{p'}^{1/2} r_1 \tag{13}$$

For $r > r_s$, air is entrained into the outflowing boundary layers until, at $r = r_e$, say, the entire mass flow rate, m_b, has been entrained. For $r > r_e$, nonentraining Ekman-type layers are formed and angular momentum in the core is no longer conserved; the radius r_e therefore corresponds to the edge of the source region.

It is useful to estimate the value of r_e that, according to Owen and Rogers (1995), will depend on the turbulent flow parameter, $\lambda_{T,b}$, and on $\beta_{p'}$. They proposed the following theoretical correlation for the nondimensional radial extent of the source region x_e:

$$\left(\frac{x_s}{x_e}\right)^{2.35} + \left(\frac{x_{e,o}}{x_e}\right)^{1.57} = 1 \tag{14}$$

where $x_{e,o}$ is the value of x_e for the case where the flow enters with zero swirl ($\beta_{p'} = 0$). The value of $x_{e,o}$ is based on the free-disk entrainment rate, where

$$x_{e,o} = 1.375\lambda_{T,b}^{5/13} \tag{15}$$

for the case where the flow is entrained equally into the boundary layers on both discs. The value of x_s in Eq. (14) is given from Eq. (13) where

$$x_s^2 = \beta_{p'} x_p^2 \tag{16}$$

Equation (14) is only valid for $x_s < 1$ and for $x_e < 1$. It is easy to show that $x_e = 1$ when

$$\lambda_{T,b} = 0.437(1 - (\beta_{p'} x_p^2)^{1.18})^{1.66} \tag{17}$$

providing $\beta_{p'} x_p^2 < 1$. For $\lambda_{T,b}$ greater than this value, the source region will fill the entire cavity and free-vortex flow will occur between the preswirl nozzles and blade-cooling passages. If $\beta_{p'} x_p^2 > 1$, there will be radial inflow in the boundary layers, with associated recirculating flow throughout the cavity. For most engine-operating conditions, it is expected that $\beta_{p'} x_p^2 < 1$ and that $\lambda_{T,b}$ will be greater than the value given by Eq. (17).

3 Computional Model

The steady-state, axisymmetric finite-volume solver used in this work is the same as that described by Wilson et al. (1997) for a related study of a direct-transfer preswirl rotor–stator system. The Launder–Sharma low-Reynolds-number k–ϵ turbulence model was used to close the coupled system of Reynolds-averaged Navier–Stokes and energy equations, and the flow was assumed to be incompressible. Turbulent heat transfer was represented using a turbulent Prandtl number equal to 0.9. A staggered grid was used with the axial and radial velocity components stored midway between the grid points, where the other solution variables were located (pressure, tangential velocity, turbulence kinetic energy and dissipation rate, and total enthalpy). The cover-plate and inner shroud (Fig. 1(b)) were represented by block obstructions within the computational grid and the equations were solved using the SIMPLEC pressure-correction algorithm.

The inlet nozzles and blade-cooling holes of the experimental rig were represented in the axisymmetric model by equivalent-area annular slots on the stator and rotor, with centerlines at $r = r_p$ and $r = r_b$, respectively. The axial velocity V_z of the preswirl air was assumed uniform at inlet and deduced from the prescribed mass flow rate m_p. Similarly, the axial velocity at the blade-cooling slot and the radial velocity at the outer seal were calculated from known mass flow rates m_b and m_s, respectively; global mass balance was achieved by ensuring that $m_p = m_b + m_s$. The inlet tangential velocity $V_{\phi,p}$ was fixed to give the required swirl ratio β_p, and Neumann (zero normal derivative) boundary conditions for V_ϕ were used at the two outlets. The remaining velocity components at flow boundaries were taken to be zero, and no-slip conditions were applied at all solid surfaces. For the computations of the adiabatic effectiveness, the static temperature was prescribed at inlet, and Neumann conditions were applied elsewhere.

The Launder–Sharma turbulence model required a very fine grid near the boundaries, with $y+ < 0.5$ for the near-wall grid nodes, and the grid spacing increased geometrically away from walls (including the cover-plate and shroud) with expansion factors of about 1.2. In total, a 223 × 223 axial by radial grid was used, with eight points covering each of the inlet and blade-cooling slots. About 55 axial grid nodes were within the cover-plate, with the remaining points divided equally between the rotor-stator system and the rotating cavity; about 70 radial grid points covered the annular pre-swirl chamber (Fig. 1(b)). Convergence of the iterative method was improved using the Gosman distributive damping term and a fixed V-cycle multigrid algorithm (Vaughan et al., 1989). Computation times were typically around 12 hours on a Silicon Graphics R10000 processor.

4 Experimental Apparatus

A schematic diagram of the rig is shown in Fig. 1. The direct-transfer rig (from which the present version was adapted) is described by Wilson et al. (1997), and so only the salient details of the cover-plate rig are described here.

The outer radius of the system, b, was approximately 207 mm, and the radial locations of the preswirl nozzles and blade-cooling holes were $r_p = 90$ mm and $r_b = 200$ mm. There were 19 preswirl nozzles of 7.92 mm diameter, angled at 20 deg to the tangential direction, and 60 blade-cooling holes of 7.7 mm diameter, with their axes normal to the disk. The axial spacing between the cover-plate, which was 5 mm thick, and the stator was 10 mm, and between the cover-plate and the rotor disk the spacing was also 10 mm. The inner and outer radii of the annular preswirl chamber were $r_i = 80$ mm and $r_o = 100$ mm, and air entered the rotating cavity through the clearance at the center of the cover-plate.

The cover-plate was made from transparent polycarbonate, and there was a window in the stator to provide optical access for LDA measurements in the rotating cavity between the cover-plate and the disk. Axial restraint of the cover-plate was provided by six cylindrical spacers of 12 mm diameter bonded to the cover-plate and to the disk at a mean radius of 142 mm. (For an inlet swirl ratio of $\beta_p = 2.5$, the design condition, free vortex flow would make $\beta = 1$ at $r = 142$ mm; at this radius, the spacers should cause the minimum of disturbance to the designed flow. When $\beta_p < 2.5$, the drag exerted by the spacers will tend to increase the angular momentum of the air for $r > 142$ mm.)

The mass flow rates of the preswirl, blade-cooling, and sealing flow, m_p, m_b, and m_s, respectively, could be independently controlled, and the flow rates were measured, with an uncertainty of ±3 percent, by orifice plates made to British Standards (BS1042). The rotor assembly could be rotated up to 7000 rpm by a variable-speed electric motor, and the speed could be measured with an uncertainty of ±1 rpm. (For the tests conducted on this rig, a speed of 7000 rpm corresponds to $\mathrm{Re}_\phi \cong 2 \times 10^6$.)

It should be pointed out that, for the results presented below, the ideal swirl ratio, $\beta_{p'}$, was used (see Section 2). This was based on the measured mass flow rate, m_p, and the continuity equation; knowing the angle and diameter of the preswirl nozzles, $\beta_{p'}$ could be calculated.

The LDA measurements were made using a TSI back-scatter optical system with a Bragg-cell frequency shift and a single-channel IFA-750 burst correlator. A Spectra-Physics 4W argon-ion laser was used, and for the tests reported here up to 350 mW on the green line (514.5 nm) was used to measure the tangential component of velocity, V_ϕ, in, or near, the midplane of the rotating cavity for $0.57 < x < 1$.

The processor could handle Doppler frequencies up to 90 MHz with signal-to-noise ratios as low as −5 dB. The beam spacing was 50 mm, and a converging lens with a focal length of 250 mm produced an optical probe volume 340 μm long and 34 μm diameter. The inlet air was seeded with micron-sized oil particles produced by a TSI 9306 six-jet atomizer. From these measurements, and those made using this LDA equipment in other rotating-disk rigs (see, for example, Gan et al., 1996), the uncertainty in the measured values of $V_\phi/\Omega r$ is expected to be approximately ±1 percent.

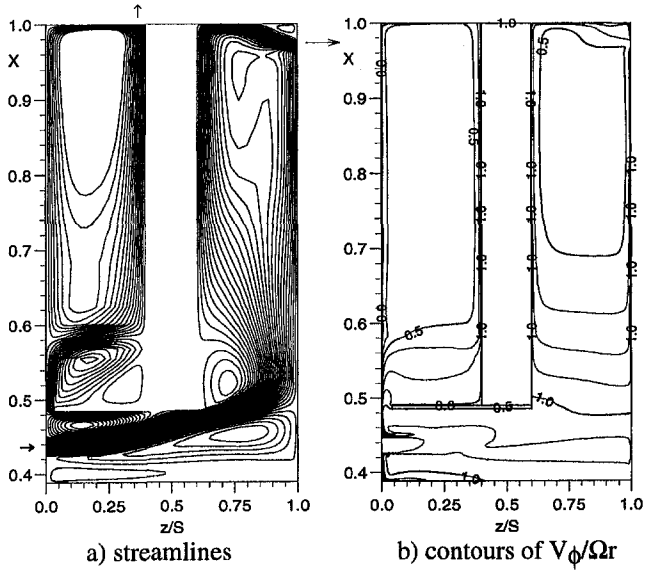

Fig. 3 Computed flow structure for cover-plate system: $Re_\phi = 1.09 \times 10^6$, $C_{w,b} = 1.21 \times 10^4$, $C_{w,p} = 1.55 \times 10^4$, $\lambda_{T,b} = 0.178$, $\beta_{p'} = 1.27$

Velocity measurements were made over the following ranges of nondimensional parameters:

$$5.3 \times 10^5 < Re_\phi < 1.25 \times 10^6$$

$$6500 < C_{w,b} < 26000$$

$$0.173 < \lambda_{T,b} < 0.363$$

$$1.18 < \beta_{p'} < 2.5$$

5 Computation and Measurements

5.1 Flow Structure. Figures 3 and 4 show the computed streamlines and contours of $V_\phi/\Omega r$ for $\lambda_{T,b} = 0.178$ and $\beta_{p'} = 1.27$ and for $\lambda_{T,b} = 0.229$ and $\beta_{p'} = 2.51$, respectively. The geometry corresponds to the experimental rig described in Section 4.

Values of Re_ϕ, $C_{w,b}$, $C_{w,p}$, $\lambda_{T,b}$, and β_p are given in the legends of Fig. 3 and 4; the nondimensional flow rate of the disk-cooling air, $C_{w,d}$, can be found from the difference between $C_{w,p}$ and $C_{w,b}$. The flow structure in the rotating cavity is determined by the magnitude of Re_ϕ, $\lambda_{T,b}$ and β_p; the magnitude of $C_{w,d}$ has an insignificant effect on the flow in the rotating cavity although it obviously has a strong effect on that in the rotor-stator system.

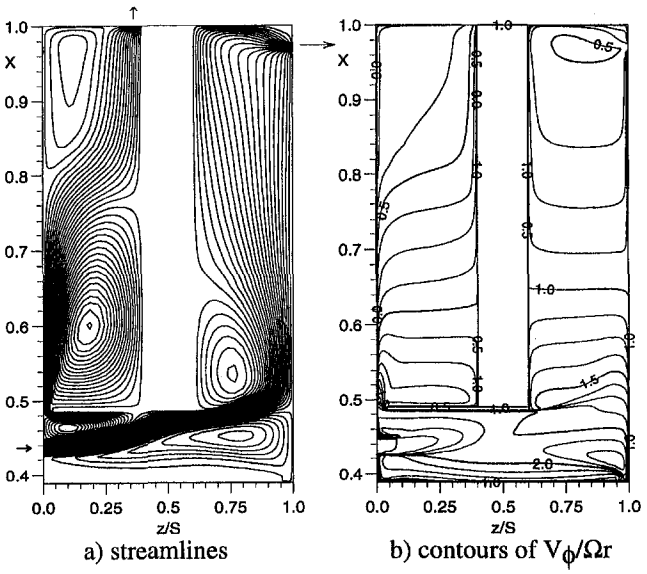

Fig. 4 Computed flow structure for cover-plate system: $Re_\phi = 0.553 \times 10^6$, $C_{w,b} = 0.902 \times 10^4$, $C_{w,p} = 1.55 \times 10^4$, $\lambda_{T,b} = 0.229$, $\beta_{p'} = 2.51$

Figure 3(a) shows the computed streamlines in three regions: the rotor–stator system (on the left-hand side of the figure); the rotating cavity (on the right-hand side); and the preswirl annulus (near the bottom). In the rotor–stator system, there is a source region for $x < 0.6$, radially outward of which there is the expected radial outflow on the rotating cover-plate and inflow on the stator, with a core of rotating fluid between the two boundary layers. The flow in rotor–stator systems is well understood and will not be discussed further here.

The preswirl flow enters the system at $z/s = 0$ and $x = 0.44$ with a swirl ratio of $\beta_{p'} = 1.27$. There are recirculation zones on either side of the swirling jet with a stagnation point on the outer wall of the preswirl annulus ($x = 0.49$, $z/s \cong 0.42$). For $z/s < 0.42$, there is an axial flow in the outer boundary layer toward the preswirl nozzles. It is this flow that enters the rotor–stator system through the clearance between the outer annular wall and the stator.

Most of the preswirl flow enters the rotating cavity, impinging on the rotating disk and separating from the cover-plate; the separation zone extends to $x \cong 0.57$. For $x < 0.75$, there is a source region, radially outward of which the flow divides into two nonentraining Ekman-type layers. (For $\lambda_{T,b} = 0.178$ and $\beta_{p'} = 1.27$, Eq. (14) gives $x_e = 0.87$, which overestimates the size of the source region shown in Fig. 3(a).) The flow leaves the rotating cavity through the annular slot in the rotating disk, at $x = 0.97$, half the flow coming from the boundary layer on the disk and the other half from the boundary layer on the cover-plate via the peripheral shroud.

Figure 3(b) shows the contours of $V_\phi/\Omega r$ for this case. For $x > 0.57$, radially outward of the separation zone, there is little axial variation of V_ϕ outside the boundary layers on the two disks.

Figure 4(a) shows the computed streamlines for $\lambda_{T,b} = 0.229$ and $\beta_{p'} = 2.51$. In the rotating cavity, the separation zone is larger than that shown in Fig. 3(a) and the source region extends throughout most of the cavity. (For $\beta_{p'} = 2.51$, Eq. (17) gives $\lambda_{T,b} = 0.173$; for $\lambda_{T,b} > 0.173$ the source region should fill the cavity, as shown in Fig. 4(a).)

Figure 4(b) shows that $V_\phi/\Omega r = 1$ at $x \cong 0.65$, which coincides with the edge of the separation zone on the cover-plate. For $x > 0.65$, there is little axial variation of V_ϕ outside the boundary layers on the disks.

Figure 5 shows the variation of $V_\phi/\Omega r$ with x^{-2} for three sets of $\lambda_{T,b}$ and $\beta_{p'}$. It is instructive to plot results against x^{-2} as free-vortex flow can be identified by straight lines passing through the origin at $x^{-2} = 0$. The "ideal free vortex," which corresponds to Eq. (12), is plotted from $x^{-2} = 0$ to $x^{-2} = 5.24$, the latter value being the radial location of the preswirl nozzles. The experimental measurements were obtained from nine tests carried out over many days. The nondimensional parameters varied slightly from test to test, but the nominal values indicated on the figure are accurate to around ±2 percent.

The "computed free vortex" in Fig. 5 is a free-vortex curve drawn through the computed values of $V_\phi/\Omega r$ at a single radius; a value of $x^{-2} = 2.2$ was arbitrarily chosen. The "computed free vortex" shows the radial extent to which the results conform to a free vortex. It is also possible to compute the "effective preswirl ratio," $\beta_{p,\text{eff}}$, corresponding to the value of the computed free vortex at $x^{-2} = 5.24$. Also shown on Fig. 5 are the locations of the centers of the blade-cooling slot, at $x^{-2} = 1.06$, and the cover-plate supports, at $x^{-2} = 2.13$.

Referring to Fig. 5(a), where $\beta_{p'} = 1.25$ and $\lambda_{T,b} = 0.18$, the computations show free-vortex flow from $1.8 < x^{-2} < 4$ ($0.5 < x < 0.75$) with $\beta_{p,\text{eff}} \cong \beta_{p'}$. The shear near $x = 1$ is associated with the boundary layer on the shroud, and the departure from the free-vortex curve at $x^{-2} \cong 1.8$ corresponds to the

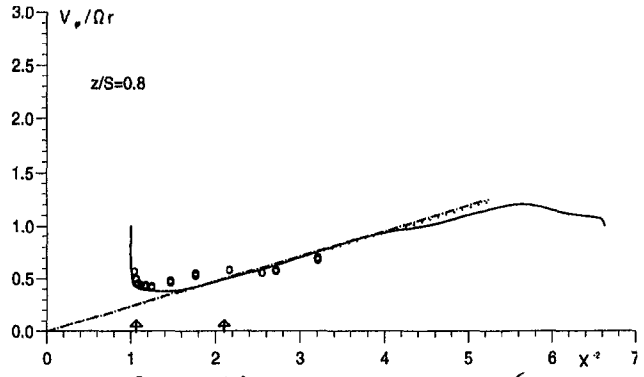

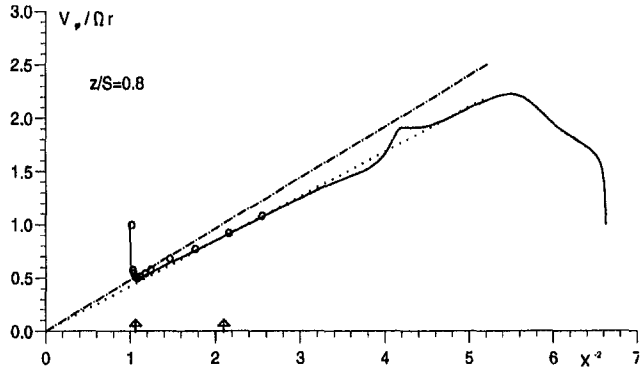

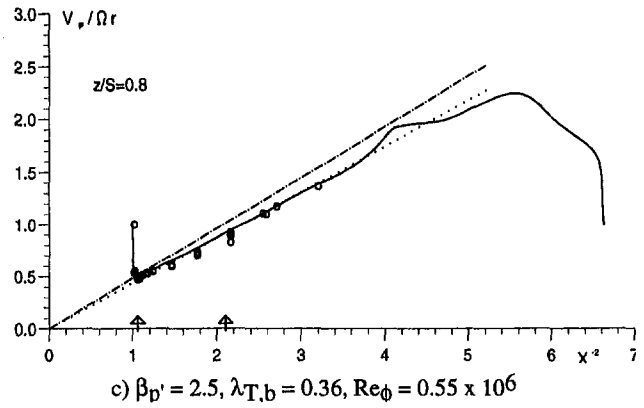

Fig. 5 Comparison between computed and measured variation of $V_\phi/\Omega r$ with x^{-2}: ○ experimental data; —— computation; – · – ideal free vortex; · · · · · · · computed free vortex; ↑ center of blade-cooling slot; ↑ center of cover-plate support

edge of the source region, which was discussed above. (It should be noted that angular momentum is not conserved outside the source region in the core flow between Ekman-type layers; see Owen and Rogers, 1995.)

The experimental data shown in Fig. 5(*a*) are consistent with a free vortex at the larger values of x^{-2} and illustrate the shear in the boundary layer near $x = 1$. Downstream of the cover-plate supports, the measurements show an increase in V_ϕ above the ideal free-vortex curve. In this region, where $V_\phi/\Omega r = 0.5$, the supports have evidently imparted angular momentum to the fluid, as suggested in Section 4.

In Fig. 5(*b*), where $\beta_{p'} = 2.5$ and $\lambda_{T,b} = 0.23$, the computations and measurements lie on a free-vortex curve that is significantly lower than the ideal one. For this case, where $V_\phi/\Omega r \cong 0.9$ near the cover-plate supports, the supports appear to have no significant effect on the flow. For these values of $\beta_{p'}$ and $\lambda_{T,b}$, the source region fills the entire cavity, and the computed and measured values of $V_\phi/\Omega r$ show that free-vortex behavior occurs up to the edge of the boundary layer on the shroud at $x = 1$.

Figure 5(*c*), where $\beta_{p'} = 2.5$ and $\lambda_{T,b} = 0.36$, shows computed and measured results similar to those in Fig. 5(*b*). These results illustrate the fact that $\beta_{p'}$ is the dominant parameter as far as $V_\phi/\Omega r$ is concerned, although $\lambda_{T,b}$ does have an effect on the size of the source region. The measurements and computations for results that are not shown here suggest that, for a fixed value of $\lambda_{T,b}$, the ratio of $\beta_{p,\text{eff}}/\beta_{p'}$ decreases significantly as $\beta_{p'}$ increases; for a fixed value of $\beta_{p'}$, the ratio increases as $\lambda_{T,b}$ increases.

5.2 Preswirl Effectiveness. Figure 6 shows a comparison between the computed values of Θ, using the definition in Eq. (7), and the theoretical curve for Θ', using Eq. (10). The geometry was based on the rig described in section 4 where $r_1/r_2 = 0.45$.

It should be pointed out that the authors were unable to make any reliable experimental measurement of Θ for the adiabatic case. Although total temperature probes were fitted in the rig to measure T_{01} and T_{t2}, it was not possible to conduct experiments under adiabatic conditions. Unlike the rig used by El-Oun and Owen (1989), the one used here was designed for heat transfer experiments. Windage heating from the heater assembly and heat input from the bearings created heat transfer from the disk to the cooling air even when no external heating was used. Heat transfer results, and the measurement of the temperature of the blade-cooling air, will be the subject of a subsequent paper.

Figure 6 shows good agreement between the computed and theoretical variation of Θ with $\beta_{p'}$ in the range $\beta_{p'} = 0$ to 4.60. It is convenient to define a nondimensional error, e_Θ, based on the difference between Θ' and Θ. From Eq. (7) it follows that

$$e_\Theta = \Theta' - \Theta = \frac{c_p(T_{t,2} - T'_{t,2})}{\frac{1}{2}\Omega^2 r_2^2} \tag{18}$$

where $T'_{t,2}$ is the theoretical value of the blade-cooling temperature, based on Eq. (10), and $T_{t,2}$ is the computed value. For 15 computed values, e_Θ ranges from 10^{-4} (for $\beta_{p'} = 2.5$) to 0.019 (for $\beta_{p'} = 4.6$). As the theoretical value given in Eq. (10) is exact, e_Θ represents the magnitude of the numerical errors in the computed values of Θ.

For the experimental rig, the conditions described above correspond to $\Omega r_2 < 84$ m/s, and the "dynamic temperature" $(\Omega^2 r_2^2/2c_p)$ is less than 3.5°C; a value of $e_\Theta = 0.019$ therefore corresponds to 0.07°C in the rig. In an engine, where dynamic temperatures can be in excess of 50°C, a value of $e_\Theta = 0.019$ would correspond to around 1°C. For practical purposes, the agreement between the computed and theoretical values of Θ can be regarded as satisfactory.

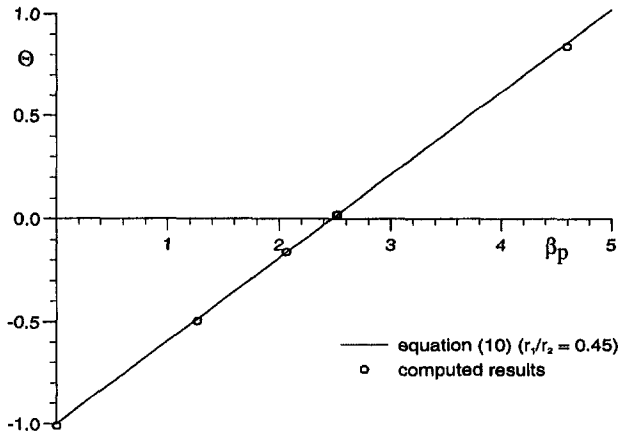

Fig. 6 Comparison between computed and theoretical variation of Θ with β_p

In engines, the effectiveness of cover-plate systems will be reduced by heat transfer from the turbine disk to the cooling air. For direct-transfer systems, the ingestion of disk-cooling air and mainstream gas into the blade-cooling passages is likely to have an even greater effect on the temperature of the blade-cooling air. However, even when heat transfer is significant, the adiabatic effectiveness provides a useful datum from which to measure preswirl performance.

6 Conclusions

Computations, made using an elliptic solver incorporating the Launder–Sharma low-Reynolds-number turbulence model, and velocity measurements, made using an LDA system in a purpose-built experimental rig, have been used to study the flow in an adiabatic cover-plate system.

The computations confirm that the flow between the cover-plate and the rotating disk is similar to that in a rotating cavity with a radial outflow of air. For sufficiently large values of $\lambda_{T,b}$, the source region fills most of the cavity and, outside the boundary layers, the flow behaves as a free vortex. The agreement between the measured and computed values of $V_\phi/\Omega r$ in the rotating cavity is mainly very good. Supports, attached to the cover-plate on the experimental rig, could disturb the flow when $V_\phi < \Omega r$ in the vicinity of the supports; at the design preswirl ratio ($\beta_{p'} = 2.5$), the effect of the supports was insignificant. The computed values of $V_\phi/\Omega r$ approximated to a free vortex with an effective preswirl ratio of $\beta_{p,\text{eff}}$. For $\beta_{p'} > 1.25$, the ratio of $\beta_{p,\text{eff}}/\beta_{p'}$ is less than unity and it decreases as $\beta_{p'}$ increases.

Values of the computed nondimensional preswirl effectiveness, Θ, were compared with theoretical values, Θ', obtained from a thermodynamic analysis of an adiabatic system. The analysis shows that Θ' depends only on the parameter $\beta_{p'}(r_p/r_b)^2$, and for $r_p/r_b = 0.45$ and $0 \le \beta_{p'} \le 4.6$ the numerical error between Θ' and Θ was less than 2 percent of the "dynamic temperature," $\Omega^2 r_b^2/2c_p$.

Acknowledgments

The authors thank the Engineering and Physical Sciences Research Council and European Gas Turbines Ltd. for funding the research described in this paper, and the Turkish Government and Kocaeli University for providing the financial support for Hasan Karabay. We also wish to thank the reviewers for their constructive comments.

References

Chen, J., Owen, J. M., and Wilson, M., 1993a, "Parallel-Computing Techniques Applied to Rotor-Stator Systems: Fluid Dynamics Computations," in: *Numerical Methods in Laminar and Turbulent Flow,* Vol. 8, Pineridge Press, Swansea, pp. 899–911.

Chen, J., Owen, J. M., and Wilson, M., 1993b, "Parallel-Computing Techniques Applied to Rotor-Stator Systems: Thermal Computations," in: *Numerical Methods in Thermal Problems,* Vol. 8, Pineridge Press, Swansea, pp. 1212–1226.

El-Oun, Z., and Owen, J. M., 1989, "Pre-swirl Blade-Cooling Effectiveness in an Adiabatic Rotor-Stator System," ASME JOURNAL OF TURBOMACHINERY, Vol. 111, pp. 522–529.

Gan, X., Mirzaee, I., Owen, J. M., Rees, D. A. S., and Wilson, M., 1996, "Flow in a Rotating Cavity With a Peripheral Inlet and Outlet of Cooling Air," ASME Paper No. 96-GT-309.

Meierhofer, B., and Franklin, C. J., 1981, "An Investigation of a Preswirled Cooling Airflow to a Gas Turbine Disk by Measuring the Air Temperature in the Rotating Channels," ASME Paper No. 81-GT-132.

Owen, J. M., and Rogers, R. H., 1989, *Flow and Heat Transfer in Rotating Disc Systems: Vol. 1: Rotor-Stator Systems,* Research Studies Press, Taunton, UK and John Wiley, New York, USA.

Owen, J. M., and Rogers, R. H., 1995, *Flow and Heat Transfer in Rotating Disc Systems: Vol. 2: Rotating Cavities,* Research Studies Press, Taunton, UK and John Wiley, New York, USA.

Popp, O., Zimmermann, H., and Kutz, J., 1998, "CFD Analysis of Coverplate Receiver Flow," ASME JOURNAL OF TURBOMACHINERY, Vol. 120, pp. 43–49.

Vaughan, C. M., Gilham, S., and Chew, J. W., 1989, "Numerical Solutions of Rotating Disc Flows Using a Non-linear Multigrid Algorithm," *Proc. 6th Int. Conf. Num. Meth. Laminar Turbulent Flow,* Pineridge Press, Swansea, pp. 66–73.

Wilson, M., Pilbrow, R. G., and Owen, J. M., 1997, "Flow and Heat Transfer in a Pre-swirl Rotor–Stator System," ASME JOURNAL OF TURBOMACHINERY, Vol. 119, pp. 364–373.

DISCUSSION

A. Mirzamoghadam[1]

The definition of flow and heat transfer in a preswirl rotor–stator cavity system using a cover-plate or direct injection to supply blade cooling air via the disk rim is critical to the design of an energy-efficient high-pressure turbine system. We in the advanced turbine design group follow the work of Professor Owen with great interest.

With respect to the cover-plate system described in Fig. 1(*b*) and for preswirl ratios greater than one in order to reduce the relative air temperature at the blade cooling passage radius of the model, to what extent would the increased radial inflow in the boundary layer offset the reduction in relative air temperature at the rim? Is there a drop in absolute air temperature on board the blade cooling passage for swirl ratios greater than one at the radius? How would you expect the disk radial Nu variation to compare with the free-disk prediction?

Referring to the direct feed system of Fig. 1(*a*) and described in Paper No. 95-GT-239, the free-disk heat transfer distributions are at least 25 percent higher even at the preswirl radius. How would this result change if: (*a*) the disk-cooling air were also preswirled, and (*b*) the stator were also a rotor?

Authors' Closure

We thank Dr. Mirzamoghadam for his comments and questions.

With respect to the cover-plate system, the results obtained in Section 2.1 are not affected by the radial inflow in the boundary layers on the rotating disks. The effectiveness defined in Eq. (7) depends on the end states of a thermodynamic process and not on the process itself: The radial inflow in the boundary layers will influence the effective preswirl ratio, $\beta_{p,\text{eff}}$, but it will not affect T_{t2}, which depends on β'_p and not on $\beta_{p,\text{eff}}$. According to Eq. (10), $T_{t2} < T_{01}$ when $\beta'_p\,(r_1/r_2)^2 > 0.5$; it follows that $T_{02} < T_{01}$ when $\beta'_p\,(r_1/r_2)^2 > 1$. This implies that $T_{02} < T_{01}$ when $V'_{\phi 2} > \Omega r_2$, where $V'_{\phi 2}$ corresponds to an "ideal free vortex." (As $\beta_{p,\text{eff}} < \beta'_p$, the actual value, $V_{\phi 2}$, will be less than the ideal value, $V'_{\phi 2}$.) Radial distributions of Nu for the cover-plate system are presented in the paper by Pilbrow et al. (1998).

With respect to the direct transfer system, Paper No. 95-GT-239 is now cited as Wilson et al. (1997) in the references given above. (*a*) If the disk-cooling air were preswirled, this would reduce the work done and, as the disk-cooling air is ingested into the blade-cooling passages, this should reduce the temperature of the air that flows into the turbine blades. Preswirling the disk-cooling air would also be expected to reduce the heat transfer from a hot disk to the air, and this would further reduce the temperature of the blade-cooling air. (b) If the "stator were also a rotor," this would be a cover-plate system with a large inlet radius: for the adiabatic case, Eq. (9) applies, but the authors have no experience of heat transfer in a large-radius cover-plate system.

Reference

Pilbrow, R., Karabay, H., Wilson, M., and Owen, J.M., 1998, "Heat Transfer in a 'Cover-Plate' Pre-swirl Rotating Disk System," ASME Paper No. 98-GT-113; ASME JOURNAL OF TURBOMACHINERY, Vol. 121, No. 2, 1999.

[1] Advanced Turbine Design, BMW Rolls-Royce AeroEngines, Eschenweg 11, 15827 Dahlewitz, Germany.

In engines, the effectiveness of cover-plate systems will be reduced by heat transfer from the turbine disk to the cooling air. For direct-transfer systems, the ingestion of disk-cooling air and mainstream gas into the blade-cooling passages is likely to have an even greater effect on the temperature of the blade-cooling air. However, even when heat transfer is significant, the adiabatic effectiveness provides a useful datum from which to measure preswirl performance.

6 Conclusions

Computations, made using an elliptic solver incorporating the Launder–Sharma low-Reynolds-number turbulence model, and velocity measurements, made using an LDA system in a purpose-built experimental rig, have been used to study the flow in an adiabatic cover-plate system.

The computations confirm that the flow between the cover-plate and the rotating disk is similar to that in a rotating cavity with a radial outflow of air. For sufficiently large values of $\lambda_{T,b}$, the source region fills most of the cavity and, outside the boundary layers, the flow behaves as a free vortex. The agreement between the measured and computed values of $V_\phi/\Omega r$ in the rotating cavity is mainly very good. Supports, attached to the cover-plate on the experimental rig, could disturb the flow when $V_\phi < \Omega r$ in the vicinity of the supports; at the design preswirl ratio ($\beta_{p'} = 2.5$), the effect of the supports was insignificant. The computed values of $V_\phi/\Omega r$ approximated to a free vortex with an effective preswirl ratio of $\beta_{p,\text{eff}}$. For $\beta_{p'} > 1.25$, the ratio of $\beta_{p,\text{eff}}/\beta_{p'}$ is less than unity and it decreases as $\beta_{p'}$ increases.

Values of the computed nondimensional preswirl effectiveness, Θ, were compared with theoretical values, Θ', obtained from a thermodynamic analysis of an adiabatic system. The analysis shows that Θ' depends only on the parameter $\beta_{p'}(r_p/r_b)^2$, and for $r_p/r_b = 0.45$ and $0 \le \beta_{p'} \le 4.6$ the numerical error between Θ' and Θ was less than 2 percent of the "dynamic temperature," $\Omega^2 r_b^2/2c_p$.

Acknowledgments

The authors thank the Engineering and Physical Sciences Research Council and European Gas Turbines Ltd. for funding the research described in this paper, and the Turkish Government and Kocaeli University for providing the financial support for Hasan Karabay. We also wish to thank the reviewers for their constructive comments.

References

Chen, J., Owen, J. M., and Wilson, M., 1993a, "Parallel-Computing Techniques Applied to Rotor-Stator Systems: Fluid Dynamics Computations," in: *Numerical Methods in Laminar and Turbulent Flow,* Vol. 8, Pineridge Press, Swansea, pp. 899–911.

Chen, J., Owen, J. M., and Wilson, M., 1993b, "Parallel-Computing Techniques Applied to Rotor-Stator Systems: Thermal Computations," in: *Numerical Methods in Thermal Problems,* Vol. 8, Pineridge Press, Swansea, pp. 1212–1226.

El-Oun, Z., and Owen, J. M., 1989, "Pre-swirl Blade-Cooling Effectiveness in an Adiabatic Rotor-Stator System," ASME JOURNAL OF TURBOMACHINERY, Vol. 111, pp. 522–529.

Gan, X., Mirzaee, I., Owen, J. M., Rees, D. A. S., and Wilson, M., 1996, "Flow in a Rotating Cavity With a Peripheral Inlet and Outlet of Cooling Air," ASME Paper No. 96-GT-309.

Meierhofer, B., and Franklin, C. J., 1981, "An Investigation of a Preswirled Cooling Airflow to a Gas Turbine Disk by Measuring the Air Temperature in the Rotating Channels," ASME Paper No. 81-GT-132.

Owen, J. M., and Rogers, R. H., 1989, *Flow and Heat Transfer in Rotating Disc Systems: Vol. 1: Rotor-Stator Systems,* Research Studies Press, Taunton, UK and John Wiley, New York, USA.

Owen, J. M., and Rogers, R. H., 1995, *Flow and Heat Transfer in Rotating Disc Systems: Vol. 2: Rotating Cavities,* Research Studies Press, Taunton, UK and John Wiley, New York, USA.

Popp, O., Zimmermann, H., and Kutz, J., 1998, "CFD Analysis of Coverplate Receiver Flow," ASME JOURNAL OF TURBOMACHINERY, Vol. 120, pp. 43–49.

Vaughan, C. M., Gilham, S., and Chew, J. W., 1989, "Numerical Solutions of Rotating Disc Flows Using a Non-linear Multigrid Algorithm," *Proc. 6th Int. Conf. Num. Meth. Laminar Turbulent Flow,* Pineridge Press, Swansea, pp. 66–73.

Wilson, M., Pilbrow, R. G., and Owen, J. M., 1997, "Flow and Heat Transfer in a Pre-swirl Rotor–Stator System," ASME JOURNAL OF TURBOMACHINERY, Vol. 119, pp. 364–373.

DISCUSSION

A. Mirzamoghadam[1]

The definition of flow and heat transfer in a preswirl rotor–stator cavity system using a cover-plate or direct injection to supply blade cooling air via the disk rim is critical to the design of an energy-efficient high-pressure turbine system. We in the advanced turbine design group follow the work of Professor Owen with great interest.

With respect to the cover-plate system described in Fig. 1(*b*) and for preswirl ratios greater than one in order to reduce the relative air temperature at the blade cooling passage radius of the model, to what extent would the increased radial inflow in the boundary layer offset the reduction in relative air temperature at the rim? Is there a drop in absolute air temperature on board the blade cooling passage for swirl ratios greater than one at the radius? How would you expect the disk radial Nu variation to compare with the free-disk prediction?

Referring to the direct feed system of Fig. 1(*a*) and described in Paper No. 95-GT-239, the free-disk heat transfer distributions are at least 25 percent higher even at the preswirl radius. How would this result change if: (*a*) the disk-cooling air were also preswirled, and (*b*) the stator were also a rotor?

Authors' Closure

We thank Dr. Mirzamoghadam for his comments and questions.

With respect to the cover-plate system, the results obtained in Section 2.1 are not affected by the radial inflow in the boundary layers on the rotating disks. The effectiveness defined in Eq. (7) depends on the end states of a thermodynamic process and not on the process itself: The radial inflow in the boundary layers will influence the effective preswirl ratio, $\beta_{p,\text{eff}}$, but it will not affect T_{t2}, which depends on β'_p and not on $\beta_{p,\text{eff}}$. According to Eq. (10), $T_{t2} < T_{01}$ when $\beta'_p\,(r_1/r_2)^2 > 0.5$; it follows that $T_{02} < T_{01}$ when $\beta'_p\,(r_1/r_2)^2 > 1$. This implies that $T_{02} < T_{01}$ when $V'_{\phi 2} > \Omega r_2$, where $V'_{\phi 2}$ corresponds to an "ideal free vortex." (As $\beta_{p,\text{eff}} < \beta'_p$, the actual value, $V_{\phi 2}$, will be less than the ideal value, $V'_{\phi 2}$.) Radial distributions of Nu for the cover-plate system are presented in the paper by Pilbrow et al. (1998).

With respect to the direct transfer system, Paper No. 95-GT-239 is now cited as Wilson et al. (1997) in the references given above. (*a*) If the disk-cooling air were preswirled, this would reduce the work done and, as the disk-cooling air is ingested into the blade-cooling passages, this should reduce the temperature of the air that flows into the turbine blades. Preswirling the disk-cooling air would also be expected to reduce the heat transfer from a hot disk to the air, and this would further reduce the temperature of the blade-cooling air. (b) If the "stator were also a rotor," this would be a cover-plate system with a large inlet radius: for the adiabatic case, Eq. (9) applies, but the authors have no experience of heat transfer in a large-radius cover-plate system.

Reference

Pilbrow, R., Karabay, H., Wilson, M., and Owen, J.M., 1998, "Heat Transfer in a 'Cover-Plate' Pre-swirl Rotating Disk System," ASME Paper No. 98-GT-113; ASME JOURNAL OF TURBOMACHINERY, Vol. 121, No. 2, 1999.

[1] Advanced Turbine Design, BMW Rolls-Royce AeroEngines, Eschenweg 11, 15827 Dahlewitz, Germany.

LDV Study of Developing Flows Through a Smooth Duct With a 180 deg Straight-Corner Turn

T.-M. Liou
email: tmliou@tmp.nthu.edu.tw

C.-C. Chen

Department of Power Mechanical Engineering, National Tsing Hua University, Hsinchu, Taiwan 30043

In view of the lack of velocity field data for flow through turbine blade internal cooling passages, laser-Doppler velocimetry measurements are presented for the flow development in a two-pass smooth rectangular duct of aspect ratio 1.1 with a 180 deg straight-corner turn with and without duct rotation. The test duct had a curvature axis normal to the rotational axis. The Reynolds number based on the bulk mean velocity and hydraulic diameter was 1.4 × 10⁴ and the rotation numbers were 0 and 0.082. Characteristics such as the upstream and downstream extents of the sharp-turn effect on the main flow profile, curvature induced Dean vortices inside the turn, turning geometry-induced separating bubble immediately downstream of the turn, and the resulting double-peak mean velocity profiles in the second pass are used to describe the developing mean flow for the case without rotation. High turbulence levels and significantly more nonuniform flow after the sharp turn in the front part of the second pass explain previously reported work showing higher but nonuniform heat transfer after that turn. Rotating the duct augments and shifts the peaks of the streamwise mean velocity and turbulence intensity profiles toward the trailing and leading walls of the first and second passes, respectively. In addition, the duct rotation skews the separating bubble and reduces its size to about 75 percent of its stationary counterpart.

Introduction

Flow fields in two adjacent ducts connected by a 180 deg turn are encountered in many practical applications such as the hot gas manifold of the space shuttle main engine power head (Kwak et al., 1986), the internal coolant path of advanced gas turbine blades, and in ventilation piping systems. The present study focuses on a two-pass rectangular smooth passage with a 180 deg sharp turn, roughly simulating the first two passes of a serpentine coolant passage internal to a cooled turbine blade, as shown schematically in Fig. 1. The space constraints in cooling blade passages dictate a small radius of curvature (R_C) for the 180 deg turn, often smaller than the duct hydraulic diameter (D_H), such that the turning geometry-induced secondary flow, flow separation, recirculation, and reattachment result in noticeable effects on the pressure loss and nonuniformity of heat transfer distribution. However, most prior studies pertaining to 180 deg turning flows, both laminar (Cheng et al., 1977; Hille et al., 1985; Fairbank and So, 1987) and turbulent (Chang et al., 1983; Azzola et al., 1986; Johnson, 1988; Choi et al., 1989), are limited to turning geometries with radii of curvature-to-duct hydraulic diameter ratios (R_C/D_H) larger than one. In such configurations, streamwise flow separation is either absent or mild. Hence, a better understanding of the local flow structures in blade cooling passages with a 180 deg turn is imperative. This information will facilitate the relevant heat transfer design and is crucial for lowering blade metal temperatures and, in turn, increasing blade life.

Among the previous studies concerning fluid flow and/or heat transfer in a smooth duct with a 180 deg sharp-turn, Metzger et al. (1984, 1986) performed pressure measurements, surface ink-streaklines visualizations, and heat transfer coefficient measurements, based on thermocouple measured segment temperatures for nine different geometries. This study included changes in the ratio of inlet to outlet channel width, and the divider tip-to-wall clearance, for Reynolds numbers ranging from 1 × 10⁴ to 6 × 10⁴. They observed a large separated recirculation flow zone along the downstream side of the divider. Considerable variations in heat transfer distribution resulted from this flow separation and reattachment region. Chyu (1991) examined both two- and three-pass channels with rectangular turns using an analogous naphthalene mass transfer technique for Reynolds numbers of 2 × 10⁴ to 7.4 × 10⁴. An important finding was that heat transfer characteristics around the second turn were virtually the same as those around the first turn. This result may suggest that, in a multiple-pass passage, heat transfer at the first turn has already reached the thermally periodic condition. The above-mentioned studies did not report secondary flow patterns. Cheng et al. (1992) visualized the secondary flow patterns at various axial cross sections in a square duct with a 180 deg sharp turn for three different divider tip-to-wall clearances and Reynolds numbers of 200, 500, and 800 using the smoke injection method. It was found that the secondary flow patterns, featuring by one to four pairs of vortices, were distorted and the flow becomes turbulent in the region two to three duct hydraulic diameters after the turn for Re = 500 and 800. Recently, Wang and Chyu (1994) presented computational results of mean secondary flow patterns and heat transfer distribution in a two-pass, square duct with a 180 deg sharp turn for three different turning configurations: (1) straight-corner turn; (2) rounded-corner turn; and (3) circular turn. Turbulence was modeled using an extended version of the $k-\epsilon$ model, and the inlet conditions were fully developed profiles for mean velocities and turbulence parameters. Results showed that overall heat transfer greatly increases in the turning region; nevertheless, spatial variation in the local heat transfer was also very significant and depended strongly on the turn geometry. Moreover, the straight-corner turn yields the highest heat transfer enhancement relative to the fully developed straight channel flow.

For serpentine smooth passages with rotation, most previous studies include heat transfer measurements (Wagner et al.,

Contributed by the International Gas Turbine Institute and presented at the 42nd International Gas Turbine and Aeroengine Congress and Exhibition, Orlando, Florida, June 2–5, 1997. Manuscript received International Gas Turbine Institute February 1997. Paper No. 97-GT-283. Associate Technical Editor: H. A. Kidd.

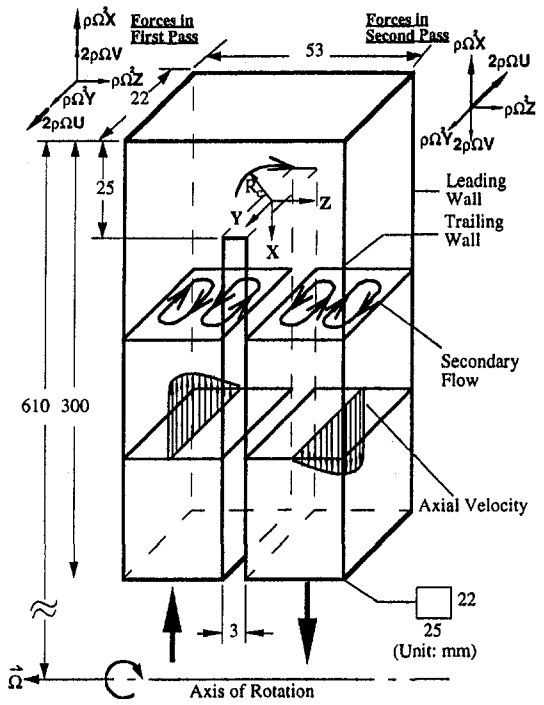

Fig. 1 Sketch of configuration, coordinate system, dimensions, and force diagrams of test section

1991a, b; Han and Zhang, 1992; Yang et al., 1992) and predictions (Tekriwal, 1994; Sathyamurthy et al., 1994; Rigby et al., 1996). However, there are few experimental data for velocity measurements. Cheah et al. (1996) reported laser-Doppler anemometry measurements of a turbulent flow field in a rotating U-bend of strong curvature ($R_C/D_H = 0.65$) with a Reynolds number of 1×10^5 and rotational number of 0, 0.2, and −0.2. Their rotational rig was designed such that the curvature axis (Y axis in Fig. 1) of the duct is parallel to the axis of rotation, although most turbine coolant passages have their axis of rotation normal to their curvature axis. Moreover, their axis of rotation was designed at the middle of the whole partition wall. They found that positive rotation, which was defined as one in which the duct trailing (pressure) side coincides with the outer side of the U-bend, doubles the length of the separation bubble and generally suppresses turbulence levels.

The preceding brief survey reveals the lack of experimental measurements of turbulent velocity fields, compared to its heat transfer counterpart, in a channel with a 180 deg sharp turn and a curvature axis normal to the rotational axis. Further, as pointed out by Johnson (1988) in his numerical simulation of local Nusselt number, for turbulent flow in a square duct with a 180 deg bend, broad agreement with experiment is achieved for local Nusselt number predictions even though significant disagreements occur between velocity field predictions in the region away from the wall and the corresponding experimental data. It is these facts that motivate the present research to perform detailed measurements of the turbulent flowfield in two-pass rectangular duct with a straight-corner turn (Fig. 1) using nonintrusive laser-Doppler velocimetry (LDV). The straight-corner (or square-corner) turn is the most common case when a 180 deg sharp turn is molded in the laboratory and adopted virtually in all of the previous studies (Wang and Chyu, 1994). The preceding survey also indicates that the square-corner turn yields the highest heat transfer enhancement among the various turning configurations examined (Wang and Chyu, 1994). To compare with these previous studies and avoid optical distortion through the curved wall in the turn region, square corners in the 180 deg sharp turn are thus used in the present work. LDV is chosen since flow reversals and large turbulence fluctuations associated with the sharp turn are expected. It is hoped that the data obtained herein lend insight to the complex flow investigation and can also be used for verification of ongoing computational predictions of internal flows in coolant passage with and without rotation.

Experimental Apparatus and Conditions

Experimental Apparatus. The flow system and LDV experimental setup in the present work are shown schematically in Fig. 2. Air was axially drawn into one end of a hollow shaft, made a 90 deg turn in one side of a settling chamber, and radially flowed into the test section. The settling chamber was an enlarged part of the hollow shaft and internally partitioned into two parts by the divider of the two-pass coolant passage. As pictured in Fig. 1, the air flow in the first and second passages of the test section was radially outward and inward, respectively. Downstream of the test section, the air flow made a 90 deg turn in the other side of the settling chamber and then flowed axially through inside the hollow shaft, a rotary joint, a curved duct, a flowmeter, a bellows, and then exhausted by a 2.2 kW turbo blower.

The LDV experimental setup is similar to that described by Liou et al. (1993). The LDV optics is a two-color four-beam two-component system. A 4-W argon-ion laser with 514.5 nm (green) and 488 nm (blue) lines provided the coherent light sources. Both forward and off-axis scattering configurations were used in the experiment; based on $1/e^2$ extent of light intensity, the former provided a probe volume of about 1.69

Nomenclature

A = half width of duct, mm
B = half height of duct, mm
D_H = hydraulic diameter = $4AB/(A + B)$ = 23.4 mm
d = divider thickness = $D_H/8$, mm
ER = encoder resolution, deg
R_c = radius of curvature, mm, Fig. 1
Re = Reynolds number = $\rho UD_H/\mu$
Ro = rotation number $\Omega D_H/U_b$
U = streamwise mean velocity, m/s
U_b = duct bulk mean velocity, m/s
u = streamwise velocity fluctuation, m/s
V = transverse mean velocity, m/s
v = transverse velocity fluctuation, m/s
W = spanwise mean velocity, m/s
X = streamwise coordinate, mm, Fig. 1
X^* = normalized streamwise coordinate = X/D_H
Y = transverse coordinate, mm, Fig. 1
Y^* = normalized transverse coordinate = Y/B
Z = spanwise coordinate, mm, Fig. 1
Z^*, Z^{**} = normalized spanwise coordinate: (*i*) $X < 0$, $Z^{**} = Z/(2A + d)$ (in the turn); (*ii*) $X \geq 0$, $Z < 0$, $Z^* = (Z + d/2)/2A$ (in the first pass); (*iii*) $X \geq 0$, $Z > 0$, $Z^* = (Z - d/2)/2A$ (in the second pass)
μ = air absolute viscosity, kg/m·s
ρ = air density, kg/m^3
Ω = rotating speed, rad/s

Subscripts

b = bulk
s = stationary

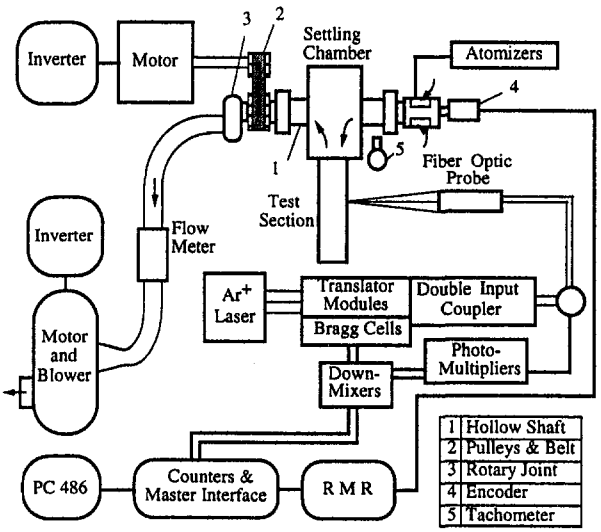

Fig. 2 Schematic drawing of overall experimental system

mm in length and 0.164 mm in diameter and the latter 0.74 mm in length and 0.164 mm in diameter inside the test section. The entire LDV system was mounted on a milling machine with four vibration-isolation mounts, allowing the probe volume to be positioned with 0.01 mm resolution. The light scattered from salt particles with a nominal 0.8 μm size was collected into the photomultiplier and subsequently downmixed to the appropriate frequency shift of 0.1 to 10 MHz. Then two counterprocessors with 1 ns resolution were used to process the Doppler signals and feed the digital outputs into a PC-486 for storage and analysis. The phase angle in a given cycle was determined with an optical encoder attached to the pulse generator (hollow shaft). A phase angle processor was used to generate a trigger pulse at any selectable phase angle. This trigger pulse was in turn input to an inhibit module, which output a variable duration pulse to inhibit the counterprocessor over a selected phase angle interval. The positioning window of each measuring location was indexed by the rotary encoder with a resolution (ER) of 0.125 deg. When a velocity measurement was validated by the counterprocessor, the phase angle-velocity data were transferred to the PC-486 and recorded in separate data bins. The circumferential length of a single data bin was from 0.71 to 1.27 mm as the measuring location varied from $X/D_H = 11.2$ to $X/D_H = 0.1$ (Fig. 1). Two circumferential traverses were performed along two close radial positions to obtain profiles along straight traverse lines by data interpolation.

Test Section and Conditions. Figure 1 shows the configuration, coordinate system, and dimensions of the test section, which was made of 3-mm-thick acrylic sheets for optical access. The flow path has a cross section of 25 mm $\times$ 22 mm with a corresponding hydraulic diameter of $D_H = 23.4$ mm. The channel height of the test section corresponds to phase angle windows of about 2 and 4 deg at radii of 585 mm and 310 mm, respectively. The lengths of the first pass, sharp turn, and second pass are 12.8 D_H, 2.3 D_H, and 12.8 D_H, respectively. At the turn, the clearance between the tip of the divider wall and the duct outer wall is kept equal to 1.07 D_H (or 25 mm) and the width of divider wall that separates the two flow passes is 0.13 D_H. For the case of rotation, the mean radius-to-passage hydraulic diameter ratio is 19.7. The coordinate origin is chosen at the tip center of the partition wall (Fig. 4) such that the X coordinates upstream and downstream of the turn are all positive, whereas in the turn they are negative. However, it should be noted that the streamwise mean velocity component U is taken positive along the main stream direction.

In the present study, the Reynolds number, based on the bulk mean velocity of $U_b = 8.94$ m/s and hydraulic diameter, is fixed at 1.4×10^4 for both the stationary and rotational cases. For the rotational case, the rotational speed is fixed at 300 rpm corresponding to a rotational number of 0.082. The velocity measurements were made at nine and ten radial stations for the first and second flow passes, respectively. In each station the streamwise velocity were made along two orthogonal lines, (Y^*, $Z^* = \pm 0.5$) and ($Y^* = 0$, Z^*). The secondary-flow velocity vector mappings were performed over nine cross-sectional planes. Moreover, detailed velocity vector mappings for the region from 1 D_H upstream of the turn to 2 D_H downstream of the turn in the $Y^* = 0$ plane were made. The inlet reference cross section is chosen at $X^* = 11.2$ of the first flow pass.

Data Uncertainty. The presented mean velocity and turbulence intensity were calculated from the probability distribution function of the measurements. Typically, 2000–4000 realizations were ensemble averaged at each measuring location for the stationary and rotational cases. Additional measurements of higher realizations (8000) in the high fluctuation regions were also taken to be sure of statistical convergence. For the latter case there were 40,000 to 80,000 realizations within the phase angle window over many revolutions. The corresponding statistical errors in the ensemble mean velocity and turbulence intensity were less than 0.018 U_b and 0.031 U_b, respectively, for a 95 percent confidence level.

There are several methods for velocity bias corrections for LDV measurements. In the present work the velocity bias was first corrected by using the well-known weighting method of Mclaughlin and Tiederman (1973) for regions where local turbulence intensity was below about 25 percent (Drain, 1980). The difference between weighted and unweighted data sets was found to be below 2 percent. For regions in the shear layer of the separation bubble and near-wall regions, the turbulence level was typically very high, and near-zero velocities frequently appear due to flow reversal resulting in very large weighting vectors and, in turn, in an overcorrection. For these regions, therefore, measurements were repeated using the equal time interval sampling, and the corrections due to velocity bias were found to be within 3.6 percent.

The phase angle broadening (or positioning window broadening) and velocity gradient broadening were coupled for the rotational case. To choose an appropriate phase angle resolution, measurements were performed for positioning window widths of 0.1, 0.125, and 0.18 deg. The results showed that there was little change in the mean velocity profiles as the positioning window width was varied. A typical example will be shown later. However, considerable differences in the turbulence intensity profiles were found between different window widths, as will be shown later. Less than 19 and 3.4 percent (relative to U_b) differences in the measured $\sqrt{u^2}/U_b$ results were found between positioning window widths of 0.18 deg and 0.1 deg, 0.125 deg and 0.1 deg, respectively. Since the maximum difference between positioning window widths of 0.125 and 0.1 deg is comparable to other uncertainties described in the Data Uncertainty, the positioning window width of 0.125 deg was chosen in the rotational case of the present work.

Uncertainty analysis pertaining to velocity gradient broadening (stationary case), data repeatability, flow-rate conservation, etc., were similar to those included in the work of Liou et al. (1990) and estimated to have overall values of $U < 0.015\ U_b$ and $u < 0.023\ U_b$.

Results and Discussion

Flow Development in $Y^* = 0$ Plane ($Ro = 0$). The streamwise evolution of the X-component mean velocity profile along the $Y^* = 0$ plane for the stationary-duct case is depicted in Fig. 3. The turning of the flow from the settling chamber

into the first pass makes the streamwise mean velocity profile at inlet reference plane $X^* = 11.2$ slightly skewed. The skewness gradually decreases as the flow proceeds from $X^* = 11.2$ to $X^* = 7.4$. Measurements of the streamwise mean-velocity distributions along $Z^* = 0.08$ and $Z^* = 0.92$ (i.e., along lines at a distance of 2 mm from inner and outer walls, respectively) reveal that downstream of $X^* = 3.0$ the flow has sensed the existence of the sharp turn and, therefore, displays an acceleration and a deceleration near the inner and the outer walls, respectively. This profile exists due to the favorable and adverse pressure gradients along the inner and outer walls, respectively, before the turning (Liou and Liao, 1995). The velocity near the inner wall can be as high as 1.33 U_b at $X^* = 0.1$, whereas the velocity near the outer wall can be as low as 0.44 U_b at $X^* = 0.1$.

Immediately downstream of the sharp turn, the flow enters the second pass. Near the turn the pressure distributions along the inner and outer walls in the second pass are completely opposite to those in the first pass (Liou and Liao, 1995) and, hence, the acceleration (convective heat transfer enhancement) is now occurring near the outer wall and the deceleration occurs near the inner wall. Owing to the inability of the flow to follow the sharp turn, Fig. 3 clearly demonstrates a large separation bubble existing adjacent to the tip of partition wall, as visualized by Metzger et al. (1984), with a maximum negative U/U_b of 0.57 and a reattachment length of about 1.75 hydraulic diameters away from the partition-wall tip. Downstream of the separating recirculation zone the flow gradually redevelops with a decrease and an increase of mean velocities near the outer and inner walls, respectively. As can be seen from Fig. 3, the flow redevelopment is, however, not completed at the exit of the second pass.

Inside the sharp turn, Fig. 4 shows the presence of the corner vortex around the outer wall corner ($X^* = -1$, $Z^{**} = -1$). It should be pointed out that this corner vortex was also found in the calculation of Wang and Chyu (1994) for the cases of straight-corner and circular-corner turns but not for the case of a U-bend. Also in their case the partition wall had a thickness of 0.50 D_H, which is about four times that of our case. The consequence is that the geometry-induced separating recirculation zone is mainly occurring on the tip region of the partition wall in their case while it exists downstream of the partition-wall tip in our case. The foregoing comparison suggests the significant effect of the divider wall thickness on the flow characteristics inside and immediately after the sharp turn.

Flow Development in $Z^* = \pm 0.5$ Plane ($Ro = 0$). The normal vector of Z^* planes is parallel to the axis of rotation and, hence, the Z^* planes approximately parallel the direction of Coriolis force in the rotating duct case (Fig. 1). As pointed out in the introduction, the streamwise flow development in $Z^* = \pm 0.5$ planes (Fig. 1) of a two-pass duct with a sharp turn has seldomly been reported in the open literature and is therefore depicted in Fig. 5 for $Ro = 0$ and $\mathrm{Re} = 1.4 \times 10^4$. Because the $Z^* = \pm 0.5$ planes are perpendicular to the curvature axis of the entry flow turning into the first pass from the settling chamber and the inflow into the sharp turn from the first pass, the streamwise mean velocity profiles in the first pass of the $Z^* = -0.5$ plane (Fig. 5) are almost unaffected by the turning curvatures and more symmetric than the counterparts in $Y^* = 0$ plane (Fig. 3), particularly around $X^* = 0.1$. In contrast, the flow development in the second pass of $Z^* = 0.5$ plane is more complex and features the double-peak streamwise mean velocity profile within the region of about 6 D_H after the turn and top-hat profile as $X^* > 6$. The double-peak mean velocity profile results from the combined effect of curvature-induced cross-section secondary flow and aforementioned sharp-turn induced separating recirculation flow, as will be made clear from the secondary flow pattern presented below.

Cross-Section Secondary Flow ($Ro = 0$). Figure 6 shows the evolution of the secondary flow pattern at several selected cross sections. The secondary-flow mean-velocity vector fields are plotted in the downstream-facing direction. Owing to the entry turning effect, the secondary flow vectors point toward the inner wall ($Z^* = 0$) in the first pass with the maximum magnitudes of velocity vector of 0.06 U_b and 0.26 U_b at $X^* = 3.7$ and $X^* = 0.1$, respectively. Inside the turn, the counterrotating Dean vortex pair appears. An example is shown in Fig. 6 for the cross section of $Z^{**} = 0$. It is noted that the cross-stream velocities are very large, as high as 1.7 U_b, near $X^* = 0$ due to thin partition wall. The reversal flow regions are confined within 0.25 D_H of the upper ($Y^* = 1$) and bottom ($Y^* = -1$) walls.

Immediately after the turn, $X^* = 0.1$ in Fig. 6, the counterrotating vortex pair is pushed toward the outer wall ($Z^* = 1$) and limited to half of the cross section ($0.5 < Z^* < 1$) by the separating bubble previously presented in Figs. 3 and 4. The cross-stream mean velocity inside the separating bubble is very low, as low as 0.05 U_b, as indicated by the shorter vectors in the region of $0 < Z^* < 0.5$ (Fig. 6, $X^* = 0.1$). It is worth mentioning here that the prevalence of a large cross-stream velocity, about 0.98 U_b, between the two counterrotating vortices, i.e., in the region $|Y^*| < 0.25$, diverts the main stream fluids in $|Y^*| < 0.25$ from $Z^* = 0.5$ plane and, hence, lowers the mainstream velocity there. The above observation provides the rationale for the formation of double-peak streamwise velocity profile at $X^* = 0.1$ (Fig. 5) of the second pass in the $Z^* = 0.5$ plane. Downstream of the separation bubble, the cross-sectional secondary flow pattern at $X^* = 3.7$ is further distorted into asymmetric vortices. There are a large counterclockwise vortex in the fourth quadrant and a very small clockwise vortex at the corner formed by the outer ($Z^* = 1$) and top ($Y^* = 1$) walls. Nevertheless, the magnitude of the maximum velocity vector has decreased to 0.09 U_b or an order of magnitude smaller than that at $X^* = 0.1$ of the same flow pass. At the further downstream cross section of $X^* = 7.4$, the secondary-flow vortices disappear and the magnitudes of the velocity vector decreased to less than 0.05 U_b, which is similar for the flow at $X^* = 7.4$ of the first pass.

Turbulence Intensity ($Ro = 0$). The sharp turn also has an effect on the fluctuation level of the two-pass duct flowfield. Figure 7 depicts the streamwise turbulence intensity profiles at

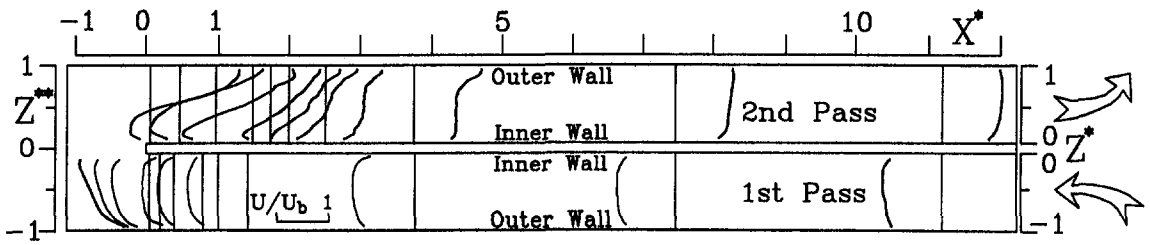

Fig. 3 Evolution of streamwise mean velocity profile in the $Y^* = 0$ plane of the first and second passes for $\mathrm{Re} = 1.4 \times 10^4$ and $Ro = 0$

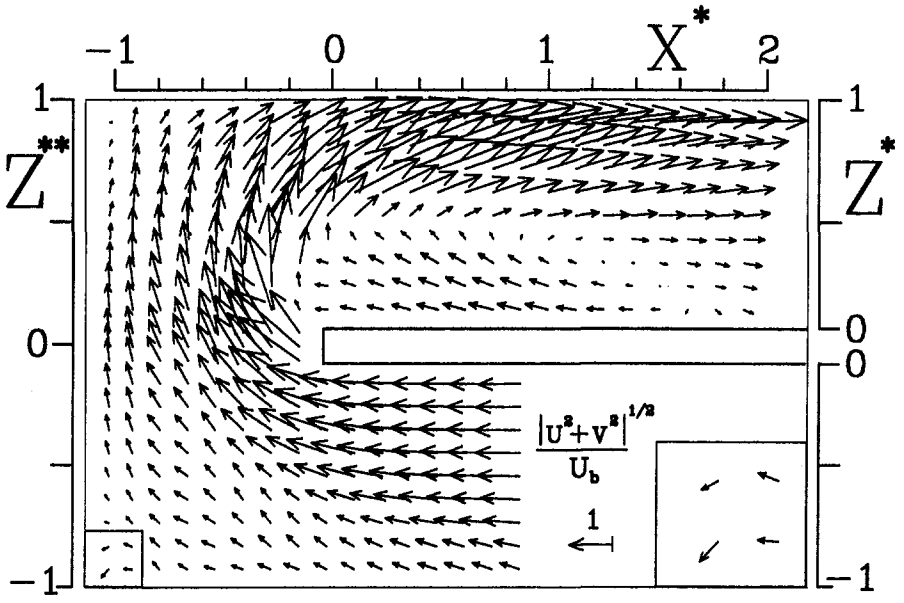

Fig. 4 Vector plot of the flow patterns near and inside the sharp turn in the $Y^* = 0$ plane for Re = 1.4×10^4 and $Ro = 0$

various X^* stations where Fig. 3 has shown the corresponding streamwise mean velocity profiles. In the first pass the $\sqrt{u^2}/U_b$ profiles are all very similar with levels of 0.09 ± 0.03, except near the wall where the levels are higher and within 0.17 ± 0.03. In contrast, Fig. 7 clearly demonstrates the significant effect of the sharp turning on raising and changing the turbulence intensity profile level and shape in the second pass. The turning geometry induced separating recirculation flow ($0 < X^* < 1.75$), the reattachment of separating shear layer ($X^* \approx 1.75$), and the core fluids' expanding through the divergent passage ($0.5 < X^* < 4$), formed by the latter part of separating bubble and outer wall, all contribute to the increase of turbulence level. Only in the convergent stream passage ($0 < X^* < 0.5$), formed by the front part of the separating bubble and outer wall, where the core fluid accelerates and the levels of $\sqrt{u^2}/U_b$ decrease. For a given streamwise turbulence intensity profile, the peak turbulence intensity generally occurs around the shear layer bounding the recirculation flow zone. For instance, the peak $\sqrt{u^2}/U_b$ occurs around $Z^* = 0.45$ (open diamond), 0.62 (solid square), 0.38 (open square), and 0.25 (solid triangle) at cross sections $X^* = 0.1$, 0.5, 1, and 1.5, respectively. Among them the peak $\sqrt{u^2}/U_b$ location $Z^* = 0.62$ at $X^* = 0.5$ corresponds to the maximum height of the separation bubble. Moreover, the maximum peak value of $\sqrt{u^2}/U_b = 0.54$ occurring at $X^* = 1.5$, slightly upstream of the reattachment point $X^* \approx 1.75$, is consistent with the general conclusion of $(\sqrt{u^2}/U_b)_{\text{Max}}$ occurring at or slightly upstream of a separated reattaching shear flow (Eaton and Johnston, 1981). Adjacent to the reattachment, the curving downward separating shear layer spreads and splits (Eaton and Johnston, 1981) with one part reattaching onto the inner wall and the other part convecting downstream. The shear layer downstream of reattachment becomes wider in thickness and weaker in velocity gradient, resulting in the lack of a sharp peak $\sqrt{u^2}/U_b$ and decreasing turbulence level for $X^* \geq 2$. As the flow proceeds to $X^* \geq 8$, the effect of turning geometry on the flow fluctuation has nearly vanished and the turbulence level is the same as that in the first pass.

The streamwise turbulence intensity profiles in the $Z^* = -0.5$ and $Z^* = 0.5$ planes of the first and second passes, respectively, are plotted in Fig. 8. As in Fig. 7, the $\sqrt{u^2}/U_b$ profiles in the $Z^* = -0.5$ plane, of the first pass, are all very similar with a turbulence level slightly higher than that in Fig. 7. In the $Z^* = 0.5$ plane of the second pass, the double-peak mean velocity profile at $X^* = 0.1$ (Fig. 5), as a result of the combined effect of curvature induced secondary flow and sharp turning induced separating bubble, raises the turbulence intensity to a value as high as $\sqrt{u^2}/U_b = 0.48$ (Fig. 8). The turbulence level subsequently decreased to a value about the same as that in the first pass for $X^* \geq 8$. At this point, it is worthwhile to point out that the high turbulence-intensity levels and significant variation in the local turbulence-intensity profiles in the front half part of second pass presented in Figs. 7 and 8, may explain the experimentally measured (Metzger et al., 1984) and computationally predicted (Wang and Chyu, 1994) high heat transfer coefficients and large variations in the heat transfer distribution around the separating recirculation and reattachment zones.

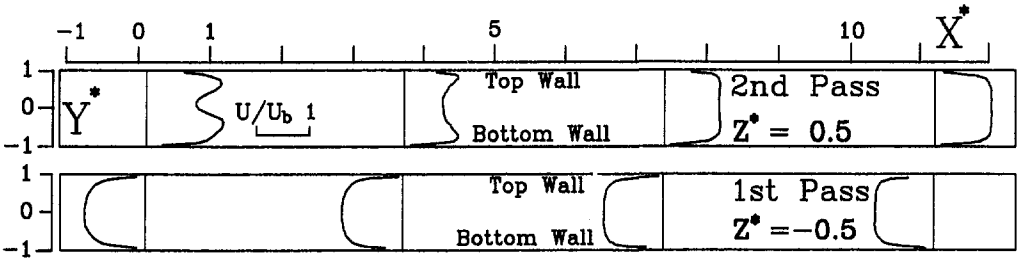

Fig. 5 Evolution of streamwise mean velocity profile in the $Z^* = \pm 0.5$ planes of the first and second passes for Re = 1.4×10^4 and $Ro = 0$

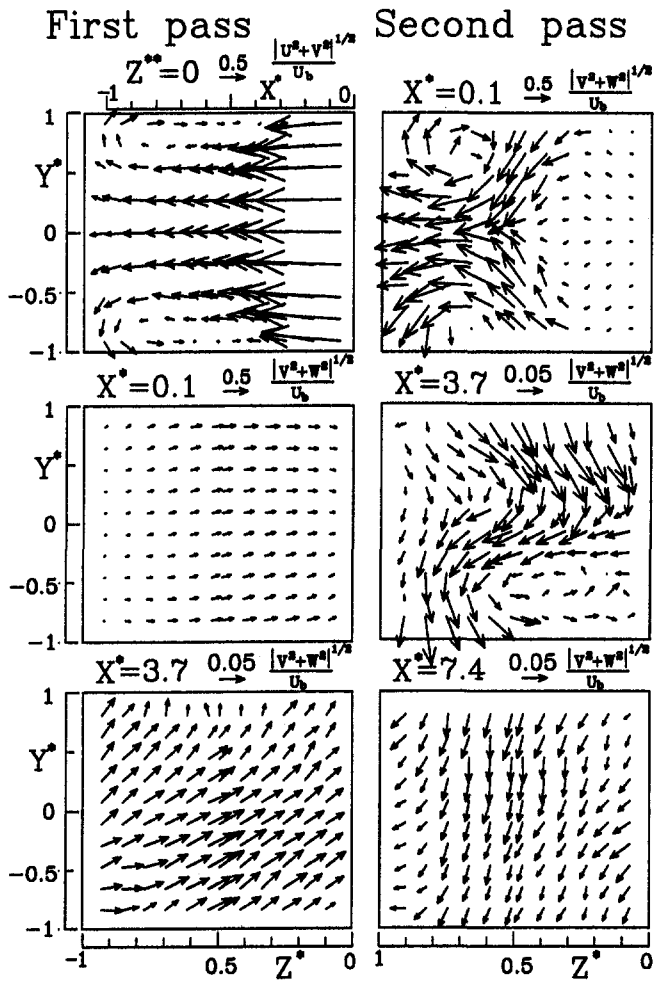

Fig. 6 Cross-stream secondary flow patterns in the first pass (left column: $X^* = 3.7$ and 0.1), inside the turn (left column: $Z^{**} = 0$), and in the second pass (right column: $X^* = 0.1$, 3.7 and 7.4) for Re = 1.4×10^4 and $Ro = 0$ (view from upstream side)

Effect of Duct Rotation. As pointed out in the foregoing discussion, there is a lack of information on the flow characteristics in the Z^* plane of rotating ducts. Figures 9 and 10 thus depict the effect of duct rotation on the evolution of streamwise mean velocity and turbulence intensity profiles, respectively, in the $Z^* = -0.5$ (first pass) and $Z^* = 0.5$ (second pass) planes. As inferred from Fig. 1, the Coriolis force was directed from

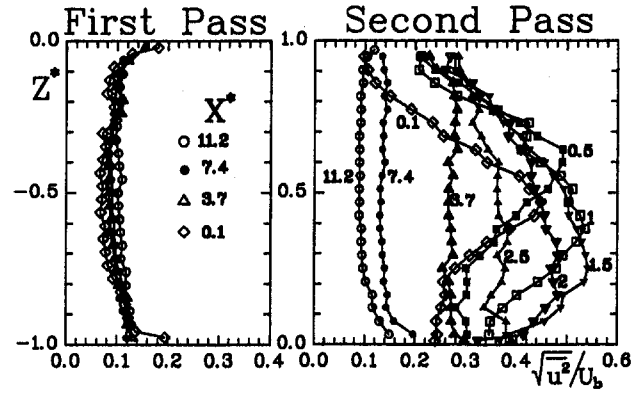

Fig. 7 Streamwise turbulence intensity profiles at various X^* stations of the first and second flow passes in the $Y^* = 0$ plane for Re = 1.4×10^4 and $Ro = 0$

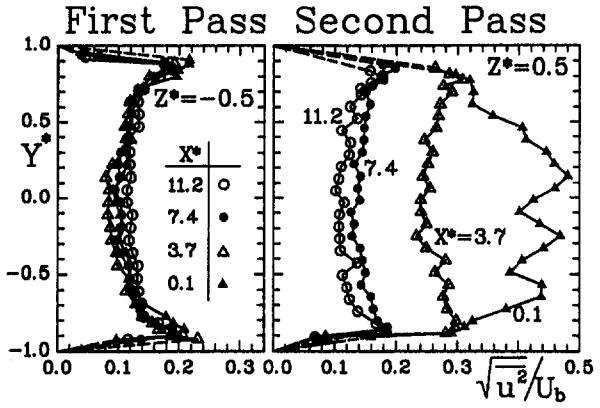

Fig. 8 Streamwise turbulence intensity profiles at various X^* cross sections in the $Z^* = -0.5$ and $Z^* = 0.5$ planes of the two-pass stationary duct for Re = 1.4×10^4 and $Ro = 0$

the leading wall toward the trailing wall in the first pass, whereas its direction is reversed in the second pass. Hence, Fig. 9 shows that relative to its stationary counterpart, the streamwise mean velocity profiles for $0.1 < X^* < 11.2$ in the first pass of the rotating duct ($Ro = 0.082$) are all skewed toward the trailing wall with a higher peak value of $U/U_b = 1.2 \sim 1.3$ occurring around $Y^* = 0.4 \sim 0.6$. Conversely, the symmetric double-peak U/U_b profile in the second pass for the stationary case is skewed towards the leading wall, say at $X^* = 0.1$, and eventually becomes a single-peak profile with peak value occurring at $Y^* \approx -0.6$, say at $X^* = 3.7$, for the rotating case. Notice that a typical example showing the sensitivity of the measured mean velocity and turbulence intensity profiles to the widths of the positioning window is also included in Figs. 9 and 10 for the measuring location of $X^* = 0.1$ and $Z^* = 0.5$ in the second pass. A detailed discussion regarding the associated uncertainty contribution has been given previously in the Data Uncertainty section.

The Coriolis force also has a significant influence on the corresponding turbulence intensity profiles. In general, it increases the turbulence intensity level, less around the duct core region ($|Y^*| < 0.5$) and more near the leading and trailing walls, as shown in Fig. 10. In the first pass of the rotating duct, the $\sqrt{u^2}/U_b$ peak shifts to the region near the trailing wall, and the corresponding $\sqrt{u^2}/U_b$ reaches a value as high as 0.3 to 0.4, or 1.5 to 2.2 times that of the stationary case. The turbulence intensity distribution in the second pass of the rotating duct is more complex. Although similar to that in the first pass, the values of $\sqrt{u^2}/U_b$ still peak near the leading and trailing walls. Immediately adjacent to the sharp turn at $X^* = 0.1$, the maximum peak $\sqrt{u^2}/U_b$ is about 0.69 or 2.1 times that of the stationary case and occurs near the trailing wall as in the first pass. Nevertheless, at a hydraulic diameter downstream of the separating recirculation zone, $X^* = 3.7$, the maximum peak in $\sqrt{u^2}/U_b$ had shifted to the leading wall due to the Coriolis force from the trailing to the leading wall in the second pass and has a value of 0.45 or 1.3 times that of the stationary case.

Rotation also has an effect on the aforementioned separating recirculation zone immediately after the turn on the downstream side of the divider. A near-wall (2 mm from the wall) scan, as shown in Fig. 11 where U/U_b is plotted versus Y^* for various X^*, clearly reveals the three-dimensional nature of the complex flowfield within the short distance after the turn. Among the X^* investigated in Fig. 11, only at $X^* = 1.62$ are the cross-sectional U/U_b all positive. At $X^* = 1.45$ the U/U_b profile had a small negative velocity zone near $Y^* = 1$ (trailing wall). An interpolation indicates that the maximum length of the separating recirculation bubble was about $X^* = 1.5$ along the trailing wall ($Y^* = 1$). Along the X axis ($Y^* = 0$ and $Z^* = 0$)

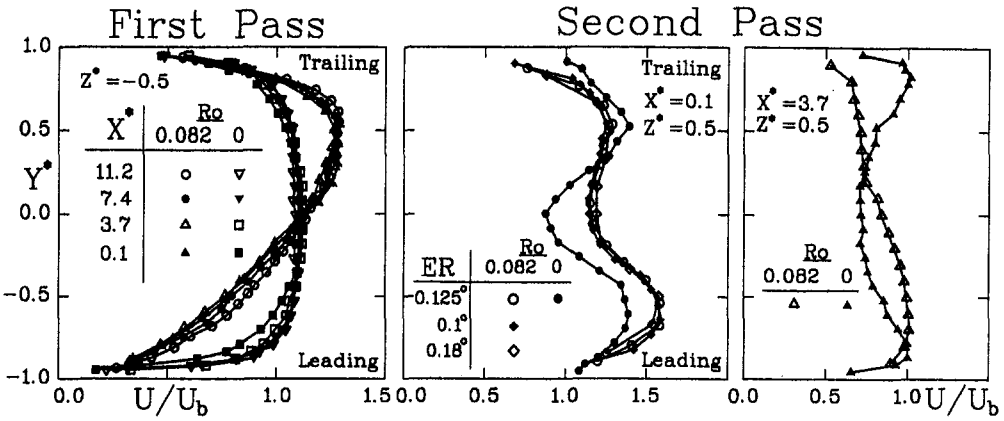

Fig. 9 Streamwise mean velocity profiles at various X^* cross sections in the $Z^* = -0.5$ and $Z^* = 0.5$ planes of the two-pass rotating duct for Re = 1.4×10^4 and $Ro = 0.082$

reattachment occurs at $X^* = 1.32$ (Fig. 11), which is about 75 percent of its stationary counterpart, $X^* = 1.75$. It is noted that the Coriolis force made the positive and negative parts of the U/U_b profile skew toward the leading ($Y^* = -1$) and trailing walls, respectively, resulting in the tail of the separation bubble being skewed toward the trailing wall and hence a decrease in the separation bubble size. It is also worth mentioning here that the present results of the rotational duct flow indicate a decrease in length of the separation bubble and an increase in turbulence levels, while Cheah et al. (1996) reported a reversed trend for the positive rotation case. The difference between the two results may be due to the difference in the angle between the curvature axis of the duct and the axis of rotation, as addressed in the introduction. For the case of Cheah et al. (1996), the direction of Coriolis force in the second pass was toward the outer wall for the positive rotation. As a result, the main flow was further shifted toward the outer wall and the bubble size increased both in height and length. In addition, the Dean-type secondary vortices were suppressed by Coriolis force, which led to a decrease in turbulence levels in their front part of the second pass. In contrast, the direction of Coriolis force in our study tended to skew the Dean vortices, which was responsible for the higher turbulence levels in our rotational case.

Summary and Conclusions

The developing and secondary flow fields in a two-pass smooth rectangular duct with a 180 deg straight-corner turn with and without rotation have been characterized using laser-Doppler velocimetry. For the stationary duct the sharp turn is found to affect the main flow up to 3 hydraulic diameters before the turn and down to 11.2 hydraulic diameters of the second pass after the turn. Inside the turn a corner vortex exists around the outer-wall corner. A separating recirculation zone resulting from the sharp straight-corner turn and thin partition wall appears immediately after the turn on the divider wall side with a maximum length and height of 1.75 and 0.62 hydraulic diameters, respectively. As a result of curvature-induced secondary flow and separating recirculation flow, the flow development along the spanwise central plane of the second pass, not reported in the past, was featured by a double-peak streamwise mean velocity profile for the region within 6 hydraulic diameters after the turn and a top-hat profile for the further downstream region. A Dean-type counterrotating symmetric vortex pair prevailed inside the turn, with a cross-stream mean velocity as high as 1.7 times bulk mean velocity. The vortex pair was limited to about half of the cross section in the region immediately after the turn due to the presence of a separating bubble, and subsequently distorted into an asymmetric complex vortex pattern in the further downstream region, about 4 hydraulic diameters, with a cross-stream mean velocity typically an order of magnitude smaller than that inside the turn. In general, the sharp turning makes the turbulence intensity levels higher and considerably more nonuniform in the front part of the second pass as compared to the first pass. This result parallels the higher but significantly nonuniform heat transfer coefficient distribution after the turn reported by previous research. Higher turbulence intensity is found along the shear layer bounding the separating recirculation zone and associated with the double-peak velocity

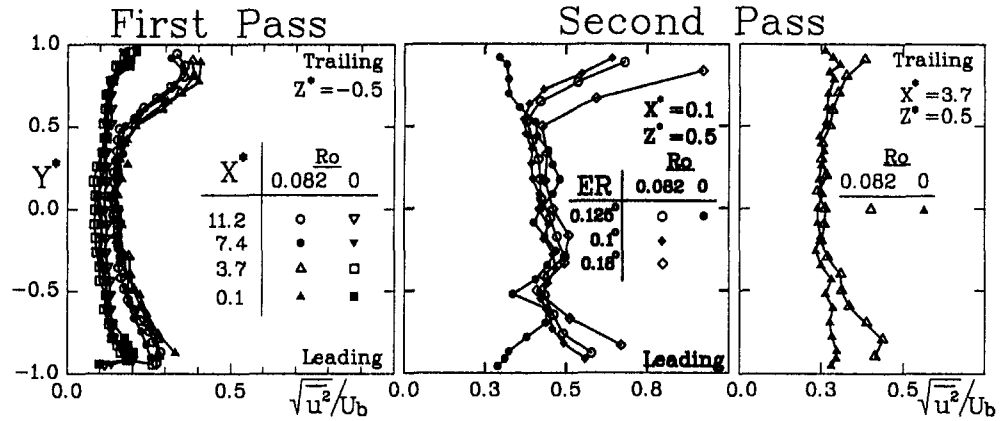

Fig. 10 Streamwise turbulence intensity profiles at various X^* cross sections in the $Z^* = -0.5$ and $Z^* = 0.5$ planes of the two-pass rotating duct for Re = 1.4×10^4 and $Ro = 0.082$

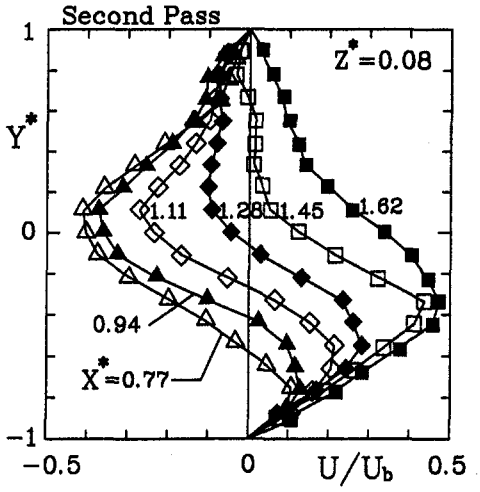

Fig. 11 Streamwise mean velocity profiles versus Y^* at various X^* in the Z^* = 0.08 plane (2 mm from divider) of the second pass for Re = 1.4 × 10^4 and Ro = 0.082

profile. The maximum peak turbulence intensity attained value of 0.54 times bulk mean velocity and occurred at 1.5 hydraulic diameters downstream of the turn or 0.25 hydraulic diameters upstream of the reattachment.

A rotation of the two-pass duct investigated made the streamwise mean velocity profiles in the spanwise plane of the first and second passes skewed toward the trailing and leading walls, respectively. The separating bubble immediately after the turn is also skewed and reduced in size to about 75 percent of its stationary counterpart. The Coriolis force generally raises the turbulence level near the leading and trailing walls of the flow pass. The augmented turbulence intensity can be as high as 1.5 to 2.2 times, 2.1 times, and 1.3 times that of its stationary counterpart in the first pass (near the trailing wall), adjacent to the sharp-turn exit (near the trailing wall), and in the second pass (near the leading wall), respectively.

Acknowledgments

Support for this work was partially provided by the National Science Council of the Republic of China under contract No. NSC-85-2212-E007-056.

References

Azzola, J., Humphrey, J. A. C., Iacovides, H., and Launder, B. E., 1986, "Developing Turbulent Flow in a U-Bend of Circular Cross-Section: Measurement and Computation," ASME *Journal of Fluids Engineering,* Vol. 108, pp. 214–221.

Chang, S. M., Humphrey, J. A. C., and Modavi, A., 1983, "Turbulent Flow in a Strongly Curved U-Bend and Downstream Tangent of Square Cross-Sections," *Physico Chemical Hydrodynamics,* Vol. 4, No. 3, pp. 243–269.

Cheah, S. C., Iacovides, H., Jackson, D. C., Ji, H., and Launder, B. E., 1996, "LDA Investigation of the Flow Development Through Rotating U-Ducts," ASME JOURNAL OF TURBOMACHINERY, Vol. 118, pp. 590–596.

Cheng, K. C., Nakayama, J., and Akiyama, M., 1977, "Effect of Finite and Infinite Aspect Ratios on Flow Patterns in Curved Rectangular Channels," *Proc. International Symposium on Flow Visualization,* Oct., Tokyo, Japan, pp. 640–645.

Cheng, K. C., Shi, L., Kurokawa, M., and Chyu, M. K., 1992, "Visualization of Flow Patterns in a 180 Deg Sharp Turn of a Square Duct," *Proc. Fourth International Symposium on Transport Phenomena and Dynamics of Rotating Machinery,* Honolulu, HI, Apr.

Choi, Y. D., Iacovides, H., and Launder, B. E., 1989, "Numerical Computation of Turbulent Flow in a Square-Sectioned 180 Deg Bend," ASME *Journal of Fluids Engineering,* Vol. 111, pp. 59–68.

Chyu, M. K., 1991, "Regional Heat Transfer in Two-Pass and Three-Pass Passages With 180 Deg Sharp Turns," ASME *Journal of Heat Transfer,* Vol. 113, pp. 63–70.

Drain, L. E., 1980, *The Laser-Doppler Technique,* Wiley, New York, pp. 136–145.

Eaton, J. K., and Johnston, J. P., 1981, "A Review of Research on Subsonic Turbulent Flow Reattachment," *AIAA Journal,* Vol. 19, pp. 1093–1100.

Fairbank, J. A., and So, R. M. C., 1987, "Upstream and Downstream Influence of Pipe Curvature on the Flow Through a Bend," *International Journal of Heat and Fluid Flow,* pp. 211–217.

Han, J. C., and Zhang, Y. M., 1992, "Effect of Uneven Wall Temperature on local Heat Transfer in a Rotating Square Channel With Smooth Walls and Radial Outward Flow," ASME *Journal of Heat Transfer,* Vol. 114, pp. 850–858.

Hille, P., Vehrenkamp, R., and Shulz-Dubois, E. O., 1985, "The Development and Structure of Primary and Secondary Flow in a Curved Square Duct," *Journal of Fluid Mechanics,* Vol. 151, pp. 219–241.

Johnson, R. W., 1988, "Numerical Simulation of Local Nusselt Number for Turbulent Flow in a Square Duct With a 180 Deg Bend," *Numerical Heat Transfer,* No. 1, 13, pp. 205–228.

Kwak, D., Chang, J. L. C., Shanks, S. P., and Chakravarthy, S. R., 1986, "A Three-Dimensional Incompressible Navier–Stokes Flow Solver Using Primitive Variables," *AIAA Journal,* Vol. 24, No. 3, pp. 390–396.

Liou, T. M., Chang, Y., and Hwang, D. W., 1990, "Experimental and Computational Study of Turbulent Flows in a Channel With Two Pairs of Turbulence Promoters in Tandem," ASME *Journal of Fluids Engineering,* Vol. 112, pp. 302–310.

Liou, T. M., Wu, Y. Y., and Chang, Y., 1993, "LDV Measurements of Periodic Fully Developed Main and Secondary Flows in a Channel With Rib-Disturbed Walls," ASME *Journal of Fluids Engineering,* Vol. 115, pp. 109–114.

Liou, T. M., and Liao, C. C., 1995, "Flows in Curved Combustor Inlet With and Without a Guide Vane," *AIAA Journal of Propulsion and Power,* Vol. 11, No. 3, pp. 464–472.

Mclaughlin, D. K., and Tiederman, W. G., 1973, "Biasing Correlation for Individual Realization of Laser Anemometer Measurement in Turbulent Flows," *The Physics of Fluids,* Vol. 16, No. 12, pp. 2082–2088.

Metzger, D. E., Plevich, C. W., and Fan, C. S., 1984, "Pressure Loss Through Sharp 180 Deg Turns in Smooth Rectangular Channels," ASME *Journal of Engineering for Gas Turbines and Power,* Vol. 106, pp. 677–681.

Metzger, D. E., and Sahm, M. K., 1986, "Heat Transfer Around Sharp 180 Deg Turns in Smooth Rectangular Channels," ASME *Journal of Heat Transfer,* Vol. 108, pp. 500–506.

Rigby, D. L., Ameri, A. A., and Steinthorsson, E., 1996, "Internal Passage Heat Transfer Prediction Using Multiblock Grids and a k–w Turbulence Model," ASME Paper No. 96-GT-188.

Sathyamurthy, P. S., Karki, K. C., and Patankar, S. V., 1994, "Prediction of Turbulent Flow and Heat Transfer in a Rotating Square Duct With a 180 Deg Bend," ASME Paper No. 94-GT-197.

Tekriwal, P., 1994, "Heat Transfer Prediction in Rotating Radial Smooth Channel: Comparative Study of k–e Models With Wall Function and Low-Re Model," ASME Paper No. 94-GT-196.

Wagner, J. H., Johnson, B. V., and Hajek, T. J., 1991a, "Heat Transfer in Rotating Serpentine Passages With Smooth Walls," ASME JOURNAL OF TURBOMACHINERY, Vol. 113, pp. 321–330.

Wagner, J. H., Johnson, B. V., and Kopper, F. C., 1991b, "Heat Transfer in Rotating Passages With Smooth Walls and Radial Outward Flow," ASME JOURNAL OF TURBOMACHINERY, Vol. 113, pp. 42–51.

Wang, T. S., and Chyu, M. K., 1994, "Heat Convection in a 180 Deg Turning Duct With Different Turn Configurations," *Journal of Thermophysics and Heat Transfer,* Vol. 8, No. 3.

Yang, W. J., Zhang, N., and Chiou, J., 1992, "Local Heat Transfer in a Rotating Serpentine Flows Passage," ASME *Journal of Heat Transfer,* Vol. 114, pp. 354–361.